ASPECTS OF THERMOCHEMICAL STORAGE AND TRANSFER OF SOLAR ENERGY USING AMMONIA

Keith Malcolm Lovegrove
June 1992

A thesis submitted for the degree of Doctor of Philosophy at the Australian National University.

Declaration

This thesis contains no material which has been accepted for the award of any other degree or diploma in any university. To the best of the author's knowledge and belief, no material previously published or written by another person has been included, except where due reference is made in the text.

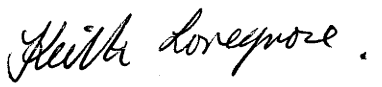

Keith Malcolm Lovegrove.

Acknowledgements

I would like to acknowledge the help and support I have received from my colleagues, family and friends during the course of this project.

Firstly I would like to thank Dr Peter Carden. Without his pioneering work this project would, of course, not been possible. He has also given inspiration and guidance throughout the project and most recently, provided a valuable critical review of the material in this text. I would like to thank Professor Stephen Kaneff for his guidance and support throughout the project and for reviewing the manuscript. Bob Whelan has also been involved with the ammonia based thermochemical experiments at the ANU since the very begining. The benefit of his experience has been invaluable for all aspects of the project. In particular his contributions to the design and construction of an ammonia level detector and a new synthesis reactor system have been major factors in the successful progress made.

Many other friends and colleagues have contributed in various ways. In particular I would like to thank: Paul Bannister, who provided his curve fitting software and assistance with modelling the flux distribution inside a cavity receiver; Warren Baker, who did an admirable job constructing the synthesis reactor cooling jacket; Seow-Wah Chin who drew several diagrams: Mark Dymond, who also drew some of the diagrams; Glen Hua-Johnston, who devoted considerable time to assistance with proof reading; and Michelle Moravec who typed some of the early chapters.

Two vacation scholars made valuable contributions to the project; Robert Hall contributed to the assembly of the experiment and the calibration of the balancing separator and James Thompson contributed to the development and testing of the ammonia level detector.

At the end of 1988 I had the privilege of spending two months at the University of Houston, working with Professor Jim Richardson. The numerical reactor model and the knowledge I brought back from that visit have been central to the success of a very large proportion of this project. I would also like to thank Professor Richardson for his personal hospitality to me and my family during our time in Houston. I would also like to thank Dr Jim Fish for his hospitality and time during a subsequent short visit to Sandia National Laboratories in Albequerque.

Finally I would like to thank my family; my mother Doreen Lovegrove who helped with proof reading and editing and my wife Kwee-Wah (Sharon) Lai and son Alexander who provided continuous support.

Abstract

The developments described in this thesis represent the continuation of an ongoing investigation into the application of the reversible dissociation of ammonia to the storage of solar energy. This investigation was begun at the Australian National University (ANU) in 1973. These developments have contributed to the theoretical analysis of the process and to the accumulation of experimentally based empirical information necessary for the design of a full scale system. The work that was carried out was done in the context of the long standing aims of developing a small scale closed loop energy transfer and storage demonstration and then incorporating an endothermic reactor/receiver prototype for a parabolic dish solar concentrator.

A detailed analysis of the thermodynamic aspects of thermochemical energy storage is presented. This analysis leads to general expressions for the thermal, exergetic (second law) and work recovery efficiencies of reaction processes which start and end at a low sink temperature. The expressions for exergetic and work recovery efficiencies are used to present constant efficiency contours, for the ammonia based system, on a temperature enthalpy diagram. The explicit connection between the characteristic temperature of these reaction processes and the attribute of spontaneous separation of reactant mixtures, (which the ammonia system possesses as a consequence of the condensation of the ammonia at low temperatures) is identified.

A pseudohomogenous two dimensional model of a packed bed catalytic reactor is described. This model was initially developed by workers at the University of Houston for modelling steam methane reforming reactors. The numerical implementation of this model has been improved and adapted to model ammonia dissociation and synthesis reactors. As well as providing theoretical predictions for comparison with the experimental results obtained, this model has been used for a preliminary design study of irradiated tube, reflux heatpipe and direct absorption reactor/receiver concepts for solar ammonia dissociation.

The final theoretical aspect considered concerns the optimisation of real systems. A general design goal of producing a required exergy output for a minimum 'generalized cost', is identified. A systematic approach to optimisation of complicated systems is outlined and the particular subsystem optimisation problem of maximising the exergy output of an exothermic reactor for a fixed catalyst volume to thermal capacity ratio, is solved by a dynamic programming technique. The solution indicates that a reaction path, chosen so as to minimise the catalyst volume required, produces close to the maximum exergy output possible.

The experimental work described is based on the construction and commissioning of a new laboratory facility and experimental layout. This culminated in an extensive series of steady state experiments using a high pressure electrically heated ammonia dissociation reactor loaded with nickel on alumina catalyst. The conditions covered included pressures up to $17MPa$, temperatures up to $720°C$ and flow rates between 0.1 and $1.5gs^{-1}$, power levels absorbed by the reactants ranged between $200W$ and $2kW$. The measured internal and external temperature profiles, absorbed flux profiles and exit reaction extents are compared with the predictions of the two dimensional model. Good agreement between the model and the experiment is found after suitable adjustment of the intrinsic rate

parameters used, an activation energy of $192 kJ mol^{-1}$ and a pre-exponential factor of $3 \times 10^7 mols^{-1} cm^{-3} atm^{-1}$ are indicated. Positive conclusions are drawn about the implications for a possible closed loop experiment and reactor/receiver prototypes.

An experimental simulation of cyclic operation of the dissociator under solar receiver conditions, in order to test a possible approach to reactor control, is also described. This simulation demonstrated that reactor temperature could be successfully controlled, under conditions of varying flux, via automated variation of inlet mass flow.

The design and almost complete installation of a new experimental reactor, primarily designed as a synthesis reactor, addresses some of the experimental shortcomings identified for the dissociation reactor and paves the way for energy transfer experiments. This provides one of many possible directions for future work, in what is a very rewarding and extremely important area of research.

Units and Nomenclature

The units used within this text have been restricted to SI, or SI derived units as much as practical. Standard decimal fraction and multiple prefixes have been used frequently, as convenient. The main exception to the use of SI units is pressure. For a number of historical reasons, including the format of data input to inherited software, atmospheres have frequently been used rather than pascals. This has occured in situations where a choice of a suitable nominal pressure was required for analysis purposes, ie. many of the graphically presented theoretical results in this text have been calculated for a pressure of 200 atmospheres rather than $20MPa$. In fact the 1.5% difference in value (200 atmospheres $\equiv 20.26MPa$) varies such results by an amount which would be indetectable in graphic form. As partial justification the author claims that in a sense an atmosphere is a 'colloquial description' as well as a unit. All experimentally measured pressures, on the other hand, have been quoted in either MPa or kPa.

Another slight variation from standard practice, is the treatment of extensive thermodynamic functions (eg enthalpy). Wherever such functions have been evaluated they have been expressed as values per mole, which actually corresponds to an intensive version of the function (eg specific enthalpy). This interchange reflects the fact that in all cases the thermodynamic system in question was equivalent to 1 mole of the primary reactant (ammonia), so that the intensive and extensive functions had the same numerical value.

The following table presents the definitions of the symbols used in this text. Where subscripts are included in the table, it indicates that the subscript is essential to the identification of the variable. In other cases, the symbols appear in the text either with or without subscripts, with the same general meaning as indicated.

Definition of symbols

Symbol	Definition	SI units	Chapter
A	Area	m^2	9,4,8
a, A, b, B	General purpose constants	—	all
C_p	Specific heat at constant pressure	$Jmol^{-1}K^{-1}$	all
C_{st}	Coefficient of storage performance	—	3
C	Concentration	$mol\ m^{-3}$	4
C	Generalised cost	—	6
d	Diameters	m	all
D	Diffusivities	m^2s^{-1}	all
e	Exergy	J, $(Jmol^{-1})$	6
e	Specific enthalpy	Jkg^{-1}	4
E_a	Activation energy	J	4
E	Void fraction	—	4

Definition of symbols continued

Symbol	Definition	SI units	Chapter
f	Functional relation	—	6
F	Friction factor	—	C
G	Gibbs free energy	J, $(Jmol^{-1})$	all
h	Heat transfer coefficient	$Wm^{-2}K^{-1}$	all
H	Enthalpy	J, $(Jmol^{-1})$	all
k	Boltzmann constant (no subscript)	JK^{-1}	4,A
k_i	Rate constants (various subscripts)	$mol\ s^{-1}m^{-3}Pa^n$	4
K_p	Equilibrium constant	Pa^n	4,A
K	Conductivities (with or without subscripts other than p)	$Wm^{-1}K^{-1}$	all
l	Length	m	all
m	Masses	kg	8,C
m	Molecular weights	$kg\ mol^{-1}$	all
$\dot{m}$	Mass flows	$kg\ s^{-1}$	all
n	Mole number	mol	3
N_i	Dimensionless parameters (various subscripts)	—	all
p	Partial pressures	Pa	4
P	Pressure	Pa	all
q	Heat flux	Wm^{-2}	9
Q	Heat	J, $(Jmol^{-1})$	all
r	Radius or radial position variable	m	all
R	Reaction rate	$mol\ s^{-1}m^{-3}$	3,4,6
R	Universal gas constant	$Jmol^{-1}K^{-1}$	A
s	Stress	Nm^{-2}	9
S	Entropy	JK^{-1}, $(JK^{-1}mol^{-1})$	all
t	Time	s	all
T	Temperature	K	all
u	Specific internal energy	Jkg^{-1}	4
U	Internal energy	$Jmol^{-1}$	all
v	Speed	ms^{-1}	4,9
v	Specific volume	m^3kg^{-1}	A
V	Volume	m^3	3,6
V	Voltage	V	C
w	Widths	m	9
W_s	Separation work	J	A
X	Mole fraction	—	3,A
z	Length variable	m	all
Z	Compressibility factor	—	A

Definition of greek symbols			
Symbol	Definition	SI units	Chapter
γ_R	Rotameter diameter ratio	—	C
δ	Reaction extent	—	all
ε	Emissivity	—	4,9
η	Efficiencies	—	all
Θ	Surface coverage	—	4
ϑ	Effectiveness factor	—	4
μ	Viscosity	$kgs^{-1}m^{-1}$	all
ρ	Density	$kg\ m^{-3}$	all
σ	Stephan Boltzmann constant	$Wm^{-2}K^{-4}$	4,9
τ	Time constant	s	8
ϕ	Thiele modulus	—	4
Φ	Exergy	J	3
Ψ	Dissipation	Wm^{-3}	4

Foreword:The Role of this Project

The Project

This project began in 1987 and ran until the beginning of 1992, for most of this time the author was essentially working alone in the field. As a result, instead of proceeding directly toward a clearly defined goal, it became broadly based and evolved in a continuous manner. Ultimately the project has made some contribution to almost every aspect of the application of the ammonia reaction to solar thermochemical systems. This thesis reports the original contributions which have been made to the field, in particular these comprise contributions to;

- efficiency analysis and optimisation;
- reactor modelling;
- receiver design;
- experimental system design and construction;
- dissociation experiments, measurement and analysis;
- synthesis reactor design.

While most of 1987 was spent investigating a relatively unrelated alternative project (Lovegrove 1987), the initial goals for the ammonia solar thermochemical project were established in early 1988. As is described in chapter 2, experimental work at ANU had essentially not progressed since the end of a NERDDC (National Energy Research Development and Demonstration Council) funded project in 1983. The major goals of this project; demonstrating closed loop thermochemical energy transfer and storage in the laboratory and then extending this to solar receiver operation, were not realized by the end of funding in 1983. They remain just as relevant, especially in view of the fact that the work at ANU still appears to be the only work in the world on the application of the ammonia reaction. There is acceptance amongst workers in the field of solar thermochemical systems, that the ammonia reaction warrants continued investigation and closed loop and receiver experiments would be very valuable original contributions.

In early 1988, a review of the status of the experimental work in conjunction with discussions with Carden and others, suggested that the most appropriate direction for the continuation of experimental work was the development of a small synthesis reactor. This idea was adopted and a reactor design developed and the necessary workshop projects were organised. An experimental arrangement based on short duration reaction runs using stored hydrogen and nitrogen gas mixtures was initially conceived, however after further consideration, this was abandoned in favour of re-commissioning the dissociation reactor developed for the NERDDC funded project and operating it as a continuous source of synthesis gas in an open loop configuration. Ultimately it was the re-commissioning and

performance analysis of this reactor together with the development of a new experimental arrangement and instrumentation and control systems, which constituted the main experimental component of this project. However construction of the synthesis reactor did continue, and at the end of this project it is ready for installation and testing in the context of the wider goals associated with continuing to work towards a closed loop experiment.

There were a number of unforseen external events, which had varying direct and indirect effects on the course of the project.

- At the end of 1987 the Research School of Physical Sciences administration made a unilateral decision to re-locate the laboratory facilities of the Energy Research Centre.
- At the end of 1988 the author had the opportunity of participating in an exchange program funded by the Department of Industry Technology and Commerce. This involved a three month visit to the USA to work with Professor J.T. Richardson of the University of Houston.
- In early 1989, following a submission in 1988 by a number of people including the author, the Energy Research Centre received a major equipment grant from the university to upgrade its data acquisition and control facilities. This grant included a large component for the thermochemical experimental program.
- In mid 1988 Dr. P.O. Carden retired from full time work within the Energy Research Centre, instead maintaining an intermittent connection via work as a consultant.

The laboratory re-location resulted in a delay of over twelve months in the experimental work, however the move did provide the opportunity (albeit forced) to completely redesign and improve the layout and interconnection of experimental equipment. The installation of equipment in the new laboratory coincided with the receipt of the large equipment grant. Receipt of the grant for data acquisition and control equipment was followed by a lengthy period of equipment evaluation and negotiations related to its purchase. Installation and testing proceeded in conjunction with the commissioning of the new experimental arrangement.

The visit to the university of Houston led directly to the work on reactor modelling that is a significant part of this project. This together with ideas gathered from short visits to other laboratories in the USA, led to the work on possible receiver designs.

The work on second law efficiency analysis and optimisation of real systems, grew first from the need to review and collate the previous work done by Carden and Williams. This process led to the identification of some areas of the thermodynamic analysis of ideal system efficiencies which needed further clarification, and then led on to the consideration of optimisation issues for real systems.

Publications

The following papers have been produced in the course of this project:

- "Alkali metal thermoelectric converters for solar applications." (In proceedings of Australian and New Zealand Solar Energy Society annual conference, Canberra, November 1987.)

- "Data acquisition and control system for experimental energy research." (Submission for ANU RSPhysSE major equipment grant, authors; P.Bannister, K.Lovegrove and S.Kaneff, Energy Research Centre, ANU, June 1988.)
- "Synthesis experiments for ammonia based thermochemical energy transfer." (In proceedings of Australian and New Zealand Solar Energy Society annual conference, Melbourne, November 1988.)
- "Report on DITAC funded visit to Department of Chemical Engineering, University of Houston." (Energy Research Centre, ANU, 1989)
- "Receiver options for ammonia based solar thermochemical systems." (In proceedings of Australian and New Zealand Solar Energy Society annual conference, Brisbane, November 1989.)
- "Testing and calibration of the balancing separator for ammonia based thermochemical experiments." (authors; K.Lovegrove and R.Hall, Technical report ER-RR-53, Energy Research Centre, ANU 1990.)
- "Demonstration of high quality energy storage and recovery by thermochemical processes involving ammonia." (Submission to NERDDC, authors; P.Carden, R.Whelan, S.Kaneff and K.Lovegrove, Energy Research Centre, ANU, May 1990.)
- "The potential role for ammonia based thermochemical energy transport and storage in large scale solar thermal systems." (In proceedings First World Renewable Energy Congress, Reading, UK, September 1990.)
- "Experimental simulation of solar energy storage via ammonia dissociation - preliminary results." (In proceedings of Australian and New Zealand Solar Energy Society annual conference, Auckland, November 1990.)
- "Performance analysis of the ammonia based thermochemical energy storage system." (Current Practices in Energy Resources and Technology, 1990-1991, publ.Geoenviron Academia, New Delhi.)
- "Experimental investigation of the ammonia dissociation reaction for solar energy transport and storage." (In proceedings of ISES Solar World Congress, Denver, Colarado USA, August 1991.)
- "Application of dynamic programming optimisation techniques to a thermochemical solar energy storage system." (In proceedings of Australian and New Zealand Solar Energy Society annual conference, Adelaide, December 1991.)

In addition to this a number of international journal articles based on the material contained in this thesis, are currently planned:

- "Thermodynamic limits on the performance of a thermochemical energy storage system." (Comprising material from chapter 3.)
- "Exergetic optimisation of a thermochemical energy storage system subject to real constraints." (Comprising material from chapter 6.)
- "High pressure ammonia dissociation experiments for solar energy transport and storage." (Comprising material from chapter 7 and chapter 8, dealing with the steady state experiments and the comparison with the numerical model.)

- "The use of ammonia dissociation for the storage of solar energy." (Comprising material from chapters 5, 7 and 8, dealing with possible receiver designs and the implications of both the qualitative and quantitative results of the dissociation experiments.)

Contents

Part I

Introduction

Chapter 1

Solar Thermochemical System Concepts

1.1 Closed Loop Thermochemical Energy Storage

Reversible chemical reactions are endothermic (energy storing) when they proceed in one direction and exothermic (energy releasing) in the other. Thermochemical energy storage systems exploit this attribute using a closed system of continuously recycled reactants. Typically the energy absorbed or released by a quantity of reactants undergoing a chemical reaction, is several times more than would be involved in a phase change, and equal to the sensible heat involved in a temperature change of many hundreds or even thousands of Kelvin. As well as promising high energy storage densities, the possibility of heating and cooling reactants before and after reaction in a manner which does not waste any of the sensible heat, offers the prospect of loss free storage at ambient temperatures.

In reality every reaction is chemically reversible; for a mixture of the reactants involved, thermodynamic equilibrium will define a relationship between the composition of the mixture and the pressure and temperature. Typically as the temperature is increased a point is reached where the equilibrium composition changes relatively quickly from close to 100% exothermic reaction products to close to 100% endothermic reaction products. The temperature at the midpoint of this change is a characteristic of the reaction in question and the value of this temperature varies slightly with pressure. Reactions proceed at finite rates and so the addition of heat results in reactants getting temporarily hotter than the equilibrium relationship indicates and conversely, colder than equilibrium when it is removed.

The essential elements of a simplified thermochemical storage system involving fluid reactants are illustrated by figure 1.1. The exothermic and endothermic reactors each operate at average temperatures respectively below and above the characteristic temperature of the reaction. The heating and cooling of reactants is achieved by the interchange of heat between in-going and out-going reactant streams as they pass through the counterflow heat exchangers associated with each reactor. The balance of the system consists of an interconnecting transport/storage circuit for the ambient temperature reactants.

An inherent assumption in the arrangement is that reactions only proceed within the two reactors, this can be readily achieved for reactions that require the presence of a catalyst to produce significant reaction rates.

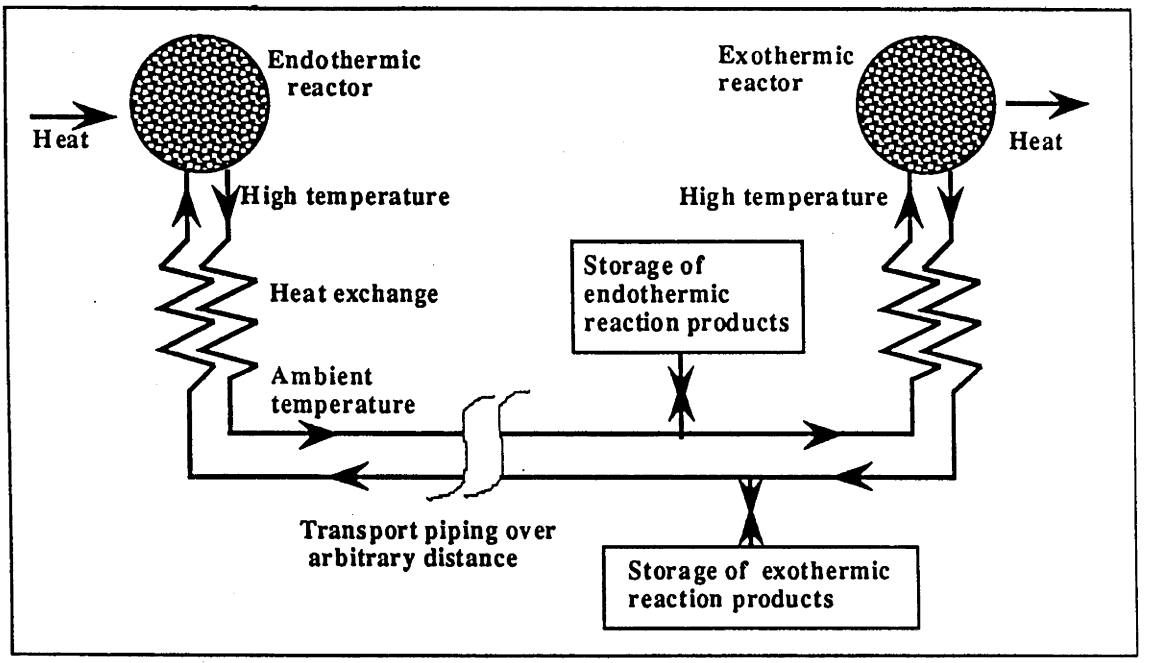

Figure 1.1: The basic elements of a thermochemical energy storage system.

1.2 Application to Solar Thermal Systems

Thermochemical energy storage is a process which could find application in any situation where thermal energy is available at a different time or place to that in which it can be most conveniently used. This is exactly the situation which must be addressed in developing the means for the large scale use of solar energy via thermal collection processes. Large scale solar thermal systems currently proposed can be categorised as; distributed parabolic dish, distributed parabolic trough, or central receiver systems. A number of potential roles for thermochemical systems can be identified:

- Energy transport from collectors to central site for distributed systems.
- Energy transport from collection site to end use site for all types of systems.
- Long and short term energy storage (at any point between collection and end use sites), for all systems.

These applications could involve carrying out the endothermic reaction within the receiver of the solar thermal system, or they may utilize some form of intermediate heat transfer process to provide heat to the endothermic reactor. It is reasonable to assume that although any one thermochemical system could fill all these roles, the optimum choice may vary in each case. The Australian National University (ANU) group has been a consistent advocate of the use of distributed arrays of parabolic dishes for large scale solar thermal systems. Currently a project to construct several prototype dish modules of $400m^2$ aperture is under way (Kaneff 1989). It is in this context, and for the particular role

of transport from a large distributed array of collectors to a central site, that development of the ammonia based system has been proceeding.

1.3 The Ammonia Based System

There have been many published discussions on different selection criteria for suitable solar thermochemical systems. Criteria can include; a reversal of reaction direction at a suitable temperature for the solar thermal system, fluid reactants and the absence of undesirable side reactions. Application of criteria like this has led to a number of different reactions receiving active investigation around the world. The requirement for fluid reactants is necessary if one of the aims is to provide energy transport by circulation of the reactants in pipelines at ambient temperature. However a number of reactions involving solid reactants, have been identified, which have higher enthalpies of reaction and could possibly be utilized for storage of solar energy. This could involve endothermic and exothermic processes being carried out within the same reactor at different times.

A thermochemical system based on the ammonia reaction;

$$2NH_3 + \Delta H \rightleftharpoons N_2 + 3H_2 \tag{1.1}$$

has been under investigation at the ANU since it was first described by Carden (1974*a*) (ΔH is the enthalpy which must be added to dissociate the ammonia). The system was chosen because of a number of perceived benefits in addition to satisfying the general criteria; both synthesis and dissociation of ammonia are common industrial processes, none of the constituents pose an environmental risk in the case of a system failure and there are no possible side reactions.

The relationship between temperature and mixture composition at equilibrium, for pressures of 100, 200 and 300 atmospheres (equivalent to 10.1, 20.2 and $30.3MPa$), is shown in figure 1.2. Given that the synthesis reaction must be carried out at temperatures less than or equal to those indicated by the equilibrium relationship, it is apparent from figure 1.2 that increasing the pressure will allow the reaction to take place at a higher temperature. Reaction rates increase strongly with temperature. To produce realistic synthesis reaction rates, system pressures up to $30MPa$ are required. While this pressure places considerable constraints on reactor and storage vessel design, it provides benefits in improved heat transfer coefficients and volumetric energy storage density.

One of the unique features of the ammonia based thermochemical system is that within the pressure range anticipated, the ammonia component of reactant mixtures begins to condense at temperatures between 300 and $400K$. The products of both exothermic (synthesis) and endothermic (dissociation) reactors can be fed into a common gas/liquid separator vessel as illustrated schematically in figure 1.3. The gas and liquid phases from the combined product streams will separate gravitationally within the vessel. The liquid phase can be drawn off the bottom to feed the dissociation reactor and the gas phase can be drawn off the top to feed the synthesis reactor. Operating as a separating system in this way allows the reaction extent endpoints for each reaction to become variables in the system design.

At $300K$ and $10MPa$ the enthalpy of the reaction is $66.5kJmol^{-1}$. Thus a $400m^2$ aperture dish collecting $400kW$ of radiation (at $1kWm^{-2}$ insolation), would require an ammonia flow rate of $6.02mols^{-1}$ ($102.5gs^{-1}$), assuming complete dissociation. Storage of $10MWh$ ($3.6 \times 10^{10}J$) of energy would require $541.7kg$ of nitrogen-hydrogen mixture, which would occupy a volume of $627l$ at these conditions. After re-synthesis the same mass of liquid ammonia would occupy $88.9l$.

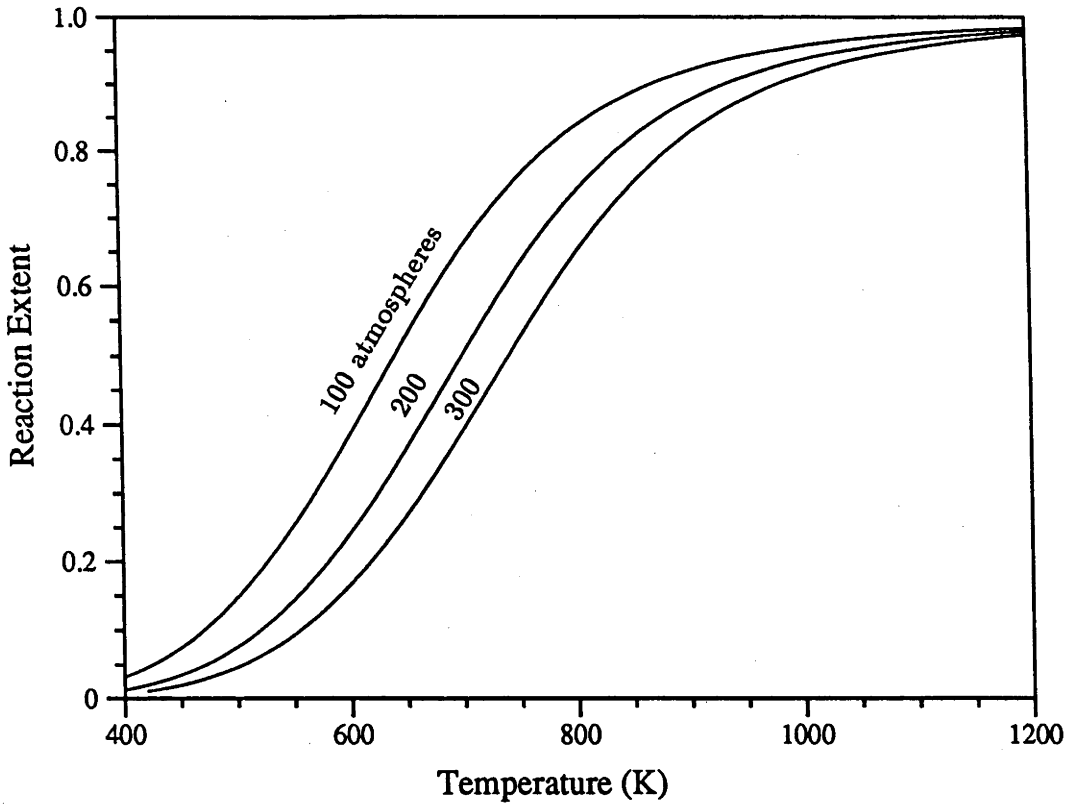

Figure 1.2: Chemical equilibrium mixture compositions for the ammonia reaction.

Figure 1.4 illustrates the currently favoured arrangement for collection of solar energy by ammonia dissociation and transport to a central site for storage and subsequent recovery by work output. In this scenario the exothermic reaction products themselves are the working fluid for work production at the central site. Elimination of heat exchange with a secondary working fluid simplifies construction and efficiency. The nearly constant specific heat of the ammonia-nitrogen-hydrogen mixture as the heat extraction fluid, allows energy to be recovered at higher overall temperatures than if a water/steam energy recovery process is used[1]. The introduction of two separate pressures has potential benefits for the reaction rates in both reactors. Current feasibility studies suggest that a complete solar thermal system constructed along these lines could reasonably expect a solar energy to electricity conversion efficiency of 26%.

1.4 Open Loop Systems

The technology that allows an endothermic reactor to be supplied with energy from concentrated solar radiation is not limited in application to systems with a fixed inventory of continuously recirculating reactants. Indeed it opens the way to establishing the direct connection between solar energy and a whole range of chemical processes which are central to our current lifestyle.

If it is considered desirable to move toward an ecologically sustainable economy, then in addition to establishing the means for renewable energy based electricity generation,

[1]The effect of the choice of heat extraction fluid on the exergetic (second law) efficiency of the exothermic process is discussed in detail in chapter 3

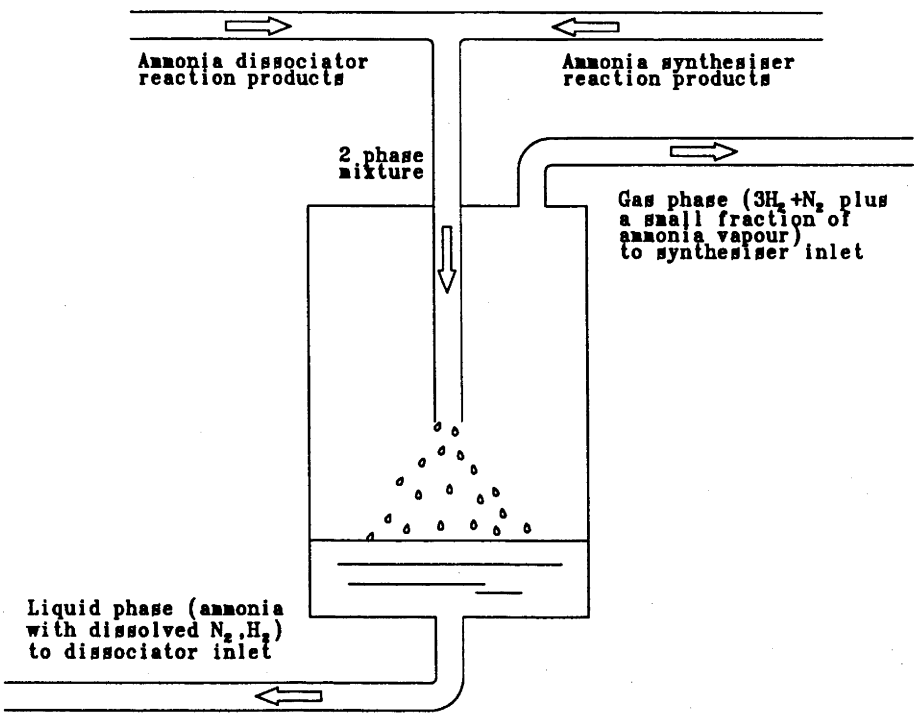

Figure 1.3: A gas/liquid separator for a closed loop ammonia based thermochemical system.

methods for replacing the use of fossil based hydrocarbons for chemical process industries and liquid fuels must be found.

The chemical reduction of water and carbon dioxide and their subsequent re-conversion to hydrocarbons would satisfy this need. The environment then provides the return path in the chemical energy transfer loop following re-oxidation of the hydrocarbons by combustion or other processes. However both reduction reactions have characteristic temperatures which are impractically high for a simple solar thermal driven process, although it is possible to develop complex multi-step methods. Biomass gasification provides a possible solution. Photosynthesis alone provides the reduction of carbon dioxide and water. Subsequent solar thermal driven pyrolysis can convert predominantly cellulose type materials into simpler hydrocarbon fluids with an enhanced energy content. Some of these hydrocarbons may then be the used in solar thermal driven steam reforming reactions in which the partial re-oxidation of carbon, simultaneously with the reduction of the water, gives an overall reaction with a lower characteristic temperature than straight water splitting , but which still absorbs a significant amount of extra solar derived energy.

Solar energy 'value adding' processes like this could of course be applied to fossil based hydrocarbons as a means of effecting a transition to completely renewable energy based processes.

In the consideration of the large scale utilisation of solar thermal energy in these ways, it is possible to conceive of integrated systems involving many interacting open and closed loop chemical processes. For example, an ammonia based closed loop process could be used to transport energy from a field of dishes to a central site where the exothermic reactor could be used as the heat source for other endothermic processes which might be too complex to incorporate into a receiver design directly. Another obvious possibility would

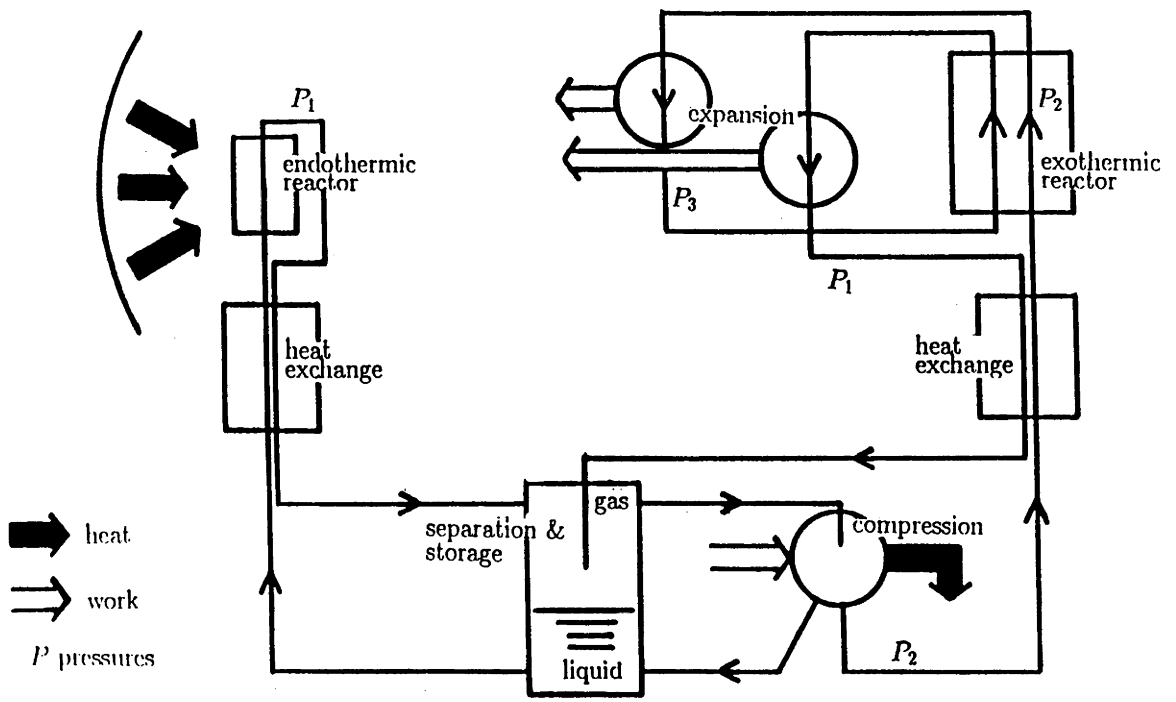

Figure 1.4: Ammonia based solar thermochemical energy transport and storage system incorporating direct work output.

be to make better use of the investment in an ammonia synthesis half of a closed loop system, by configuring the plant as a net producer of ammonia via inputs from associated sources of hydrogen and nitrogen.

Thermochemical processes are of course not the only means for making the connection between solar energy and chemical reactions. Electrochemical processes such as the electrolysis of water require an initial conversion of radiation to electricity. Photon driven processes (ie photolytic or photocatalytic reactions), can produce significant reaction rates for reactions which would otherwise require impractically high temperatures. These together with hybrid combinations may all contribute to the chemical aspects of a renewable energy based economy.

Chapter 2

Previous Work

2.1 Closed Loop Thermochemical Storage

Thermochemical energy storage appears to have first attracted interest for the transport of energy from nuclear reactors to remote locations with a thermal energy end use requirement. The concept was patented by Hilberath & Teggers (1968) and construction of a $1MW$ pilot plant based on the steam reforming of methane, began in Germany in the early 1970s (the 'EVA-ADAM' demonstration, see Hafele (1974) and Fedders, Harth & Holhein (1975)).

The idea of using thermochemical energy storage for solar thermal systems became popular in the early 1970s, coincident with the increased interest in and support for solar energy research at that time. Carden, at the ANU, was one of the pioneers in the field, with a patent application and a preliminary description of an ammonia based system appearing in 1974 (Carden 1974*b*, Carden 1974*a*). Chubb (1975) presented a comprehensive preliminary design study of a system which used a closed loop based on the dissociation of sulphur trioxide to transport the energy from a field of parabolic dishes to a central electricity generation plant. At around the same time Hildebrandt (1975) suggested the use of closed loop thermochemical processes for the storage of the energy collected from a central receiver solar thermal system. He considered the application of reactions based on the steam reformation of methane, the decomposition of methanol, the dissociation of sulphur trioxide and the carbon dioxide reformation of methane.

Numerous authors have attempted a systematic review of possible reactions using various criteria. One of the earliest was that of Wentworth & Chen (1976), who adopted a set of ten essentially pragmatic criteria for the selection of reactions for storage of solar energy. These included, high enthalpy of reaction and characteristic temperatures between 500 and $1000°C$. Because they were interested in storage without transport they did not confine themselves to fluid phase reactants and identified a considerable number of reactions involving solids which had larger enthalpies of reaction and volumetric energy storage densities than the fluid phase reactions considered.

A thorough review carried out by the Rocket Research Corporation (1977) was the first of a number of such extensive studies commissioned in the USA. In this case 85 reactions were initially selected for evaluation for energy storage applications. This selection was reduced to 24 reactions which were subjected to a detailed feasibility study and rankings were produced according to criteria which included; energy storage density, estimated thermal efficiency and estimated cost. The ammonia reaction was included in the list of 24 but ranked fairly poorly in their listings.

Some years after the ANU group had begun working with the ammonia based sys-

Reaction	Turning temperature (K)	ΔH at $298K$ ($kJmol^{-1}$)	Solar to electric conv. efficiency
$SO_3 \rightleftharpoons SO_2 + \frac{1}{2}O_2$	1000	98.2	23%
$NH_4HSO_4 \rightleftharpoons NH_3 + H_2SO_4$	1013	132	
$\frac{1}{2}CH_4 + \frac{1}{2}H_2O \rightleftharpoons \frac{3}{2}H_2 + \frac{1}{2}CO$	1285	103.1	16%
$\frac{1}{2}CH_4 + \frac{1}{2}CO_2 \rightleftharpoons H_2 + CO$	1285	123.4	
$NH_3 \rightleftharpoons \frac{3}{2}H_2 + \frac{1}{2}N_2$	751	66.5	19%

Table 2.1: Five previously investigated solar thermochemical energy storage reactions. Estimated solar to electric conversion efficiencies are taken from Williams (1980*a*).

tem, Williams (1980*a*) published a comparison of reactions. He limited consideration to reactions with fluid reactants for which widespread industrial knowledge was available. On these grounds he chose to consider, in addition to the ammonia reaction, the decomposition of sulphur trioxide, the decomposition of methanol and the steam reforming of methane. He estimated a conversion efficiency for a complete distributed receiver solar thermal-electric system with chemical energy transport, for each case. His efficiency figures ranked the ammonia system second to the sulphur trioxide system, with the choice of the ammonia system rationalised by pragmatic considerations.

Fox (1983) presented another very thorough study of reactions for energy transport purposes. He presented an extensive review of all the relevant literature up to 1983 and a summary of most of the work being carried out at that time. Fifteen plausible fluid phase reactions were selected from the literature for preliminary screening and this was reduced to four which were considered in more detail. These were: ammonia decomposition, sulphur trioxide decomposition, steam reforming of methane and carbon dioxide reforming of methane.

Fish (1984) used the results of Fox to choose a reaction for a 'Closed Loop Efficiency Analysis' project at Sandia National Laboratories. He used a number of qualitative criteria, including the wish to avoid the duplication of other research programs, and ultimately selected the carbon dioxide reforming of methane.

Since the mid 1970s five reactions have been the subject of a significant amount of research work. They are listed in table 2.1 together with some relevant properties.

2.1.1 Decomposition of Sulphur Trioxide

As previously mentioned, the interest in the sulphur trioxide decomposition cycle was initiated by Chubb. He continued systems studies for a number of years, including developing some possible designs for parabolic dish reactor receivers (Chubb 1975, Chubb, Nemecek & Simmons 1979*a*, Chubb 1976, Chubb, Nemecek & Simmons 1979*b*). This initial work prompted the commissioning of a number of experimental studies by Sandia National Laboratories (eg Won & Voecks (1986)). These culminated in a closed loop experiment which was operated at a 1-2kW power level (McCrary & McCrary 1987). Although the sulphur trioxide system appears feasible, there are two significant drawbacks. Sulphur trioxide forms a viscous liquid in piping at ambient temperatures, requiring pipes to be maintained at around $100°C$ for reactant transfer. Also both sulphur dioxide and sulphur trioxide are quite toxic and pose an environmental and health risk in the case of a pipe failure.

2.1.2 Decomposition of Ammonium Hydrogen Sulphate

Prengle & Sun (1976) at the University of Houston picked the decomposition of methanol and the decomposition of ammonium hydrogen sulphate, from the list produced by Wentworth and Chen, for a detailed study. Being primarily interested in energy storage rather than transport, they were impressed by the relatively large enthalpy of reaction for ammonium hydrogen sulphate and the fact that all reactants were liquid or solid at ambient temperature with a resulting high energy storage density at low pressure. Subsequent work by this group (Lee & Prengle 1986, Ranade, Lee & Prengle 1986, Prengle & Lee 1986) assembled reaction rate and mass transfer data and established the basis of a system design. The drawbacks with this system appear to be a lack of industrial experience and the fact that the process appears fairly complex, involving for example, two separate reaction processes for the energy recovery half of the loop. The ammonium hydrogen sulphate itself has a melting point of $147°C$, which permits reasonably easy supply to the reactor and does not rule out some level of energy transport.

At present there does not appear to be any active work on the ammonium hydrogen sulphate system.

2.1.3 Methane Reforming

Thermochemical loops based on the reforming of methane have been the subject of the major part of the research carried out to date. As noted previously the interest in the steam reforming reaction pre-dates the application of closed loop thermochemical processes to solar thermal systems. The work initiated by the EVA-ADAM I demonstration in Germany has continued, the successful operation of a $10MW$ EVA-ADAM II demonstration was reported in 1981 (Holhein, Menzer & Range 1981). The EVA reforming reactors are heated by a high temperature gas heat transfer medium.

Richardson & Das-gupta (1978), among others, examined the feasibility of linking a steam methane loop to a solar central receiver system. Two more recent papers (Richardson, Paripatyadar & Shen 1988) (Parypatyadar & Richardson 1988) reported the results of a major experimental effort at the University of Houston on the development of a reforming reactor for the simulation of solar operation. The concept utilizes a sodium heat pipe as a means for making the flux conversion between the levels expected in a solar receiver and those required by the reactor. Successful cyclic operation of a $25kW$ electrically heated pilot unit was reported.

Work in Europe has continued, and recently the preliminary results of an experimental program to couple an EVA-ADAM type system to the central receiver facility at Almeria (Spain), using air as a heat transfer medium, have been reported (Bohmer, Langnickel, Rodriguez & Sanchez 1991).

The carbon dioxide reforming and steam reforming reactions involve essentially the same reactant systems. Maintaining one or the other as the dominant reaction requires a careful choice of operating conditions and catalyst materials. The carbon dioxide reaction has the benefit of avoiding the condensation and evaporation of water in the reactant heating and cooling processes, with the attendant problems of having to degrade energy at reaction temperatures to provide the latent heat. However the lack of industrial experience with reactor construction and catalysts for the carbon dioxide reforming system has meant that its development initially lagged that of the steam reforming system.

Chubb (1980) proposed a solar thermal system based on the carbon dioxide reforming of methane, this was followed up by experimental investigations (McCrary, McCrary, Chubb, Nemecek & Symons 1982). Sandia National Laboratories (USA) has operated a

continuing program of research, a closed loop efficiency analysis experiment was successfully operated in 1986 (Hawn & Fish 1986, Fish & Hawn 1987). Work since then has concentrated on receiver developments, with work on a $100kW$ volumetric reactor receiver in conjunction with DLR (German Aerospace Research Establishment, Stuttgart) reported (Hogan & Skocypec 1989, Skocypec & Hogan 1989). This receiver unit, constructed from segments of ceramic foam catalyst support material, was subsequently successfully tested with DLR's $150kW$ parabolic dish collector unit (Buck, Muir, Hogan & Scocypec 1991).

A group at the Weizmann Institute of Science (Israel) has also done a considerable amount of work on the carbon dioxide reforming system, starting with work on a $10W$ bench scale closed loop (Fraenkel, Levitan & Levy 1986). Experiments with a $3kW$ tubular reforming reactor mounted directly in a cavity receiver have been reported (Levitan, Rosin & Levy 1989, Levy, Rosin & Levitan 1989) and also the theoretical modelling of the performance of this reactor (Meirovitch, Segal & levy 1990). Recently this work has been extended to the operation of a complete solar driven closed loop at power levels up to $6.4kW$ (Levitan, Levy, Rosin & Rubin 1991).

Their has been considerable interaction between the various groups working on carbon dioxide reforming. A recent paper (Diver, Fish, Levitan, Levy, Meirovitch, Rosin, Parypatyadar & Richardson 1992) described tests of a $7.5kW$ receiver based on Richardson's sodium reflux heat pipe concept. This was a cooperative effort between the Sandia, Weizmann and University of Houston groups.

2.1.4 Decomposition of Ammonia

Work on various aspects of the mass utilization of solar energy began at ANU in 1971. A concept for a large scale solar power plant based on a distributed array of dishes with thermochemical energy transport and storage using ammonia, was described by Carden (1974*a*). The work has continued since then as is detailed in the following section. A small group at Colarado State University is the only other group to have worked actively on the ammonia based system. Starting in 1978, their work focussed on the endothermic half of the system, and included a design study of a $10kW$ reactor receiver unit (Lenz, Wright & Chubb 1978, Wright & Lenz 1980) and some experimental work to evaluate catalysts and measure reaction rates (Nandy & Lenz 1984).

The principle advantages of the ammonia based system are that; the components are environmentally benign and basically nontoxic[1], there are no possible side reactions, the reaction is well understood and there is a considerable body of industrial experience to draw upon. Against this, the disadvantages are that the enthalpy of reaction is somewhat lower than the other candidates and its characteristic temperature is lower than desirable. The low characteristic temperature has a detrimental effect on exothermic reaction rates and on the amount of work that can be produced from the energy output. However the use of high system pressures, although placing extra restrictions on component design, shifts the equilibrium towards higher temperatures and helps to make the system feasible. The use of high pressures provides the additional benefits of improved heat transfer coefficients and greater volumetric energy storage densities. As with the water component in the steam reforming of methane system, ammonia condenses at the ambient temperature and pressures encountered. The disadvantage of the condensation is that at the endothermic reactor the latent heat of vapourisation is usually provided by degrading energy which is available at the reaction temperatures. However to offset this negative effect, the condensation of ammonia allows the separation of endothermic and exothermic reaction products

[1]Ammonia however does have caustic effects when it combines with moisture at high concentrations.

and thus gives more freedom in the choice of reactor operating conditions.

2.1.5 Summary

It would appear that a consensus has developed that there are four reactions worth pursuing for closed loop solar thermochemical application, (sulphur trioxide, ammonia and the methane reactions), with the current emphasis being for their use primarily for the purposes of energy transport. Of the four the carbon dioxide reforming of methane is currently the most favoured.

There is a danger in placing too much emphasis on systematic evaluations of various candidate reactions. The true feasibility of competing systems is not apparent until they have reached at least an advanced 'solar pilot project' stage. Ultimately it is the relative economic performances that are most important, and there is always the possibility of new technological or design developments which will favour one system over the other.

It should also be noted that research on any system is likely to produce developments and techniques which are, either directly or indirectly, applicable to others and to the general field of solar driven chemical processes.

2.2 Work at ANU on the Ammonia System

Carden's initial description (Carden 1974*a*) of a large scale solar plant using the ammonia based thermochemical energy storage system, looked at the feasibility of all aspects by drawing upon existing engineering data. At that stage the collector modules planned were $10m^2$ pressed metal units, this small size necessitated keeping the components associated with each dish simple to achieve an economic design. A preliminary examination of the thermodynamics suggested a theoretical upper limit of 53% for the conversion of absorbed energy to work. Commercially available catalyst materials were identified, and it was noted that reactant handling could be achieved with standard mild steel tubing and components. A hemispherical receiver design constructed from pressed steel plates welded together, was suggested. A modified Stirling cycle was proposed for the recovery of heat from the exothermic process, and its conversion to work.

During the following four years basic research proceeded on all aspects of the concept, with up to half a dozen people working in the team. An updated description of the system was published by Carden in a journal article in 1977 (Carden 1977*a*), this article has been frequently cited since then. Members of the team produced numerous conference papers summarizing the concept and giving updated accounts of the research (Carden, Edwards, Revie & Williams 1975), (Carden 1975), (Carden, Williams & Revie 1976), (Carden, Edwards, Revie & Williams 1976*a*), (Carden, Edwards, Revie & Williams 1976*b*) (Revie 1976), (Carden, Edwards, Revie & Williams 1977), (Carden, Revie & Williams 1977) and (Carden 1978*b*).

Considerable effort was spent assembling a logically consistent body of thermodynamic data. This is described in some detail in appendix A, and three technical reports addressing the subject were produced (Revie 1975, Williams 1976, Williams 1978*b*). Using this data Carden and Williams analysed the theoretical limits on performance in detail, considering both thermal efficiencies and the limits on the efficiency of work production. Two technical reports address these issues, (Carden 1977*b*, Williams 1978*d*) and the major results were presented in two key journal articles (Carden & Williams 1978*b*, Williams & Carden 1979*c*).

Experimental work was initially directed at developing the laboratory facilities and techniques for handling reactants and carrying out reactions at the high pressures involved (up to 300 atmospheres). This included the development of techniques for measuring flow rates (Whelan 1979, Cantor & Williams 1976) and measurements of heat transfer processes in packed catalyst beds (Carden & Whelan 1976). Early reaction experiments yielded essentially qualitative results and unfortunately do not appear to have been written up. The culmination of the early experimental work involved tests with a small electrically heated dissociator constructed as a cylindrical arrangement of parallel catalyst filled passages in a direct simulation of a possible cavity receiver geometry (Williams & Carden 1979*a*, Williams & Carden 1979*b*). The experimental arrangement also incorporated a counterflow heat exchanger and so tested some of the concepts on heat exchangers studied by Edwards (1974).

At the end of 1978 the group made efforts to obtain funding from outside the university to mount a closed loop experiment. Initially it was necessary to answer a number of criticisms (largely founded on ignorance) from within government circles (Carden & Williams 1978*a*). Williams (1978*a*) prepared a detailed research proposal, describing a closed loop ammonia based thermochemical experiment to operate at a $10kW$ power level. In early 1979 funding for this was secured from the National Energy Research Demonstration and Development Council (NERDDC). The objectives for the project also included monitoring developments on other thermochemical storage systems, and producing a detailed system study of a $10MW$ solar thermochemical power plant.

The first two years of this program were extremely productive, in addition to the major papers already mentioned, the $10MW$ system study was completed, the relevant overseas work was reviewed and the design and construction of the $10kW$ experiment progressed well (Carden 1979, Carden 1980*a*) .

The $10MW$ system study was carried out in conjunction with the engineering consultants Davy Pacific Pty. Ltd. Their report (Davy Pacific Pty. Ltd. 1979), described a feasible design, based on existing technology, for a $10MW$ solar plant. The plant design used a steam based heat recovery and electricity generation system to give an overall solar to electric conversion efficiency of 13.3%. Cost projections indicated a reasonable prospect of achieving economic viability in the future, even without the use of a number of identified future technological developments which were expected to improve efficiencies.

Carden and Williams made visits to laboratories in Europe and USA in keeping with the requirement to keep abreast of other developments and to place the work at ANU in context. The work they reported on (Carden & Williams 1979) has been discussed in the previous section. The general conclusion was that the ANU work was well advanced and in many respects ahead of work elsewhere in the world at that time. Theoretical aspects of a number of alternative thermochemical systems were considered (Carden 1980*b*, Carden 1980*c*, Williams 1980*f*, Williams 1980*h*) and two papers on the subject of screening and the choice of reaction system were published (Williams & Carden 1979*d*, Williams 1980*a*).

Williams (1980*c*) presented a detailed design of the closed loop experiment which was then intended to be of $5kW$ capacity. Many of the major components had been constructed and installed, including the dissociation reactor which was about to be tested. The synthesis reactor was under construction, and its design, which utilized the reactants themselves for heat extraction in counterflowing passages, was the subject of a patent application (Williams 1980*e*). Carden (1981), addressed the control problems associated with exothermic reactors of this kind, identifying the conditions under which they can become dynamically unstable.

Theoretical system studies during this period included cost optimisation applied to sys-

tem pressure and other variables (Williams 1978*c*),and aspects of receiver design (Williams 1980*b*, Williams 1980*d*). General system descriptions and summaries of the research were presented in Williams (1981*a*), Williams (1980*g*), Williams (1981*c*) and Williams (1981*b*).

At the end of 1981 an unfortunate accident involving the explosion of an ammonia storage vessel which was inadvertently over heated, although causing only a minor amount of damage, resulted in a major disruption to the experimental program. This was followed early in 1982 by the sudden departure of Williams from the project and subsequently by the loss of a number of other team members. Carden summarised the position in a mid-1982 progress report (Carden 1982*c*), identifying shortcomings in the experimental system design and tasks that remained for the demonstration of energy transfer. The work that followed addressed these aspects and sought to consolidate the progress that had been made up to that time. This included a reappraisal of the synthesiser pressure vessel design (Carden 1982*b*), the design and construction of a balancing separator for mass flow calibrations and reaction extent measurement (Carden 1982*a*) and the publication of details of the liquid nitrogen pumping system developed for the production of high pressure gas (Carden 1983*a*, Carden 1984*a*).

At the end of NERDDC funding in 1983 Carden (1983*b*) noted that under the circumstances resources had been insufficient to complete the energy transfer demonstration but that considerable valuable progress had been made nonetheless. During the period of NERDDC funding 10 journal articles, 6 conference papers and 14 detailed technical reports were produced.

Somewhat independently of the NERDDC funded program, Carden and Paterson (Carden 1978*a*, Carden & Paterson 1979, Carden & Patterson 1980, Paterson 1981) worked on a theoretical and experimental investigation of the fundamental aspects of the underground storage of hydrogen and hydrogen containing mixtures. This work was motivated by the possibility of providing long term energy storage using underground storage of nitrogen and hydrogen mixtures.

From 1983 until the beginning of this project in 1987, Carden was the only person working on the ammonia based thermochemical system. In anticipation of continuation of the experimental work the construction of a large cold walled pressure vessel, as an alternative containment method for synthesis reactors, was commissioned. The major accomplishment of the period was the theoretical development that led to the 'direct work recovery' concept. This concept involves the use of the exothermic reaction products themselves as the working fluid in a heat engine cycle, together with heat extraction from the exothermic reactor via the use of counterflowing heat exchange passages. This concept was the subject of a patent application (Carden 1985) and Davy McKee Pacific Pty. Ltd. (1987), made a preliminary reappraisal of the $10MW$ system study using it. Carden (1987) presented the concept in a journal article and concluded that an overall solar to electric conversion efficiency of 26% was feasible.

Part II

Theoretical analysis

Chapter 3

Thermodynamic Aspects

3.1 Basic Principles

A thermochemical energy transfer or storage system is based on a chemically reversible reaction, which can be represented in a generalised manner as;

$$\Delta H_0 + \mathsf{A} \rightleftharpoons j\mathsf{B} \tag{3.1}$$

where A and B are mixtures of reaction components in stoichiometric proportions and ΔH_0 is the change in enthalpy associated with converting 1 mole of A mixture to j moles of B mixture.

The fact that the reaction can proceed in both directions implies the existence of thermodynamic states of a system where various amounts of A and B mixtures are present. The composition is frequently quantified using the mass fraction of B mixture, referred to as the reaction extent or the conversion (δ) and defined as;

$$\delta = \frac{n_B m_B}{n_A m_A + n_B m_B} \tag{3.2}$$

where m_A and m_B are molecular weights and n_A and n_B are the number of moles of each mixture in a given sample. Since $m_A = j m_B$ (from the stoichiometry of equation 3.1), the reaction extent is related to the mole fraction (X) of B according to:

$$\delta = \frac{X}{j(1-X)+X}. \tag{3.3}$$

It is convenient to examine a thermodynamic system which is equivalent to 1 mole of A mixture but which at any given time could contain various amounts of A and B according to the current value of δ. This is a closed system which may gain and lose heat but requires the addition of a heat engine to produce external work. This is the thermodynamic system which is considered in the analysis throughout this text unless otherwise specified. For the particular case of the ammonia reaction, the system is equivalent to 1 mole of ammonia.

The state of the system is specified by its temperature (T), pressure (P), reaction extent and volume (V). If an equation of state is available this could be reduced to T, P and δ. When the system is in chemical equilibrium, there must also be a relationship between T, P, and δ, defined by the requirement that the total entropy of the system and its surroundings be maximised. Figure 1.2 in chapter 1 presents equilibrium composition as a function of temperature for the ammonia reaction at several constant pressures.

For a thermochemical energy storage process the thermodynamic system is sometimes regarded as a reacting system, in which case chemical equilibrium is a necessary prerequisite for thermodynamic equilibrium, but at other times as a non-reacting system, in which case the system can be in thermodynamic equilibrium whilst being far from chemical equilibrium. This is quite a realistic approach for reactions such as the ammonia reaction where reaction rates in the absence of a catalyst are negligible.

Carden (1977*a*) chose the temperature enthalpy diagram as being the most comprehensive way of presenting information about thermochemical processes in a single diagram. In the simplest form, a closed loop thermochemical process is assumed to operate at an approximately constant pressure throughout. When the loop involves more than one pressure as in the direct work output configuration discussed in section 3.6, each reactor will still be operated at a constant pressure. Having chosen as the thermodynamic system in question, 1 mole equivalent of A, a thermochemical process will involve only exchanges of heat and flow work (associated with volume changes) with its environment. Thus, as a consequence of the first law, the isobaric conditions and the lack of external work production, heat exchanged with the environment will have the same magnitude as the enthalpy variation of the system. Since it is the amount of heat transferred at various temperatures which is of primary interest, the temperature enthalpy diagram is an ideal vehicle for the presentation of information.

Figure 3.1 shows the equation of state for the ammonia system at several constant pressures, plus the locus of points of chemical equilibrium, on a temperature enthalpy diagram. The origins of the thermodynamic data represented in figure 3.1 and a more detailed description of it are given in appendix A. A number of important features can be noted:

- The equation of state is represented by contours of constant δ from $\delta = 0$ (pure NH_3) to $\delta = 1$ (completely dissociated NH_3). The slope of each line of constant δ is equal to the inverse of the specific heat at constant pressure of the non-reacting mixture.
- The horizontal distance between $\delta = 0$ and $\delta = 1$ represents the enthalpy of formation of the dissociated mixture at any given temperature.
- The dewline marks the boundary between gaseous and two-phase mixtures, it is the locus of points where the partial pressure of ammonia is equal to its vapour pressure.
- The line $\delta = 0$ does not have a horizontal section corresponding to a phase change when the pressure exceeds the critical pressure for ammonia.

A transition of the system from one point to another at the same temperature and pressure is characterized by the change in reaction extent ($\Delta\delta$). Associated with this are corresponding changes in all the thermodynamic functions, which must be related to the changes associated with the reaction. If $\Delta H_0(T), \Delta G_0(T)$ and $\Delta S_0(T)$ are the enthalpy, Gibbs free energy and entropy of the reaction at temperature T respectively, then in general:

$$\begin{aligned} \Delta H(T) &= \Delta\delta\Delta H_0(T) + H_m(\delta_1,T) - H_m(\delta_2,T) \\ \Delta S(T) &= \Delta\delta\Delta S_0(T) + S_m(\delta_1,T) - S_m(\delta_2,T) \\ \Delta G(T) &= \Delta\delta\Delta G_0(T) + H_m(\delta_1,T) - H_m(\delta_2,T) - T(S_m(\delta_1,T) - S_m(\delta_2,T)) \end{aligned} \quad (3.4)$$

where H_m and S_m are the heat and entropy of mixing respectively[1]. At reaction temperatures, mixtures can usually be regarded as ideal solutions, for which mixing heats are

[1]The heat and entropy of mixing refered to here, are the contributions associated with the mixing of A

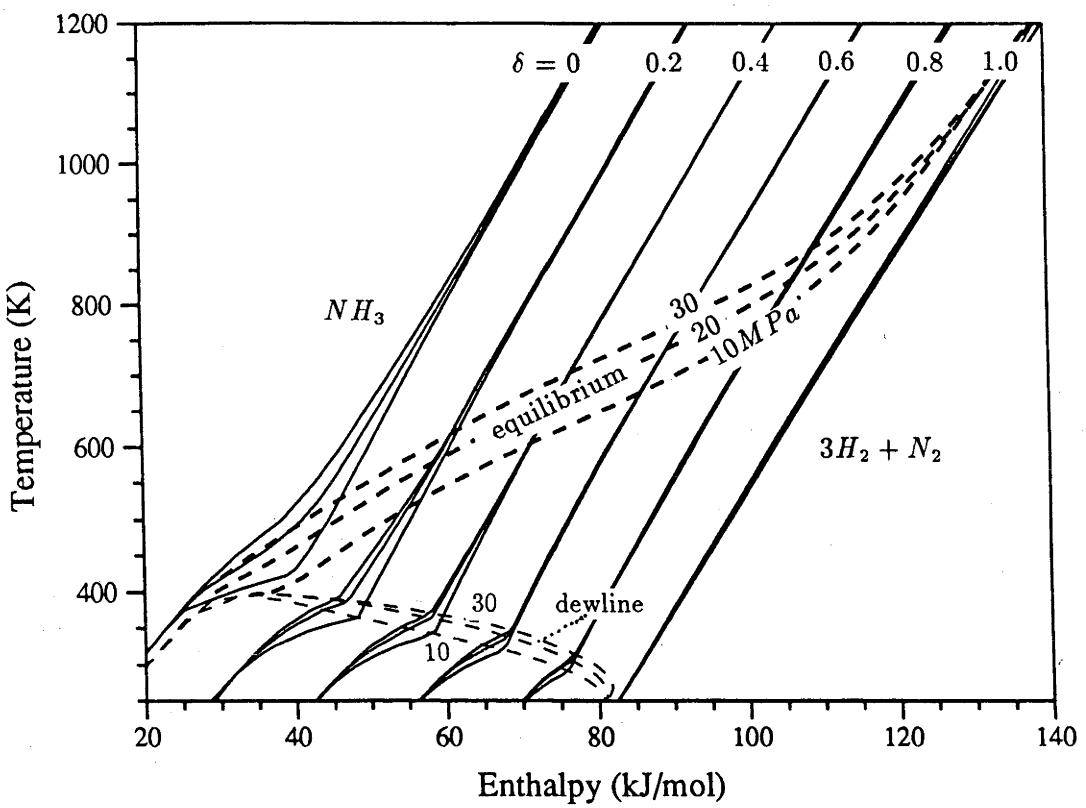

Figure 3.1: Temperature enthalpy characteristics for ammonia/ 3:1 hydrogen-nitrogen in the range 10-30MPa .

zero. For the ammonia reaction, ammonia preferentially condenses from mixtures at low temperatures. If the temperature is sufficiently low, then the fraction of nitrogen and hydrogen dissolved in the liquid phase and the fraction of ammonia remaining in the gas phase will be low enough that the mixing heat and mixing entropy will be negligible.

Figure 3.2 shows a possible reversible process that the system may undergo. Paths 1–2 and 3–4 along lines of constant δ represent reversible cooling/heating of a mixture in the absence of catalyst. The path 2–3 along the equilibrium line corresponds to a quasistatic addition or removal of heat in the presence of a catalyst. Travelling from 4–1 is obviously an exothermic process. The total energy released is $\Delta H(T_s)$. Conversely in the endothermic direction a total amount of energy $\Delta H(T_s)$ must be provided.

It can be seen that with such a cycle it is theoretically possible to achieve loss free thermodynamically reversible storage of energy. The problem with translating such a scheme into reality is that at equilibrium reaction rates are zero. A non-zero reaction rate in a reacting thermodynamic system is a manifestation of a system which is not in thermodynamic equilibrium spontaneously and irreversibly returning to equilibrium. Reaction kinetics are discussed in detail in chapter 4, however the qualitative behaviour of reaction rates can be described simplistically as being the product of a 'composition' factor, that is to first order proportional to the 'distance' (eg increment in δ) from equilibrium, and a Boltzmann type temperature dependant factor. Clearly the thermodynamically reversible

and B. If A and B themselves contain a number of components (ie B $\equiv N_2 + 3H_2$), then the contributions to their enthalpy and entropy due to mixing, will be reflected in ΔH_0 and ΔS_0 for the reaction.

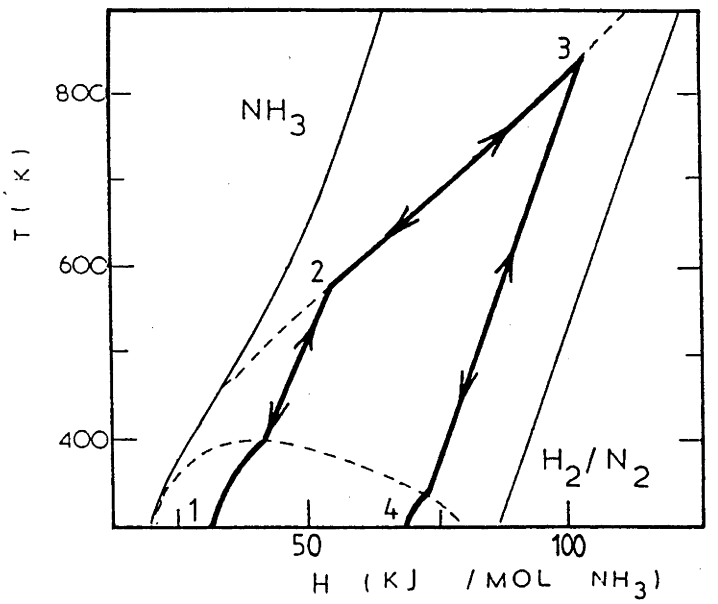

Figure 3.2: A possible thermodynamically reversible process.

process shown in Figure 3.2 is not possible in a real system; exothermic reactions must always operate at temperatures somewhere below equilibrium and endothermic reactions at temperatures above equilibrium.

The series of states that the thermodynamic system passes through in a transition from one value of δ to another is referred to as a reaction path. Figure 3.3 illustrates three possible isobaric exothermic reaction paths that may be followed from a common starting point. On the temperature enthalpy diagram these paths indicate the amount of heat that

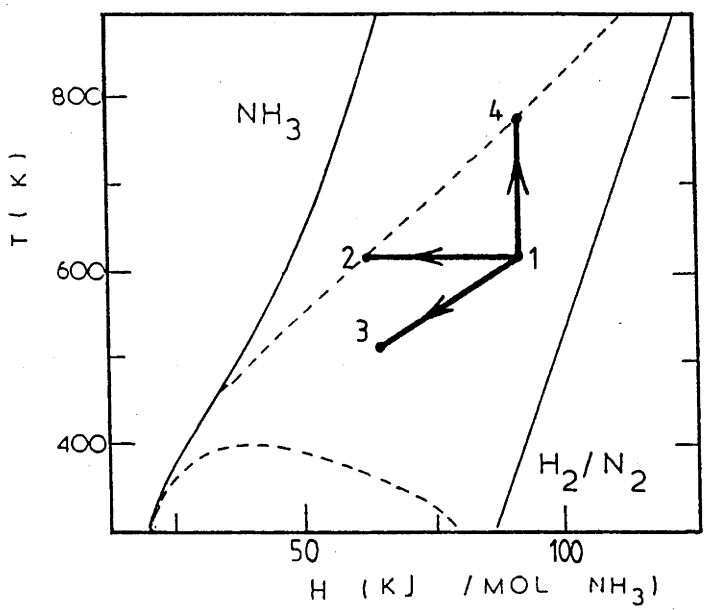

Figure 3.3: Isothermal (1–2), isenthalpic (1–4) and constant slope (1–3) exothermic reaction paths.

must be transferred between the system and its environment for each δ increment. The

thermodynamic system, based on one mole of ammonia, could trace out these paths in a number of ways. For example, a mixture of ammonia and hydrogen/nitrogen, with a composition corresponding to point 1, could be placed inside a constant pressure reaction vessel in perfect thermal contact with a controlled temperature heat sink. The reaction paths would be spontaneously traced out as the temperature of the heat sink varied with time and the total heat absorbed varied with the integral of the reaction rate. Thus the isothermal path from 1–2 would be produced by placing the reaction chamber in perfect thermal contact with an isothermal heat sink. The time dependence of composition would be entirely dependent on the values of the reaction rate encountered as the system traversed its isothermal path. Given the qualitative behaviour of reaction rates described previously, an asymptotic approach to equilibrium conditions would be expected.

The isenthalpic path from 1–4 corresponds to a completely insulated reaction vessel proceeding to equilibrium, with the enthalpy change due to reaction being exactly balanced by the increase in temperature, ie:

$$dH = 0 = \frac{\partial H}{\partial \delta} d\delta + \frac{\partial H}{\partial T} dT. \tag{3.5}$$

In this case both the composition and temperature would proceed in an asymptotic manner towards their equilibrium values. Both the isothermal and isenthalpic reaction paths could equally well be traced out by the passage of the closed thermodynamic system (the 1 mole equivalent of ammonia) through a one dimensional steady state reactor. In a steady state reactor, the temperature and composition at any point do not vary with time, a constant flow rate of reactants and transfer of heat is maintained and the reactants themselves experience a variation in conditions as they traverse the reactor. The time dependent behaviour observed in the 'batch' type arrangement just described would be replaced by a similar spatial behaviour, with the reactor length increment required for each δ increment being inversely proportional to the average reaction rate.

In the context of a steady state one-dimensional reactor, the constant slope path from 1–3 could correspond to the effect of a counter flowing heat transfer fluid of constant specific heat; in this situation if perfect heat transfer is assumed, the reaction path must have a slope equal to the product of the fluid's specific heat and the ratio of heat transfer fluid to reactant flow rates.

When the idealisation of perfect heat transfer within a reactor is removed, and a two or greater dimensional description becomes necessary, these simple paths spread out to form a reaction path envelope. Furthermore, when the assumption of perfect heat transfer between reactor and heat sink is dropped, a 'heat transfer' path at a lower temperature than the lowest curve in the reaction path envelope results.

All of the above points apply equally to endothermic reaction paths with the appropriate reversal of reaction and heat transfer direction.

The idealised paths of a real separating ammonia based closed loop thermochemical system may look qualitatively as shown in figure 3.4. In this case the gas/liquid separator is operated at $300K$, ammonia liquid is fed to the endothermic reactor and the gas mixture is fed to the exothermic reactor. For the liquid, δ is slightly greater than zero due to a small amount of dissolved nitrogen and hydrogen gas. The composition of the gas is dictated by the intersection of the $300K$ isotherm with the dewline. Maintaining a constant thermal power level for different exit reaction extents, requires proportional variations in the flow rate to the reactor in question. Reaction paths are determined by the heat flux profiles of the two reactors, and exit reaction extents are chosen by trading off factors such as reaction rate limitations, pressure drops and heat exchanger performance.

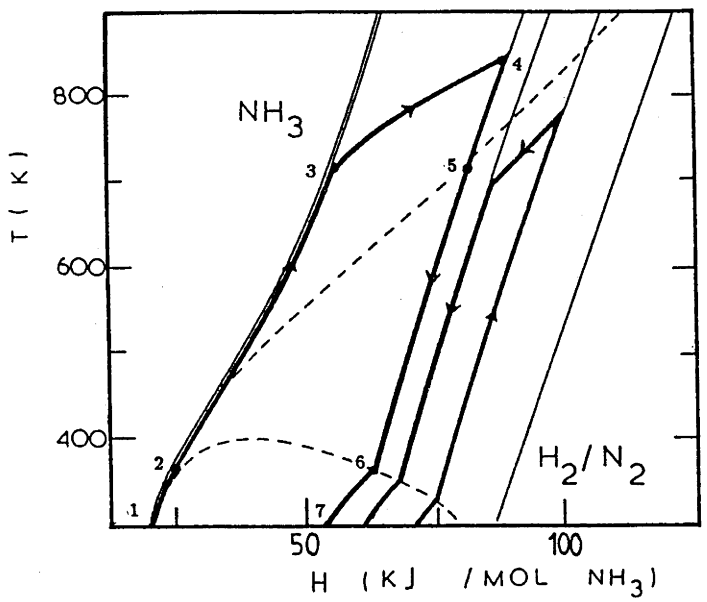

Figure 3.4: Possible real endothermic and exothermic paths for a closed loop system.

3.2 Performance Analysis

With energy handling processes of this type, performance analysis is concerned with quantifying both direct losses of energy and loss in the potential to do useful work.

Associated with every amount of energy is a fraction of that amount which can theoretically be converted to work. This quantity is variously referred to as 'available energy', 'available work', 'availability' and 'exergy' among other terms. Exergy is used throughout this text, although it is a term which does not have universal acceptance, it has the advantage of being a unique word which is less likely to be misinterpreted. An amount of energy which is in the form of work is 100% exergy. An amount of energy in the form of heat has an exergy content which is related to the temperature it can be extracted at and the lowest sink temperature available, by the Carnot efficiency relationship. The exergy contained in an isolated thermodynamic system, is a function of its thermodynamic state. It is equal to the amount of work which would be obtained if the system was brought reversibly to thermodynamic equilibrium with the lowest temperature and pressure sink available, using appropriate heat engines and expansion devices. Exergy is lost in proportion to energy lost, but it can also be destroyed by thermodynamically irreversible processes.

The two types of loss can be quantified using some combination of the 'thermal efficiency' (the first law efficiency);

$$\eta_I \equiv \frac{\text{Energy out}}{\text{Energy in}} \tag{3.6}$$

the 'Exergetic efficiency' (the second law efficiency);

$$\eta_{II} \equiv \frac{\text{Exergy out}}{\text{Exergy in}} \tag{3.7}$$

or a 'conversion efficiency';

$$\eta_c \equiv \frac{\text{Exergy out}}{\text{Energy in}}. \tag{3.8}$$

Many authors have discussed thermal efficiency issues in relation to thermochemical energy storage. Fish (1984) is one of the few to discuss factors relating to the exergetic efficiency. The most comprehensive analysis of efficiencies of solar thermochemical systems so far appears to be that of Carden & Williams (1978*b*) and Williams & Carden (1979*c*). Their analysis proceeds from the definition of two efficiencies; the energy storage efficiency, which is a thermal efficiency for the endothermic part of the thermochemical loop; plus the work recovery efficiency, which is a conversion efficiency for the exothermic half of the loop. The product of these is a conversion efficiency for the complete thermochemical system, which is consistent with the usual practice of comparing solar thermal electric conversion systems via conversion efficiencies. The analysis presented here reproduces and builds upon their results.

3.3 Thermal Efficiency

Given that energy is stored as an enthalpy variation at the sink temperature for a thermochemical system, the endothermic and exothermic thermal efficiencies are;

$$\begin{aligned} \eta_{I_{end}} &= \frac{\Delta H_{end}(T_s)}{Q_{in}} \\ \eta_{I_{ex}} &= \frac{Q_{out}}{\Delta H_{ex}(T_s)} \end{aligned} \tag{3.9}$$

where Q_{in} and Q_{out} are heat inputs and outputs.

These definitions are in terms of molar quantities, hence $\Delta H_{end} \neq \Delta H_{ex}$ in reflection of the different reaction extent endpoints. Multiplying numerator and denominator by a molar flow ($\dot{m}$) in each case would reconfigure them as a ratio of power levels, and the product of enthalpy change and flow rate would be equal in the two cases if the thermochemical process is not accumulating excesses of either reactants. In this manner the overall thermal efficiency reduces to the ratio of thermal input and output as it should.

$$\begin{aligned} \eta_{I_{sys}} &= \eta_{I_{end}} \times \eta_{I_{ex}} \\ &= \frac{\Delta H_{end}(T_s)\dot{m}_{end}}{Q_{in}\dot{m}_{end}} \times \frac{Q_{out}\dot{m}_{ex}}{\Delta H_{ex}(T_s)\dot{m}_{ex}} \\ &= \frac{Q_{out}\dot{m}_{ex}}{Q_{in}\dot{m}_{end}}. \end{aligned} \tag{3.10}$$

For either reaction the enthalpy change of the reaction at the sink temperature is equal to the path integral of the incremental enthalpy variation, starting at the initial reaction extent and sink temperature and ending at the final reaction extent, also at the sink temperature:

$$\Delta H(T_s) = \int_{(T_s,\delta_1)\ \text{path}}^{(T_s,\delta_2)} dH(T,\delta). \tag{3.11}$$

Complete paths consist of; heating inlet reactants, supplying or withrawing heat from the reaction and cooling the products. If these steps can be carried out with 100% thermal efficiency, then the whole system will have a thermal efficiency of 100%.

Given that the heating of reactants and the cooling of products occurs simultaneously for steady state operation, it is the net surplus or deficit of heat for each temperature increment which is of primary importance. Equation 3.11 can be rewritten as;

$$\Delta H(T_s) = \int_{T_s}^{T_{max}} d(\Delta H) \tag{3.12}$$

where $\Delta H = H(T, \delta_2') - H(T, \delta_1')$, δ_2' and δ_1' being the two possible values of reaction extent at each temperature (equal to δ_2 and δ_1 except within the reactor).

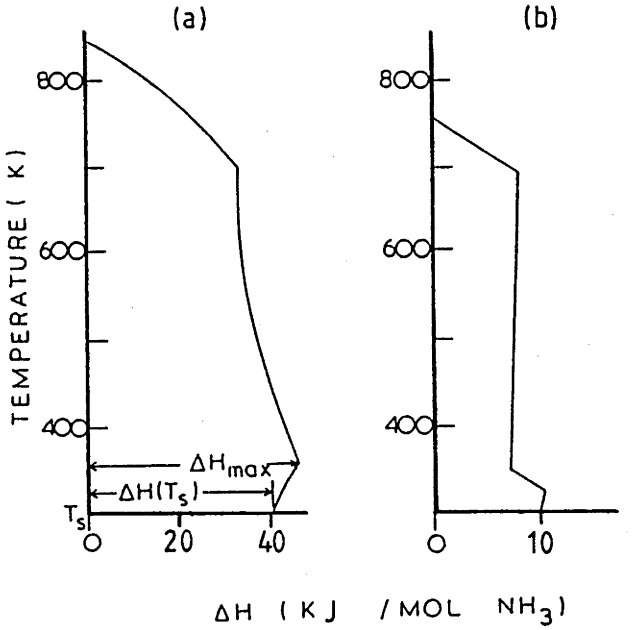

Figure 3.5: The temperature profile of enthalpy changes associated with the endothermic (a) and exothermic (b) paths in figure 3.4, reproduced from Carden & Williams (1978*b*).

Figure 3.5 shows the temperature dependence of ΔH for the representative endothermic and exothermic paths of figure 3.4. The temperature profile for the endothermic path is divided into three regions. The high temperature region, with a negative $\frac{d\Delta H}{dT}$ corresponds to the large heat requirement of the reaction dominating the small amount recovered from the cooling of the products. The next region also has a negative value of $\frac{d\Delta H}{dT}$, indicating that more heat is required to heat the ammonia than is recovered from cooling the products over this range. In the lowest temperature section, the reverse is true, with the heat recovered from product cooling exceeding that required to heat the ammonia. The interpretation of the profile for the exothermic path is similar, but with the opposite interpretation of the sign of $\frac{d\Delta H}{dT}$, negative values indicate a net heat output, in view of the reversal of reaction direction.

Some assumptions about the practical method of implementation allow further observations to be made.

For the endothermic reactor, a solar parabolic dish installation will consist of a receiver/reactor plus a counterflow heat exchanger. In the absence of any other mechanism, the heat deficit between 360 and $700K$, must be provided by degrading heat from the receiver. Refering back to figure 3.4, this is done by sending the reaction products to the heat exchanger at point 4 rather than first recovering some of their heat back to the reactor and starting at point 5. The temperature of point 3 must be such that $\Delta H_{3-4} = \Delta H_{2-6}$ ($= \Delta H_{max}$ in figure 3.5), this the amount of energy which is absorbed from the collected solar radiation.

Carden & Williams (1978*b*) in their analysis of energy storage efficiency, point out that for the endothermic process, a simple heat exchanger design determined by cost-driven simplifications for distributed solar collector operation, would result in the heat released at the low temperature end (between 360 and $300K$) being lost to the environment. With

this assumption, a limiting value for the thermal efficiency of the endothermic process is:

$$\eta_{I_{end}} = \frac{\Delta H(T_s)}{\Delta H_{max}} \tag{3.13}$$

In a later paper (Williams & Carden 1979*c*) they present the results of calculations using this relationship for paths that begin at $\delta = 0$; these have been reproduced in figure 3.6. The major conclusion that can be drawn is that low values of change in reaction extent result in poor thermal efficiencies as a consequence of the large value of $\frac{\partial H}{\partial \delta}$ in the region of the dew line for low values of δ.

For the exothermic reaction process, the added complexity acceptable for a large central plant in a solar thermochemical system would be more conducive to a system with a 100% thermal efficiency. However it would be possible to carry out a similar analysis to that performed on the endothermic process . As shown in figure 3.5b, the exothermic process produces a component of heat surplus at around 340K which, after reabsorbing a small amount around 310K, would represent the component most likely to be wasted. Calculations of exothermic thermal efficiency could be made using:

$$\eta_{I_{exo}} = \frac{\Delta H(T_s) - \Delta H_{waste}}{\Delta H(T_s)}. \tag{3.14}$$

For a given inlet reaction extent, these calculations would indicate a value for the exit reaction extent for which the thermal efficiency would be a maximum. This could prove to be a significant factor in the choice of an exit reaction extent.

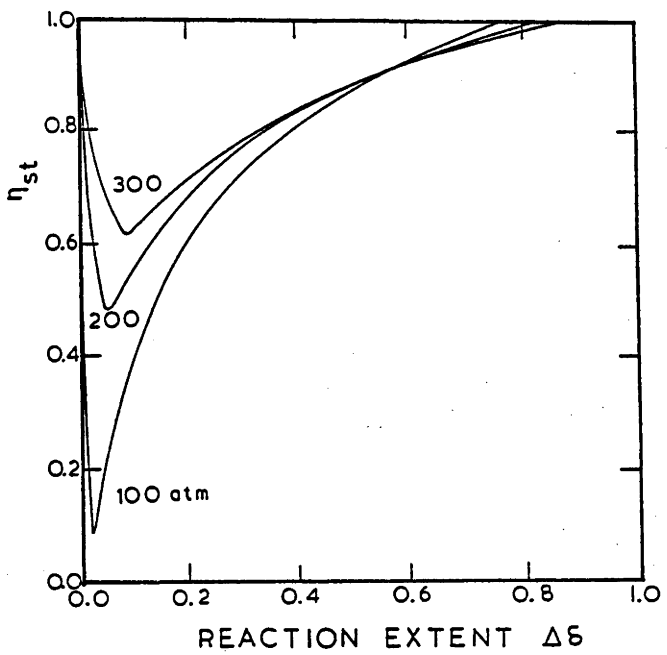

Figure 3.6: Energy storage efficiencies for $\delta = 0$ input, reproduced from Williams & Carden (1979*c*).

3.4 Exergetic and Work Recovery Efficiencies

The functional dependence of the amount of exergy contained by a hydrostatic[2] thermodynamic system on its state, can be derived by applying the first and second laws to a combined system consisting of the hydrostatic system plus a reversible heat engine. Kinetic energy and gravitational or other potential energy contributions are assumed absent in this analysis.

In a quasistatic transition the combined system will do work equal to the loss of exergy (Φ) from the hydrostatic system ie:

$$\begin{aligned} -d\Phi &= -dQ\left(1-\frac{T_s}{T}\right)+(P-P_o)dV \\ &= -dQ+T_s dS+(P-P_o)dV \end{aligned} \tag{3.15}$$

where T_s is the heat sink temperature and P_o its pressure. Application of the first law to the hydrostatic system and substitution for heat transfered (dQ) gives:

$$\begin{aligned} -d\Phi &= -dU-PdV+T_s dS+(P-P_o)dV \\ &= -dU+T_s dS-P_o dV. \end{aligned} \tag{3.16}$$

Integrating yields:

$$\Phi(P,T,V)=U-T_s S+P_o V. \tag{3.17}$$

In trying to determine the exergetic or conversion efficiencies for thermochemical processes, the quantity of interest is the exergy released in an isobaric transition from one value of reaction extent at the sink temperature to a different value of reaction extent also at the sink temperature. Since the system remains always at the same pressure, this can be equated with P_o. Under these conditions, using the definition of Gibbs free energy ($G \equiv U+PV-TS$), the exergy change for the 1 mole equivalent thermodynamic system becomes:

$$d\Phi_{\text{system}} = dG = \left.\frac{\partial G}{\partial \delta}\right|_{(T_s,\delta)} d\delta. \tag{3.18}$$

The amount of exergy released or absorbed by the heat source/sink to or from the thermochemical process, will depend on the extent of irreversibility involved. Carden & Williams (1978*b*) addressed this issue in their derivation of work recovery efficiency. They analysed an idealised process consisting of a thermodynamically reversible counter flow heat exchanger operating between T_s and T_f, together with an isothermal reactor at T_f in which system composition was changed by a finite value of $\Delta\delta$. Initially they conceptually contrived to operate the isothermal reactor reversibly, through the use of semi-permeable membranes and isothermal expansions and compressions. They identified all the possible sources of work from this process and confirmed the equality of the total with $\Delta G(T_s)$. Dropping the assumption of reversible behaviour in the isothermal reactor, allowed identification of the loss in work that could be produced and yielded an expression for the work recovery efficiency for this semi-realistic process. The expression was subsequently generalized to cover an infinitesimal change in reaction extent to give an expression that could be integrated along a non-isothermal reaction path.

There are some conceptual benefits to performing a similar analysis which assumes an infinitesimal transition in reaction extent from the beginning. Consider an infinitesimal

[2] A hydrostatic system is a system of constant mass which exerts a uniform hydrostatic pressure on its surroundings, it may still move relative to other frames of reference.

isobaric transition from (T_s, δ) to $(T_s, \delta + d\delta)$ consisting of; heating from (T_s, δ) to (T_f, δ), reaction to $(T_f, \delta + d\delta)$, followed by cooling to $(T_s, \delta + d\delta)$. In this general analysis $d\delta$ could be positive, corresponding to an endothermic transition, or negative, corresponding to an exothermic transition. The exergy change experienced by the heat source/sink linked to the reactor and heat exchanger will be:

$$d\Phi_{\text{process}} = \int_{(T_s,\delta)\ \text{path}}^{(T_s,\delta+d\delta)} dH \left(1 - \frac{T_s}{T}\right). \tag{3.19}$$

This exergy increment can be divided up according to the stages already identified, ie:

$$d\Phi_{\text{process}} = d\Phi_{\text{heating}} + d\Phi_{\text{reaction}} + d\Phi_{\text{cooling}}. \tag{3.20}$$

The reaction contribution can be readily identified as:

$$d\Phi_{\text{reaction}} = \left.\frac{\partial H}{\partial \delta}\right|_{(T_f,\delta)} d\delta \left(1 - \frac{T_s}{T_f}\right). \tag{3.21}$$

The heating and cooling contributions which combine to form the heat exchanger contribution are:

$$\begin{aligned} d\Phi_{\text{heat exchanger}} &= d\Phi_{\text{heating}} + d\Phi_{\text{cooling}} \\ &= \int_{T_s}^{T_f} \left.\frac{\partial H}{\partial T}\right|_{(T,\delta)} \left(1 - \frac{T_s}{T}\right) dT + \int_{T_f}^{T_s} \left.\frac{\partial H}{\partial T}\right|_{(T,\delta+d\delta)} \left(1 - \frac{T_s}{T}\right) dT \\ &= \int_{T_s}^{T_f} \left(\left.\frac{\partial H}{\partial T}\right|_{(T,\delta)} - \left.\frac{\partial H}{\partial T}\right|_{(T,\delta+d\delta)} \right) \left(1 - \frac{T_s}{T}\right) dT \\ &= -d\delta \frac{\partial}{\partial \delta} \left(\int_{T_s}^{T_f} \left.\frac{\partial H}{\partial T}\right|_{(T,\delta)} \left(1 - \frac{T_s}{T}\right) dT \right). \end{aligned} \tag{3.22}$$

Since it has been assumed that the heat exchanger is operated reversibly (and at constant pressure), the identity;

$$\frac{1}{T}\frac{\partial H}{\partial T} = \frac{\partial S}{\partial T} \tag{3.23}$$

can be used, hence the heat exchanger contribution becomes:

$$\begin{aligned} d\Phi_{\text{heat exchanger}} &= -d\delta \frac{\partial}{\partial \delta} \int_{T_s}^{T_f} \left(\left.\frac{\partial H}{\partial T}\right|_{(T,\delta)} - T_s \left.\frac{\partial S}{\partial T}\right|_{(T,\delta)} \right) dT \\ &= d\delta \left.\frac{\partial H}{\partial \delta}\right|_{(T_s,\delta)} - T_s d\delta \left.\frac{\partial S}{\partial \delta}\right|_{(T_s,\delta)} - d\delta \left.\frac{\partial H}{\partial \delta}\right|_{(T_f,\delta)} + T_s d\delta \left.\frac{\partial S}{\partial \delta}\right|_{(T_f,\delta)} \\ &= d\delta \left.\frac{\partial G}{\partial \delta}\right|_{(T_s,\delta)} - d\delta \left.\frac{\partial H}{\partial \delta}\right|_{(T_f,\delta)} + T_s d\delta \left.\frac{\partial S}{\partial \delta}\right|_{(T_f,\delta)}. \end{aligned} \tag{3.24}$$

Finally combining this with the reaction contribution yields:

$$\begin{aligned} \frac{d\Phi_{\text{process}}}{d\delta} &= \left.\frac{\partial G}{\partial \delta}\right|_{(T_s,\delta)} - \left(\frac{T_s}{T_f} \left.\frac{\partial H}{\partial \delta}\right|_{(T_f,\delta)} - \frac{T_s T_f}{T_f} \left.\frac{\partial S}{\partial \delta}\right|_{(T_f,\delta)} \right) \\ &= \left.\frac{\partial G}{\partial \delta}\right|_{(T_s,\delta)} - \frac{T_s}{T_f} \left.\frac{\partial G}{\partial \delta}\right|_{(T_f,\delta)}. \end{aligned} \tag{3.25}$$

If the infinitesimal reaction is carried out at $T_f = T_{equil}$, the temperature of chemical equilibrium corresponding to the value of δ, then the identity $\frac{1}{T} dH = dS$ could also be

used in evaluating the reaction contribution and equation 3.25 would then be identical to equation 3.18. This also demonstrates the origin of the criterion that $\frac{\partial G}{\partial \delta} = 0$ for chemical equilibrium in an isobaric system. The derivative $\frac{\partial G}{\partial \delta}$ is positive for temperatures below equilibrium and negative above equilibrium. As a consequence, equation 3.25 shows that the exergy change of the heat source/sink is greater than the exergy change of the 1 mole equivalent thermodynamic system if $T_f > T_{\text{equil}}$. Conversely the exergy change is less if $T_f < T_{\text{equil}}$. These two inequalities are the conditions for endothermic and exothermic reaction direction respectively. The term $-\frac{T_s}{T_f}\frac{\partial G}{\partial \delta}|_{(T_f,\delta)}$ in equation 3.25 can be anticipated without the benefit of the derivation by considering the alternatives of transition between (T_f, δ) and $(T_f, \delta + d\delta)$ either reversibly or irreversibly. In the exothermic direction, proceeding irreversibly at $T_f < T_{\text{equil}}$ amounts to converting the exergy contribution $\frac{\partial G}{\partial \delta}|_{(T_f,\delta)}$ into heat at T_f. In doing so $\frac{T_s}{T_f}\frac{\partial G}{\partial \delta}|_{(T_f,\delta)}$ is the exergy that is destroyed; the corresponding net increase in entropy is $\frac{1}{T_f}\frac{\partial G}{\partial \delta}|_{(T_f,\delta)}$. In the endothermic direction, proceeding irreversibly at $T_f > T_{\text{equil}}$ amounts to unnecessarily providing the extra exergy $\frac{T_s}{T_f}\frac{\partial G}{\partial \delta}|_{(T_f,\delta)}$ ($\frac{\partial G}{\partial \delta} < 0$ for $T > T_{\text{equil}}$), which is subsequently destroyed.

Using this result for the exergy transfer from an infinitesimal reaction step coupled to a reversible heat exchanger, the corresponding exergetic and work recovery efficiencies can be presented.

For an endothermic process;

$$\begin{aligned} \eta_{\text{IIend}} &= \frac{\text{Exergy stored in reaction}}{\text{Exergy input}} \\ &= \frac{\int_{\delta_1}^{\delta_2} \frac{\partial G}{\partial \delta}|_{(T_s,\delta)}\, d\delta}{\int_{\delta_1 \text{reaction path}}^{\delta_2} \left(\frac{\partial G}{\partial \delta}|_{(T_s,\delta)} - \frac{T_s}{T}\frac{\partial G}{\partial \delta}|_{(T,\delta)} \right) d\delta} \end{aligned} \tag{3.26}$$

for an exothermic process;

$$\begin{aligned} \eta_{\text{IIexo}} &= \frac{\text{Exergy output}}{\text{Exergy stored in reaction}} \\ &= \frac{\int_{\delta_1 \text{reaction path}}^{\delta_2} \left(\frac{\partial G}{\partial \delta}|_{(T_s,\delta)} - \frac{T_s}{T}\frac{\partial G}{\partial \delta}|_{(T_s,\delta)} \right) d\delta}{\int_{\delta_1}^{\delta_2} \frac{\partial G}{\partial \delta}|_{(T_s,\delta)}\, d\delta} \end{aligned} \tag{3.27}$$

and the work recovery efficiency is given by;

$$\begin{aligned} \eta_R &= \frac{\text{Exergy output}}{\text{Heat stored in reaction}} \\ &= \frac{\int_{\delta_1 \text{reaction path}}^{\delta_2} \left(\frac{\partial G}{\partial \delta}|_{(T_s,\delta)} - \frac{T_s}{T}\frac{\partial G}{\partial \delta}|_{(T,\delta)} \right) d\delta}{\int_{\delta_1}^{\delta_2} \frac{\partial H}{\partial \delta}|_{(T_s,\delta)}\, d\delta}. \end{aligned} \tag{3.28}$$

For the sake of completeness, the endothermic counterpart of the work recovery efficiency, a coefficient of performance for energy storage, can also be defined:

$$\begin{aligned} C_{St} &\equiv \frac{\text{Heat output}}{\text{Exergy stored in reaction}} \\ &= \frac{\int_{\delta_1}^{\delta_2} \frac{\partial H}{\partial \delta}|_{(T_s,\delta)}\, d\delta}{\int_{\delta_1 \text{reaction path}}^{\delta_2} \left(\frac{\partial G}{\partial \delta}|_{(T_s,\delta)} - \frac{T_s}{T}\frac{\partial G}{\partial \delta}|_{(T,\delta)} \right) d\delta}. \end{aligned} \tag{3.29}$$

Returning to the consideration of infinitesimal change of reaction extent paths, these four performance indices can be reduced to their corresponding combination of thermodynamic function derivatives. In this form they are also functions of the thermodynamic state and can be presented as contours on a temperature enthalpy diagram. The finite reaction path performance indices can be written in terms of their respective infinitesimal versions, for example:

$$\eta_{\text{IIexo}} = \frac{\int_{\delta_1 \text{reaction path}}^{\delta_2} \eta_{\text{IIexo}}(T,\delta)\, \frac{\partial G}{\partial \delta}\big|_{(T,\delta)}\, d\delta}{\int_{\delta_1}^{\delta_2} \frac{\partial G}{\partial \delta}\big|_{(T_s,\delta)}\, d\delta}. \tag{3.30}$$

In general these expressions cannot be equated with expressions of the form;

$$\overline{\eta} = \frac{\int_{\delta_1 \text{reaction path}}^{\delta_2} \eta(T,\delta) d\delta}{\int_{\delta_1}^{\delta_2} d\delta} \tag{3.31}$$

as Carden and Williams have done with the work recovery efficiency. This is simply the average value of the performance index over the reaction extent range of the path. It will, however, give the correct value for the overall performance index of the path for the two exothermic indices if $\frac{\partial G}{\partial \delta}|_{(T_s,\delta)}$ and $\frac{\partial H}{\partial \delta}|_{(T_s,\delta)}$ are constants, which is the case under conditions in which the reactants spontaneously separate at the sink temperature.

Carden and Williams used the expression for the infinitesimal path work recovery efficiency (based on equation 3.28) to manually produce contours of constant efficiency within the reaction extent range in which spontaneous separation occurs. This has been extended to cover the whole reaction extent range and to encompass contours of constant exothermic and endothermic exergetic efficiency as well. The procedure developed for the numerical calculation of constant efficiency contours is described in appendix B and utilizes two dimensional curve fits to $\frac{\partial G}{\partial \delta}$ and $\frac{\partial H}{\partial \delta}$, which are presented in appendix A.

Figure 3.7 shows constant contours for a range of values of all three efficiency quantities, for a system pressure of 200 atmospheres and a sink temperature of $300K$. The equilibrium line is of course a contour of unity exergetic efficiency in both the exothermic and endothermic directions. Less than unity exergetic efficiency contours run in a semi-parallel manner to the equilibrium line and decrease in value moving away from the equilibrium line. Those contours at higher temperatures than equilibrium correspond to endothermic processes and those below to exothermic processes. At $\delta = 0$ all contours should terminate at $T = T_s$ and at $\delta = 1$ they should go to $T = \infty$. The plotted contours however do not extend this far because the two dimensional curve fits used are not valid to these limits. Although the efficiency expressions can be evaluated down to the sink temperature (which would be a contour of zero efficiency), they would have no real meaning below the dewline since there is no practical mechanism for reaction to occur other than in the gas phase.

In the reaction extent region for which the dewline is above the sink temperature, (ie reactant mixtures separate when cooled), the constant work recovery efficiency contours are also constant exergetic efficiency contours. The relative values differ by the constant factor $\frac{\partial G}{\partial \delta}|_{(T_s,\delta)} / \frac{\partial H}{\partial \delta}|_{(T_s,\delta)}$ (hence this is the value of work recovery efficiency along the equilibrium line). At the reaction extent at which the dewline intersects the sink temperature the discontinuous change to a higher value of $\frac{\partial H}{\partial \delta}|_{(T_s,\delta)}$ is reflected in a discontinuous drop to a lower temperature for the contours.

Repeating the calculations for a sink temperature of $350K$ produces the results shown in figure 3.8. The intersection of the dewline with the sink temperature and the associated

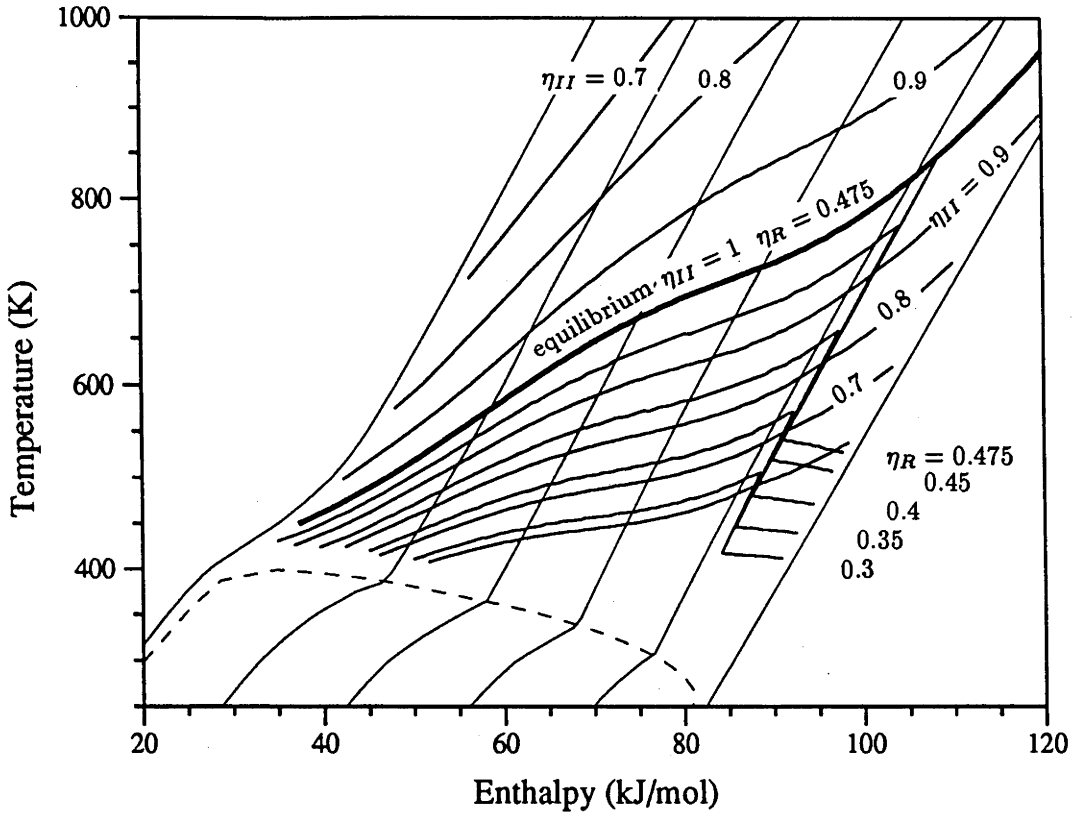

Figure 3.7: Constant exergetic and work recovery efficiency contours for $T_s = 300K$ and a pressure of 200 atmospheres.

discontinuity occurs at a lower value of reaction extent. The equilibrium line remains the same but its corresponding work recovery efficiency in the spontaneous separation region is lower as a consequence of the higher sink temperature. Raising the sink temperature (the zero efficiency contour) also has the effect of moving all the contours closer to the equilibrium line.

Raising the sink temperature to $400K$ (figure 3.9) results in the dewline remaining below the sink temperature for all values of reaction extent. As a result no spontaneous separation occurs at the sink temperature, $\frac{\partial G}{\partial \delta}|_{(T_s,\delta)}$ and $\frac{\partial H}{\partial \delta}|_{(T_s,\delta)}$ are not constant and the contours of exergetic efficiency are no longer equivalent to the contours of work recovery efficiency in any region.

In regions above the dewline, $\frac{\partial G}{\partial \delta}$ and $\frac{\partial H}{\partial \delta}$ vary in a manner roughly proportional to the reaction extent, for all temperatures and as a result work recovery efficiency contours are nearly isothermal. This is typical of a thermochemical system without spontaneous separation, for example Carden (1980*b*) examined the sulphur trioxide based system and found that work recovery efficiency contours were almost exactly isothermal.

To illustrate the effect of sink temperature more explicitly, figures 3.10 and 3.11 show contours of $\eta_{II} = 0.7$ and $\eta_r = 0.3$ respectively, for a range of sink temperatures. Figure 3.10 shows both the exothermic and endothermic exergetic efficiency contours moving closer to the equilibrium line as the sink temperature is raised. Figure 3.11 also reflects this trend but in addition shows the transition to an almost isothermal curve which intersects the equilibrium line.

The figures presented here all correspond to a system pressure of 200 atmospheres.

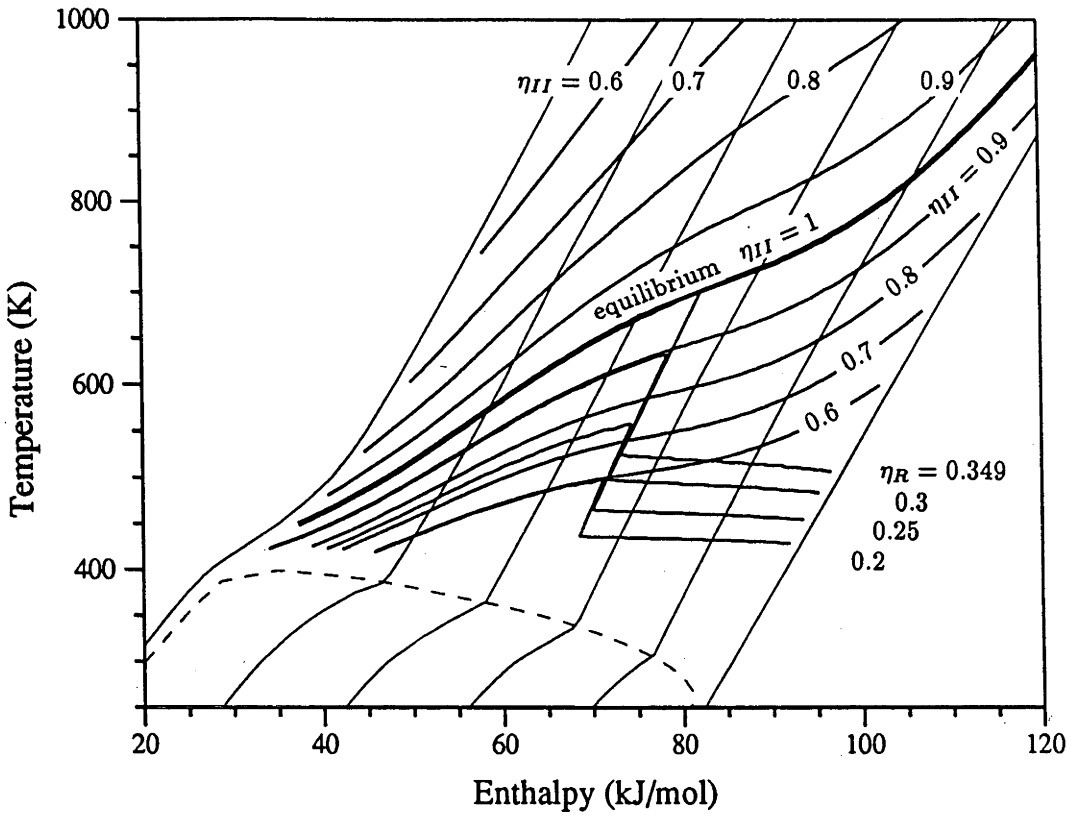

Figure 3.8: Constant exergetic and work recovery efficiency contours for $T_s = 350K$ and a pressure of 200 atmospheres.

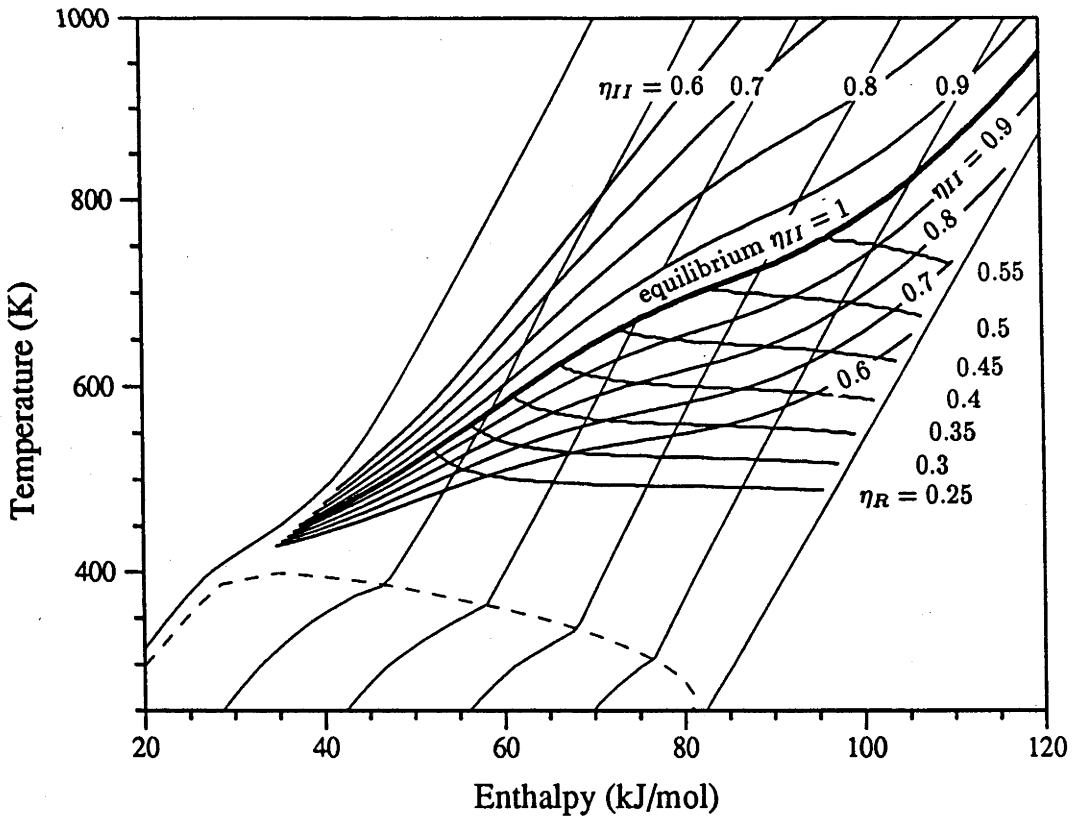

Figure 3.9: Constant exergetic and work recovery efficiency contours for $T_s = 400K$ and a pressure of 200 atmospheres.

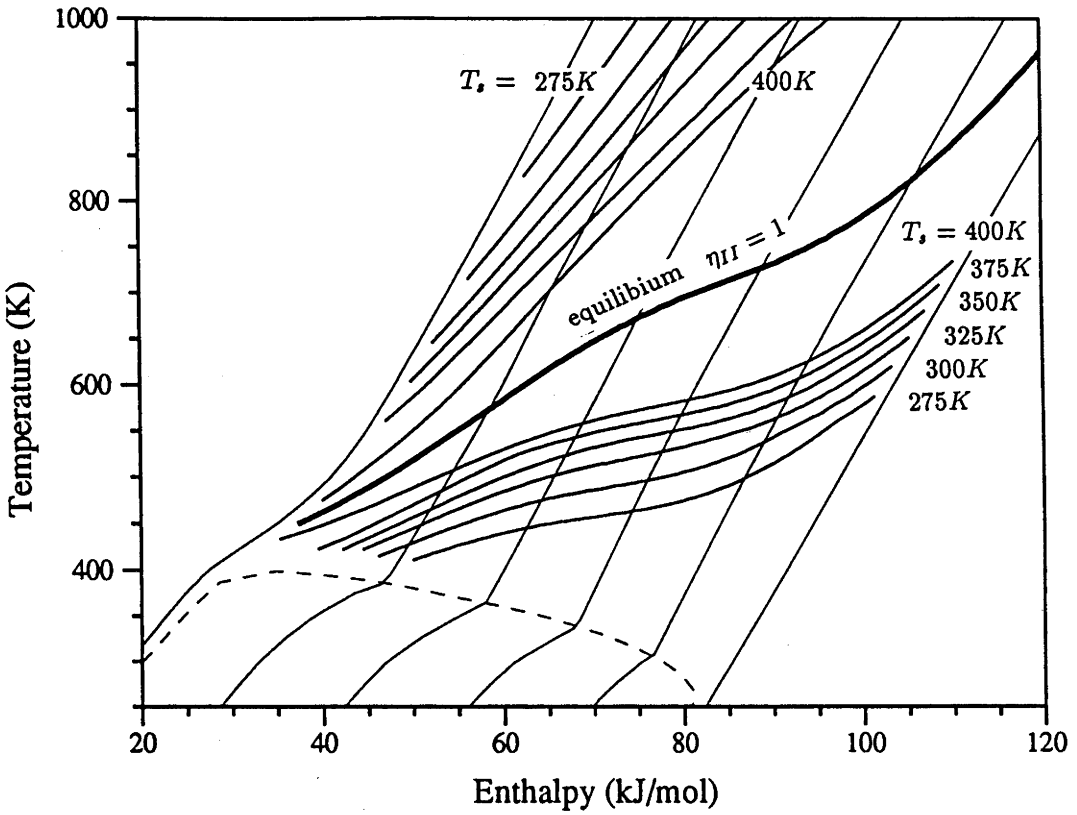

Figure 3.10: Constant exergetic efficiency =0.7 contour for $T_s = 275K - 400K$ and a pressure of 200 atmospheres.

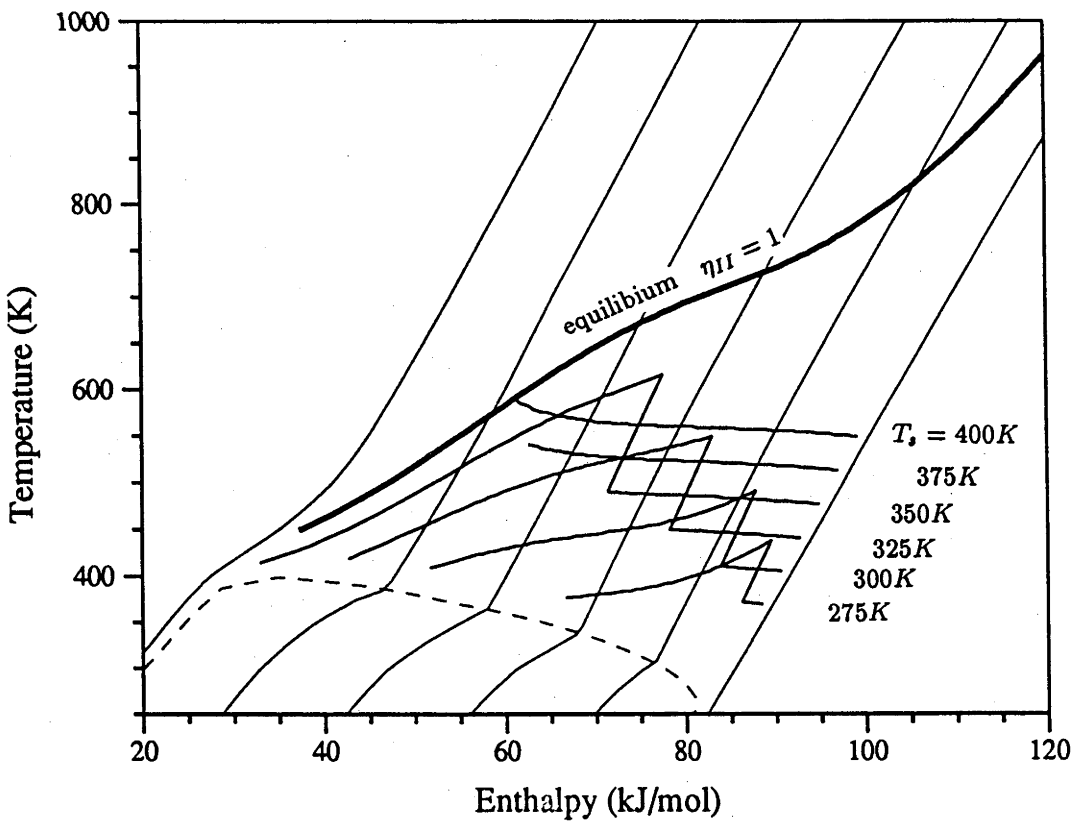

Figure 3.11: Constant work recovery efficiency =0.3 contour for $T_s = 275K - 400K$ and a pressure of 200 atmospheres.

Variation of the pressure moves the equilibrium line as indicated in figure 3.1, other constant efficiency contours simply move in proportion to there relative proximity to the equilibrium line

To extend an exergetic analysis to a more realistic situation, the assumptions about heat exchanger irreversibility which were used in the discussion of first law efficiency could be included. In this case, analysis must be based on a direct evaluation of equation 3.19. Introducing heat exchanger irreversibilities does not alter the path which the 1 mole equivalent thermodynamic system traverses. Instead, it determines the temperature which each enthalpy increment is degraded to or from, and it is this series of temperatures which must be used in equation 3.19.

Although an analysis of an infinitesimal transition could be made on this basis, it is of reduced significance since a finite transition is no longer equivalent to an integral of infinitesimals. A more relevant approach is to compare similar finite paths which share major common features such as inlet reaction extent.

3.5 Characteristic Temperatures

The analysis of the exergy transfers associated with a heat transfer process is equivalent to determining the characteristic temperature of the heat transfer process. A characteristic temperature (T_c) can be defined such that:

$$\Delta\Phi = \int dH \left(1 - \frac{T_s}{T}\right) \equiv \left(1 - \frac{T_s}{T_c}\right) \int dH. \tag{3.32}$$

It can be recognised that the term $\left(1 - \frac{T_s}{T_c}\right)$ is equal to the work recovery efficiency for an exothermic thermochemical process. This illustrates the essential difference between the work recovery efficiency and the exergetic efficiency. The work recovery efficiency for an irreversible path primarily quantifies its characteristic temperature and only implicitly gives information on the degree of irreversibility. The exergetic efficiency explicitly measures the degree of irreversibility, but does not contain enough information to identify the characteristic temperature. Comparison of equation 3.32 with equation 3.23 shows that the characteristic temperature for an equilibrium process is:

$$T_{c\ \text{equil}} = \frac{\Delta H(T_s)}{\Delta S(T_s)}. \tag{3.33}$$

The value of $T_{c\ \text{equil}}$ for reaction from $\delta = 0$ to $\delta = 1$ is a characteristic temperature for the reaction, ie;

$$T_c^* = \frac{\Delta H_o(T_s)}{\Delta S_o(T_s)} \tag{3.34}$$

where ΔH_o and ΔS_o are the enthalpy and entropy changes of the reaction.

T_c^* is a useful parameter for evaluating reaction systems for energy storing applications. Williams & Carden (1979*d*) discuss this characteristic temperature and relate it to the turning temperature, a characteristic temperature defined by the condition that the equilibrium constant be equal to unity (Wentworth & Chen 1976).

Another consequence of the spontaneous separation attribute of the ammonia system is the equality of $T_{c\ \text{equil}}$ and T_c^*. The fact that the equilibrium line is a contour of constant (maximum) work recovery efficiency is an expression of this. This means that equilibrium paths between values of δ which are both less than approximately 0.5, operate over a range of temperatures which are always less than the characteristic temperature. This is only

possible if the net enthalpy change of such paths is the result of both positive and negative changes with the positive contribution occurring at a higher average temperature than the negative contribution.

Examination of the temperature enthalpy diagram for the ammonia system suggests that this condition is satisfied as a consequence of the variation in $\frac{\partial H}{\partial T}$ associated with the phase change of the ammonia component. The precise nature of this connection can be demonstrated. Rewriting equation 3.32 for an infinitesimal process that starts and ends at the sink temperature gives:

$$\frac{d\Phi}{dH} = \frac{d\Phi}{d\delta}\left.\frac{\partial \delta}{\partial H}\right|_{T_s,\delta} = \left(1 - \frac{T_s}{T_c}\right). \tag{3.35}$$

Thus for a separating system with constant $\left.\frac{\partial H}{\partial \delta}\right|_{T_s,\delta}$, the condition $T_{c\ equil}$ = const. is equivalent to the condition $\left.\frac{d\Phi}{d\delta}\right|_{(T_s,\delta)}$ = constant, or $\left.\frac{d^2\Phi}{d\delta^2}\right|_{(T_s,\delta)} = 0$, for any infinitesimal path.

Referring back to equations 3.21 and 3.22, the exergy transferred when an infinitesimal reversible reaction path is followed is:

$$\frac{d\Phi}{d\delta} = -\frac{\partial}{\partial \delta}\left(\int_{T_s}^{T_f} \left.\frac{\partial H}{\partial T}\right|_{(T,\delta)} \left(1 - \frac{T_s}{T}\right) dT\right) + \left.\frac{\partial H}{\partial \delta}\right|_{(T_f,\delta)} \left(1 - \frac{T_s}{T_f}\right). \tag{3.36}$$

Substitution of $\left.\frac{\partial H}{\partial \delta}\right|_{(T,\delta)} = \Delta H_o(T) + \left.\frac{\partial H_m}{\partial \delta}\right|_{(T,\delta)}$ (where H_m is the contribution to the enthalpy due to the mixing of non-ideal components) in the heat exchanger contribution and $\frac{1}{T}\frac{\partial H}{\partial \delta} = \frac{\partial S}{\partial \delta}$ for the reversible reaction contribution yields:

$$\frac{d\Phi}{d\delta} = -\int_{T_s}^{T_f} \frac{\partial}{\partial T}\left(\Delta H_o(T) + \left.\frac{\partial H_m}{\partial \delta}\right|_{(T,\delta)}\right)\left(1 - \frac{T_s}{T}\right) dT + \left.\frac{\partial H}{\partial \delta}\right|_{(T_f,\delta)} - T_s \left.\frac{\partial S}{\partial \delta}\right|_{(T_f,\delta)} \tag{3.37}$$

from which:

$$\frac{d^2\Phi}{d\delta^2} = \frac{\partial^2}{\partial \delta^2}\left(-\int_{T_s}^{T_f} \left.\frac{\partial H_m}{\partial T}\right|_{(T,\delta)} \left(1 - \frac{T_s}{T}\right) dT + H_m(T_f,\delta) - T_s S_m(T_f,\delta)\right). \tag{3.38}$$

The factor in brackets can be at most a linear function of δ if $\frac{d^2\Phi}{d\delta^2}$ is to equal zero. At reaction temperatures, thermochemical systems can be regarded to good approximation as ideal mixtures, so the mixing enthalpy term $H_m(T_f,\delta)$ can be taken as zero. The term $T_s S_m(T_f,\delta)$ is the work that would be required to separate the components at the sink temperature if the mixture remained ideal at all temperatures. The integral term represents the reduction in exergy transferred, on cooling from T_f, as a consequence of non-zero mixing enthalpy. Carden & Williams (1978*b*) have shown that this reduction in exergy is equal to the separation work for the equivalent ideal mixture, as might be expected. Thus for a spontaneously separating system, the temperature dependence of mixing enthalpy is not only a reflection of the need for separation to proceed without violation of the second law, but also naturally results in all equilibrium reaction paths having the same characteristic temperature.

The opposite extreme to a spontaneously separating system is a situation where the specific heat at constant pressure is independent of δ. In this case the only exergy contribution will be that of the reaction and hence the characteristic temperature will be equal to the average equilibrium temperature for a reversible path.

A non-separating system, with its consequently varying characteristic temperature, introduces the possibility of choosing reaction composition endpoints (obviously the same

for exothermic and endothermic reactions) so as to match the characteristic temperature to an available heat source. A spontaneously separating system does not have this option, although decisions may be influenced by the temperature range of enthalpy transfer associated with different reaction endpoints.

The possibility of variation of characteristic temperature through choice of reaction endpoints also suggests the interesting possibility of operating an otherwise non-separating system as a chemical heat pump via the application of the necessary separation work. A spontaneously separating system could also be considered as a heat pump if the heat transfers to and from the heat exchangers are considered equivalent to the external supply of work. Viewed in this way, the enthalpy change in the reactor is the component which is absorbed and then subsequently largely released at a higher temperature.

3.6 Direct Work Recovery.

As was described in section 3.1, the ideal reaction path of an exothermic reactor from which the heat is extracted by a secondary fluid will have a slope linearly dependent on the specific heat of the secondary fluid. This dependence can be expressed formally as:

$$\left.\frac{\partial H}{\partial T}\right|_{(T,\delta)\ \text{reaction path}} = C_{p_{\text{second}}} \frac{\dot{m}_{\text{second}}}{\dot{m}_{\text{reactant}}} + \left.\frac{\partial H}{\partial T}\right|_{(T,\delta_1)}. \tag{3.39}$$

The second term on the right is the contribution due to the assumed preheating of the reactants in a heat transfer passage from the coldest to the hottest end of the reactor. This constraint on reaction path slope defines the possible exit conditions that can be reached from a given inlet condition, noting of course that the path must remain on the exothermic side of the equilibrium line. In practice it is the inlet reaction extent and inlet temperature of the secondary fluid (which must then become the exit temperature for the reactor) which are predetermined. The reactor inlet temperature and exit reaction extent are then determined by the condition that;

$$\int_{\delta_1\ \text{reaction path}}^{\delta_2} \frac{A d\delta}{R(T,\delta)} = \text{reactor volume} \tag{3.40}$$

where A is a constant which reconciles the dimensions of reaction rate (R), with volume.

When the ammonia based thermochemical system was conceived in the context of solar thermal electric systems, an early assumption made was that the thermochemical system would be coupled to a steam-based heat engine which would otherwise have been supplied by heat directly from the solar receivers. However, the exergetic efficiency of reaction paths that are obtainable with steam as a secondary fluid are limited by the inflexion points caused by the water/steam phase change and the need to preheat the inlet water. Carden (1987) has pointed out these difficulties and presented a new concept termed 'direct work recovery'. The essence of the concept is to use the reaction products themselves as the working fluid for a heat engine. The reaction products extract the thermal output of the reactor by flowing through reheat passages which take them from the reactor exit temperature back to the higher reactor inlet temperature. The slope of the reaction path can no longer be varied by a continuous variation in flow rate. However there is the option of varying the number of expansion plus reheat stages used. Fortuitously the path that results from the combination of two reheat paths in combination with the incoming reactant preheat path has a slope almost parallel to the equilibrium line, thus providing no limit on the maximum possible exergetic efficiency that can be obtained. Figure 3.12,

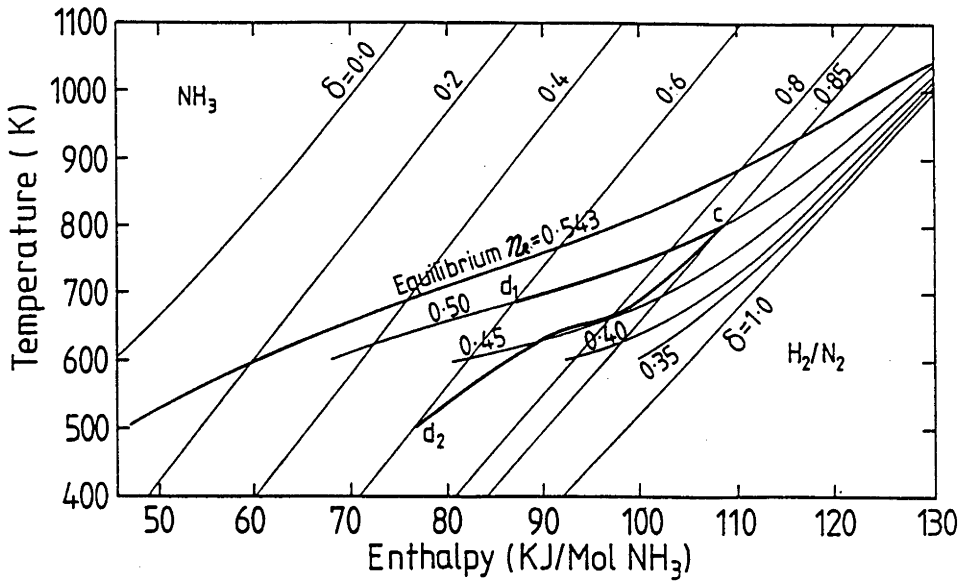

Figure 3.12: Comparison of reaction paths, between $\delta = 0.85$ and $\delta = 0.6$, from steam based heat recovery (c–d_2) and direct work recovery (c–d_1), taken from Carden (1987) (pressure 300 atmospheres).

compares possible steam-based or direct work reaction paths that share a common initial reaction extent and temperature.

The currently favoured arrangement is shown schematically in chapter 1, figure 1.4. This arrangement incorporates two stages of adiabatic expansion of the outlet reactants (one following each reheat process), producing the work output in conjunction with the isothermal compression of inlet reactants. The first stage of expansion should be stopped at the point where the temperature has again dropped to the lowest reactor temperature so that the three parallel heat extraction processes remain consistent. This arrangement has the endothermic half of the system operating at the lower pressure. The exothermic reaction products could equally well be recompressed before the separator, allowing the endothermic reactor to operate at the higher pressure. The option of operating the endothermic reactor at a lower pressure, has the advantage that the resulting shift in the chemical equilibrium compositions will give improved reaction rates. This shift in the position of equilibrium lowers the characteristic temperature of the endothermic process. Although the exergy output of the exothermic process is unchanged, the exergy absorbed by the endothermic process is reduced. The difference is equal to the extra work that must be done to recompress the exothermic reaction inlet reactants compared to the alternative of recompressing the exothermic products (which consist of a greater liquid fraction and a smaller total number of molecules). The net result is a reduction in the total system exergetic efficiency.

Carden has assumed that, particularly in the context of large scale solar thermal electric systems, the expansion and compression stages would use turbines. He points out that for ammonia $\frac{dS_{dew}}{dP}$ for an adiabatic process is negative, so eliminating the possibility of droplet formation during the expansions which could cause damage in high speed turbines. He also notes that the high system pressure should result in compact and, hence, cost-efficient turbine construction.

The analysis of exergy transfer and the resulting efficiencies presented in section 3.4 assumed only that the heating and cooling processes were reversible and the initial and

final endpoints at the sink temperature were at the same pressure as the reactor. As a result, provided the expansion and recompression processes are reversible, the results can be applied to the direct work recovery situation as well. The analysis of the direct work recovery system when expansion and compression are not reversible is more complicated. Carden addressed this problem by treating each component (heat exchanger, reactor, expanders and compressor) as a separate open thermodynamic system.

Chapter 4

Kinetics and Reactor Modelling

4.1 Chemical Reaction Mechanisms

4.1.1 Introduction

Chemical reaction systems are frequently classified as homogeneous or heterogeneous according to whether there is either one phase or more than one involved in the system. The simplest is a homogeneous reaction and the most frequently encountered situation involves all the reactants in the gas phase. Reactions involving gas reactants and solid catalysts (such as ammonia dissociation or synthesis) are heterogeneous, although the possibility remains that a homogeneous reaction could proceed in parallel with the heterogeneous catalysed reaction.

A consideration of homogeneous gas reactions provides an insight into some of the basic processes which are common with heterogeneous catalytic reactions. For a simple single step reaction;

$$\mathsf{A} + \mathsf{B} \rightleftharpoons \mathsf{C} \tag{4.1}$$

reactant molecules A and B may react to form a product molecule C after a collision if the AB complex has an energy, derived from the combined energies of translation, rotation and vibration etc, which exceeds a certain activation energy. This can be explained simplistically by the need to break existing bonds in the reactants before making the new product molecules. This process is often illustrated with the mechanical analogy of a particle on a hill (figure 4.1), with one side representing the reactants, the peak the activated complex, and the other the products. The height of the peak represents the activation energy for the process and the difference between the levels of A + B and C is the change in energy of the reaction, either positive or negative.

For an ideal gas system the frequency of collisions will be proportional to the product of partial pressures (pressures raised to the stoichiometric coefficients if these are not unity). The probability that the energy of the AB complex will exceed a certain activation energy is given by the Boltzmann relation. Hence the reaction rate for the forward reaction (R_1) is given by;

$$R_1 = k_1 e^{\left(\frac{-E_{a1}}{kT}\right)} p_A p_B \tag{4.2}$$

where E_a is the activation energy, k_1 a rate constant k the Boltzmann constant and p_A and p_B are the partial pressures of A and B. The same holds for the reverse reaction rate (R_2):

$$R_2 = k_2 e^{\left(\frac{-E_{a2}}{kT}\right)} p_C. \tag{4.3}$$

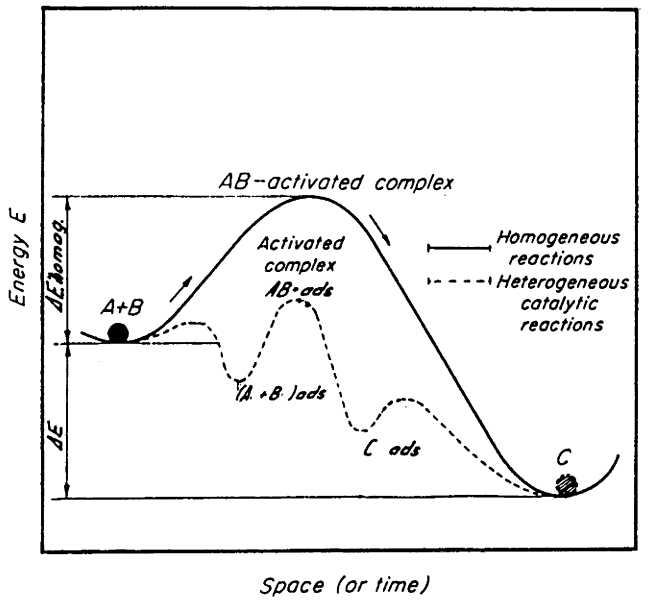

Figure 4.1: Mechanical analogy of homogeneous and heterogenous catalytic reaction mechanisms, adapted from Vancini (1971) (*ads* ≡ species adsorbed on catalyst surface).

Thus the overall reaction rate will be:

$$R = k_1 e^{\left(\frac{-E_{a_1}}{kT}\right)} p_A p_B - k_2 e^{\left(\frac{-E_{a_2}}{kT}\right)} p_C. \tag{4.4}$$

If E_a is taken as the average of E_{a_1} and E_{a_2} (which differ by the free energy change of the reaction), and substituting for the equilibrium constant ($K_p = \frac{k_2}{k_1}$), this becomes;

$$R = k_0 e^{\left(\frac{-E_a}{kT}\right)} [p_A p_B - K_p p_C] \tag{4.5}$$

which will equal zero at chemical equilibrium. This rate expression assuming, as it does, ideal gas behaviour and a constant activation energy, none the less fits observed behaviour for many homogeneous gas reactions.

4.1.2 The Role of Catalysts

For many gas reactions the activation energy is low enough that simply heating the products will produce an appreciable reaction rate (for example the reaction $2H_2 + O_2 \rightarrow 2H_2O$). For other reactions however the magnitude of the activation energy is such that reactants must be heated to impractically high temperatures to observe an appreciable reaction rate. The synthesis or dissociation of ammonia falls in the latter category.

The role of a catalyst is to introduce extra steps into the reaction system, without changing the overall reaction. If successful these steps will each have activation energies lower than the single activation energy of the homogeneous reaction. In the mechanical analogy this amounts to replacing the large hill with a series of small ones (figure 4.1).

Heterogeneous catalytic reactions such as the ammonia reaction involve gaseous reactants and solid catalysts. The catalyst is usually in the form of porous particles, with the pores serving to maximise the surface area of catalyst available to reactants. As a result, a series of processes control the overall rate at which products are formed:

1. mass transfer to the particle surface;

2. diffusion into the pores;
3. chemical adsorption of reactants onto the catalyst surface;
4. reaction on the surface;
5. desorption of the products;
6. diffusion of products out of the pores;
7. mass transfer away from the particle.

Processes 3, 4 and 5 combine to determine the so called intrinsic reaction rate of a heterogeneous catalytic reaction. Processes 1, 2, 6 and 7 are dependent on the structure of the catalyst particles and the conditions within the reactor. Processes 3,4 and 5 are likely to involve several steps each. The adsorption and desorption of each reactant/product being a separate step, and the reaction on the surface also being a multistep process. Frequently it is the case that one of these steps will be substantially slower than the others and hence the 'rate determining' step for the heterogeneous reaction. A single rate determining step greatly simplifies the task of developing a reaction rate expression.

If one of the surface reaction steps is the slowest, then a rate expression similar to equation 4.5 is expected, but with the surface coverage (the fraction of the sites suitable for adsorption occupied) rather than the pressure determining the frequency of interaction. In this situation, the adsorption process will be an equilibrium between adsorption and desorption. The surface coverage can be related to system partial pressures (at constant temperature) via a model of the adsorption equilibrium process. A common model used is the 'Langmuir isotherm'; this is derived by assuming the adsorption rate for a particular substance is proportional to its partial pressure and the uncovered surface area, and the desorption rate is proportional the substance's partial pressure and the covered area, with the two rates being equal at equilibrium. Reaction rate expressions derived from this model are known as 'Langmuir Hinshelwood' rate expressions and are frequently encountered in the literature. Other adsorption models which have proved empirically useful include the 'Freundlich' isotherm which gives a surface coverage proportional to a power of the partial pressure, and the 'Frumkin Slygen' expression which consists of a logarithmic dependence.

In contrast to the above are reaction systems where one of the adsorption or desorption steps is the slowest; in this case the surface reaction is assumed to be in equilibrium. The ammonia reaction appears to fall in this category.

4.1.3 Mechanism for the Ammonia Reaction

For the ammonia synthesis/dissociation reaction;

$$N_2 + 3H_2 \rightleftharpoons 2NH_3 \tag{4.6}$$

carried out on a solid catalyst, six steps have been identified (Vancini 1971).

adsorption	$H_2 \rightleftharpoons 2H_{ad}$
	$N_2 \rightleftharpoons 2N_{ad}$
Reaction	$N_{ad} + H_{ad} \rightleftharpoons (NH)_{ad}$
	$(NH)_{ad} + H_{ad} \rightleftharpoons (NH_2)_{ad}$
	$(NH_2)_{ad} + H_{ad} \rightleftharpoons (NH_3)_{ad}$
desorption	$(NH_3)_{ad} \rightleftharpoons NH_3$

All these steps are chemically reversible as is the overall reaction, so proceeding in the dissociation direction is simply a matter of reversing all the steps and their order, with the adsorption steps becoming desorption and vice versa.

By conducting experiments using such techniques as radioisotope exchange, it is possible to measure the rate of each individual step and thus determine which is the slowest and hence the rate determining step. It is generally accepted that nitrogen adsorption is the slowest step and the major determinant in the overall intrinsic rate for the ammonia reaction.

The most commonly used rate expression for the ammonia reaction is the 'Temkin-Pyzhev' rate expression. This rate expression, in common with many functional expressions used for predicting effects in catalyst reaction systems, is semi-empirical. Expressions of this type are derived by assuming a simplified model for the process in question, then deriving an analytical expression often based on plausibility arguments. The expression is tested for correlation with experimental results and, if deemed successful, the empirical constants included are fitted to available data to yield an expression capable of predicting behaviour at least over some range of applicability. The arguments leading to the Temkin-Pyzhev rate expression which are given here largely follow those presented by Vancini (1971).

The rate determining step is the chemisorption of nitrogen ie:

$$N_2 \rightleftharpoons 2N_{ad}. \tag{4.7}$$

The rate of this single reaction step will be given by an expression similar to that for a homogeneous gas reaction, however the assumption is made that the activation energy, rather than being constant, is linearly dependent on surface coverage (Θ) thus;

$$\begin{aligned} R &= R_{ad} - R_{des} \\ &= k_a p_{N_2} e^{-\left(\frac{E_a}{RT} + A\Theta\right)} - k_d e^{-\left(\frac{E_a}{RT} - B\Theta\right)} \end{aligned} \tag{4.8}$$

where A and B are products of $\frac{1}{T}$ and constant factors and have dimensions of inverse surface coverage. Although the nitrogen adsorption process is not in equilibrium, all other steps, including the surface reaction and ammonia desorption, are assumed to be. Thus it follows that the surface concentration of adsorbed nitrogen will be in a resultant equilibrium with the gas concentrations of ammonia and hydrogen. Temkin and Pyzhev expressed this as being equivalent to a situation of adsorption equilibrium between surface nitrogen and a 'virtual' partial pressure of nitrogen (p'_{N_2}), derived from the ammonia and hydrogen pressures and the homogeneous reaction equilibrium constant;

$$p'_{N_2} \equiv K_p^{-1} \left(\frac{p^2_{NH_3}}{p^3_{H_2}} \right) \tag{4.9}$$

where K_p is the equilibrium constant for the reaction as presented in equation 4.6. They then use the Frumkin Slygen expression for the adsorption isotherm to relate the surface coverage to this virtual gas pressure:

$$\Theta = \frac{1}{A+B} ln \left(\frac{k_a}{k_d} p'_{N_2} \right). \tag{4.10}$$

This expression removes all but the activation energy term from the exponential in equation 4.8 and leads to;

$$R = e^{-\frac{E_a}{kT}} \left(k_a p_{N_2} \left(\frac{k_a}{k_d K_p} \frac{p_{NH_3}^2}{p_{H_2}^3} \right)^{\frac{-A}{A+B}} - k_d \left(\frac{k_a}{k_d K_p} \frac{p_{NH_3}^2}{p_{H_2}^3} \right)^{\frac{B}{A+B}} \right) \tag{4.11}$$

which, after defining $\alpha = \frac{A}{(A+B)}$ and reconfiguring the constants, becomes;

$$R = k_0 e^{-\frac{E_a}{kT}} \left(K_p^{-1} p_{N_2} \left(\frac{p_{H_2}^3}{p_{NH_3}^2} \right)^{\alpha} - \left(\frac{p_{NH_3}^2}{p_{H_2}^3} \right)^{1-\alpha} \right) \tag{4.12}$$

where k_0 is the pre-exponential rate constant. This is the form of the Temkin-Pyzhev rate equation that has been used in the reactor simulation program discussed later. An empirical value of $\alpha = 0.5$ is frequently quoted.

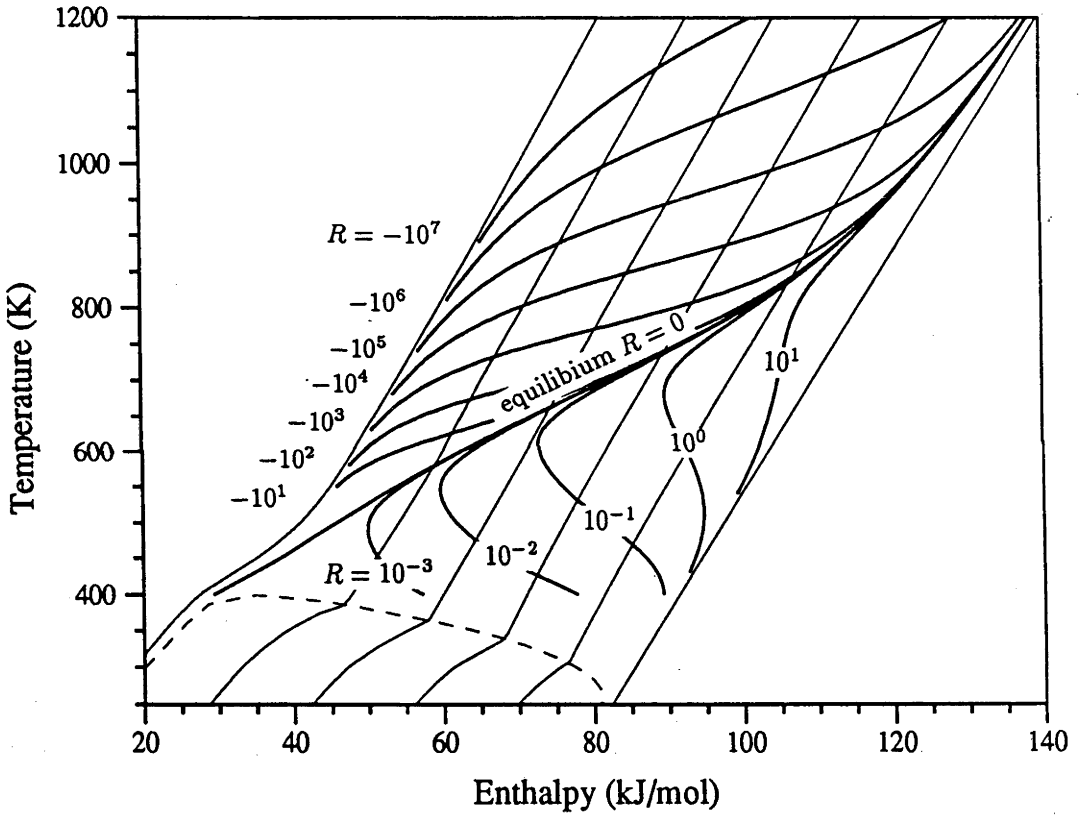

Figure 4.2: Constant relative rate contours for an activation energy of $1.59 \times 10^5 kJmol^{-1}$ (promoted iron synthesis catalyst), system pressure 200 atmospheres.

As mentioned before, rate expressions such as this are semi-empirical and cannot be expected to work universally. Replacing the partial pressures by fugacities helps to extend the range to higher pressures, but aside from this, the simplifying assumptions embodied in the derivation are the limiting factor. Nielsen (1970), in a review article, discusses experimental results which point to a more complex series of reaction steps which may actually vary with conditions. The possibility of the existence of two consecutive rate determining steps is also raised and some more complex rate equations based on this are presented.

Figure 4.2 and figure 4.3 show contours of constant relative reaction rate, calculated using equation 4.12 with two different activation energy values. The unity rate contour has

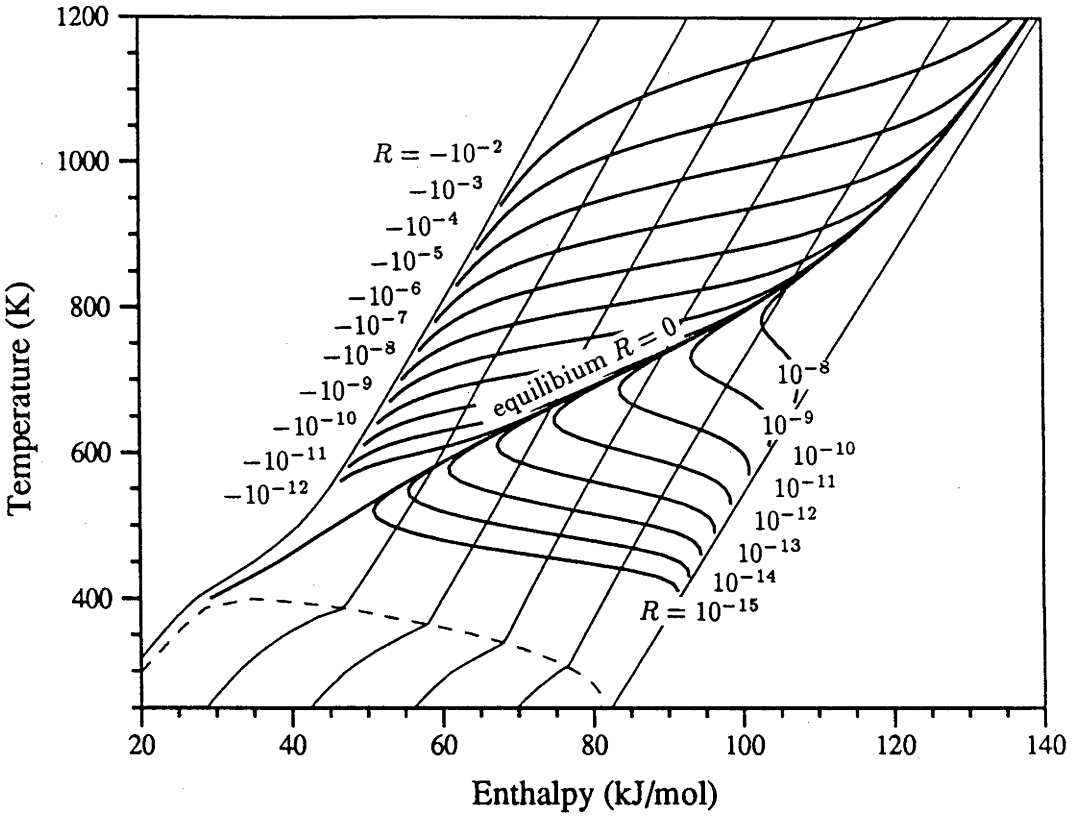

Figure 4.3: Constant relative rate contours for an activation energy of $2.58 \times 10^5 kJmol^{-1}$ (nickel on alumina dissociation catalyst), system pressure 200 atmospheres.

been arbitrarily chosen as the exothermic contour passing through $T = 600K$ and $\delta = 0.8$ for the $1.59 \times 10^5 kJmol^{-1}$ activation energy. The rate expression consists of a product of a strongly temperature dependant factor (the Arrhenius factor) and a factor which quantifies the degree of departure ('distance') from equilibrium. For the endothermic reaction this produces constant rate contours with average slopes in between isothermal and that of the equilibrium line. For the exothermic reaction, the two factors are in conflict, ie moving away from the equilibrium line to lower temperatures results in a decrease in the first factor and an increase in the second. Near the equilibrium line the 'distance' factor, which is equal to zero at equilibrium, changes rapidly and dominates the final result. At lower temperatures the temperature dependant factor dominates, hence the characteristic change in direction of the rate contours at the point where $\frac{\partial R}{\partial T}|_\delta = 0$.

Increasing the activation energy (with the pre-exponential rate constant unchanged) decreases the magnitude of both endothermic and exothermic rates. It also has the effect of bringing the constant reaction rate contours closer together and bringing the points at which $\frac{\partial R}{\partial T}|_\delta = 0$ closer to the equilibrium line.

4.2 Modelling Catalytic Reactors

4.2.1 Introduction

Since reactions on a solid catalyst are surface reactions, a catalyst structure which maximises surface area to volume ratio is desirable. However there is also the sometimes

conflicting requirement that the desired flow rate of reactants through the reactor be maintained without an excessive pressure drop.

The most common method of achieving these aims is to fill a volume with porous catalyst particles of a uniform size, usually between 1 and $20mm$ in diameter. The pores within the particles give effective surface areas of around $40m^2$ per cm^3 of bed, whilst the voids between the particles, often around 40% of the total volume, allow the reactants to flow without excessive pressure drop. The catalyst particles may be entirely composed of the catalyst material, as is the case for example with 'promoted iron' ammonia synthesis catalysts, or may consist of an inert support which is impregnated with the catalyst material, such as the 'nickel on alumina' ammonia dissociation catalyst used in the course of this project.

There are other possible configurations, such as constructing the reactor from a single piece of ceramic foam catalyst support or employing a fluidised bed of fine particles. The reactor model discussed here deals with a conventional packed bed of catalyst particles.

4.2.2 Processes in a Packed Bed Reactor

Numerous processes combine to determine the conditions at any point within a packed catalyst bed, these are illustrated schematically in figure 4.4. These processes can be

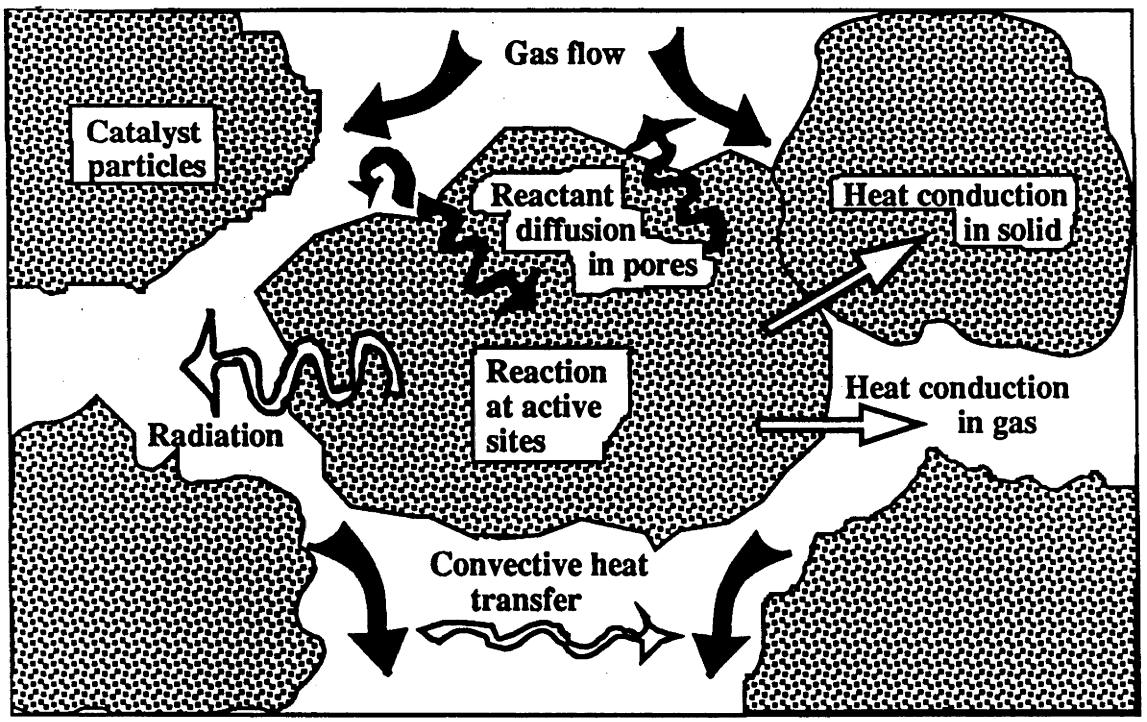

Figure 4.4: Heat mass transfer and reaction processes within a catalyst bed.

categorised as follows:

- Heat transfer processes (both within the bed and to the walls);

- radiation between solids
- conduction in the solid
- conduction in the fluid
- convection in the fluid

- Mass transfer processes;
  - diffusion in particle pores
  - diffusion in the bed
  - dispersion in the bed
  - average flow

- Reaction;
  - within the pores with rate determined by local conditions
  - acts as a source or sink of heat and reactants.

Exactly specifying the conditions within a packed bed reactor would require values for all the thermodynamic variables at each point as well as specifying whether each point was within a particle or void. This represents an extremely complex three dimensional problem. Although a numerical solution might be attempted for one or two catalyst particles, it is impractical for an extended catalyst bed.

4.2.3 The Two-Dimensional Steady State Pseudo Homogeneous Model

A more realistic approach than attempting a numerical solution of the complete heterogeneous problem, is to use a 'pseudo homogeneous' model. This means treating the catalyst bed as a continuum and representing the conditions at each point by local averages of the various quantities.

If all the mass and heat transfer processes, with the exception of those due to the average gas velocity, are lumped together then the standard heat conduction and Fick's law diffusion equations can be applied. This is done by defining an 'effective conductivity' (K_{eff}) and an 'effective diffusivity' (D_{eff}), both of which will vary with local conditions. Having done this, application of the principles of energy, mass and momentum conservation to a differential volume element yields the basic governing equations.

The general three dimensional energy conservation equation with heat conduction as the only heat transfer process is (see for example Incropera & Dewitt (1985));

$$\rho \underline{v}.\underline{\nabla} e - \underline{\nabla}.(K_{eff}\underline{\nabla} T) - R\Delta H - \Psi - \underline{v}.\underline{\nabla} P = -\frac{\partial(\rho u)}{\partial t} \tag{4.13}$$

where ρ is the density, e is the specific enthalpy, u the specific internal energy, $\underline{v}$ the velocity, Ψ the 'dissipation' (quantifying the contribution due to frictional forces) and $\underline{\nabla}$ the vector differentiation operator ($\equiv \frac{\partial}{\partial x}\underline{i} + \frac{\partial}{\partial y}\underline{j} + \frac{\partial}{\partial z}\underline{k}$ in cartesian coordinates). similarly the three dimensional mass conservation equation, in terms of reaction extent is;

$$\frac{C_0}{\rho_0}\underline{\nabla}.(\underline{v}\rho\delta) - \frac{C_0}{\rho_0}\underline{\nabla}.(D_{eff}\underline{\nabla}(\rho\delta)) - R = -\frac{C_0}{\rho_0}\frac{\partial(\rho\delta)}{\partial t} \tag{4.14}$$

where C_0 is the initial concentration of the primary reactant (ammonia) and ρ_0 is the initial density.

The computer program for numerical solution used for this project is an extension of a program developed at the University of Houston specifically for modelling steam methane reforming reactors. The original program and the assumptions embodied in the model have been presented by Richardson et al. (1988). The algorithm and the changes made to the original program are described in appendix B.

The model covers steady state behaviour in radially symmetric constant diameter annular cylindrical beds (including tubular reactors as a limiting case). Using the simplifying assumptions that average longitudinal flow dominates longitudinal diffusion (the plug flow assumption), that viscous forces and pressure drops are insignificant, that the average velocity and the density are constant and that the gradients of the specific heat, the effective conductivity and the effective diffusivity are much smaller than the temperature and reaction extent gradients, leads to simplified governing equations. The energy conservation equation becomes;

$$\frac{\rho v C_p}{m}\frac{\partial T}{\partial z} - K_{eff}\left(\frac{\partial^2 T}{\partial r^2} + \frac{1}{r}\frac{\partial T}{\partial r}\right) - R\Delta H = 0 \tag{4.15}$$

where v is the average longitudinal flow velocity, C_p is the local value of specific heat at constant pressure for the mixture and m the average molecular weight. The boundary conditions are;

$$\begin{aligned} T &= T_{in} \quad \text{at} \quad z = 0 \\ (h_w \Delta T)_{wall} &= \left(-K_{eff}\frac{\partial T}{\partial r}\right)_{r_{wall}} \end{aligned} \tag{4.16}$$

where h_w is an effective heat transfer coefficient for the wall. The mass conservation equation becomes:

$$\frac{\partial \delta}{\partial z} - \frac{D_{eff}}{v}\left(\frac{\partial^2 \delta}{\partial r^2} + \frac{1}{r}\frac{\partial \delta}{\partial r}\right) - \frac{R}{C_0 v} = 0. \tag{4.17}$$

Turbulent diffusion processes are frequently parameterized with a Peclet number;

$$N_{PE} \equiv \frac{d_p v}{D_{eff}} \tag{4.18}$$

using this definition the mass conservation equation can be rewritten as:

$$\frac{\partial \delta}{\partial z} - \frac{d_p}{N_{PE}}\left(\frac{\partial^2 \delta}{\partial r^2} + \frac{1}{r}\frac{\partial \delta}{\partial r}\right) - \frac{R}{C_0 v} = 0. \tag{4.19}$$

The boundary conditions for mass conservation are:

$$\begin{aligned} \delta &= \delta_{in} \quad \text{at} \quad z = 0 \\ \frac{\partial \delta}{\partial r} &= 0 \quad \text{at} \quad r = r_{wall}. \end{aligned} \tag{4.20}$$

4.2.4 Correlations Used in the Model

Solution of these equations requires some method of relating the effective conductivity, the effective diffusivity, the overall reaction rate and the wall heat transfer coefficient to the local conditions, in addition to knowledge of the thermodynamic properties of all the reactants. This is done via the use of semi empirical correlations, ie expressions based on a simplified model of the process involved, which contain one or more empirical constants. Values for the empirical constants are evaluated by fitting available experimental data to

the expressions. The Temkin Pyzhev rate equation discussed previously is an example of this process. Richardson et al. (1988) surveyed the literature and selected the most appropriate expressions for incorporation in their model. In view of the success with which they were able to predict their experimental results, there was no reason to modify their formulation. The details of the correlations used are reproduced here.

For the effective conductivity they referred to a review article by Kulkarni & Doraiswamy (1980) before selecting the method presented by Argo & Smith (1953). In this correlation method the effective conductivity is given by an average of conductivities calculated for the gas and solid phases, weighted by their respective cross section areas. The gas phase contribution is the result of independent parallel contributions from conduction, radiation and convection. The solid phase contribution results from heat transfer through the surface film on the outside of each pellet in series with conduction within its bulk. Thus the resultant expression is;

$$K_{eff} = E(K_c + K_{cv} + K_r) + (1 - E)K_{series} \tag{4.21}$$

where E is the void fraction. The fluid conduction contribution (K_c) is taken as the average thermal conductivity of the fluid mixture components. Each of the other terms is evaluated from separate correlations involving variables usually associated with the individual mechanisms. The convective contribution (K_{cv}) is given by;

$$K_{cv} = \frac{\rho v C_p d_p}{mEN_{PE}} \tag{4.22}$$

where d_p, the effective particle diameter is determined from the average particle volume by assuming a spherical shape. The correlation for the radiative contribution is;

$$K_r = (2.29 \times 10^{-7} W K^{-4} m^{-2}) d_p \frac{\varepsilon_s}{(2 - \varepsilon_s)} T^3 \tag{4.23}$$

where ε_s is the emissivity of the solid catalyst. The solid phase contribution (K_{series}) depends on both the conductivity of the solid particles (K_s) and the particle to particle heat transfer coefficient (h_p):

$$K_{series} = \frac{h_p K_s d_p}{2K_s + h d_p}. \tag{4.24}$$

The particle to particle heat transfer coefficient is itself made up of conductive, convective and radiative components;

$$h_p = h_c + h_{cv} + h_r \tag{4.25}$$

$$h_c = \left(10^{(-1.52+(74.5 W^{-1} mK) K_s/E)} W m^{-1} K^{-1}\right) \frac{2K_s + h_p d_p}{d_p K_s} \tag{4.26}$$

$$h_{cv} = 1.95 \frac{\rho v C_p}{m} \frac{N_{RE}^{-0.51}}{N_{PR}^{2/3}}, N_{RE} < 350 \tag{4.27}$$

$$= 1.06 \frac{\rho v C_p}{m} \frac{N_{RE}^{-0.41}}{N_{PR}^{2/3}}, N_{RE} > 350$$

$$h_r = K_r \frac{2K_s + h d_p}{d_p K_s} \tag{4.28}$$

where the Reynolds (N_{RE}) and Prandtl (N_{PR}) numbers are related to average mixture properties via the definitions:

$$N_{PR} \equiv \frac{C_p \mu_m}{m K_m} \tag{4.29}$$

$$N_{RE} \equiv \frac{\rho v d_p}{m\mu_m}.$$

The correlation used for the Peclet number is;

$$N_{PE} = 9.0\left(1 + 19.4\left(\frac{d_p}{d_t}\right)^2\right) \tag{4.30}$$

which Kulkarni & Doraiswamy (1980) suggest is a satisfactory form for high Reynolds number flow (d_t is the equivalent diameter of the reactor).

The heat transfer coefficients for the reactor wall/s are also taken as the sum of convective and radiative contributions;

$$h_w = (h_{cv} + h_r)_{wall} \tag{4.31}$$

with the radiative contribution given by;

$$(h_r)_{wall} = \frac{\sigma}{(1/\varepsilon_{wall} + 1/\varepsilon_s - 1)}\left(\frac{T_{wall}^4 - T_0^4}{T_{wall} - T_0}\right) \tag{4.32}$$

where σ is the Stephan-Boltzmann constant and T_0 the temperature of the first layer of catalyst (which is assumed to absorb all radiation). Under reaction conditions the correlation from Chao, Caban & Irizarry (1973) is used for the convective contribution:

$$(h_{cv})_{wall} = 0.39\frac{K_m N_{RE}^{0.6}}{d_p} \tag{4.33}$$

where K_m is the conductivity of the reactant mixture. The resultant wall heat transfer coefficient must also be combined with the effect of the wall conductivity and the coefficient for the outer surface of the wall in order to determine the total temperature drop or heat flux between the bed and the heat source/sink.

The Temkin Pyzhev equation provides the method for calculation of the intrinsic reaction rate, however the diffusion of products and reactants through catalyst particle pores also contributes to the determination of the overall reaction rate. The diffusion process is driven by concentration gradients within the pores. The intrinsic reaction rate at any particular site will reflect the conditions there. Concentrations near the surface of a particle will be close to those of the free stream but towards the centre of the particle they will progressively approach the chemical equilibrium values, with a corresponding decrease in local reaction rate. For a pseudo homogeneous reactor model this is quantified by defining an effectiveness factor (ϑ) according to:

$$\vartheta = \frac{\textit{actual local average reaction rate}}{\textit{intrinsic rate at free stream conditions}}. \tag{4.34}$$

The reaction rate terms presented in this section are evaluated as the product of the intrinsic rate and the effectiveness factor, (plus any necessary density factors to convert rates to units per volume of bed). Evaluation of the effectiveness factor requires knowledge of an effective diffusivity of the pore diffusion process and for this Richardson et al. (1988) chose the correlations suggested by De Deken, Devos & Froment (1982). The effectiveness factor is related to the 'Thiele modulus' (ϕ) by:

$$\vartheta = \frac{3\phi coth(3\phi) - 1}{3\phi^2}. \tag{4.35}$$

The Thiele modulus is evaluated from;

$$\phi = \frac{V_p R_{surface} \rho_p}{A_p (2D_e)^{1/2}} \left(\int_{C_1^{equil}}^{C_1^{surf}} R \rho_p dC_1 \right)^{-1/2} \tag{4.36}$$

where C_1 is the concentration of the primary reactant (ammonia), V_p, A_p and ρ_p the average volume, surface area and density of a pellet respectively and D_e the effective diffusivity for the pellet.

Finally, although the pressure dependent terms have been dropped from the energy equation, it is desirable to be able to predict the magnitude of the pressure drop through the bed. The commonly accepted correlation for pressure drop through a packed bed is the Ergun equation (see for example Hill (1977)) which relates the pressure drop per unit length to the void fraction and the Reynolds number:

$$\frac{\Delta P}{l} = \frac{\rho v^2 (1 - E)}{d_p E^3} \left(\frac{150(1 - E)}{N_{RE}} + 1.75 \right). \tag{4.37}$$

Given that heat transfer processes are the major determining factor in the behaviour of a packed bed reactor, Richardson et al checked the applicability of heat transfer coefficient calculations by conducting no flow and non-reacting flow experiments. This revealed the need for a quadratic correction applied to the radiative heat transfer term, but showed that the convective terms were satisfactory.

Chapter 5

Receiver Concepts

5.1 Introduction

There are a number of characteristics of endothermic catalysed reactions in general and ammonia dissociation in particular, which impose fundamentally different requirements on receiver designs than those for heat collection in non-reacting fluids. The heat flux absorbed by a catalyst bed is determined by the heat transfer mechanisms operating and the behaviour of the reaction rate. It is usually considerably lower at a given temperature than could be expected for a non reacting fluid flowing in an unobstructed passage. This combined with the limitation of maximum surface temperature, as a result of materials constraints, means that heat fluxes must be kept well below the maximum levels that can be achieved at the focus of paraboloidal concentrators.

In the case of ammonia dissociation the intrinsic reaction rate of the commonly used nickel dissociation catalyst is such that the volume of catalyst needed to achieve the necessary rate of reactant consumption is a significant design constraint. Another characteristic which is a feature of the ammonia based thermochemical system is the high operating pressure, which is between 10 and $30MPa$. This operating pressure together with the requirement for high catalyst temperatures represents a difficult containment problem, given the usual wish to minimise volumes, weights and materials costs.

5.2 Past Work on Receiver Designs

5.2.1 Ammonia Dissociation

The high pressure used for the ammonia system has lead to laboratory reactors based on catalyst filled heavy walled tubing of suitable alloys. For receiver designs, the logical extension of this, when combined with the limitation on the energy flux into the catalyst bed, is some form of of cavity constructed from catalyst filled tubes.

Williams & Carden (1979*a*) reported the results of experimental work with a laboratory dissociator constructed as a direct simulation of such a receiver geometry. The electrically heated dissociator consisted of a $90mm$ deep $90mm$ diameter $5.5mm$ wall thickness inconel cylinder, with longitudinal passages drilled in the wall to hold the catalyst particles. They suggested a similar geometry for an actual receiver design, but with the variation that the reactant passage be a spiral within the cylindrical cavity geometry. They pointed out that the expected flux distribution within such a cavity, involving higher levels near the entrance, is relatively consistent with the requirements of the reaction if the incoming ammonia starts at the front and moves toward the back.

Williams (1980*b*) developed the concept of a single helical coil cavity receiver into a detailed design of a unit for a $10m^2$ paraboloidal dish with a 60° rim angle. The design parameters chosen were; a system pressure of $20MPa$, a maximum wall temperature of $750°C$, a lifetime[1] of $100,000hr$, a thermal input of $10kW$ and a reactant flow rate of $2.2gs^{-1}$.

The configuration is shown in figure 5.1, the cavity internal shape was chosen to pro-

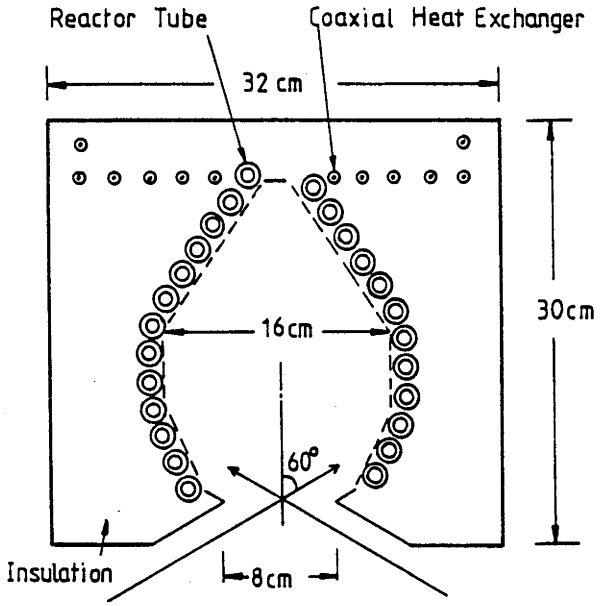

Figure 5.1: Optimized cavity geometry for an ammonia dissociation receiver, taken from Williams (1980*b*).

duce a flux profile which would maintain as much of the reactor tube as possible at near to the maximum permissible wall temperature. In this way reaction rates would be maximised and necessary catalyst volume minimised. Economic optimisations lead to the final design details, which were also based on the assumption that a catalyst with 10 times the activity of the ICI 47-1 nickel catalyst used in the earlier laboratory experiments could be found.

The group at Colarado State University (Wright & Lenz 1980, Lenz et al. 1978) also carried out a design study of an ammonia based receiver/reactor. They chose a similar set of design parameters; a system pressure of $300bar$ ($30.79MPa$), a maximum wall temperature of $700°C$, a lifetime of $10,000hr$ and a $10kW$ thermal input. In addition, they decided to limit pressure drop through the reactor to $20psi$ ($138kPa$) in contrast to Williams' design, which ultimately had a design pressure drop of $2.5MPa$. This was the major reason why they rejected the concept of a cavity based on a single helical winding, in favour of a cylindrical cavity based on parallel longitudinal catalyst filled tubes mounted between two manifolds. They also pointed out that this arrangement makes catalyst replacement easier, an important consideration for an experimental prototype. They did not give any analysis of expected flux profiles, presumably flux levels will be always low enough to keep wall temperatures below the operating limit. They did however employ the device of leaving a significant gap between and behind each reactor tube to allow

[1]For the extremes of temperature and pressure anticipated, lifetime is determined by the rate of creep of the tube wall material.

radiation to pass behind and be reradiated to the back of the tubes, thus helping to reduce circumferential flux and temperature gradients.

5.2.2 Other Thermochemical Systems

Receiver design studies for other thermochemical systems have followed similar lines, although more moderate system pressures have allowed more imaginative methods of construction to be considered. For example, Chubb et al. (1979*b*) described a cavity type design for a $24kW$ SO_3 dissociation receiver which uses a cylindrical spiral ceramic sandwich to provide passages for a counterflow heat exchanger and the reactor itself.

The group at the Weizmann Institute are one of the few, if not the only, workers in the field to publish accounts of experimental results obtained by direct irradiation of catalyst filled tube reactors. They successfully trialled two small tubular reactor designs which utilised a modest fraction of the $15kW$ of radiation incident on the aperture of a ceramic cavity structure (Levitan et al. 1989). Since then this work has been extended to tests with a similar u-shaped tubular reactor design operating at a power level of up to $6.4kW$ as part of a complete solar driven closed loop system.

Other recent work has been done on some more 'exotic' receiver/reactor concepts which may well be applicable to the ammonia system. In a review article on receiver/reactor concepts Diver (1987) identifies in addition to tube/cavity designs, concepts based on heat transfer via liquid vapour reflux or liquid heat transfer fluids and also direct absorption of radiation on the catalyst bed. Reflux heat pipe based receivers and direct absorption receivers are considered here.

5.2.3 Reflux Heat Pipe Receivers

Richardson et al. (1988) have described the development of a steam methane reforming reactor supplied with heat by a sodium reflux heat pipe. A reflux heat pipe, by virtue of its extremely high effective conductivity, can maintain the reactor walls at essentially isothermal conditions, thus providing a flux profile that is determined by the reaction requirements. Sodium heat pipes can also readily cope with very high heat fluxes in the energy input region, provided that it remains wetted with liquid. Thus for solar energy receiver design, the transformation of high flux at the focal region to the more moderate values required by endothermic catalysed reactions, is achieved. The reactor can also be maintained at a uniform optimised operating temperature irrespective of any changes in conditions such as gradual ageing of the catalyst. This is a major advantage over cavity designs such as that of Williams, since even if such designs match the radiation flux profile to the reaction requirements successfully, correct operation is dependent on parameters such as catalyst activity not changing. A progressive poisoning or ageing of the catalyst produces a corresponding drop in the extrinsic reaction rate. For a cavity design with a fixed radiation flux profile, this results in localised increases in wall temperatures and possible tube failures.

In a related paper, Parypatyadar & Richardson (1988) describe cyclic experiments with the same reactor, designed to simulate operation in a solar energy collecting context. They also present a conceptual design for a $1MW$ receiver, consisting of two annular coaxial cylindrical catalyst beds encapsulated in a large cylindrical heat pipe structure, on one end of which is a hemispherical sodium evaporation/receiver section. This work lead to a collaborative project with workers from Sandia National Laboratories and the Weizmann Institute, to construct and test a receiver prototype based on the concept (Diver, Fish, Levitan, Levy, Meirovitch, Rosin, Parypatyadar & Richardson 1992). The

prototype consisted of seven $48.2mm$ i.d. reactor tubes mounted vertically in a box like sodium reflux assembly. This unit operated successfully with $7.5kW$ of the $15kW$ of flux input being absorbed by the carbon dioxide methane reforming reaction. It was subsequently damaged by an inadvertent drying out of the wick responsible for returning liquid sodium to the solar flux collecting region.

This design concept could be directly applied to ammonia dissociation. Indeed the high operating pressure with the more stringent limitations that this places on tube wall temperatures, make the advantages of the reflux concept even more significant.

5.2.4 Direct Absorption Receivers

A receiver structure which allows the solar radiation to be directly absorbed by the catalyst material, eliminates the limitations imposed by using metal tubing and allows the catalyst bed to operate at temperatures up to the considerably higher maximum values imposed by the catalyst material itself.

There has been a considerable amount of work in recent years on direct absorption receivers (sometimes called volumetric receivers) for various applications. A number of groups have looked at the application of the concept to chemical reactor receivers.

Levy et al. (1989) tested a unit consisting of a ceramic honeycomb catalyst substrate irradiated via a hemispherical saphire window. This reactor operated at a power level of up to $2.4kW$ for carbon dioxide methane reforming.

Fish and others (Fish 1989) at Sandia National Laboratories have worked with a similar prototype both for chlorinated hydrocarbon decomposition and methane reforming reactions. Their receiver was based on a concave dish of alumina ceramic foam substrate with an impregnation of Ruthenium as the metallic catalyst. The catalyst block was mounted in a ceramic cavity structure and the whole assembly was contained within two quartz hemispheres, with reactants directed to flow from the front to the rear of the receiver. For the destruction of hazardous waste such as chlorinated hydrocarbons closed system catalytic decomposition has obvious environmental advantages over combustion, and the direct absorption receiver design allows bed temperatures of $1000°–1200°C$ to be reached which is necessary for successful decomposition.

This reactor was the precursor of the CAESAR (Catalytically Enhanced Solar Absorption Receiver) project operated in conjunction with DLR of Germany (Hogan & Skocypec 1989, Skocypec & Hogan 1989). As with the Sandia prototype, the reactor was based on a rhodium catalyst on a ceramic foam support structure composed largely of alpha-alumina. The reactor consists of a cylindrical structure $640mm$ diameter and $100mm$ deep assembled from 18 blocks of the catalyst material. The reactor was mounted in a cylindrical receiver structure with a $10mm$ thick plane quartz window, with reactants directed to flow from the front to the back of the catalyst assembly. This unit has been tested in an open loop configuration, at absorbed power levels of up to $97kW$, with the carbon dioxide methane reforming reaction (Buck et al. 1991). Maximum catalyst temperatures of $1200°C$ were reached, the experimental tests were eventually terminated after the catalyst assembly began to fall apart due to fractures apparently caused by the thermal stresses encountered.

A major difficulty experienced in trying to implement the direct absorption concept has been window failure due to thermal stresses. To date, successful experiments have involved low, sometimes below atmospheric, pressures. To apply the concept to ammonia dissociation will require a window design which can also cope with the high system pressure.

Although a direct absorption process involves reactants being heated by the portion of the catalyst material which absorbs the radiation, rather than the other way around, reaction processes are fundamentally the same. At each position in the bed the reactants and catalyst will still be close to thermal equilibrium, with the local temperature determining the corresponding chemical equilibrium composition which the reaction will tend towards.

Direct absorption however does introduce the possibility of photon dependent processes also taking place. In particular the phenomenom of photo-enhanced catalysis is now well documented. In general, reaction rates are proportional to the number of 'active site/reactant complexes' on the catalyst surface with energy greater than the activation energy. In the case of thermal equilibrium this leads to the usual exponential temperature dependence (Arrhenius relation). Photo-enhanced catalysis depends on the existence of energy levels for the active sites which are above the activation energy and have lifetimes long enough that direct absorption of photons of the appropriate wavelength can maintain greater than thermal equilibrium populations, giving a consequent enhancement of the reaction rate.

Wentworth et al (Wentworth, Batten & Gong 1987, Wentworth, Batten & Gong 1990) report experiments to determine the photo contribution to hydrocarbon reactions using transition metal oxide catalysts. Their work reveals that the existence of a strong photo catalytic effect is very hard to predict and is dependent on numerous factors including the nature of the supposedly inert catalyst support materials. Their motivation for investigation is the hope that an economically competitive method for using solar energy to produce value added hydrocarbon products may result. Moshfegh & Ignatiev (1987) report experiments with methanation reactions using polycrystalline nickel as the catalyst. They attempt to identify the mechanisms involved in the observed photo catalytic effect. The observation of such an effect with a nickel catalyst suggests that there is a strong possibility of finding a catalyst combination for ammonia dissociation which could also benefit from photo enhancement.

For a direct absorption reactor to benefit significantly from such an effect radiation would need to be absorbed by a significant portion of the catalyst surface area. Wentworth and others have considered fluidized beds which continuously expose fresh catalyst particles to the incident flux. Incorporating this concept in the receiver of a tracking concentrator would be a challenging design task. Alternatively a solid structure with suitable cavities to allow radiation to penetrate, or a translucent substrate such as a porous glass material (Corning Glass Works 1987) could be used.

5.3 Feasibility of Concepts For Ammonia Dissociation

Three possible receiver concepts have been identified;

- tube based cavity receivers;
- heat pipe receivers;
- direct absorption receivers.

At the current stage of the experimental program at the ANU, it is worthwhile to look at the plausibility of some prototype experimental designs which could be tested with the ANU's $20m^2$ parabolic dish. At an insolation of $1kWm^{-2}$ the dish will intercept $20kW$ of radiation. The capacity required of the reactor will obviously depend on the

overall thermal efficiency of the collector and receiver structure, however based on the performance measured with steam generating receivers, it is expected that it will be close to $15kW$.

Economic or other optimisations have not been considered at this stage and a number of assumptions are made about the operating parameters. The operating pressure has been taken as 100 atmospheres ($10.1MPa$). Following Williams (1980*b*), a minimum exit reaction extent of 84% has been chosen, at 100 atmospheres and $300K$ no liquid will condense from such a mixture and so only single phase reactant streams must be handled. Use of the ICI 47-1 nickel on alumina dissociation catalyst currently available has also been assumed. The most suitable rate parameters located in the literature for nickel on alumina catalysts for ammonia dissociation were those of Nandy & Lenz (1984) (the ICI company unfortunately regards such information as proprietry). They tested three different formulation and pressure combinations, based on their results, an activation energy of $2.58 \times 10^5 Jmol^{-1}$ and a pre-exponential factor of $9.647 \times 10^9 mols^{-1}cm^{-3}atm^{-1}$ have been used in the reactor model.

5.3.1 Reflux Heat Pipe Receivers

Analysis of reflux heat pipe based reactors has the advantage that the isothermal conditions make a qualitative understanding of the behaviour easier. This can provide a stepping stone to understanding the behaviour of designs with more complicated temperature profiles.

For this design exercise the $9mm$ i.d. $18mm$ o.d. inconel tube, with a $750°C$ maximum temperature, previously suggested by Williams in his design study, has also been used. The receiver concept consists of the necessary number of straight tubes running parallel to the axis of a cylindrical reflux container, with a concave flux collection region in the bottom end. A $500mm$ tube length has been adopted and tubes would be connected in U-shaped pairs to give a total reactor length of $1m$.

Figure 5.2 shows predicted profiles of average temperatures, average reaction extent and absorbed heat flux for various inlet flow rates with the heat pipe maintained at $750°C$. The curves of all show an asymptotic approach to equilibrium conditions, with smaller flow rates allowing equilibrium to be reached sooner. At equilibrium the composition will coincide with the chemical equilibrium value corresponding to the final temperature, the internal temperature will be the same as the outside and as a result the heat flux is zero. The temperature at $z = 0$ has been set at $600°C$, this corresponds to the estimated temperature of incoming reactants after being preheated by a suitable counterflow heat exchanger. Although figure 5.2(c) shows the absorbed flux reaching a peak a small distance beyond the beginning of the reactor, this simply reflects the spacing of the plotted points, theoretically the flux will jump straight to its peak value at $z = 0$.

The results are relatively insensitive to inlet temperature since the variation in sensible heat of the incoming gas over a range of a few hundred degrees is a small fraction of the energy absorbed by the reactor. At $z = 0$ the reaction proceeds at the rate dictated by the inlet temperature, as does the rate of heat transfer. If the heat flux does not match the energy consumed in the reaction, the temperature quickly changes until it does. Figure 5.3 shows the effect of increasing the inlet temperature to $750°C$. The initial reaction rate is quite high yet the initial rate of heat transfer is zero as a consequence of the equality of internal and external temperature. The reaction consumes the sensible heat of the inlet gas and the temperature quickly drops until the heat transfer rate equals the energy requirements of the reaction. In this case the peak flux occurs at the same position as the

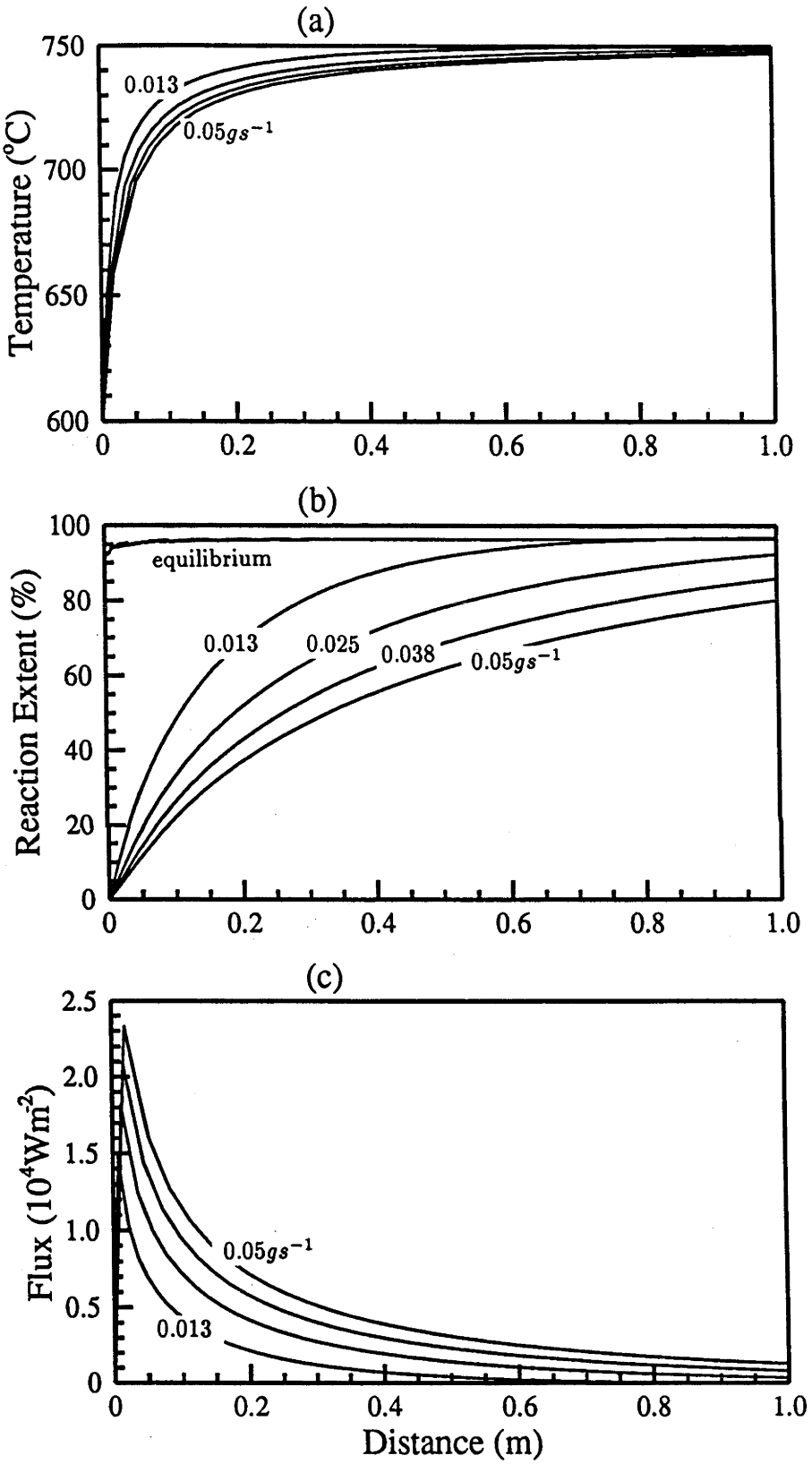

Figure 5.2: Average temperature, average reaction extent and absorbed flux profiles for a $1m$ long tubular reactor operated with a $750°C$ outside temperature and a $600°C$ inlet temperature. Mass flow rates 0.013, 0.025, 0.038 and $0.05gs^{-1}$.

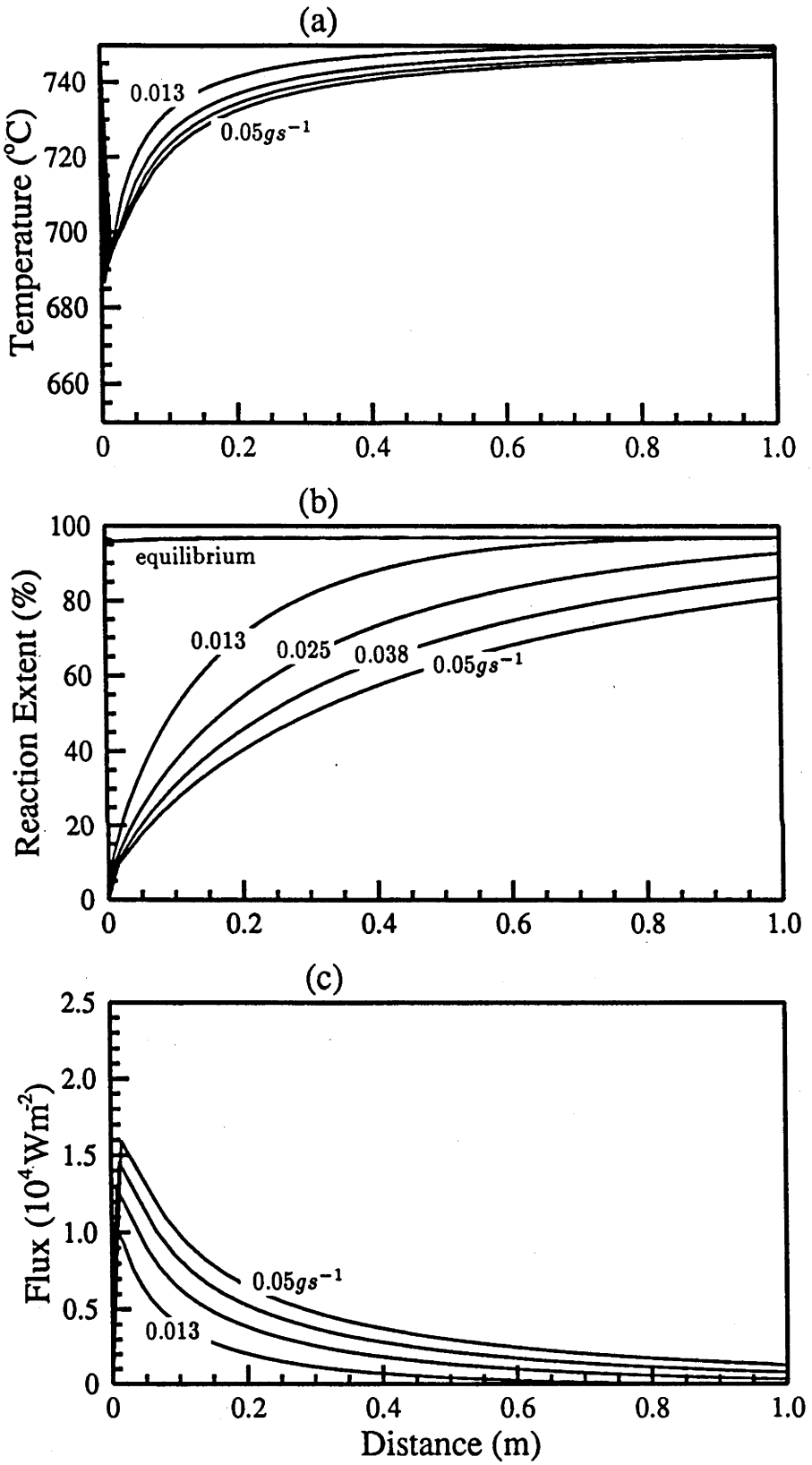

Figure 5.3: Average temperature, average reaction extent and absorbed flux profiles for a $1m$ long tubular reactor operated with a $750°C$ outside temperature and a $750°C$ inlet temperature. Mass flow rates 0.013, 0.025, 0.038 and $0.05gs^{-1}$.

point of minimum temperature.

Figure 5.4 shows the dependence of exit reaction extent and reactor power level on inlet flow rate explicitly. An increased flow rate requires a greater length of reactor before

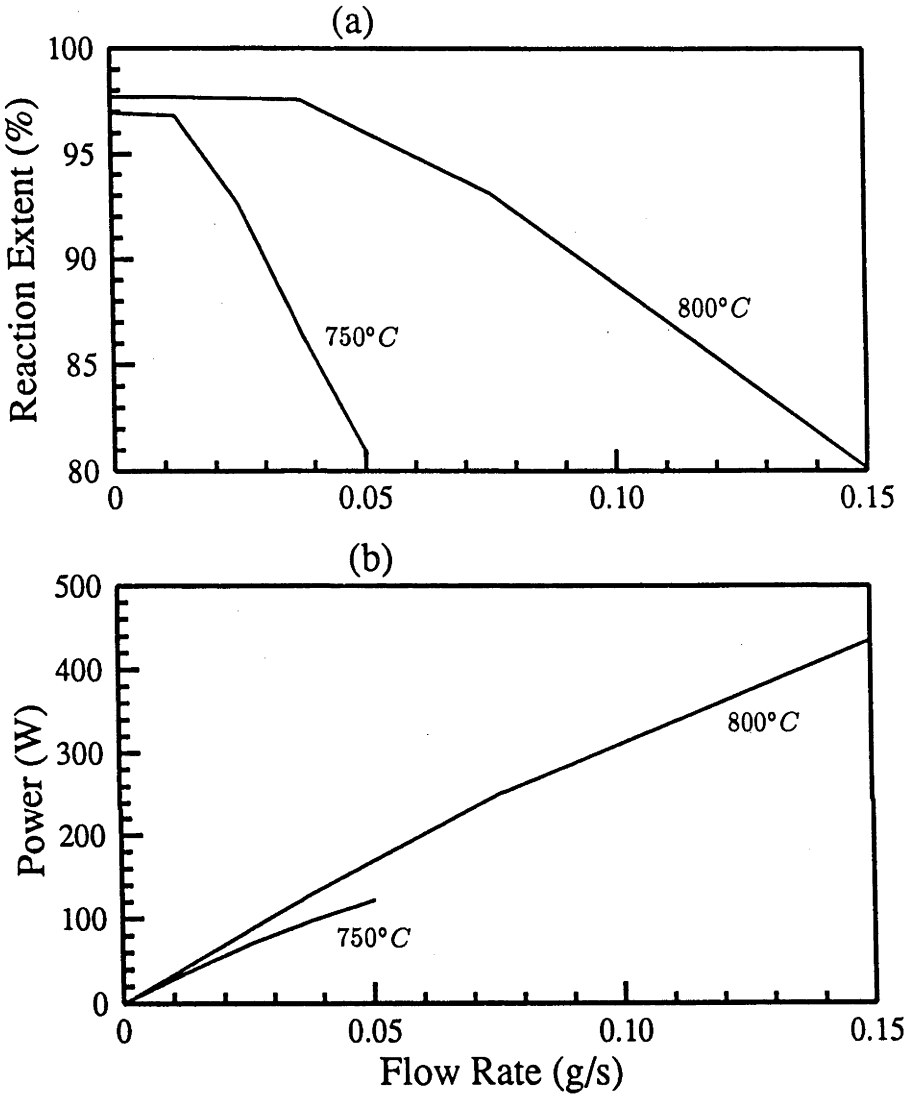

Figure 5.4: dependence of exit reaction (a) and absorbed power level per tube (b) on flow rate for 750°C (600°C inlet temperature) and 800°C (650°C inlet temperature) reactors.

chemical equilibrium is reached. This has the effect of keeping the reaction rate higher over a greater length and hence increasing the net power level. An output reaction extent of 84% is given by a flow rate of $0.042gs^{-1}$, corresponding to a power level of $125W$ for each pair of $500mm$ long tubes. The estimated $15kW$ capacity required can thus be provided by 120 tube pairs. If a 30% void fraction is allowed for vapour transport within the heat pipe, these could be encapsulated as shown in figure 5.5, in a cylindrical structure $650mm$ long by $350mm$ diameter. Although a little large for a $5m$ diameter dish, especially when a $50 - 100mm$ insulation layer is included, it is nonetheless a plausible receiver design.

Figure 5.4 also includes values for an 800°C heat pipe temperature with a 650°C inlet temperature. With this heat pipe temperature, an output reaction extent of 84% can

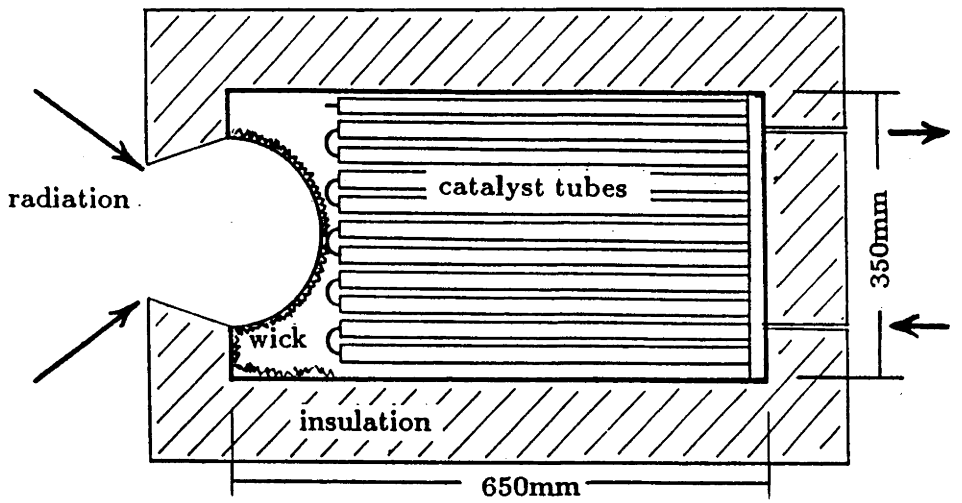

Figure 5.5: $15kW$ reflux heat pipe receiver design for $750°C$ operation.

be produced with the higher flow rate of $0.125gs^{-1}$, illustrating the strong temperature dependence of the overall reaction rate. Operating at this temperature would produce $380W$ per pair of $500mm$ reactor tubes, reducing the number of tube pairs to 40 and nearly halving the heat pipe diameter. This increased operating temperature may be tolerable in view of the reduction in operating pressure from Williams' value of $20MPa$ to $10MPa$ (100 atmospheres), if necessary the tube wall thickness could be increased. For a detailed design study, temperature versus receiver volume and mass would be one of a number of areas subject to optimisation.

5.4 Cavity Receivers

If a performance equal to the $800°C$ isothermal tubes could be maintained, then the 80 tubes required could be arranged axially to form a cylindrical cavity $500mm$ long and $500mm$ internal diameter. However with directly irradiated reactor tubes it is virtually impossible to design a receiver structure which would give a flux profile that would result in isothermal operation. Thus a given maximum operating temperature limit would inevitably result in a lower average external temperature. If the maximum temperature limit was relaxed to $800°C$, it is unlikely that that even the performance level of the $750°C$ isothermal case could be achieved. In this case there does not appear to be a feasible way of constructing a cavity with 240 such tubes. This supports Williams' conclusion that an improvement in catalyst activity would be needed to make a cavity reactor feasible.

Attempts to model the case of a single long reactor tube, such as would be encountered with Williams' helical tube reactor, produced predicted pressure drops in excess of the system pressure. This casts some doubt on the pressure drop calculations he has made and supports the conclusion of Wright & Lenz (1980), that parallel flow in multiple short tubular segments is the most plausible approach.

5.5 Direct Absorption Receivers

A strong motivation for considering the direct absorption option at this stage is that the ANU group has available a windowed pressure vessel of close to the right specifications. The unit, pictured in figure 5.6, was designed as a direct absorption receiver for steam generation (Mayer 1989), however it lends itself to configurations very similar to the direct absorber concepts suggested by Diver (1987).

Figure 5.6: $15MPa$ working pressure windowed pressure vessel for direct absorption receiver applications shown with the remains of the first quartz window prototype (the window fitted to the vessel is a plastic mock up only).

The design working pressure is $15MPa$ at $200°C$, which would be ideal for operation with internal insulation between the catalyst bed and the pressure vessel walls. The aperture diameter is $150mm$, which although a little small for the ANU dish, would be adequate for experimental operation as long as some form of cooling was provided for the front flange. The original design included a hemispherical $6mm$ thick quartz window for which modelling of internal temperature distributions had predicted stresses within acceptable limits at the working pressure. However the first window prototype failed a low temperature static pressure test, apparently due to manufacturing deviations from the design geometry in the region of its mounting flange.

To test the direct absorption concept two configurations have been modelled; a cylindrical plug of catalyst immediately behind the window, and a cylindrical cavity arrangement within the interior of the vessel. The reactor model does not include the reflection and absorption of directly incident solar radiation, but it can be used to get a reasonable

estimate of reactor behaviour.

In the case of the plug configuration, the flux profile across the front surface was assumed uniform and calculated from the estimated $15kW$ power level. It was estimated that radiation would penetrate up to $5mm$ into a bed of $2mm$ diameter particles. The model was used to predict the one-dimensional behaviour of a small cylindrical core $5mm$ in diameter, with the energy input provided by a 'pseudo flux profile' for the reactor model program. This profile was approximated by a cubic polynomial falling to zero after $5mm$. The resultant profiles are shown in figure 5.7. The flux profile in part (c), represents energy absorbed per circumferential area element of the $5mm$ diameter core. The flux profile is fixed and determines the behaviour of temperature and reaction extent within the bed, in contrast to the heat pipe reactor where the reactor conditions determine the flux. Thus in the first $2mm$ the high flux levels drive the temperature and reaction rate up until a point is reached where the reaction rate energy consumption matches the flux level. After this point the flux level falls below the rate of energy consumption by the reaction and so temperatures fall also. After $5mm$ the flux has dropped to zero and the reactor becomes adiabatic. The reaction proceeds, converting sensible heat into chemically stored energy, moving towards a temperature/reaction extent combination which would be in chemical equilibrium.

Since catalyst volume is no longer an overriding concern, a cavity configuration, of greater catalyst volume, within the pressure vessel would reduce the radiation losses. Figure 5.8 illustrates a possible cylindrical cavity configuration consisting of a catalyst bed $160mm$ internal diameter, $200mm$ long and $10mm$ thick. Figure 5.9 shows the results from modelling the behaviour of this configuration. The absorbed flux profile for this case was calculated by Bannister (1991*a*) using a receiver model which calculates the incident profile from a knowledge of the collector geometry and then includes the effect of reradiation from the cavity walls to get the total distribution. This calculation was made by assuming a uniform $1000°C$ internal temperature as a first approximation.

The reactor was modelled by assuming that the radiation would be absorbed by the exposed surface of the bed, rather than allowing it to penetrate as in the plug reactor case. As a result the surface temperature is overestimated by approximately 10–20%, although the average bed conditions are relatively unaffected. The flux is higher near the entrance of the cavity, this coincides with the region of highest reaction rate and as a result the average temperature does not vary greatly from inlet to exit. The surface temperature on the other hand, varies over a considerable range in direct reflection of the flux levels. The radial profiles predicted by the model are of interest, these are presented in figure 5.10. At $z = 0$ the radial temperature profile starts at the uniform $750°C$ inlet temperature, and the reaction extent is zero. Progressing along the cavity, the reaction extent and temperature close to the irradiated surface rise sharply up to the point where the flux level begins to diminish. At this point the difference in conditions between inner and outer radial positions also begins to reduce.

The results for both direct absorption configurations also illustrate the strong effect of temperature on reaction rate, with the total necessary catalyst volume being approximately 10^3cm^3 in both cases, compared to 10^4cm^3 for the $800°C$ heat pipe configuration.

5.6 Conclusion

These preliminary calculations with the numerical reactor model indicate that, on the basis of the rate parameters used, both reflux heat pipe and direct absorption based receiver concepts appear feasible for ammonia dissociation with standard nickel catalyst,

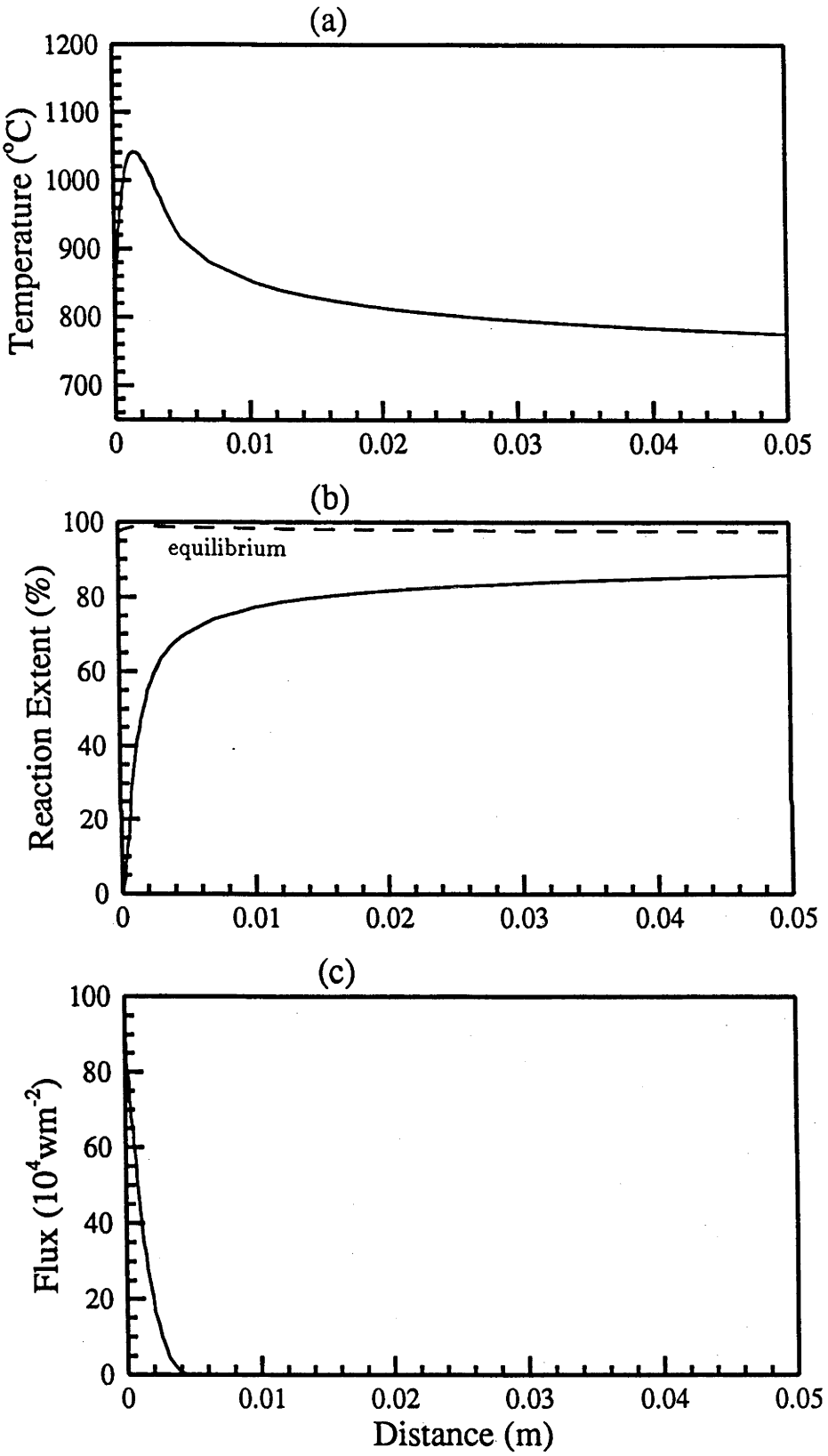

Figure 5.7: Temperature, reaction extent and absorbed flux profiles for a $5mm$ diameter section of a $5cm$ deep catalyst plug. Uniform radiation on the front surface of $9.05 \times 10^5 Wm^{-2}$ and reactant massflux of $3.36 \times 10^2 gs^{-1}m^{-2}$.

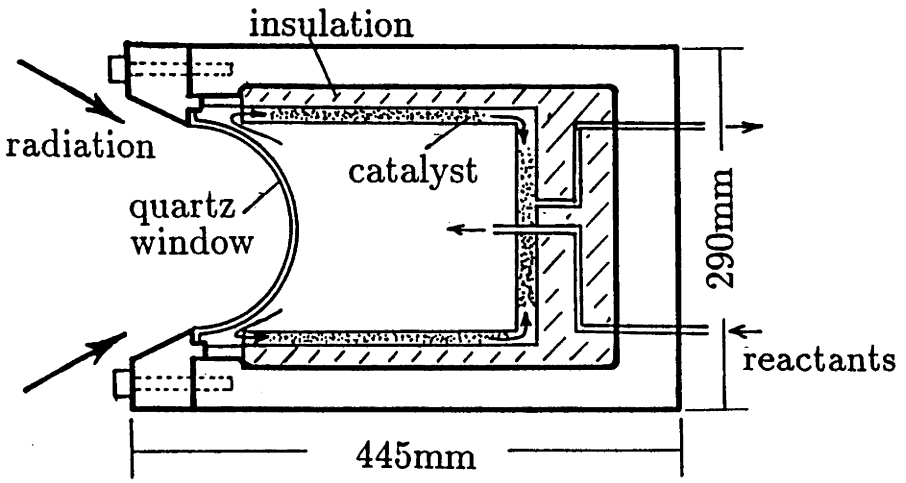

Figure 5.8: Cavity design for a direct absorption reactor based on a windowed pressure vessel.

but a cavity design using irradiated tubing seems difficult to implement. However, this study was carried out prior to the dissociation experiments presented in chapter 8, which ultimately indicated that the 47-1 catalyst has a considerably higher activity than has been assumed. In the light of those results an approximately four-fold increase in reactor performance can be predicted. This would result in considerably more compact reflux heat pipe designs and allow operation of direct absorption receivers at lower temperatures (giving associated improvements in thermal efficiency). It also appears that a tube/cavity construction of reasonable size may also be possible.

All three concepts appear worth pursuing, each has its advantages and particular engineering problems to overcome. In the case of a tube cavity design the main challenge is matching the flux profile to the requirements of the reactor so as to avoid exceeding the maximum temperature limit. Thermal stresses due to local variations in tube wall temperatures would also have to be addressed. Although these problems are common with other thermochemical systems, they are exacerbated by the high operating pressure proposed for the ammonia based system. A reflux heat pipe design overcomes these problems and as such may be even better suited to ammonia dissociation than methane reforming reactions carried out at lower pressures. Ensuring correct and reliable operation of a wick mechanism within the reflux heatpipe appears to be the major challenge for this concept. The major challenge with the direct absorption approach is producing a suitably robust window. If this could be achieved, then the windowed pressure vessel design has advantages in the ease with which the internal design could be varied or the catalyst changed during the course of an experimental program.

In consideration of receiver designs, the primary aim has been to maintain reactor sizes within reasonable bounds. Given that this is possible with some margin available, then exergetic efficiency could be addressed. From the reaction point of view, exergetic efficiencies will be maximised with a reactor temperature profile that starts at a lower value and increases as reaction extent also increases along the bed. The result of this is that the same exergy content will be achieved in the products for a reduced thermal exergy input, at the cost of increased catalyst volume. However, in the context of a solar receiver

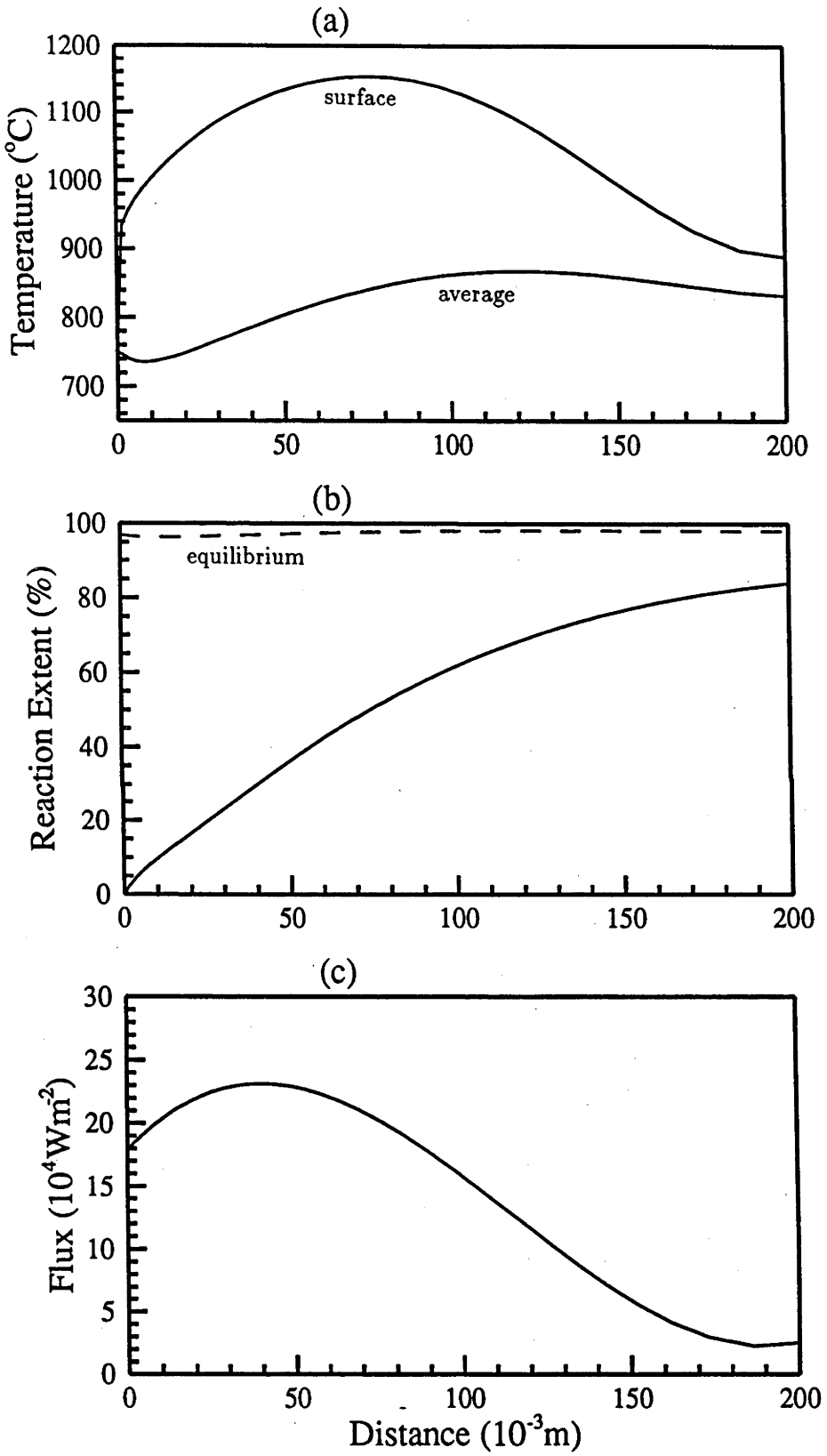

Figure 5.9: Temperature, average reaction extent and absorbed flux profiles for a cylindrical cavity with $14kw$ absorbed by a $5.2gs^{-1}$ reactant flow.

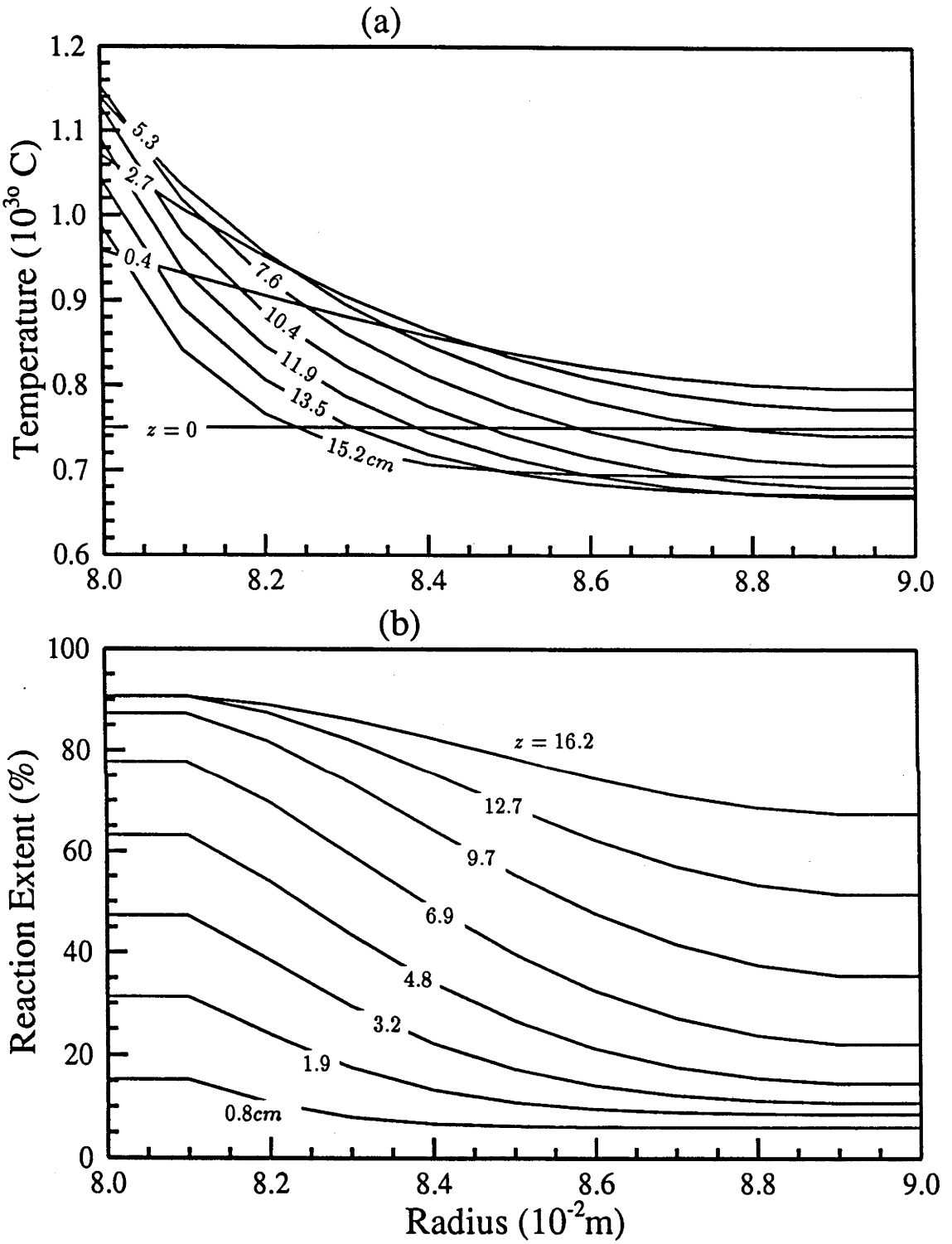

Figure 5.10: (a) Radial temperature and (b) reaction extent profiles for a cylindrical cavity with $14kw$ absorbed by a $5.2gs^{-1}$ reactant flow.

this has little value since the exergy input as radiation has not changed, a percentage of the irreversibility has simply been shifted from the heat to chemical conversion process to the radiation to heat conversion process. There will be some benefit in that a lower

average temperature reduces thermal losses (particularily radiation) from the absorber.

Given that the exergy content of the received energy is fixed, exergetic efficiency of the combined receiver reactor system could be improved by including a topping cycle such as a thermoelectric process (Lovegrove 1987) or by increasing the exergy/energy ratio in reactants leaving the receiver. For the ammonia system it has been pointed out in chapter 3 section 3.5 that this can not be achieved by variation of the inlet reactant stream composition (although it may be for other thermochemical systems). The only possibility is to increase the operating pressure of the dissociator further so as to move the equilibrium towards higher temperatures.

Chapter 6

Optimisation of Real Systems

6.1 Optimisation of Energy Conversion Systems

6.1.1 Design Goals

The development of a system for conversion of solar energy, like any design exercise, must begin as a purely creative process. On the other hand, the need to achieve the best possible economic and/or thermodynamic efficiencies suggests the application of systematic analytical optimisation techniques. As a result design development is typically an iterative application of alternate creative and analytical processes.

A significant fraction of the published literature on energy conversion systems is devoted to optimisation issues of various kinds. In situations in which it is desired to improve the thermodynamic performance of systems which contribute to work production, there is an increasing acceptance that second law analysis via the maximisation of exergetic efficiencies or the minimisation of entropy production, is the appropriate path to design improvement. Bejan (1987), in a review article, covered the application of this approach to the design of heat and mass transfer devices. Other recent examples include: Suzuki, Okamura & Oshida (1987), who established the optimum operating conditions for a flat plate collector; Nag & Kumar (1988), who applied Bejan's ideas to optimise the Reynolds number in a duct subject to a constant heat flux; and Bannister (1991*b*) who determined the optimum pipe radius to use in a tube based receiver for a parabolic dish collector.

This type of optimisation typically involves trade-offs between conflicting sources of thermodynamic irreversibility. The consideration of appropriate real constraints in the analysis of energy conversion systems places fundamental limits on the maximum exergetic efficiencies achievable. Curzon & Ahlborn (1975) pioneered the theoretical analysis of such limits by establishing the upper limit on the efficiency of a Carnot engine constrained to work at maximum power. The implications of this result for solar driven heat engines were investigated by Gordon (1988). In a recent publication Won-yong & Sang-soo (1991) carried out a similar analysis of an organic Rankine cycle constrained to operate at maximum power.

The ammonia based solar thermochemical system with direct work output belongs to a large class of solar thermal systems for which the design goal is to produce work from solar radiation with a minimisation of cost either per unit of work output or unit of installed capacity. The design problem usually incorporates a number of constraints such as; an upper limit on initial financial investment, restriction on physical size and location, and constraints associated with the characteristics of the conversion process. Consideration of complicated 'whole' systems can involve determining the optimum operating conditions

for a given design, as has been considered by Bannister (1991*a*), for the case of a small solar thermal power system. Alternatively an examination of cost efficiency trade-offs for the various parts of a system, such as that carried out by Gordon (1988) for a system made up of various types of series connected solar collectors, can determine a minimum cost design for a required output.

6.1.2 Systematic Optimisation with Financial Constraints

Taken as a whole, energy conversion systems such as the ammonia based thermochemical system have so many variables that a direct approach to optimisation is impractical. Instead, breaking down the system into a series of subsystems which can be dealt with individually is more appropriate. for systems with a single output this can be represented schematically as in figure 6.1. If the thermodynamic performance of the system is quanti-

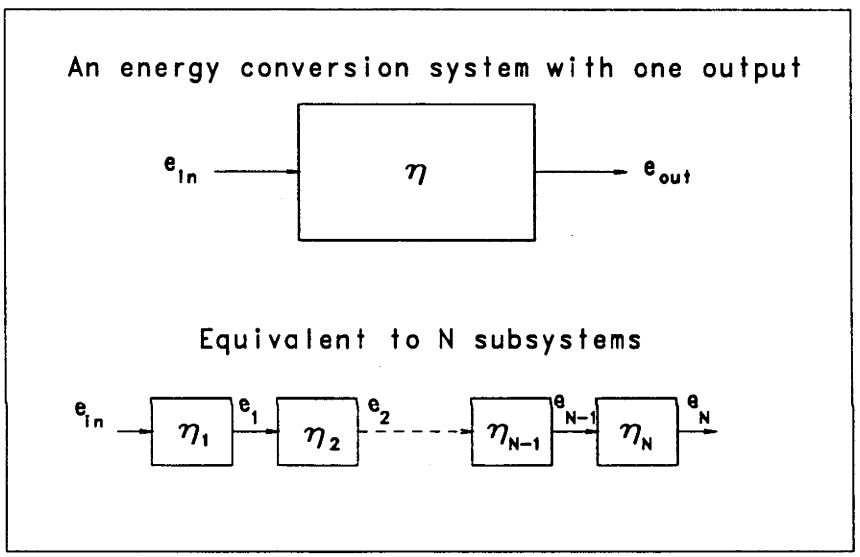

Figure 6.1: Considering an energy conversion system as a series of subsystems with exergy outputs e_i and efficiencies η_i.

fied by its exergetic efficiency, then this has the advantage that the overall system efficiency is the product of the exergetic efficiencies of the individual subsystems. If 'cost' is taken as a generalised term which indicates either cost per unit of work produced or cost per unit of installed capacity, then the design problem can be re-expressed as; 'produce a required exergy output for the minimum cost subject to specified constraints'.

If the subsystems are chosen in such a way that each is characterised by a single cost determining variable, then systematic optimisation can proceed in two stages:

- for each subsystem, the optimum design is determined for a range of values of the cost determining variable;
- the whole design is optimised by choosing the best distribution of cost amongst the various subsystems, in a way that produces the required output.

Typically a subsystem design has an efficiency cost relationship which starts at zero efficiency non-zero cost, increases in some manner with cost and ultimately asymptotically

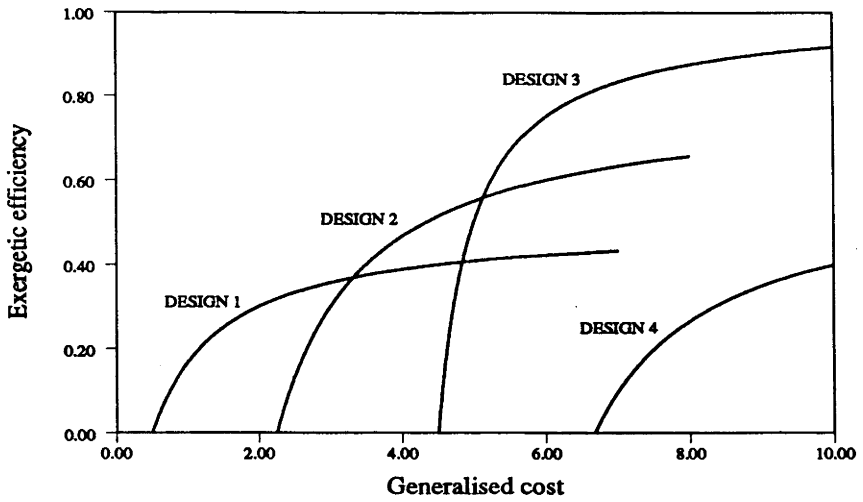

Figure 6.2: Conceptual efficiency cost relationship for 4 alternative designs.

approaches a maximum efficiency $\leq 100\%$. The creative process which produces a design implicitly involves an intuitive determination of the likely range in which the optimum value of the cost determining variable for each subsystem will fall. In a sense the allocation of financial resource amongst subsystems under these conditions is a 'linearised' version of a more complex problem. If the solution of the cost distribution problem suggests a value of the cost determining variable for a particular subsystem, which is at either extreme of its assumed realistic range (ie close to the zero efficiency value, or beyond the point where efficiency increases significantly with cost), then this is an indication that the particular subsystem design deserves re-assessment. This point is illustrated conceptually in figure 6.2, which represents the efficiency cost relationship for a task for which four alternative designs are available. Clearly design 4 is a 'poor' design under all circumstances; however the choice between designs 1, 2 and 3 would depend on the value of the optimisation of cost distribution suggested for the task. Thus creative and analytical methods are used in an iterative manner to arrive at a final total system design.

6.1.3 Application of Dynamic Programming

Optimisation tasks which simply require the maximisation or minimisation of functions can be completed by, for example, determining the roots of function derivatives. However when the maximisation or minimisation must be performed subject to possibly complicated constraints, more sophisticated methods are required. Dynamic programming, (see for example Norman (1975)) is a general technique which appears to be particularly suitable for application to energy conversion system design problems. Dynamic programming is essentially a systematic approach to presenting optimisation problems and solving them in a recursive manner. It can be applied to discrete problems such as the distribution of cost amongst a fixed number of subsystems and it can also provide a numerical approach to solving continuous problems with complicated constraints.

If each subsystem has in turn been subjected to an optimisation procedure for a range of values of its cost determining variable, then its cost can be presented as a function of the value of efficiency desired (Cost $= C(\eta_i)$). The design goal for the system of N subsystems is to produce a desired value of the work (or exergy e_N) output from the Nth subsystem, for the minimum cost. A design policy is specified by a series of values of η_i, these in turn determine the cost of the system. In the dynamic programming description

the problem itself is described as a 'system' which must be taken from an initial 'state' to a final 'state' in a number of 'stages', via a path which optimises the appropriate path dependent function.

For the problem of cost distribution amongst subsystems, each subsystem can represent a stage. The stage number n is equal to the number of subsystems involved in producing the required exergy output from subsystem n, and the required exergy output (e_{out}) is the single variable which specifies the system state. The decision to be made at each stage is the size of the cost allocation ($C(\eta_n)$) to that energy conversion subsystem. The decision results in a transition from stage n to stage $n-1$, at stage $n-1$ the required exergy output is higher than at stage n by the amount of exergy that is lost from stage n ie:

$$e_{out_{n-1}} = \frac{e_{out_n}}{\eta_n}. \tag{6.1}$$

The optimum value of the total cost of subsystems up to the current stage is represented by a 'functional relation' $f_n(e_{out})$. The similarity of the decision at each stage naturally leads to the recursive expression for the functional relation which is the basis of the dynamic programming method:

$$\begin{aligned} f_n(e_{out}) &= \text{Min}_{(constraints)}(\text{cost of producing } e_{out} \text{ using } n \text{ subsystems}) \\ &= \text{Min}_{(constraints)}(\text{cost of } \eta_n + \text{cost of necessary input to stage } n) \\ &= \text{Min}_{(constraints)}\left(C(\eta_n) + f_{n-1}\left(\frac{e_{out}}{\eta_n}\right)\right). \end{aligned} \tag{6.2}$$

Evaluation begins with[1];

$$f_1(e_{out}) = \text{Min}_{(constraints)}(C(\eta_1) + C(e_{in_1})) \tag{6.3}$$

where the cost of the required exergy input $C(e_{in_1})$ is given by, for example, the cost per unit area of the basic solar collector structure multiplied by the average flux. If each f_n is evaluated for a range of values of e_{out} then the combined set of values of optimum efficiency $\eta_i^*(e_{out_i})$ will implicitly contain the information on the optimum cost distribution for a range of outputs from the whole system.

If m discrete different values of e_{out} are considered at each stage, then there are $m^{(N-1)}$ different possible paths from initial to final state. Testing each of these for optimality would require some multiple of $m^{(N-1)}$ calculations. On the other hand the dynamic programming solution requires m evaluations of $f_n(x)$ at each stage, only a multiple of $N \times m$ calculations altogether.

For subsystem optimisation the states are more likely to be continuous rather than discrete. In this case dynamic programming provides an algorithm for a numerical solution. If the recursive definition of $f(x)$ is taken to the limit of infinite stages then it can be manipulated to produce a partial differential equation initial value problem. When formulated for an appropriate general case with equality constraints, this can be shown (Norman 1975) to be equivalent to the Euler Lagrange equation of variational calculus.

6.2 Optimisation of Thermochemical Energy Storage

The investigation by Carden & Williams (1978*b*) of work recovery efficiencies for the exothermic half of an ammonia based thermochemical system was essentially motivated

[1] $\text{Min}_{(constaints)}$ means minimisation subject to specified constraints.

by a perceived need to maximise this efficiency (equivalent in effect to the exergetic efficiency). This line of investigation was continued by Carden (1987) in developing the direct work recovery system which improved upon the efficiency limit imposed by the previously considered steam based heat recovery system. Independently of this line of investigation, Williams (1978*c*) optimised the thermochemical energy transport costs for a distributed solar power plant. His calculations involved trading off installation cost versus pumping power to determine optimum transport piping size for various operating pressures and thus allowed an identification of an optimum system pressure. Fish (1984) discussed the irreversibility associated with the isothermal operation of an exothermic reactor. He presents the results of a brief analysis which suggests an optimum operating temperature based on the trade-off of this irreversibility and the thermal efficiency. Aside from this work, there does not appear to be any published material on the optimisation of thermochemical energy storage systems.

The conceptual arrangement for an ammonia based solar thermochemical energy transport and storage system with direct work output has been described in chapter 1 and chapter 3. To develop this concept into a design, involves determining the general construction details of all the individual components and the values of a number of important parameters. Specifically, these parameters are: the pressures for operation of the endothermic and exothermic halves of the system, and the inlet and outlet reactant compositions for the two reactors. Table 6.1 presents a possible identification of subsystems which could then be the subject of individual optimisation studies followed by an overall examination of resource allocation.

Whilst there is probably a number of optimisation issues associated with the design of reflective materials and turbine, they are both areas which do not specifically relate to thermochemical energy storage processes. In the context of thermochemical system development it is more appropriate to rely on the options commercially available to define their efficiency cost relationship.

In the case of the connecting piping, the subsystem efficiency cost relationship is straight forward. Given that the length required and the operating pressure have been pre-determined, the efficiency, being determined by the pressure drop, is a monotonically increasing function of pipe diameter. The cost would also increase with diameter in a simple manner.

The cost of reactant storage is obviously determined by the storage volume required and the method chosen. The issue of a non-unity exergetic efficiency only arises if the method chosen relies on a continual work input, or has an inherent leakage of reactants associated with it. The first situation would be encountered with refrigerated low pressure storage of liquid ammonia, in which case the efficiency cost relationship would be determined by the effectiveness of the thermal insulation. A possible scenario for storage with continual leakage could be some form of underground storage in which reactants continually diffused into ground water or geological strata. In such a situation a cost related determination of efficiency might be provided by the possible application of a surface treatment for the storage cavern. For reactant storage on a smaller scale, the relative costs of different connection fitting or gasket material types, with different associated rates of leakage, may prove relevant.

In the context of a generalized theoretical examination, the heat exchanger and reactor subsystems are of most interest. For the two heat exchangers there are three factors which determine their exergetic efficiency; the pressure drop, the effectiveness of the inter-passage transfer of heat, and the mismatch in specific heats of reactants in the two passages. Specific heat mismatch can be a significant limiting factor on heat exchanger ex-

n	Subsystem	Cost determining variable	Efficiency determining factor
1	Reflective surface	Choice of material	Reflectivity
2	Receiver structure	Size	Temperature
3	Endothermic reactor	Catalyst volume	Reaction path
4	Dish heat exchanger	Passage length	Reynolds number
5	Reticulation piping	Diameter	Pressure drop
6	Reactant storage	—	Leak rate
7	Heat exchanger for exothermic reactor	Passage length	Reynolds number
8	Exothermic reactor	Catalyst volume	Reaction path
9	Turbines	Construction tolerance	—

Table 6.1: A possible identification of subsystems for a solar thermochemical energy transport and storage system.

ergetic efficiency. Unless surplusses or deficits can be met reversibly at each temperature, then either a net surplus is irreversibly degraded to the outgoing reactant exit temperature (and possibly completely lost to the environment), or a net deficit must be irreversibly made up within the reactor. For the ammonia based system the issue of specific heat mismatch arises largely because the phase boundary (the dewline) is encountered at different temperatures for mixtures of different composition. The endothermic reactor heat exchanger will have a net energy surplus which varies with the choice of inlet and outlet reaction extent. In the context of the operation of parabolic dish solar energy collector units, it has always been assumed that this surplus will be wasted, hence this is a major factor in the determination of inlet and outlet reaction extents. Specific heat mismatch is of less concern for the exothermic reactor subsystem since there is a greater chance of meeting energy surplusses or deficits reversibly in the context of a single large installation.

If inlet and outlet reactant mixture compositions and the method of construction have been specified, the actual efficiency of a heat exchanger subsystem will be determined by a combination of the pressure drop and the effectiveness of the heat transfer process. Taking the length of the passages as a plausible cost determining variable, the optimisation task is the determination of the Reynolds number which gives the best trade-off between convective heat transfer coefficients and pressure drop. This is one of the problems which has been addressed by Bejan (1987).

The cost determining variable identified for the two catalytic reactors is the catalyst volume per unit of thermal capacity. The subsystem optimisation task is the choice of reaction path between nominated inlet and exit mixture compositions.

The exergy content of solar radiation and of energy stored in chemical form are both fixed, hence the exergetic efficiency of the combination of receiver and endothermic reactor is determined by their thermal efficiencies. However a determination of highest exergetic efficiency reaction paths for the endothermic reactor is equivalent to producing the lowest possible average reactor temperature and is thus related to the thermal efficiency. The determination of optimum reaction paths for the endothermic reactor would however have considerable significance in the context of generalised thermochemical energy storage systems applied to arbitrary sources of heat, or to solar thermal-electric systems which incorporated topping cycles between the receiver and the endothermic reactor.

For the exothermic reactor, exergetic efficiency maximisation directly effects the total

work output of the system. The determination of the optimum reaction path for an exothermic reactor is the theoretical problem which has been studied in detail in the course of this project.

6.3 Optimization of Exothermic Reaction Path

The exergetic efficiency of reaction paths has been discussed in detail in chapter 3. Figure 6.3 shows contours of constant exergetic efficiency and relative intrinsic reaction rate for the exothermic reaction on the relevant region of a temperature enthalpy diagram for the ammonia system.

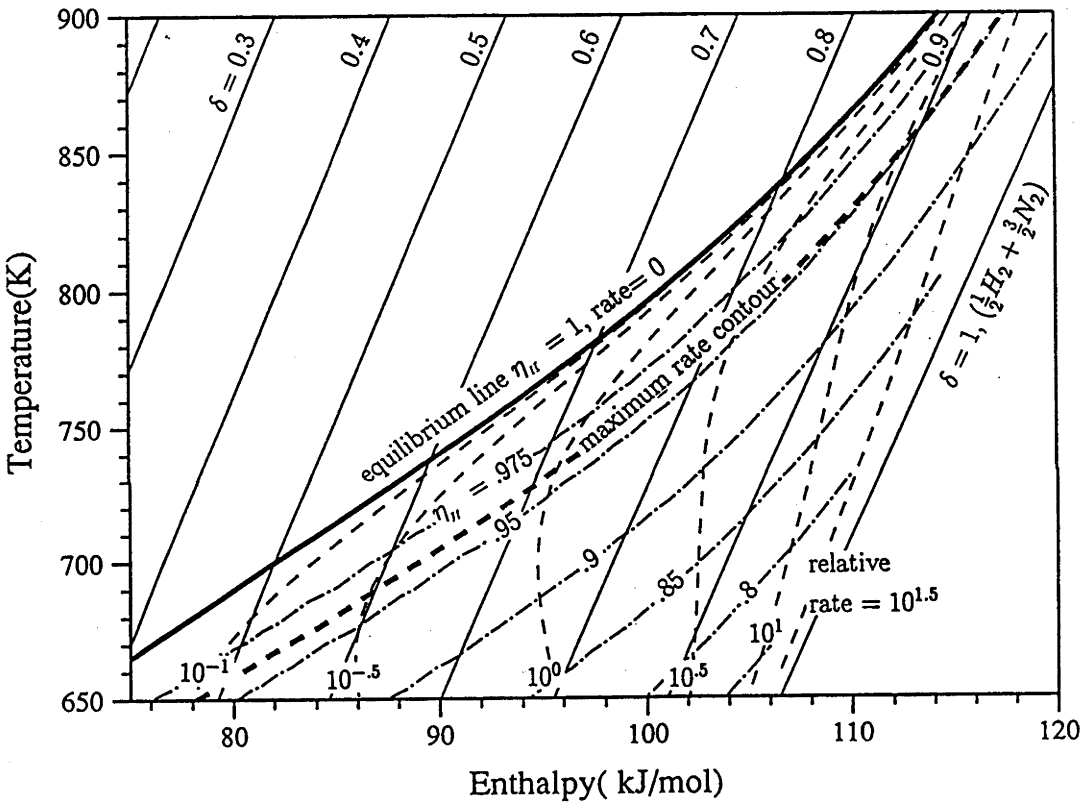

Figure 6.3: Temperature enthalpy diagram for the ammonia system showing contours of constant exergetic efficiency (– · –), and relative reaction rate (- - -) (200 atmospheres).

The catalyst volume required for a mole of reactants to traverse a given reaction path is related to the reaction rate encountered according to;

$$V = A \int_{\delta 1}^{\delta 2} \frac{d\delta}{R(T,\delta)} \tag{6.4}$$

where A is a constant which reconciles the dimensions of volume and reaction rate (R). As discussed in chapter 4, actual rates for a real reactor are lower than the intrinsic rate; however the shape of relative rate contours would not be expected to vary greatly. for the purposes of the investigation of this general optimisation problem, the Temkin-Pyzhev intrinsic rate expression has been used, with an activation energy of $159 kJ mol^{-1}$

(corresponding to a promoted iron ammonia synthesis catalyst), and a system pressure of 200 atmospheres.

If the reaction extent of the inlet mixture is such that it spontaneously separates into gas and liquid phases at the sink temperature, then $\frac{\partial G}{\partial \delta}(T_s, \delta)$ is constant and the exergetic efficiency of a particular reaction path (equation 3.27) reduces to:

$$\eta_{ex} = \frac{\int_{\delta 1}^{\delta 2} \eta_{ex}(T, \delta) d\delta}{\int_{\delta 1}^{\delta 2} d\delta} \tag{6.5}$$

where $\eta_{ex}(T, \delta)$ represents the local value of exergetic efficiency for an infinitesimal path, as indicated by the contours in figure 6.3. For the exothermic reaction, the reaction rate for a given value of reaction extent starts at zero at equilibrium, initially increases with decreasing temperature as the thermodynamic system is taken away from equilibrium, but then begins to decrease as the reduction in average molecular kinetic energy begins to dominate. Thus there is a contour, defined by temperatures at which $\frac{\partial R(T,\delta)}{\partial T} = 0$, which represents the maximum reaction rate achievable at a given value of reaction extent, this contour is also indicated in figure 6.3. The distance between the maximum rate contour and the equilibrium line increases if the catalyst activation energy is decreased.

Any reaction paths which lie on the maximum rate contour are paths of minimum required catalyst volume. In the same way that the work recovery efficiency of reversible paths along the equilibrium line is analogous to the Carnot efficiency limit for engines operating between constant temperature sources and sinks, the work recovery efficiency of paths along the maximum rate contour is analogous to the Curzon Ahlborn efficiency (Curzon & Ahlborn 1975) of such engines operating at maximum power. When the volume available exceeds the minimum required, the optimum path will lie somewhere in the region bounded by the maximum rate (minimum volume) contour and the equilibrium line (paths of infinite required volume).

The determination of the optimum path between initial and final reaction extents belongs to a general class of 'allocation' problems which are particularly suited to a dynamic programming solution. The definition of a state for the problem can be taken as the local value of the temperature and the reaction extent and the value of specific reactor volume available to take reactants to the desired final reaction extent. If the reaction extent interval is divided into N stages, then reaction extent is determined by the stage number and the problem becomes two dimensional.

Although an exothermic reaction proceeds from high values of reaction extent to low values, the dynamic programming problem and the evaluation of path efficiencies and volume requirements can be calculated in either direction. Nominating the reaction extent at stage N as δ_1 and at stage 0 as δ_2, the decision to be made at each stage is the choice of temperature increment (ΔT) for the transition:

$$\begin{aligned} \delta &\rightarrow \delta - \Delta\delta = \delta - \frac{\delta_2 - \delta_1}{N} \\ T &\rightarrow T + \Delta T \\ V &\rightarrow V - \Delta V = V - A \int_{\delta}^{(\delta+\Delta\delta)} \frac{d\delta}{R(T,\delta)}. \end{aligned} \tag{6.6}$$

The functional relation for this problem is:

$$f_n(V,T) = \mathrm{Max}_{\left(\int_{\delta_n}^{\delta_2} \frac{A}{R} d\delta \leq V\right)} \left(\int_{\delta_n}^{\delta_2} \eta_{ex}(T, \delta) d\delta \right)$$

$$= \text{Max}_{\left(\int_{\delta_n}^{\delta_2} \frac{A}{R} d\delta \leq V\right)} \left(\int_{\delta_n}^{\delta_n - \Delta\delta} \eta_{ex}(T,\delta) d\delta + f_{n-1}(V - \Delta V, T + \Delta T) \right) . \quad (6.7)$$

Solution begins with:

$$f_1(V,T) = \text{Max}_{\left(\int_{(\delta_2 - \Delta\delta)}^{\delta_2} \frac{A}{R} d\delta \leq V\right)} \left(\int_{(\delta_2 - \Delta\delta)}^{\delta_2} \eta_{ex}(T,\delta) d\delta \right) . \quad (6.8)$$

The Fortran implementation of this algorithm is described in appendix B. This investigation of optimum reaction paths has used a system pressure of 200 atmospheres, a sink temperature of $300K$ and a fixed maximum reaction extent path limit of 0.8 (this value is close to the dewline value at $300°K$ and hence the limit of applicability of the simplified path efficiency expression given by equation 6.5). Path optimisations have been carried out for various values of minimum reaction extent between 0.6 and 0.8. Computational effort increases with the product of the number of temperature and volume divisions used at each stage. Partly as a consequence of the unsophisticated maximisation algorithm used, the number of intervals was limited to less than 50 in order to complete the optimisation using between 1/2 and 1 hour of cpu time on a DEC Vaxstation.

Optimised linear reaction paths (corresponding to a single stage solution) have been considered in addition to multiple stage paths. Linear paths would be encountered when the heat recovery method is via a counter flowing heat extracting fluid of constant specific heat, as is the case with the direct work recovery system. For comparison, families of non-optimum linear paths which are parallel to minimum volume paths have also been considered.

Figures 6.4 and 6.5 show the calculated optimum linear paths and optimised 5 stage paths (dividing δ_1 to δ_2 into five intervals) for transition between δ =0.6 to 0.8 and δ = 0.7 to 0.8 for various available volumes. Available volume is normalised with respect to the minimum volume required for the transition between the reaction extent endpoints, and takes values between 1 and 3, divided into exponentially increasing intervals.

The paths in these figures exhibit a degree of imperfection which reflects the limitations of the program's subroutine algorithms and the finite number of temperature volume and reaction extent intervals used. The families of linear paths contain a number of examples where adjacent lines are converging in the opposite direction to the local trend. This reflects the fact that they are constrained to pass through one of the discrete available temperatures at δ = 0.8 and so their slope is compromised accordingly. The multiple reaction extent interval paths exhibit a degree of interval to interval oscillation about what can be assumed is a true optimum path. Superimposed oscillations produce a path of the same efficiency, but requiring slightly higher available volume than a smoothed path. The oscillations have their origin in the same limitation on temperature at $\delta = 0.8$ as in the linear case, combined with approximation errors in the interpolation method for determining $f_{n-1}(V,T)$ at each stage.

The general trend for both linear and general optimised paths as the available volume is increased, is a smooth transition between paths which run parallel to the maximum rate path, to paths which run parallel to the equilibrium line. The high reaction extent endpoint temperatures initially increase faster than the low reaction extent endpoint temperatures. The plausibility of these results can be confirmed by consideration of the behaviour of reaction rates with temperature and reaction extent. As illustrated by figure 6.3, $\frac{\partial R}{\partial \delta}(T,\delta)$ is positive and increases with δ, whilst $\frac{\partial R}{\partial T}(T,\delta)$ is zero at the maximum rate contour and becomes increasingly negative as the equilibrium line is approached. If a supposedly optimum linear reaction path is subject to an infinitesimal rotation in the temperature

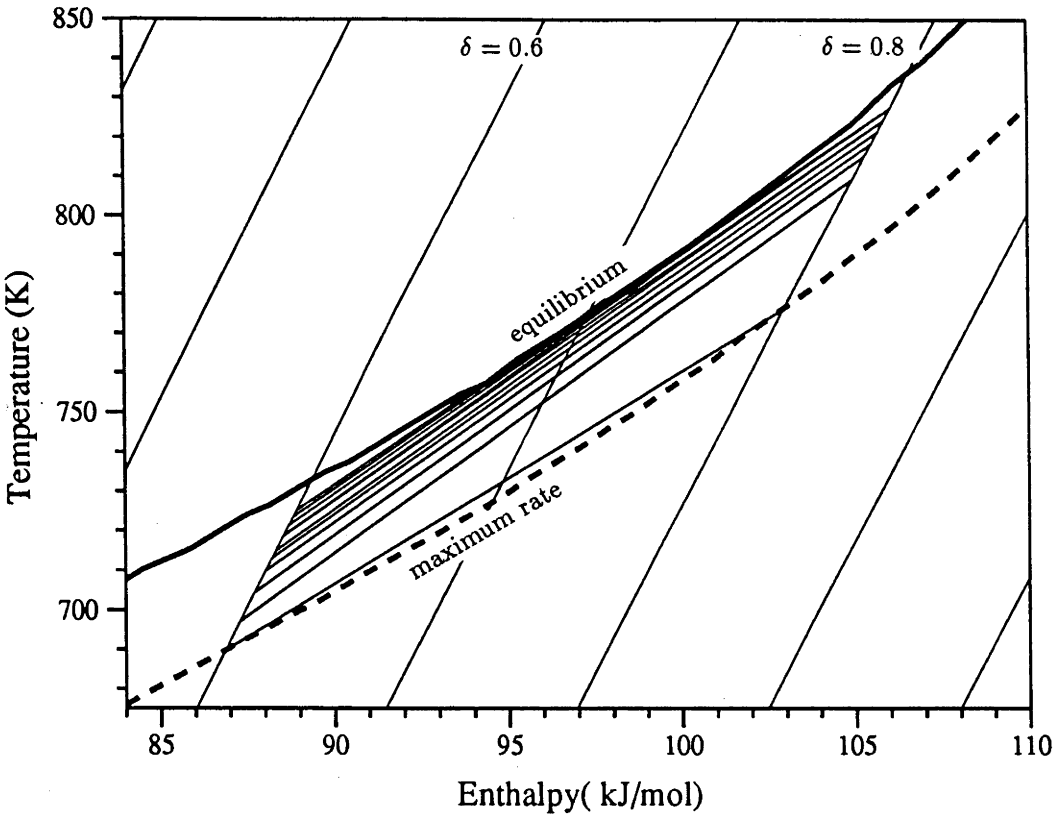

Figure 6.4: Optimised linear paths between $\delta = 0.6$ and $\delta = 0.8$, for available catalyst volume to minimum required volume ratios between 1 and 3 ($\frac{V}{V_{min}} = 10^{(n \times 0.0477)}$, $n = 0$ to 10) (200 atmospheres).

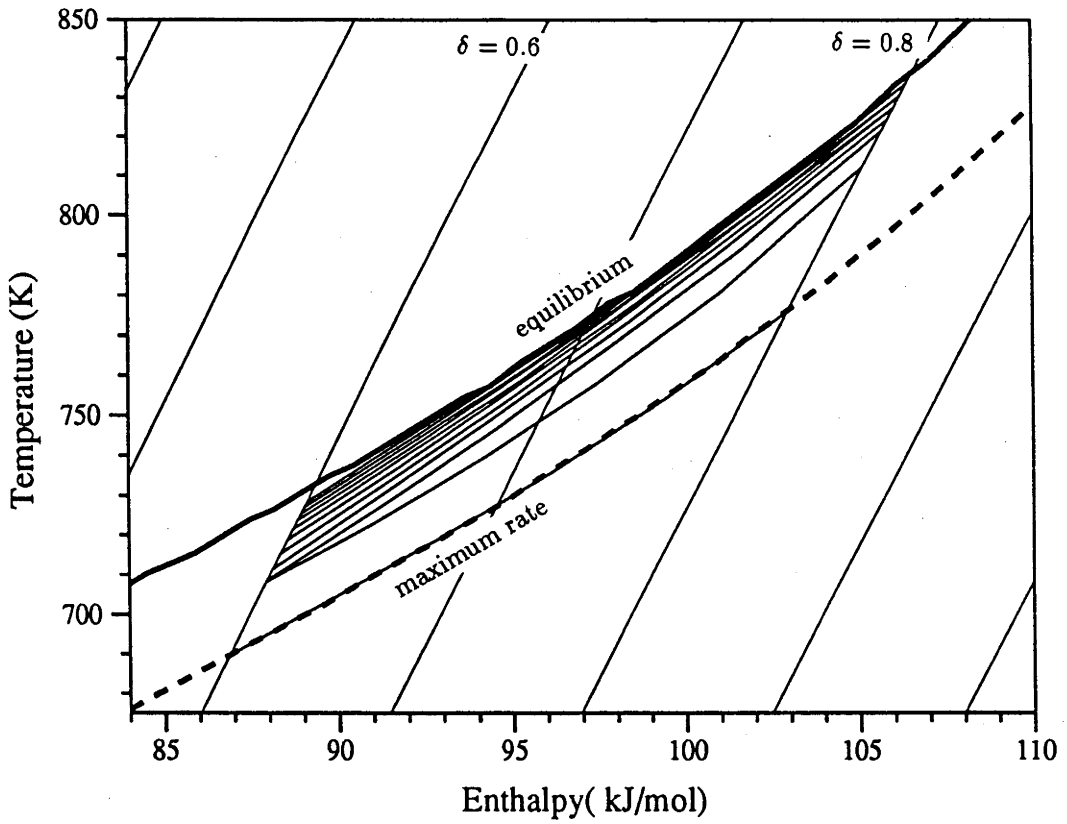

Figure 6.5: Optimised 5 stage paths between $\delta = 0.6$ and $\delta = 0.8$, for available catalyst volume to minimum required volume ratios between 1 and 3 ($\frac{V}{V_{min}} = 10^{(n \times 0.0477)}$, $n = 0$ to 10) (200 atmospheres).

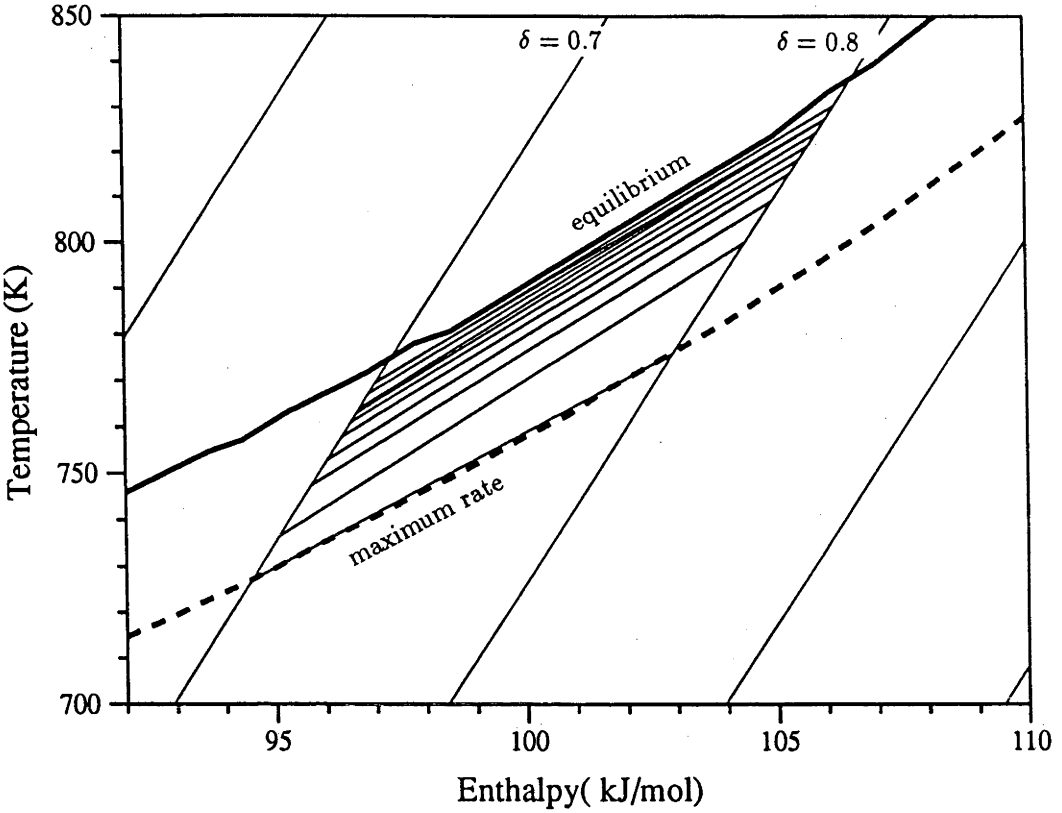

Figure 6.6: Optimised linear paths between $\delta = 0.7$ and $\delta = 0.8$, for available catalyst volume to minimum required volume ratios between 1 and 3 ($\frac{V}{V_{min}} = 1$ and $10^{((2n-1)\times 0.0236)}$, $n = 1$ to 10) (200 atmospheres).

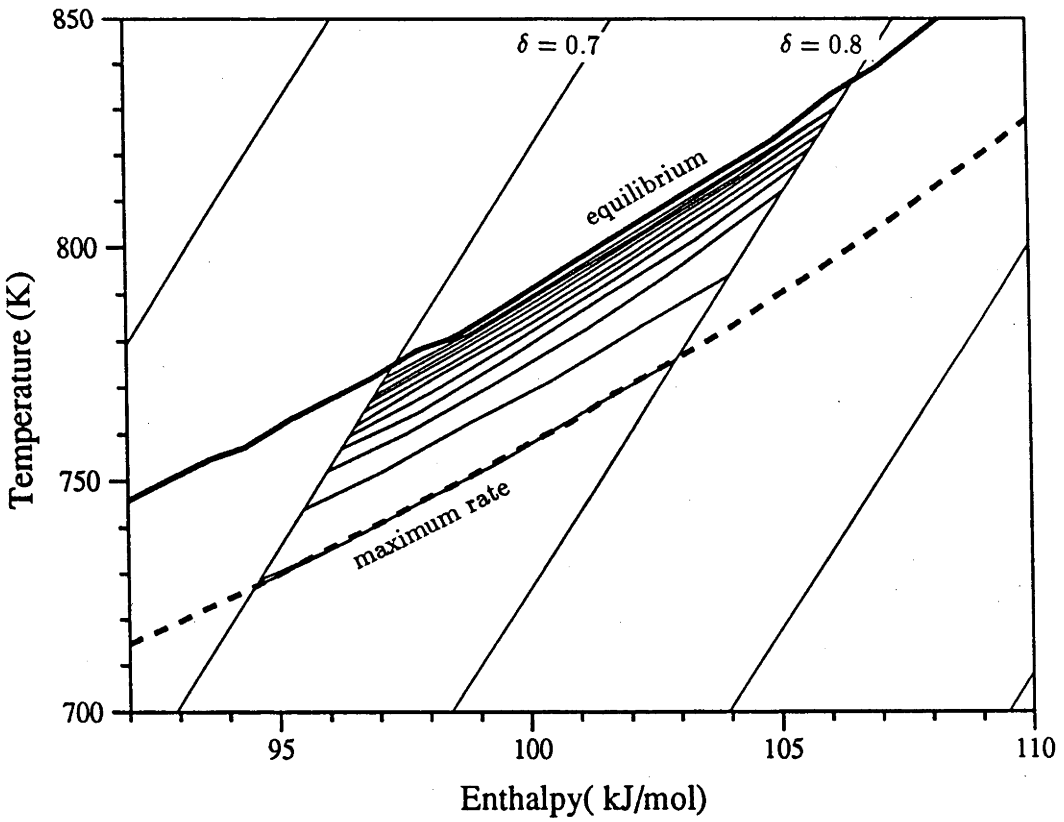

Figure 6.7: Optimised 5 stage paths between $\delta = 0.7$ and $\delta = 0.8$, for available catalyst volume to minimum required volume ratios between 1 and 3 ($\frac{V}{V_{min}} = 1$ and $10^{((2n-1)\times 0.0236)}$, $n = 1$ to 10) (200 atmospheres).

enthalpy plane, then since the contours of constant efficiency are very nearly straight, its efficiency will be unchanged. If it is an optimum path then the required volume should not change also, this would be the case if $\frac{\partial V}{\partial T}|_{\delta 1}$ is equal to $\frac{\partial V}{\partial T}|_{\delta 2}$. In the light of equation 6.4, this will be the case if $\frac{1}{R^2}\frac{\partial R}{\partial T}$ is equal at each end. Examination of the families of optimum linear paths in conjunction with the constant rate contours suggests that this is indeed the case. Extending this argument to the general optimum paths, given that the efficiency contours are approximately straight and evenly spaced, $\frac{1}{R^2}\frac{\partial R}{\partial T}$ should be approximately constant along each optimum path, which it appears to be. This discussion also points the way to a possible variational calculus approach to the optimisation problem.

The determination of optimum linear reaction paths was tested for a specific case, by evaluating the efficiency and required volume of a range of linear paths generated from all combinations of a series of representative temperature endpoints, and manually estimating the optimum paths. The validity of the calculations for multiple stages is supported by the observation of a smooth transition from linear to multiple stage paths, and that use of around five stages is sufficient to produce a general optimum profile, which remains unchanged if more stages are used. Figure 6.8 shows superimposed 1, 5 and 20 stage paths for the interval $\delta = 0.7$ to $\delta = 0.8$. If the computational 'noise' is ignored, the transition from single stage to large stage number paths is smooth and consistent.

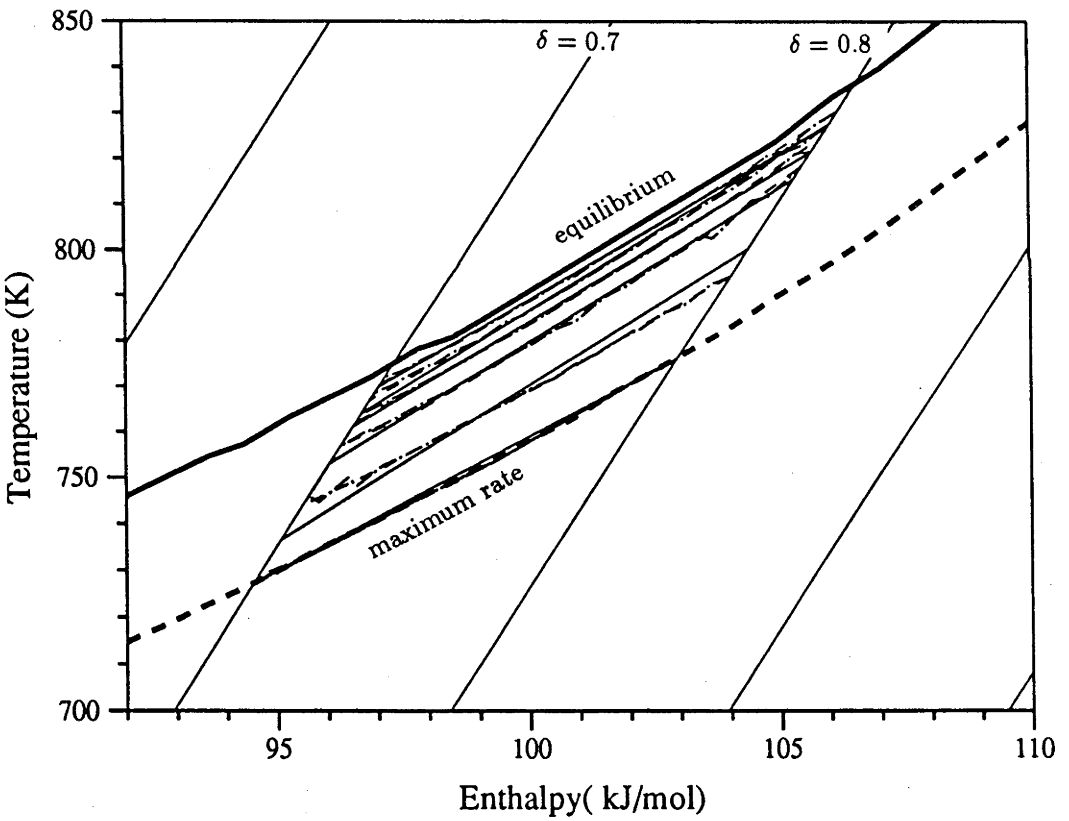

Figure 6.8: Superimposed optimised 1 (—), 5 (– –) and 10 (– · –) stage paths between $\delta = 0.7$ and $\delta = 0.8$, for available catalyst volume to minimum required volume ratios between 1 and 3 ($\frac{V}{V_{min}} = 1$ and $10^{((5n-4)\times 0.0236)}$, $n = 1$ to 5) (200 atmospheres).

It is apparent from the families of optimum paths presented in figures 6.4 to 6.7, that the relationship between available volume and the proximity of optimum paths to the equilibrium line is very non-linear. This non-linearity is reflected in the relationship between path efficiencies and available volume. Figure 6.9 shows the relationship for optimum

linear, optimum 5-stage and non-optimum paths of the same slope as the maximum rate contour. It is apparent that an available volume of approximately three times the mini-

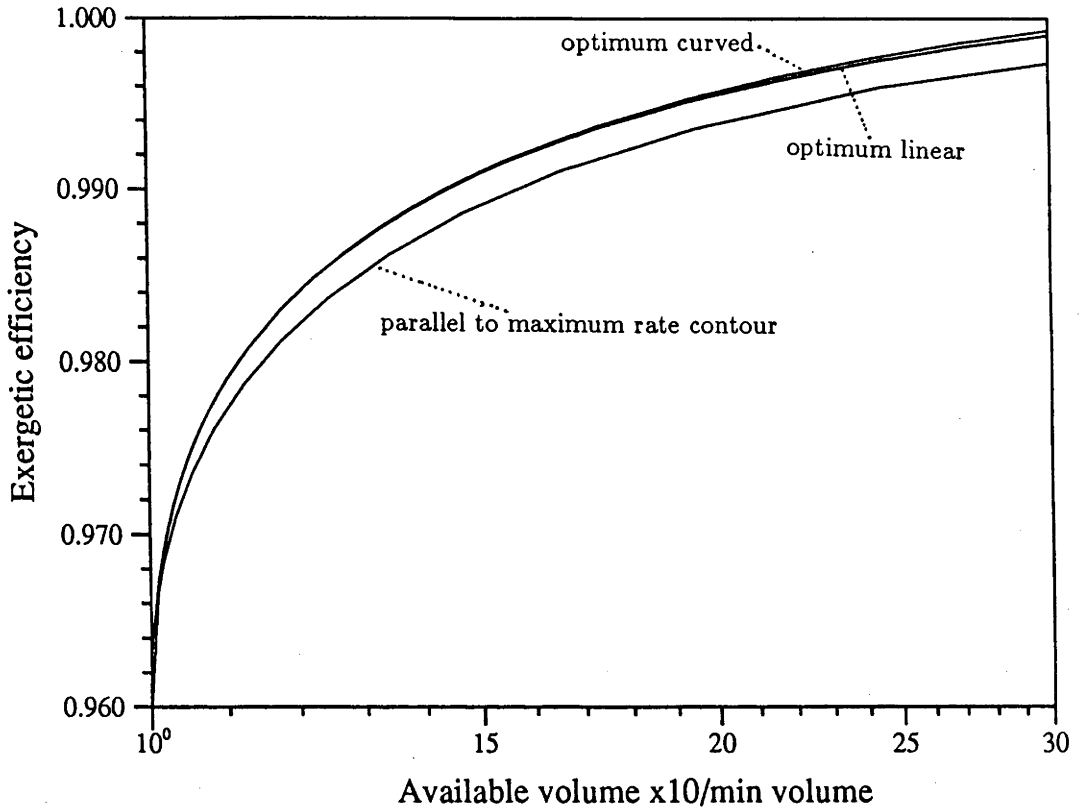

Figure 6.9: Relationship between efficiency and available volume for optimised general paths, optimised linear paths and paths parallel to the minimum volume path between $\delta = 0.6$ and $\delta = 0.8$ (200 atmospheres).

mum required provides nearly all of the possible efficiency gain. Increasing the available volume by only 10% above the minimum required is sufficient to produce a significant efficiency improvement.

It is also apparent that 5-stage optimum paths have efficiencies which are only marginally higher than the optimum linear paths, suggesting that there would be little reason to modify a heat recovery system design to produce a non-linear reaction path. However, when the available volume exceeds the minimum necessary, there is a significant efficiency improvement in choosing an optimised path over a path chosen simply so as to be parallel to the minimum volume path.

The variation in slope of optimised linear paths for various minimum reaction extent endpoints is shown in figure 6.10. The limitation of the possible temperature endpoints at the maximum reaction extent to one of 100 discrete values, results in errors in the slope of optimised paths which are reflected in the curves of figure 6.10. The slope error for a given temperature error obviously increases as the width of the reaction extent interval is decreased. This is in contrast to the efficiency volume curves which are relatively unaffected due to the insensitivity of efficiency to path slope.

The greatest deviation from the slope of the minimum volume paths occurs for available volumes which are approximately 10% higher than the minimum. The size of the maximum deviation does not vary significantly with the choice of minimum reaction extent, however as the average reaction extent of paths is increased, the effect is to lower $\frac{\partial H}{\partial T}$ for all available

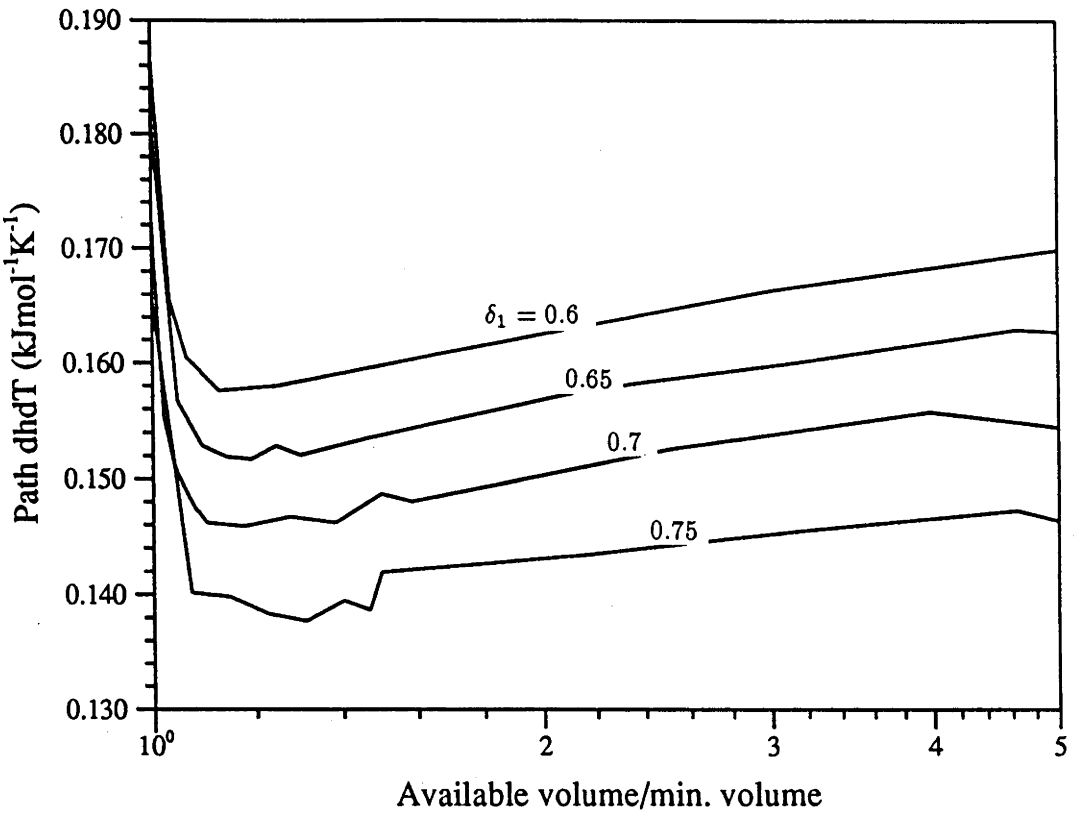

Figure 6.10: Relationship between $\frac{\partial H}{\partial T}$ and available volume for optimised linear paths between $\delta_1 = 0.6, 0.65, 0.7, 0.75$ and $\delta_2 = 0.8$ (200 atmospheres).

volumes in line with the changing slope of both the equilibrium line and the maximum rate line.

The direct work recovery concept as originally conceived by Carden (1987), involves three heat exchange paths carrying reactants to extract heat from the exothermic reactor. This gives an essentially linear reaction path with $\frac{\partial H}{\partial T} = 0.173 Jmol^{-1}K^{-1}$. This is close to that of a minimum volume path between reaction extents of 0.7 and 0.8. It is apparent from figure 6.10 that a range of reaction extent intervals exist for which the optimum linear reaction path for a particular available volume would have the same value of $\frac{\partial H}{\partial T}$ as that produced by the direct work recovery method. For example, the reaction extent interval of 0.55 to 0.8 would have an optimised linear path with $\frac{\partial H}{\partial T}$ close to $0.173 Jmol^{-1}K^{-1}$, for an available volume approximately three times the minimum.

These results have established the form of the relationship between the efficiency of optimised reaction paths and normalised available volume for a given reaction extent interval. In order to address the choice of reaction extent endpoints, the efficiency volume relationship for alternative intervals must be considered on the same relative scale. Figure 6.11 presents the efficiency volume relationship for optimised linear paths for various reaction extent intervals with required volumes normalised against the minimum volume required for a path between $\delta = 0.75$ and $\delta = 0.8$. The curves demonstrate the reduction in required volume that results from operating at the higher average temperatures encountered for paths of higher average reaction extent. This advantage must ultimately be traded off against the increased reactant mass flow rate required to maintain the same thermal capacity with a smaller reaction extent interval, with its associated effects on pressure drops and heat exchanger performance.

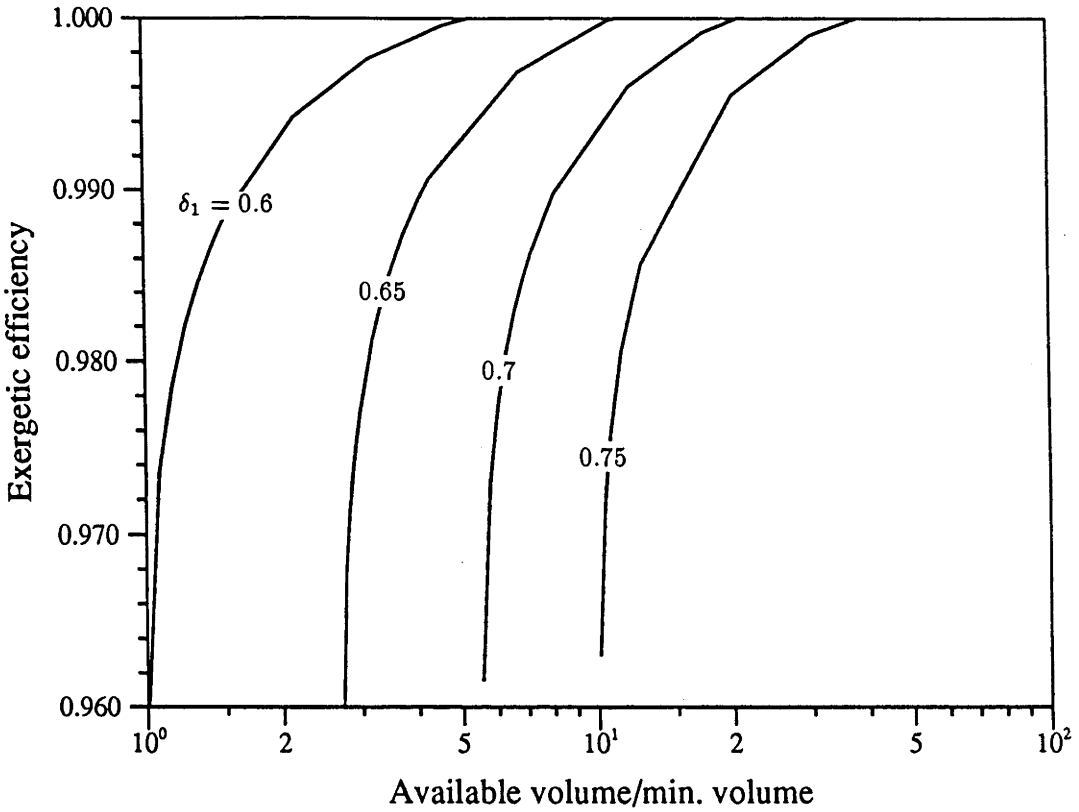

Figure 6.11: Relationship between efficiency and relative available volume for optimised linear paths between $\delta_1 = 0.6, 0.65, 0.7, 0.75$ and $\delta_2 = 0.8$ (200 atmospheres).

6.3.1 Conclusions

A systematic approach to energy conversion system design, based on identifying subsystems with a single cost determining variable and applying dynamic programming optimisation techniques, is a useful approach to analytical analysis which can be combined with creative processes in an iterative way. These ideas have been developed into a method for the analysis of an ammonia based solar thermochemical energy transport and storage system. Dynamic programming has provided a suitable approach to optimisation of exothermic reaction paths subject to the constraint of constant volume per thermal capacity and appears suitable for application to other similar problems. A number of specific conclusions can be drawn from the exothermic reaction path analysis.

- Increasing the available catalyst volume by a factor of three is sufficient to increase the exergetic efficiency from the minimum available volume value to close to the maximum achievable value, while small increases of the order of 10% are sufficient to achieve a significant fraction of the possible efficiency gain.
- There is very little efficiency improvement to be obtained by utilizing an optimum path of arbitrary shape in favour of an optimised linear path.
- There is a small but possibly significant efficiency improvement to be obtained by using an optimum linear path in favour of a path parallel to the maximum rate contour.
- It is possible to choose available volume and reaction extent interval combinations which have optimum linear paths which are compatible with the method of heat

recovery inherent in the direct work recovery concept.

The algorithm developed should be directly applicable to other thermochemical systems, with suitable adaptation the approach could also be applied to situations where energy is recovered from staged adiabatic reactors with intermediate reactant cooling. In the context of the optimisation of a complete ammonia based thermochemical system, the choice of reaction extent endpoints for the exothermic reactor is probably the most significant issue, solution of the optimum reaction path problem has provided one of the necessary prerequisites for consideration of this choice.

Part III

Experimental Work

Chapter 7

Experimental Arrangement

7.1 New Laboratory

The old laboratory contained all the major components needed for the 1978-1983 NERDDC funded closed loop demonstration. Most of the reactant handling apparatus and the dissociator were housed in a partitioned area, while the synthesis reactor, the ammonia supply cylinder and two 20*l* storage pressure vessels, were mounted on a roof area above the laboratory. The old closed loop arrangement was designed with a philosophy of achieving a high level of operational flexibility from operation of the panel mounted valves. All the control valves for the system were mounted in panels built into the walls of the partitioned area, so that experiments could be operated by personnel working from outside and so afforded some protection in the event of leaks or equipment failure. Valves were arranged on control panels in a manner which schematically reflected their sequence in the system, the mild steel connecting piping was built up in layers behind the wall panels.

There were a number of inherent shortcomings with this experimental arrangement. The combination of physically unrelated positioning of major components and their control valves, plus the high level of built in operational flexibility resulted in an extremely complex network of piping. The identification of the actual flow paths within the system from casual observation of the experimental arrangement was extremely difficult. The degree of complexity, together with the relatively unreliable performance of the "Ermeto" single ferruled pipe fittings used, meant the system was troubled by leaks which were difficult to locate and rectify. In addition, the high density of pipes and connections behind the wall panels made modifications difficult and presumably contributed to the effort required during the original construction.

The new experimental arrangement has the experimental components housed in a prefabricated shed on the reinforced concrete roof of a laboratory/workshop area. The lower area houses the data aquisition computer and this allows experiments to be monitored remotely. Whilst it is considered satisfactory for the operator to be present in the experimental area during experimental runs, being able to monitor the progress from the lower level and terminate it if necessary, reduces the exposure time to the risks of the potential effects of leaks or equipment failure. As the experimental arrangement is currently configured, experiment start up, and routine adjustments must be done from within the experimental area. Many of these operations could be performed remotely or automatically, with minor extensions to the current control systems.

In contrast to the old laboratory, rather than build in operational flexibility, a construction technique that allows easy extension and modification was chosen. The actual system constructed was designed to satisfy the immediate experimental goals with the

minimum number of valves and interconnections. Considerable attention was given to the layout of components. The floor plan adopted has the major experimental components, namely the dissociation and synthesis reactor assemblies, located in the centre and the majority of the reactant and gas supply and handling items arranged around the walls. Although this project only involved open loop dissociation experiments, the arrangement has been designed to evolve in stages to the complete closed loop system planned for the future. Interconnections have been routed as directly as possible, with control valves incorporated in convenient locations throughout the system. The result is a system in which, despite a moderate but unavoidable level of complexity, it is possible to deduce the function of any interconnection or control valve by a casual observation of piping paths. Such an identification process is also aided by appropriate colour coding of piping and labelling of valves. Figure 7.1 is a view of the layout in the new experimental area.

The construction technique employed is central to the 'ergonomic' success of the arrangement. The walls of the experimental area have been lined with a network of "Unistrut" channel. The Unistrut system is a commercially produced range of modular products which includes special purpose nuts and pipe clips which allow attachment of items of equipment and piping quickly and easily anywhere on the network of channel. The network is based on a series of permanently fixed vertical sections of channel mounted $200mm$ out from the walls and with a uniform $793mm$ lateral spacing. Horizontal sections are affixed to the vertical sections with unistrut nuts wherever they are required and the uniform lateral spacing allows standard horizontal sections to be used anywhere in the system. Bolting horizontal sections of channel onto the face of the vertical sections means that the face of these sections is offset by the channel thickness plus the thickness of spacers which are also added. This technique was chosen so that vertical elements of piping, (which are clipped to horizontal channel sections) are all in a different plane to the horizontal pipe sections (which are attached to vertical channel sections). This requires that 90° pipe bends must incorporate the change in plane. The advantage is that additions to the system can be added without interference from pipes already in situ.

The openness of the whole arrangement allows 360° access to most fittings, which is of considerable benefit during assembly and modification. As in the old laboratory the majority of the connecting pipe is $1/4inch$ o.d. 16 gauge mild steel. This gauge is considerably stronger than is required for a $30MPa$ maximum expected working pressure, however, the extra thickness has the advantage of providing increased rigidity and reduced susceptibility to tube bore collapse when fittings are opened and retightened. The "Autoclave Engineering" control valves from the previous arrangement have been re-used. Although the control valves have single ferrule pipe end fittings, they have given less trouble in the past than the Ermeto pipe fittings. The use of Ermeto fittings, has been abandoned, in favour of superior double ferruled "Swagelock" fittings, in all sections of the system which handle reactants. This combined with the reduction in the number of connections and the improved access, has made the elimination of leaks a relatively easy task.

Although presence in the laboratory area during experiments is considered reasonably safe, the precaution of wearing face protection when approaching high pressure equipment is taken. The laboratory area is fitted with compressed air breathing hoods, which although not routinely worn, are kept operating during experiments for use in case of malfunctions that result in a major leakage of ammonia. In the event of accidents involving ammonia splashes to face or body, the laboratory has emergency shower and eye-wash units immediately outside an emergency exit door.

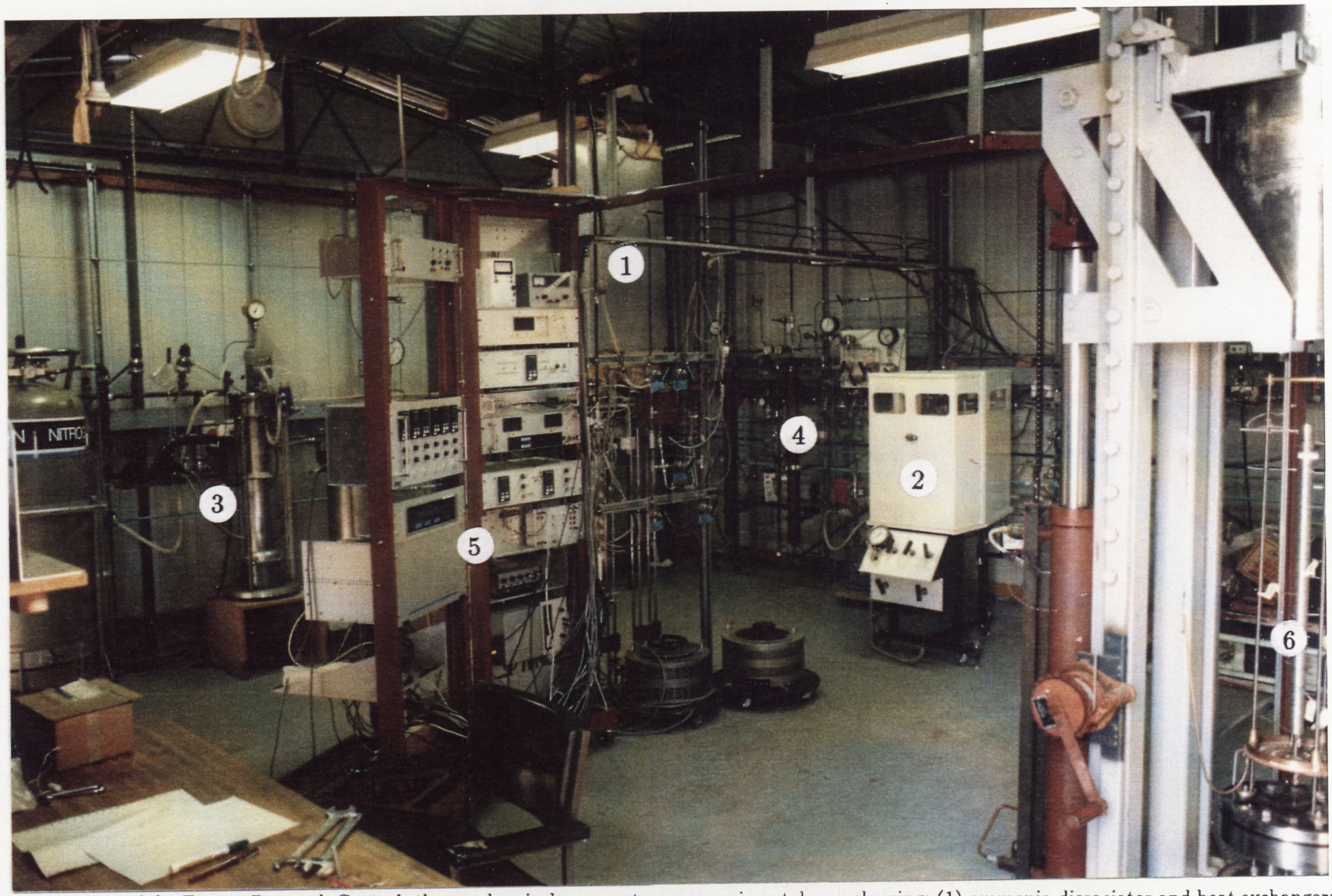

Figure 7.1: View of the Energy Research Centre's thermochemical energy storage experimental area showing; (1)-ammonia dissociator and heat exchanger; (2)-balancing separator; (3)-high pressure nitrogen supply; (4)-ammonia accumulator and metering valve; (5)-data acquisition and control electronics; (6)-ammonia synthesis reactor.

7.2 Experimental Apparatus

The open loop experimental arrangement as it currently stands is shown schematically in figure 7.2. For the dissociation experiments which constituted the experimental component of this project, reactants followed the 'synthesiser bypass' path. At present, the components required to include the synthesis reactor in the system are largely ready for assembly, but have not yet been tested, the details of the synthesis reactor design are discussed in chapter 9.

'Technical grade' 99.98% pure ammonia for the open loop dissociation experiments was obtained from "Ajax Chemicals Pty Ltd". This ammonia is supplied as a liquid in a $34kg$ supply vessel, which is mounted in an inverted position on the roof of the experimental area. A "Sprague" air driven positive displacement pump is used to fill a two litre, high pressure, accumulator vessel with ammonia from the roof mounted supply. This is done prior to and sometimes during experiments. The Sprague pump compresses liquid ammonia up to $40MPa$, depending on the setting of the compressed air supply regulator. To prevent cavitation on the inlet stroke of this ammonia pump, a combination of gravity feed from roof level, and the cooling of the incoming ammonia and the pump body is employed. The cooling is achieved with a circulating ethylene glycol based fluid cooled to $-15°C$ by a refrigeration unit.

The flow rate of liquid ammonia is determined by a manually adjusted needle valve (Whitey SS22RS4) with a micrometer handle. To ensure a steady flow rate, a constant pressure drop must be maintained across the valve. This is done by separately maintaining the ammonia accumulator vessel and the system exit at constant pressure. The pressure difference between these two is kept considerably larger than the pressure drop associated with the reactor, so that variations in the conditions within the reactor have very little effect on the flow rate.

The method of pressure control makes use of the high pressure nitrogen gas supply previously developed by Carden (1984*a*). This system, which is based on the compression of liquid nitrogen, is discussed in detail in appendix C. The pressure control is achieved by using the nitrogen as a buffer gas, with pressures set by two Circle Seal LR20CB4112HG pressure regulators. These regulators require a continuous minimum flow of gas to function correctly, because a difference in cracking and reseating pressures for the regulating valve, is discernable, and because they are unable to close off gas flow entirely (either by design or due to wear). One regulator pressurises the ammonia accumulator. The necessary minimum flow for this regulator is maintained by continuously bleeding nitrogen from a vent valve. At the system exit the reactant stream combines with a continuous stream of nitrogen from the second regulator before flowing through a throttle valve to a vent line. The throttle valve must be adjusted so that the desired pressure is not exceeded under conditions of maximum expected reactant flow, the pressure regulator then attempts to maintain a constant pressure by varying the nitrogen flow to compensate for reactant flow variations. The regulators are imperfect pressure controllers so reactant flow variations do result in some fluctuation in exit pressure. Opening the throttle valve further results in an increased flow of nitrogen, reducing the effect of reactant flow variations at the cost of increased nitrogen consumption.

The pressure control arrangement resulted from an evolutionary process over a period of 7 months. In the initial attempt, the ammonia accumulator pressure was determined by continuous operation of the Sprague pump, with a fixed volume of gas contained within the accumulator serving to filter out pressure pulses from pump strokes. Exit pressure was set with a spring loaded pressure relief valve operating as a back pressure regulator. This

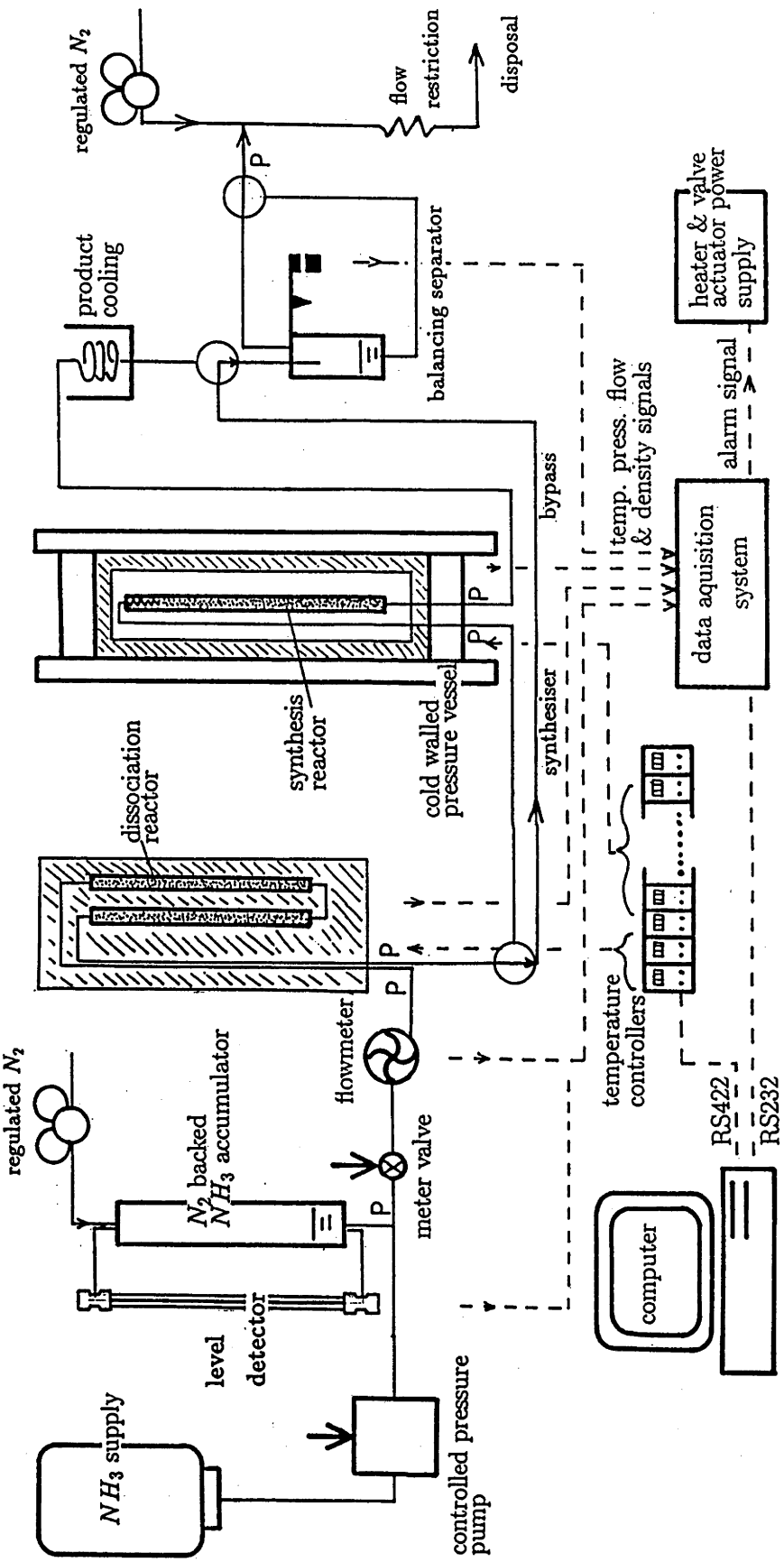

Figure 7.2: The open loop energy transfer experimental layout.

was not a satisfactory arrangement as the output pressure of the Sprague pump proved to be strongly effected by pumping rate, and the exit relief valve possessed an unacceptable level of hysteresis. The two elements combined, through the feedback path provided by the ammonia flow-rate, to produce a very unstable system. This initial attempt grew by a series of stages to the final successful arrangement. During the evolutionary period, interpretation of system behaviour was complicated by problems of intermittent blockages of the flow metering needle valve, and later the exit throttle valve. These were overcome by the installation of suitable inline filter units.

The original intention was that, after initial calibration with the balancing separator, the rate at which liquid ammonia left the metering valve, would be measured by the rotary flow meter unit developed previously by Whelan (1979). However to date this unit has not been re-commissioned following damage to its bearing mechanism. Instead inlet mass flows were determined either from the measured pressure drop across the metering valve, or later using an electronic liquid level detecting probe which was fitted to the accumulator vessel. These methods are discussed in detail in appendix C.

Ammonia flows to the dissociator via the inlet passage of a counterflow heat exchanger, reaction products leave the exit passage of the heat exchanger at close to ambient temperature. Reaction products from the dissociator are a mixture of nitrogen, hydrogen and undissociated ammonia. Measurement of the mixture composition is central to a quantitative determination of the reactor's behaviour. This role is performed by the balancing separator.

The balancing separator (Carden 1982*a*) is a small pressure vessel, mounted on an electronically monitored balance. It has flexible connections to inlet, vent and drain ports. The reaction product mixture that leaves the exit passage of the counterflow heat exchanger that is associated with the dissociator, is typically a two phase mixture. In the balancing separator the liquid ammonia component is allowed to settle out while the gaseous fraction passes on to the system exit. Measurement of the rate of liquid accumulation allows the reaction extent of the mixture to be deduced. When full, the gas vent port is closed and a liquid drain port opened to allow the accumulated liquid to leave via the system exit. The balancing separator, although constructed previously, had not been tested or calibrated. A considerable amount of time during early 1990 was spent doing this (Lovegrove & Hall 1990). A more detailed description of the unit and the results of the calibration process are also presented in appendix C.

The mixture of reaction products and nitrogen from the pressure regulator, that leaves the throttle valve at the system exit, passes to a gas disposal system. This consists of a cabinet with a water spray to remove ammonia and a connection to a manifold which allows the scrubbed gas to vent to the atmosphere.

There are a number of details to the system which are not conveyed by figure 7.2. The dissociator, the ammonia accumulator and the nitrogen accumulator are all protected from over-pressure by suitable rupture disc units which are all connected to a common vent manifold. Bourden tube dial pressure gauges are included at various places in the system, mainly to assist the operator rather than provide quantitative information. Non-return valves (Autoclave Engineering SWB4400) immediately at the exit of the two nitrogen pressure regulators serve to prevent back flow of gas containing ammonia in situations when the nitrogen supply pressure drops. Autoclave Engineering, SWF4-35, 35 micron metal frit, line filters are incorporated at the ammonia pump exit, in front of the ammonia metering valve, at the dissociator exit, and prior to the system exit throttle valve. In addition, a Whitey SS-4TF filter unit with a 2 micron metal frit element gives additional protection to the metering valve.

In addition to the balancing separator and the ammonia accumulator level measurement, the instrumentation of the experimental arrangement consists of pressure transducers at the points indicated in figure 7.2, plus a large number of thermocouples. The operation and calibration of the pressure transducers is presented in appendix C. The majority of the thermocouples are associated with the dissociator and the heat exchanger, however, in addition, the temperature at the balancing separator inlet and the ambient temperature adjacent to the dissociator are measured. Approximately half of the thermocouples used are commercially manufactured stainless steel sheathed, mineral insulated, shielded junction, K type (chromel-alumel) thermocouples. These are $1mm$ diameter units with calibration accuracies quoted by the manufacturer of $\pm 0.75\%$. The balance is made up of a combination of exposed junction type K and type J (iron-constantan) thermocouples.

The establishment of the new laboratory facility has been enhanced by the purchase of a computer-based data acquisition and control system. This system includes a "Chessel 4500" data acquisition unit plus 15 "Eurotherm 808" self tuning proportional-integral-differential (PID) temperature controllers. The Chessel unit currently has 48 channels of analogue input and provides analogue to digital conversion, thermocouple linearisation, and alarm level detection, amongst other features. The Chessel unit and the controllers are linked to an IBM compatible personal computer via RS232 and RS422 serial communications lines respectively. Data is recorded and displayed on the PC using "Lab Tech Notebook", a commercial data acquisition package. For the dissociation experiments measurements of all variables were recorded every 20 seconds. There is also a safety control system which can close the experimental system down as a result of an alarm signal from the Chessel or the operation of one of three panic switches. The details of the implementation and operation of these data aquisition and control aspects are also discussed in detail in appendix C.

Chapter 8

Dissociation Experiments

8.1 The Experimental Program

The first test of the dissociator in the new experimental arrangement was on the 14th of March 1990 and experimental work for this project continued until the 28th of May 1991. Graphical results and tabulated steady state data from every run are presented in chronological order in appendix D. The program was characterised by a continual process of evolution in the understanding of the system behaviour and improving the instrumentation, control and analysis. As a result many of the earlier runs are of little value in providing quantitative results.

The investigation of steady state behaviour has explored a range of pressures, inlet mass flows, and setpoint temperatures. Although the conditions covered have come close to the limits achievable with the current experimental system, the investigation has by no means covered the whole range of possible combinations. Rather, it has been limited to a reasonably comprehensive investigation of the effect of varying each parameter over an achievable range of values whilst maintaining the others at 'typical' operating values.

Interspersed with the dissociation runs, investigations of behaviour without flow and with nitrogen flow were also made in order to examine thermal loss and internal heat transfer mechanisms. In addition to this a series of non steady state runs, aimed at simulating the operation of a dissociation reactor in a dish receiver context, was also carried out.

8.2 The Dissociation Reactor

8.2.1 Reactor design

The dissociator unit was developed for the 1978-1983 closed loop demonstration project and has been described previously by Williams (1980*c*). The unit incorporates a counter-flow heat exchanger in an all welded construction as detailed in Figure 8.1. The reactor is based on two parallel sections of $21.3mm$ o.d. $15.8mm$ i.d. inconel tubing. These two sections are filled with catalyst particles, with access provided via removable plugs at each end. Heat at a rate of up to approximately $2.3kW$ can be provided to each section by "Pyrotenax" stainless steel sheathed mineral insulated heating elements, which are wound around the outside. A $5mm$ o.d. tube runs up the centre of each column, these tubes pass through the bottom end plugs and extend to the top of the columns where they have blanked ends. These tubes allow internal temperatures to be measured using thermocouple probes.

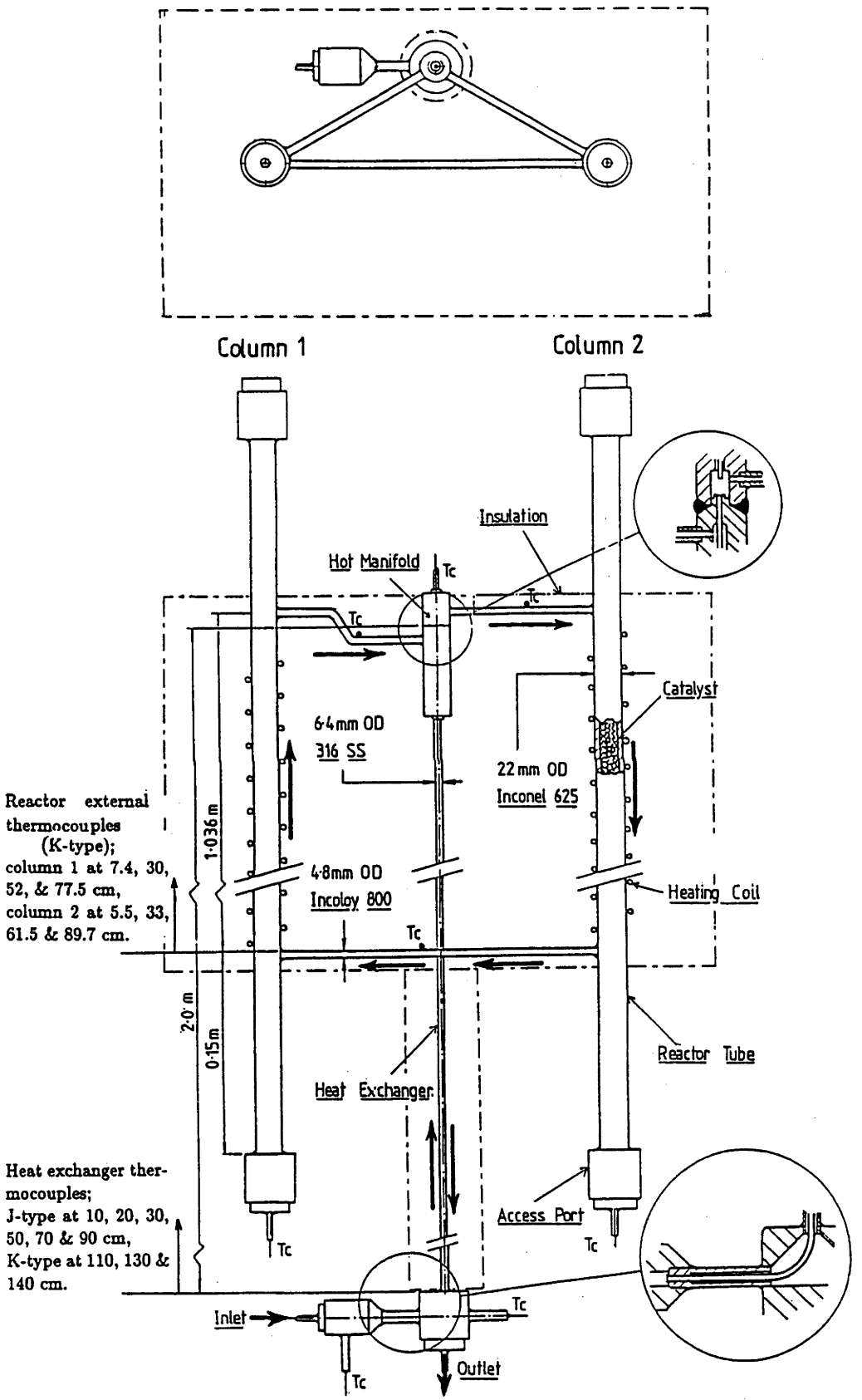

Figure 8.1: Construction of the ammonia dissociator and counterflow heat exchanger. Tc ≡ thermocouple.

Reactants enter via one of the heat exchanger passages, flow down one reactor column, pass through a $4.8mm$ o.d. transfer passage to the bottom of the other column, and flow up this column before leaving via the other passage of the heat exchanger. Figure 8.1 also shows the dissociator/heat exchanger unit in plan view with the reactor columns identified as column 1 and column 2. The heat exchanger is a construction of two co-axial tubes, with a spiral of Nickel wire in the annular space between the two. According to Williams (1980*c*), the design is the same as that used for the 'Mark iv' dissociator experiments reported previously (Williams & Carden 1979*a*). This implies a construction consisting of a thin walled $1.5mm$ diameter 304 stainless steel tube inside a $6.4mm$ diameter, 16 gauge, 316 stainless tube, with nickel wire spirals wound inside and outside the inner tube to promote turbulent flow. For the early runs, pipe connections were made so that incoming ammonia passed through the outer passage, and outgoing reactants passed through the inner one. With this arrangement the first reactor column encountered was that which has been designated column 1. However this arrangement resulted from a misinterpretation of the heat exchanger design. The outgoing reactants, with smaller expected heat transfer coefficients than the incoming ammonia, are intended to flow in the outer passage and benefit from the greater surface area available. Pipe connections were changed accordingly, but the labelling of data acquisition system channels has remained the same. Hence the distinction is made, in this text, that reference to column 1 and column 2 is according to figure 8.1, while reference to the 'first' or 'second' 'reaction chamber' indicates the order as seen by the reactants during the experimental run in question.

The pressure/temperature combinations that the dissociator was designed to operate under mean that it has a finite lifetime due to eventual creep failure of the inconel 625 wall material. Williams has presented the results of the design lifetime calculations. At $800°C$ and $20MPa$ the expected lifetime is 10^3 hours, however at $750°C$ and $10MPa$ the lifetime is of the order of 10^7 hours. Presumably the fraction of the lifetime remaining can be deduced from integrating the 'normalised' contributions to lifetime consumption from the various operating conditions encountered. Apart from some preliminary tests during 1980-82 the reactor has remained unused until this project. The total operating time for the period 1988 to June 1991, was less than 100 hours. Taking the conditions very conservatively as $720°C$ and $10MPa$ throughout that period suggests that only a negligible fraction of the lifetime has been consumed.

Figure 8.1 also indicates the position and type of thermocouples used for temperature measurements. The J type thermocouples on the heat exchanger were spot welded to the outer wall during manufacture. These have been augmented by some type K unshielded junctions which have been attached with nickel wire ties. The thermocouples on the exterior of the reactor columns are K type shielded junction probes. These have been inserted between windings of the heater coils, with their tips in as close contact as possible with the reactor wall. Temperature measurement of inlet and exit fluid temperatures is by similar type K probes inserted into the fluid stream via appropriate Swagelock fittings.

In the old laboratory, the dissociator was insulated with slabs of "Microtherm" block insulation. This was removed, in order to position the thermocouples, and replaced with a more convenient arrangement of a hinged aluminium case filled with a combination of rigidised fibreglass and "Kaowool" ceramic fibre insulation material. With both arrangements the column endcaps are uninsulated and are thus protected from the temperature extremes experienced by the main body of the reactor.

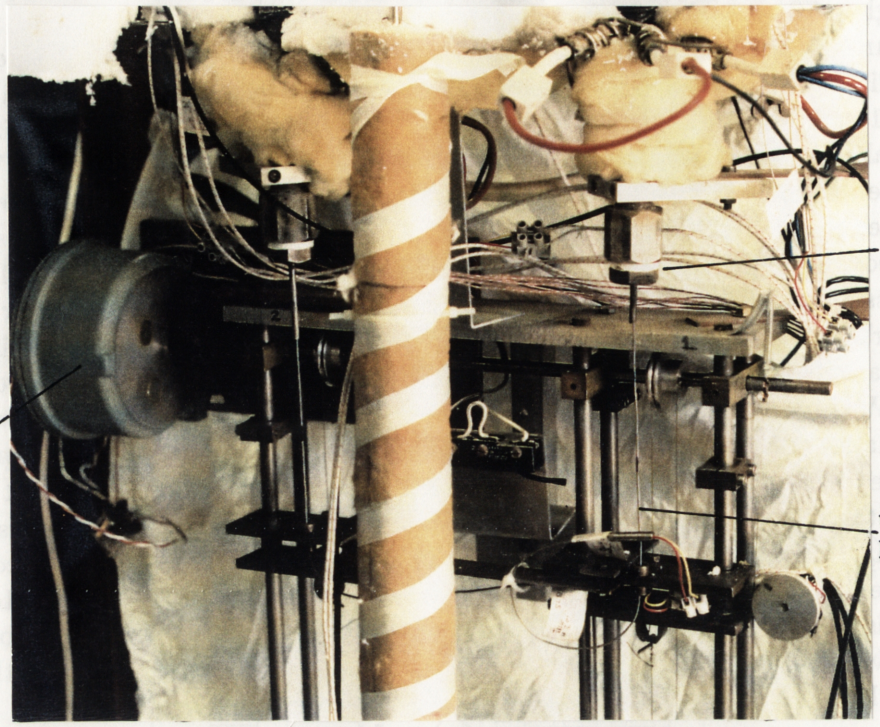

Figure 8.2: Thermocouple scanning mechanism for dissociator internal temperature profile measurement.

8.2.2 Internal Temperature Scanning System

Temperatures within the central passages of the two reaction chambers can be measured using two $1.3m$ long $1.5mm$ diameter stainless steel sheathed, shielded junction type K thermocouple probes.

In the laboratory the dissociator is mounted with the bases of the reaction chambers $1375mm$ above the floor. As well as allowing for the extra length of the counterflow heat exchanger, this vertical space is used for the mechanism which moves the two probe thermocouples. The mechanism, which is shown in figure 8.2, consists of a frame which moves on vertical tracks. The outer ends of the thermocouples are attached to the frame, which can be moved up and down by two cables which are driven by a $15V$ dc motor with a reduction gearbox. The position of the thermocouples is measured by a multi-turn potentiometer attached to the moving framework. This potentiometer has a pulley fitted to it, which is rotated by a separate cable suspended alongside the vertical tracks.

The limits of motion of the moving framework have been adjusted to give a fully withdrawn position in line with the bottom reactant transfer tube and a fully inserted position in line with reactant inlet and exit tubes. The stainless steel sheathed probes are sufficiently rigid that reinsertion does not cause them to collapse. However, associated with the reinsertion process is a degree of uncertainty in tip position due to the interaction between the variable sliding friction forces and elastic buckling in the exposed sections of the probes.

During experimental runs the probes were kept in their fully inserted positions; when conditions were considered sufficiently steady a temperature profile was taken by moving

the probes downward. This operating regime was adopted for several reasons;

- using the fully inserted position as the normal resting position allows exit and inlet temperatures to be measured during transient behaviour. The probes are also protected from accidental damage;
- scanning down for measurements avoids the tip position uncertainty just described;
- a downward scan produces no noticeable thermal disturbance, in contrast to the reinsertion of the cold probes which causes a detectable short duration drop in reactor temperatures.

The choice of scanning speed for profile measurement is governed by the response time of the thermocouple and the rate at which the data acquisition system makes measurements. Initially the scanning speed was reduced by reducing the dc voltage applied to the motor. This approach limited the maximum scan time to 3 minutes, because the motor stalled when encountering tight spots on the guide tracks when slower scans were attempted.

This scan duration proved insufficient because the probes were unable to respond quickly enough to the temperature variations encountered and because the 20 second sample period of the data acquisition system resulted in insufficient measurements for a detailed profile. Subsequently a different approach was adopted; currently a pulse generator with adjustable duration and frequency is used to operate a relay and send $12V$ pulses to the motor. This produces a stepped motion of the probe which, with appropriate adjustment, approximates a smooth scan with no upper limit on duration.

Figure 8.3 shows the results of tests to determine the response time of the two probes. These tests were done using one of the Eurotherm 808 controllers as a temperature sensor and recording the output at $4Hz$. Step changes were produced by disconnecting the motor and manually raising and lowering the drive frame, with an approximately 1/2 metre movement made in a fraction of a second. It is apparent from the curves that the thermocouple's thermal characteristics can be modelled to a good approximation by a single RC network. On this basis the time constants determined are:

- column 1: $\tau = 4.13 \pm 0.8sec$
- column 2: $\tau = 5.7 \pm 1.0sec.$

The large variation in these values does not reflect random errors in the measurement technique, rather it reflects the different values encountered for each individual step change. This can be attributed to variations in the thermal resistance encountered. This may be the result of varying degrees of oxidation within the internal passages or the fact that the thermocouple probe is somewhat smaller than the passage so that contact between the tip and the wall is not consistently maintained. Differing degrees of contact between tip and wall could also explain the difference in average time constants for the two probes. Alternatively this difference may reflect manufacturing differences between the two.

The magnitude of these time constants results in significant discrepancies between instantaneous measured and actual internal temperatures, even at slower scan rates. Given the qualitative nature of the response function described, the measured (T_m) and actual (T_{act}) internal temperatures are related by;

$$T_{act} = \tau \frac{dT_m}{dt} + T_m \tag{8.1}$$

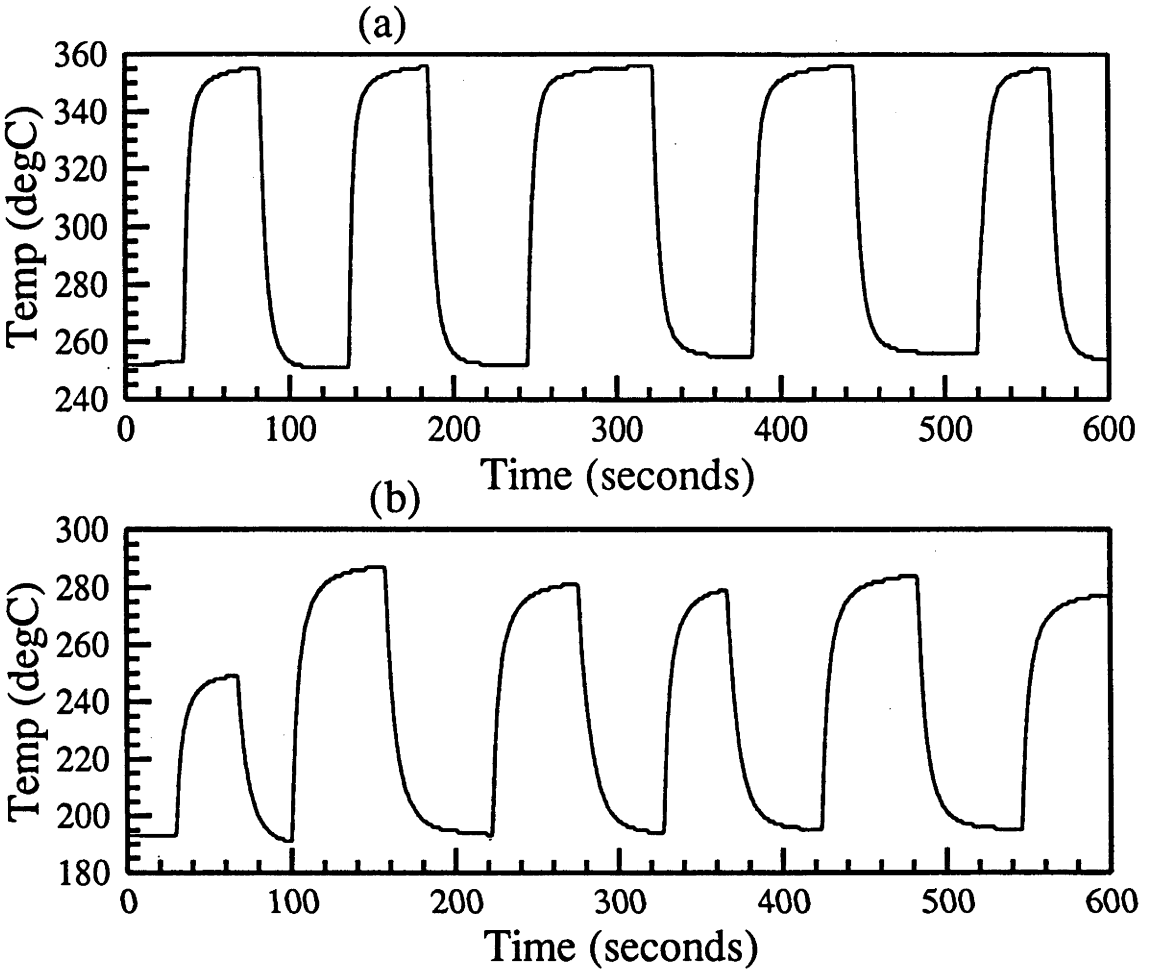

Figure 8.3: Step responses of dissociator scanning thermocouples, (a) column 1, (b) column 2.

where τ is the appropriate time constant. The internal temperature profiles presented in appendix D have been corrected using equation 8.1 with the point-to-point temperature variation used to determine a value for the derivative.

Figure 8.4 shows corrected and uncorrected values for scans taken with short and long scan durations under the same reactor conditions. Clearly the correction process does not alter the fact that the reduced number of points obtained with a fast scan results in a loss of detail in the temperature profile.

8.2.3 Dissociation Catalyst Material

When the dissociation reactor was first trialled in the old laboratory, it was loaded with ICI 47-1 nickel on alumina dissociation catalyst. Although these early trials were not properly documented, it is known that the reactor was only operated for a small number of hours. For this project the emphasis of the experimental work has been on perfecting the operation of the dissociator and associated experimental components and testing the predictions of the numerical reactor model. There for, it was reasonable to continue using the catalyst material already loaded.

The 47-1 catalyst material is manufactured in the form of cylindrical pellets $4.5mm$ long and $4.5mm$ in diameter. These pellets are composed of finely-porous gamma alumina

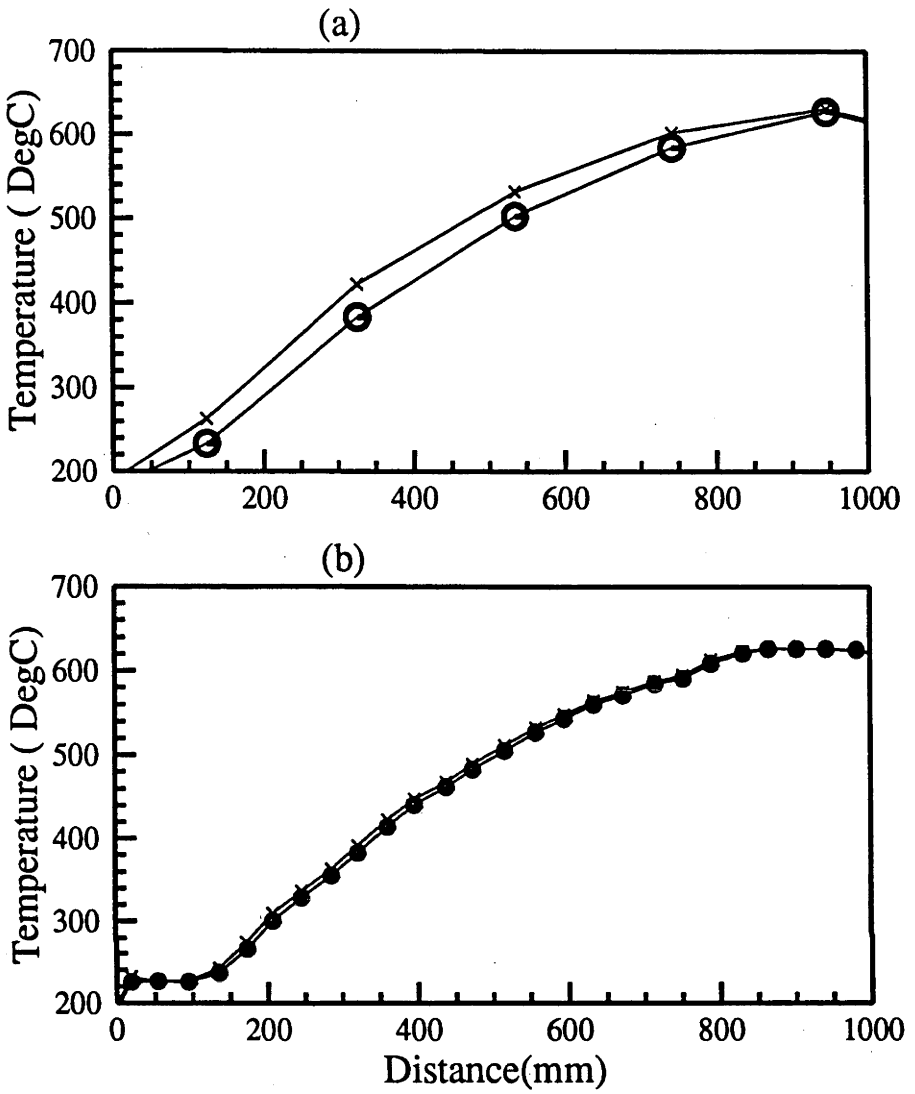

Figure 8.4: Comparison of first chamber uncorrected (o) and corrected (x) internal temperature profiles from (a) 2.5 minute and (b) 25 minute scans (Data from 27th March 1991).

with an impregnation of nickel of the order of 10% by weight. The catalyst is supplied in a largely oxidised state and, hence, after installation in the reactor it must be reduced. The simplest approach is to begin operation with ammonia, in which case the hydrogen produced by those parts of the catalyst which are not oxidised will serve to reduce those parts which are. This being so, it is safe to assume that, if the catalyst in the dissociator had become partially re-oxidised in the time since the first trials, it would have been re-reduced during the first few runs of this project.

The ICI Company have now replaced the 47-1 material with 27-2. The main difference in these two products appears to be the ceramic substrate which for 27-2 is calcium aluminate; the physical dimensions of the pellets are unchanged. Companies such as ICI appear to regard reaction rate parameters for their catalysts as proprietry information, which is unfortunate. They do however claim that the 27-2 material should give close to the same performance (ie extrinsic rate) as the 47-1, when used under the same conditions.

Parameter	Value
average particle mass	0.0769±0.0002 g
average particle volume	0.04457±0.0004 cm^3
effective particle diameter	0.440±0.004 cm
void fraction	0.4642±0.005

Table 8.1: Dissociator catalyst particle parameters.

At the completion of this project further work to compare the performance of these two catalysts, and others which could be obtained, would be worthwhile. As described in section 8.2, the two reaction chambers of the dissociator are fitted with threaded plugs at each end. The bottom plugs have the thermocouple probe tubing attached to them. A preliminary test revealed that, although the frictional force on this tubing, due to the catalyst particles, causes resistance to unscrewing the bottom plugs, it is not so great that it would prevent their removal. Thus catalyst replacement could be accomplished relatively easily by removing the bottom plugs, shaking out the old material, then refilling from the top openings[1].

Catalyst material is supposedly homogeneous and may be crushed to any desired particle size for use. Inspection of the material within the reactor through one of the top ports, confirmed the recollection of workers involved in the original installation, that it had been loaded with particles produced by manually cleaving individual cylindrical catalyst particles longitudinally into two.

The effective particle size and void fraction are important parameters in the reactor model. Values for these parameters were determined from a sample of the prepared particles left over from the loading. The void fraction was determined using a mock up of the dissociator geometry using metal tubing of the same radial dimensions. Figure 8.5 illustrates this and shows a typical distribution of particles around the central thermocouple probe passage. A sample of 263 particles was poured into the tube and settled by vibration and the occupied volume was then measured to determine the void fraction. This process was repeated several times. An average particle volume was determined by displacement of alcohol in a measuring cylinder. The measurement used was made with particles that had been pre-soaked in the alcohol[2].

The parameters determined are presented in table 8.1. The uncertainties quoted represent the uncertainties in the measurement processes; there is, however, a considerably larger particle-to-particle variation in values of approximately ±30%. The assumption has been made that particle sizes are uniformly distributed along the reactor.

8.3 Qualitative Behaviour

All the dissociation experiments followed a common start up procedure. Preliminary preparations involved starting the high pressure nitrogen supply, setting the ammonia accumulator and system exit pressures, filling the accumulator with ammonia and priming the system up to the balancing separator inlet with liquid ammonia. The balancing separator volume was initially filled with nitrogen gas. At this point operation of the data

[1]The alternative method of removing the catalyst would be to remove the top endplugs and invert the reactor, this would be a more inconvenient and time consuming procedure.

[2]The volume displaced by completely dry particles was 36% less than with presaturated particles, confirming their highly porous nature.

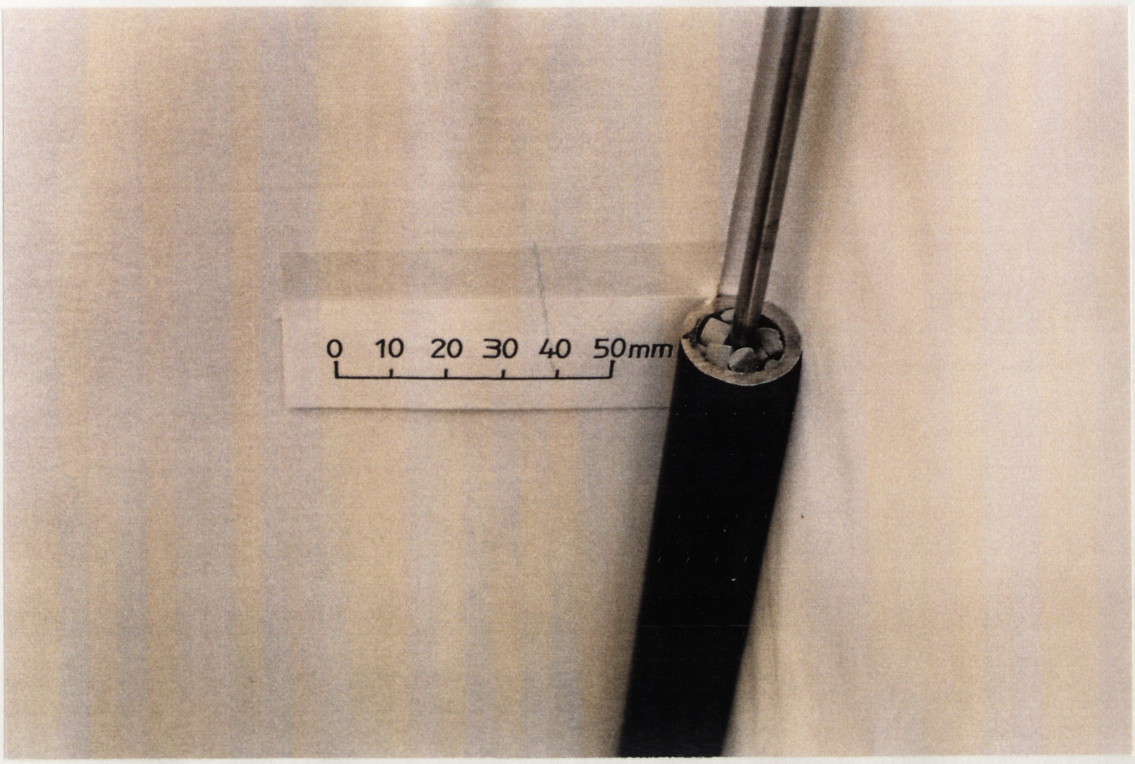

Figure 8.5: Re-creation of the dissociator reaction chamber geometry and catalyst particle distribution.

acquisition system was begun. A period of several minutes without flow was allocated to allow measurement of pressure and ammonia level signals for later normalisation purposes. Ammonia flow was then commenced by opening the accumulator shut off valve. This was usually followed by one or two fill and 're-zero' cycles with the balancing separator to calibrate inlet flow rate. After this, the mains power supply to the heater units was turned on.

Figure 8.6 shows the typical start up behaviour of the important system variables. The initial positive slope of the balancing separator signal represents the inlet mass flow passing through the system undissociated. Prior to turning heater power on, the balancing separator was left with vent closed and drain open. Without reaction the mass signal remained constant under this situation and the observation of a latter decrease provides positive evidence of the presence of gaseous dissociation products.

After power on, the reactor external temperatures rose quickly, with the two controlled temperatures levelling off at their setpoint values within 12 minutes. The controller power signals showed a corresponding rapid decrease as the setpoint temperatures were approached. The external temperatures of the reactor sections reached a steady state level when the heater power, the thermal losses, and the heat input to the reaction all balanced. The controller thermocouples were located in the positions of highest expected external temperature. As a result, the other external temperatures slowly approached various lower equilibrium values after the initial high heater power period had passed. Reactor internal

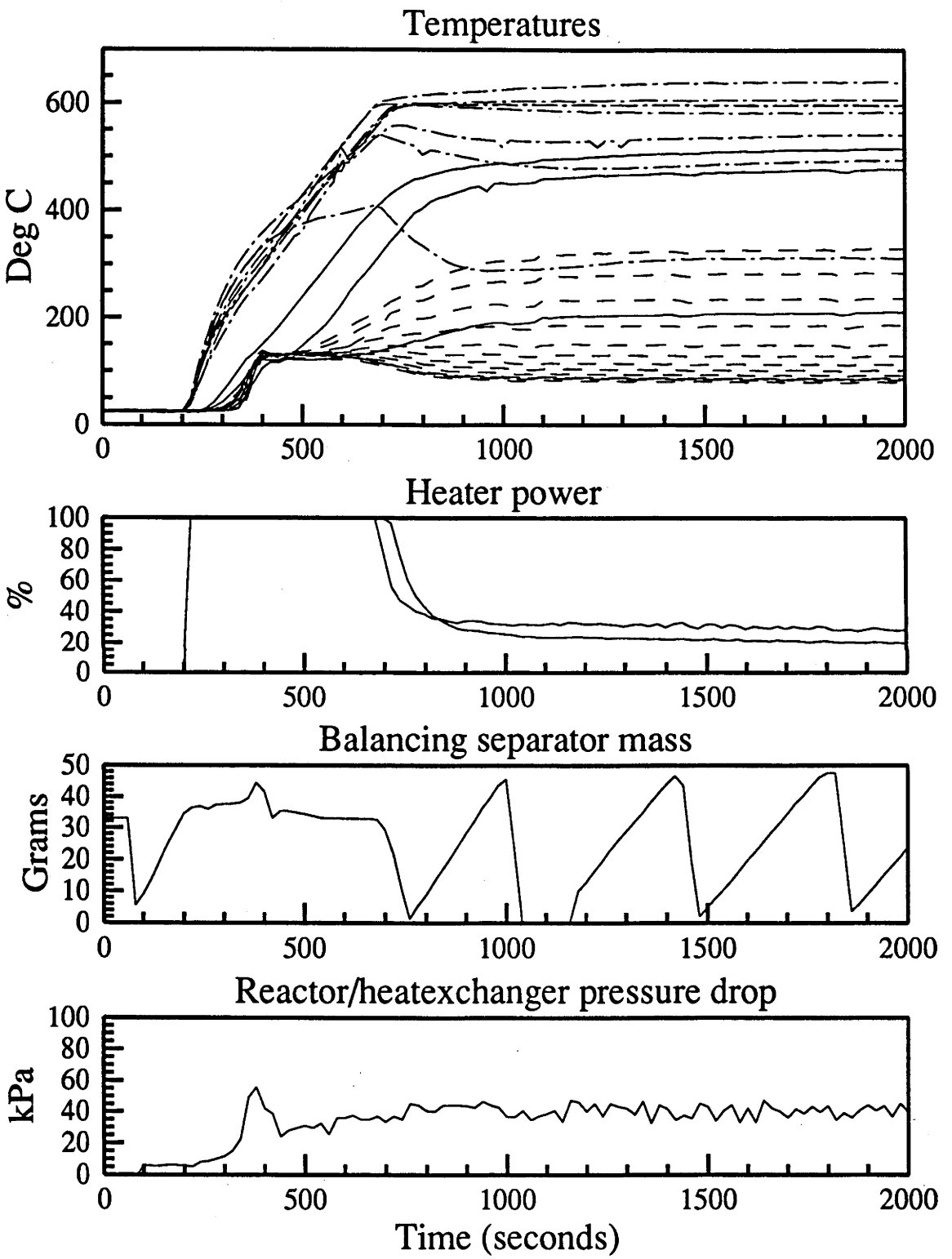

Figure 8.6: Start up transient behaviour of the ammonia dissociator, $0.3gs^{-1}$ inlet mass flow, $12MPa$ system pressure, $600°C$ setpoint temperatures, from the 21st of February 1991. Temperature curves show reactor external temperatures (— · —) internal and connecting tube temperatures (—) and heat exchanger temperatures (- - -).

temperatures rose more slowly, in reflection of the time constants associated with heat transfer processes within the catalyst bed.

Heat exchanger temperature measurements (exit passage) showed an initial transient overshoot 2 minutes after power on. This coincided with a large exit mass flow that was produced when the liquid ammonia, that was initially present in the reaction chambers, boiled. This exit mass flow transient was reflected as a short duration spike in the pressure drop across the reactor/heat exchanger system. It also appeared as an excursion in the balancing separator mass signal, presumably because the high flow rate increased the pressure within the separator vessel, temporarily reducing the size of the gas pocket within it. Some 5 minutes after this excursion, the mass signal began to reduce, indicating that gaseous dissociation products had begun to displace liquid within the separator vessel. From power on approximately 40 minutes was required for complete steady state behaviour to be obtained. Subsequent variations in operating conditions required a further 20 minutes before steady state measurements could be made.

A number of conclusions can be drawn from the transient behaviour of the system temperatures. The external temperatures reached a maximum rate of increase within a few seconds of power on, indicating a correspondingly small time constant for the heater element and reactor wall. The temperatures of fluid leaving the reactor chambers did not begin to rise for approximately 1 minute after power on, but then reached their maximum rate of increase within approximately 40 seconds, indicating an effective time constant of between 1 and 2 minutes for the reactor itself. It is apparent that the time limiting factor in reaching reaction temperatures within the reactor, is the maximum power level available from the heaters. Although the dynamic behaviour of the whole system is obviously very complex, it would appear that the factor which determines the period required to obtain steady state conditions must be the relatively large effective time constant of the insulation package.

The selection of time intervals for steady state analysis has been made on the basis of the examination of graphical results. Given the relative magnitudes of the various time constants, it is reasonable to assume that even if system temperatures continued to change slightly, the reactor would be behaving in a steady state manner relative to the instantaneous wall temperatures.

Figure 8.7 shows the internal and external temperature profiles corresponding to the steady state interval which followed the transient process shown in figure 8.6. The distance scale in this and subsequent reactor temperature profile plots, corresponds to position along the reactor measured from the inlet port of the first chamber. The connecting tube between the two chambers is ignored, with the position of the inlet of the second chamber set to equal the position of the exit of the first chamber. The discontinuity between the profiles from the two reaction chambers and the drop in temperature near their ends indicates that there are considerable thermal losses from the reactor column ends and the interconnecting tubes. The relatively low temperature at the beginning of the first reaction chamber is consistent with the greater average value of specific heat for the incoming ammonia relative to the outgoing product mixture in the counterflow heat exchanger. A large fraction of the first chamber is responsible for simply heating the ammonia, the change to a smaller value of $\frac{dT}{dx}$ about half way along indicates the transition from temperature increase to the reaction rate as the dominant energy sink.

The $100mm$ unheated section at the beginning of the first chamber is clearly reflected in unchanging internal temperatures in that region. A number of 'bumps' in the internal temperature profile are common to all recorded profiles. They presumably indicate the presence of inhomogeneities in either the packing or the activity of the catalyst pellets. At

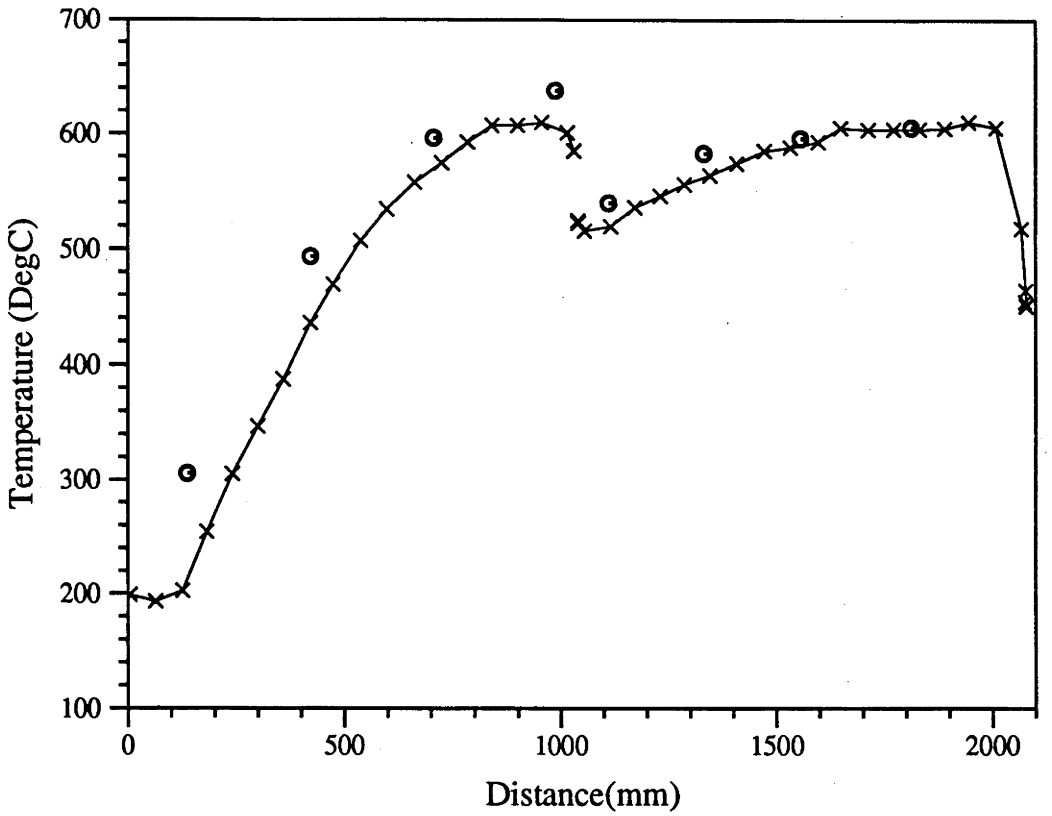

Figure 8.7: Internal (×) and external (•) steady state temperatures from the 21st February 1991, 2500-3800 second interval.

the end of the second chamber temperatures drop as they do for the first chamber, however the main reactant flow does not drop to the lowest temperature measured. The lowest values correspond to the final resting position of the probe, which was slightly beyond the reactant exit port in the side of the chamber.

8.4 Determination of Energy Balance

An experimentally determined absorbed heat flux profile is necessary for the determination of the enthalpy input to reactants. It is also the most suitable boundary condition for input to the two dimensional reactor model.

As described in section 8.2, the two reactor columns are heated by "Pyrotenax" electrical heating elements. Power is supplied to these heaters from a $240V$ mains supply modulated on a variable duty cycle basis by two "Eurotherm" model 808 temperature controllers.

For determination of an absorbed flux profile, the primary experimental data available is the power supplied by these heaters and the temperature profiles of the two reactor columns. Determination of the flux profile requires an analysis of the heat transfer and loss mechanisms operating.

8.4.1 Measurement of Heater Power

At $20°C$ the reactor heater elements have resistances of 26.2Ω for the first column and 24.4Ω for the second column. The difference between the two reflects the different lengths of the heaters. The manufacturer (Pyrotenax Australia Pty Ltd 1988) specifies a thermal dependence factor of $0.0079\Omega K^{-1}$ for the heater material.

Heater power calculations have been made by assuming that the elements had uniform resistivities corresponding to the estimated average temperatures for each set of experimental conditions. This approach leads to errors of up to 3% in heater fluxes at the extreme coldest ends of the elements, however the contribution to the uncertainty in the net heater power is less than 0.5%.

The two heaters are supplied with power from separate phases from a three phase power outlet in the laboratory. The voltage applied to each heater was measured separately during the full power startup period of each run using an RMS voltmeter. The spiral construction of the elements could be expected to introduce an inductive component to the load. An investigation of the relationship between voltage and current waveforms, however, revealed no detectable phase difference. Hence, the heater power levels for a 100% duty cycle were determined directly from measured voltages and the adjusted values of resistance.

The actual average heater power level is determined by the temperature controller for each element. The Eurotherm 808 units employed have time proportional output. They operate by switching power on to the heaters for between 0 and 100% of every heat cycle. The heat cycle length is one of many parameters determined by the operator. The circuitry employed incorporates zero crossing switching[3] to avoid excessive generation of harmonic noise. This means that on time is limited to integral numbers of half cycles, thus the resolution of an individual heat cycle for a $50hz$ supply is $0.01sec$ divided by the chosen cycle time. The value of the heater 'fractional on time', in addition to the measured temperature, is available via an RS422 serial communication facility on the controllers. These variables were logged by the data acquisition system. Actual heater power levels were determined from the product of the 100% power level determined from element resistance and voltage, and the fractional on-time indicated by the controller.

Initially a heater cycle time of 2 seconds was chosen as a reasonable compromise between the resolution of the output power and the assumed order of magnitude of system time constants. The controller variables were logged every 20 seconds along with all other system variables. The power data recorded in this way (as illustrated by figure 8.8(a)) proved to be considerably noisier than other variables. With a 20 second data acquisition sample period, averages of steady state power levels over periods of 10 minutes produced mean values with random uncertainties of the order of 15%, compared to less than 1% for temperature data from thermocouples.

This level of variation in recorded power values resulted from a combination of the method employed by the controllers to calculate power values and the way in which data was recorded. The controllers carry out analogue to digital conversion of the input signal, and an associated update of the power signal calculated from the PID algorithm, 8 times per second. At the beginning of each heater cycle only the most recent value is used to determine the fractional on time for that cycle. As a consequence, in situations in which there is noise on the input signal, a significant amount of information is lost in the unused calculations. If the resulting fluctuations in the power signal exceed the resolution

[3]Zero crossing switching involves the solid state component which switches the heater power, being triggered on or off at or close to a zero dc level of the ac power supply signal.

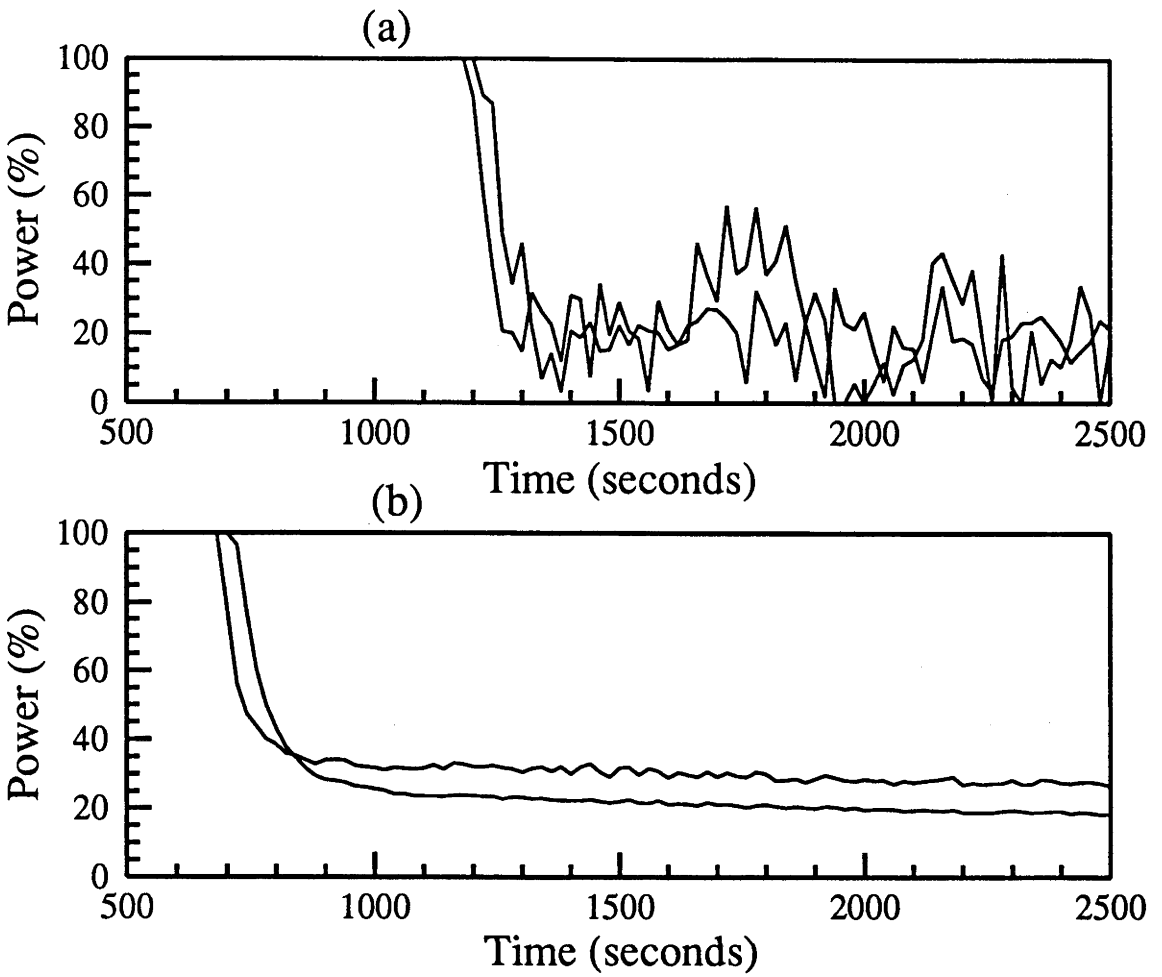

Figure 8.8: Recorded power data; (a) heater cycle time of 2 seconds, 20 second measurement period (21st November 1990), (b) heater cycle time of 5 seconds, 10 sample running average (21st February 1991).

provided by the cycle time, then it is beneficial to reduce the cycle time and utilise a greater number of input measurements.

When logging the power level, the data acquisition system records the most recent calculated value rather than the value adopted for the most recent heater cycle. Thus recorded data does not record actual instantaneous power levels, but rather a series of values with a long term average which should equal the long term average of actual cycle power levels.

These considerations led to the adoption of a 0.5 second cycle time and the modification of the data acquisition software set up to record values which were a 10 sample running average of values measured every 2 seconds. As shown in figure 8.8(b), these measures resulted in a dramatic improvement in the quality of the recorded heater power data.

Figure 8.9 shows the response of heater temperature to an initial power on, with greater temporal resolution than in figure 8.6. It is apparent from the time taken to reach the maximum rate of temperature increase, that the time constant of the heater elements is only of the order of 1 second. This suggests that the 2 second heater cycle time would also have been directly contributing to fluctuations in heater temperatures.

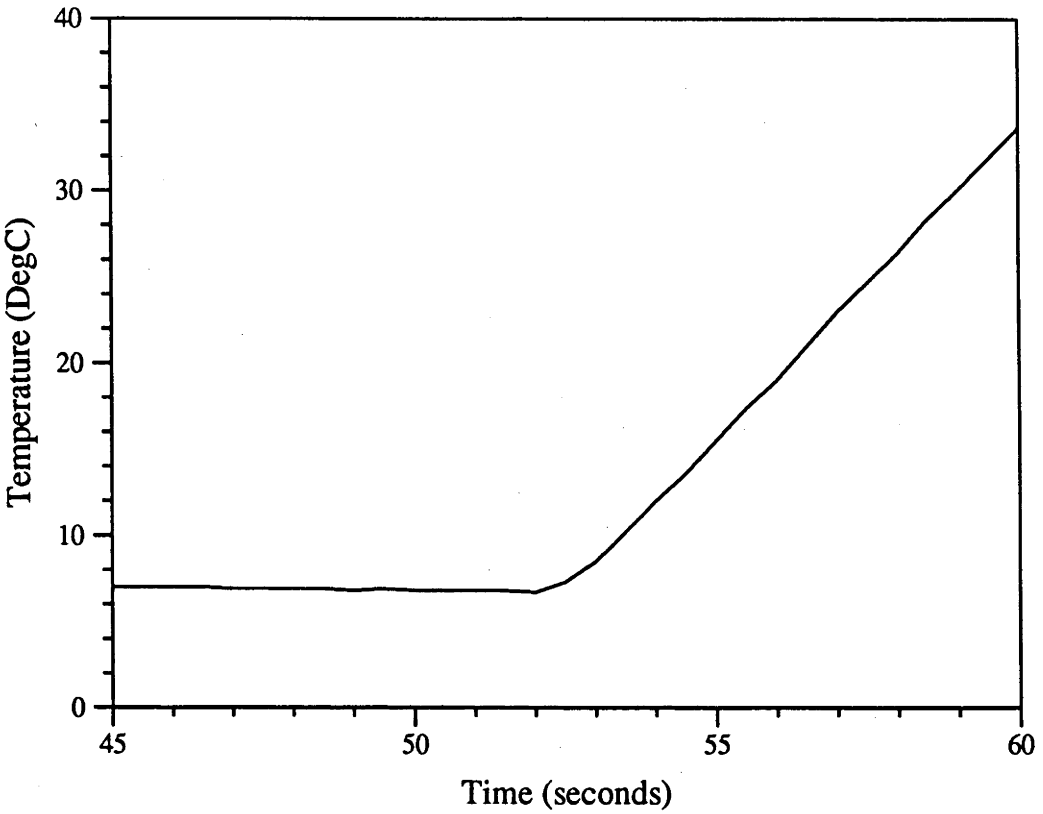

Figure 8.9: Response of heater temperature to power on at 51.7 seconds.

8.4.2 Quantifying Thermal Losses

A considerable fraction of the power provided by the heaters is consumed by thermal losses. As has been described, the insulation on the dissociator, although substantial along most of the length, reduces to nothing at the column ends. As a consequence, although the flux profile from the heaters is uniform, the profile of the flux absorbed by the reactor columns is far from uniform.

Determination of this profile for a given set of conditions requires determining the energy balance of each element of reactor wall. At each point the heat flux into the catalyst bed is the resultant of the heater contribution, heat conduction within the reactor tube wall and the loss through the insulation. It is reasonable to assume that loss through the insulation is, at least to a first order approximation, linearly dependant on wall to ambient temperature difference. Thus the appropriate form of the energy equation is:

$$q = KA\frac{d^2T}{dx^2} + q_h - h_l \pi d(T - T_0) \tag{8.2}$$

where, K is the conductivity of the reactor wall material, A its cross-sectional area, q_h the heater flux, d the outer diameter of the tube, T_0 the ambient temperature and h_l an effective heat transfer coefficient for losses through the insulation.

The conductivity of Inconel is well known, for this analysis a linear relationship to temperature was assumed:

$$K = (6.5612 + (1.7492 \times 10^{-2} K^{-1})T) w m^{-1} K^{-1}. \tag{8.3}$$

In order to determine the value of the effective loss heat transfer coefficient as a function of position, a number of runs with no gas flow were carried out. These produced the

'inverted U' shaped temperature profiles expected for a situation of large losses at the end regions. Figure 8.10(a) shows the profiles from such a run on the 6th March 1991. Surprisingly however, the heater power required to maintain the same setpoint temperature for each column differed markedly. This implies a large difference in the effectiveness of the insulation of the two columns. To confirm this, the wiring of the temperature controllers was modified to allow both heaters to be controlled from the one unit. Runs with identical heater power levels produced in this way resulted in different maximum steady state temperatures, confirming the apparent variation between the two columns. The reason for the variation in insulation is not apparent, but must presumably be the result of some variation in the type or packing density of the insulation material used.

Solution of equation 8.2 for the loss heat transfer coefficient requires the determination of the second derivative of the wall temperature. Since there was no gas flow for these runs the internal temperature profiles are equivalent to wall temperature profiles. Two methods of analysis were tried; polynomial fitting to temperature profile measurements, and for later runs with slower scan rates, derivative calculations from discrete measurements. Although both methods ultimately produced the same results, the use of polynomial fitting was initially distrusted due to the large systematic errors in derivatives that can be produced by apparently well fitted polynomials.

The results from the 6th of March 1991 have been analysed using discrete point derivative calculations. Part(b) of figure 8.10 shows the known heater flux profile, the calculated wall conduction contribution and the resultant flux through the insulation needed to produce zero net flux along the length of the reactor. Part (c) presents the insulation loss heat transfer coefficient profile, that was implied by the energy balance. As expected the coefficient jumps to a higher value at the ends of the two columns. In the supposedly uniformly insulated regions the coefficient appears to reflect the temperature profile. This is consistent with the temperature dependence of the conductivity of such insulation materials. The 'noise' level, which originates from the second derivative calculation, largely obscures the slight spatial variations that must be responsible for the small irregularities in the original temperature profiles.

To confirm the temperature dependence of the loss coefficient the same analysis was performed for a lower temperature no flow run on 3rd April 1991. $450°C$ temperature controller set points were used for both columns. The results for this, shown in figure 8.11, are qualitatively similar and indicate lower values of loss coefficient at the lower temperatures.

Results for the insulation loss heat transfer coefficient in the uniform region from both cases are presented versus temperature in figure 8.12. Least squares linear fits give for the loss coefficient temperature dependence:

Parameters for $h_l = AT + B$		
Column	A $(10^{-3}Wm^{-2}K^{-2})$	B $(Wm^{-2}K^{-1})$
1	6.937 ± 0.12	−2.152± 0.06
2	6.098 ± 0.19	−3.116± 1.5

Although the uncertainties associated with these parameters are quite high, this reflects the limited temperature range of the experimental points. For temperatures in the 300 to $700°C$ range, loss coefficients calculated using these values will have an uncertainty of $\pm 0.1 Wm^{-2}K^{-1}$, which is of the order of 1%. Outside the 'uniformly insulated' regions, the loss coefficient is not as well determined.

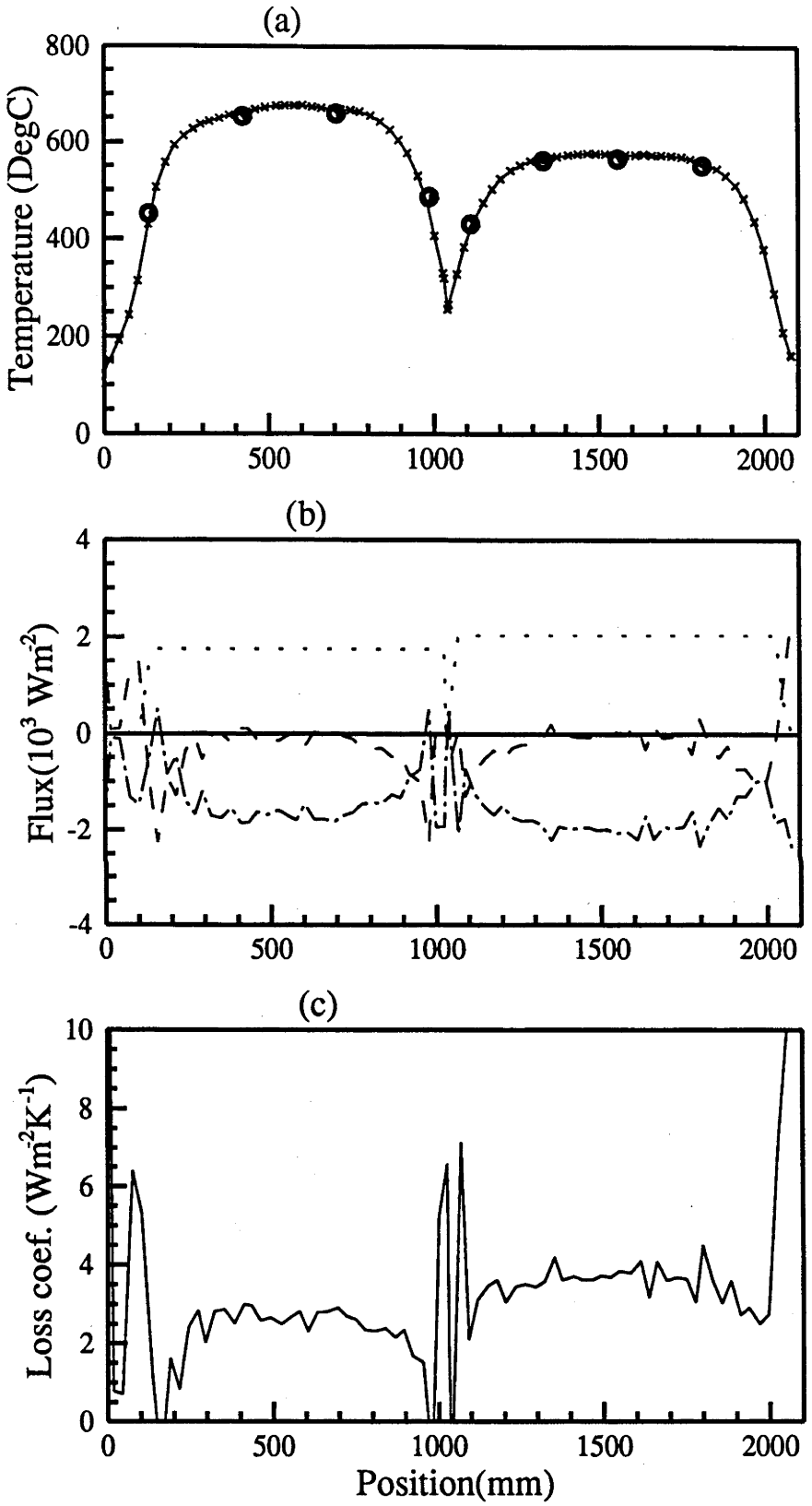

Figure 8.10: Analysis of thermal losses from no-flow run on the 6th of March 1991; (a) internal (×) and external (o) temperatures, (b) heater (···), wall conduction (– –) and insulation loss (– · –) contributions to zero net flux, (c) deduced insulation loss heat transfer coefficient profile.

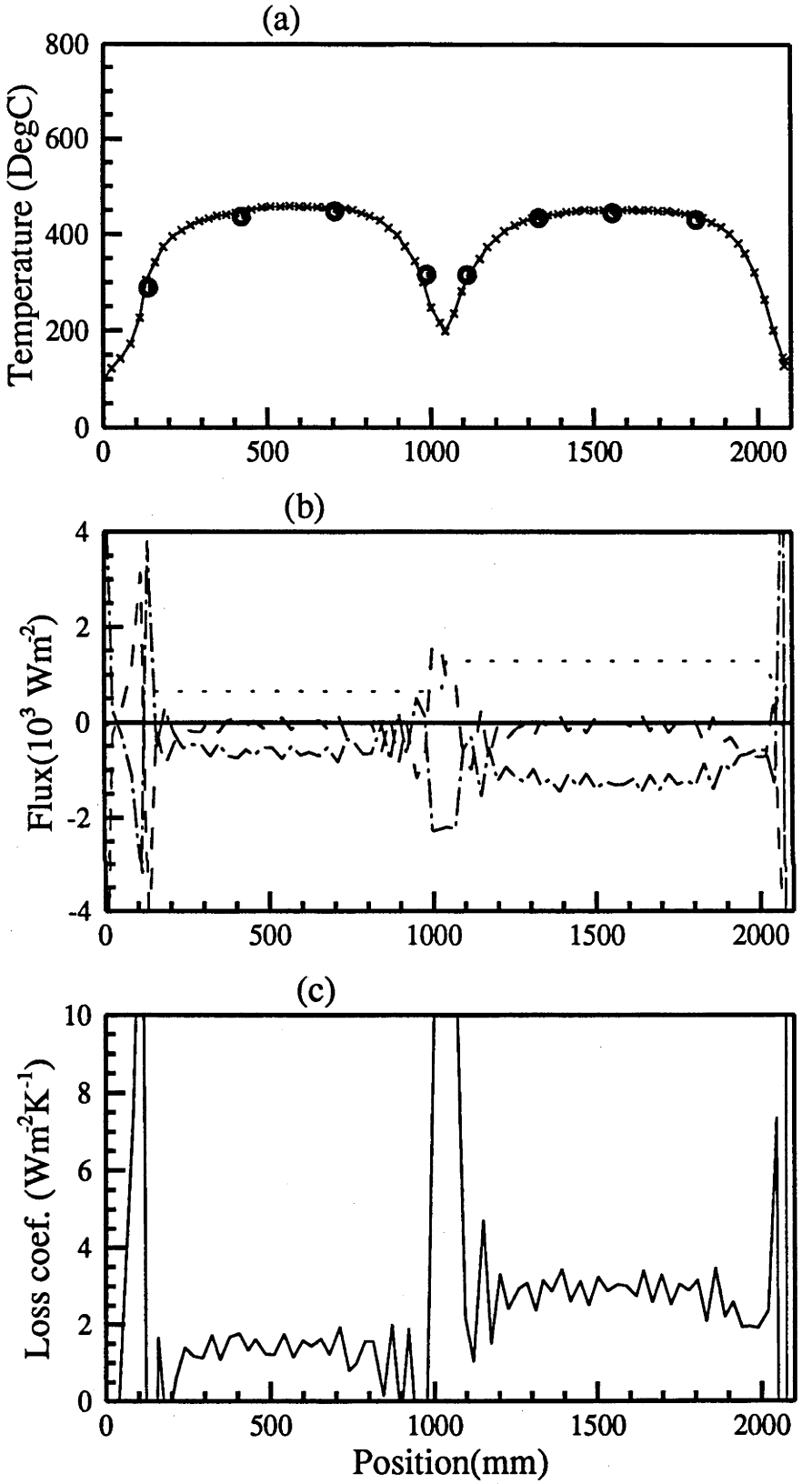

Figure 8.11: Analysis of thermal losses from no-flow run on the 3rd of April 1991 ($450°C$ setpoints); (a) internal (×) and external (o) temperatures, (b) heater (· · ·), wall conduction (——) and insulation loss (— · —) contributions to zero net flux, (c) deduced insulation loss heat transfer coefficient profile.

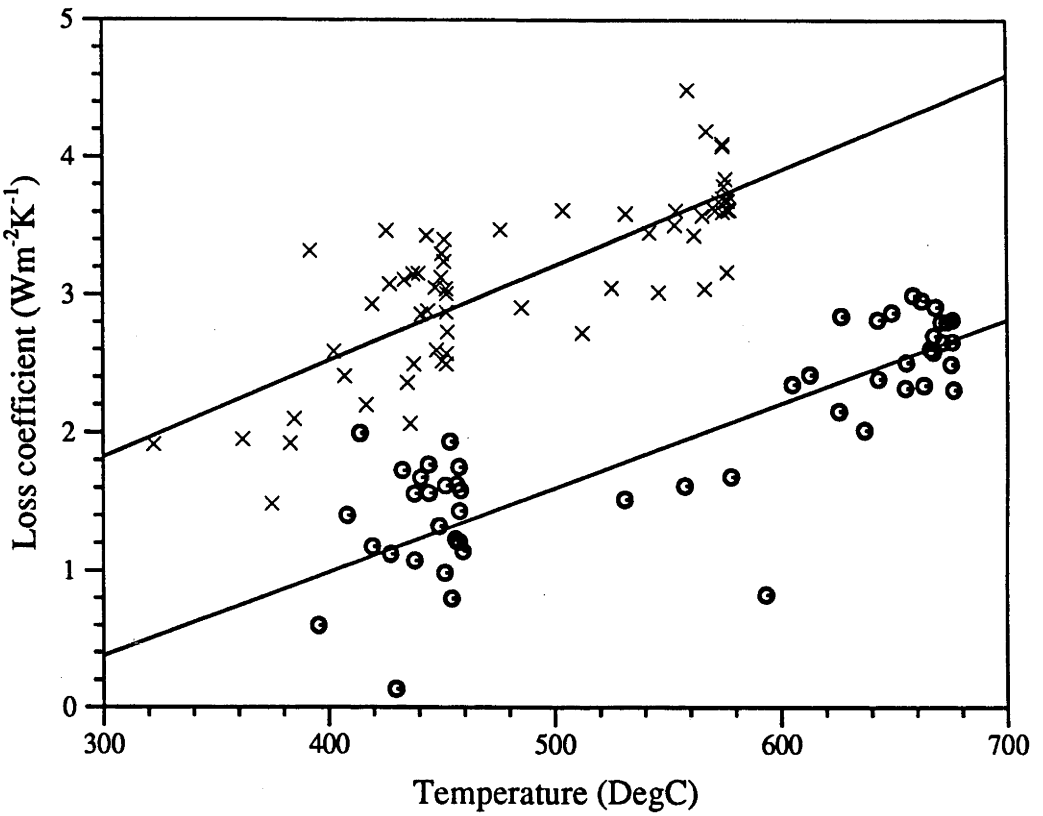

Figure 8.12: Temperature dependence of the insulation loss coefficient in the uniformly insulated regions from the results of 6th March 1991 and 3rd of April 1991, column 1 (×) column 2 (o).

8.4.3 Runs with reactant flow.

With the heat loss mechanisms quantified, the same energy balance analysis can be used to determine the profile of the heat flux absorbed by the reactor. Under conditions of net heat transfer to flowing reactants, the wall temperature profile is no longer identical to that measured by the internal probe. However, external temperature measurements obtained with the four thermocouples on the outside of each reactor column, indicate that within the uniformly insulated regions, the difference between external and internal temperatures is, to a good approximation, a linear function of position. For the analysis of runs with reactant flow, the wall temperature profiles were determined by the appropriate adjustment to the linear terms in cubic polynomial fits to the internal profiles.

For each of the four 'tail' regions, sufficient information is available to make a reasonable determination of the average energy balance. The points for transition from the energy balance analysis for the middle regions to that for the tail regions were selected to include the positions at which $\frac{dT}{dx} = 0$ within the tail regions. The observation of sections of internal temperature profiles with $\frac{dT}{dx} \leq 0$, indicates the existence of a point of zero net flux[4], at which the internal and external temperature must coincide. This allows a reasonable estimate of tail section average temperature to be made. The uninsulated column endcaps are $100mm$ beyond the end of the inlet/exit ports of the reaction chambers. An estimate of net conduction loss from reaction chamber ends was provided by assuming that

[4]In the absence of reaction the zero net flux point will be the point where $\frac{dT}{dx} = 0$, when reaction is taking place it will be at a point where $\frac{dT}{dx} < 0$.

Column/tail	Transition point (mm)	Heat transfer coefficient ($Wm^{-2}K^{-1}$)
1 top	1969 ± 15	16.15 ± 1.6
1 bottom	1100 ± 15	3.0 ± 0.3
2 top	130 ± 15	6.0 ± 0.6
2 bottom	923 ± 15	11.72 ± 1.2

Table 8.2: Parameters for thermal loss calculations in the tail regions.

the ambient to average tail temperature difference occurs across a $100mm$ length reactor tube material. The temperature gradient, calculated from the polynomial fit to the middle region temperatures, evaluated at the chosen transition points, plus the contribution of the heater elements, complete the net energy balance for the tail sections. For the purposes of input for the reactor model, the average flux calculated for the tail sections was allocated to their midpoints, and linear interpolation/extrapolation used between these points, the ends of the reactor and the uniformly insulated regions.

Results obtained from runs with nitrogen flow, provided a means for testing this analysis process. Figure 8.13 shows the temperature profiles obtained from a run with nitrogen flow. Internal temperatures are very close to the average gas temperatures and thus the profile can be converted directly to a flux profile, using the temperature enthalpy relationship for nitrogen. This was done by fitting fourth order polynomials to the middle regions of the temperature profile and using linear approximations to the regions at the chamber ends. The empirical flux profile obtained in this way has been compared with the flux profile obtained by the analysis of thermal losses and used to adjust the thermal loss heat transfer coefficients for the tail regions to give the correct enthalpy change in each region. The final values, which have been used in subsequent analysis of reaction runs, are presented in table 8.2.

Figure 8.14 superimposes the two flux profiles. It is apparent that the analysis of thermal losses is reasonably successful at predicting the net energy input to the reactor, at least for temperatures within a limited range of those in figure 8.13. It would appear that the temperature dependence of the effective heat transfer coefficient in the middle regions is more complicated than the simple linear approximation adopted, and so the flux profiles calculated by this approach are only an approximation to the exact shape.

Later reaction runs, for which reasonably accurate internal temperature profiles were obtained, were analysed in a similar manner. As an example, figure 8.15 presents the results from the first steady state interval of a run with ammonia dissociation from the 28th May 1991-B. Part(a) presents the assumed external temperature profile together with the measured values of internal and external temperatures, part(c) the calculated loss coefficient profile used to determine the insulation loss contribution, and part(b) presents the various contributions to the net flux profile. It is apparent that loss through the insulation is the dominant loss mechanism over most of the reaction chamber length, accounting for approximately 10% of the heater flux for the first chamber, and 30% for the second. It should be noted that for the tail sections, the contributions only balance at the midpoint, corresponding to the average calculation. With the exception of the net flux profiles, the linear interpolations in the tail region are notional and have not contributed to the calculations. In reality the actual flux profile will obviously be smooth, with the net power reduction from 'rounder' shoulders being offset by reduced values of negative flux in the extreme ends.

This analysis is presented quantitatively in figure 8.16. Thermal loss through the insulation in the uniformly insulated regions, is the most accurately determined contribution

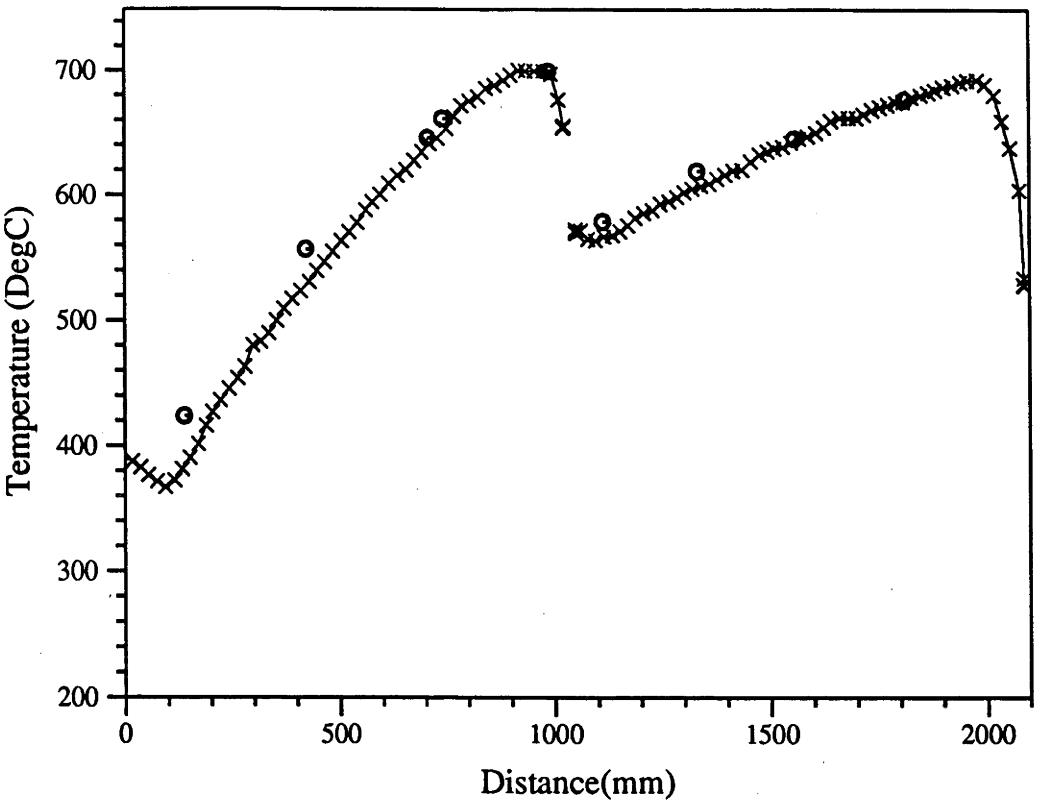

Figure 8.13: Temperature profiles from nitrogen flow run, 28th May 1991-A.

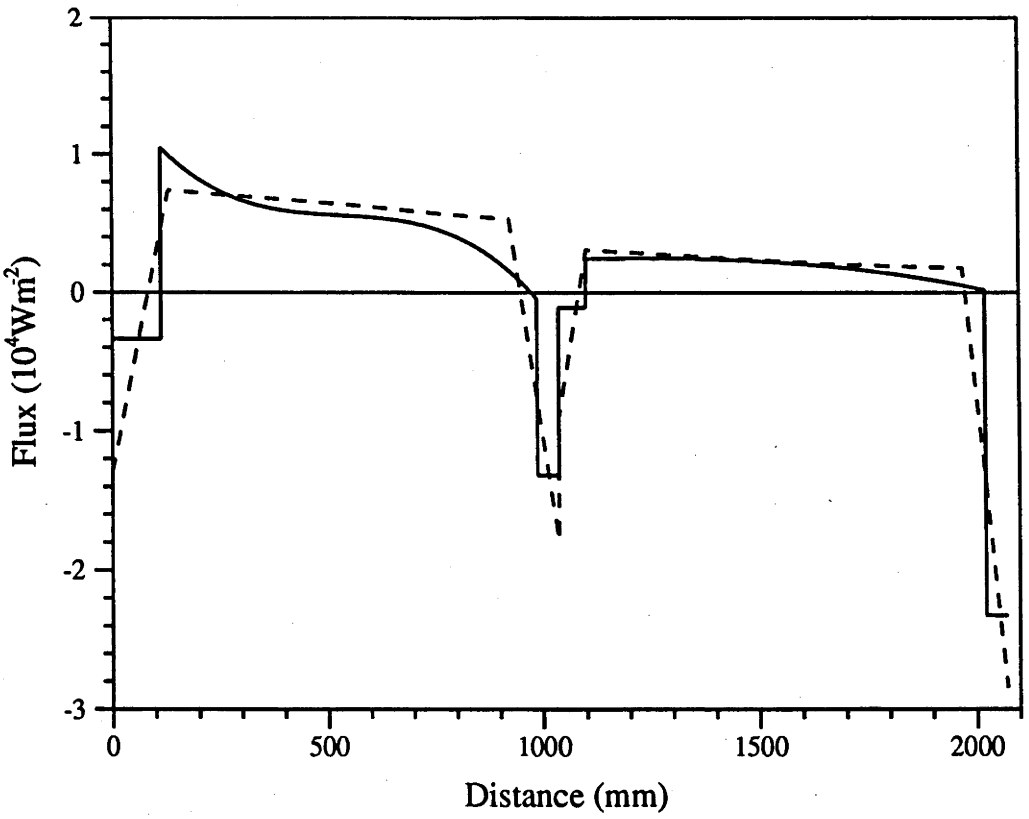

Figure 8.14: Comparison of flux profiles derived from enthalpy variation (—) and loss analysis (- - -), for nitrogen flow run, 28th of May 1991-A.

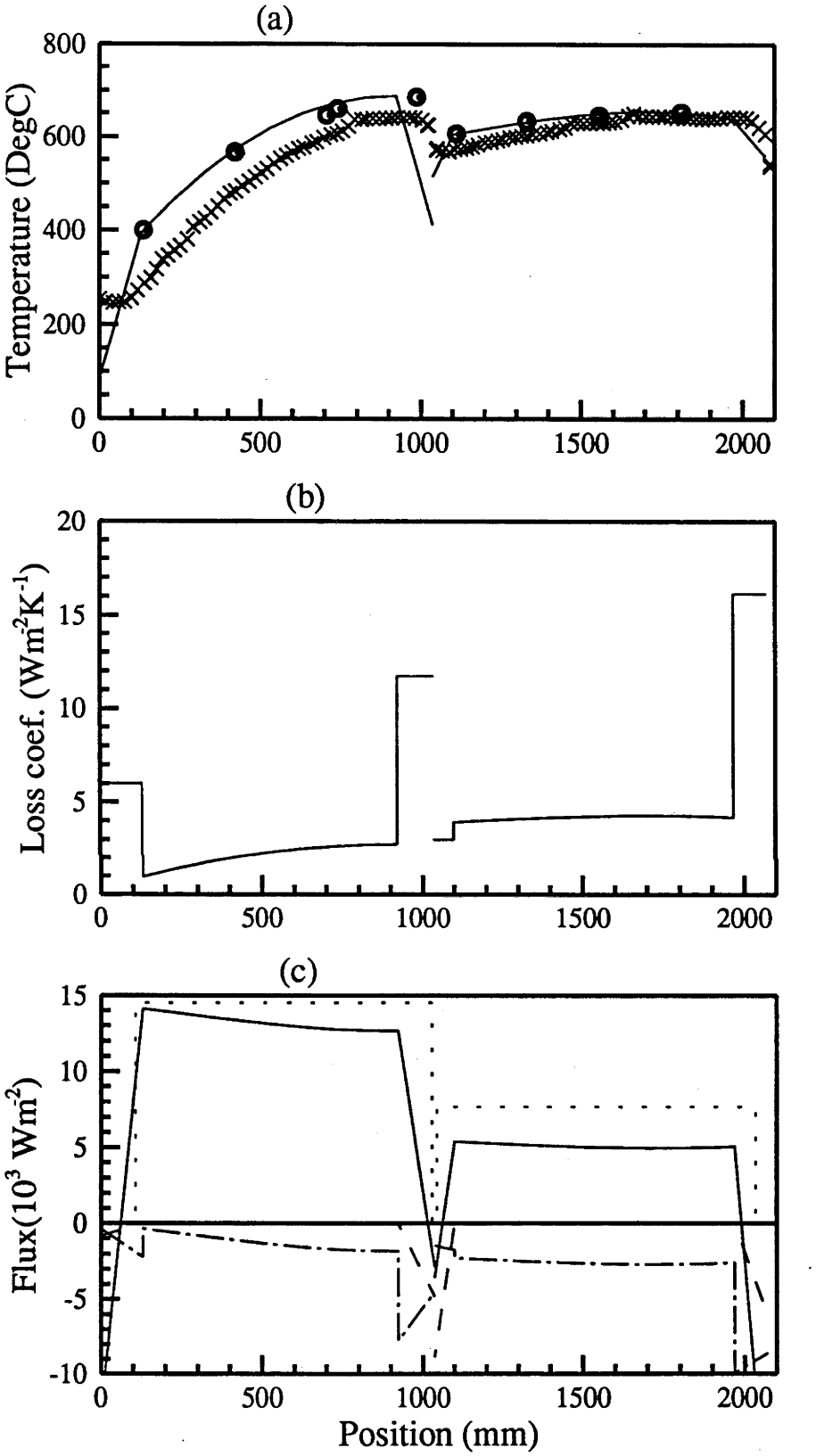

Figure 8.15: Analysis of thermal losses from 28th May 1991-B, first interval; (a) measured external (×) and internal (o) temperatures and the assumed external temperature profile (—), (b) insulation loss heat transfer coefficient profile, (c) heater (· · ·), wall conduction (– – –), insulation (– · –) and net (—) flux profiles.

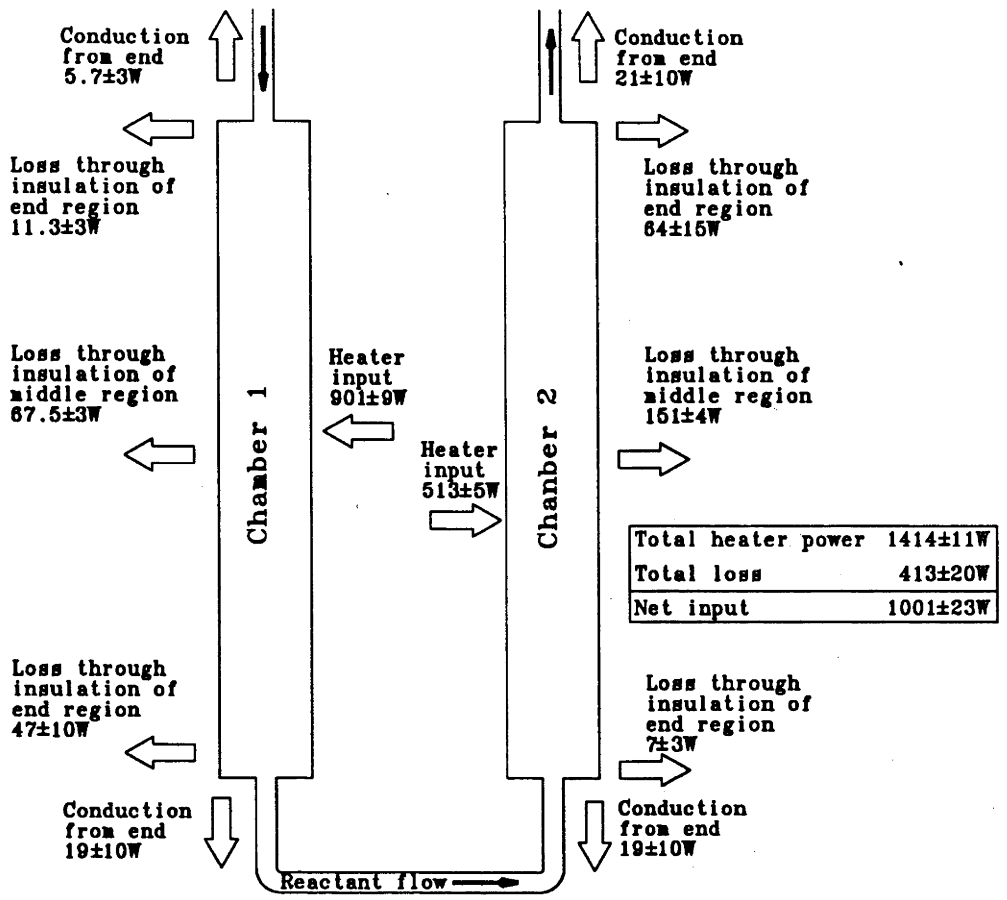

Figure 8.16: Energy balance for 28th May 1991-B, first interval.

and so only contributes modestly to the overall uncertainty. In the tail regions, the uncertainty in the insulation loss component largely reflects the uncertainty in the value of the loss coefficients used. The determination of loss via conduction from chamber ends, is the least accurately determined contribution, as a result of the reliance on simplifying assumptions to determine $\frac{dT}{dx}$. The $\pm 15mm$ uncertainty in the position of tail region boundaries results in a relatively insignificant contribution of between $\pm 1W$ and $\pm 3W$ for each tail section.

Given that the various sources of uncertainty do not share a common systematic origin, the overall result in this case, is an uncertainty in the magnitude of total thermal losses of $\pm 20W$ (ie $\pm 5.3\%$). The uncertainty in the determination of net heater power is 1%, the overall uncertainty in the determination of net power into the reactor is thus only 2.2%. Table 8.3 contains the values for the net power inputs to the reactor chambers, plus values of summed enthalpy changes calculated from the inlet and exit temperatures and reaction extents for the two chambers (note, this is not the net enthalpy change for the whole reactor). The results from the 18th April 1991 and the 8th April indicate a reasonable agreement between the determined values of net power input and effective enthalpy change. On the other hand the remainder, and most particularly the results from 10th April, indicate a deduced net power input that is the order of 15% too small to account for the enthalpy change. The conclusion that has been drawn from this is that there is a factor in the thermal loss process which varies on a daily basis. The most obvious

Interval	Absorbed power (kW) calculated from: enthalpy changes	analysis of thermal losses
	8th of April 1991	
1	0.764 ± 0.036	0.711 ± 0.023
2	0.723 ± 0.031	0.577 ± 0.034
	10th of April 1991	
1	0.726 ± 0.045	0.776 ± 0.031
2	0.976 ± 0.053	0.680 ± 0.027
3	0.758 ± 0.038	0.597 ± 0.024
4	0.693 ± 0.036	0.604 ± 0.024
5	0.913 ± 0.045	0.607 ± 0.024
6	0.860 ± 0.038	0.591 ± 0.024
7	0.754 ± 0.033	0.569 ± 0.023
8	0.698 ± 0.032	0.570 ± 0.023
9	0.679 ± 0.032	0.551 ± 0.021
	16th of April 1991	
1	0.404 ± 0.01	0.383 ± 0.018
2	0.536 ± 0.018	0.399 ± 0.019
3	0.926 ± 0.04	0.850 ± 0.024
	18th of April 1991	
1	0.708 ± 0.053	0.737 ± 0.023
2	1.54 ± 0.12	1.515 ± 0.024
3	2.05 ± 0.17	1.864 ± 0.030
4	2.46 ± 0.21	2.018 ± 0.032
5	1.99 ± 0.18	1.424 ± 0.023
6	1.95 ± 0.22	1.901 ± 0.030
7	2.33 ± 0.23	2.085 ± 0.033
8	2.12 ± 0.22	2.182 ± 0.035
	28th of May 1991	
1	1.321 ± 0.053	1.001 ± 0.022
2	1.22 ± 0.065	1.015 ± 0.023
3	1.309 ± 0.053	1.105 ± 0.023
4	1.205 ± 0.051	1.249 ± 0.030

Table 8.3: Reactor absorbed power levels calculated from thermal loss analysis and effective enthalpy changes.

possibility is the amount of air movement within the laboratory, which does indeed vary considerably as a consequence of the unsealed nature of the laboratory and the fact that the doors are left open during runs for extra ventilation as a precaution against the effects of leaks.

Although the thermodynamic data used for the calculation of enthalpy changes from temperature and reaction extent variations (as discussed in appendix A), has not been rigorously validated by experimental results, it is unlikely that it would be responsible for errors in calculated enthalpy changes of more than a few percent. The uncertainties

associated with the determination of net power inputs, preclude making any conclusions about the quality of the thermodynamic data. The tentative conclusion that has been drawn, is that the effective enthalpy change values are in agreement with the net power values for those occasions when the laboratory conditions were close to those that were present when the heat transfer parameters were initially determined. As such, given that the calculation of effective enthalpy changes relies on the measured values of exit reaction extent, this agreement suggests that the method and calculations used to determine exit reaction extents, are basically sound.

8.5 Determination of Reaction Extent

8.5.1 Balancing Separator Measurements

To date, reaction extents have been determined from the difference between inlet ammonia mass flows and the measurement of ammonia mass flow in the exit reactant stream obtained with the balancing separator.

The balancing separator directly measures the mass contained within its pressure vessel. A change in this mass when the liquid fraction of a 2 phase mixture is allowed to accumulate, is the net result of the mass of the liquid that accumulates, minus the mass of the gas which is displaced by the liquid. Thus a rate of increase of liquid mass ($\frac{dm}{dt}_{liq}$) is related to a measured net rate of mass change ($\frac{dm}{dt}_{bal}$) by;

$$\frac{dm}{dt}_{liq} = \frac{dm}{dt}_{bal}\left(1 + \frac{\rho_g}{\rho_l - \rho_g}\right) \tag{8.4}$$

where ρ_l is the density of the liquid and ρ_g the density of the gas. The gas that leaves the balancing separator also contains a percentage of ammonia in vapour form as a consequence of the gas/liquid phase equilibrium which is established within the vessel. Thus the mass flow of ammonia in the reactant mixture entering the balancing separator ($\frac{dm}{dt}_{NH_3}$), is the sum of the rate of increase of liquid mass and the rate at which ammonia vapour is leaving the vessel, ie;

$$\frac{dm}{dt}_{NH_3} = \frac{dm}{dt}_{liq} + \frac{dm}{dt}_{vap} \tag{8.5}$$

$$= \frac{dm}{dt}_{liq}\left(1 + \frac{\rho_g}{\rho_l}(1 - \delta_g)\right)$$

$$= \frac{dm}{dt}_{bal}\left(1 + \frac{\rho_g}{\rho_l - \rho_g}\right)\left(1 + \frac{\rho_g}{\rho_l}(1 - \delta_g)\right) \tag{8.6}$$

where δ_g is the reaction extent of the gas phase leaving the balancing separator.

The densities and gas phase reaction extents used for these calculations, have been derived from the data which is presented in appendix A, using measured values for the temperature and pressure within the balancing separator vessel. The gas mixture density values so obtained had an overall uncertainty of $\pm 6.5\%$, the ammonia liquid densities $\pm 1\%$ and the mass fraction of ammonia in pure gas mixtures $(1 - \delta_g)$ an uncertainty of $\pm 5\%$. After including the contribution of the uncertainty associated with linear fits to balancing separator mass, the net uncertainty in the value for the mass flow of ammonia in exit reactant streams was between 3 and 4%.

The reaction extent for the dissociator reaction products is given by:

$$\delta = \left(1 - \frac{\frac{dm}{dt}^{out}_{NH_3}}{\frac{dm}{dt}^{in}_{NH_3}}\right). \tag{8.7}$$

The uncertainty in outlet ammonia mass flow rate generally dominated the uncertainty in inlet mass flow. It can be seen from equation 8.7 that the effect on the uncertainty in the exit reaction extent value will reduce as the exit mass flow reduces and the reaction extent increases. Values obtained had uncertainties which ranged from $\pm 15\%$ at reaction extents around 0.2, to $\pm 1.5\%$ at reaction extents around 0.75.

8.5.2 Gas Analysis

There is no reason to doubt the validity of the reaction extent values obtained by the above method and the enthalpy input determination from the analysis of thermal losses has lent a reasonable degree of support to them. However the lack of some form of gas analysis apparatus to give a direct and unequivocable measurement of the composition of the gas component of the exit reactant stream, is the main shortcoming of the present experimental system.

Towards the end of the experimental work some time was spent investigating the options available, both for future improvement of the experimental facility and for an immediate rapid analysis of a gas sample in order to verify the reaction extent values obtained with the balancing separator. A number of general possibilities were identified however unfortunately no other group at the ANU had the facilities necessary to offer an analysis of a gas sample without a further major investment in experimental effort.

Infra-red spectroscopy, gas chromotography, mass spectroscopy and ammonia selective electrodes are possible methods which can be considered. Infra-red analysis would be limited to the detection of the ammonia fraction in gas mixtures. There are facilities at the ANU for the analysis of gas samples, however to produce quantitative results requires the preparation of a number of reference samples for calibration purposes. Detection of a single absorbing species (ie ammonia), could be done with a much simpler arrangement than a spectrometer, with proper calibration a simple absorption cell using a single wavelength should be sufficient. Such an arrangement could be incorporated into the experimental arrangement, at a future date, to give a continuous measurement of gas composition.

Gas chromotography appears to offer the most thorough means of quantitative analysis of all the components of an arbitrary gas mixture, however the necessary facilities do not appear to be readily available. Other groups at the ANU only use chromotography methods on liquid samples. CIG ("Commonwealth Industrial Gases") offer an analysis service at their Sydney laboratory, but utilising this would require procuring high pressure sample bottles for shipment.

Mass spectroscopy may also offer a means of identifying all the components of an arbitrary gas mixture, however the facilities available at the ANU could not readily give quantitative information, and there is some doubt as to whether an ammonia component would not be further dissociated within the spectrometer and recorded as an increase in the levels of nitrogen and hydrogen.

Capture of the ammonia component of a gas mixture by passing it through an aqueous solution, which can be subsequently analysed appears to offer a relatively simple method of ammonia detection. After some investigation it appears that the analysis might reasonably be done with an ammonia selective electrode and these are available commercially. Con-

siderable attention would need to be given to the methodology of the use of ion selective electrodes to achieve reliable results.

Although no instant answer to the problem of gas analysis was found, it is an area which deserves a high priority in future experimental work if the resources are available.

8.6 Numerical Modelling of Dissociator Behaviour.

The assumptions and the semi-empirical correlations embodied in the numerical reactor model have been discussed in chapter 4 and the Fortran implementation and the format of the required input data are discussed in some detail in appendix B. In addition to thermodynamic data for all the reactants, input data comprises a number of parameters relating to the catalyst particle properties and intrinsic kinetics, plus inlet mass flow and temperature and some specification of the conditions which apply at the reactor walls. For modelling of dissociation experiments the wall conditions have been specified by the net absorbed flux profile. The program allows the specification of multiple reactor sections such as the two chambers of the dissociator used for this project. This is accomplished by calling the reactor simulation block of the program once for each section. The average exit reaction extent and pressure from the first section are used as the inlet values for the second section in conjunction with the specified inlet temperature.

The determination of parameters that reflect the size and packing of the catalyst particles has been described in section 8.2, all other parameters which relate to diffusion or heat transfer processes have been taken directly from the values used by Richardson et al. (1988). The intrinsic rate parameters, namely the activation energy and pre-exponential factor, were initially taken from Nandy & Lenz (1984), but were treated as the main variables for fitting the model to the experimental results.

In the light of the conclusions drawn about the analysis of thermal losses, the flux profiles derived, were scaled to agree with the effective enthalpy change deduced from experimental inlet and exit temperatures and reaction extents, before being used with the model. After adjustment of the intrinsic rate parameters, the model proved very effective in reproducing the longitudinal internal and external temperature profiles observed experimentally.

Three 'baseline' conditions corresponding to approximately midrange values from the main investigations of the effects of flow, pressure and temperature variations were chosen. Figures 8.17 to 8.22 present measured and predicted temperature profiles plus predicted reaction extent profiles and measured exit reaction extents for these.

The predicted temperature profiles are in fairly good agreement with the measured values. Irregularities in the measured profiles, which are common to all cases, and which have been attributed to inhomogeneities in the catalyst bed, are of course not predicted by the model. The model quite successfully predicts the magnitude of the external to internal temperature drop along the length of both chambers. This provides some support for its ability to predict radial temperature distributions. In all cases both measured and predicted temperature profiles for the first reactor chamber show a noticeable shoulder at around $550°C$. The shape of the predicted reaction extent profiles confirms that this corresponds to the point at which the reaction rate increases rapidly and thus reduces the rate of temperature increase produced by the heat flux. Examination of all the experimental profiles presented in appendix D indicates that this transition appears to occur at around $550°C$ for reaction runs, irrespective of the maximum temperature of the reactor, however it is absent from nitrogen flow runs.

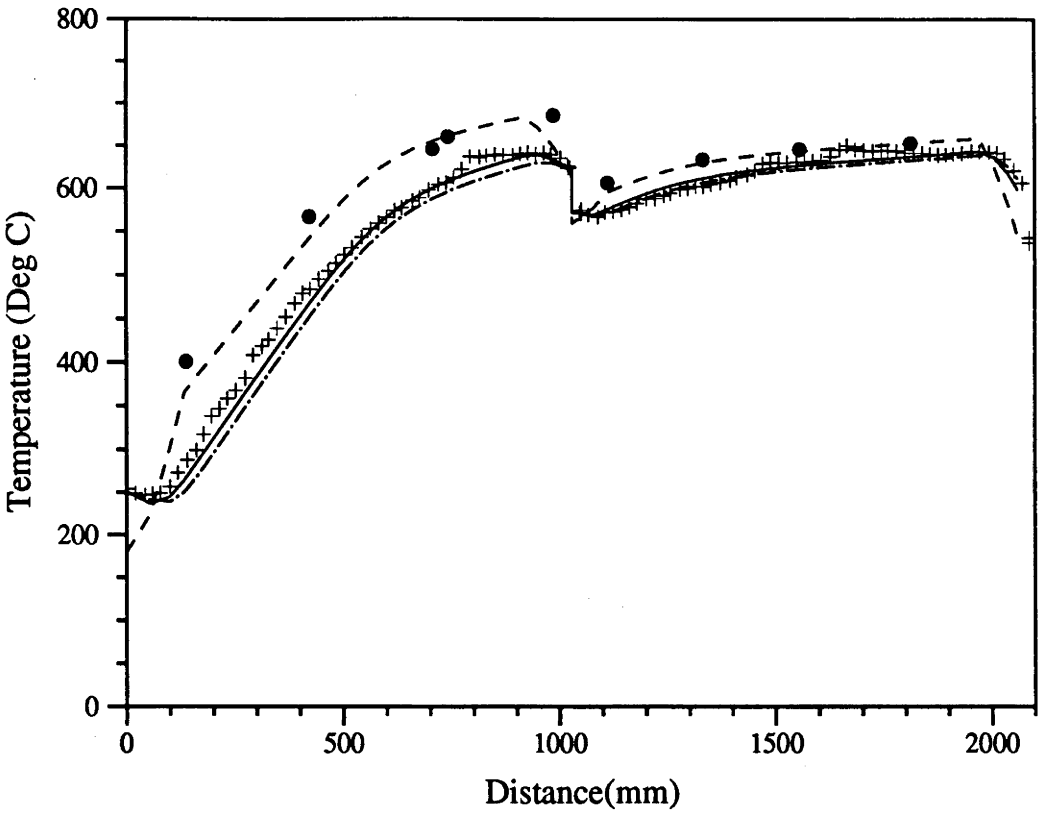

Figure 8.17: External (- - -), average (—) and internal (— · —) modelled temperature profiles and internal (+) and external (•) experimental values for 28th of May 1991-B first interval ($0.507gs^{-1}$, $11.4MPa$, $650°C$, temperature variation baseline condition).

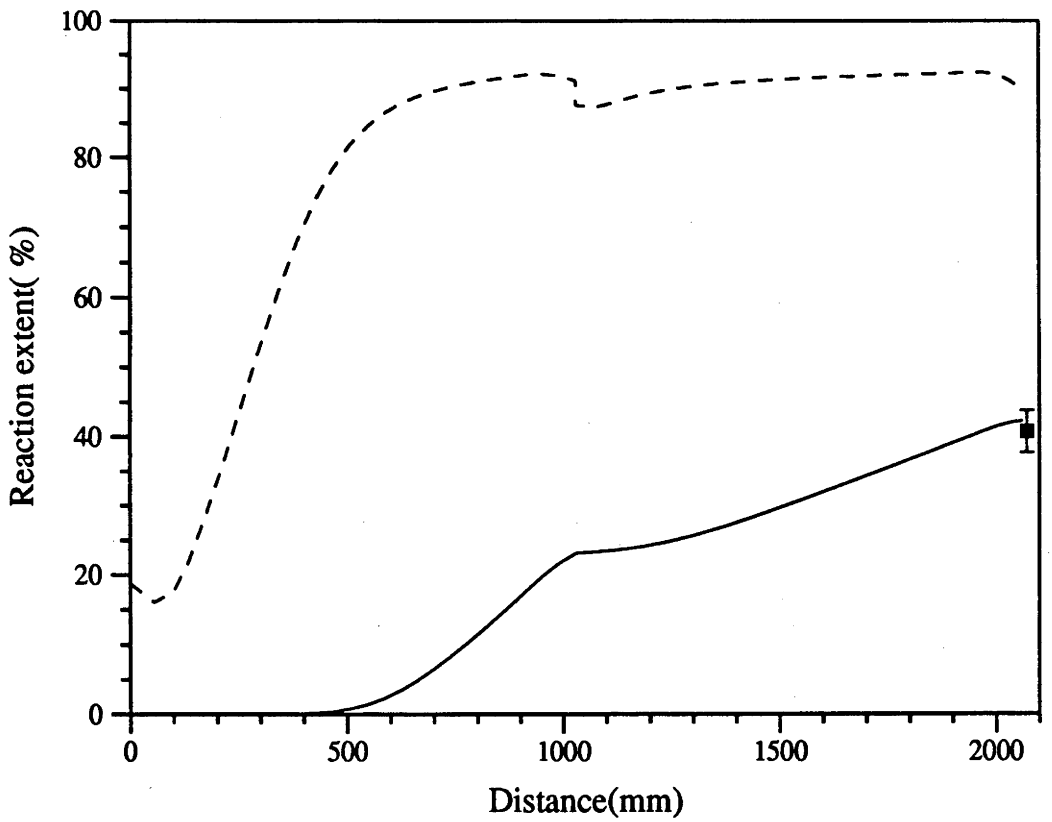

Figure 8.18: Equilibrium (- - -) and average (—) modelled reaction extent profiles with the neasured exit value for 28th of May 1991-B first interval.

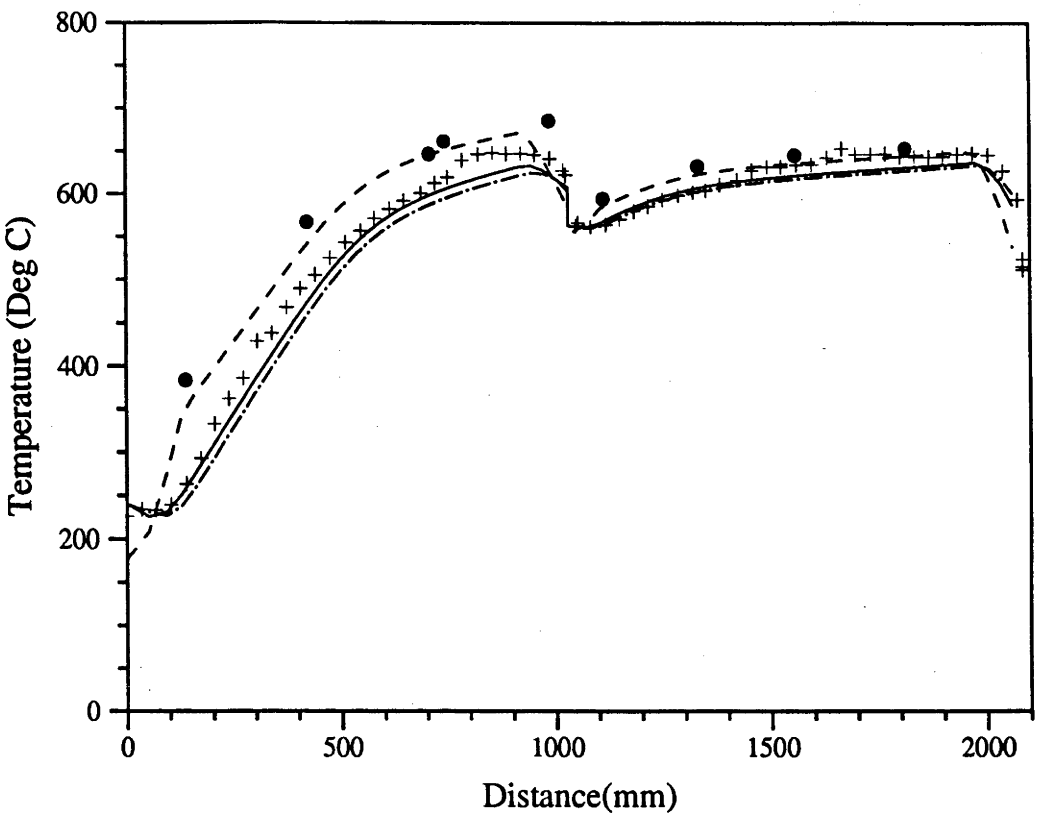

Figure 8.19: External (- - -), average (—) and internal (— · —) modelled temperature profiles and internal (+) and external (•) experimental values for 16th of April 1991 third interval ($0.338gs^{-1}$, $9.9MPa$, $650°C$, mass flow variation baseline condition).

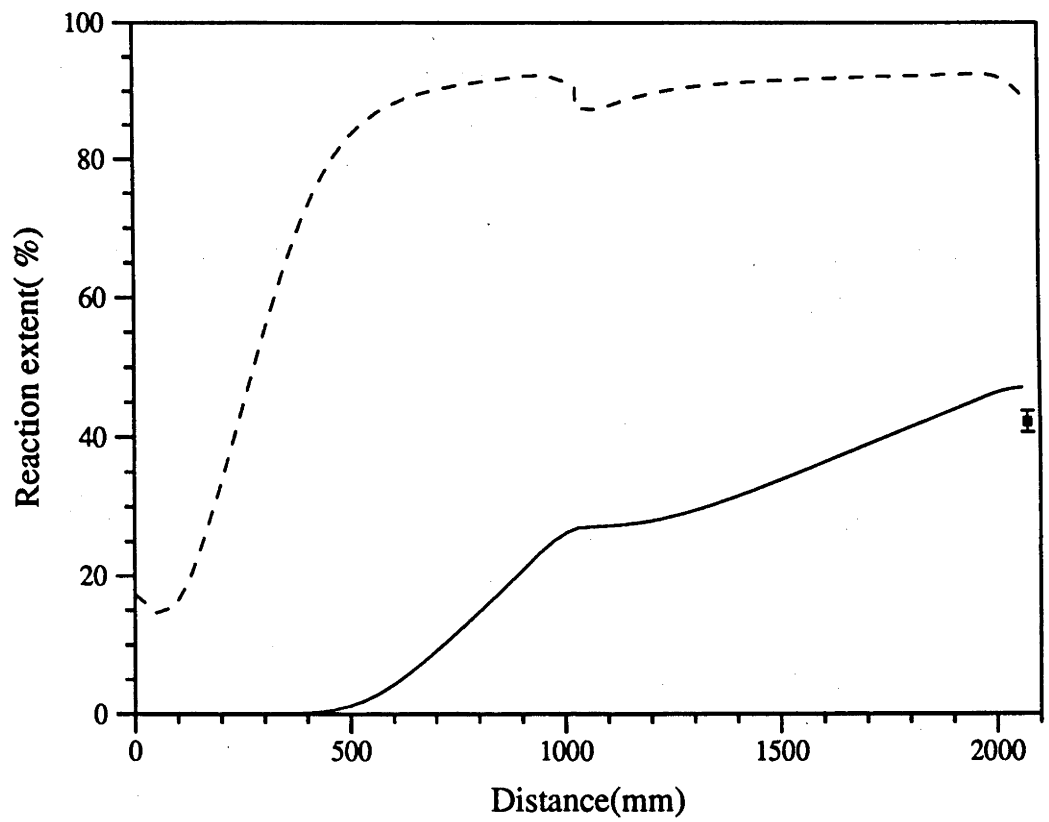

Figure 8.20: Equilibrium (- - -) and average (—) modelled reaction extent profiles with the neasured exit value for 16th of April 1991 first interval.

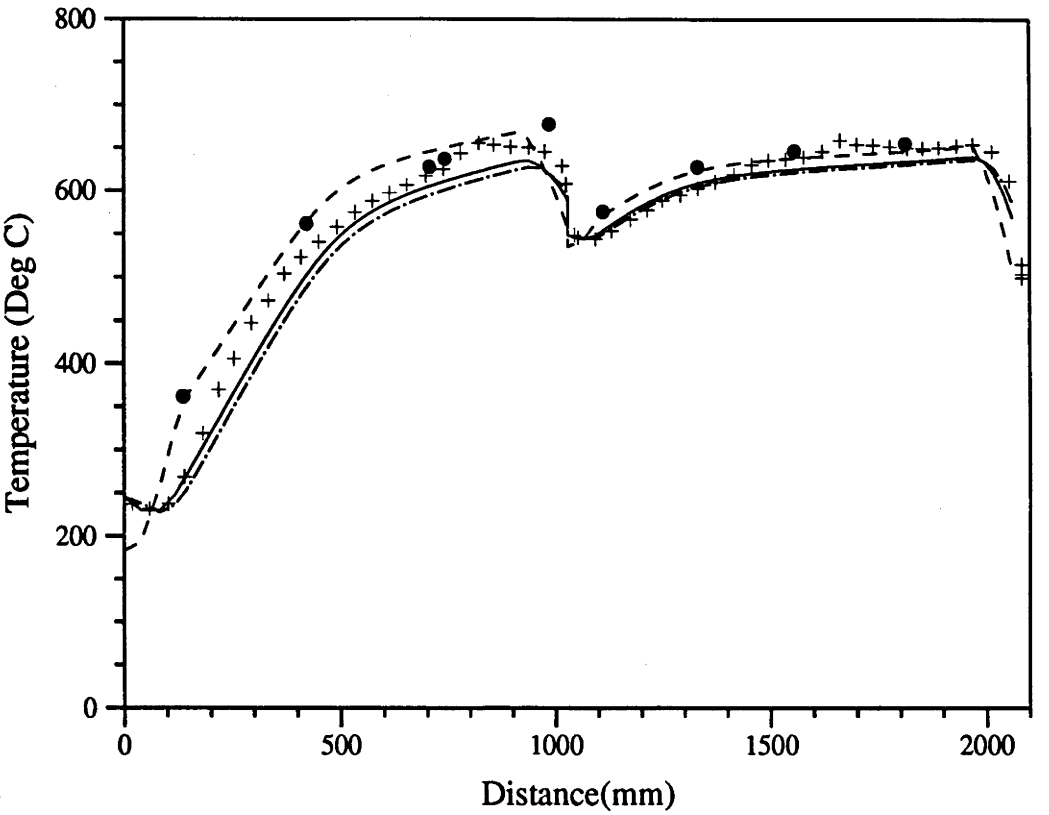

Figure 8.21: External (- - -), average (—) and internal (– · –) modelled temperature profiles and internal (+) and external (•) experimental values for 10th of April 1991 fourth interval ($0.235gs^{-1}$, $9.01MPa$, $650°C$, pressure variation baseline condition).

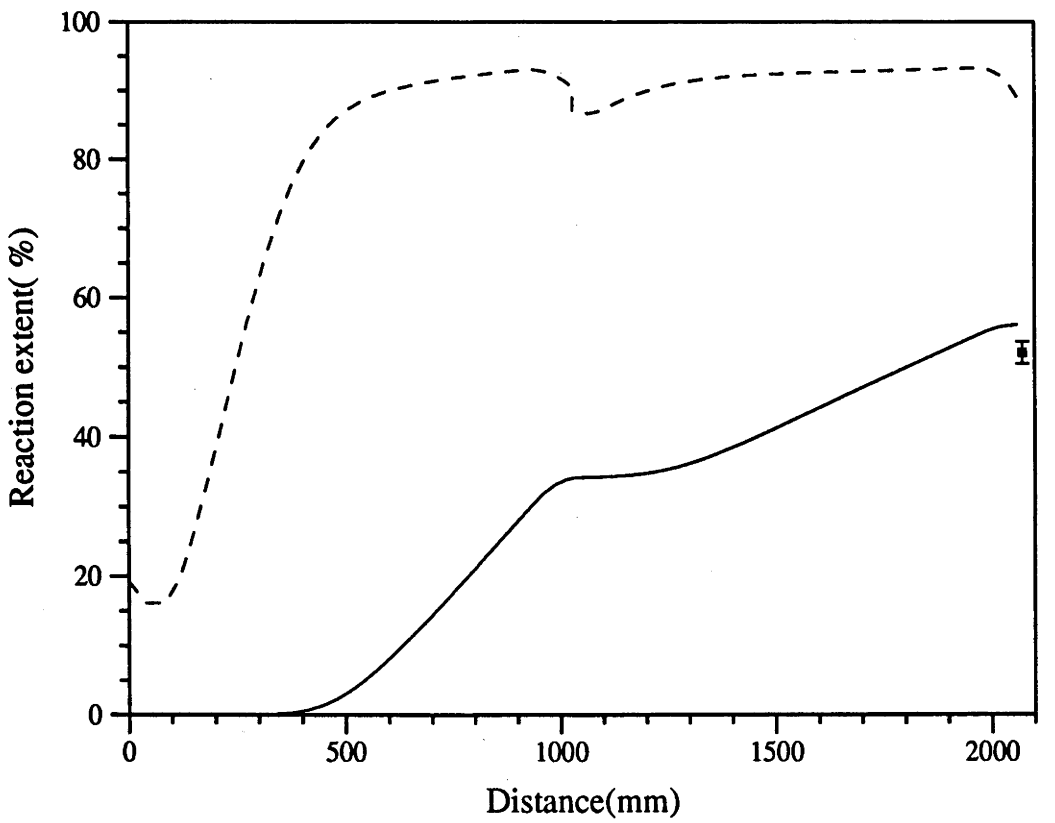

Figure 8.22: Equilibrium (- - -) and average (—) modelled reaction extent profiles with the neasured exit value for 10th of April 1991 first interval.

8.6.1 Nitrogen Runs

Experimental measurement of temperature profiles with pure nitrogen flowing in the reactor was intended to provide, in addition to a means for validating the analysis of thermal losses, a method for the examination of heat transfer processes in the absence of other factors. Richardson et al. (1988) used a similar approach in their original validation of the model. Their experimental set up involved an annular shaped reactor heated from the inside surface. As a consequence they were able to examine radial heat transfer processes, in the absence of flow, by measuring radial temperature profiles as heat flowed from the inner wall through the bed to the outer wall and then through a finite amount of insulation material to the surroundings. They did this in addition to measurements under conditions of nonreacting flow, and hence had the advantage of being able to examine radiative and convective heat transfer processes more or less independently. They found that an empirical correction to the radiative component of the effective conductivity was required. A factor quadratic in temperature successfully reconciled their heat transfer measurements with the predictions of the model.

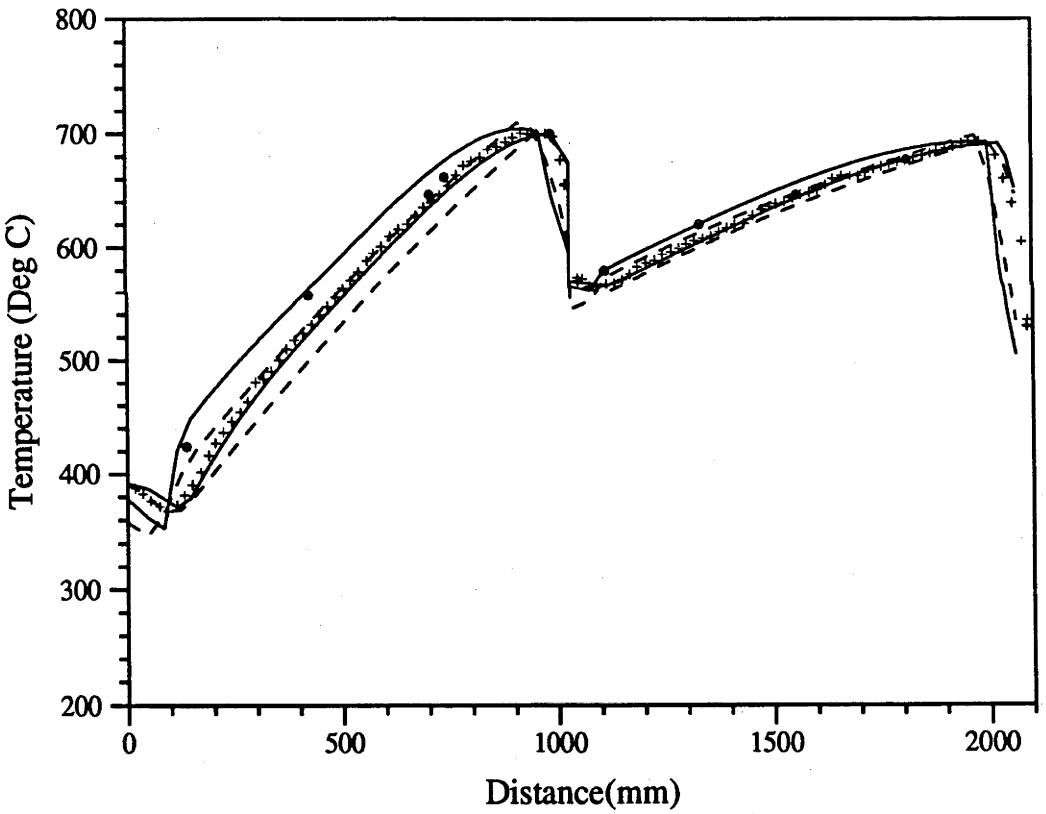

Figure 8.23: Experimental and predicted temperature profiles for 28 May 1991-A $0.63gs^{-1}$ nitrogen flow, modelled using flux profiles for model from thermal loss analysis (– –) and from the experimental temperature profile (—).

Figure 8.23 superimposes the experimental temperature measurements from the nitrogen flow run on the 28th May 1991-A with the predictions of the model using the empirical flux profile calculated from the temperature profile and the flux profile from the analysis of thermal losses (as shown in figure 8.14). The internal temperature profile that has resulted from running the model with the flux profile deduced from measured temperature

changes is in good agreement with the experimental points and simply confirms that the conversion from temperature to enthalpy was consistent with the conversion from enthalpy to temperature within the reactor model program. On the other hand, the profile that has resulted from the flux profile suggested by the analysis of thermal losses, although in agreement at inlet and exit, is substantially less curved than the measured results. This is as expected from the comparison of the two flux profiles in figure 8.14.

The extent of agreement between the predictions of the model and the experimental results for external to internal temperature difference under reaction conditions suggests that the prediction of heat transfer behaviour is fairly good. Surprisingly the agreement is not quite as good under nitrogen flow conditions.

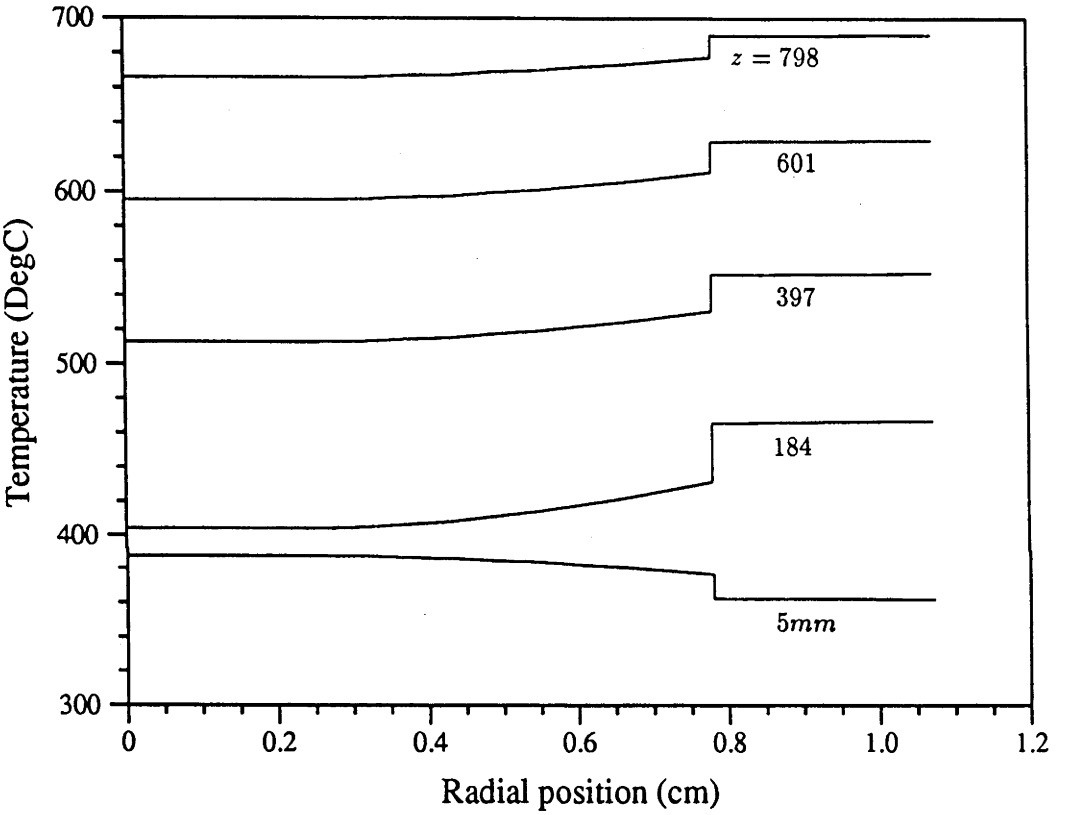

Figure 8.24: Radial profiles, 28th of May 1991-A nitrogen flow.

Using the flux profile deduced from experimental temperatures with the model, allowed the internal to external temperature difference to be examined without confusion from localised errors in the value of the flux. The sensitivity of the temperature difference to a number of parameters was examined, the first being the correction factor applied to the radiation contribution by Richardson et al. (1988). However variation of this factor by plus or minus an order of magnitude effected the internal to external temperature difference by only approximately 2%. Consequently, in the absence of any other evidence this factor has been left as formulated by Richardson et al. (1988). Addition of a single correction factor to the effective conductivity also had only a limited effect. The selected radial profiles presented in figure 8.24, show that the most significant single contribution to the internal to external temperature difference is the temperature drop across the wall boundary layer.

Figure 8.25 illustrates the effect of applying a correction factor to the heat transfer coefficient at the wall. It is apparent that a correction factor of approximately 1.5 brings the predictions of the model for nitrogen flow, to reasonable agreement with the experimental

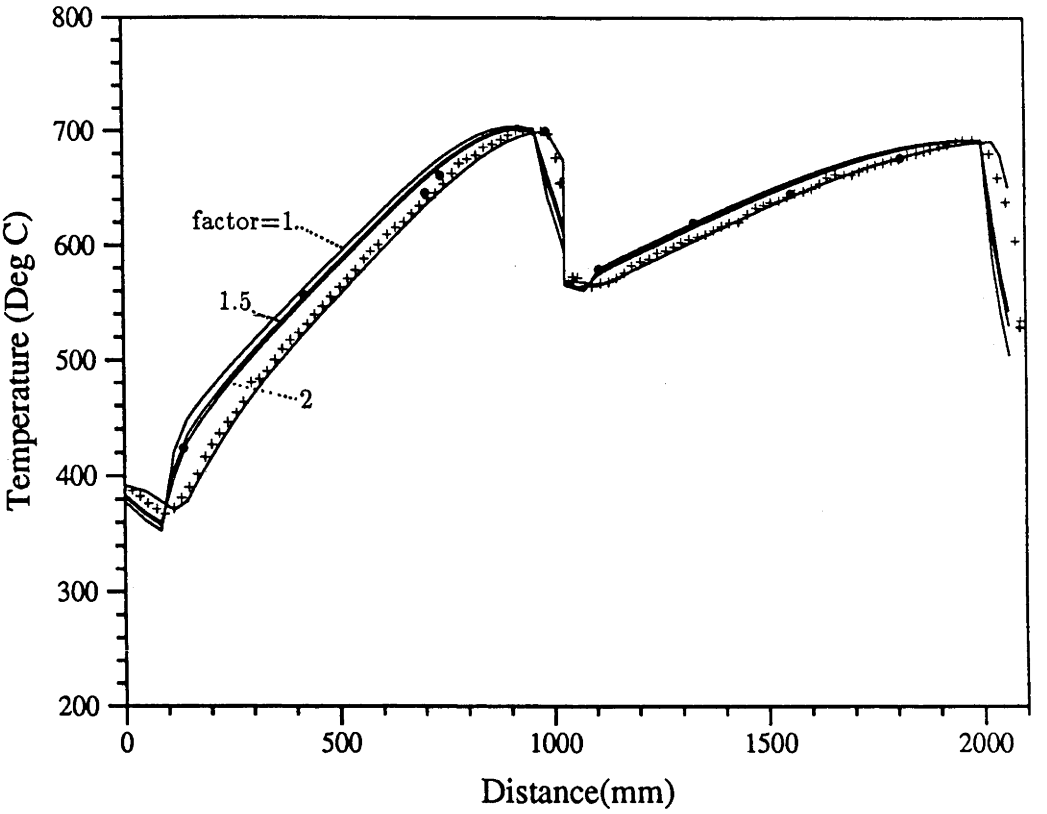

Figure 8.25: The effect of variation of wall heat transfer coefficient correction factor on modelled temperature profiles for 28 May 1991-A, nitrogen flow.

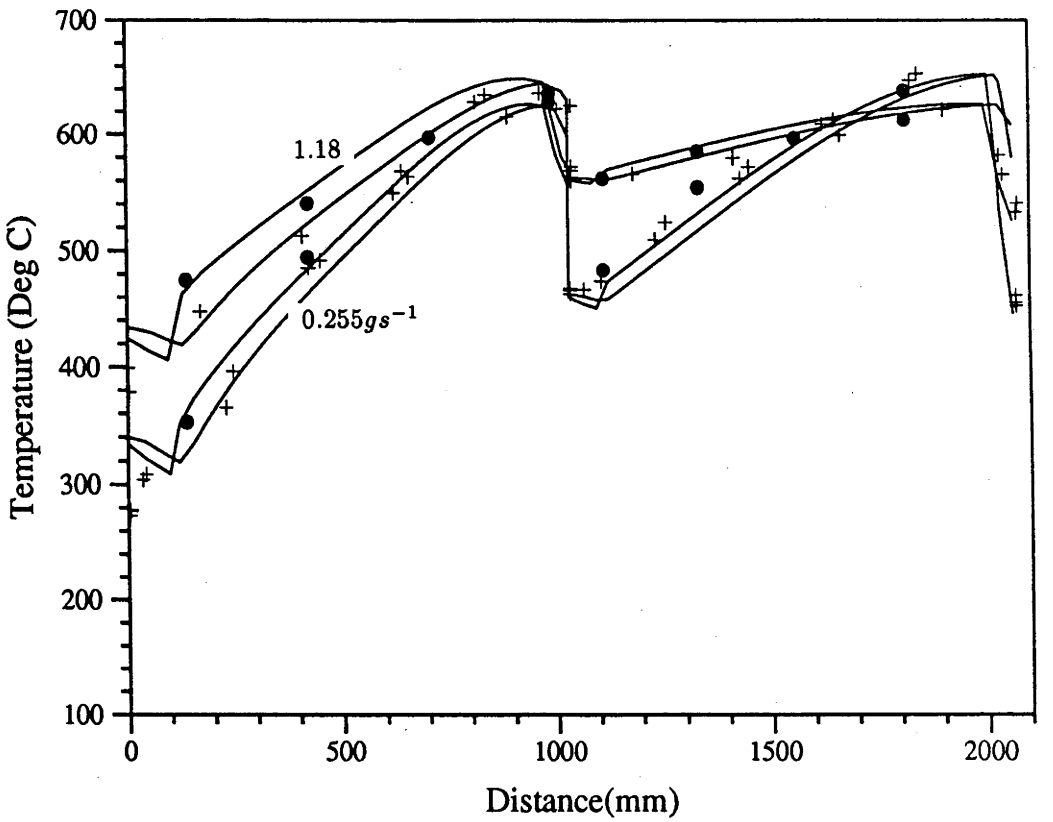

Figure 8.26: The effect of variation flow rate on nitrogen flow temperature profiles. Measurements from the 15th of January 1991, 600°C setpoints.

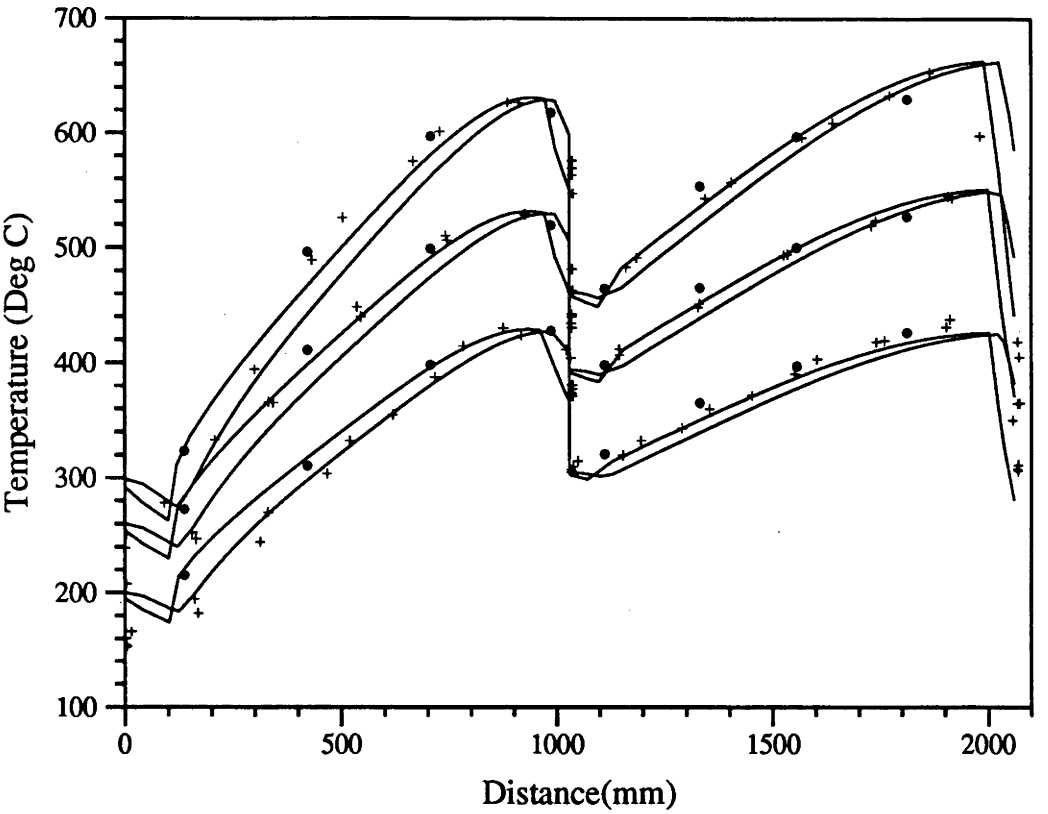

Figure 8.27: The effect of variation of setpoint temperature on nitrogen flow temperature profiles. Measurements from the 17th of January 1991, $0.25gs^{-1}$ average flowrate.

values. As has been noted, this discrepancy is not observed with results from reaction runs and so in general, a correction factor is not needed . There does not appear to be an obvious reason for the model to predict wall heat transfer coefficients for pure nitrogen less successfully than for reactant mixtures.

The first experimental runs with nitrogen flow were made prior to the improvement of the spatial resolution of internal temperature profiles. These early runs did however investigate the effect of temperature and flow rate variation. The experimental results indicated only mild sensitivity to these variables and this was also indicated by the model. Figures 8.26 and 8.27 demonstrate this. The predictions of the model shown in these figures were not produced by an exact modelling of the individual experimental runs, but were produced using the observed inlet temperatures together with the flux profile from the 28th of May 1991-A, scaled to produce the correct outlet temperatures.

8.7 Variation of Operating Conditions

The exit reaction extent results for all the experimental runs analysed, are plotted versus the maximum external temperature of the reactor, in figure 8.28, together with the equilibrium mixture compositions for $5MPa$ and $10MPa$. The temperature controller thermocouples were positioned at the estimated points of maximum external temperature, so that maximum external temperature is equivalent to the controller setpoints (which were kept the same for both columns). This figure gives an indication of the range of the various

operating parameters (temperature, mass flow and pressure) investigated and the range of exit reaction extents measured.

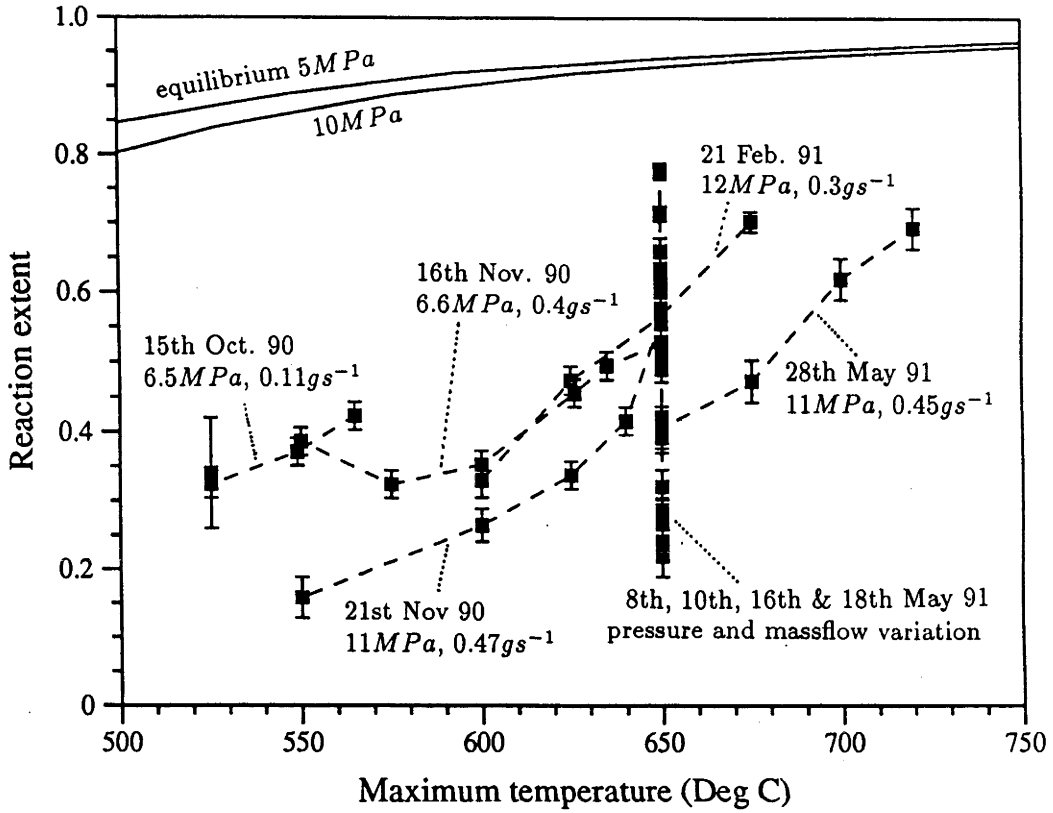

Figure 8.28: Exit reaction extents from all analysed experimental runs.

Rather than attempt to model the exact conditions of every run, the model was used to produce relationships between the various operating parameters and the conditions at reactor exit. After successful reconciliation with the experimental results, these relationships allow a smooth interpolation between the conditions tested experimentally and extrapolation beyond the conditions tested.

The dependence of reactor temperatures and reaction extents on operating conditions, reflects the behaviour of the dissociator in conjunction with the counterflow heat exchanger. The heat exchanger is essentially a positive feedback mechanism for the reactor. Its behaviour can be characterised by two observations; if other factors are equal, the inlet temperature seen by the first reaction chamber increases with the exit temperature of the second reaction chamber; and if the exit temperature of the second chamber remains unchanged, the inlet temperature for the first chamber increases with flow rate and exit reaction extent.

Whilst it would be possible to model the heat exchanger behaviour in conjunction with the reactor, it is the behaviour of the reactor which is of primary interest. The approach taken has been to relate the inlet temperatures for the two chambers to the varying operating parameter using a one dimensional curve fit to the experimental values in each case. Interpolated values from these fits have been used as input data for the reactor model Similarly the experimentally observed effective enthalpy changes[5] have been the

[5]The effective enthalpy change is the sum of the enthalpy changes associated with each reactor chamber.

subject of curve fitting, with interpolated effective enthalpy change values being used to calculate scale factors which were applied to the flux profiles from the three chosen baseline conditions.

8.7.1 Variation of Temperature

The results of the main experimental investigation of the effect of operating temperature on exit reaction extent and the pressure drop across the reactor plus the heat exchanger are presented in figures 8.29 and 8.31 respectively, together with the predictions of the model. The average flow rate for these runs was $0.447gs^{-1}$ and the pressure was $11.4MPa$, actual flow rates differed by up to $0.06gs^{-1}$ and pressures by $0.7MPa$. As is expected there is a fairly dramatic increase in exit reaction extent as the operating temperature is increased. The temperature reaction extent relationship predicted by the model is confirmed by the experimental points, close to within the bounds of their error bars. The curve generated by the model indicates an asymptotic approach to equilibrium conditions that begins at approximately $750°C$, the experimental points however, do not extend to a high enough temperature to observe this trend. The curve generated by the model was obtained using intrinsic rate parameter values selected to give the best overall prediction of reaction extents for all the conditions presented in figure 8.28.

The error bars associated with the experimental values represent the uncertainty in the calculation of exit reaction extent based on the determination of inlet and exit ammonia mass flow. Point to point fluctuations are the result not only of random errors, which have been quantified by the error bars, but also of variations in the operating conditions or of deviations from steady state behaviour.

Occasionally measurements have been obtained which lie well outside the range of the general trend, but for which no obvious correlating variation of an operating parameter can be found. The last point from the 21st of February 1991 (at $650°C$) falls in this category, its measured mass flow is very close to the other points measured on this occasion, yet the reaction extent is indicative of a much lower value. This point also has a lower measured reactor/heat exchanger pressure drop than the others, which would be consistent with a lower flow rate. The data taken on the 21st of November 1990 pre-dates the installation of the electronic level sensor on the ammonia accumulator, thus flow rates were determined from the pressure drop across the metering valve. The flow rate may have been reduced by a partial blockage of the valve which was undetected by the measurement of pressure drop across it.

The predictions of the model indicate that pressure drop across the reactor increases with the maximum external temperature, presumably in direct correlation with the increased molar flux associated with higher reaction extents. The experimental results are somewhat inconclusive, with the values from the 21st of February 1990 being considerably lower than those from 28th of May 1991. The earlier run pre-dated refinements to the pressure transducer instrumentation and so these values must be treated with less confidence than the later ones. A possible explanation for a real increase in the pressure drop could be a progressive accumulation of powdered catalyst material within passages of the reactor or the heat exchanger. The results from the 28th of May, when taken in isolation, do confirm the increase with temperature predicted by the model. Measured values of pressure drop considerably larger than predicted for the reactor alone could indicate that the heat exchanger was responsible for a large fraction of the total pressure drop.

Figures 8.31 and 8.32 show the measured inlet temperatures and effective enthalpy changes respectively, together with the curve fits used for interpolation for operation of

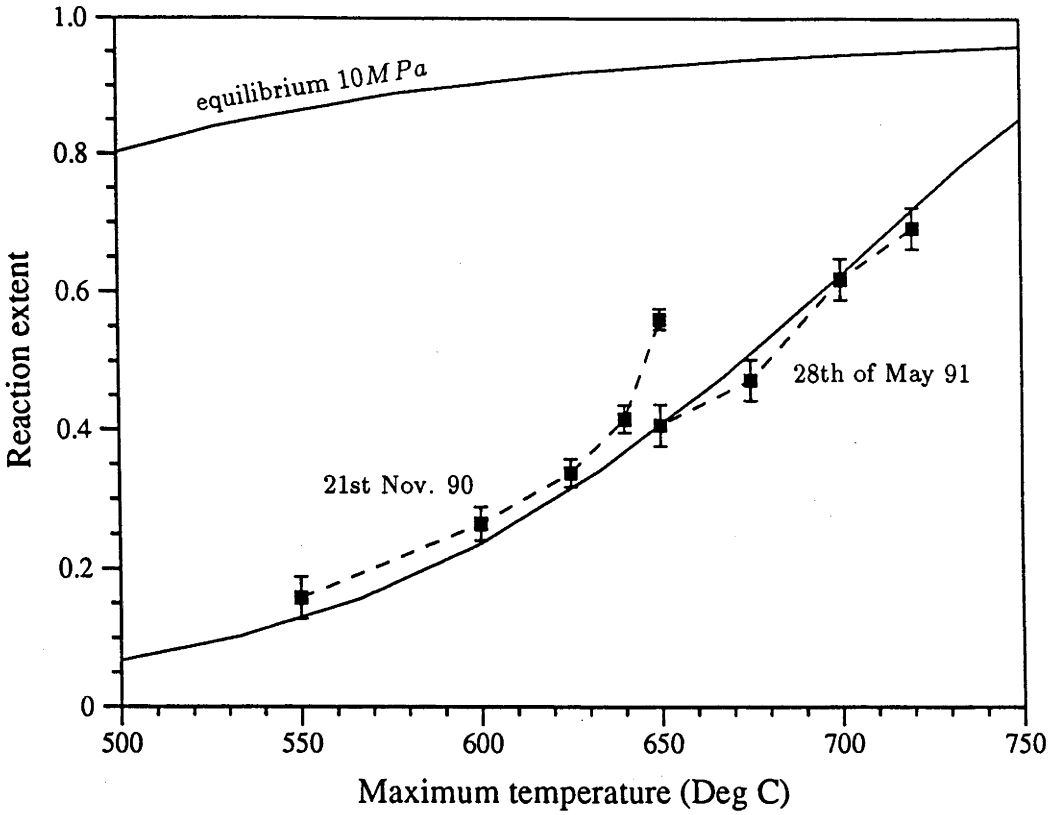

Figure 8.29: The effect of variation of operating temperature on exit reaction extent, for $11.4MPa$ and $0.447gs^{-1}$.

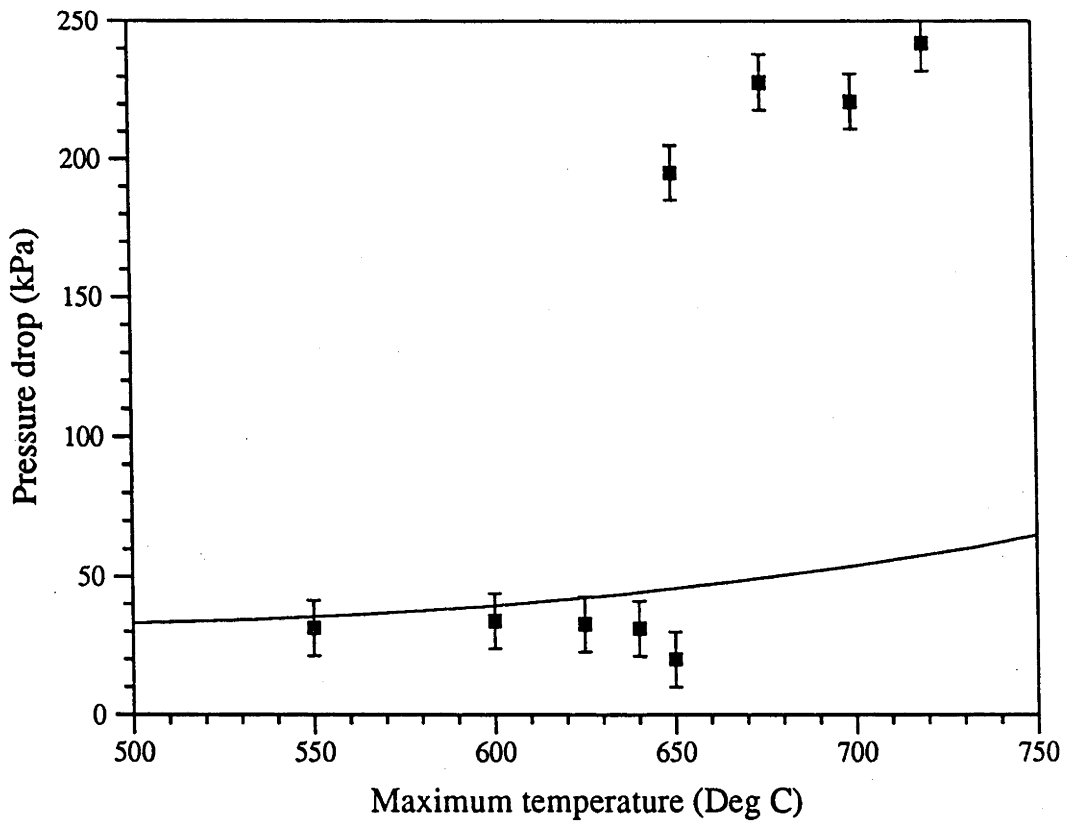

Figure 8.30: The effect of variation of operating temperature on modelled reactor pressure drop and measured reactor plus heat exchanger pressure drop, for $11.4MPa$ and $0.447gs^{-1}$.

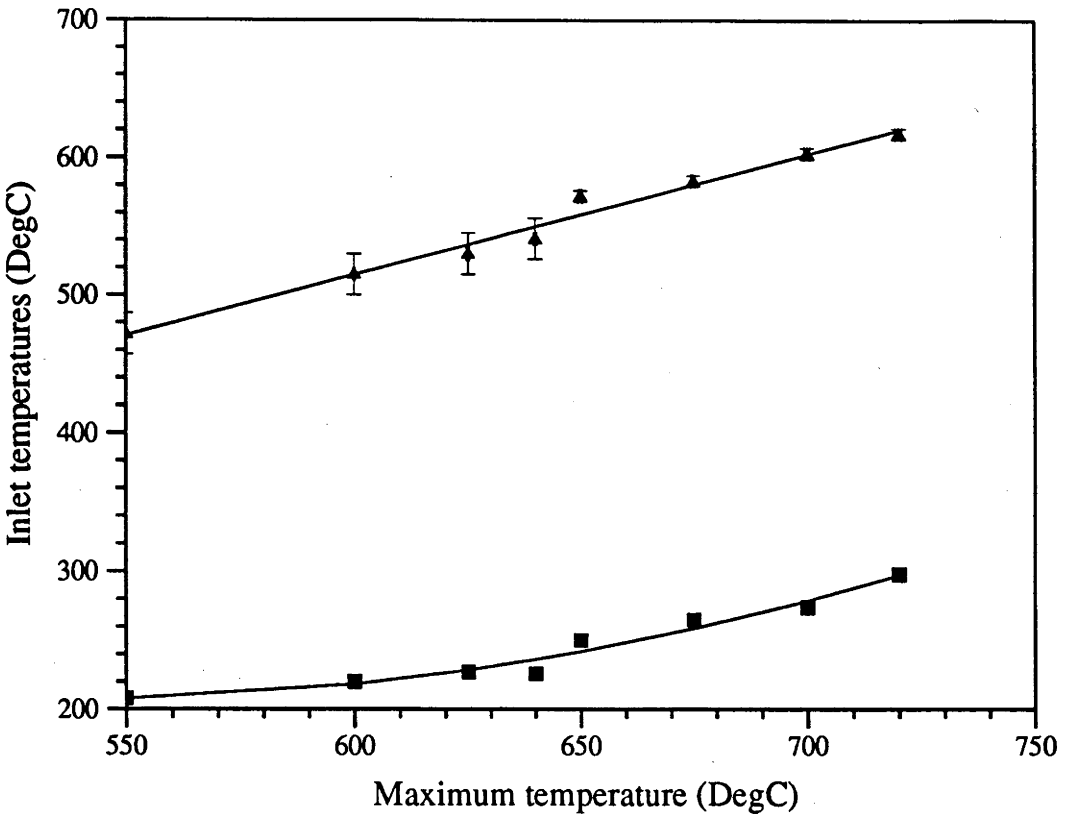

Figure 8.31: The effect of variation of operating temperature on reactor inlet temperatures, for $11.4MPa$ and $0.447gs^{-1}$ (□ – chamber 1, △ – chamber 2).

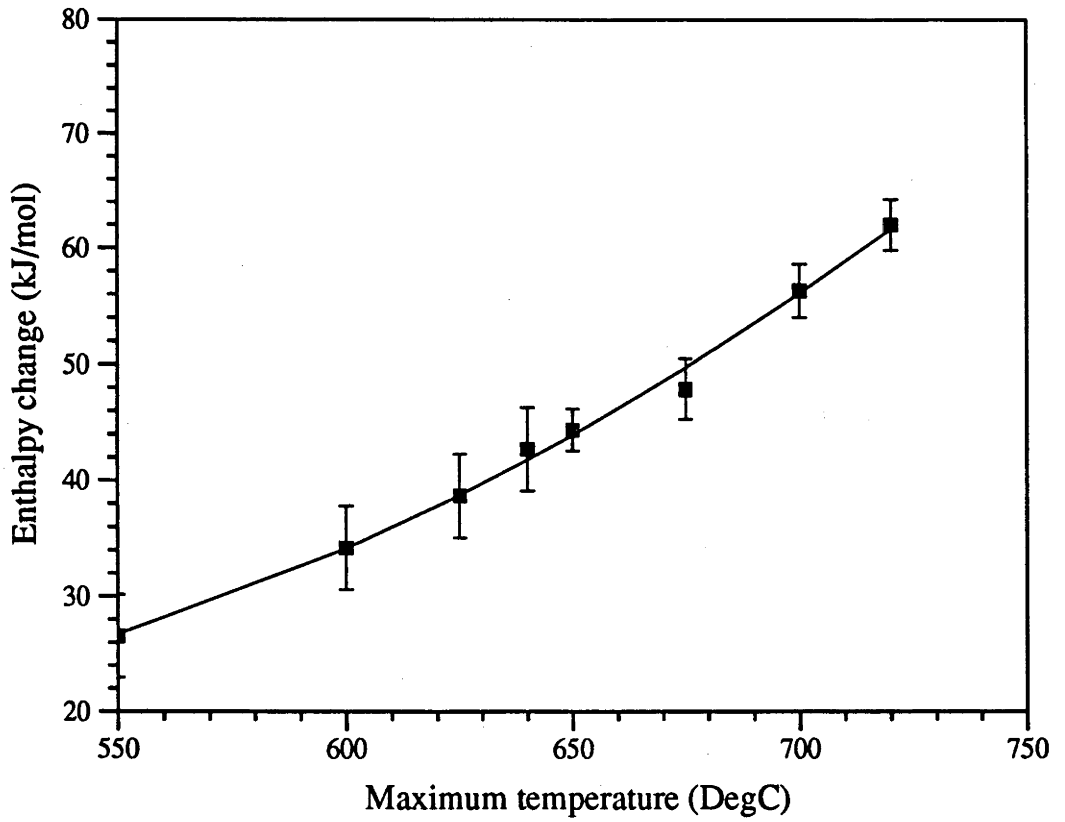

Figure 8.32: The effect of variation of operating temperature on the effective enthalpy change, for $11.4MPa$ and $0.447gs^{-1}$.

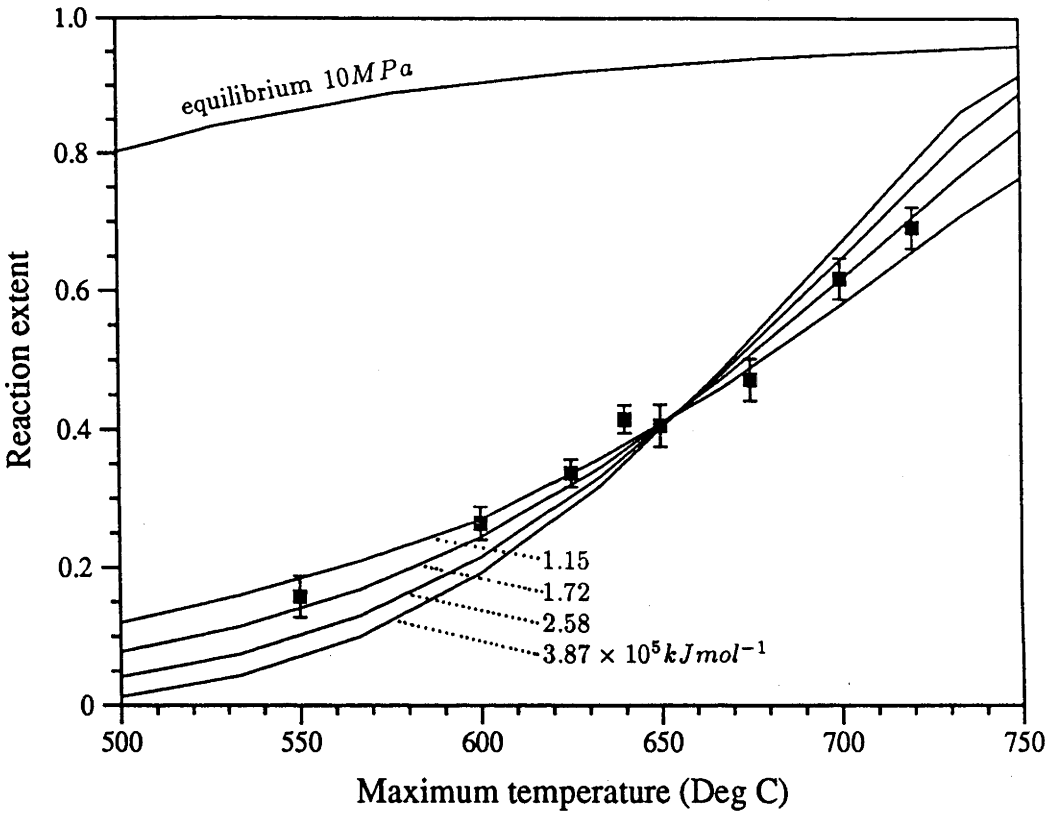

Figure 8.33: The effect of variation of operating temperature on exit reaction extent modelled using different activation energies.

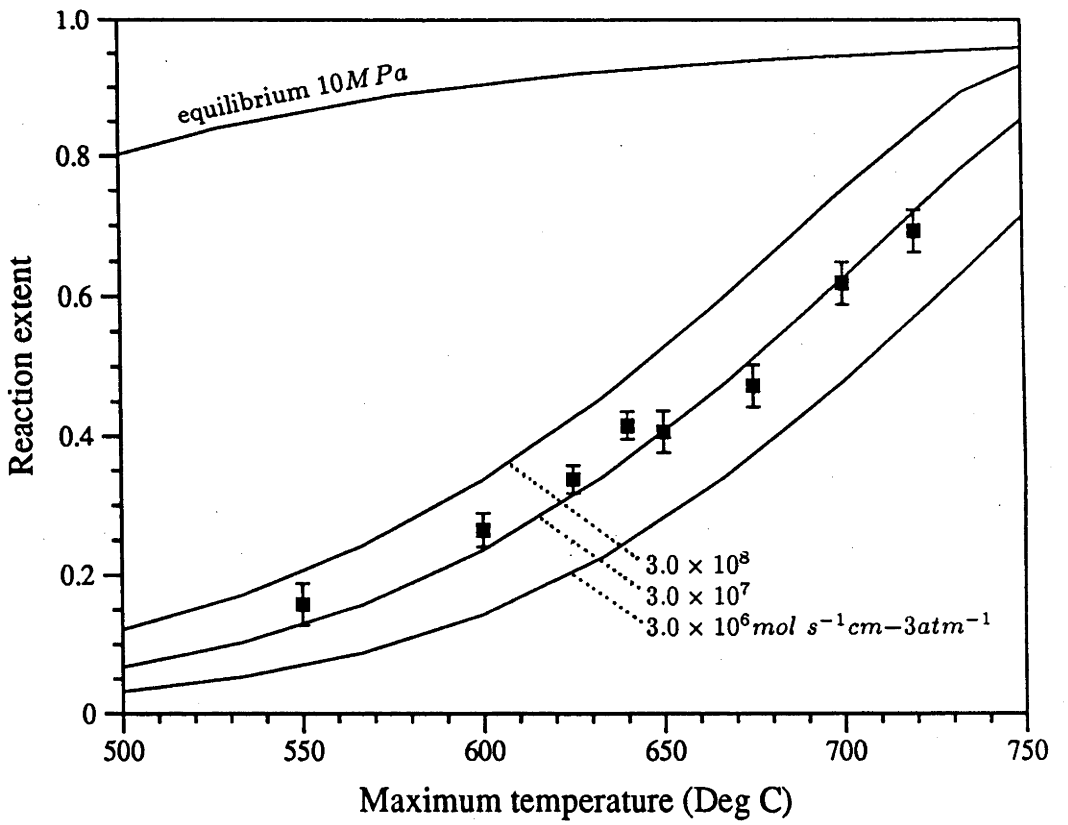

Figure 8.34: The effect of variation of operating temperature on exit reaction extent modelled using different pre-exponential factors (activation energy $1.92kJmol^{-1}$).

the model. The inlet temperatures increase in line with the overall temperature of the reactor. The curve fit used for the first chamber is;

$$T_{in} = (959.6 - 2.813(°C)^{-1} \times T + 2.6295 \times 10^{-3}(°C)^{-2} \times T^2)°C \tag{8.8}$$

with a standard deviation of fit of $5.8°C$, and for the second chamber;

$$T_{in} = (-11.82 + .8774(°C)^{-1} \times T)°C \tag{8.9}$$

with a standard deviation of $6.7°C$. The net enthalpy change increases essentially in proportion to the change in reaction extent, and has been fitted by;

$$\Delta H = (101.98 - 0.3981(°C)^{-1} \times T + 4.750 \times 10^{-4}(°C)^{-2} \times T^2)kJmol^{-1} \tag{8.10}$$

with a standard deviation of $8.2kJmol^{-1}$.

Although diffusion and heat transfer processes are effected by the operating temperature, the most significant affect on reactor behaviour is via the temperature dependence of the intrinsic reaction rate. Figure 8.33 illustrates the affect of varying the activation energy on the predictions of the model. These curves were obtained by making compensating changes to the pre-exponential factor so that the intrinsic rate at a temperature of $640°C$ would remain constant. The fact that the family of curves pivots around a maximum external temperature value of approximately $660°C$ indicates that this is the value at which the reaction rate weighted average temperature within the reactor is $640°C$.

Nandy & Lenz (1984) determined activation energies for two nickel based catalysts for high pressure ammonia dissociation. For 6.9 wt.% nickel on alpha-alumina they obtained values between 258 and $283kJmol^{-1}$, for 8.1 wt.% nickel on gamma-alumina, which corresponds closely to the composition of the ICI 47-1 material used for this project, they obtained a value of $192kJmol^{-1}$. An activation energy of $192kJmol^{-1}$ produces a maximum temperature exit reaction extent relationship which is in good agreement with the experimental points, although a slightly lower value of $170kJmol^{-1}$ produces the best fit. The magnitude of the random uncertainties and the fact that the results are composed of values obtained on two separate occasions (with an associated risk of the introduction of a systematic error such as a decline in catalyst activity), suggests an uncertainty in this result of approximately $\pm 30\%$. The experiments performed by Nandy and Lenz were more appropriate for the direct determination of intrinsic rate parameters than the ones reported here, hence the most appropriate conclusion is that the experimental results reported here support their value of $192kJmol^{-1}$.

On the other hand it can be seen from figure 8.33 that an activation energy of $349kJmol^{-1}$ as suggested by Williams & Carden (1979*a*), is not supported by these results. Although they used the identical ICI 47-1 catalyst material, their determination of activation energy must be questioned since it involved the use of Arrhenius plots of measurements of extrinsic rates made using large catalyst particles, rather than finely crushed catalyst which is necessary for direct measurement of intrinsic rates.

Figure 8.34 illustrates the sensitivity of the predictions of the model to variation of the pre-exponential factor using the $192kJmol^{-1}$ activation energy. The value determined on the basis of all the experimental results to date is $3.0 \times 10^{(7.0 \pm 0.18)} mols^{-1}cm^{-3}atm^{-1}$.

8.7.2 Variation of Mass flow

The investigation of the effect of mass flow variation was carried out at an average pressure of $10.3MPa$, (with variations up to $0.6MPa$) and with temperature setpoints of $650°C$.

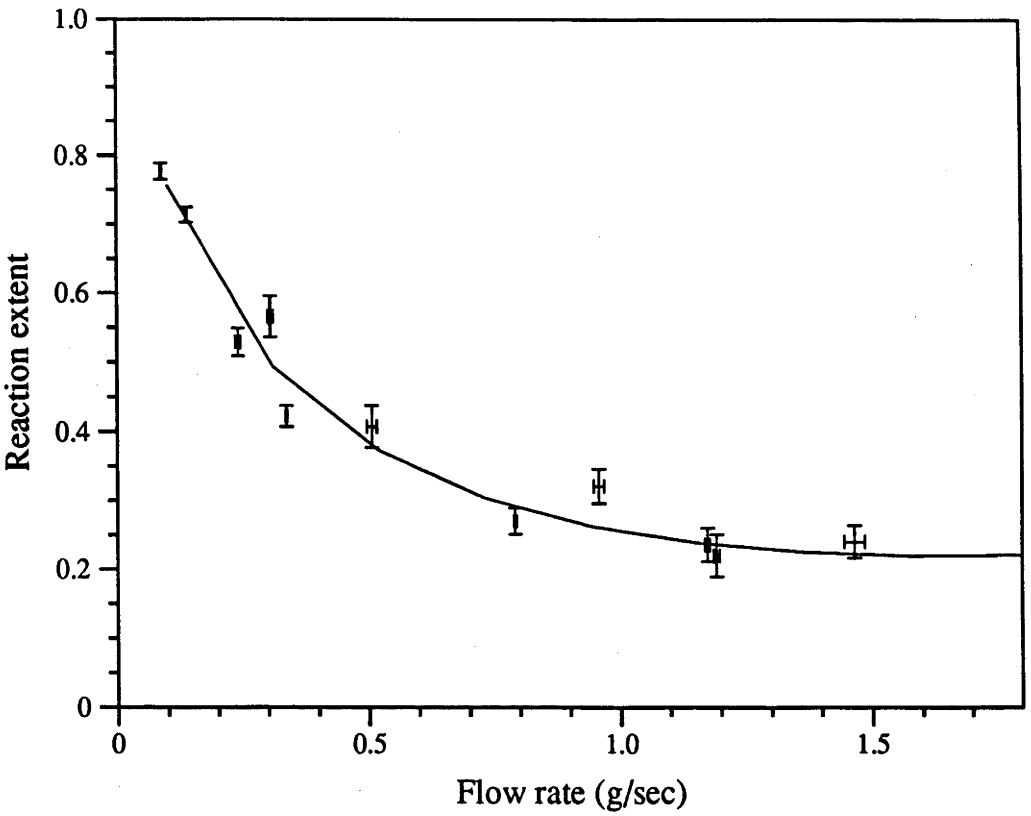

Figure 8.35: The effect of variation of mass flow on exit reaction extent, for $10.3MPa$ and $650°C$ maximum temperature.

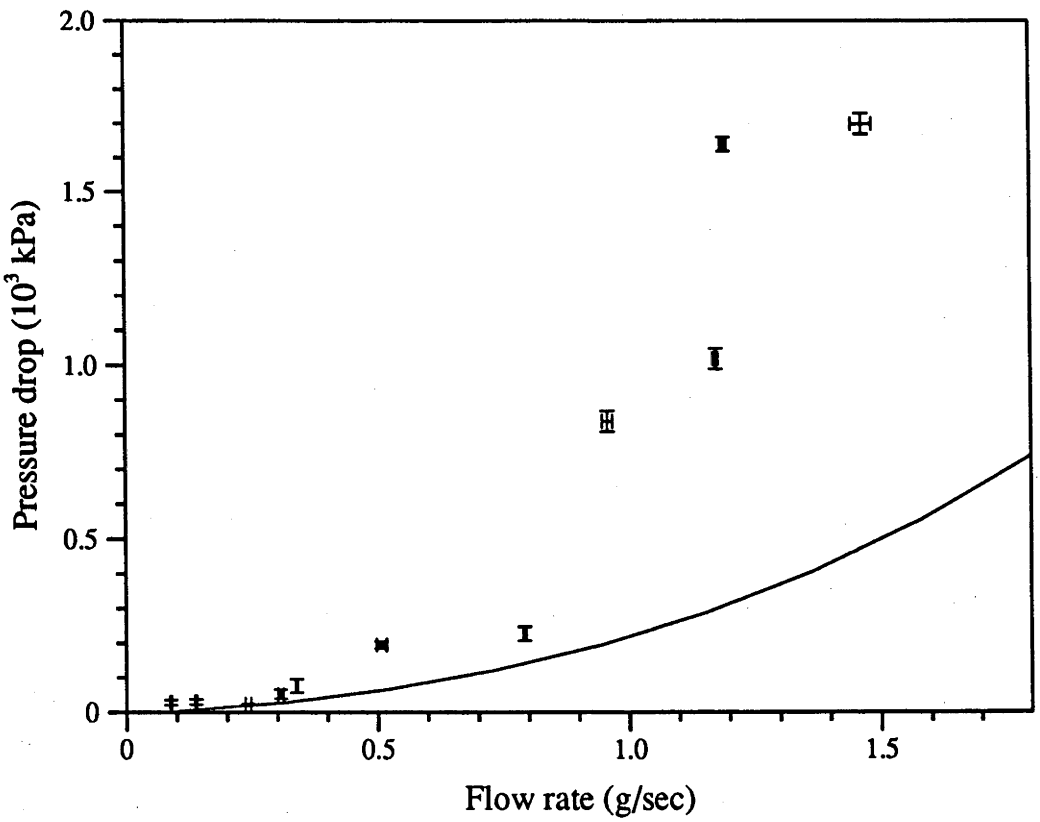

Figure 8.36: The effect of variation of mass flow on measured reactor/heat exchanger pressure drop and modelled reactor pressure drop, for $10.3MPa$ and $650°C$ maximum temperature.

Figure 8.35 shows the experimental points and the modelled variation of reaction extent with mass flow. The experimental values are largely from runs carried out on the 16th and 18th of April 1991, with 2 supplementary points, one from the 21st of February 1991 (at $0.31gs^{-1}$) and the other from the 28th of May 1991 (at $0.51gs^{-1}$), for which the same nominal operating pressure and temperature setpoints were used.

As expected the exit reaction extent decreases as the residence time[6] within the catalyst bed is decreased by increasing the mass flow. However the relationship is not linear. This presumably is a consequence of a combination of the effect of increased mass flow on the performance of the heat exchanger (giving a higher inlet temperature), and in enhanced heat transfer and diffusion processes within the bed.

Using the rate parameters discussed above, the model has predicted a behaviour for the reaction extent mass flow relationship which is in good agreement with that indicated by the experimental points. The deviation of experimental values from the model curve is, in a number of cases, outside the range of the uncertainty associated with the reaction extent calculation. No correlation between the point to point variation and the pressure or chamber inlet temperatures has been identified, indicating the possible presence of other systematic effects. It can be noted, that with the exception of one point at $0.96gs^{-1}$, the points from the 16th and 18th of April lie on or below the model curve, whereas the points from the 21st of February and the 28th of May (at 0.31 and $0.51gs^{-1}$ respectively), lie above the curve. This may be an indication of a systematic effect that changes from run to run.

Figure 8.36 presents the measured values of pressure drop across the reactor heat exchanger combination, together with the predictions of the model for pressure drop across the reactor. Although there are considerable fluctuations between the measured values the general trend follows that predicted by the model, ie pressure drop increases in an almost exponential manner with flow rate. The predicted values are considerably lower than the experimental points, consistent with the results obtained on the 28th of May 1991, further suggesting that the heat exchanger may be a major contributor to the measured pressure drop. This could be tested at a future date by the removal of catalyst from the reactor to allow the pressure drop across the heat exchanger alone to be measured using nitrogen flow.

The reactor inlet temperatures together with the curve fit used for interpolation for the model are presented in figure 8.37. At low flow rates the thermal losses from the heat exchanger and the connection tubes become increasingly significant and result in the dramatic drop in inlet temperatures observed. The curve fits used for interpolation purposes are, for the first chamber;

$$T_{in} = (5.112 - 179.89(gs^{-1})^{-1} \times \dot{m} + 469.84(gs^{-1})^{-0.5} \times \dot{m}^{0.5})^{\circ}C \qquad (8.11)$$

with a standard deviation of fit of $6.6^{\circ}C$, and for the second chamber;

$$T_{in} = (325 - 281.1(gs^{-1})^{-1} \times \dot{m} + 546.1(gs^{-1})^{-0.5} \times \dot{m}^{0.5})^{\circ}C \qquad (8.12)$$

with a standard deviation of $9.3^{\circ}C$ ($\dot{m}$ is the mass flow). These curves are only valid over a limited range of mass flows. Below $0.1gs^{-1}$ a linear extrapolation is necessary, and at high mass flows the values are essentially constant (above $1.2gs^{-1}$ for the first chamber

[6]In chemical engineering literature residence time is frequently indicated by the space velocity, which is defined as the frequency with which a quantity of reactants which would occupy the whole reactor volume at standard temperature and pressure, passes through it. Thus for the dissociator with a volume of $358cm^{-3}$ a mass flow of $1gs^{-1}$ ($0.0587mols^{-1}$) represents a space velocity of $1.32 \times 10^4 hr^{-1}$.

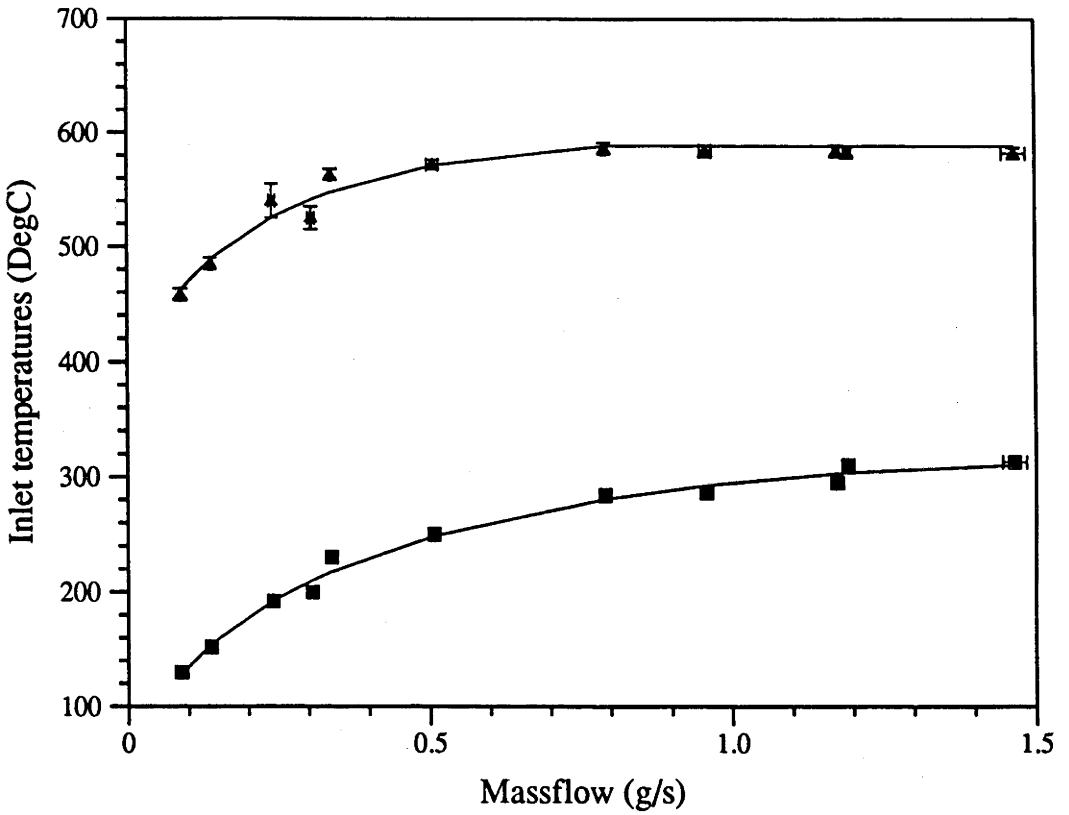

Figure 8.37: The effect of variation of mass flow on reactor inlet temperatures, for $10.3MPa$ and $650°C$ maximum temperature (□ - chamber 1, △ - chamber 2.

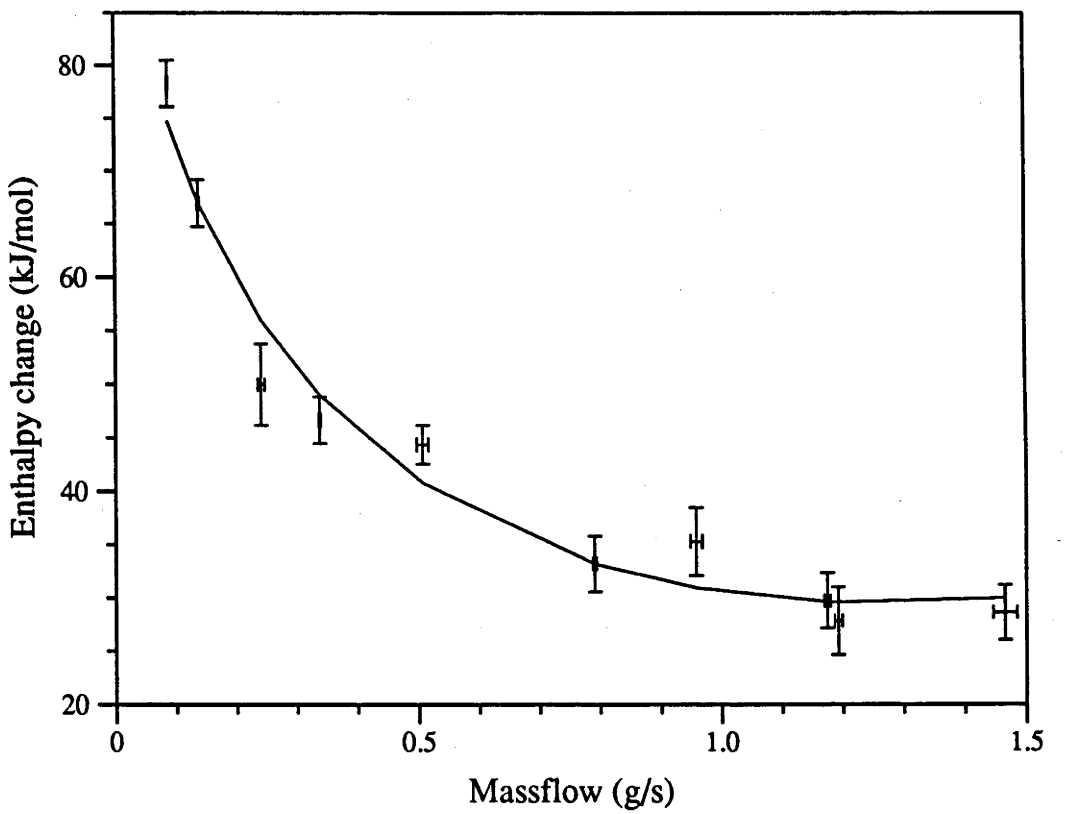

Figure 8.38: The effect of variation of mass flow on the effective enthalpy change, for $10.3MPa$ and $650°C$ maximum temperature.

and above $1gs^{-1}$ for the second). The effective enthalpy change decreases with mass flow, essentially in proportion to the change in reaction extent, and has been fitted by;

$$\Delta H = (112.8 + 65.63(gs^{-1})^{-1} \times \dot{m} - 147.83(gs^{-1})^{-0.5} \times \dot{m}^{0.5})kJmol^{-1} \qquad (8.13)$$

with a standard deviation of $3.2kJmol^{-1}$. For enthalpies, a linear extrapolation is also needed below $0.05gs^{-1}$ and the value is essentially constant for extrapolation above $1.5gs^{-1}$.

Given that the model has been shown to predict the results of the baseline condition satisfactorily, the qualitative nature of the predicted relationship between mass flow and reaction extent is partly a reflection of the empirically determined inlet temperatures and enthalpy changes. However, the variation of mass flow does affect heat transfer and diffusion processes, and also the average reactor temperature and hence the intrinsic rates encountered. Thus the degree of agreement between experiment and model does offer vindication of the model and the parameter values used.

8.7.3 Variation of Pressure

The investigation of the effect of variation of system pressure involved runs on the 8th and 10th of April 1991. A supplementary point from the 18th of April 1991 for which the same mass flow and operating temperature were used has also been included in the analysis. These results together with model predictions are presented in figure 8.39. The average mass flow used was $0.229gs^{-1}$, with variations up to $0.07gs^{-1}$. Setpoint temperatures were maintained at $650°C$.

Both the experimental results and the predictions of the model show the exit reaction extent increasing at lower pressures, however the model predicts exit reaction extents which are just above the upper limit of the range of uncertainty associated with most of the experimental points. The measured pressure drop values shown in figure 8.40 increase in proportion to the exit reaction extent, as would be expected from an increased molar flux. Once again the pressure drop predicted by the model for the reactor alone is substantially less than that measured across the heat exchanger and reactor.

Although the model predictions for exit reaction extent are higher than most of the experimental values, an adjustment to the intrinsic rate pre-exponential factor would produce good agreement. The model curve has been produced using the previously quoted value which was chosen to give the best overall agreement with all the experimental results. It can be noted that the measurement from the 18th of April ($9.9MPa$) is consistent with the majority of experimental points and is less than the modelled variation of pressure curve by approximately the same amount as it is less than the modelled variation of flow rate curve ($0.24gs^{-1}$ in figure 8.35).

Two experimental points are noticeably different from the general trend. The point at $7Mpa$ (from the 8th of April) is higher than the general trend although only just beyond the range of the error bars, it corresponds to the lowest inlet flowrate of the series, the variation of $-0.05gs^{-1}$ from the average is almost sufficient to account for the discrepancy. The point at $14.3MPa$ is considerably lower than the general trend. Although it has one of the higher measured inlet flow rates, other points with the same or higher value do not show the same variation. Being the first measurement from the 10th of April, the variation may be a result of non-steady state behaviour at the beginning of the run.

The effect of pressure on the exit reaction extent is relatively minor, however in terms of the primary quantity measured under experimental conditions, ie. the liquid ammonia mass flow in the exit reactant stream, the effect was dramatic. The lowest pressure measurement at $5.27MPa$ resulted in no liquid accumulation in the balancing separator.

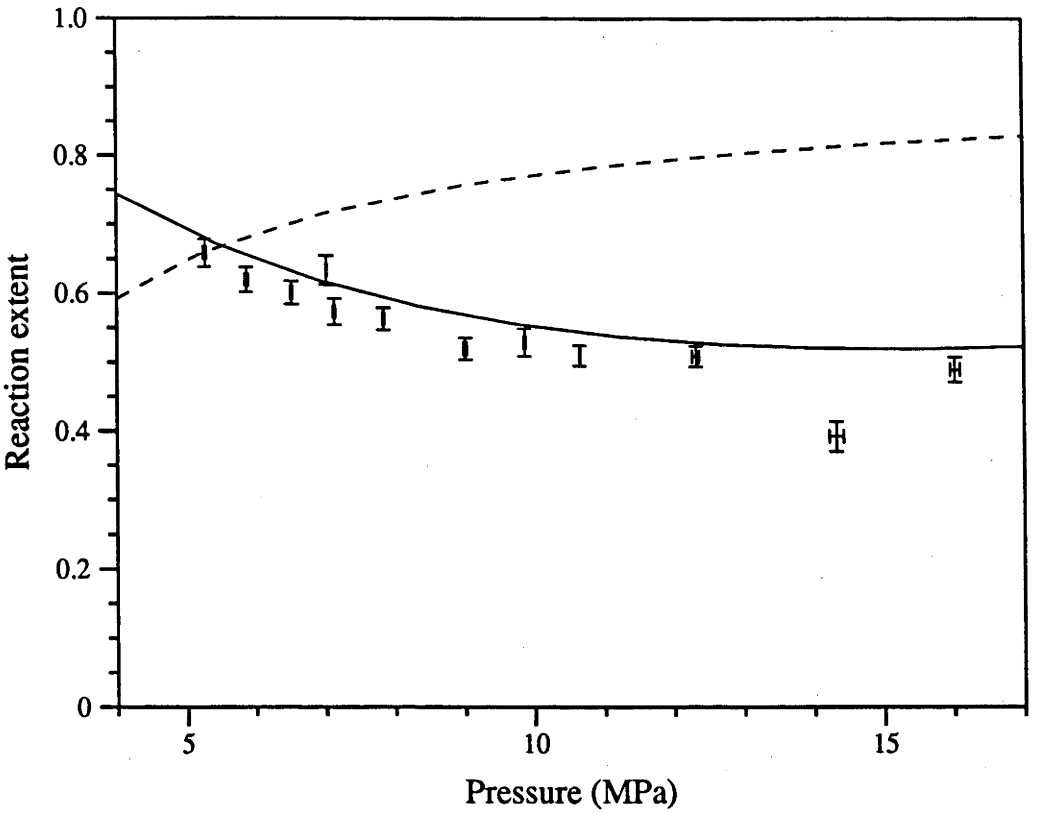

Figure 8.39: The effect of variation of pressure on exit reaction extent, for $0.23gs^{-1}$ and $650°C$ maximum temperature (— model predictions, - - - mass fraction of H_2/N_2 in the gas component at $25.0°C$.

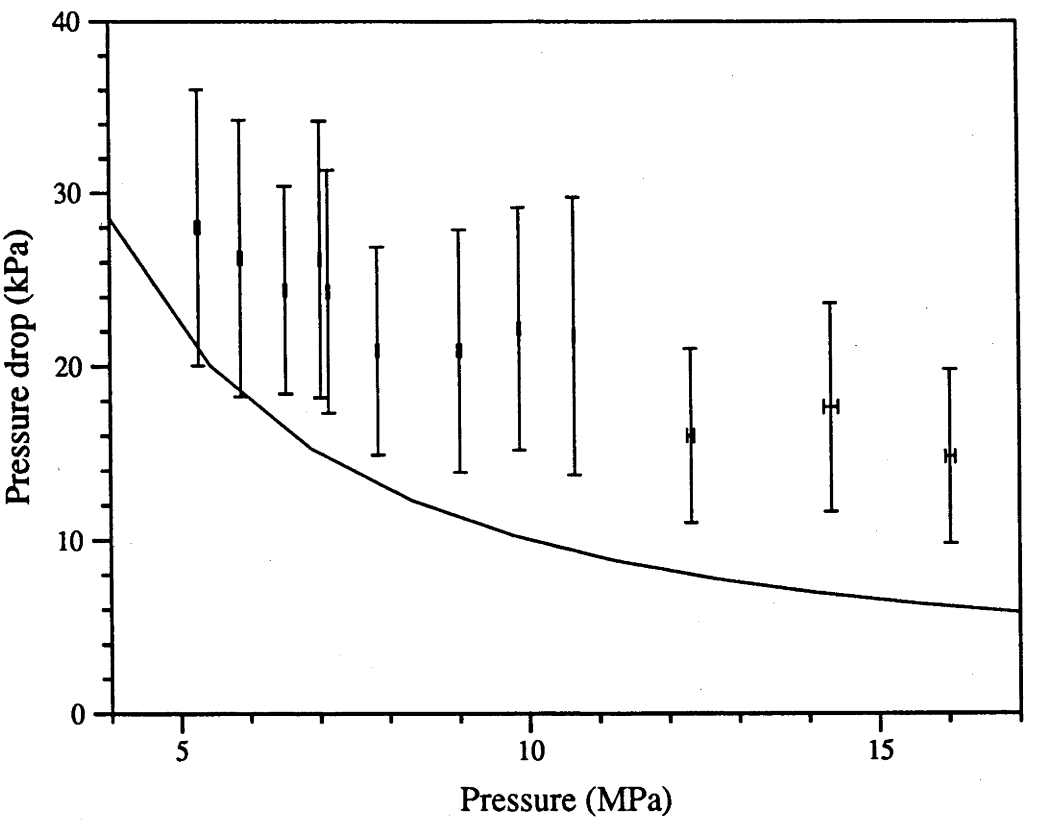

Figure 8.40: The effect of variation of pressure on reactor heat exchanger pressure drop, for $0.23gs^{-1}$ and $650°C$ maximum temperature.

The extra contour plotted in figure 8.39 represents the mass fraction of H_2/N_2 in the gas phase of a two phase reactant mixture, at a temperature of $25.0°C$ (the temperature of the reactant stream entering the separator for the $5.27MPa$ measurement). This contour intercepts the experimental points at the pressure of which the ammonia vapour pressure is a sufficiently large enough fraction to prevent the formation of a liquid phase.

When the exit liquid mass flow is small relative to the inlet mass flow, the calculation of reaction extents from balancing separator measurements relies heavily on the validity of the gas phase composition data used, but becomes progressively less affected as the exit liquid mass flow increases. Thus the calculation of exit reaction extent at $5.27MPa$ is entirely based on the gas composition data used, whereas the calculation for $16Mpa$, is almost independant of the data. If the composition data was erroneous the effect would be to vary the curvature of the experimental reaction extent pressure relationship whilst leaving the high pressure values unaffected. Whilst there is no reason to believe that the composition data is not at least reasonably correct, the consistency between shape of the the modelled and the experimental reaction extent pressure relationships suggests not only has the model successfully predicted the effect of pressure, but the method and data used for reaction extent calculations are essentially sound.

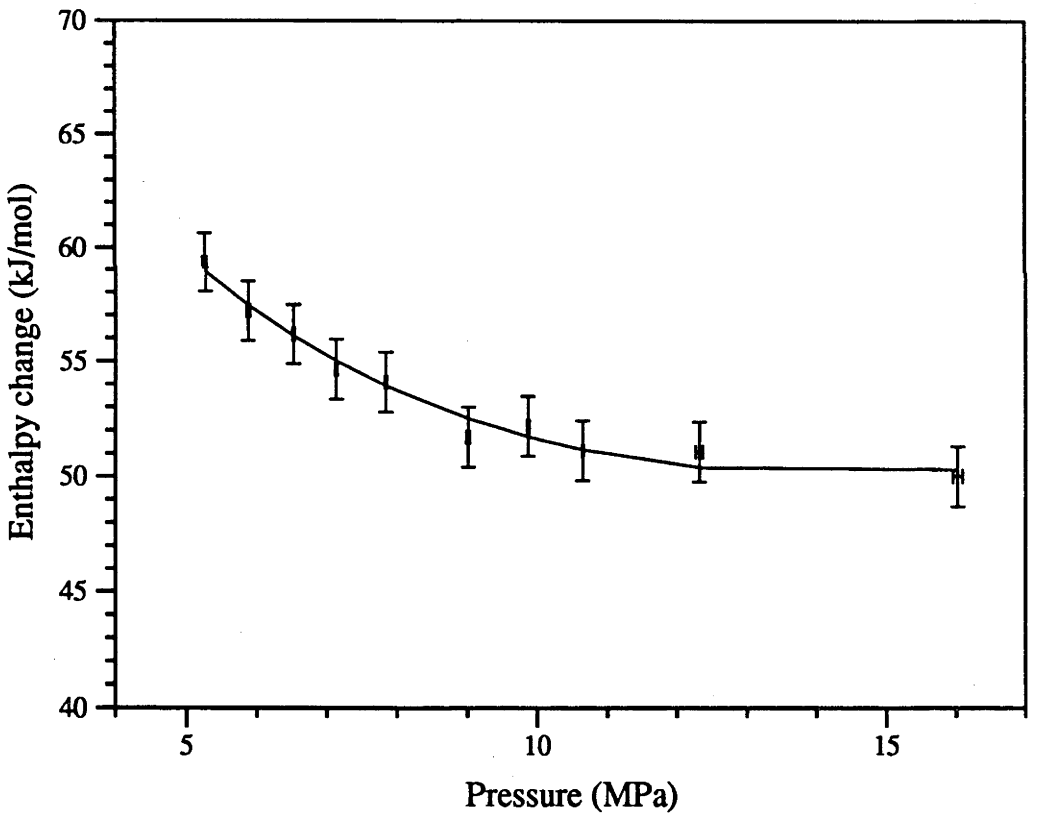

Figure 8.41: The effect of variation of pressure on the effective combined enthalpy change, for $0.23gs^{-1}$ and $650°C$ maximum temperature.

The inlet temperatures for the two reactor chambers demonstrated no resolvable variation with pressure. For modelling purposes the average values of $(211 \pm 5)°C$ for the first chamber, and $(546 \pm 10)°C$ for the second chamber were used. The empirical values for the effective combined enthalpy change reflect the observed variation in reaction extent, however since this variation is relatively small, the variation in enthalpy change values is

largely obscured by the variations introduced by the random variation in inlet and exit temperature values. To remove this random component, enthalpy changes were recalculated using the average values for inlet and exit temperatures. These recalculated effective enthalpy change values, together with the curve fit used for interpolation, are shown in figure 8.41.

The equation of the curve fit used is;

$$\Delta H = (107.2 + 3.998(MPa)^{-1} \times P - 30.22(MPa)^{-0.5} \times P^{0.5}) kJmol^{-1} \qquad (8.14)$$

this fit has a standard deviation of $0.447 kJmol^{-1}$.

Clearly the application of this empirical enthalpy variation to the model would produce qualitatively similar changes in the exit reaction extent to those measured, even if the behaviour of the reactor did not vary with pressure. However the model predictions indicate a variation in exit temperatures of only $\pm 3°C$, consistent with the apparently constant value indicated by the experimental measurements, and so indicating that the variation in reaction extent has indeed resulted from pressure related variations in the average extrinsic reaction rate.

8.8 Heat Exchanger Performance

Appendix D includes heat exchanger external temperature profiles for every steady state condition investigated. As well as this, the tabulated data presented for each condition includes hot end and cold end temperatures for the reactants in both the inlet and outlet passages of the heat exchanger. The cold end temperatures have been measured with thermocouple probes within the reactant streams. At the hot end the inlet passage temperatures have been measured with a similar internal thermocouple, while the exit passage temperatures have been deduced from measurements with an external thermocouple on the connecting tube between the end of the second reaction chamber and the heat exchanger.

The temperature profiles within the two passages of the heat exchanger, reflect the energy balance which is maintained at each point along the heat exchanger. If longitudinal conduction within the walls is neglected, this energy balance is affected by three factors; the specific heats of the two reactant streams, the inter-passage heat transfer coefficient and the magnitude of thermal losses from the outer passage through the insulation material. Given that the thermal losses could be quantified relatively easily, and the relationship between specific heat and temperature for reactant mixtures is known fairly well, the measurement of temperature profiles provides a means for determining inter-passage heat transfer coefficients for this heat exchanger design. The heat exchanger temperature measurements made in the course of this project, could provide a comprehensive empirical relationship between heat transfer coefficient and temperature, pressure, mass flow and exit reaction extent. To date, this analysis has not been performed, however it deserves a high priority in future work.

For an annular counterflow heat exchanger with the hotter fluid in the outer passage (and hence subject to thermal losses) the energy balance is given by;

$$\dot{m} C_{p_2} \frac{dT_2}{dx} = -hC(T_2 - T_1) - q_l C_{out} \qquad (8.15)$$

for the outer passage and;

$$\dot{m} C_{p_1} \frac{dT_1}{dx} = hC(T_2 - T_1) \qquad (8.16)$$

for the inner passage. h is an interpassage heat transfer coefficient which applies at a radial position where the heat transfer area per unit length is given by the 'circumference' constant C. q_l is the thermal loss heat flux from an outer surface of circumference C_{out}. The mass flow ($\dot{m}$) is the same in each passage. The specific heats (C_p) in this case have dimensions of energy/temperature/mass and they are functions of temperature pressure and composition. The inter-passage heat transfer coefficient will be a function of the mass flow plus the temperature, pressure and composition in both passages. The thermal loss will depend on the outer passage temperature alone. If all these quantities are known as functions of the various variables, the simultaneous solution of the two differential equations, using the cold end temperature of the inlet stream plus the hot end temperature of the outlet stream as boundary conditions, will yield theoretical temperature profiles for the two passages.

For the situation where the specific heats, the losses and the temperature profile of the outer passage are known, the temperature profile of the inner passage can be established by integrating equations 8.16 and 8.15 from a single known inner passage temperature, independently of the inter-passage heat transfer coefficient. The known and deduced temperature profiles can then be used to calculate an inter-passage heat transfer coefficient profile. Since the inner passage temperature has been measured at each end, the complete temperature profile could be calculated from both ends to check for consistency. The use of an average of the two profiles (with weighting factors based on the distance from one end) could yield more reliable results for the interpassage heat transfer coefficients.

Although a thorough analysis has not been completed it is possible to make some qualitative observations based on the recorded temperature profiles. Figure 8.42 shows external temperature profiles together with inlet and exit fluid temperatures for both passages, from a run with constant mass flow and pressure and a series of reactor setpoint temperatures. The profiles are qualitatively as would be expected given that the specific heat of the hotter exit reactant mixture is less than that of the colder incoming ammonia for temperatures above 50 to 100°C (ie above the dewline temperature), and greater than it for lower temperatures. Thus, after the first $300mm$, the slope of the hotter outlet passage profile is always greater than the slope of the inner passage profile, while prior to this the opposite is true. In the limit of perfect heat transfer, all the heat transfer and change in temperature would occur at the extreme ends of the heat exchanger, thus the extent to which the profile slopes steepen at the end, is an indication of the overall thermal resistance of the heat exchanger.

Increasing the reactor setpoint temperatures has the effect of increasing the hot end temperature of the exit passage in line with the increase in the exit temperature of the reactor. The cold end temperatures of the exit passage, however, decrease as the reactor temperature increases. The exit reaction extent is increased by increasing the reactor temperature, so this result appears to be a direct qualitative vindication of the calculation of energy storage efficiency presented by Williams & Carden (1979*c*), which indicated that the energy surplus in the exit reactant stream leaving such a heat exchanger, would decrease with increasing reaction extent. This is a consequence of the fact that increasing the reaction extent lowers the dewline temperature and so reduces the temperature interval over which the exit reactants have a higher specific heat than the ingoing ammonia.

The effect of the variation of mass flow is shown in figure 8.43. The hot end temperature of the exit reactant passage increases with flowrate in line with the increase in reactor exit temperatures associated with higher power levels and the proportionate reduction in the significance of thermal losses. At the cold end, low flow rates are associated with low exit passage temperatures. This results from the combination of high reaction extents reducing

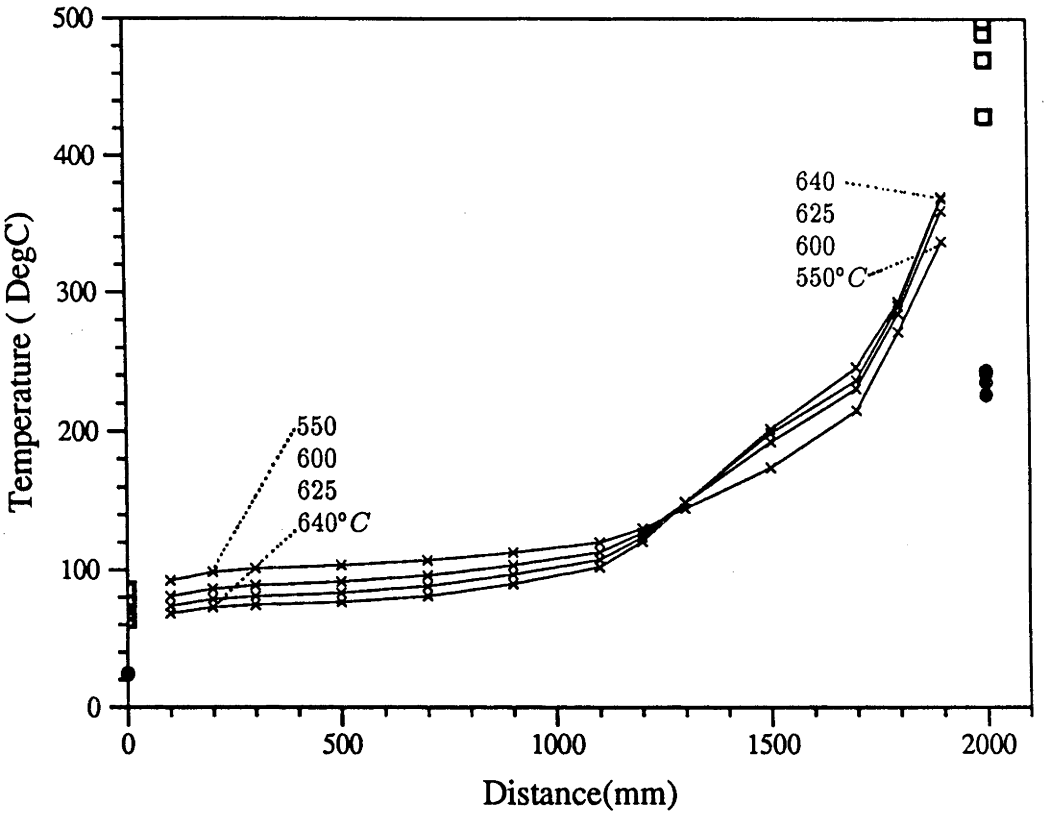

Figure 8.42: The effect of reactor setpoint temperature on heat exchanger temperatures. Outer passage (exit passage) external temperatures (×), outer passage extreme end fluid temperatures (□) and inner passage extreme end fluid temperatures (o) from the 21st of November 1990.

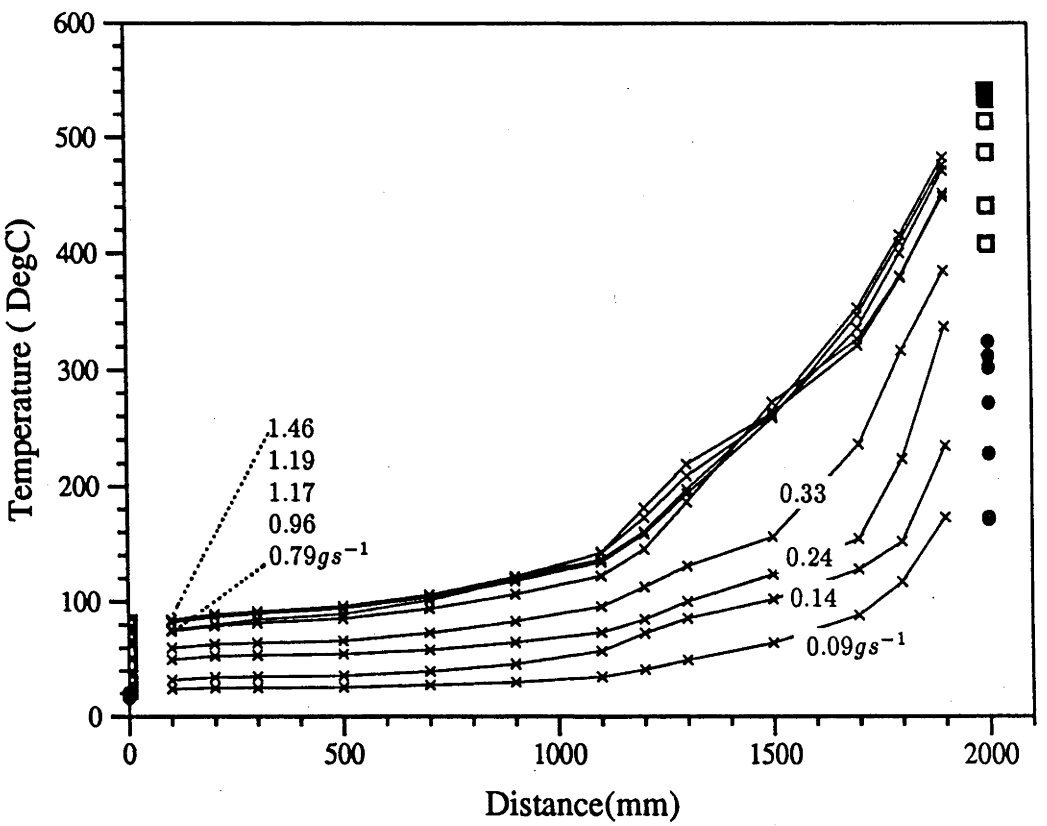

Figure 8.43: The effect of mass flow rate on heat exchanger temperatures. Outer passage (exit passage) external temperatures (×), outer passage extreme end fluid temperatures (□) and inner passage extreme end fluid temperatures (o) from the 16th and 18th of April 1991.

the specific heat mismatch, low hot end temperatures and the increased significance of thermal losses from the heat exchanger. Above $0.7gs^{-1}$, the profiles vary very little. This appears to indicate that the factors mentioned become less sensitive to mass flow as it is increased. The improvement in the heat transfer coefficient associated with higher Reynolds numbers, would also tend to cancel the effect of the other factors.

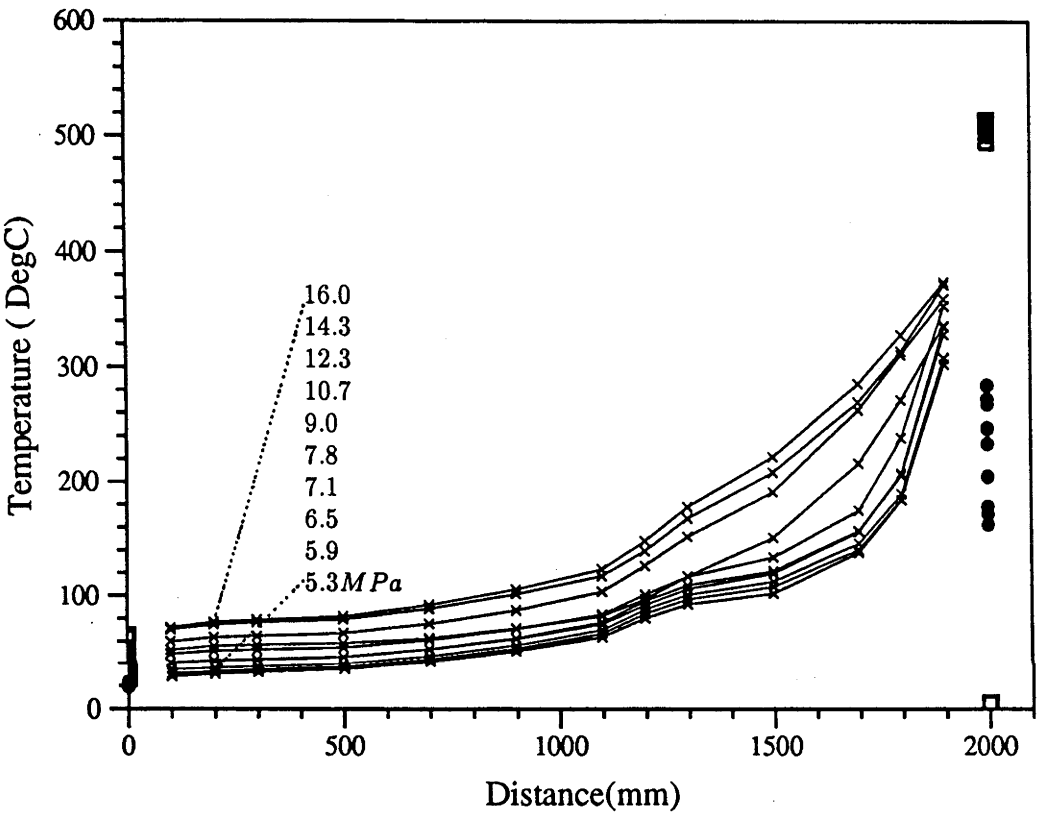

Figure 8.44: The effect of pressure on heat exchanger temperatures. Outer passage (exit passage) external temperatures (×), outer passage extreme end fluid temperatures (□) and inner passage extreme end fluid temperatures (o) from the 8th and 10th of April 1991.

Figure 8.44 illustrates the effect of pressure variation. In this case hot end exit passage temperatures remain essentially constant, reaction extents are known to vary over a relatively small range and thus the behaviour is a direct indication of the dependence of the heat transfer coefficient on pressure. It can be seen that the heat transfer coefficient must increase strongly with a decrease in pressure; cold end temperatures are reduced and an increased proportion of the overall temperature change occurs at the high temperature end of the heat exchanger. This trend presumably reflects the effect of the increased gas velocity required to maintain the same mass flow at reduced pressures.

8.9 Solar Flux Simulation

In early considerations on ammonia dissociation in receivers of parabolic dishes Williams & Carden (1979*a*) suggested that it would be possible to successfully operate receiver/reactors

with a constant ammonia flowrate. If a mass flow is chosen so as to keep temperatures within design limits under conditions of maximum expected solar flux, then the system will operate under lower flux levels, at a lower temperature and hence with a lower exit reaction extent. However the consequence of this approach is that energy storage efficiencies may be lower than desirable for a considerable fraction of the time. The motivation for suggesting constant mass flow operation stemmed from the relatively small $10m^2$ dish modules proposed at that time, with the associated need to keep the components needed for individual dish units simple and cheap. Currently proposed dish modules have apertures of $400m^2$, this larger size can justify the development of more sophisticated control systems. The most obvious alternative is to vary the ammonia flow rate in a manner which adjusts the receiver/reactor operating conditions in a way which continuously optimises the efficiency of the endothermic half of the system.

In order to test the plausibility of this approach to reactor control, a number of tests were carried out with the heater power level varied in a manner which simulated a diurnal variation of solar flux, whilst the reactor temperature was controlled by variation of the ammonia flowrate.

Automated flow rate control was achieved by replacing the flow metering valve by a similar unit to which an electric motor drive and a variable inductance displacement transducer to measure the valve position, had been fitted. The balance of the control system comprised a Eurotherm 808 temperature controller, with a $0 - 10V$ dc output module, whose signal acted as the setpoint for a proportional control circuit which varied the drive motor supply voltage in order to determine the valve position.

Heater power was controlled using a single Eurotherm 808 controller for both heaters. This controller was programmed for; a linear millivolt input signal, direct (rather than 'reverse') output and derivative and integral components of the transfer function where turned off. This produced heater power levels proportional to a low voltage input signal. To produce a simulation of a diurnal flux profile, the controller was driven by a single half sine wave from a waveform synthesiser. A flat topped flux profile typical of a real daily solar flux cycle was produced by increasing the period of the sinewave whilst the power level was above approximately 80% of its maximum value. Short duration transients typical of intermittent cloud were produced by temporarily removing the signal.

Some unsuccessful attempts were made to use the self tuning facility on the temperature controller governing the flow rate, to determine the parameters for its 'PID' control function, however given that the primary aim was not to keep the control temperature exactly at the setpoint value, this was not pursued. Instead proportional only control was used, with a relatively wide proportional band chosen to achieve a progressive increase and decrease in flow rate at the ends of the cycle.

The effective 'gain' of the whole control system depends not only on the proportional band of the temperature controller, but also on the pressure drop across the valve (via its effect on the aperture/flow rate relationship) and on the relationship between temperature and flowrate for the particular position monitored on the reactor. After initial testing a pressure drop across the valve of $690kPa$ was used. This is approximately 1/3 of that used for the steady state runs and it allowed the valve to operate over a greater position range and hence reduced the effect of errors in the position control.

The metering valve requires 10 turns to take it from fully open to fully closed. The needle is mounted telescopically within the end of the stem, with a spring loaded action so that a further 5 turns from fully closed are possible, with the needle maintaining a constant pressure on its seat. The position transducer was adjusted to read just greater than $0V$ at the fully closed position, the corresponding reading at fully open was $9V$.

Although the arrangement did successfully demonstrate the feasibility of reactor temperature control by flow rate variation, it was apparent that the in-house constructed motorised valve system was not suitable for long term operation. The valve itself was not designed for this sort of application and consequently its teflon stem packing deteriorated with the frequent rotation. The 'grub screw' couplings between motor and valve also required frequent re-tightening.

Figure 8.45 shows the results of the final successful simulation of a complete 'abbreviated' diurnal cycle. The heater power was taken through a compound sinusoid half period of just over 2 hours duration, with a peak value of 23.7%. Some short duration transients were superimposed approximately 2/3 through the cycle. The controlled temperature (highlighted in figure 8.45) was that measured by the external thermocouple $707mm$ from the beginning of the first reaction chamber. A setpoint of $710°C$ with a proportional band of $150°C$ was used.

At the beginning of the cycle, reactor temperatures rose under no flow conditions until the controlled temperature reached $560°C$ (the edge of the proportional band). At this point the valve began to open and reactants began to flow. After an initial overshoot, the valve position, inlet mass flow and controlled temperature reached relatively steady values. The steady valve position signal of $1.7V$ corresponds to an opening of only 14%. Ideally the valve should be fully open at the maximum expected power, resulting in a controlled temperature much closer to the nominal setpoint. The pressure control system however could not reliably maintain smaller pressure differences across the valve, a valve with a smaller orifice area would solve the problem.

It is apparent that this non-optimised control system has successfully limited the magnitude of the temperature variations resulting from both transient power fluctuations and the overall cyclic variation. The measured inlet and exit ammonia liquid flow rates indicate that the reaction extent remained relatively constant at approximately 0.4.

A notable feature of the run is that the first 25% of the energy supplied by the heater is used to heat up the reactor and is ultimately lost after reactant flow has stopped at the end of the cycle. In a true diurnal cycle of approximately 10 hours duration such a loss would be reduced to slightly less than 10% of the total energy absorbed. A loss of this magnitude is worth addressing in consideration of reactor design and control strategy. Reducing the mass of the reactor for a given thermal capacity would improve the situation, the apparent poor performance in this demonstration is largely a consequence of the choice of a maximum power level only 25% of that possible.

The possibility of improving the overall performance through the choice of control strategy introduces a new class of optimisation problems worth studying. While the operating conditions of a receiver reactor could be optimised on the assumption of steady state conditions, the actual goal should be a performance which is maximised when integrated over the period of the cycle. This problem could be addressed retrospectively for a known diurnal cycle of solar flux. Ultimately a control strategy, which makes use of statistical information to choose a series of operating conditions with the highest probability of producing the best performance during the course of a cycle of unknown characteristics, would be desirable.

8.10 Conclusions

The experimental investigation of the behaviour of the ammonia dissociator, has shown the experimental arrangement, the instrumentation and the analysis techniques used, all to be successful. The results obtained have provided a considerable amount of quantitative

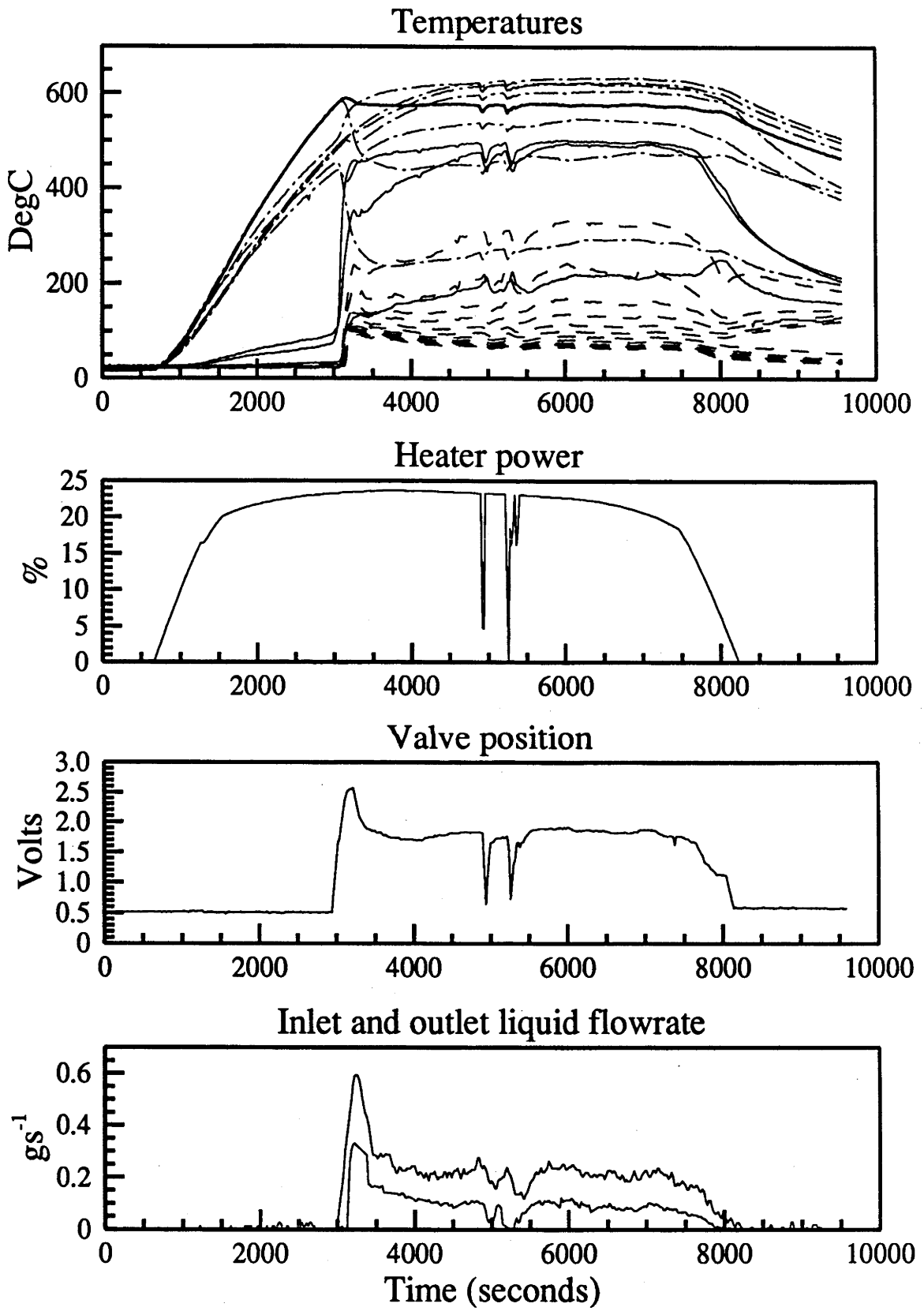

Figure 8.45: Simulation of an abbreviated diurnal solar flux variation, with flow rate control of reactor temperatures on the 5th of April 1991. The temperature curves show the reactor external temperatures (– · –)(the controlled external temperature is the thicker solid trace), internal and connecting tube temperatures (—), and heat exchanger temperatures (- - -).

information on steady state behaviour and qualitative information on the nature of both steady state and transient behaviour.

The work done by the author on the Fortran implemented numerical reactor model of Richardson et al. (1988) involved the generalization of the geometry, the reaction system, the wall boundary conditions and improvements in the algorithm. The 'model' itself, as embodied in the physical assumptions made and the choice of empirical correlations for the calculation of effective conductivity, effective diffusivity and other properties has not been changed. This model performed well in comparison with the experimental results for steam reforming of methane of Richardson et al. (1988). With the input of the appropriate thermodynamic properties for the ammonia system reactants and parameters for the catalyst particles in the dissociator, a simple adjustment of the pre-exponential factor for the intrinsic rate was all that was required to reproduce the experimentally observed effects of the variation of temperature, pressure and flow rate. This degree of success suggests that the model could now be used with reasonable confidence for simulation of reactor configurations and operating conditions outside the range covered by these experiments.

The success of the model is all the more remarkable considering that the ratio of catalyst particle diameter to reactor diameter is considerably larger than is usual for the application of a pseudo-homogeneous model. It should be noted that the model is inherently semi-empirical and that the adjustment of the pre-exponential factor is acting as a calibration of the whole model. Thus it would not be appropriate to use the derived pre-exponential factor outside the model as other than a rough indication of its true magnitude.

For the purposes of a closed loop energy transfer demonstration, it is apparent from the experimental results obtained, that operation at a nominal power level of $1kW$ is possible using the present catalyst. This could be achieved with an inlet flowrate of $0.41gs^{-1}$, and with setpoint temperatures at $725°C$ to give an exit reaction extent of 0.75. This performance would not be significantly affected by variation of the pressure between 10 and $30Mpa$.

It is apparent from the experimental results obtained so far, that there remain some unexplained systematic effects. These could include; a long term loss in catalyst activity, physical influences on the experimental system which cause day to day variations in the performance or influences on the technique for measurement of reaction extent which cause apparent variations in performance. Although further experiments would certainly shed light on these possibilities, they would not affect the conclusions that have been made about the success of the model and the capacity of the reactor. This being so, the returns for continuing dissociation experiments with the same catalyst material would be small. The immediate priorities for further work would more profitably include investigation of other catalyst materials and the commissioning of the reactor described in chapter 9.

The amount of effort required for analysis and modelling of this reactor configuration together with the somewhat inconclusive nature of the analysis of the energy balance has highlighted the shortcomings of the design for quantitative experiments. These shortcomings, namely the use of two separate reactor chambers and the high thermal losses through the uninsulated ends, were anticipated at the beginning of the project. It should be noted that the design was originally conceived primarily for the purposes of a closed loop demonstration, and these experiments have confirmed its suitability for that purpose. These issues were instrumental in the development of the new synthesis reactor design presented in chapter 9.

The steady state experiments conducted, have also demonstrated the success of the counterflow heat exchanger design. With further analysis, the measurements taken of heat

exchanger temperatures could give the general heat transfer coefficient data needed for the design of similar units for different mass flow ranges.

Finally, the operation of the ammonia dissociator under conditions which simulated typical solar flux input, has confirmed the feasibility of a control system based on the variation of the ammonia flow rate. This test has also helped in identifying some of the issues that must be addressed in developing an optimised control strategy for receiver-reactors.

Chapter 9

Synthesis Reactor Design

9.1 Introduction

As part of the previous NERDDC funded closed loop demonstration, a synthesis reactor was constructed and reached the stage of preliminary testing. The design (Williams 1980*c*) was similar in concept to the dissociation reactor, in that it involved a cylindrical catalyst chamber, constructed from high strength nickel alloy tubing (Inconel 601) which was maintained at high temperature and pressure over most of its length, but with the end regions kept close to ambient temperature. One end consisted of a flange with a bolted endplate, through which passed reactant inlet and outlet passages plus passages for heat extraction. The stresses associated with the thermal gradients and pressures on the reactor ends were analysed in considerable detail (Carden 1982*b*). In the reappraisal of the project which followed the end of NERDDC funding and the storage vessel accident (Carden 1982*c*) it was decided that this approach to reactor construction was potentially too dangerous in view of the higher volume needed for the synthesis reactor.

The alternative chosen (Carden 1984*b*) was to use a larger pressure vessel, but to operate it at ambient temperature, with internal insulation between the vessel walls and the hot reactor. A vessel design was finalised and construction largely completed prior to the start of this project.

In developing an initial reactor design to test the cold walled vessel concept, priority was given to the simplicity and ease of construction and the ease of experimental measurement and analysis. The problems encountered with the analysis of the dissociator experiments were mainly associated with the twin catalyst chamber construction and the high thermal losses in the end regions. These problems were anticipated at the beginning of this project and in developing the synthesiser design, effort was made to avoid them.

The design developed consists of a simple tubular reactor with a number of electrical heaters (constructed in a similar fashion to those of the dissociator), acting as thermal shields. For the heaters to work as thermal shields, the thermal losses from the reactor to the buffer gas within the pressure vessel, must exceed the output of the exothermic reaction. The deficit is then made up by the heaters, which are used to control the reactor external temperatures. The heat absorbed by the buffer gas must be extracted from the vessel. This is done using a water cooled jacket which completely surrounds the reactor. Insulation material fills the void between the cooling jacket and the vessel walls.

For simplicity of construction, no counterflow heat exchanger has been incorporated in the initial design. Instead, a reactant preheat section, consisting of a heated spiral passage, has been incorporated at the beginning of the reactor. Exit reactants will leave the pressure vessel at high temperature to be cooled with a simple gas/water heat exchanger consisting

of a coil of pipe in a cold bath.

The cooling jacket also serves as a calorimeter, providing a simple and accurate method of measuring the combined heat output of the heaters and reactor. The use of a number of individually controlled thermal shield heaters allows a predetermined external temperature profile to be maintained irrespective of the conditions within the reactor. The flux profile of the reactor can be determined in a simple manner by taking the difference of heater flux profiles required to produce the same temperature profile under reaction and no flow conditions. The difficulty with the determination of inlet and exit reactant temperatures encountered with the dissociator, is avoided by having thermocouples placed in the reactant stream at each end of the catalyst bed.

9.2 Pressure Vessel

The pressure vessel is a cylindrical unit with two identical removeable end plates. The internal volume is $1000mm$ long and $300mm$ diameter. Overall the vessel is $1520mm$ long and its outside diameter is $416mm$. The two $314mm$ diameter $90mm$ thick endplates are fitted with O-ring plus backup ring seals and slide into a smooth section of the vessel of slightly greater inside diameter than the main internal region. The endplates are retained at the shoulder at the inner end of this section by $250mm$ i.d. annular collars which are screwed into the ends of the vessel. Both endplates have a series of holes to accommodate various feedthroughs. Twelve $16mm$ diameter holes are distributed at a radius of $102mm$ from the centre, in addition there is a $5mm$ diameter hole at the centre of each endplate. Unused holes are blocked with bolts and copper washers.

The vessel was designed for a working pressure of $33.4MPa$ for temperatures between 10 and $100°C$. For safe operation it has been fitted with a relief valve set at $29.8MPa$. Following a hydrostatic test to $50MPa$ the vessel has been certified by the Australian Capital Territory boiler inspector for operation at the designed working pressure.

For experimental operation, the experience with the dissociator has confirmed that it is frequently necessary to work on the outside of the reactor, either to check or modify thermocouples, heaters or pipe fittings. It is clearly an advantage if this can be done without disturbing reactant or electrical connections. To achieve this, it was decided to fix the reactor and all the associated feedthroughs to one of the two endplates and to mount this endplate rigidly within the laboratory. Access is then gained to the reactor by removing the vessel from the fixed endplate.

Initially, in view of the approximately $700kg$ mass of the vessel, it was planned to mount the reactor horizontally and place the vessel on a movable trolley. However the horizontal operation of a packed bed reactor can result in uneven 'channelling' of the reactant stream as a consequence of the catalyst settling[1]. Thus the mechanically more demanding approach of removing the vessel by lifting it vertically, was pursued.

The task of the lifting and replacing the vessel is made more exacting by the need to maintain alignment with the fixed endplate. This alignment must be maintained within approximately $\pm 0.5mm$ in order to avoid knocking the endplate O-ring from its groove. The solution adopted consists of a hoist based on two $100mm \times 100mm$ square section tubular steel columns guiding a trolley which carries the vessel and is lifted by a hydraulic ram[2]. The vessel is shown in its fully lifted position on the hoist in figure 9.1.

[1]This was pointed out by Professor J.T.Richardson during the author's 1988 visit to the University of Houston.

[2]The pressure vessel hoist was designed and constructed by Bob Whelan of the ANU Energy Research Centre.

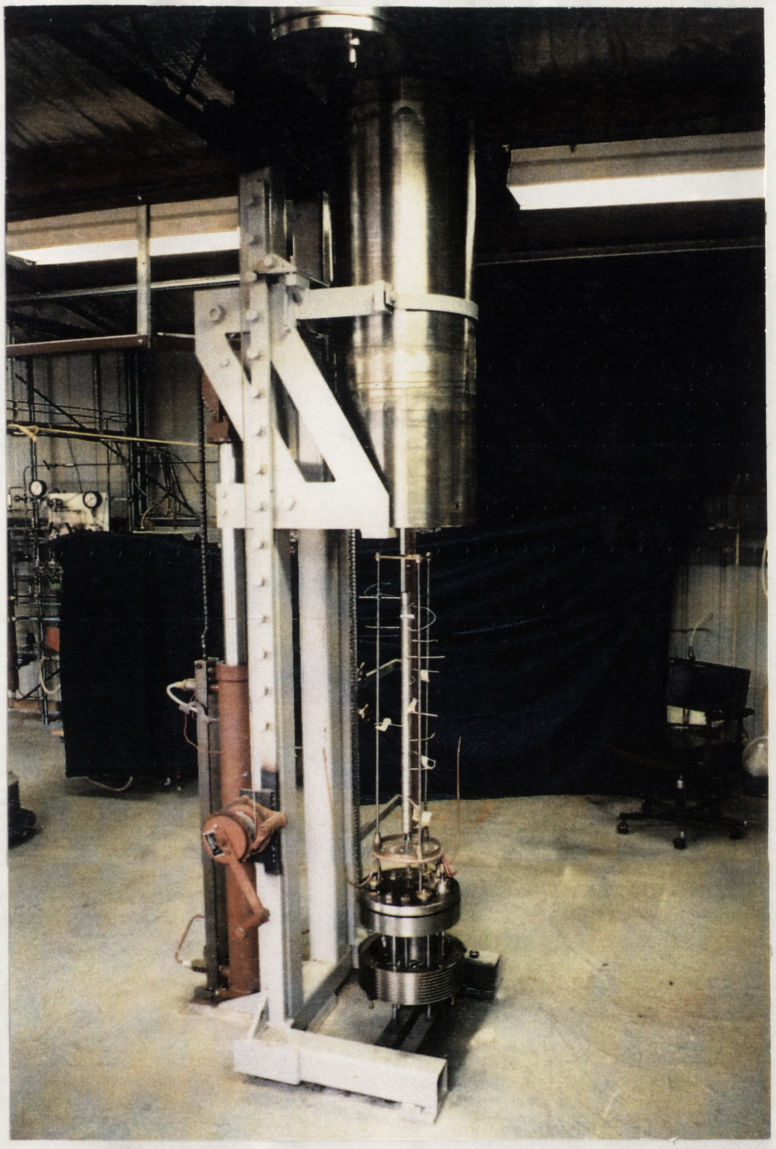

Figure 9.1: View of the synthesiser pressure vessel fully lifted on the hydraulic hoist, with the reactor mounted on the fixed endplate.

9.3 Reactor

The reactor prototype is based on a section of $25.2mm$ o.d. $1.6mm$ wall thickness stainless steel tubing. The length of this cylinder is less than the $1000mm$ internal length of the pressure vessel by an amount that allows for the vessel insulation and end connections. The construction details are shown in figure 9.2.

Values for average reaction rates achieved with promoted iron synthesis catalysts were taken from Vancini (1971), Weale (1967) and Imperial Chemical Industries (1970). These gave a mean result of $39mol\ m^{-3}s^{-1}$, at 300 atmospheres, $450°C$ and $\delta = 0.8$, with a variation of $\pm 20mol\ m^{-3}s^{-1}$. Based on relative reaction rates calculated from the Temkin

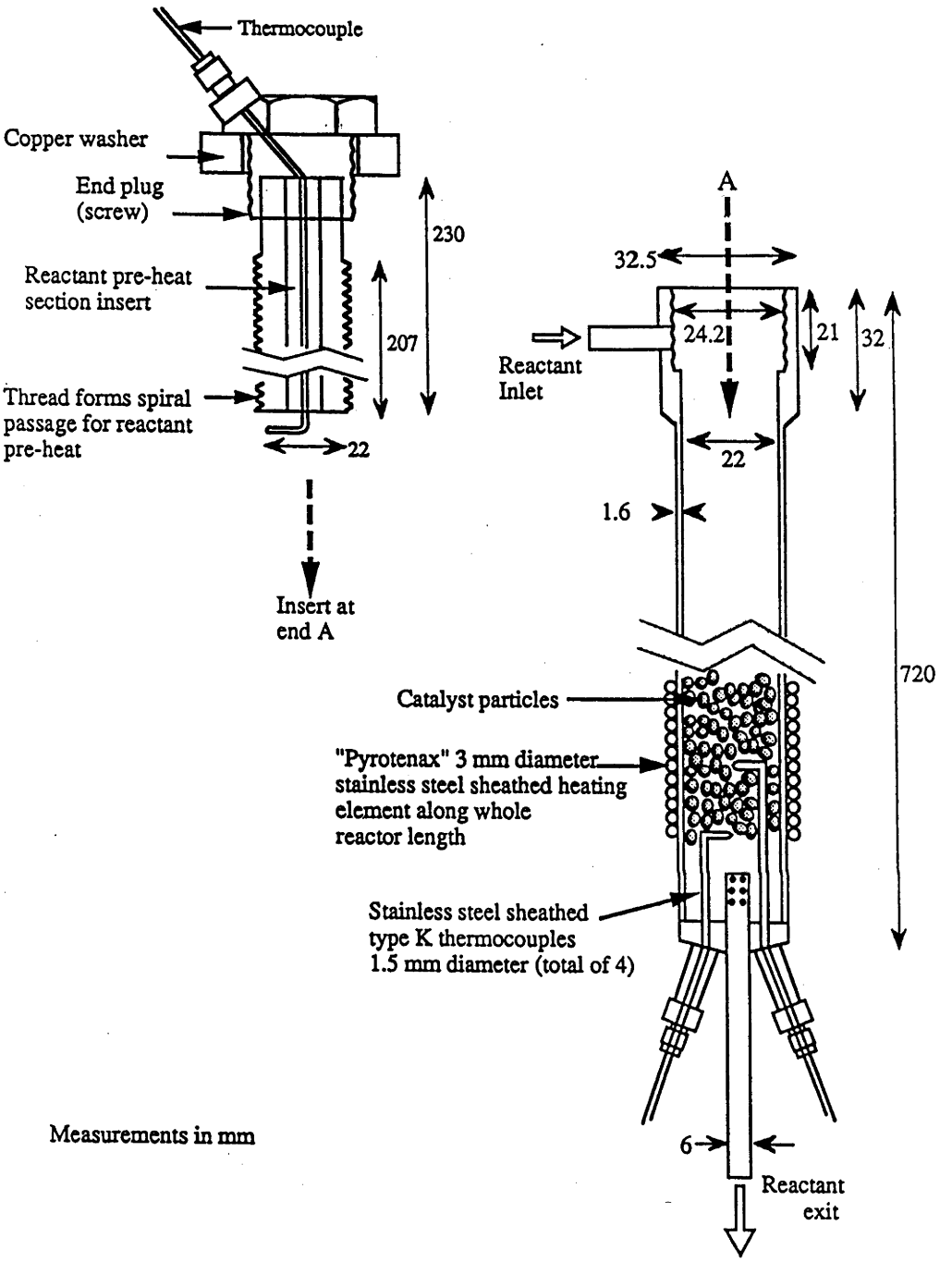

Figure 9.2: Construction details of the prototype synthesis reactor.

Pyzhev intrinsic rate equation, this suggests an average reaction rate of $25mol\ m^{-3}s^{-1}$ for a maximum rate reaction path between $\delta = 0.8$ and $\delta = 0.6$. Thus with a $333cm^3$ reactor volume and an enthalpy of reaction of $56.85kJmol^{-1}$, a power level of $473W$ is expected, with the variation in reaction rate values suggesting an uncertainty in the power level expected, of $\pm 250W$. Operation at this power level with the specified reaction extent change implies a flow rate of $0.708gs^{-1}$ ($0.042mol\ s^{-1}$ ammonia equivalent).

If the heating elements surrounding the outside of the reactor are to be capable of reproducing the external temperature profile under a no reaction situation, then their

maximum power output must be at least equal to the maximum reaction power level expected. For controllability it is also necessary that the heat losses from the outside of the reactor will be great enough that some level of electrical heating will also be required during reaction.

Eight thermal shield heaters wound from "Pyrotenax" 32.S.10000 stainless steel sheathed mineral insulated heating cable, are used. This cable has an outside diameter of $3.2mm$, the combined length of the tightly wound elements along the entire length of the reactor is $17.7m$. Given the maximum specific power level suggested for the heating cable of $110wm^{-1}$ (Pyrotenax Australia Pty Ltd 1988), this results in a maximum total heater power level of $1.94kW$, which should be adequately in excess of the maximum reactor power expected.

The heat loss from the reactor depends on heat transfer between the reactor tube and the catalyst bed, plus the heat transfer between the outer surface and the cooling jacket of the pressure vessel. The heat transfer processes within the reactor should not differ greatly from those experienced with the dissociator. The highest flux levels will occur near the reactor inlet, a reaction rate of $40mol\ m^{-3}s^{-1}$ in this region corresponds to a flux level of $2.3 \times 10^4 Wm^{-2}$. The numerical reactor model was used for examination of radial temperature distributions[3] Modelling a short $22mm$ diameter reactor section with a $0.71gs^{-1}$ mass flow, a reaction extent of 0.8 and a temperature of approximately $800K$ suggested an effective bed conductivity of $2.5Wm^{-1}K^{-1}$ and an overall wall heat transfer coefficient of $9.0Wm^{-2}K^{-1}$, this produced a temperature drop across the bed of $42K$ and across the wall of $26K$. It would appear that rate of heat transfer from the reactor through the walls will be sufficient to remove the exothermic reaction heat expected. If this proves not to be the case, then chemical equilibrium conditions would limit internal temperatures to less than approximately $577°C$.

Heat transfer between the outside of the reactor and the cooling jacket will be a combination of convection and radiation, with radiation becoming more significant at higher temperatures. The radiation contribution to the thermal loss (Q_r) can be calculated from;

$$Q_r = \sigma A_{react}(\varepsilon_2 T_2^4 - \varepsilon_1 T_1^4) \tag{9.1}$$

where σ is the Stephan-Boltzmann constant, A_{react} the exposed surface area of the heater elements and ε_1 and ε_2 are the emissivities of the cooling jacket and the heater element surface (0.78 for copper and 0.6 for stainless steel at high temperature). An average reactor temperature of $T_2 = 400°C$ and an average cooling jacket temperature of $T_1 = 40°C$ gives thermal losses of $Q = 595W$. Considering that convection losses will be added to this it seems there will be sufficient heat loss to keep reactor temperatures under control. It is anticipated that either insulation or cooling fins might be added to the outside of the reactor on an ad hoc basis to adjust any discrepancies in heat transfer.

The boundaries between heating elements represent points of discontinuity in the heater flux profile. Longitudinal heat conduction in the tube wall will have the effect of smoothing possible flux and temperature discontinuities. To estimate the degree of smoothing expected, the simplified case of an infinite heat conducting element divided into two sections of different heating flux level and with thermal losses assumed to be linearly proportional to the temperature difference with the surroundings, has been con-

[3]The determination of effective heat transfer parameters and temperature drops is largely independant of the reaction rate so parameters for the dissociator catalyst were used.

sidered. The temperature distribution will satisfy the longitudinal heat transfer equation;

$$\frac{d^2T}{dz^2} = \frac{C_1}{C_0}(T - T_0) - \frac{q_h}{C_0} \tag{9.2}$$

where q_h is the heater flux, C_0 is the product of cross section area and conductivity of the bar and C_1 is the product of an effective heat transfer coefficient and the circumference. The boundary conditions are;

$$\begin{aligned} q_h &= q_1 \text{ for } z \leq 0 \\ q_h &= q_2 \text{ for } z \geq 0 \end{aligned} \tag{9.3}$$

The solution is;

$$\begin{aligned} T &= \frac{(q_2 - q_1)}{2C_1} \exp\left(\sqrt{\frac{C_1}{C_0}}z\right) + \frac{q_1}{C_1} + T_0, \qquad z \leq 0 \\ T &= \frac{(q_1 - q_2)}{2C_1} \exp\left(-\sqrt{\frac{C_1}{C_0}}z\right) + \frac{q_2}{C_1} + T_0, \qquad z \geq 0 \end{aligned} \tag{9.4}$$

This result is plotted in figure 9.3 using a conductivity of $78 W m^{-1} K^{-1}$ for the steel, $q_1 = 1532 W m^{-2}$, $q_2 = 1332 W m^{-2}$ and $C_1 = 4 W m^{-1} K^{-1}$ (chosen to give temperatures at $z = \pm\infty$ of 450 and $500°C$), for three thicknesses of tubing.

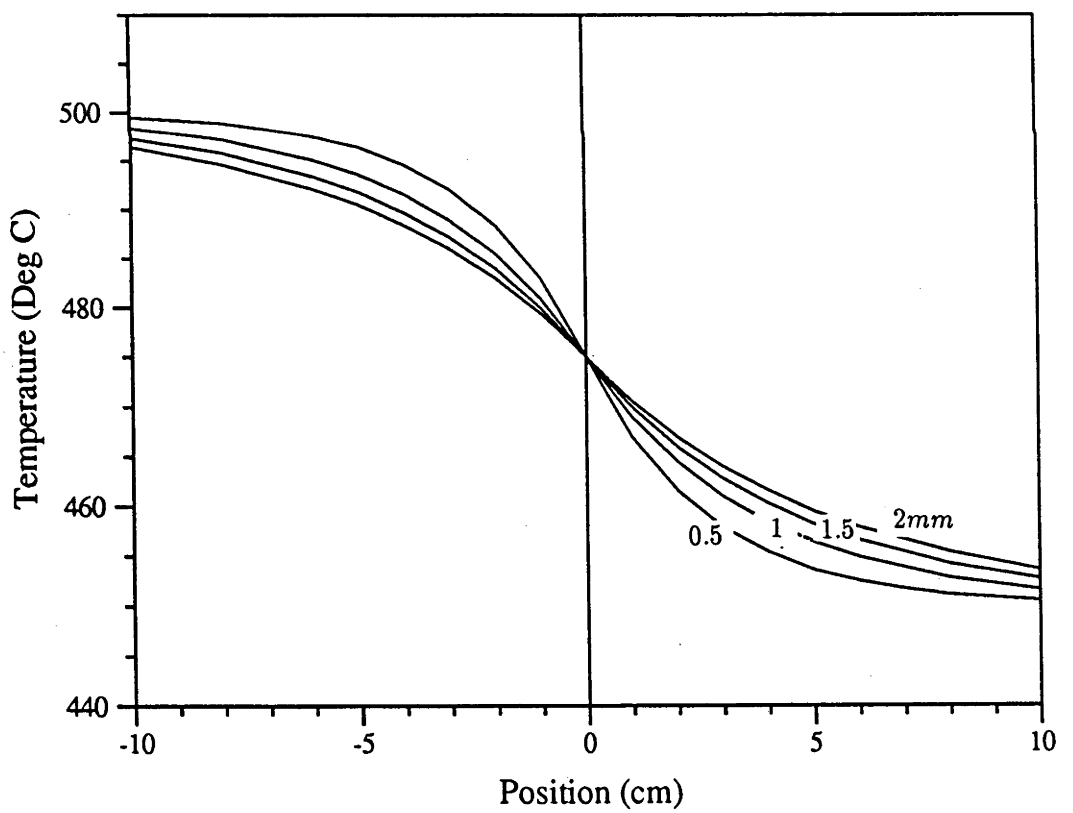

Figure 9.3: Temperature profiles resulting from a discontinuity in heater power levels, in $2.2cm$ diameter stainless steel tubes of various thicknesses.

The eight separate heating elements are wound according to figure 9.4, with each element divided into three sections, a middle section of closely packed windings and two

end sections in which it is wound interspersed with its neighbours. The elements at the ends of the reactor have only one neighbour and hence are only divided into two sections. The result is that the reactor is divided into thirteen $40mm$ long sections of constant heater power level (plus a $65mm$ section at each end). As indicated by figure 9.3, a $40mm$ section centred on a heater power level discontinuity will have very close to a linear temperature profile even for a $0.5mm$ tube wall thickness. Thus the wall temperature profile produced by the thermal shield heaters should be a smooth fit to the element centre point temperatures.

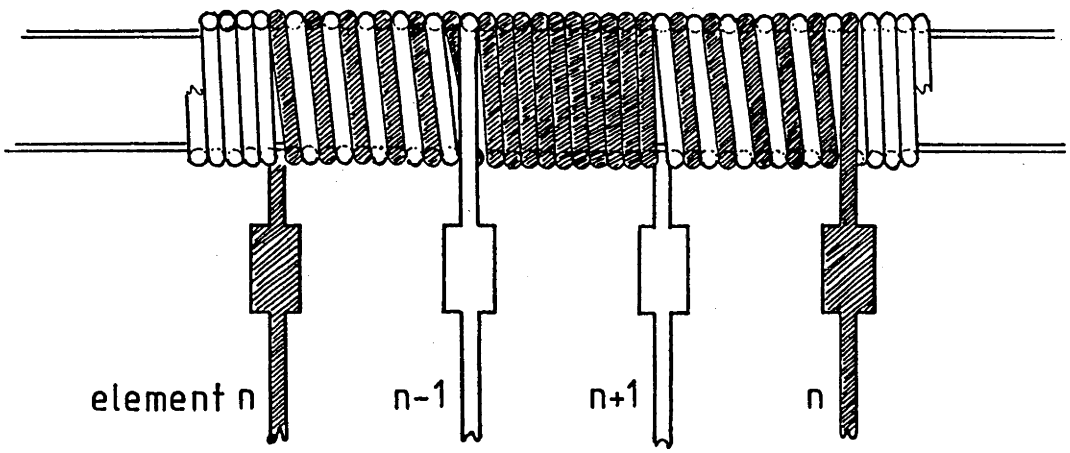

Figure 9.4: Heating element construction details.

The spiral reactant preheat passage at the beginning of the reactor is formed by a $3mm$ deep triangular profile thread cut in a stainless steel plug which fits inside the reactor tube. It forms a $2.9m$ long path which will have an essentially isothermal wall temperature. Assuming a constant value for the heat transfer coefficient, the rate of increase in reactant temperature with position in the passage will be proportional to the temperature at each point, ie;

$$\dot{m}C_p\frac{dT}{dz} = ha(T_{wall} - T) \tag{9.5}$$

where $\dot{m}$ is the mass flow in the passage, a is the surface area per unit length and h is the heat transfer coefficient. If the inlet temperature is T_0, the solution is;

$$T = T_{wall} - (T_{wall} - T_0)exp\left(\frac{-haz}{C_p\dot{m}}\right). \tag{9.6}$$

A mass flow of $0.708gs^{-1}$ gives a Reynolds number of 1.7×10^8, indicating turbulent flow. The usual expression for heat transfer coefficient in turbulent pipe flow is (Ozisik 1985);

$$\frac{hd}{K} = 0.023N_{RE}^{0.8}N_{PR}^{0.4} \tag{9.7}$$

where N_{RE} and N_{PR} are the Reynolds and Prandtl numbers and K is the fluid conductivity. This expression should give a reasonable estimate of the behaviour within the triangular

passage. It can be rearranged to give;

$$h = 0.0279\dot{m}^{0.8}d^{-1.8}C_pN_{PR}^{-0.6}\mu^{0.2} \tag{9.8}$$

where μ is the viscosity. Williams (1978*b*) presents data for μ and $C_pN_{PR}^{-0.6}$, values for an average temperature of $450K$ and a reaction extent of 0.8, with $d = 3mm$ give $h = 161.23Wm^{-2}K^{-1}$. Thus for a mass flow of $0.708gs^{-1}$ with $C_p = 3.45 \times 10^3 Jkg^{-1}K^{-1}$, inlet reactants can be expected to increase in temperature from $25°C$ to $500°C$ within the $2.9m$ passage, if the walls are maintained at $600°C$.

The hot reaction products leaving the reactor will flow straight out of one of the gas feedthroughs. They could subsequently be cooled using a coil of tubing of approximately the same passage length as the preheater, immersed in a cold water bath.

9.4 Cooling Jacket

The cooling jacket is to serve the dual purposes of keeping the pressure vessel cool and providing a measurement of the total heat output within the vessel. The design was arrived at by trading off the following conflicting requirements:

- minimising the fraction of the internal volume of the vessel filled with insulation material;
- minimising the difference between pressure vessel and room temperatures;
- producing a temperature in the water large enough for accurate calorimetry measurements.

The jacket has been made in two parts, the main part, comprised of a copper cylinder with a single closed end, is intended to remain inside the pressure vessel when it is raised and lowered. The other part comprising the other end of the cylinder, is mounted on the fixed pressure vessel endplate and the two parts fit together when the vessel is lowered onto the fixed endplate. The jacket is constructed from $2mm$ thick copper sheet, it is $215mm$ diameter and $800mm$ long, this allows for $42.5mm$ of insulation material between it and the pressure vessel wall ($96mm$ at the ends). Both parts of the jacket have coils of $6.3mm$ o.d. $4.0mm$ i.d. copper tubing attached to carry cooling water. The cooling water is provided to the two parts separately via feedthroughs in the top pressure vessel endplate, for the main cylinder, and the bottom fixed endplate for the cylinder bottom end. The unit is shown separate from the pressure vessel in figure 9.5.

The heat generated by the combination of the reactor and the heating elements could be up to $2kW$. A temperature change between ingoing and outgoing cooling water of $10K$ has been chosen as the minimum required for calorimetric measurements. This dictates a flow rate of $3l\ min^{-1}$ at a $2kW$ total power level. The cooling coils are spaced $30mm$ apart, the resulting $19m$ has been divided into 2 parallel circuits of $9.5m$ each, in order to reduce the pressure drop. This gives a Reynolds number of 7.84×10^3, which lies within the laminar flow range.

The pressure loss is given by Darcie's equation (Vennard 1961);

$$\Delta P = \frac{F\rho v^2 l}{2d} \tag{9.9}$$

where l and d are the pipe length and diameter, v is the fluid velocity and F is a friction factor which is 0.034 for smooth drawn pipe at $N_{RE} = 7.84 \times 10^3$. Thus at $3l\ min^{-1}$,

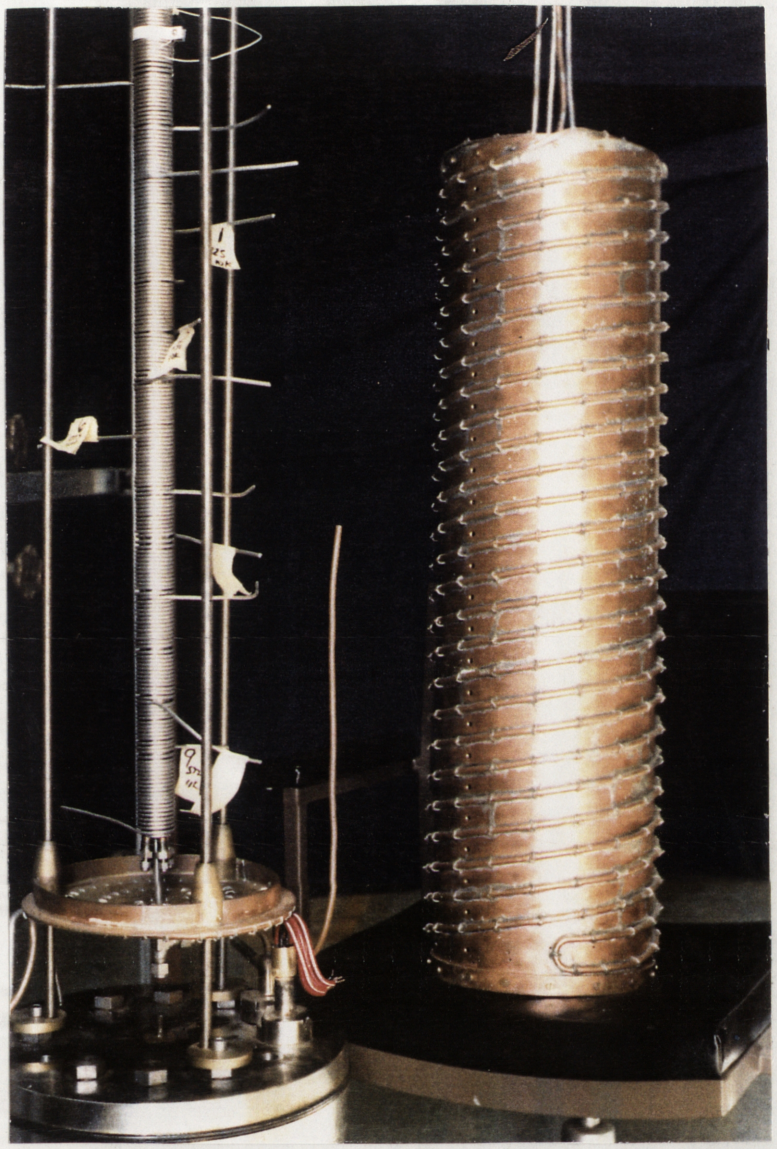

Figure 9.5: The synthesiser pressure vessel cooling jacket and the fixed pressure vessel endplate.

the pressure drop will be $158kPa$. Mains water pressure is 3 or 4 times higher than this, hence it will be possible to increase the flow rate if the vessel and cooling jacket are used for experiments at higher power levels.

For laminar flow the ratio $\frac{hD}{K}$ approaches 3.66 (Ozisik 1985), giving $h = 547Wm^{-2}K^{-1}$. This results in a temperature difference across the boundary layer of 14.5K.

By making the cooling water return parallel to its outgoing path, ie. alternating hot and cold coils down the length of the jacket, the average temperature can be maintained constant throughout.

An estimate of the temperature distribution between adjacent coils was obtained by assuming that the thermal flux absorbed by whatever mechanism (convection + radiation)

is uniform throughout. Then the one dimensional variation between coils at T_1 and T_2 is given by;

$$\frac{dT}{dz} = (l - z)\frac{q}{Kw} \tag{9.10}$$

where K is the conductivity of the jacket material, w its wall thickness, l the coil spacing and q the constant flux. The solution is;

$$T = \frac{qz(l - z)}{2Kw} + (T_1 - T_2)\frac{z}{l} + T_2. \tag{9.11}$$

This parabolic temperature profile gives an average temperature of:

$$\overline{T} = \frac{T_1 + T_2}{2} + \frac{l^2 q}{12Kw}. \tag{9.12}$$

For a jacket of $2mm$ thick copper ($K = 390Wm^{-1}K^{-1}$) with a flux of $3.66kWm^{-2}$, the average temperature of the jacket will be $0.33K$ higher than the average temperature of the coils and hence approximately $15K$ hotter than the average temperature of the water.

"Kaowool" ceramic fibre insulation material, or something similar, will be used.This material has a conductivity of approximately $0.05Wm^{-1}K^{-1}$ at 50°C. If the cooling jacket is maintained at an average temperature that is $20K$ above that of the vessel, then the thermal loss through the insulation will be $15.5W$, which is less than 1% of the heat absorbed by the cooling jacket. This energy must be lost by convection from the outer surface of the pressure vessel. Using empirical heat transfer coefficients for free convection taken from Ozisik (1985) indicated that $15.5W$ will be dissipated if the vessel temperature is $4.7K$ above ambient air temperature.

9.5 Pressure Vessel Feedthroughs

Pressure vessel feedthroughs are required for;

- reactant gases;
- cooling water;
- N_2 buffer gas;
- thermocouples;
- power for heating elements.

The basic feedthrough design is shown in figure 9.6, examples of the units adapted for the various required functions are shown in figure 9.7. If the tubular section of a feedthrough was subjected to the pressure within the vessel, then the radial stress (S) in the tube wall would be;

$$s = \frac{rP}{w} \tag{9.13}$$

where r is the tube radius and w the wall thickness. The yield stress of stainless is $207MPa$ at room temperature, thus the feedthroughs, with an inside diameter of $11.1mm$ and an outside diameter of $16.0mm$, have a wall thickness safety factor of 3.13. A prototype was fitted to the pressure vessel and successfully passed the $50MPa$ hydrostatic test.

The electrical power feedthrough has been constructed by silver soldering a length of 7 core mineral insulated Pyrotenax conducting cable into a basic feedthrough body. The

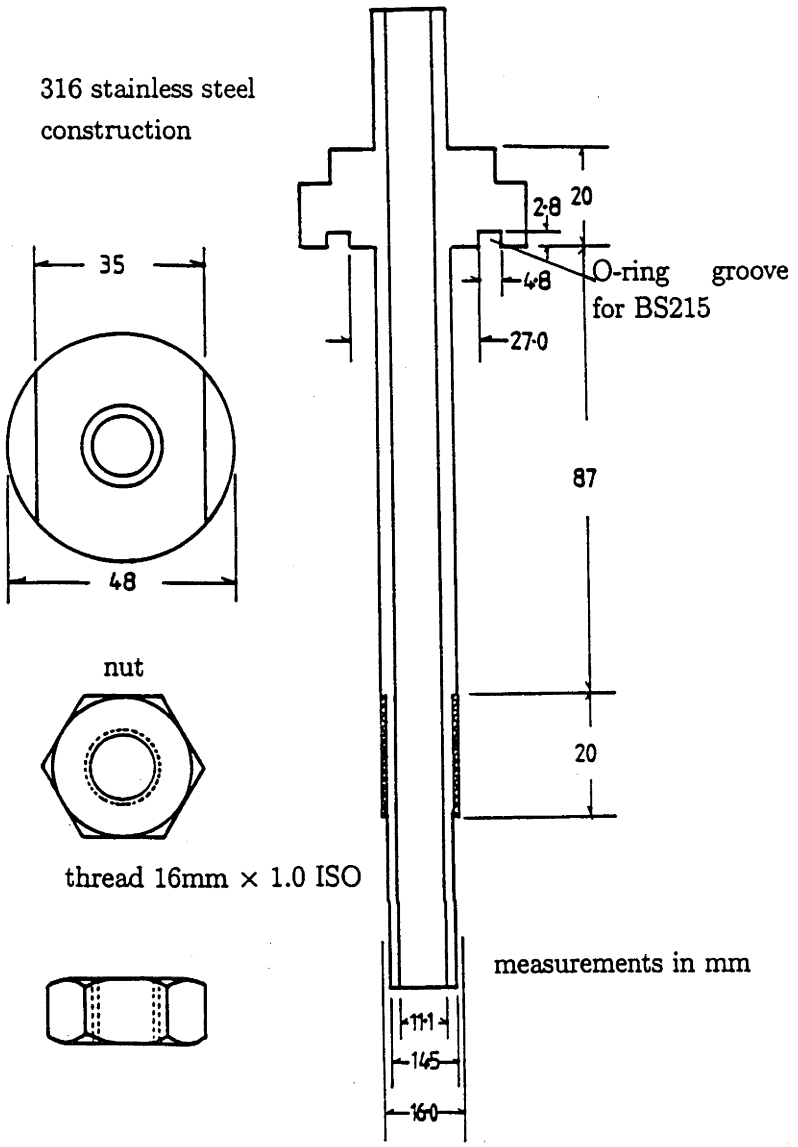

Figure 9.6: Basic pressure vessel feedthrough design.

inside end of the mineral insulated cable has been capped with epoxy resin to prevent gas seepage down the insulating material.

The design for combined cooling water/gas feedthroughs essentially consists of a short annular counterflow heat exchanger. Reactants pass through a central tube while the cooling water passes through the annular passage between it and the main body of the feedthrough thus preventing a flow of heat from the reactants into the pressure vessel endplate. Based on the calculations for the reactant preheater, the reactants flowing through the feedthrough will experience a temperature drop of $42K$ and give up $104W$ to the cooling water. A cooling water flow of $0.3l\ min^{-1}$ for the endplate of the cooling jacket will experience a corresponding temperature increase of only $5K$, without any significant flow of heat into the pressure vessel endplate. In the case of a cooling water failure, the end plate would be separated from the hot gas by three gas boundary layers, giving a resultant heat transfer coefficient of approximately $10Wm^{-2}K^{-1}$. This would mean heat would flow into the end plate at $4.2W$. The resulting temperature drop from the inside

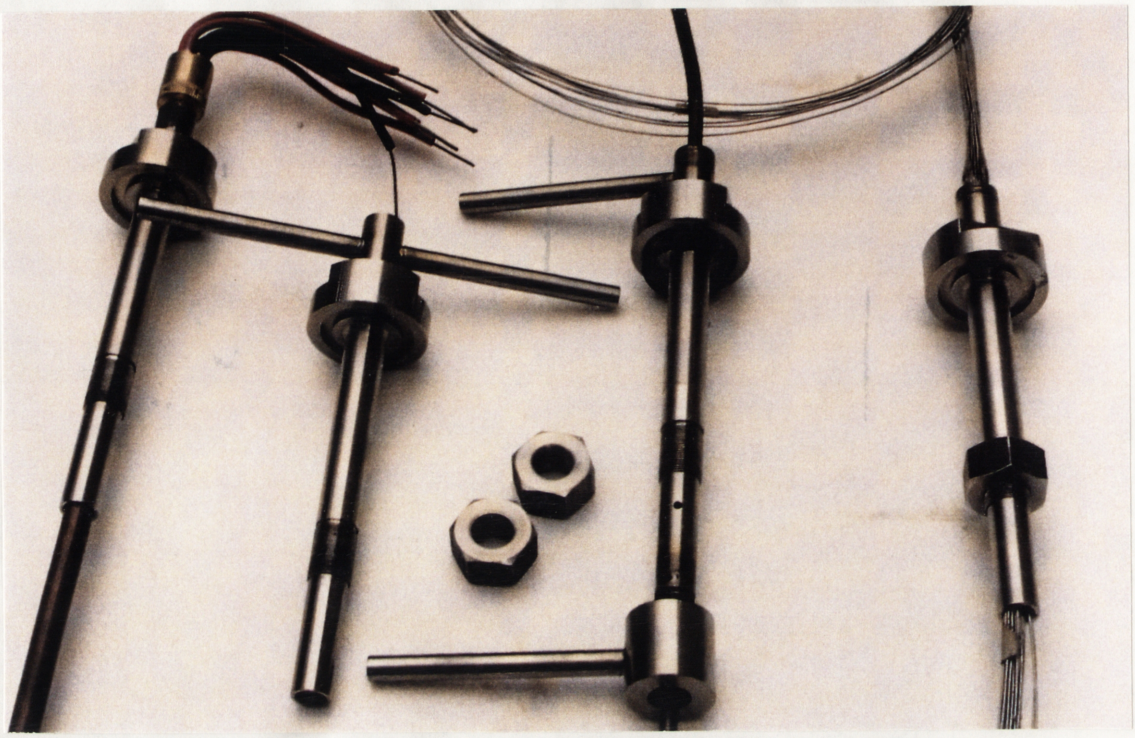

Figure 9.7: Pressure vessel feedthroughs for, from left to right; heater connections, cooling water, combined reactants and cooling water and thermocouples.

to the outside of the end plate would be $0.25K$. The resulting thermal stresses would not threaten the integrity of the pressure vessel.

9.6 Future Work

Currently a number of technical tasks remain before the synthesiser can be tested, these are;

- making electrical connections from feedthrough to heaters and from temperature controllers to feedthrough;
- connecting thermocouples to reactor and connecting extensions from the thermocouple feedthrough to the data aquisition system and temperature controllers;
- filling reactor with catalyst;
- installing reaction product cooling system;
- connecting water lines to cooling jacket;
- installing valves and piping for nitrogen and reactant reticulation.

When theses tasks are complete, commissioning will be carried out in a number of steps. The logical first stage of this process would be to test the heaters, temperature controllers, cooling jacket and temperature measurement systems at atmospheric pressure with the reactor filled with nitrogen. When these systems are functioning correctly the tests could be repeated at pressure and with nitrogen flow, with attention given to perfecting a method for maintaining a minimal pressure differential between the interior and exterior of the reactor. This could be followed by reduction of the catalyst with hydrogen, with measurement of the rate of water production using a weighable bed of dessicant or other methods. For simplicity, reaction tests could begin by operation of the unit as a dissociator. Before beginning synthesis reaction experiments consideration needs to be given to achieving a reliable flow of high reaction extent gas from the dissociator, which may involve the installation of another separator vessel (possibly cooled) to remove any liquid ammonia from the dissociator product mixture.

The new reactor system promises to be a source of reliable quantitative data and in conjunction with the dissociator, will provide a concrete demonstration of thermochemical energy transfer with ammonia. It will hopefully also eventually be part of a complete closed loop system. Ultimately this small reactor will be replaced by a larger and more sophisticated unit which will incorporate the important aspects of the direct work recovery concept. The pressure vessel and cooling jacket should continue to serve their purposes for other larger reactors.

Part IV

Summary

Chapter 10

Achievements and Conclusions

This project can claim to have encompassed a significant contribution to every aspect of the implementation of thermochemical transport and storage of solar energy using ammonia. This being so there is no single achievement or conclusion which dominates the final results.

It can be said that the technical and economic feasibility of the concept of storage and transport of solar energy using a closed loop thermochemical process based on ammonia, will only be established beyond doubt when a relatively large pilot plant has been constructed and operated. However the considerable body of research that has preceded this project has clearly demonstrated that the concept appears technically feasible and has a reasonable prospect of being economically feasible under the right conditions. Under these circumstances it can be said that this project has not identified any factor which would place the possibility of technical feasibility in doubt. Rather, by adding to the body of information upon which the details of implementation can be based, the project has shown that technical feasibility seems more certain.

In the foreword, the various areas to which this project can have claimed to have made a contribution, were listed. The specific achievements and conclusions which each chapter has presented can now be summarized.

This doctoral thesis is the first to directly address the work at the ANU on the ammonia based solar thermochemical energy transport and storage system, it is also the first document to attempt to discuss all aspects of the work in detail. As a result it is hoped that it may serve as a useful introductory reference for anyone interested in continuing the work. In view of this the review of previous work at ANU, presented in chapter 2, has encompassed every significant document produced to date. Also an attempt has been made, in chapters 1 and 3, to present a fairly thorough and hopefully clear description of the theoretical aspects of the concept and its implementation.

Chapter 3 attempts to present a thorough analysis of the thermodynamic aspects of thermochemical energy storage, with particular reference to the situation encountered with the ammonia reaction where the endothermic and exothermic reaction products separate spontaneously due to the condensation of one component at ambient temperature. The presentation draws on well known thermodynamic principles and previous work done by Carden & Williams (1978*b*), however some credit can be claimed for clarifying a number of aspects. The derivation of the exergy change associated with an infinitesimal change in reaction extent starting and ending at the sink temperature, although based on Carden and Williams' derivation of work recovery efficiency, represents a clarification and generalisation of their result. It led to the derivation of exact expressions for the exergetic efficiency of both endothermic and exothermic finite reaction paths. It was pointed out

that the expression for work recovery efficiency for such paths, quoted by Carden and Williams, is only valid for the range of reaction extents for which spontaneous separation occurs at the sink temperature.

The generation of constant contours of exergetic and work recovery efficiencies, via the Fortran code described in appendix B, represents an extension of the work recovery efficiency contours derived manually by Carden and Williams. The effect on work recovery efficiency of the transition from a process with spontaneous separation to one without, was illustrated. In addition to this an analysis which demonstrated the direct connection between the presence of spontaneous separation and the characteristic temperature of finite paths was presented.

The discussion of general reaction mechanisms, processes within catalyst beds, and specific mechanisms for the ammonia reaction, in chapter 4, is a compilation of textbook material. The discussion of the reactor model essentially reproduces the work of Richardson et al. (1988). The original contribution that can be claimed is in the adaptation of their model for application to ammonia dissociation and synthesis reactors, this was via modifications to the Fortran code as described in appendix B. This adaptation amounted to the generalisation of a very reaction specific and geometry specific implementation. The final result is that not only was the model successfully applied to predicting the performance of the dissociation reactor tested, but the program can now be applied to almost any packed bed reactor system, with a variety of geometries and wall conditions possible.

The use of the model to test the application of some of the latest ideas in receiver/reactor design to ammonia dissociation (chapter 5) has demonstrated the feasibility of these concepts in a quantitative way. This is in contrast to previous receiver design studies for ammonia dissociation which have relied on 'engineering estimates' of reactor performance. This modelling exercise was carried out prior to the experimental work which subsequently demonstrated that the intrinsic rate parameters used gave reaction rates which were conservatively small and implementation of the receiver concepts would be easier than indicated.

Although the concepts relating to the optimisation of real energy conversion systems, which have been introduced in chapter 6, are directly related to other recent work, this appears to be the first time these ideas have been applied to a thermochemical energy storage process. The description of a systematic approach to optimisation of an ammonia based solar thermochemical storage system and the solution of the reaction path optimisation problem using a dynamic programming technique, is claimed as a major original contribution of this project. The specific conclusions drawn from the analysis of this problem have been related in chapter 6, in general terms the results indicated that intuitively chosen paths, such as those produced by the direct work recovery system, produced very close to optimum performance.

Establishing a new laboratory facility, as related in chapter 7, is a reasonably significant accomplishment in its own right, but really only of direct interest to persons interested in continuing experimental work at the ANU. In a wider context, the layout and construction techniques used may be of some interest to others contemplating similar high pressure reaction experiments.

The experimental results obtained using the dissociation reactor, which have been presented in chapter 8, are the most thorough quantitative results which have been produced from work at the ANU to date. The most important direct conclusion drawn is that the adapted reactor model, following a simple adjustment to the intrinsic rate parameters, is able to adequately predict reactor performance under all the conditions tested. The model can now be used with confidence for the analysis of future reactor designs.

The experiments have provided empirical performance data which could be utilized in receiver designs even without the model. The data may well represent a higher pressure measurement of ammonia dissociation than any previously published. In addition to this, the experimental work has demonstrated the suitability of the dissociation reactor for a $1kW$ energy transfer experiment, provided empirical data on heat exchanger performance and tested a possible approach to the control of a receiver/reactor.

The completion of construction of the new reactor design presented in chapter 9 and its almost completed installation means that the facilities are now immediately available to advance experimental work towards the goal of an energy transfer experiment. The ideas embodied in the design were inspired from a number of sources, P.O. Carden and R.E. Whelan must take credit for many aspects. However the author claims the credit for providing the creative input which assembled these ideas into a specific design and determining most of the details of its construction.

In summary, this project has advanced experimental work on the implementation of an ammonia based solar thermochemical energy storage system and provided a good foundation for such work to continue in a productive manner. It has established a theoretical basis for optimisation of the performance of a real system. The project has also provided the analytical tools and sufficient empirical information to allow solar receiver based ammonia dissociation reactors to be designed with acceptably accurate predictions of performance.

Chapter 11

Future Work

The broad nature of this project has lead to the identification of opportunities for future work on all aspects of the topic. There are opportunities for valuable theoretical contributions in the areas of system optimisation, receiver and synthesis reactor design and control strategy formulation.

Further work on receiver/reactor design is probably the theoretical area which deserves the highest priority. The modelling of temperature profiles for the direct absorption receiver concept presented in chapter5, used an input flux profile produced by the model developed by Bannister (1991*a*). This model started with a simplified assumption about the actual temperature distribution, to deduce a net flux profile. Joining the reactor model and the receiver model in an iterative routine which generated consistent temperature and flux profiles would be a valuable first step.

This combined collector/receiver/reactor model would be a necessary tool for detailed design studies of various receiver design concepts. Design studies which aimed to produce cost comparisons as well as testing technical feasibility would be worthwhile. The availability of a detailed model of one or more receiver designs would provide the opportunity to pursue the problem of the choice of optimum exit reaction extent for the receiver. This would involve a trade-off between the energy storage efficiency of the reactor heat exchanger combination and the thermal efficiency of the receiver assembly.

There are numerous other aspects of generalised subsystem optimisation problems which can be identified. For the endothermic half of the system the corresponding reaction path optimisation, to that considered in chapter 6 for the exothermic reactor, would be of interest. Such a path may find application if a non-solar application was considered or if the incorporation of a topping cycle within a receiver construction was contemplated. For the exothermic half of the system determination of the optimum choice for exit reaction extent by considering the effects on pressure drop, heat exchanger irreversibilty, and required catalyst volume is of major importance.

The approach to real system optimisation outlined in chapter 6 could be pursued to its ultimate conclusion. In particular, applying it to an updated case study of a $10MW$ system would be worthwhile.

The endothermic and exothermic halves of the system pose different problems in the determination of control strategies. For the endothermic half, the determination of a control strategy which maximises the net exergy collection over daily cycles and through cloud cover transients deserves considerable study. For the exothermic reactor it is assumed that steady state operation will be possible, the main aspect of interest is to insure stable operation.

Two other areas which deserve some theoretical attention are the modelling of heat

exchanger behaviour and a further revision of the thermodynamic data for ammonia nitrogen/hydrogen mixtures. The ground work for heat exchanger modelling has been done. Completion of a numerical model would allow the quantification of heat transfer processes using the unanalysed experimental temperature measurements made during this project. Although the thermodynamic data used to date appears satisfactory, a number of minor shortcomings with the numerical program that calculates properties for mixtures should be addressed.

The potential for continuation of experimental work is clear. Work could continue immediately with the present experimental arrangement, although there are of course many improvements that could be made. The lack of facilities for continuous gas composition analysis and for direct measurements of intrinsic rates are the main shortcomings of the facility at present. Given the appropriate resources, these two aspects deserve a high priority.

Continuation of experiments with the dissociator would provide further useful results. If this was contemplated, measurement of the performance of the ICI 27-2 catalyst, possibly prepared in a range of particle sizes, should be the highest priority. However, future effort would be more profitably spent on the new reactor system. The new reactor, although conceived for synthesis experiments, could equally well be used for dissociation tests to investigate alternative catalyst materials. As has been noted its design avoids the shortcomings of the existing dissociator, for example making the determination of flux profiles and energy balance considerably easier. Its use for quantitative measurements of synthesis reaction behaviour would be most valuable. The design of the thermal shield heaters would also allow an investigation of the stability issues, associated with various heat extraction methods, in a controlled manner.

The commissioning of the new reactor, and its operation as a synthesizer in conjunction with the dissociator, would provide an immediate demonstration of open loop energy transfer. Development of a system for reactant recirculation would then be the only impediment to a small closed loop experiment.

Somewhat separately from this laboratory based work, the early operation of a receiver based reactor should be a high priority. This could initially be with a small tube based reactor of around $1kW$ level, utilizing a small fraction of the radiation collected within a cavity structure. Such tests would provide experience with the problems associated with reactor control under solar operation, and the effects of the associated thermal cycling on catalyst material.

There remains a great deal of rewarding research to be done on the implementation of solar thermochemical energy storage using ammonia. It is part of a general field of solar driven chemical processes which currently receives very little attention in Australia and insufficient attention on a world scale. The technologies that arise from this area of research are almost certainly going to be of enormous significance in the not too distant future. At the end of a fairly trying project, the author would nonetheless strongly recommend the field to any person seeking an intellectually challenging area of research which has a good prospect of making a valuable contribution to the quality of life on this planet.

Bibliography

Argo, W. & Smith, J. (1953), 'Heat transfer in packed beds', *Chemical Engineering Progress* **49**(8), 443–451.

Bannister, P. (1991*a*), An Experimental and Analytical Assessment of a Steam Rankine Solar Thermal System, PhD thesis, Research School of Physical Sciences and Engineering, Australian National University.

Bannister, P. (1991*b*), 'Maximization of exergy gain in high temperature solar thermal receivers by choice of pipe radius', *Journal of Heat Transfer* **113**(2), 337–340.

Bejan, A. (1987), 'The thermodynamic design of heat and mass transfer processes and devices', *Journal of Heat and Fluid Flow* **8**(4), 258–276.

Bohmer, M., Langnickel, U., Rodriguez, J. & Sanchez, M. (1991), Solar steam reforming of methane, *in* 'Proceedings ISES Solar World Congress, Denver, Colarado USA', pp. 828–833.

Breedveld, G. & Prausnitz, J. (1973), 'Thermodynamic properties of supercritical fluids and their mixtures at very high pressures', *American Institute of Chemical Engineers Journal* **19**, 783–796.

Buck, R., Muir, J., Hogan, R. & Scocypec, R. (1991), 'Carbon dioxide reforming of methane in a solar volumetric receiver/reactor: the CAESAR project', *Solar Energy Materials* **24**, 449–463.

Budenburg Gauges Pty Ltd (1990), 'Test report - pressure transducer'. Ringwood, Victoria.

Cantor, H. & Williams, O. (1976), 'A hot wire sensor for liquid level detection', *Journal of Physics E: Scientific Instruments* **9**, 1136–1139.

Carden, P. & Paterson, L. (1979), 'Physical chemical and energy aspects of underground hydrogen storage', *International Journal of Hydrogen Energy* **4**, 559–569.

Carden, P. & Patterson, L. (1980), Physical and energy aspects of underground hydrogen storage, *in* 'Proceedings of World Hydrogen Energy conference', Tokyo.

Carden, P. & Whelan, R. (1976), Radial heat transfer in packed catalyst tube, Technical Report EC-TR-12, Department of Engineering Physics, RSPhysS, ANU.

Carden, P. & Williams, O. (1978*a*), ANU solar energy project. a response by the ANU research team to a report commissioned by the Department of Science, Technical report, Department of Engineering Physics, RSPhysS, ANU.

Carden, P. & Williams, O. (1978*b*), 'The eficiencies of thermochemical energy transfer', *International Journal of Energy Research* **2**, 389–406.

Carden, P. & Williams, O. (1979), Thermochemical energy transport: Relation between work by energy conversion group, ANU, and work elsewhere, Technical report, Department of Engineering Physics, RSPhysS, ANU.

Carden, P., Edwards, B., Revie, R. & Williams, O. (1975), Thermochemical energy transfer and storage for large scale solar energy utilisation, *in* 'Proceedings of Symposium on Solar Energy Resources: Applications and Techniques', Canberra.

Carden, P., Edwards, B., Revie, R. & Williams, O. (1976*a*), Thermochemical energy transfer and storage for large scale solar energy utilization, *in* 'Proceedings of Conference on Energy Management', Sydney.

Carden, P., Edwards, B., Revie, R. & Williams, O. (1976*b*), The reversible ammonia reaction for large scale solar energy utilization, *in* 'Proceedings of Royal Australian Chemical Institute, Solid State Division - National Meeting', Sydney.

Carden, P., Edwards, B., Revie, R. & Williams, O. (1977), Large scale utilization of solar energy by the solar ammonia system, *in* 'Proceedings of ISES conference', Palm Springs, California.

Carden, P., Revie, R. & Williams, O. (1977), The solar ammonia system, *in* 'Proceedings of Electrochemical Society, Spring Meeting', Philadelphia, Pennsylvania.

Carden, P., Williams, O. & Revie, R. (1976), Thermochemical methods for the transport and storage of solar derived energy, *in* 'Proceedings of ANZAAS Conference', Hobart.

Carden, P. (1974*a*), A large scale solar plant based on the dissociation and synthesis of ammonia, Technical Report EC-TR-8, Department of Engineering Physics, RSPhysS, ANU.

Carden, P. (1974*b*), 'Means and methods for the utilization of solar energy'. Australian Patent no.PB-9168.

Carden, P. (1975), Corradiation using the reversible ammonia reaction, *in* 'Solar Use Now - a resource for people: extended abstracts', Los Angeles.

Carden, P. (1977*a*), 'Energy corradiation using the reversible ammonia reaction', *Solar Energy* **19**, 365–378.

Carden, P. (1977*b*), Thermodynamic gain of thermochemical energy transfer systems, Technical Report EC-TR-13, Department of Engineering Physics, RSPhysS, ANU.

Carden, P. (1978*a*), Hydrogen rich gas storage in sedimentary formations, Technical Report EC-TR-17, Department of Engineering Physics, RSPhysS, ANU.

Carden, P. (1978*b*), Solar power for remote area, *in* 'Proceedings of ISES Symposium', Perth.

Carden, P. (1979), Solar power for remote areas - chemical heat pipes. progress report to NERDDC, Technical report, Department of Engineering Physics, RSPhysS, ANU.

Carden, P. (1980*a*), Demonstration of a laboratory scale chemical heat pipe, progress report to NERDDC, Technical report, Department of Engineering Physics, RSPhysS, ANU.

Carden, P. (1980*b*), Work recovery efficiency of ideal gas thermochemical energy transfer systems and SO_3 synthesis, Technical Report EC-TR-23, Department of Engineering Physics, RSPhysS, ANU.

Carden, P. (1980*c*), Work recovery efficiency of the methanation process, Technical Report EC-TR-21, Department of Engineering Physics, RSPhysS, ANU.

Carden, P. (1981), Stability and control of a converter coupled to a multipass steam generator, Technical Report EC-TR-24, Department of Engineering Physics, RSPhysS, ANU.

Carden, P. (1982*a*), A balancing separator for the ammonia thermochemical energy transfer demonstration, Technical Report EC-TR-26, Department of Engineering Physics, RSPhysS, ANU.

Carden, P. (1982*b*), Thermal stresses in the hot wall reaction vessel for the synthesis of ammonia, Technical Report EC-TR-25, Department of Engineering Physics, RSPhysS, ANU.

Carden, P. (1982*c*), Thermochemical energy transfer (chemical heat pipe) demonstration based on the system $2NH_3/N_2 + 3H_2$. progress report to NERDDC, Technical report, Department of Engineering Physics, RSPhysS, ANU.

Carden, P. (1983*a*), Manufacture of high pressure nitrogen gas from the liquid phase, Technical Report EC-TR-26, Department of Engineering Physics, RSPhysS, ANU.

Carden, P. (1983*b*), Thermochemical energy transport using the ammonia reaction. final report to NERDDC, Technical report, Department of Engineering Physics, RSPhysS, ANU.

Carden, P. (1984*a*), 'Manufacture of high pressure nitrogen gas from the liquid phase', *Journal of Physics E: Scientific Instruments* **17**, 890–895.

Carden, P. (1984*b*), Specification for synthesiser, Department of Engineering Physics, RSPhysS, ANU.

Carden, P. (1985), 'Utilisation of solar energy'. Australian Patent no.PHO-0440.

Carden, P. (1987), 'Direct work output from thermochemical energy transfer systems', *International Journal of Hydrogen Energy* **12**, 13–22.

Chao, R., Caban, R. & Irizarry, M. (1973), 'Wall heat transfer to chemical reactors', *Canadian Journal of Chemical Engineering* **51**, 67–70.

Chessel Ltd (1990), '4500 installation and operation manual'. Worthing, Sussex, UK.

Chubb, T., Nemecek, J. & Simmons, D. (1979*a*), 'Application of chemical engineering to large scale solar energy', *Solar Energy* **20**, 219–224.

Chubb, T., Nemecek, J. & Simmons, D. (1979*b*), 'Design of a small thermochemical receiver for solar thermal power', *Solar Energy* **23**, 217–221.

Chubb, T. (1975), 'Analysis of gas dissociation solar thermal power system', *Solar Energy* **17**, 129–136.

Chubb, T. (1976), 'A chemical approach to solar energy', *Chemtech* pp. 654–657.

Chubb, T. (1980), 'Characteristics of $CO_2 - CH_4$ reforming- methanation cycle relevant to the SOLCHEM thermochemical power system', *Solar Energy* **24**, 341–345.

Corning Glass Works (1987), *Product Information*, Corning Glass Works, New York.

Curzon, F. & Ahlborn, B. (1975), 'Efficiency of a Carnot engine at maximum power output', *American Journal of Physics* **43**, 22–24.

Davy McKee Pacific Pty. Ltd. (1987), Assessment of solar thermochemical power plant, Technical report, Department of Engineering Physics, RSPhysS, ANU.

Davy Pacific Pty. Ltd. (1979), Report on the chemical heat pipe project for solar power for remote areas, Technical report, Department of Engineering Physics, RSPhysS, ANU.

De Deken, J., Devos, E. & Froment, G. (1982), 'Steam reforming of natural gas: Intrinsic kinetics, diffusional influences, and reactor design', *American Chemical Society Symposium Ser.-Chemical Reaction Engineering* **196**, 181–197.

Diver, Fish, Levitan, Levy, Meirovitch, Rosin, Parypatyadar & Richardson (1992), 'Solar test of an integrated sodium reflux heat pipe receiver/reactor for thermochemical energy transport', *Solar Energy* **48**(1), 21–30.

Diver, R. (1987), 'Receiver/reactor concepts for thermochemical transport of solar energy', *Journal of Solar Energy Engineering* **109**, 199–204.

Edwards, B. (1974), Heat exchangers, Technical Report EC-TR-10, Department of Engineering Physics, RSPhysS, ANU.

Eurotherm Corporation (1988), 'Installation and operation manual; models 808 and 847 digital controllers'. Reston, Virginia, USA.

Fedders, R., Harth, R. & Holhein, B. (1975), 'Experiments for combining nuclear heat with methane steam reforming process', *Nucl. Eng. and Design* **34**, 119–127.

Fish, J. & Hawn, D. (1987), 'Closed loop thermochemical energy transport based on CO_2 reforming of methane', *Solar Energy Engineering* **109**, 215–220.

Fish, J. (1984), Overture to CLEA: The closed loop efficiency analysis project, Technical Report SAND84-0502, Sandia National Laboratories.

Fish, J. (1989), High-temperature solar destruction of hazardous wastes, *in* 'Proceedings of the Annual Solar Thermal Technology Research and Development Conference', pp. 134–152.

Fox, J. (1983), Thermochemical energy transport systems study, Technical Report JCS-PR-002, Sandia National Laboratories, USA.

Fraenkel, D., Levitan, R. & Levy, M. (1986), 'A solar thermochemical pipe based on the $CO_2 - CH_4(1:1)$ system', *International Journal of Hydrogen Energy* **11**(4), 267–277.

Gordon, J. (1988), 'On optimized solar-driven heat engines', *Solar Energy* **40**(5), 457–461.

Gunn, R., Chueh, P. & Prausnitz, J. (1966), *American Institute Chemical Engineers Journal* **12**, 937–941.

Haar, L. & Gallagher, J. (1978), 'Thermodynamic properties of ammonia', *Journal of Physical and Chemical Reference Data* **7**(2), 635–792.

Hafele, W. (1974), 'Energy choices that Europe faces', *Science* **84**, 360–367.

Hawn, D. & Fish, J. (1986), CLEA: The closed loop efficiency analysis facility for thermochemical energy transport studies, Technical Report SAND86-0590, Sandia National Laboratories.

Hilberath, E. & Teggers, H. (1968). West German Patent 298233.

Hildebrandt, A. (1975), Solar tower thermo-chemical energy cycles, *in* 'Proceedings of Hydrogen Energy Fundamentals symposium, Miami, Florida, March 3-5', pp. 51–53.

Hill, C. (1977), *Chemical Engineering Kinetics and Reactor Design*, John Wiley and Sons, New York.

Hogan, R. & Skocypec, R. (1989), 'Analysis of catalytically enhanced solar absorbtion chemical reactors: I-basic concepts and numerical model description', *Solar Energy Technology ASME SED* **8**, 31–37.

Holhein, B., Menzer, R. & Range, J. (1981), 'High temperature methanation in the long distance nuclear energy transport system', *Applied Catalysis* **1**, 125–139.

Imperial Chemical Industries (1970), *Catalyst Handbook*, Wolfe Scientific Books, London.

Incropera, F. & Dewitt, D. (1985), *Fundamentals of Heat and Mass Transfer*, John Wiley and Sons, New York.

Kaneff, S. (1989), On the design of viable paraboloidal dish solar collector systems, *in* 'Proceedings of ISES Solar World Congress', Kobe.

Kelly, D. (1989), Data logger instruction manual, Technical Report J368, Electronics Unit, RSPhysS, ANU.

Kulkarni, B. & Doraiswamy, L. (1980), 'Estimation of effective transport properties in packed bed reactors', *Catalysis Reviews in Science and Engineering* **22**(3), 431–483.

Laboratory Technologies Corporation (1989), 'Labtech notebook version 5'. Wilmington, MA, USA.

Lee, M. & Prengle, H. (1986), 'Chemical storage of solar energy - kinetics of heterogenous NH_3 and H_2SO_4 reactions I. analysis of experimental reaction and mass transfer data', *Solar Energy* **37**, 301–311.

Lenz, T., Wright, J. & Chubb, T. (1978), Engineering design study of conversion of solar energy to chemical energy through ammonia dissociation, Technical report, Department of Agricultural and Chemical Engineering, Colarado State University.

Levitan, R., Levy, M., Rosin, H. & Rubin, R. (1991), 'Closed-loop operation of a solar chemical heat pipe at the Weizmann Institute solar furnace', *Solar Energy Materials* **24**, 464–477.

Levitan, R., Rosin, H. & Levy, M. (1989), 'Chemical reactions in a solar furnace - direct heating of the reactor in a tubular reciever', *Solar Energy* **42**(3), 267–272.

Levy, M., Rosin, H. & Levitan, R. (1989), 'Chemical reactions in a solar furnace by direct irradiation of the catalyst', *Journal of Solar Energy Engineering* **111**, 96–97.

Lovegrove, K. & Hall, R. (1990), Testing and calibration of the balancing separator for ammonia based thermochemical experiments, Technical Report ER-RR-53, Energy Research Centre, RSPhysS, ANU.

Lovegrove, K. (1987), Alkali metal thermoelectric converters for solar applications, *in* 'Proceedings of Australian and New Zealand Solar Energy Society nual conference, Annual Conference', Canberra.

Lovegrove, K. (1992*a*), Fortran implementation of a two dimensional pseudo homogenous packed bed catalytic reactor model, Technical Report ER-RR-62, Energy Research Centre, RSPhysS, ANU.

Lovegrove, K. (1992*b*), Fortran programs for study of the ammonia based thermochemical system, Technical Report ER-RR-61, Energy Research Centre, RSPhysS, ANU.

Mayer, I. (1989), Volumetric receiver pressure vessel, Technical Report Private Communication, Energy Research Centre ANU.

McCrary, J. & McCrary, G. (1987), Experimental studies of a closed-loop sulfur oxide energy conversion and transport system, Technical Report Sand86-7040, Sandia National Laboratories.

McCrary, J., McCrary, G., Chubb, T., Nemecek, J. & Symons, D. (1982), 'An experimental study of the $CO_2 - CH_4$ reforming-methanation cycle as a mechanism for converting and transporting solar energy', *Solar Energy* **29**, 141–151.

Meirovitch, E., Segal, A. & levy, M. (1990), 'Theoretical modelling of a directly heated solar-driven chemical reactor', *Solar Energy* **45**(3), 139–148.

Michels, A., Skelton, G. & Dumoulin, E. (1950), 'Gas-liquid phase equilibrium in the system ammonia-hydrogen-nitrogen', *Physica* **16**(11-12), 831–838.

Moshfegh, A. & Ignatiev, A. (1987), 'Photo-enhancement of the catalytic methanation reaction', *Energy* **12**(3/4), 227–282.

Nag, P. & Kumar, N. (1988), 'Second law optimization of convective heat transfer through a duct with with constant heat flux', *International Journal of Energy Research* **13**, 537–543.

Nandy, S. & Lenz, T. (1984), 'Observations on the catalytic decomposition of ammonia at high temperatures and pressures', *American Institute of Chemical Engineers Journal* **30**(3), 504–507.

Nielsen, A. (1970), 'Review of ammonia catalysis', *Catalysis Reviews* **4**, 1–25.

Norman, J. (1975), *Elementary Dynamic Programming*, Edward Arnold, London.

Ozisik, M. (1985), *Heat Transfer, a Basic Approach*, McGraw-Hill, New York.

Parypatyadar, S. & Richardson, J. (1988), 'Cyclic performance of a sodium heat pipe solar reformer', *Solar Energy* **41**(5), 475–485.

Paterson, L. (1981), Viscous fingering and Underground hydrogen storage, PhD thesis, Department of Engineering Physics, RSPhysS, ANU.

Prengle, H. & Lee, M. (1986), 'Chemical storage of solar energy - the Flood-Forland-Lindeman hypotheses and the decomposition of pyrosulfate ions', *Solar Energy* **37**, 293–299.

Prengle, H. & Sun, C. (1976), 'Operational chemical storage cycles for utilization of solar energy to produce heat or electric power', *Solar Energy* **18**, 561–.

Pyrotenax Australia Pty Ltd (1988), 'Pyroheat'. Industrial electrical heating systems catalogue.

Ranade, S., Lee, M. & Prengle, H. (1986), 'Chemical storage of solar energy - kinetics of heterogenous NH_3 and H_2SO_4 reactions II. process and reactor design', *Solar Energy* **37**, 375–388.

Revie, R. (1975), The enthalpy diagram for the ammonia synthesis reaction, Technical Report EC-TR-9, Department of Engineering Physics, RSPhysS, ANU.

Revie, R. (1976), Solar energy for a future society, *in* 'Proceedings of Australian Petroleum Exploration Association conference', Adelaide.

Richardson, J. & Das-gupta, S. (1978), Interfacing methane-carbon monoxide chemical heat pipes with solar towers: Preliminary design and economic study, *in* 'Proceedings of Solar High-Temperature Industrial Processes Workshop', Atlanta, Georgia.

Richardson, J., Paripatyadar, S. & Shen, J. (1988), 'Dynamics of a sodium heat pipe reforming reactor', *American Institute of Engineers Journal* **34**(5), 743–752.

Rocket Research Corporation (1977), Reversible chemical reactions for electric utility energy applications, Technical Report RRC-77-R-559, Contract TPS 76-658, Electric Power Research Institute.

Rutt, H. & Bonilla, I. (1975), 'A wide range linear capacitance meter', *Journal of Physics E; Scientific Instruments* **8**, 239–241.

Skocypec, R. & Hogan, R. (1989), 'Analysis of catalytically enhanced solar absorbtion chemical reactors: II-predicted characteristics of a $100kW_{thermal}$ reactor', *Solar Energy Technology ASME SED* **8**, 39–47.

Suzuki, A., Okamura, H. & Oshida, I. (1987), 'Application of exergy concept to the analysis of optimum operating condidions of solar heat collectors', *Journal of Solar Energy Engineering* **109**, 337–342.

Vancini, C. (1971), *Synthesis of Ammonia*, Macmillan, London.

Vargaftic, N. (1983), *Handbook of Physical Properties of Liquids and Gases: Pure Substances and Mixtures*, Hemisphere Publishing Corporation.

Vennard, J. (1961), *Elementary Fluid Mechanics*, John Wiley, New York.

Weale, R. (1967), *Chemical Reactions at High Pressures*, E. and F.N. Spon, London.

Wentworth, W. & Chen, E. (1976), 'Simple thermal decomposition reactions for storage of solar thermal energy', *Solar Energy* **18**, 205–214.

Wentworth, W., Batten, C. & Gong, W. (1987), 'The photoassisted thermal decomposition of methanol and isopropanol in a fluidized bed', *Energy* **12**(3/4), 319.

Wentworth, W., Batten, C. & Gong, W. (1990), 'Evaluation of photo contribution to a chemical reaction using concentrated solar energy', *Solar Energy* **44**(1), 37–42.

Whelan, R. (1979), 'A miniature low flow rate turbine flowmeter', *Journal of Physics E; Scientific Instruments* **12**, 553–555.

Williams, O. & Carden, P. (1979*a*), 'Ammonia dissociation for solar thermochemical absorbers', *International Journal of Energy Research* **3**, 129–142.

Williams, O. & Carden, P. (1979*b*), Ammonia dissociation for solar thermochemical absorbers, *in* 'Proceedings of ISES Silver Jubillee Congress', Atlanta, Georgia.

Williams, O. & Carden, P. (1979*c*), 'Energy storage efficiency for the ammonia/hydrogen-nitrogen thermochemical energy transfer system', *International Journal of Energy Research* **3**, 29–40.

Williams, O. & Carden, P. (1979*d*), 'Screening reversible reactions for thermochemical energy transfer', *Solar Energy* **22**, 191–193.

Williams, O. (1976), Thermodynamic data for the ammonia synthesis and dissociation reactions, Technical Report EC-TR-11, Department of Engineering Physics, RSPhysS, ANU.

Williams, O. (1978*a*), Demonstration of an ammonia-based chemical heat pipe: A research proposal, Technical Report EC-TR-19, Department of Engineering Physics, RSPhysS, ANU.

Williams, O. (1978*b*), Generation of thermochemical energy transfer data for the ammonia/hydrogen-nitrogen system, Technical Report EC-TR-16, Department of Engineering Physics, RSPhysS, ANU.

Williams, O. (1978*c*), 'Thermochemical energy transport costs for a distributed solar power plant', *Solar Energy* **20**, 333–342.

Williams, O. (1978*d*), A thermodynamic study of thermochemical energy transfer systems, Technical Report EC-TR-15, Department of Engineering Physics, RSPhysS, ANU.

Williams, O. (1980*a*), 'A comparison of reversible chemical reactions for solar thermochemical power generation', *Revue Physique Appliquee* **15**, 453–461.

Williams, O. (1980*b*), 'Design and cost analysis for an ammonia-based solar thermochemical cavity absorber', *Solar Energy* **24**, 255–263.

Williams, O. (1980*c*), Development of the 5kW ammonia-based thermochemical energy conversion experiment, Technical Report EC-TR- 20, Department of Engineering Physics, RSPhysS, ANU.

Williams, O. (1980*d*), 'Evaluation of wall temperature difference profiles for heat absorption tubes exposed nonuniformly to solar radiation', *Solar Energy* **24**, 597–600.

Williams, O. (1980*e*), 'A heat transfer system for chemical reactor thermal control', Australian Patent Application. PE 06364.

Williams, O. (1980*f*), Organic thermochemical energy conversion and storage based on reversible cycloaddition reactions, Technical report, Department of Engineering Physics, RSPhysS, ANU.

Williams, O. (1980*g*), Prospects for solar thermochemical power generation, *in* 'Proceedings of ISES ANZ section annual conference', Melbourne.

Williams, O. (1980*h*), Solar thermochemical energy storage using reversible cycloaddition reactions, *in* 'Proceedings of ISES ANZ section annual conference', Melbourne.

Williams, O. (1981*a*), 'Ammonia thermochemical energy transport in a distributed collector solar thermal power plant', *Solar Energy* **27**, 205–214.

Williams, O. (1981*b*), ANU solar thermochemical research, *in* 'Proceedings of ISES ANZ section annual conference', Sydney.

Williams, O. (1981*c*), The thermodynamics of solar thermochemical power generation, *in* 'Proceedings of the Second National Thermodynamics Conference', Melbourne.

Won, Y. & Voecks, G. (1986), 'Experimental and theoretical study of a solar thermochemical receiver module', *Solar Energy* **37**, 109–118.

Won-yong, L. & Sang-soo, K. (1991), 'An analytical formula for the estimation of a Rankine-cycle heat engine efficiency at maximum power', *International Journal of Energy Research* **15**, 149–159.

Wright, J. & Lenz, T. (1980), Solar energy collection using the reversible ammonia dissociation reaction, *in* 'Proceedings of 15th Intersociety Energy Conversion Engineering Conference', pp. 140–144.

Appendix A

Thermodynamic Data

A.1 Introduction

This project has largely relied on the thermodynamic data for ammonia-hydrogen/nitrogen mixtures compiled by Williams (1978*b*). The need for adequate thermodynamic data was addressed early in the investigation of the ammonia system by the ANU group. Revie (1975) assembled, from various sources, temperature enthalpy data for ammonia and 3:1 hydrogen nitrogen mixtures. Williams (1976) built on this and assembled a complete set of data including intermediate mixtures for the single phase region. This was subsequently extended to cover the two phase region as well (Williams 1978*b*). For this project, extra information on thermal conductivities and viscosities has been taken from Vargaftic (1983).

A.2 Enthalpies and Gibbs Free Energies

Williams (1976) found that reliable published thermodynamic data was only available for pure components and for temperatures below $600K$. To extend this to higher temperatures he relied on calculations based on the principle of corresponding states. This is a semi-empirical method which involves extrapolating from limited data by reference to generalised relationships based on accumulated empirical data from similar materials.

For fluids which can be described by a simple central field interaction, the equation of state can be successfully reduced to the common form;

$$\frac{Pv}{RT} = Z\left(\frac{T}{T_c}, \frac{P}{P_c}\right) \tag{A.1}$$

where Z is the compressibility factor, R is the universal gas constant, v is the specific volume (volume per mole) and the critical temperature (T_c) and pressure (P_c) for a particular fluid are related to the energy and distance parameters in its intermolecular potential function. Derived functions such as enthalpy also become functions of the reduced temperature and pressure. When a central field description of the intermolecular interaction is not adequate, this 'two parameter' corresponding states principle can be extended by, for example, introducing a third fluid specific parameter, making T_c and P_c temperature dependant or using effective values derived from empirical data and applicable over a limited range of conditions.

Williams addressed the problem for each of the pure components and single phase mixtures. Nitrogen deviates only slightly from the central field description, the appropriate generalized results of Breedveld & Prausnitz (1973) were used and found to be in good

agreement with the low temperature tabulated data. Hydrogen is classified as a 'quantum fluid' and deviates strongly from the simple corresponding states principal predictions, Williams used the temperature dependant critical constants quoted by Gunn, Chueh & Prausnitz (1966), and found that results were also in good agreement with low temperature data. For ammonia, empirical data was assembled over the pressure and temperature range of interest, the choice of suitable effective critical constants allowed successful interpolation using corresponding states calculations.

For fluid mixtures, Williams followed Breedfeld & Prausnitz in the use of the Van der Waals one fluid and two fluid models for deriving 'pseudocritical constants'. The Van der Waals approach treats the mixture as a mixture of two hypothetical fluids whose critical constants are derived from a non-linear combination of the constants of the actual component fluids. In the single fluid model, overall critical constants for the mixture are given by the molar averages of the pseudocritical constants. For the two fluid model, the two hypothetical fluids are treated separately and thermodynamic properties of the mixture are calculated from the molar averages of the values determined for each of the two hypothetical fluids. Williams employed single fluid calculations for hydrogen and nitrogen mixtures, and two fluid calculations for hydrogen nitrogen and ammonia mixtures. He noted that above approximately $800K$ and below 600 atmospheres, mixtures of hydrogen nitrogen and ammonia are 'ideal solutions' in that enthalpies calculated with the two fluid model did not differ significantly from plain molar averages based on the properties of ammonia and pure synthesis gas,

To extend the enthalpy data into the two phase region at low temperatures, Williams (1978*b*) relied on the relationship between separation work (W_s, the work required to separate the components of an equivalent ideal mixture at the sink temperature T_s) and mixing heat (H_m) (Carden & Williams 1978*b*);

$$W_s = T_s S_m(T_f, \delta) = -\int_{T_s}^{T_f} \left.\frac{\partial H_m}{\partial T}\right|_{(T,\delta)} \left(1 - \frac{T_s}{T}\right) \tag{A.2}$$

together with the phase equilibrium data of Michels, Skelton & Dumoulin (1950). For each value of the mixture composition the temperature at the dewline (the phase boundary) was taken from the data of Michels et al and the dewline enthalpy value was derived by iterative solution of equation A.2 after calculation of the mixing entropy of the equivalent ideal mixture (S_m) from the composition. It was assumed that the enthalpy of mixing was zero above $900K$, and polynomial interpolation was used between the known high temperature enthalpy values and the assumed value at the dewline.

Gibbs free energies can be deduced from the enthalpy data via the Gibbs-Helmholtz relation;

$$\frac{G(\delta,T)}{T} = \frac{G(\delta,T_0)}{T} + \int_{T_0}^{T} H(\delta,T) d\left(\frac{1}{T}\right) \tag{A.3}$$

where T_0 is sufficiently low that $G(\delta,T_0)$ is given by the combination of pure ammonia and synthesis gas values. Gibbs free energies in turn yield the composition of mixtures at chemical equilibrium, which at constant pressure is equated with the condition $\frac{\partial G}{\partial \delta} = 0$.

Williams (1978*b*) has presented tabulated values of enthalpies, Gibbs free energies and other quantities together with a listing of the Fortran program used to produce them. Figure A.1 presents the complete enthalpy data for 200 atmospheres. It is apparent that there is a bug in the calculation of enthalpies for $\delta = 0.2$, with the enthalpy values intercepting those for $\delta = 0$ at approximately $500K$. This error becomes even more noticeable for enthalpy data generated for lower pressures. Aside from this the values produced by Williams' program are consistent with the derivations described and after discarding the

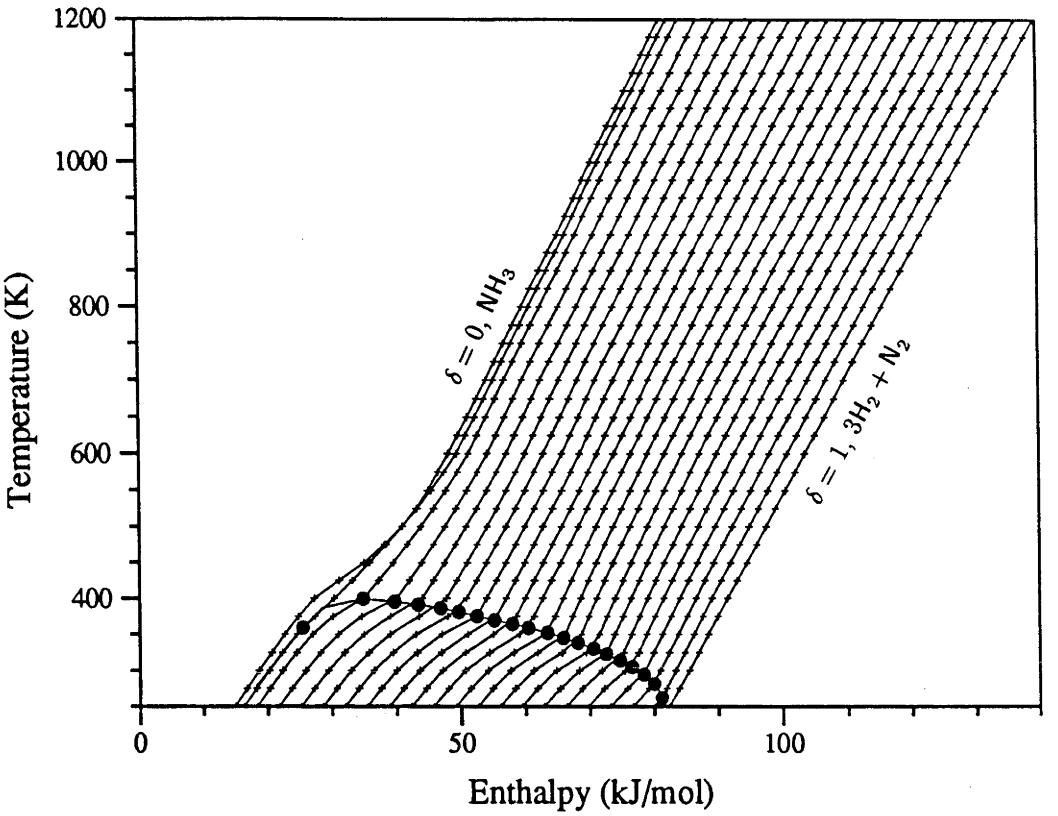

Figure A.1: Enthalpy data for 200 atmospheres shown as constant reaction extent contours between $\delta = 0$ and $\delta = 1.0$ in steps of 0.05, with an extra contour at $\delta = 0.02$. Dewline interception points are shown by • symbols.

$\delta = 0.2$ values they have been used for all the thermodynamic data manipulation involved in this project.

Figure 1.2, in chapter 1, illustrates the manner in which enthalpies vary with pressure. Figures A.2 and A.3 show the tabulated Gibbs free energy data corresponding to the enthalpy values of figure A.1 plotted as G vs T and G vs δ respectively.

In the course of this project this data has been utilised in a number of ways. As described in appendix B, Williams' original program has been converted to a subroutine and combined with other modules to produce additional tables of derivatives of enthalpy and Gibbs free energy with respect to T and δ. This expanded data set has been used during analysis by a combination of linear interpolation and one dimensional and two dimensional curve fitting techniques.

A.3 Data for Reactor Modelling

The Fortran implementation of the two dimensional reactor model described in chapter 4 and appendix B uses curve fits for the various thermodynamic properties required; cubic polynomial fits are used for specific heat at constant pressure and enthalpy, power fits are used for thermal conductivities and viscosities and an exponential fit is used for the equilibrium constant.

Cubic polynomials for enthalpy and specific heat at constant pressure have been obtained by fitting curves to the data for $\delta = 0$ and $\delta = 1$ and $T \geq 450K$. Coefficients

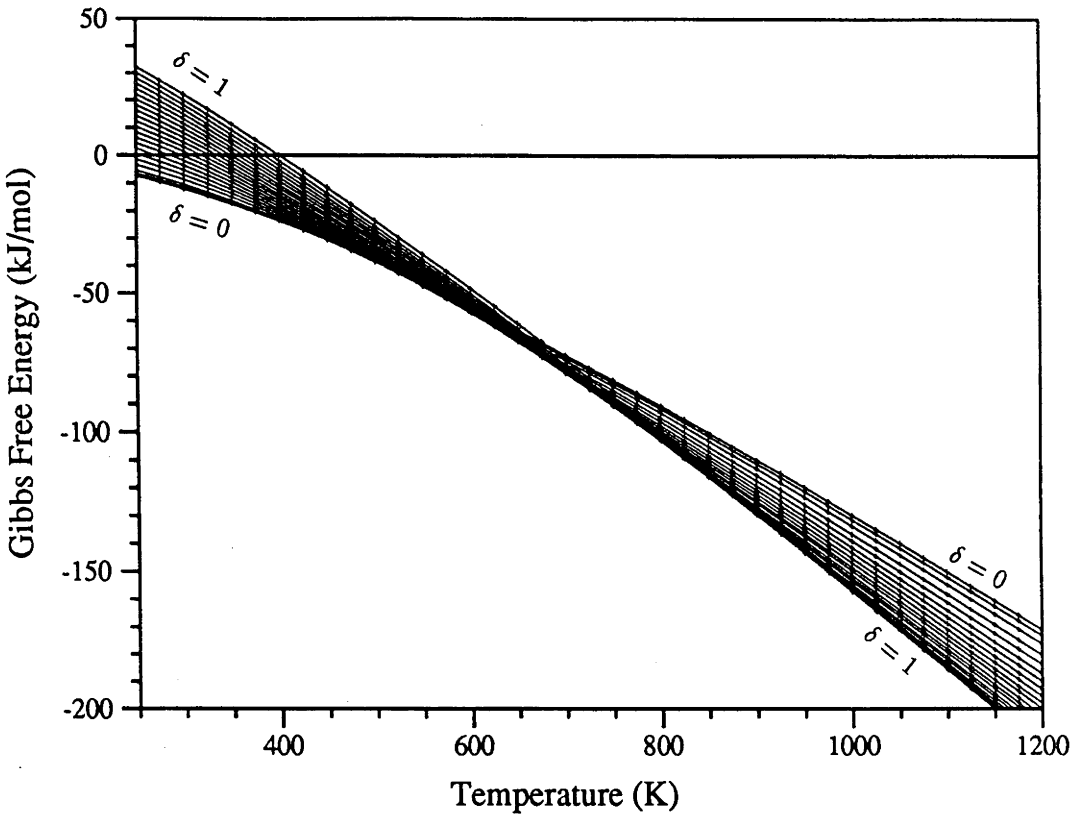

Figure A.2: Gibbs free energy data for 200 atmospheres plotted as constant reaction extent contours between $\delta = 0$ and $\delta = 1.0$ in steps of 0.05, with an extra contour at $\delta = 0.02$.

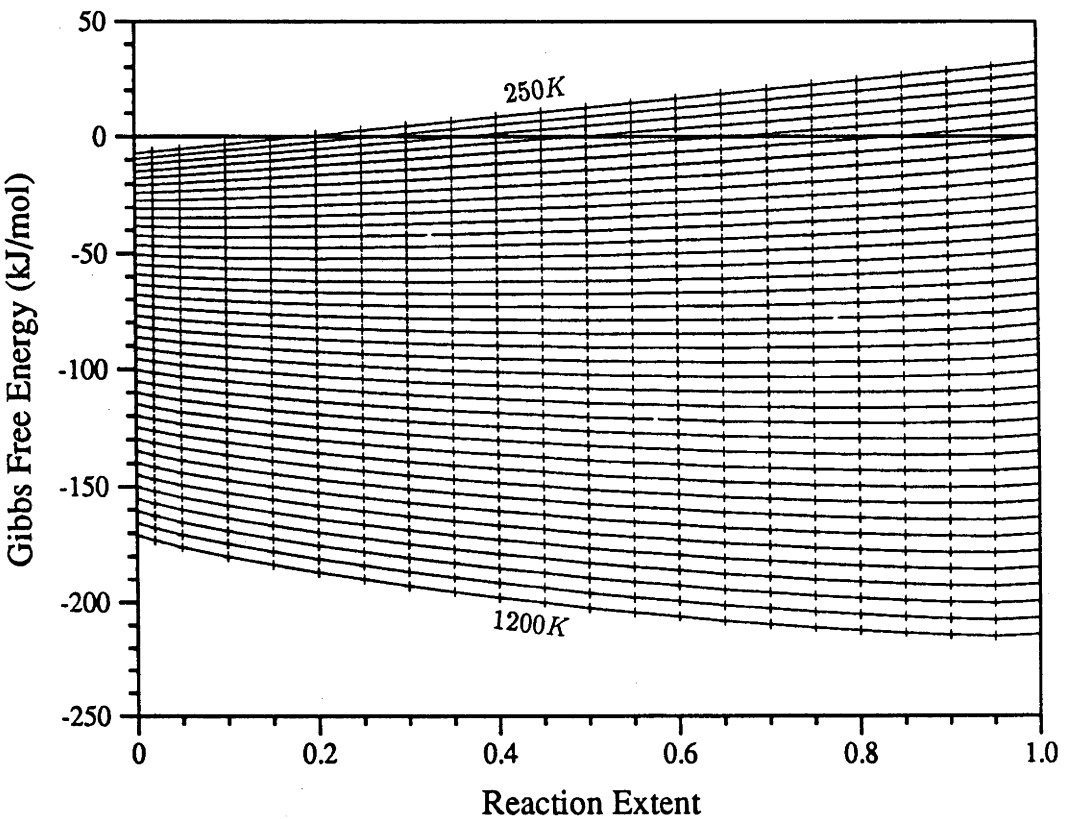

Figure A.3: Gibbs free energy data for 200 atmospheres plotted as constant temperature contours. Temperatures range from 250 to $1200K$ in steps of $25K$.

corresponding to a range of pressures are presented in Tables A.1 and A.2. The coefficients quoted for hydrogen and nitrogen were obtained from those for the synthesis gas mix ($\delta = 1$), by assuming that values for the two components remained in the same average ratio as for 1 atmosphere. Hence these coefficients will not necessarily produce correct pure component values, but when used in the reactor modelling program they will reproduce the correct values for mixtures. For synthesis gas mixtures these polynomials reproduce enthalpy values to within 0.1% and specific heat values within 1% (for temperatures greater than $500K$). For ammonia the quality of fit is not quite as good. For temperatures greater than $500K$ enthalpy values are reproduced within 1% and specific heat values within 6%. However, ultimately, the curve fits to specific heat values in table A.2 were not used with the reactor model program. The program calculates enthalpy changes by integrating the specific heat values available to it, hence it is important that the specific heat functions used are, the exact derivative of the enthalpy functions, thus quadratic curves obtained from differentiating the enthalpy curve fits in table A.1 were used instead.

Hydrogen and nitrogen viscosity data has been taken from Vargaftic (1983), values between $250K$ and $1200K$ for 100 atmospheres yielded the power fits given in table A.3. These fits both have correlation coefficients which differed from unity by less than 5×10^{-5}. Viscosity increases with pressure, however hydrogen viscosities vary by less than 1% over the range 1 to 200 atmospheres. Nitrogen viscosities vary by up to 3% over the same range. The fit for ammonia was based on the two dimensional linear fit quoted by Williams (1978*b*):

$$\mu = (0.15P + 0.368T - 25.5) \times 10^{-7} Nsm^{-1} \tag{A.4}$$

Thermal conductivity data was also taken from Vargaftic. The power fits in table A.4 cover temperatures in the range $450K$ to $1200K$ for 100 atmospheres. Correlation coefficients for the curves are greater than 0.995. Thermal conductivity increases with pressure and in this temperature range the variation between 0 and 200 atmospheres is up to 1% for hydrogen, 3% for nitrogen and 10% for ammonia.

Figure A.4 presents equilibrium mixture compositions for various pressures using data from Williams (1978*b*) and Vancini (1971). It can be seen that both sources are in reasonable agreement. There is some variation at low temperatures, however data in this region is of little importance. The reactor model program deduces equilibrium compositions from an exponential fit to an equilibrium constant based on partial pressures. Since the conditions encountered do not correspond to ideal gas behaviour, a characterisation of the reaction equilibrium with a fugacity based constant would be more appropriate. However a pressure based constant will yield the appropriate composition provided that it is also treated as a function of pressure. The equilibrium composition data from Williams plus the 10 atmosphere values from Vancini have been converted to corresponding values of the equilibrium constant for the reaction;

$$2NH_3 \rightleftharpoons N_2 + 3H_2 \tag{A.5}$$

using the relationship;

$$K_p = P^2 \frac{X_{N_2}(X_{H_2})^3}{(X_{NH_3})^2} = P^2 \frac{27}{16} \frac{\delta^4}{(1-\delta^2)^2} \tag{A.6}$$

where X are mole fractions.

Fitting these values as exponential functions of temperature for each pressure yielded the results of table A.5. The worst correlation coefficient is 0.994 for the 300 atmosphere

Coefficients in fit to enthalpy values ($kJmol^{-1}$)
$H = A + BT + CT^2 + DT^3$

Reactant	A	B	C	D
		100 atmospheres		
NH_3	1.368×10^{1}	6.984×10^{-2}	-2.085×10^{-5}	8.339×10^{-9}
$\frac{3}{2}H_2 + \frac{1}{2}N_2$	6.828×10^{1}	5.581×10^{-2}	5.383×10^{-6}	-2.399×10^{-9}
H_2	3.390×10^{1}	2.771×10^{-2}	2.673×10^{-6}	-1.191×10^{-9}
N_2	3.484×10^{1}	2.848×10^{-2}	2.747×10^{-6}	-1.224×10^{-9}
		125 atmospheres		
NH_3	4.666	9.830×10^{-2}	-5.091×10^{-5}	1.883×10^{-8}
$\frac{3}{2}H_2 + \frac{1}{2}N_2$	6.823×10^{1}	5.618×10^{-2}	4.940×10^{-6}	-2.146×10^{-9}
H_2	3.388×10^{1}	2.790×10^{-2}	2.453×10^{-6}	1.066×10^{-9}
N_2	3.482×10^{1}	2.867×10^{-2}	2.521×10^{-6}	-1.095×10^{-9}
		150 atmospheres		
NH_3	-4.569	1.276×10^{-1}	-8.207×10^{-5}	2.977×10^{-8}
$\frac{3}{2}H_2 + \frac{1}{2}N_2$	6.794×10^{1}	5.751×10^{-2}	3.309×10^{-6}	-1.420×10^{-9}
H_2	3.374×10^{1}	2.856×10^{-2}	1.643×10^{-6}	-7.049×10^{-10}
N_2	3.467×10^{1}	2.935×10^{-2}	1.689×10^{-6}	-7.245×10^{-10}
		200 atmospheres		
NH_3	-2.279×10^{1}	1.853×10^{-1}	-1.431×10^{-4}	5.112×10^{-8}
$\frac{3}{2}H_2 + \frac{1}{2}N_2$	6.805×10^{1}	5.747×10^{-2}	3.403×10^{-6}	-1.307×10^{-9}
H_2	3.379×10^{1}	2.854×10^{-2}	1.690×10^{-6}	6.489×10^{-10}
N_2	3.473×10^{1}	2.933×10^{-2}	1.737×10^{-6}	-6.669×10^{-10}
		250 atmospheres		
NH_3	-2.809×10^{1}	1.970×10^{-1}	-1.518×10^{-4}	5.311×10^{-8}
$\frac{3}{2}H_2 + \frac{1}{2}N_2$	6.807×10^{1}	5.807×10^{-2}	2.601×10^{-6}	-1.003×10^{-9}
H_2	3.380×10^{1}	2.883×10^{-2}	1.292×10^{-6}	4.983×10^{-10}
N_2	3.474×10^{1}	2.963×10^{-2}	1.328×10^{-6}	5.121×10^{-10}
		300 atmospheres		
NH_3	-3.351×10^{1}	2.093×10^{-1}	-1.610×10^{-4}	5.533×10^{-8}
$\frac{3}{2}H_2 + \frac{1}{2}N_2$	6.813×10^{1}	5.850×10^{-2}	2.007×10^{-6}	-7.835×10^{-10}
H_2	3.384×10^{1}	2.905×10^{-2}	9.964×10^{-7}	3.890×10^{-10}
N_2	3.477×10^{1}	2.985×10^{-2}	1.024×10^{-6}	-3.998×10^{-10}

Table A.1: Polynomial fits to enthalpy data.

Coefficients in fit to specific heat at constant pressure ($kJmol^{-1}K^{-1}$)
$C_p = A + BT + CT^2 + DT^3$

Reactant	A	B	C	D
		100 atmospheres		
NH_3	2.130×10^{-1}	-5.810×10^{-4}	6.796×10^{-7}	-2.569×10^{-10}
$\frac{3}{2}H_2 + \frac{1}{2}N_2$	5.437×10^{-2}	1.569×10^{-5}	-1.257×10^{-8}	1.876×10^{-12}
H_2	2.692×10^{-2}	7.767×10^{-6}	-6.227×10^{-9}	9.286×10^{-13}
N_2	2.799×10^{-2}	8.075×10^{-6}	-6.474×10^{-9}	9.654×10^{-13}
		125 atmospheres		
NH_3	3.393×10^{-1}	-1.004×10^{-3}	1.143×10^{-6}	-4.236×10^{-10}
$\frac{3}{2}H_2 + \frac{1}{2}N_2$	5.518×10^{-2}	1.362×10^{-5}	-1.095×10^{-8}	1.751×10^{-12}
H_2	2.732×10^{-2}	6.743×10^{-6}	5.420×10^{-9}	8.669×10^{-13}
N_2	2.841×10^{-2}	7.011×10^{-6}	5.635×10^{-9}	9.013×10^{-13}
		150 atmospheres		
NH_3	4.654×10^{-1}	-1.426×10^{-3}	1.607×10^{-6}	-5.901×10^{-10}
$\frac{3}{2}H_2 + \frac{1}{2}N_2$	5.604×10^{-2}	1.136×10^{-5}	-9.083×10^{-9}	1.533×10^{-12}
H_2	2.775×10^{-2}	5.625×10^{-6}	-4.497×10^{-9}	7.590×10^{-13}
N_2	2.885×10^{-2}	5.848×10^{-6}	-4.675×10^{-9}	7.891×10^{-13}
		200 atmospheres		
NH_3	4.143×10^{-1}	-1.183×10^{-3}	1.276×10^{-6}	-4.528×10^{-10}
$\frac{3}{2}H_2 + \frac{1}{2}N_2$	5.766×10^{-2}	7.239×10^{-6}	-5.846×10^{-9}	1.294×10^{-12}
H_2	2.855×10^{-2}	3.584×10^{-6}	-2.894×10^{-9}	6.405×10^{-13}
N_2	2.968×10^{-2}	3.726×10^{-6}	-3.009×10^{-9}	6.659×10^{-13}
		250 atmospheres		
NH_3	6.172×10^{-1}	-1.876×10^{-3}	2.055×10^{-6}	-7.384×10^{-10}
$\frac{3}{2}H_2 + \frac{1}{2}N_2$	6.119×10^{-2}	-5.394×10^{-6}	8.367×10^{-9}	-3.883×10^{-12}
H_2	3.030×10^{-2}	-2.670×10^{-6}	4.143×10^{-9}	-1.923×10^{-12}
N_2	3.150×10^{-2}	-2.776×10^{-6}	4.307×10^{-9}	-1.999×10^{-12}
		300 atmospheres		
NH_3	5.165×10^{-1}	-1.482×10^{-3}	1.575×10^{-6}	-5.535×10^{-10}
$\frac{3}{2}H_2 + \frac{1}{2}N_2$	6.461×10^{-2}	-1.757×10^{-5}	2.201×10^{-8}	-8.829×10^{-12}
H_2	3.199×10^{-2}	-8.697×10^{-6}	1.089×10^{-8}	-4.371×10^{-12}
N_2	3.326×10^{-2}	-9.042×10^{-6}	1.133×10^{-8}	-4.545×10^{-12}

Table A.2: Polynomial fits to specific heat at constant pressure data.

Viscosities AT^B (Nsm^{-2})		
Reactant	A	B
NH_3	3.781×10^{-8}	9.905×10^{-1}
H_2	2.048×10^{-7}	6.638×10^{-1}
N_2	6.618×10^{-7}	5.955×10^{-1}

Table A.3: Power fits to viscosities at 100 atmospheres

Thermal Conductivities AT^B $(wm^{-1}K^{-1})$		
Reactant	A	B
NH_3	7.418×10^{-6}	1.448
H_2	2.770×10^{-3}	.7382
N_2	7.509×10^{-4}	.6466

Table A.4: Power fits to thermal conductivities at 100 atmospheres

values. The largest errors occur below $500K$, where the fitted expression overestimates the original value by over 100% at 300 atmospheres. However this will only result in an

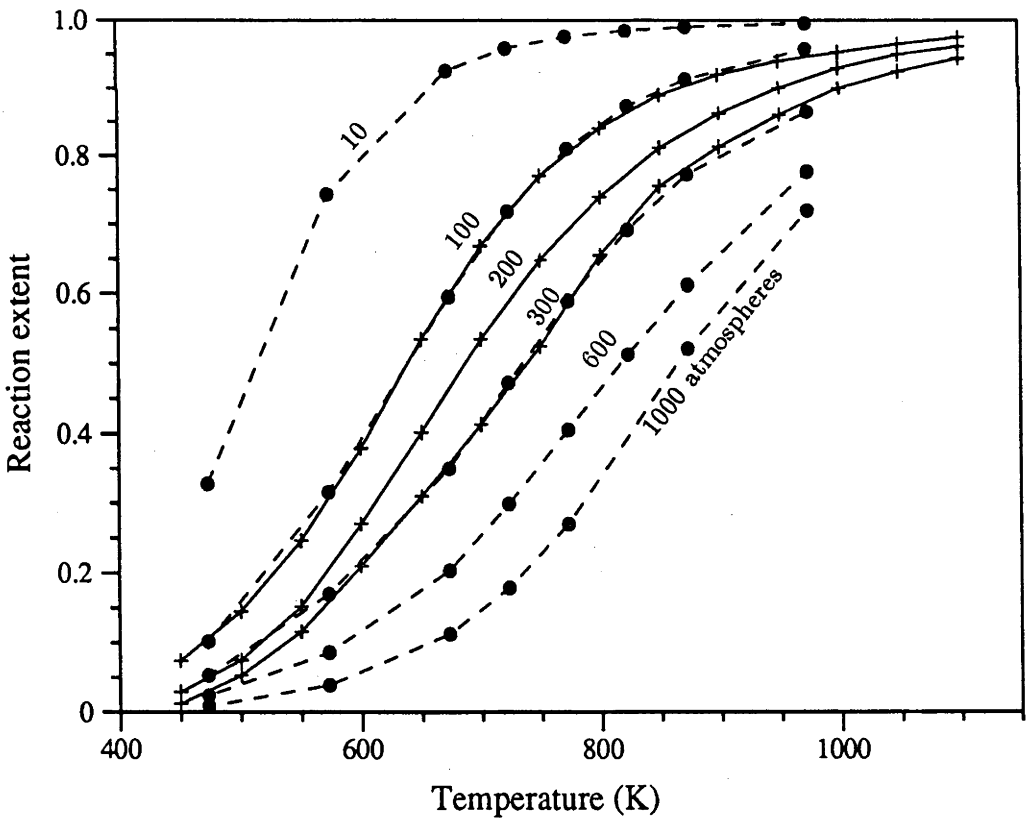

Figure A.4: Equilibrium mixture compositions from Williams (1978*b*) (+) and Vancini (1971) (•).

Equilibrium Constant $K_p = exp(A + B/T) atmos^2$		
Pressure (atmos)	A	B
10	27.271	-1.2475×10^4
100	26.847	-1.2372×10^4
200	29.165	-1.4168×10^4
300	30.567	-1.5445×10^4

Table A.5: Exponential fits to equilibrium constants.

over estimate of the equilibrium mass fraction by less than 50% under conditions when it is close to 0 in any case.

A.4 Data for Reaction Extent Calculations

Calculation of reaction extents from balancing separator measurements requires knowledge of the densities of the liquid and gas phases within the separator and the composition of the gas phase.

Ammonia liquid densities in the temperature range $280K$ to $380K$ and pressure range 2 to $20MPa$ were taken from Haar & Gallagher (1978). This data was subjected to a two dimensional least squares curve fit for use in the reaction extent calculation routine. The coefficients for the function used are given in table A.6, this function reproduces densities with an uncertainty of $\pm 1\%$. Hydrogen and nitrogen densities were taken from Vargaftic

Function component	Coefficient $(gcm^{-3})/(MPa^{-i}K^{-j})$
Const.	-1.185
T	-9.246×10^{-3}
P	-5.2466×10^{-3}
TP	2.060×10^{-5}
$T^{0.5}$	2.632×10^{-1}

Table A.6: Two dimensional fit to ammonia liquid density in the range $280K$ to $380K$ and 2 to $20MPa$.

(1983) and subjected to the same curve fitting procedure. For hydrogen, data in the range 280 to $400K$ and 4 to 20 MPa is reproduced to within 4% by the curve in table A.7. For

Function component	Coefficient $(gcm^{-3})/(MPa^{-i}K^{-j})$
PT^{-1}	.23798
P^2T^{-1}	-1.5209×10^{-3}
P^3T^{-1}	1.1273×10^{-5}

Table A.7: Two dimensional fit to hydrogen gas density in the range 280 to $400K$ and 4 to $20MPa$.

nitrogen, data in the range 280 to $380K$ and 2 to $15MPa$ is reproduced within 3% by the curve in table A.8.

Function component	Coefficient $(gcm^{-3})/(MPa^{-i}K^{-j})$
PT^{-1}	3.332
P^2T^{-1}	-1.0025×10^{-2}

Table A.8: Two dimensional fit to Nitrogen gas density in the range 280 to $380K$ and 2 to $15MPa$.

For mixtures of hydrogen and nitrogen the assumption was made that the interaction between hydrogen and nitrogen molecules would not be very different from the interaction between like molecules and thus the mixture density was taken as the molar average. For occasions where small amounts of ammonia gas were also present in mixtures, the density of the hydrogen nitrogen mix was corrected by scaling by the average molecular weight of the whole mix.

Gaseous mixture compositions have been determined from the phase equilibrium data embodied in Williams (1978*b*), dewline points for 100, 200 and 300 atmospheres. For the purposes of curve fitting, these points have been converted to effective vapour pressures on an ideal gas basis, and supplemented by vapour pressures from Vargaftic to extend them to lower pressures. Data in the temperature range 280 to $360K$ yielded the curve fit in table A.9, this curve reproduces the original points to within 1%.

Function component	Coefficient $(gcm^{-3})/(MPa^{-i}K^{-j})$
Const	1.055×10^{-1}
T	1.803×10^{-2}
T^2	-8.575×10^{-5}
T^3	-2.361×10^{-7}
T^4	1.1716×10^{-9}
P	5.155×10^{-1}
PT	-1.9495×10^{-3}
PT^2	-6.886×10^{-6}
PT^3	2.753×10^{-8}
PT^4	-1.0515×10^{-12}

Table A.9: Two dimensional fit to ammonia effective vapour pressure in the range 280 to $360K$ and 0 to 300 atmospheres.

A.5 Data for Efficiency Calculations

Second law efficiency and work recovery efficiency calculations use the derivatives $\frac{\partial G}{\partial \delta}(T, \delta)$ and $\frac{\partial H}{\partial \delta}(T, \delta)$. Linear interpolation from tables of derivatives derived from Williams' enthalpy and Gibbs free energy data proved unsatisfactory due to the amplification of round off errors and other sources of uncertainty by the derivative process. To produce smooth constant efficiency contours and to investigate the generation of optimised reaction paths required that the necessary derivatives be represented by continuous functions. Two dimensional curve fits were employed for this purpose.

The fits used are applicable to specific ranges of conditions. Table A.10 presents coefficients for $\frac{\partial G}{\partial \delta}(T, \delta)$ above the dewline. This fit was obtained from derivative values calculated from tabulated Gibbs free energy data for conditions above the dewline and for values of reaction extent less than 0.95, supplemented by extra equilibrium line values

derived from the fitted equilibrium constants. These fits reproduce $\frac{\partial G}{\partial \delta}(T, \delta)$ between

Coefficients for $\frac{\partial G}{\partial \delta}(kJmol^{-1}K^{-i})$			
Function component	100 atmos.	200 atmos.	300 atmos.
Const.	6.3056×10^{1}	6.0932×10^{1}	6.9754×10^{1}
δ	-9.2306×10^{1}	-7.8763	-5.3315×10^{1}
δ^2	2.2757×10^{2}	-1.1585×10^{1}	5.8821×10^{1}
δ^3	-1.5582×10^{2}	1.3874×10^{1}	-1.7215×10^{1}
T	-1.5338×10^{-1}	-1.4135×10^{-1}	-1.5185×10^{-1}
$T\delta$	3.8671×10^{-1}	2.5948×10^{-1}	3.4628×10^{-1}
$T\delta^2$	-7.2436×10^{-1}	-3.8133×10^{-1}	-5.2481×10^{-1}
$T\delta^3$	4.5787×10^{-1}	2.1863×10^{-1}	2.8520×10^{-1}

Table A.10: Two dimensional fit to $\frac{\partial G}{\partial \delta}(T, \delta)$ above the dewline, $0.05 \leq \delta \leq 0.95$.

$\delta = 0.05$ and $\delta = 0.95$ to within 5% of the correct values. Outside this reaction extent range the results are not valid as $\frac{\partial^2 G}{\partial \delta^2}$ should be infinite at $\delta = 0$ and $\delta = 1$, which is clearly not possible with this functional form.

The addition of the derived equilibrium line values to the input data ensured reasonable consistency between equilibrium lines obtained from $\frac{\partial G}{\partial \delta} = 0$ and by the contour of zero reaction rate produced using the intrinsic rate expression with an exponential fit to the equilibrium constant. For investigation of optimum exothermic reaction paths for reaction extents above 0.5, the alternative fits presented in table A.11 were used. These are based

Coefficients for $\frac{\partial G}{\partial \delta}(kJmol^{-1}K^{-i})$			
Function component	100 atmos	200 atmos	300 atmos
Const	2.1296×10^{1}	8.8283	1.9160×10^{1}
δ	1.8146×10^{1}	6.8263×10^{1}	8.7428×10^{1}
δ^2	1.4876×10^{2}	8.6896×10^{1}	-2.5422×10^{1}
δ^3	-1.4956×10^{2}	-1.2360×10^{2}	-3.2431×10^{1}
T	-5.4314×10^{-2}	-2.1959×10^{-2}	-4.4860×10^{-2}
$T\delta$	4.3119×10^{-2}	-9.110×10^{-2}	-5.1419×10^{-2}
$T\delta^2$	-3.2739×10^{-1}	-1.0529×10^{-1}	-6.2023×10^{-2}
$T\delta^3$	3.0800×10^{-1}	1.8656×10^{-1}	1.2003×10^{-1}

Table A.11: Two dimensional fit to $\frac{\partial G}{\partial \delta}(T, \delta)$ above the dewline, applicable for temperatures greater than $500°K$ and $0.05 \leq \delta \leq 0.95$.

on calculated derivative values for conditions above the dewline, with δ greater than 0.5 and less than 0.95, supplemented with extra equilibrium line values derived from the fitted equilibrium line constants. These fits give better consistency between the two equilibrium line derivations in this region of reaction extent, but are not valid for reaction extents less than 0.5.

Below the dewline, $\frac{\partial G}{\partial \delta}$ does not vary with temperature, it is also continuous across the

dewline, hence values below the dewline were deduced from the fits for conditions above the dewline, evaluated at the point of intersection with the dewline.

$\frac{\partial H}{\partial \delta}$ is discontinuous across the dewline, hence separate fits are required. Values below the dewline are reproduced to within 6% by the fits in table A.12. Values above the dewline are reproduced by the fits in table A.13 to within 10%.

Coefficients for $\frac{\partial H}{\partial \delta}(kJmol^{-1}K^{-i})$			
Function component	100 atmos	200 atmos	300 atmos
Const	5.4897×10^{2}	1.5541×10^{2}	1.5547×10^{2}
T	-3.5132	-6.8491×10^{-1}	-6.6643×10^{-1}
T^2	6.4010×10^{-3}	1.3435×10^{-3}	1.2678×10^{-3}

Table A.12: One dimensional fits to $\frac{\partial H}{\partial \delta}(T, \delta)$ below the dewline.

Coefficients for $\frac{\partial H}{\partial \delta}(kJmol^{-1}K^{-i})$			
Function component	100 atmos	200 atmos	300 atmos
Const	2.8519×10^{1}	2.6982×10^{1}	2.5300×10^{1}
δ^{-1}	8.2794	1.2597×10^{1}	1.5639×10^{1}
T	5.5433×10^{-2}	5.8558×10^{-2}	5.9368×10^{-2}
$T\delta^{-1}$	-1.9134×10^{-2}	-2.7661×10^{-2}	-3.2460×10^{-2}
T^2	-2.7322×10^{-5}	-2.7980×10^{-5}	-2.6845×10^{-5}
$T^2\delta^{-1}$	1.0585×10^{-5}	1.4740×10^{-5}	1.6581×10^{-5}

Table A.13: Two dimensional fits to $\frac{\partial H}{\partial \delta}(T, \delta)$ above the dewline,

Appendix B

Computer Software

A substantial amount of work was done during the course of this project on the development of computer software. The three areas of greatest significance were; the manipulation of thermodynamic data, the two dimensional reactor model and the optimisation of exothermic reaction paths. There was also a considerable number of less involved tasks related to the analysis of experimental data. All the software was developed using Fortran source code (with the exception of the program used for two dimensional curve fitting[1]) and compiled and run on various "DEC Vax" systems.

Listings of the Fortran source code and a detailed description of the input and output data formats for, the important applications, are given in two technical reports (Lovegrove 1992*b*, Lovegrove 1992*a*). The basic algorithms used are described here.

B.1 Thermodynamic Data Manipulation

As described in appendix A, the bulk of the thermodynamic data used for this project is based on the work of Williams (1978*b*). In addition to describing the origins of the data, he presents a listing of the Fortran code of a program which generates tables of selected thermodynamic properties for a given pressure input. This program has been converted to a subroutine (PROCGANEF) for use in conjunction with other subroutines and programs developed for this project. In this form the calling parameters include, in addition to the pressure, a number of arrays which allow the data produced to be passed directly to the calling program.

The thermodynamic data manipulation software is based around a set of subroutines which are used variously by programs for;

- returning individual values of thermodynamic properties from keyboard input of temperature and reaction extent;
- calculating constant efficiency and reaction rate contours;
- calculating optimum reaction paths.

The primary subroutine used (MAKETABLES), reads curve fit parameters for $\frac{\partial G}{\partial \delta}$, $\frac{\partial H}{\partial \delta}$, the equilibrium constant and the intrinsic reaction rate from a data file (if available). It then calls PROCGANEF twice to generate the basic enthalpy and Gibbs free energy

[1]Two dimensional least squares curve fits were obtained using a Pascal program developed by P.Bannister.

arrays and calls derivative subroutines DVDDELTABLE and DVDTTABLE, to generate arrays of the function derivatives.

Other subroutines return values of the required thermodynamic properties by various methods. Subroutines for enthalpy, Gibbs free energy and their derivatives with respect to temperature (FENTH, FGIBBS, FDHDT and FDGDT) use a linear interpolation subroutine (INTERPOL) which also takes into account the discontinuities which occur at the dewline. Subroutines for derivatives with respect to reaction extent and the intrinsic reaction rate (FDGDDEL, FDHDDEL and RATE) use the curve fit parameters read by MAKETABLES. Localised work recovery and exothermic and endothermic exergetic efficiency subroutines (FWREC, F2EFFEX and F2EFFEN) use calls to FDGDDEL and FDHDDEL. A path integral subroutine (FINTEGRAL) evaluates path integrals of $\frac{\partial G}{\partial \delta}$, $\frac{\partial H}{\partial \delta}$ or the inverse of reaction rate. FINTEGRAL requires a path specified as an array of temperature/reaction extent values, a finite summation is then performed over a linear path element between each point of the specified path. FINTEGRAL is used by EFFEXPATH and EFFENPATH to find the exergetic efficiency of exothermic and endothermic reaction paths and by VOLPATH to find the catalyst volume needed for the specified reaction path.

These routines are used extensively by the reaction path optimisation program discussed in section B.3. They are also used for producing thermodynamic quantity values at individual points and for the calculation of constant efficiency and reaction rate contours. The constant contour calculation is carried out by a program called EFFCONT. After input of the type and range of contour required, this program uses a simple iterative algorithm based on the progressive halving of a temperature interval to find the temperature of the contour at each reaction extent value considered.

B.2 Two Dimensional Reactor Simulation

The original Fortran source code for the implementation of the two dimensional pseudo-homogeneous reactor model was written by S.Parypatyadar of the University of Houston. It was written specifically for the steam reforming of methane, proceeding in the endothermic direction only. The geometry was restricted to the situation of heat supplied from an isothermal source to a reactor constructed from two concentric cylinders with the catalyst bed within the annulus. The program accounted for the simultaneous 'water gas shift' reaction by assuming that this second reaction was always at equilibrium. The numerous subroutines which implemented the semi-empirical correlations discussed in chapter 4 and calculated equilibrium reaction extents, average mixture properties, mole fractions etc were written with many of the actual values of parameters and stoichiometric coefficients within the code.

In the course of adapting the program for application to ammonia reactors, this author has made a number of generalisations and improvements. The program has been generalised to handle any two reaction system where one reaction is assumed to remain in equilibrium. This has been done by converting every relevant parameter, including stoichiometric coefficients, into variables which are read from a data file, together with all the necessary thermodynamic data and initial and boundary conditions. This task is performed by the subroutine DATAINPUT. Modifications have been made to allow other generalisations including the modelling of exothermic reactions and reactor geometries based on a single tube and series connections of multiple catalyst chambers. More importantly the assumption of an isothermal heat source outside the reactor wall has been replaced by the specification of an arbitrary temperature profile, flux profile or heat trans-

fer fluid (specific heat/temperature relationship specified), with the profile specified either as a polynomial or tabulated function of position along the reactor.

General improvements have included the correction of a number of minor bugs, reorganisation of the program structure and the addition of more thorough explanatory annotation within the source code.

There are many subroutines for the implementation of correlations and property calculations, these include:

- RATE - intrinsic reaction rate;
- CON2 - equilibrium conversion of the secondary reaction;
- EQUIL - equilibrium conversions for both reactions (uses CON2 for 2nd reaction);
- MODINT - modified Thiele modulus (uses RATE and CON2);
- RATER - extrinsic reaction rates (using RATE and MODINT);
- PROCAL - specific heat viscosity and thermal conductivities from polynomial curve fits;
- PRESUR - pressure from calculation of pressure drop for latest z increment;
- QCALC - adds to a sum of total heat flow for each z increment;
- NEWMFR - mole fractions of components from reaction extents;
- HEAT - effective thermal conductivity and wall heat transfer coefficient;
- AVDATA - areal averages of thermodynamic properties;
- T2ND - wall temperature or flux at each z according to profile specified.

The subroutine REATORSIMULATION is responsible for initialising many of the important variables, it in turn calls REACTR which carries out the actual step by step integration of the differential equations. When the integration is finished the subroutine DATAOUTPUT is responsible for producing the various output data files.

The integration of the differential equations is carried out using a chosen number of radial positions between the radius of the inner wall (which may be 0) and the radius of the outer wall. The conditions at each radial position are taken to represent the average of those of the annulus centred on it. Given the temperature and reaction extent at each radial position for a given position (z) along the reactor, all the associated properties are evaluated by calls to the appropriate subroutines, and values for $\frac{\partial T}{\partial z}$ and $\frac{\partial \delta}{\partial z}$ are calculated from difference equation approximations to the differential equations presented in chapter 4. The values obtained are used to extrapolate to the values of temperature and reaction extent at the next value of z. The conditions at the reactor walls are determined separately by using the wall boundary conditions. The original program used a fixed step size between z positions. An additional improvement initiated by the author was to replace this with a variable step size. At each step, the step size is now chosen such that the percentage change in temperature or absolute change in reaction extent (which ever is larger) equals a value specified in the input data file. Since conditions typically change much more rapidly in some sections of reactors than others, this change resulted in a much more time efficient execution for a given integration resolution.

The organisation of the program into data input and output and reactor simulation subroutines facilitated the construction of temporary program modules for repeated simulations of dissociator operation with the variation of a single variable (ie temperature, pressure or flow rate). This was achieved by repeated calls of REACTORSIMULATION after modifications to the variables in question.

B.3 Reaction Path Optimisation

The program OPTIMISE implements the dynamic programming algorithm described in chapter 6 using a number of subroutines. The initial inputs required are; the maximum and minimum reaction extents, the number of stages (reaction extent intervals) the number of temperature intervals, the maximum volume factor and the number of volume intervals. The subroutine BOUNDARIES establishes the region in which the optimum exothermic path must lie, by determining the position of the equilibrium line and the contour of maximum reaction rate, using a similar approach to that used by the program EFFCONT.

The calculation proceeds from the low reaction extent limit to the high limit. At each stage the temperature interval between the equilibrium line and the maximum rate (minimum required volume) contour is divided into the number of temperature intervals specified at the beginning. The available volume values considered are given by dividing the interval between the minimum required volume[2] and the maximum volume factor times this minimum value, in a logarithmic manner.

The solution of the optimisation problem is represented by the determination of the elements in a 'policy matrix'. This 3-dimensional matrix contains an element for each temperature and available volume combination considered at each stage. The elements are the optimum temperatures to use for the transition to the next lowest reaction extent value, from the temperature, reaction extent and available volume combination represented by the element's indices.

The policy matrix is built up by stage by stage operation of a subroutine (MAKFN) which calculates the functional relation values for the problem (ie the maximum values of exergetic efficiency possible, subject to the volume constraint). The recursive nature of the functional relation calculation (equation 6.7) is satisfied by the subroutine FNMI1 which uses linear interpolation on a matrix of previous stage functional relation values to return a value for any given previous stage temperature/available volume combination. MAKFN uses a simple 'interval halving' iterative maximisation algorithm to find the best temperature for each policy matrix element. The functional relation values are stored in a matrix which is used to replace the previous stage functional relation matrix at the end of each stage calculation.

When all the policy matrix elements have been calculated, subroutine BESTPATH is used to determine the actual optimum paths for a given available volume. BESTPATH uses FINDPATH, to find an optimum path for a specific starting temperature at the maximum reaction extent value by interpretation of the policy matrix. This is repeated by BESTPATH for various starting temperatures until the overall optimum path is found. FINDPATH starts at the maximum reaction extent with a specified starting temperature. It calculates the optimum temperature to adopt for the next lowest reaction extent value, by interpolation between the policy matrix elements which are closest to corresponding to the temperature available volume combination in question. This is repeated at the next

[2] At each stage the minimum required volume is that needed to make the transition back to the minimum reaction extent limit via the maximum rate contour.

reaction extent value after reducing the available volume by the amount required for the single interval transition.

Appendix C

Experimental Equipment

C.1 Data Acquisition and Control

The current combination of data acquisition and control equipment was assembled and installed simultaneously with the establishment of the new laboratory. The system comprises a "Chessell 4500" data acquisition unit, fifteen "Eurotherm 808" self-tuning PID temperature controllers, a safety protection system based on relays and solenoid valves, plus an IBM compatible personal computer with "Labtech Notebook" data acquisition software.

The Chessell unit and the Eurotherm controllers communicate with the PC via RS232 and RS422 serial communication lines respectively. The safety protection system is activated either by alarm signals from the Chessell or manually.

The purchase and assembly of this system followed a lengthy evaluation of alternatives. In addition to cost benefit considerations, this process involved a number of choices about the type of system desired. Choices included:

- systems remote from the PC versus systems based on internal plug-in input/output circuit boards;
- serial versus parallel communication for a remote system;
- separately implemented control functions versus PC software implementation.

The main feature of the system chosen is that the various tasks have been spread amongst three almost independent subsystems. This has advantages for safety, reliability and flexibility of application. The data acquisition unit is responsible for alarm level detection and fulfills this role independently of the PC or the controllers. The PC can collect data from either the data acquisition unit or the controllers or both. The data acquisition unit and the controllers both provide numerical displays independently of the PC. The system is modular and hence easily expandable and RS232 communication allows the remote location of the PC.

C.1.1 Chessell 4500 Data Acquisition Unit

The Chessell 4500 (Chessel Ltd 1990) is an expandable rack-based system with on board microprocessor and a choice of various input and output boards. The present system in the thermochemical laboratory incorporates four 15 channel analogue input boards and one 15 channel combination digital input/output board. The extensive configuration menus

are accessed either from a front panel or using an offline configuration program from the PC.

Configuration of analogue input channels involves choices of input type, conversion function, filter time constant, and scaling and offsets. Selection of thermocouple input and the appropriate linearisation function results in a displayed output in $°C$. A choice of reference junction type is also needed. With the current experimental arrangement, thermocouples are joined to twin-core shielded conductors at two locations, with the ambient temperature of these locations measured by two thermocouples terminated directly at Chessell inputs. For these two channels, 'internal' cold junction compensation is used. The other thermocouple channels use 'remote' cold junction compensation, with the Chessell making the correct compensation from the value of the nominated reference channel.

During the commissioning of the system this method of operation gave considerable problems: large variations in the output from channel to channel for a common input were observed when 'internal' compensation was employed. This was resolved by the manufacturer providing an improved input module. Systematic temperature measurement variations from this source are now less than $\pm 0.5°C$. Operation of 'remote' compensation was only successful after an upgrade to the current version 2.1 of the operating system.

DC inputs can be nominated either as volts or millivolts, in either case the signal should not exceed $10V$ with the non-attenuating input modules currently used. The significance of the choice of volts or millivolts is only a shift in decimal place for the Chessell, however the data acquisition software only captures measurements to two decimal places, leading to a loss of significant figures if volts are used inappropriately. The Chessell also has the facility for a number of user-defined linearisation functions. Scaling and offsets can be added via the appropriate selection of end values for 'input', 'function' and 'display' ranges.

All analogue input boards function independently, with every channel addressed by the Chessell's processor every two seconds, irrespective of the number of boards. The filter facility is implemented within the Chessell operating system, selection of a non-zero time constant results in an output that is updated many times a second. The appropriate choice of filter time constant would be approximately 25% of the data logging period used, however, the noise level of the signals measured has not been a limiting factor, so this facility was not used.

Currently a single digital output channel is employed for the emergency shutdown circuitry, alarms on appropriate channels trigger the digital output from active to inactive.

C.1.2 Eurotherm Temperature Controllers

The Eurotherm 808 temperature controllers are small self contained microprocessor based units. The features of these units and the configuration parameter list available to the operator via front panel operation is extensive (Eurotherm Corporation 1988).

All the units were purchased with 'time proportioning' triac outputs. With this system the control signal calculated from the proportional-integral-differential (PID) control algorithm is converted into a duty cycle for the AC voltage supplied to the heater. Zero crossing switching is incorporated to minimise harmonic noise and this limits the resolution of each cycle to one-half AC period per heater cycle period. The period of the heater cycle is one of the parameters chosen by the operator. The significance of the value chosen has been discussed in chapter 8, section 8.4.

For the dissociator heaters (with $5.2A$ peak current requirements), the $1A$ current limitation of the triac outputs was insufficient, so they were used to drive $25A$ solid state

relays. Similarly, the controllers needed for the synthesis reactor have been coupled to larger $10A$ triacs to satisfy the 3 - $4A$ peak current requirement.

Activation of the self tune facility during operation causes the controllers to produce a series of small amplitude step changes in power level. The built in software determines optimised parameters for the PID algorithm based on the system response. Although the operator may manually select the PID parameters, the self-tuning process resulted in very good temperature control for the experimental conditions encountered so far.

The RS422 communications facility provides access to the measured temperatures and the power level (as a percentage). The analogue-to-digital conversion process and subsequent update of the control signal are repeated every 125 milliseconds. A data acquisition prompt simply returns the most recent values determined. Similarly, the beginning of a heat cycle sees the most recently calculated control signal adopted. This approach unfortunately means that a large amount of error signal information is not used to determine actual power levels, and measured power levels only equate to actual power levels when averaged over an appropriate time scale. The significance of these points has also been discussed in chapter 8, section 8.4.

A number of the controllers incorporate extra features, including the possibility of choosing a linear input as a sensor type. With this option the unit becomes a generalised PID controller, not limited to temperature applications. The faster measurement frequency, compared to the Chessell system, has led to their use for data acquisition tasks involved in investigating faster transient behaviour of both millivolt and temperature signals.

C.1.3 Data acquisition Software

The Eurotherm and Chessell hardware is used in conjunction with an IBM compatible, 386 processor, personal computer running Labtech Notebook version 5.03. The Labtech Notebook package (Laboratory Technologies Corporation 1989) supports a wide range of hardware including RS232 communicating devices.

Version 5.03 of the package, however, can only produce one prompt string per communication port. To produce the series of prompt strings needed to address a range of channels in the Chessell 4500, and to combine the resulting reply strings, required the development of a protocol converter unit. Similarly conversion of a single RS232 prompt string into a series of strings addressing 808 controllers connected in parallel on an RS422 bus also required a protocol converter. The design and operation of these units has been described by Kelly (1989).

The package is menu based, operation requires the configuration of parameters for data channels, the screen display and files for data storage. A data channel is required for every variable, ie time, Chessell channel, 808 temperature value or 808 power value. Data channels corresponding to Chessell channels are "RS232 type", they use communications "port 1" and they must all share the same prompt string of the form; "$PVabcxyz%", where abc is the first Chessell channel to be polled, and xyz the last. The parsed start and stop positions, which identify which section of the reply string to use, are; $(n-1)\times 9+2$ and $(n-1)\times 9+8$, for the nth channel scanned (ie abc+n). 808 channels use "port 2", with prompt string; "$PVOPabxy%" where ab is the first controller polled and xy the last. Parsed start and stop positions for the nth controller in the sequence are; $(n-1)\times 18+4$ and $(n-1)\times 18+8$ for temperature and $(n-1)\times 18+13$ and $(n-1)\times 18+17$ for power.

Sample rate is limited by two factors, the rate at which the system can address channels and receive replies (largely determined by the protocol converter) and the buffer size for

data channels. The two ports are addressed independently and addressing the Chessell channels is usually the slowest process, approximately 0.1 second per channel is required. Asking for a higher than possible sample rate will cause the system to run as fast as it can, but to record time values incorrectly, as if it was working at the requested rate. If a small number of channels are measured at a relatively high rate the system may be unable to write to the hard disc and update the screen between measurements, in this case it will run until a data buffer overflows. Increasing the buffer size of all channels too far ultimately exceeds the memory allocation of the PC.

Different data channels may have different sample rates provided that all the channels which share the same port have the same rate and all the variables saved in a given data file share the same rate. This feature was used to improve the resolution of power measurements as discussed in chapter 8. Chessell channels were logged and recorded once every 20 seconds, but 808 channels were logged every 2 seconds, with a 10 measurement block average calculated channel recorded every 20 seconds. The results of the block averages were stored together with Chessell channels and a time channel in a single ASCI data file.

C.1.4 Emergency Shutdown Circuitry

The laboratory is protected by a circuit based around a series of relays and solenoid actuated valves, which disconnect heater power and prevent reactant flow in the absence of a $24V$ signal.

Heater power circuits have relays mounted in series with the solid state relays or triacs which are activated by the 808 temperature controllers. The air driven "Sprague" pump which fills the ammonia accumulator vessel with ammonia has a "Goyen" $240V$ solenoid valve in its air line, this solenoid is activated by a $24V$ relay. Reactant flow isolation is achieved with "Whitey SS-33VS4" ball valves operated by "Whitey MS-131-SR" spring return air actuators. These air actuators are supplied with air by "Festo" $24V$ solenoid valves. At present, ball valves operated in this way stop reactant flow at the outlet of the accumulator and at the exit to the gas disposal system. Two additional ball valves connected in a 'toggling' configuration to a single actuator are used for vent drain cycles of the balancing separator. This is not a direct safety function but it is intended to ultimately contribute to remote operation of the whole system.

The $24V$ supply can be broken by any one of four series connected switches. Three of these are 'panic button' switches, two within the experimental area and one in the lower level with the data acquisition computer. The fourth switch is a relay operated by a circuit based on the alarm driven output of the Chessell data acquisition system. The Chessell alarms are non-latching, although they do have the facility for providing up to 10% hysteresis. For safety purposes a latched system with manual reset is preferable. This has been achieved with a relay based circuit which incorporates indicator lamps and manual reset and override switches.

C.2 High Pressure Nitrogen Supply

The thermochemical laboratory makes extensive use of high pressure nitrogen gas for leak testing and as a buffer gas for pressure control applications. For these purposes, in addition to being inert and non-toxic, nitrogen has the obvious advantage that it is itself one of the reactants in the ammonia based system. This means that traces of nitrogen that enter the

reactor system (for example, by dissolving in liquid ammonia) are not a contaminant but simply a small shift away from a perfect stoichiometric mixture.

The system pressures encountered are close to or can exceed the pressure of bottled gas supplies. This, together with the relatively large volumes of gas consumed, led to the construction of an alternative source of high pressure nitrogen by Carden (1984*a*).

The system is based on a high pressure pumping system for liquid nitrogen. This approach benefits from the ready availability of liquid nitrogen and the reduced work input required for the compression of the liquid phase. The pump consists of a small bore piston driven, via a long connecting shaft, by a double acting air driven piston. Reciprocating motion is achieved with mechanical limit switched air control valves. The pumping piston does not have a sealing ring but instead relies on close tolerance construction for successful operation. The pump is supplied by liquid nitrogen from a 170 litre dewar via a tube running to a small manifold feeding an inlet non-return valve. Compressed liquid leaves via a second non-return valve and then passes through coils in a temperature controlled water bath maintained at approximately 60°C.

The pump body and a number of coils of the inlet tube are kept immersed in liquid N_2 in a vacuum flask. The liquid N_2 in this flask is at atmospheric pressure in contrast to the pressure at inlet to the pump, which remains at the supply dewar pressure. As pointed out by Carden, the boiling liquid in the flask will be at a lower temperature than the pressurised liquid in the dewar. As a result, the inlet line to the pump is cooled further, so helping to prevent cavitation during the throttling process which occurs through the inlet valve.

The N_2 dewar supply pressure can be adjusted through the operation of a 'pressure buildup' valve on the dewar manifold. This valve determines the rate at which heat can be admitted to the dewar, via heat exchange tubing mounted near its outer skin, to increase the vapour pressure. To avoid cavitation by the pump, an inlet pressure greater than approximately $280kPa$ is necessary.

It is extremely important to exclude any moisture from the internal sections of the pump. To ensure this, reticulated dry nitrogen 'boil-off ' gas from a bulk supply vessel is blown into the vacuum flask and through the pump, via the inlet line assembly, during shutdown and prior to start up. It is particularly important to maintain the inside of the pump at above atmospheric pressure so that any moisture which does precipitate around the top of the pump cannot run down the close tolerance seal.

When the dewar is removed for refilling, the connecting hose is also back flushed with dry nitrogen via the pump inlet line. Failure to remove all moisture can result in one or other of the non-return valves not operating properly on start up, necessitating completely reheating and flushing the whole system.

A typical start up procedure involves:

- filling the vacuum flask with liquid nitrogen;
- allowing 5–10 minutes for the pump assembly to reach thermal equilibrium;
- shutting the dry nitrogen connection to the inlet line to prevent back flow of liquid;
- opening the connection from dewar to inlet line and ensuring that the dewar pressure is high enough;
- opening the compressed air regulator to begin pumping.

For a given nitrogen gas pressure at system exit and pumping frequency, the amount of leakage from the close tolerance seal is approximately proportional to the downstroke

duration. For this reason the pressure differential across the air driven piston for the downstroke, is kept as high as possible. A regulator setting of $400kPa$ is used, this is slightly below the supply pressure, so that variations in supply pressure do not alter the pump performance. With the downstroke air pressure difference kept constant, stroke repetition rate is controlled by an air-throttling valve which reduces the rate at which air leaves the upper side of the driving piston during the upstroke. Operated in this manner, the pump can run continuously with stroke rates between 0 and approximately $1Hz$.

The vacuum flask must be kept full of liquid nitrogen, during the first half hour of operation, an occasional refill is required. As peripheral parts of the apparatus gradually cool, a point is reached where the leakage past the close tolerance seal is usually sufficient to keep the vacuum flask filled.

The high pressure nitrogen supply system was installed and recommissioned in the new thermochemical laboratory in mid-1989. Initially some work was required to achieve the performance originally reported by Carden. The inlet valve and seat required lapping with fine abrasive paste to remove corrosion damage resulting from past residual moisture. It was also necessary to renew the seal coupling the inlet line to the inlet manifold on the base of the pump body. Following this work and some improvement in the systematic approach to the exclusion of moisture, the pump performed well.

The air drive piston and cylinder assembly has, at times, not operated smoothly. Dismantling this assembly revealed corrosion damage to the cylinder wall from moisture in the compressed air supply. Polishing with abrasive paper and relubricating was sufficient to return to smooth operation. However, care must be taken to regularly drain the water from the air regulator moisture trap and to ensure adequate lubrication from the oil feed unit attached to the regulator.

The balance of the high pressure nitrogen supply system comprises:

- an electrically-heated water bath in which high pressure nitrogen liquid is converted to gas with heat exchange tubing;
- a dead-weight pressure relief valve with blow off pressure set by a series of calibrated weights;
- a 2-litre 'buffer' pressure vessel.

During an experimental run, gas is drawn from the buffer vessel via high pressure regulators as needed. The buffer remains at the pressure determined by the relief valve, which is kept at the point of blow off via appropriate adjustment of the pump stroke rate.

C.3 Mass Flow Determination

C.3.1 Introduction

For thermochemical experiments, determination of inlet mass flow and exit mixture composition are the most fundamental measurements required. For experiments with the dissociation reactor, this required measurement of the inlet flow rate of liquid ammonia and a determination of the liquid fraction of the two phase mixture of cooled reaction products. Both of these areas have been addressed in the past by the ANU group.

Whelan (1979) developed a rotary flow meter for measurement of liquid ammonia flows. However, the ammonia supply arrangement used for this project, involving progressive displacement of liquid ammonia from the prefilled accumulator vessel, caused problems with this instrument. Consuming all the ammonia in the accumulator allows the nitrogen

buffer gas to flow through the system, whilst this does no harm to the reactor or other components, the consequences for the rotary meter are disastrous. The design of the device relies on the viscosity of the liquid to keep the rate of revolution of the turbine wheel low and proportional to the mass flow rate. Operation with gas results in overspeeding and very quickly destroys the needle and seat bearings.

For this reason the use of the rotary flow meter was suspended until a level detection device could be developed for the accumulator to provide protection against complete liquid loss. Ultimately, an electronic level probe was developed which provided an analogue signal proportional to liquid level. This detector itself has sufficient resolution to determine inlet flow rates and was used for this purpose for later runs.

Carden (1982*c*) identified the need for a device which would provide an absolute measurement of masses of liquids and gases and integrate liquid flow rates. This led to the construction of a balancing separator (Carden 1982*a*). This device, which is essentially a small pressure vessel on a beam balance, satisfied most of the mass flow determination requirements for this project. In particular, it was used to calibrate inlet ammonia mass flow rates prior to heating the dissociation reaction, and during runs it provided a continuous measurement of the liquid component of the cooled reaction products.

Prior to the installation of the electronic level probe, experiments were conducted under conditions of close to constant inlet flow rate. Inlet flow rate was calibrated with the balancing separator and then corrected according to any subsequent variation in pressure drop across the metering valve.

For the nitrogen flow experiments, none of these techniques were appropriate. For these tests three "Gilmot rotameters" were connected after the exit throttle valve, to measure gas flow rates at atmospheric pressure.

C.3.2 The Balancing Separator

Figure C.1 illustrates the construction of the balancing separator. A $358cm^{-3}$ pressure vessel and a moveable counterweight are attached to a balance beam on opposing sides of a fulcrum. The vessel has three connections, via flexible helices of small bore stainless steel tubing, to an external fluid handling system. As shown, these connections are to a drain port at the bottom of the vessel, an exit port at the top of the vessel, and an inlet port taken to approximately half way down the interior of the vessel.

In the event of a change in mass within the vessel, motion of the beam is constrained by a spring constant provided by two torsion bars in line with the fulcrum and the combined effect of the tubing helices, plus two oil-filled damping arms. The balance beam is fitted with a sliding counterweight moved by a motor driven screw. A control circuit which uses an electronic proximity sensor on the balance beam can return the beam to its equilibrium position via motion of this counterweight. Indication of net vessel mass is provided either by a voltage reading from the proximity sensor on the balance beam (with the counterweight fixed) or via a counter mounted on the screw thread which moves the counterweight. These two modes of operation have been refered to by Carden as dynamic and static mode operation respectively, reflecting their vastly different response times.

Testing and calibration of the balancing separator was carried out using ethanol as a density reference. The details of the experimental method and the analysis of the results for both the static and dynamic modes of operation are described by Lovegrove & Hall (1990).

For the dissociation experiments described in chapter 8, the unit was used in its dynamic mode, with the voltage signal from the proximity sensor recorded and converted to

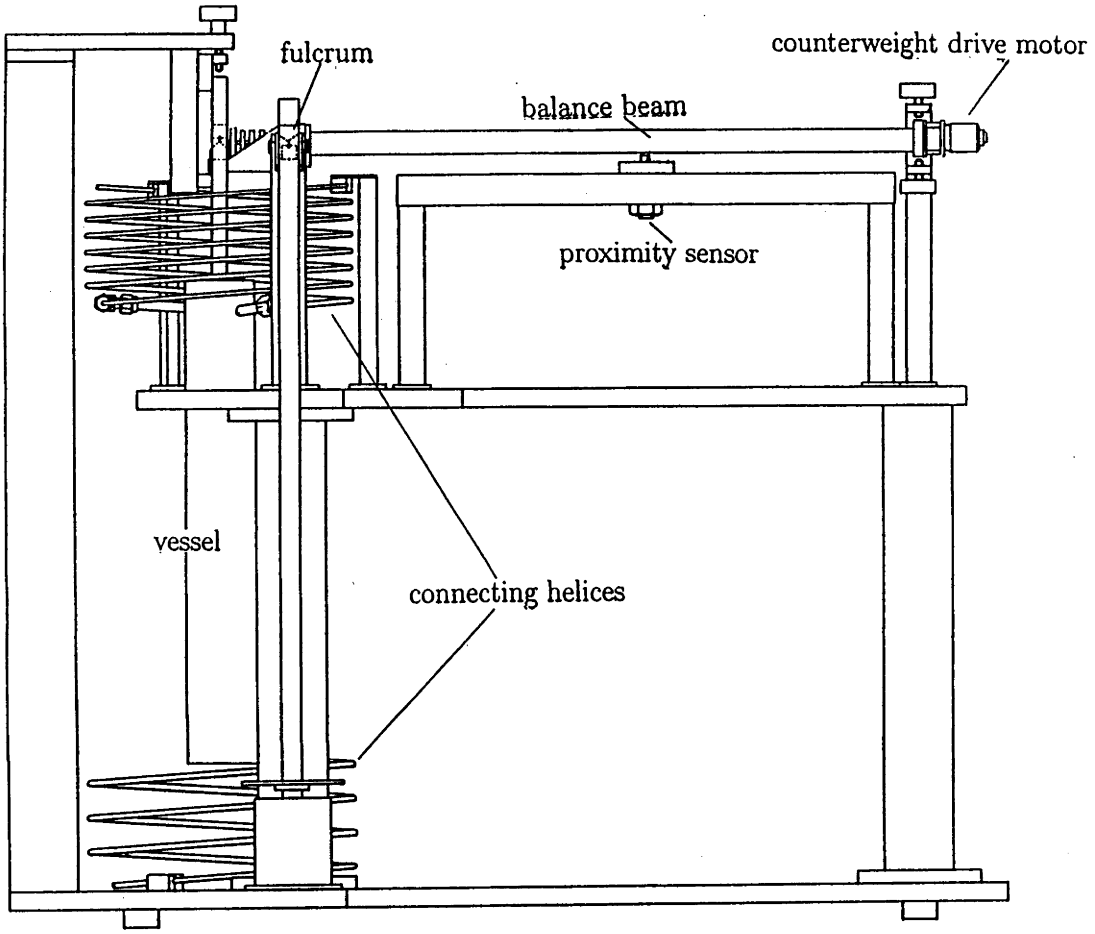

Figure C.1: Construction of the balancing separator.

a mass signal by the data acquisition system. The results of the calibration process for the dynamic mode of operation are summarized here.

For dynamic mode operation, the counterweight is left in a fixed position and the proximity sensor provides an analog signal which reflects the displacement of the balance beam. The beam displacement is determined by the equilibration of torques associated with extra mass in the vessel and the combined elastic forces from the torsion bars and helical coils. Provision has been made to position the transducer at positions between $120mm$ and $403mm$ from the fulcrum. Moving the transducer away from the fulcrum increases the sensitivity of mass measurement at the price of a reduced mass range covered within the transducers operating region.

The balancing separator employs a "Bentley Nevada model 3100N" inductive proximity sensor to measure balance beam displacement. The signal from this sensor saturates at $0V$ at the minimum displacement limit of its operating range and at close to the supply voltage at the maximum displacement limit. In its normal operating range there are significant deviations from linear behaviour.

The transducer response was measured in situ with the transducer positioned $402.7mm$ from the fulcrum. The balance beam was progressively displaced using one of the clamping screws and the resulting displacement measured with a "Mercer" dial gauge. To provide the required conversion of sensor voltage to absolute displacement, the results were subjected to least squares curve fitting to give displacement as a polynomial function of sensor voltage within the normal operating region. The result of a fifth order polynomial fit to

j	a_j $10^{-4} in V^{-j}$	b_j $10^{-4} in$
0	1.4911×10^2	1.5054×10^2
1	28.135	3.695×10^2
2	11.1613	1.7293×10^3
3	-2.2677	-4.5071×10^3
4	0.18024	4.5685×10^3
5	-5.0708×10^{-3}	-1.6361×10^3

Table C.1: Coefficients in Polynomial curve fits: Displacement $= \sum_{j=0}^{5} a_j$ (volts)^j and Displacement $= \sum_{j=0}^{5} b_j$ (relative signal)^j

points between $0.05V$ and $12.51V$ is given in table C.1. This fit has a regression coefficient which differs from unity by less than 3×10^{-4}. Table 3 also gives normalized values obtained by dividing signal voltages (minus the zero offset voltage) by the saturation voltage, thus removing any instrument dependent systematic error.

A number of calibration tests were carried out using ethanol, with the proximity sensor in four different positions. In each case the initial displacement was brought as close to zero as possible by adjusting the position of the counterweight. The measurements were normalized with respect to saturation and offset voltages, then converted to displacements using the conversion function in table C.1.

The linearity of the results obtained, supported the implicit assumption that the elastic forces associated with the balancing separator obey Hook's Law within the range of the sensor and also that the variation of the beam angle/displacement relationship with distance from fulcrum, does not significantly affect the signal/displacement relationship. Least squares linear fits were made to the linear regions of the transformed data and the slopes were used to calculate values for the constant:

$$C_d = \frac{displacement}{mass \times l} \tag{C.1}$$

where l is the distance between the fulcrum and the proximity sensor. Taking the mean of the values, weighted by the inverse of their squared uncertainties, yielded a final result of;

$$C_d = (27.129 \pm 0.054) \times 10^{-7} in g^{-1} mm^{-1} \tag{C.2}$$

This corresponds to a spring constant of $5.89\ N mrad^{-1}$.

Given the normal operating range of the sensor of (140 to 600) $\times 10^{-4}$ in, the mass range will depend on distance from fulcrum according to;

$$\text{mass range} = \frac{1}{l} \times (16.96 \times 10^3 g\ mm). \tag{C.3}$$

The trade-off for decreasing l to improve the mass range is an increasing uncertainty in mass determination (Δm) for a given sensor voltage resolution (ΔV), ie;

$$\Delta m = \frac{\Delta V}{l} \times (1.4 \times 10^{-3} g\ mm\ V^{-1}). \tag{C.4}$$

For the duration of this project the sensor was kept at the maximum possible distance from the fulcrum, in order to get the largest possible mass range.

It should be noted however, that since the effective spring constant of the system is a result of a combination of the torsion bars and the connecting helices, interference with either will result in the need for re-calibration.

C.3.3 The Electronic Level Detector

The electronic level detector exploits the large difference in the dielectric constants of liquid ammonia and nitrogen buffer gas. The first prototype comprised a $5mm$ o.d. stainless steel rod inserted longitudinally within the accumulator vessel. The capacitance between the rod and the vessel wall varied with the mean dielectric constant within the vessel, which is linearly dependent on the level. Both electrodes were in contact with the ammonia. A modified circuit based on the diode pump arrangement of Rutt & Bonilla (1975) was developed[1]. This circuit was expected to be insensitive to the moderate leakage resistance expected from conduction within the ammonia. Although limited success was achieved with this design, the circuit proved to be affected by the magnitude of the leakage resistance. The apparent conductivity of the ammonia also behaved in a manner which was not fully understood.

As a consequence of this problem, a second prototype was developed with the centre electrode electrically insulated from the ammonia within a teflon sleeve. The limited size of the entry ports to the accumulator did not permit this method of construction within the accumulator itself. Instead the arrangement shown in figure C.2 was adopted. The level detector is now an external device consisting of a $12.5mm$ o.d. $8.5mm$ o.d. mild steel tube with a concentric, teflon sheathed, $4mm$ diameter stainless steel electrode. The level detector is connected to the accumulator at the top and the bottom.

Both prototypes were constructed with the centre electrode divided into two, with a $100mm$ long reference element positioned near the bottom. The intention was that the reference electrode would remain immersed in liquid and provide a signal which would vary with changes in the dielectric constant caused by temperature or other variable factors. This signal would then provide the information needed to convert the level measurement signal to a height.

In practice, both empty and full signals from both capacitance elements were observed to vary by a few percent on an hourly time scale. The factors responsible for these variations have not been properly identified. On some occasions, proportional variations in the signals from the two elements were observed, however apparently uncorrelated variation was also observed. As a result the reference element proved of little use. The best results were obtained by ensuring the detector passed through at least one full-to-empty cycle during the course of an experimental run. The empty and full signals were then used for normalisation.

Prior to installation in the laboratory, both the capacitance measurement circuit and the complete unit were calibrated. The circuit was calibrated with a manually varied air plate capacitor working over the expected range of values of 0.05 to $40.4nF$. A least squares fit to the results gave:

$$\text{Signal} = (15.448 \pm .016)V/nF \times \text{Capacitance} + (2.959 \pm .004)V. \qquad \text{(C.5)}$$

[1]The level detector was designed and constructed by R.Whelan, J.Thompson built and tested the circuit and performed some of the calibrations.

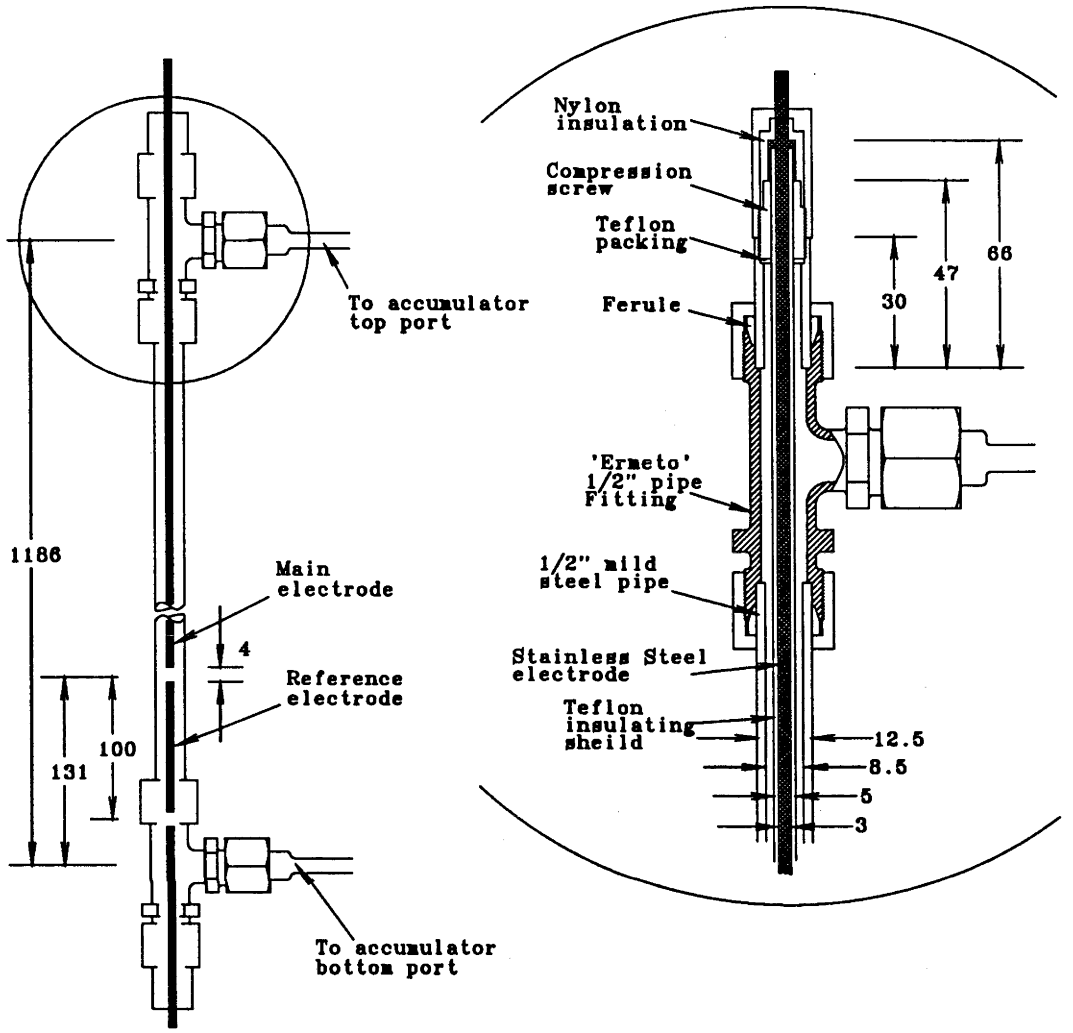

Figure C.2: Construction details of the electronic level detector.

The detector and circuit were calibrated using ethanol in the accumulator vessel. Ethanol levels were measured in a transparent sight tube fixed to the side of the accumulator. The level was varied by addition and removal of ethanol through the bottom port. Figure C.3 shows the results of the calibration performed on the 28th of April 1991. The deviation from linearity is attributed to distortion of the centre electrode during the assembly process. Consequently any subsequent dismantling and reassembly would require a recalibration. Table C.2 gives the coefficients in the fourth order polynomial fit (correlation coefficient greater than 0.999) used for linearizing measurements made from the 28th of April 1991 onwards, this polynomial is also plotted in figure C.3.

The combination of the accumulator vessel and the level detector tube provide a storage volume of approximately 2 litres, with a volume to length ratio of $(1.9062 \pm 0.0005) cm^3 mm^{-1}$.

At the top end of the accumulator, the level detector continues to read a variation as the liquid level rises above the end cap and into the connecting tubing. If care is taken to maintain the system at constant pressure during and after filling, the full signal

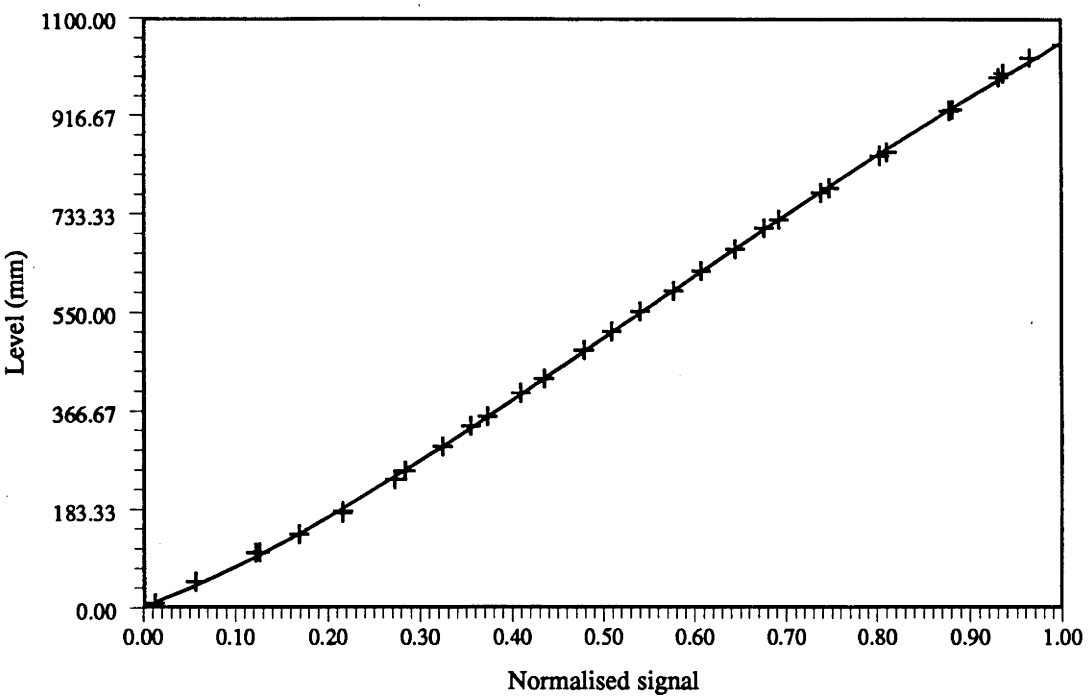

Figure C.3: Calibration curve for the electronic level detector as measured on the 28th of April 1991.

	$L = a_1 + a_2S + a_3S^2 + a_4S^3 + a_5S^4$ (mm)
a_1	2.5620
a_2	6.1942×10^2
a_3	1.288×10^3
a_4	-1.2694×10^3
a_5	4.1489×10^2

Table C.2: Polynomial fit to level (L) as a function of normalized signal (S).

obtained will correspond to a liquid level at the top internal diameter of the manifold tube which connects the level detector to the accumulator. Measurements for the purpose of calculating mass flow are only made with the liquid level within the main volume of the accumulator.

For calculation of mass flows during dissociation experiments, the density of liquid ammonia was determined from the pressure upstream of the flow metering valve and the temperature measured at the inlet to the heat exchanger, using the data presented in appendix A.

The noise associated with the circuit and the data acquisition system is such that2 three measurements in the space of one minute are sufficient to give a signal measurement with an uncertainty of less than 0.5%. The unpredictable drift reflected in changes in the full and empty signals used for normalisation contributed an uncertainty of 1% to level values. The major source of uncertainty in ammonia mass flow determinations is that associated with linear fitting to limited numbers of level values.

C.3.4 Gilmot Rotameters

A rotameter is a variable orifice area flow meter. The variable area orifice is formed by a float which moves in a vertically mounted tapered tube. For a given flow rate, the equilibrium position of the ball is that at which the drag forces balance its weight.

Three "Gilmot" rotameters of different capacity were used for measurements of nitrogen gas flow rates. Each instrument is supplied by the manufacturer with a calibration chart which relates diameter ratio (γ_R) to the scale readings marked on the side of the tube. A correlation chart which relates flow coefficient (C_R) to the Stokes (N_{ST}) number is also provided.

The Stokes number is given by:

$$N_{ST} = 1.042 \frac{m_f(\rho_f - \rho)\rho}{\mu^2 \rho_f} \gamma_R^3 \tag{C.6}$$

where m_f is the float mass in grams, ρ_f the float density (gcm^{-3}), ρ the fluid density (gcm^{-3}), and μ the fluid viscosity (centipoise). With the flow coefficient determined, the mass flow ($\dot{m}$) is given by:

$$\dot{m} = 0.238 \rho d_f C_R \sqrt{\frac{g m_f(\rho_f - \rho)}{\rho_f \rho}} \gamma_R \left[\frac{\gamma_R}{100} + 2\right] \tag{C.7}$$

where d_f is the float diameter and g is the acceleration due to gravity. The accuracy claimed by the manufacturer is 2.0% or one scale division, whichever is greater.

The appropriate parameters for the three rotameters used in the thermochemical laboratory are given in table C.3.

Size	Serial Number	ρ_f (gcm^{-3})	m_f (g)	d_f (in)
3	D–738	2.53	0.339	0.250
4	B–959	2.53	1.142	0.375
5	B–560	2.53	2.715	0.500

Table C.3: Gilmot rotameter specifications.

For the nitrogen flow runs the appropriate rotameter was chosen in each case to keep readings near the upper half of the scale. The exiting gas was vented at atmospheric pressure and its temperature measured with a J-type thermocouple. As discussed in appendix A, nitrogen viscosities and densities were taken from Vargaftic (1983). Combining uncertainties associated with the reading and calculation process, and density and viscosity determinations with the 2% calibration accuracy, yielded figures with a 3% uncertainty.

C.3.5 Mass Flow Measurement via Pressure Drop

The needle valve used for inlet flow rate control for steady state experiments was a "Whitey SS-22RS4" unit fitted with a micrometer handle. The manufacturer claims that mass flow through this valve is determined by;

$$\dot{m} = C_v \rho \left(\frac{\Delta P}{SG}\right)^{0.5} \tag{C.8}$$

where ΔP is the pressure drop across the valve, and SG the specific gravity of the fluid. The flow coefficient (C_v) for this valve has a maximum value of $0.007 GPM_{(water)}/(psi)^{.5}$ and is claimed to be linearly proportional to the number of turns from closed.

The mass flow characteristics of the valve where investigated using the balancing separator for absolute mass flow measurements. Investigation of the effect of valve position at constant pressure indicated that the relationship departed from linearity near the fully closed position. At other positions there was considerable fluctuations from the apparently linear behaviour. These were attributed to the scoring damage observed on the valve needle on occasions when it was dismantled. Since no attempt was made to rely on valve setting to deduce mass flow, these variations were not important.

The results of an investigation of the effect of pressure drop on mass flow with a valve setting of 0.35 turns from closed, are shown in figure C.4. They support the validity of the square root dependence on pressure drop, a least squares fit gave a value for $\Delta P^{0.5}/\dot{m}$ of $2.25 MPa^{0.5} g^{-1} s$. On the basis of this investigation, mass flow for early experimental runs was deduced by limiting a run to a single valve and pressure setting combination, precalibrating the inlet mass flow using the balancing separator and then correcting this initial value according to any small variations in valve pressure drop measured.

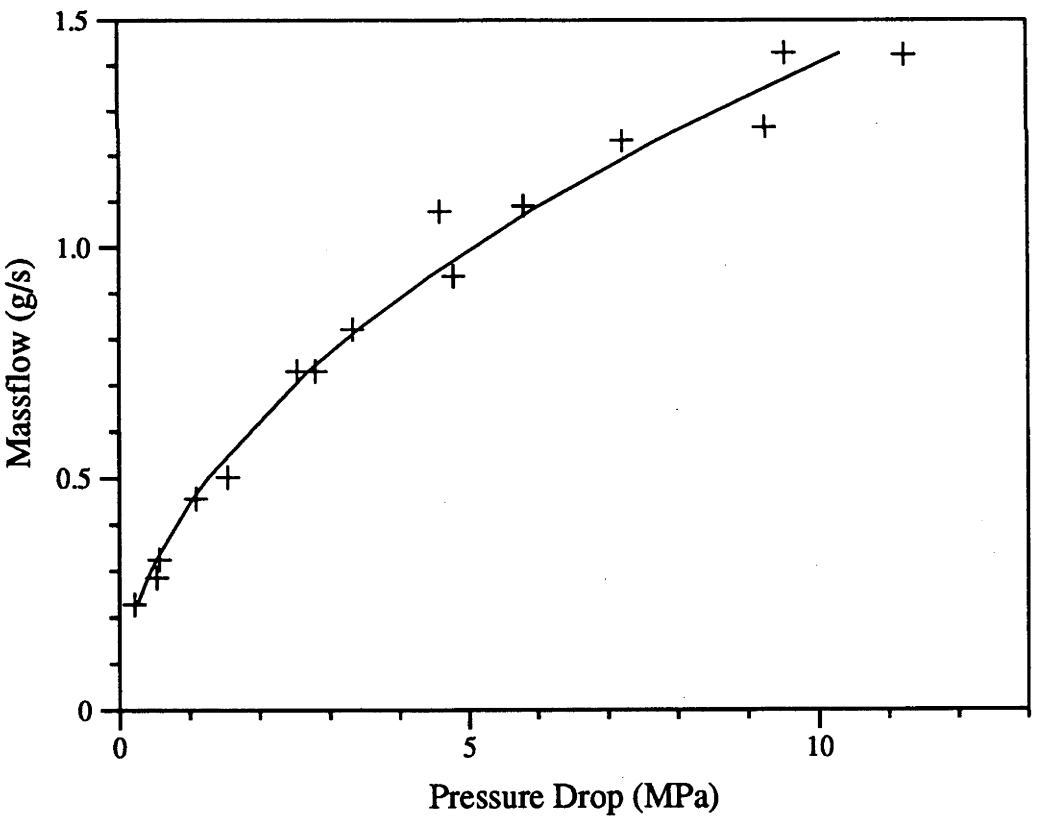

Figure C.4: mass flow pressure relationship for Whitey SS-22RS4 valve at a setting of 0.35.

C.4 Pressure Measurement

At the commencement of this project the thermochemical laboratory had three "Tyco model AB" semiconductor strain gauge pressure transducers. From the beginning of 1991 these were supplemented by the purchase of four "data instruments mediamate" semiconductor strain gauge pressure transducers.

These transducers have been marked as 1 through to 7 to identify them for calibration purposes. Both types of transducer share the same power supply range and wiring details. They produce a millivolt output that nominally varies linearly with both pressure and supply voltage.

During June 1990, transducer number 1 was tested and calibrated to AS1349 (Budenburg Gauges Pty Ltd 1990). The test report gives a signal voltage pressure dependence for a 5.035 V supply of;

$$V_{\text{signal}} = (0.00293\ mV/kPa)\ P - 1.3148\ mV \tag{C.9}$$

with an uncertainty from combined random and systematic sources of less than 0.25% of full scale reading. This relationship is equivalent to;

$$P = (0.3413 \pm 0.0009) MPa/mV \times V_{\text{signal}} + (0.449 \pm 0.045) MPa. \tag{C.10}$$

Subsequently transducer number 1 was used to calibrate the others. The results of a progressive reduction in pressure from $20 MPa$ to 0, are shown in figure C.5. All the transducers shared a Hewlett Packard power supply unit adjusted to $5.035V$ to match the calibration conditions of transducer number 1. Least squares linear fits yielded the results in table C.4.

		Coefficients for $P = A \times V_{\text{signal}} + B$	
Transducer	Chessell Channel	$A\ (MPa/mV)$	$B\ (MPa)$
1	3	0.3413 ± 0.0009	0.449 ± 0.045
2	4	0.3340 ± 0.001	0.6486 ± 0.014
3	5	0.3292 ± 0.001	0.3092 ± 0.008
4	-	0.6653 ± 0.002	0.3048 ± 0.028
5	11	0.6736 ± 0.009	0.9465 ± 0.14
6	15	0.6611 ± 0.002	0.3304 ± 0.028
7	14	0.6688 ± 0.002	0.6327 ± 0.0022

Table C.4: Coefficients for linear fits to pressure transducer calibration curves for a $5.035V$ Supply.

The uncertainties in these values are a combination of the effect of the 0.25% uncertainty in pressure determined with transducer 1 and the statistical uncertainty in the least squares fit. Although this calibration process indicated uncertainties in measured pressures would potentially be less than 1%, experience showed that the offsets differed relative to each other on a long term basis. To compensate for this, a period of no flow pressure equalisation was included during experimental runs. The signals recorded during these periods were used to determine an offset correction relative to the mean for each transducer. The estimated systematic uncertainty in pressure measurements following a recalibration by this method is $\pm$ 1%. A statistical uncertainty considerably less than

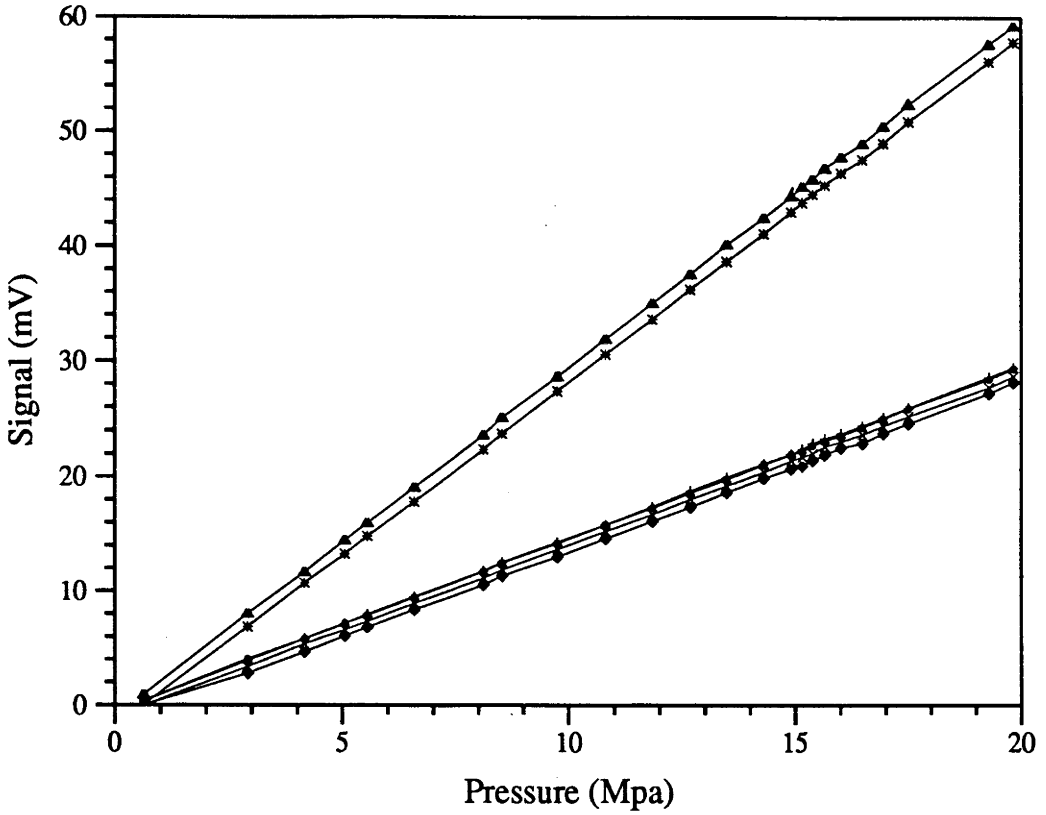

Figure C.5: Calibration curves for transducers 2 ($\star$), 3 ($\triangle$), 4 ($\bullet$), 5 ($\diamond$), 6 ($\times$) and 7 (+), obtained with pressure measurements from transducer 1.

this was easily achieved during steady state measurements, so the systematic contribution dominates the uncertainties in pressure measurements.

For pressure difference measurements, the 1% systematic uncertainty being common to all transducers, transfers to pressure differences as a percentage rather than an absolute error. The statistical uncertainties from two separate transducers, however, must be combined in the usual manner and usually dominate the systematic contribution for a pressure difference measurement.

Pressure drop measurements across the dissociator plus heat exchanger were provided by a transducer at exit and inlet and also by a "Validyne DP303-30" differential pressure transducer (Serial No 41913) connected between inlet and exit. The differential pressure transducer is a variable reluctance design, functioning through small deflections of a stainless steel diaphragm mounted between two coils. It was used in conjunction with a "Validyne CD223" transducer indicator which provided a panel display and also a suitable DC signal for the data acquisition system.

The installation and calibration of appropriate diaphragms for the validyne transducer was not properly investigated during this project and, as a result, the unit was of limited use for quantitative measurements. The validyne transducer did however provide a good low noise signal for the qualitative interpretation of transient pressure drops. It was used for quantitative measurements in situations when the pressure drop could not be adequately resolved using the absolute pressure transducers. For an individual run this involved measurement of zero offset during a no-flow period and calibration against measurements using absolute transducers during conditions of higher pressure drop. The

zero offset varied over the range -3 to $0.9V$ and the proportionality between 0.015 and $0.050VkPa^{-1}$. There was some evidence that the large variation in proportionality was indicative of a non-linearity in the response but this was not conclusive. The net result was measurements with uncertainties of around 30%.

Appendix D

Summary of Experimental Runs

D.1 Introduction

The Energy Research Centre's new thermochemical laboratory and experimental arrangement was assembled during 1989. Testing and calibration of individual items of equipment began in mid 1989. Preliminary experimental runs with the data acquisition system operational, began at the begining of 1990.

This appendix presents the raw data from all the experimental runs that were recorded in the course of this project. The runs from the 14th of March 1990 to the 8th of August 1990 illustrate the evolution of the experimental arrangement and techniques up to the first successful steady state run. After this, improvements continued until early in 1991. The later runs have provided the backbone of the results presented in chapter 8.

The following table is a key to the various line and symbol types used in the graphs in this appendix.

Symbol or line type	Graph type	Identification
– · – · –	temperature versus time	reactor external temperatures
———	"	reactor internal and connecting tube temperatures
– – – –	"	heat exchanger temperatures
———	power versus time	column 2 power level
– – – –	"	column 1 power level
– · – · –	pressure versus time	reactor inlet pressure
———	"	system exit pressure
– – – –	"	accumulator pressure
• •	reactor temperature profiles	reactor external temperatures
× ×	"	reactor internal temperatures
× ×	heat exchanger temperature profiles	heat exchanger external temperatures

D.2 Runs 1990-1991

14th of March 1990

- First test of data acquisition system during reactor heating.
- Heaters powered directly from variac.
- System pressurised to $5MPa$ with N_2 from cylinder supply, negligible flow.

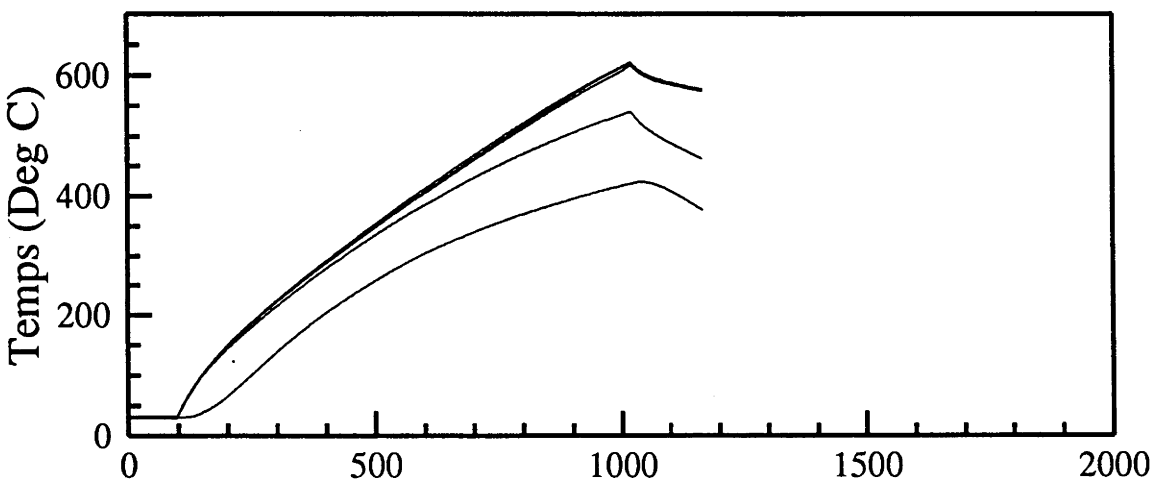

Figure D.1: Time dependance, of temperatures 14th of March 1990.

15th of March 1990 A

- First test of dissociator with ammonia present.
- System prefilled with liquid, no flow.
- Manual variation of power with variac, to limit temperatures.
- Transient behaviour associated with liquid boil off and expansion illustrated.
- Temperature measurements lagging others due to too high a sample rate.

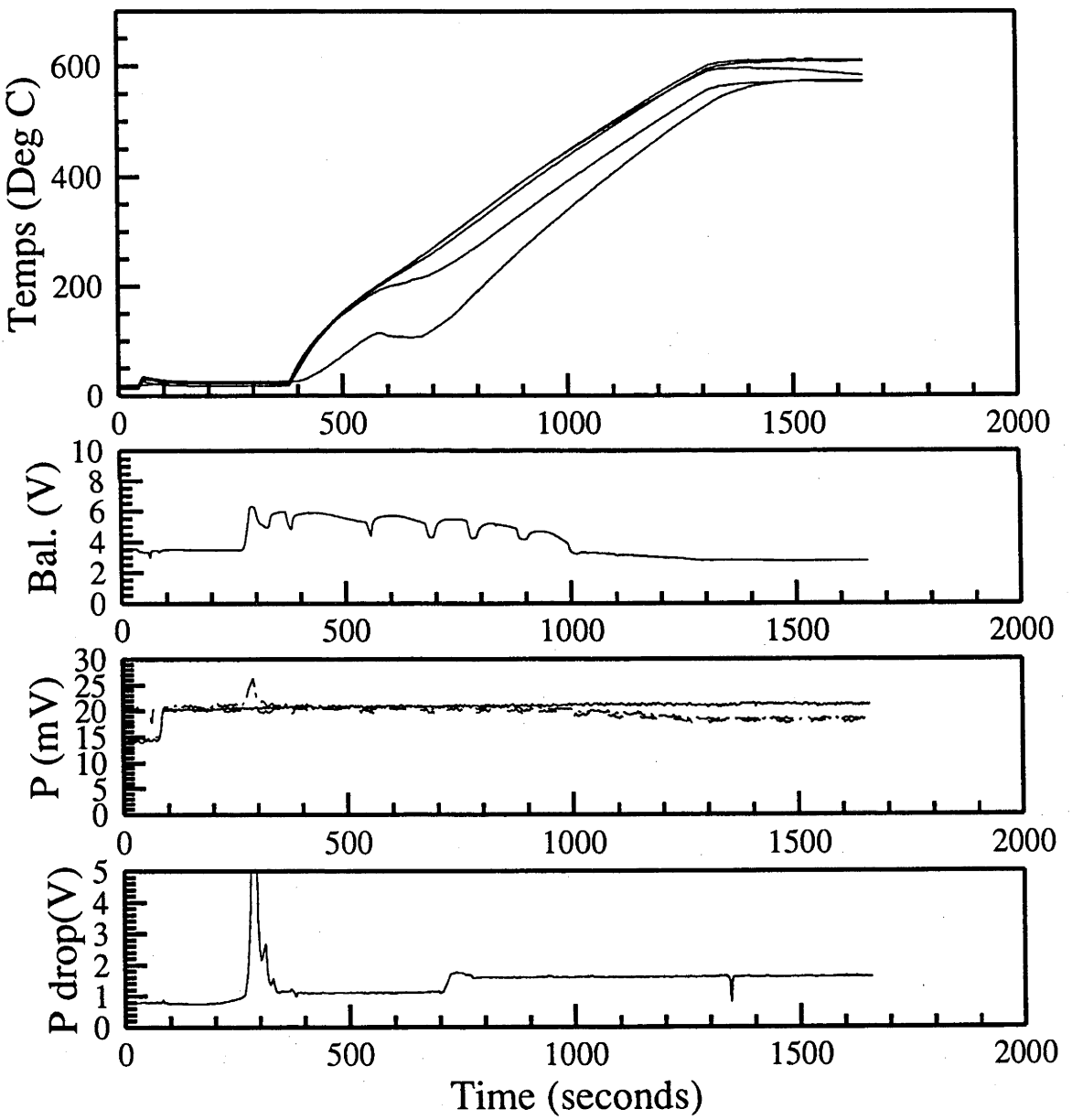

Figure D.2: Time dependance, 15th of March 1990, first run.

15th of March 1990 B

- First test of dissociator with ammonia flow.
- Variation of flow rate with metering valve.
- Correlation between pressure drop and flow rate and temperature observed.
- Correct operation of balancing separator through several vent - drain cycles establishes the presence of gaseous reaction products.
- Still time errors in temperature measurements from data acquisition system.

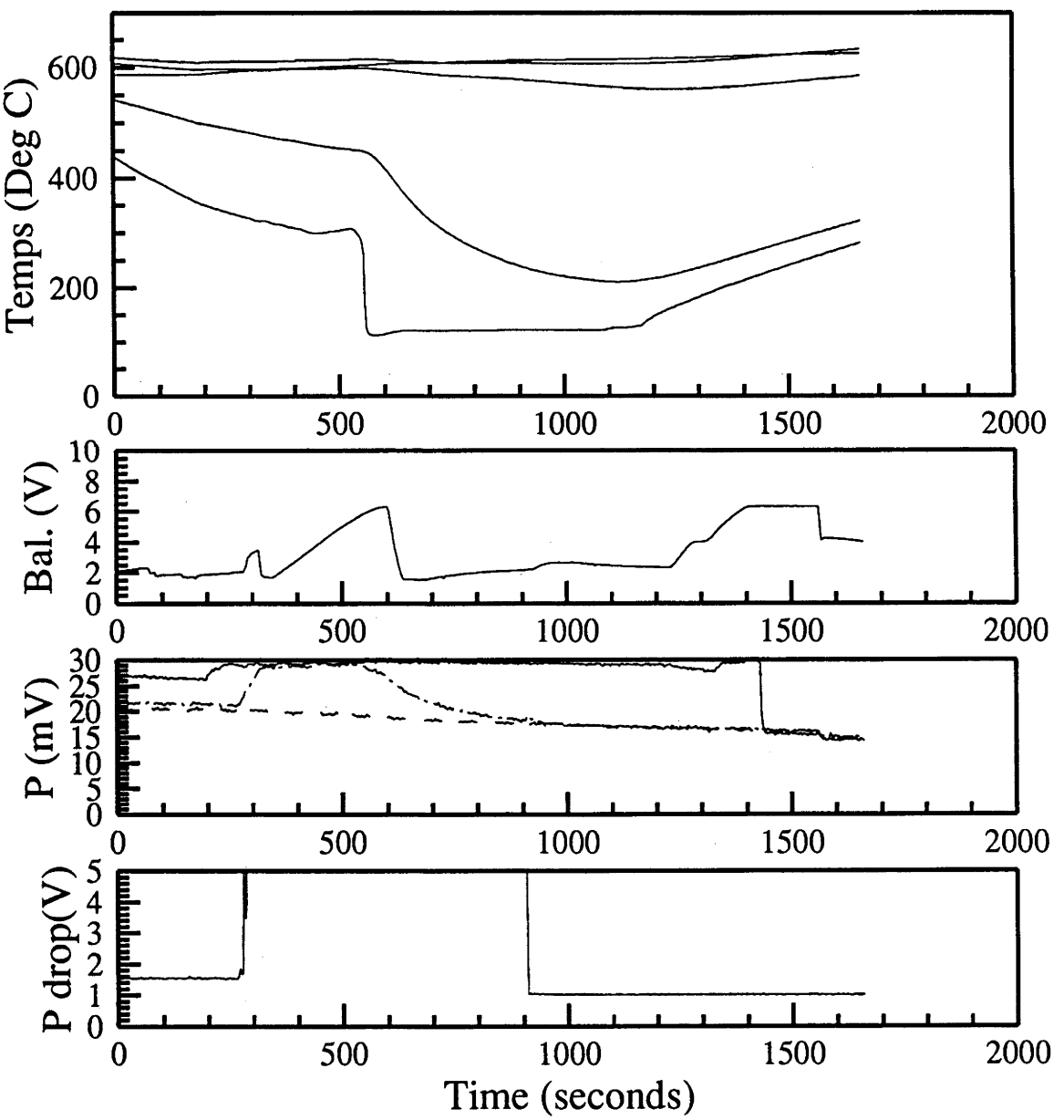

Figure D.3: Time dependance, 15th of March 1990, second run.

31st of April 1990

- First trial of Eurotherm temperature controllers, setpoints 500°C first chamber (column 1), 550°C second chamber (column2), successful operation.
- System running well except unable to achieve steady conditions.
- Heater power measurements unavailable.
- Inlet flow rate approximately 0.07 gs^{-1}.
- Problems with data acquisition time signals resolved.
- Heat exchanger temperatures measured for the first time.
- Temperature probe scanning mechanism tested.

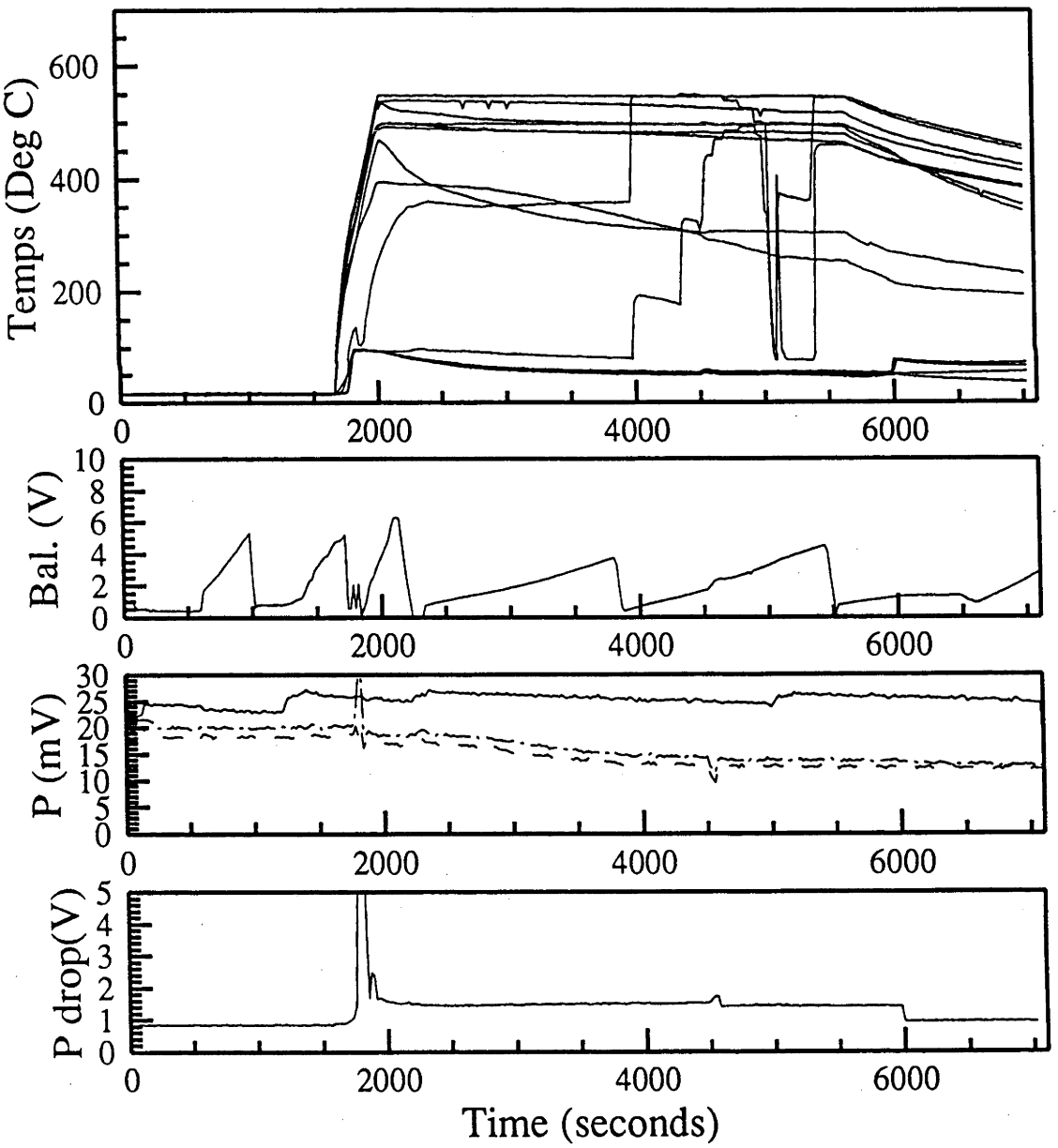

Figure D.4: Time dependance, 31st of April 1990.

22nd of May 1990

- Still unable to achieve steady conditions, correlation between variations in power, temperature and pressure drop signals indicates unsteady mass flow as the cause.
- Apparent short term fluctuations plus an overall reduction in mass flow with time due to a combination of an inadequate pressure control arrangement and possible blocking of valves.
- Power on approximately 2 minutes before opening dissociator inlet caused an interesting transient in heat exchanger temperatures due to fluid expansion.

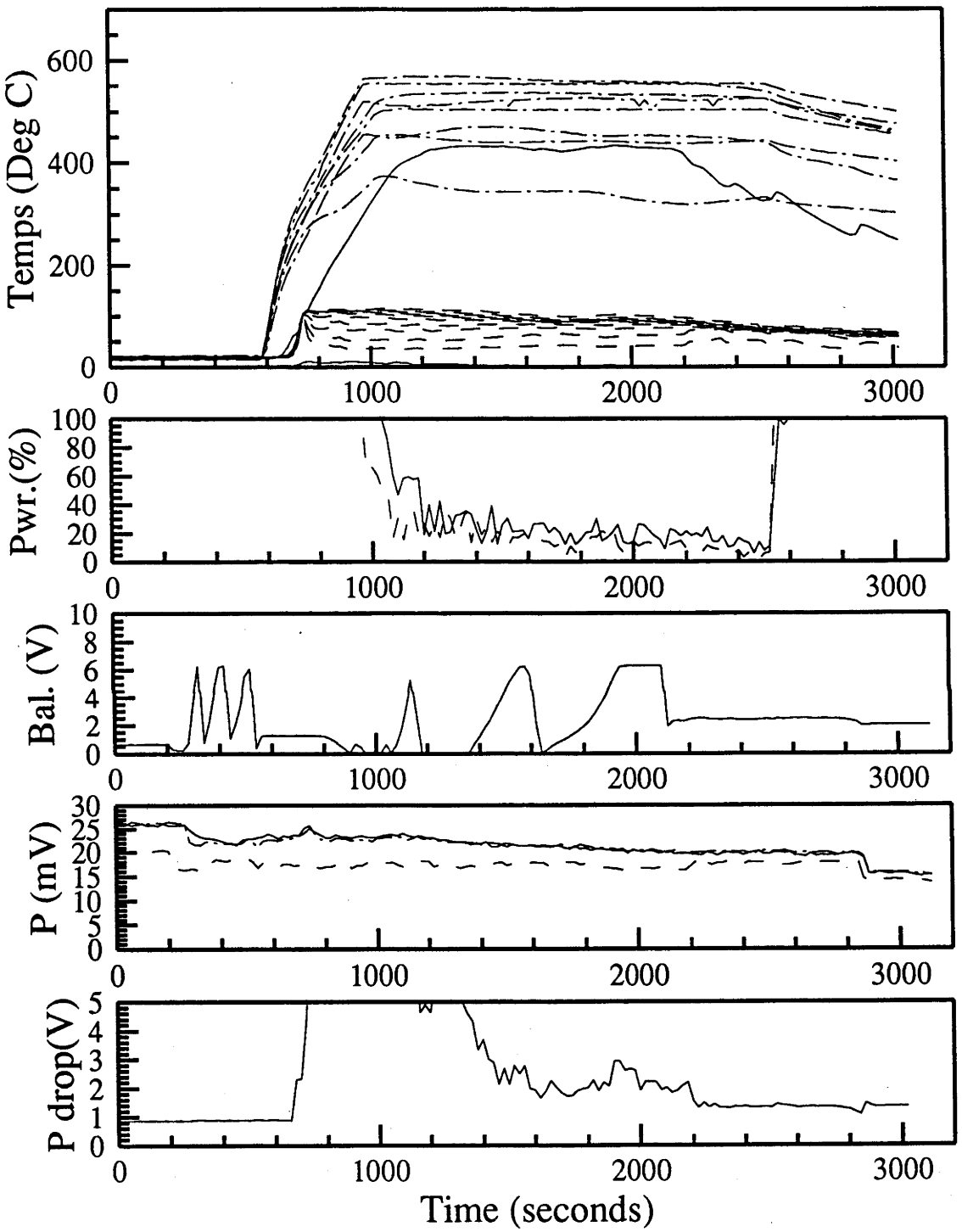

Figure D.5: Time dependance, 22nd of May 1990.

26th of July 1990

- First trial of improved pressure control system; both ammonia accumulator and system exit pressures set with regulated nitrogen, throttle valve at exit in place of pressure relief valve.
- Reasonable behaviour observed until ammonia supply exhausted.

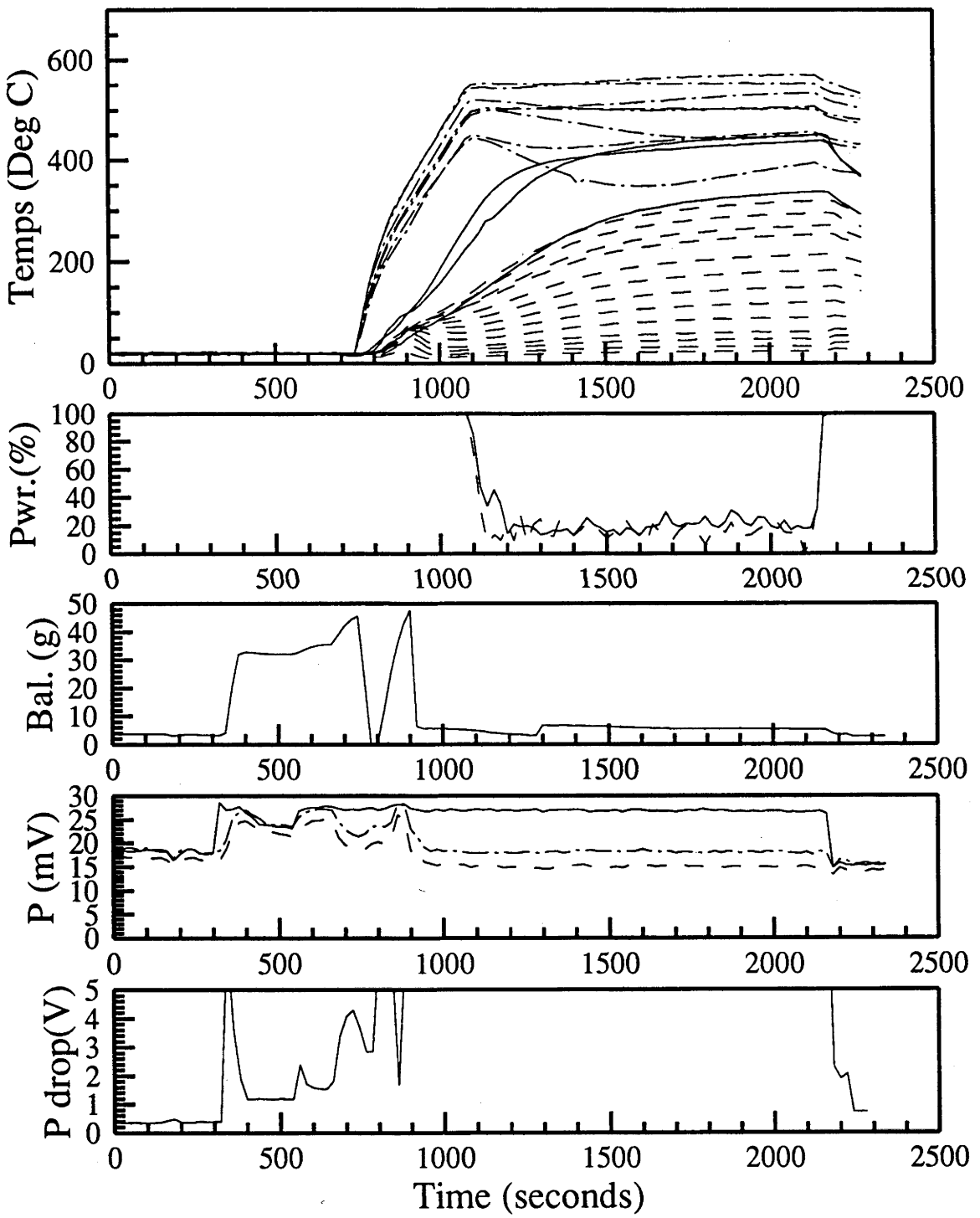

Figure D.6: Time dependance, 26th of July 1990.

2nd of August 1990

- Operation with new ammonia supply, complete failure due to apparent blockage of exit throttle valve.

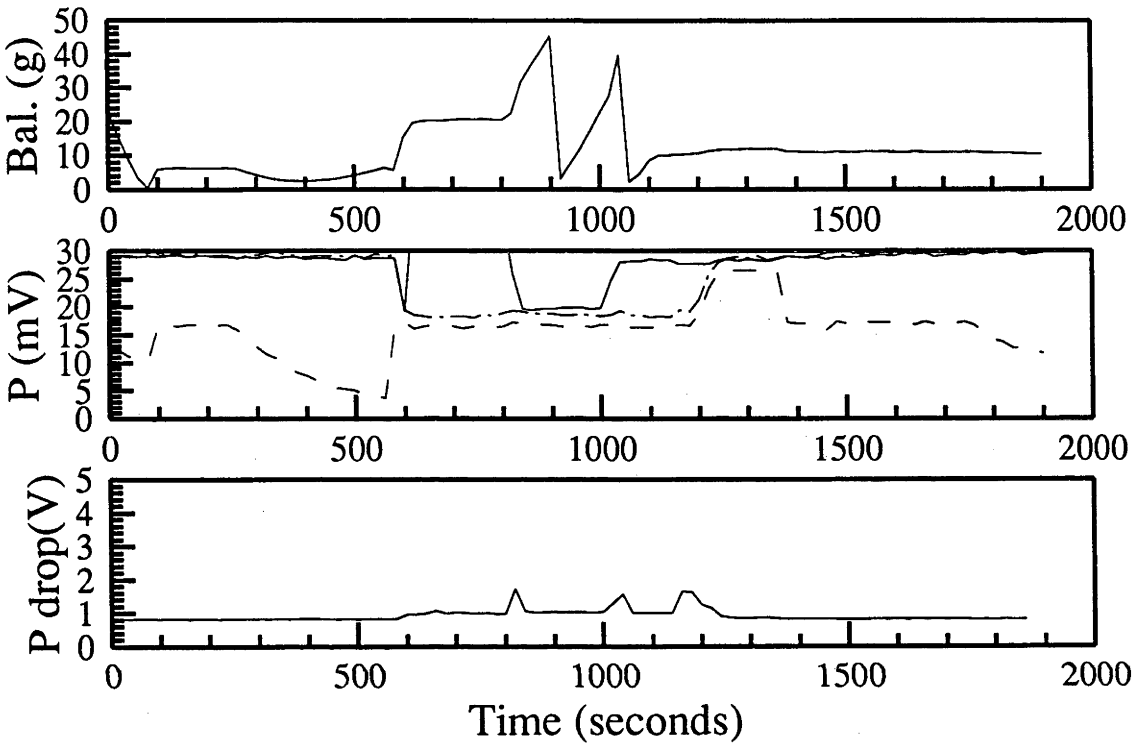

Figure D.7: Time dependance, 2nd of August 1990.

8th of August 1990

- First successful steady state operation following overhaul of throttle valve and installation of an inline filter.
- Three flow rates tested for constant setpoint temperatures.
- Flow rates deduced from previous calibration of metering valve.

Time interval (seconds)	3300-3600	5000-5350	6250-6550
Pressure (MPa)	5.34±0.1	5.47±0.1	5.71±0.1
Inlet mass flow (gs^{-1})	0.114±0.01	0.38±0.03	1.06±0.1
Reaction extent	0.34±0.08	0.29±0.09	0.34±0.08
Pressure drop (kPa)	21.4±2	54.2±5	216±20
	First chamber (column 1)		
Temperature setpoint ($°C$)	500	500	500
Heater power (W)	243±1	520±4	849±8
Inlet temp ($°C$)	83.8±3	128.5±3	171.0±3
Outlet temp ($°C$)	490±15	500±15	485±15
	Second chamber (column 2)		
Temperature setpoint ($°C$)	550	550	550
Heater power (W)	252±1	326±2	367±3
Inlet temp ($°C$)	345±10	441±10	451±10
Outlet temp ($°C$)	420±15	490±15	510±15
	Heat exchanger		
Inlet cold end temp ($°C$)	21.6±1	19.6±1	19.5±1
Inlet hot end temp ($°C$)	113±10	159±10	201±10
Outlet hot end temp ($°C$)	200±5	352±5	430.2±5

Table D.1: Steady state values, 8th of August 1990.

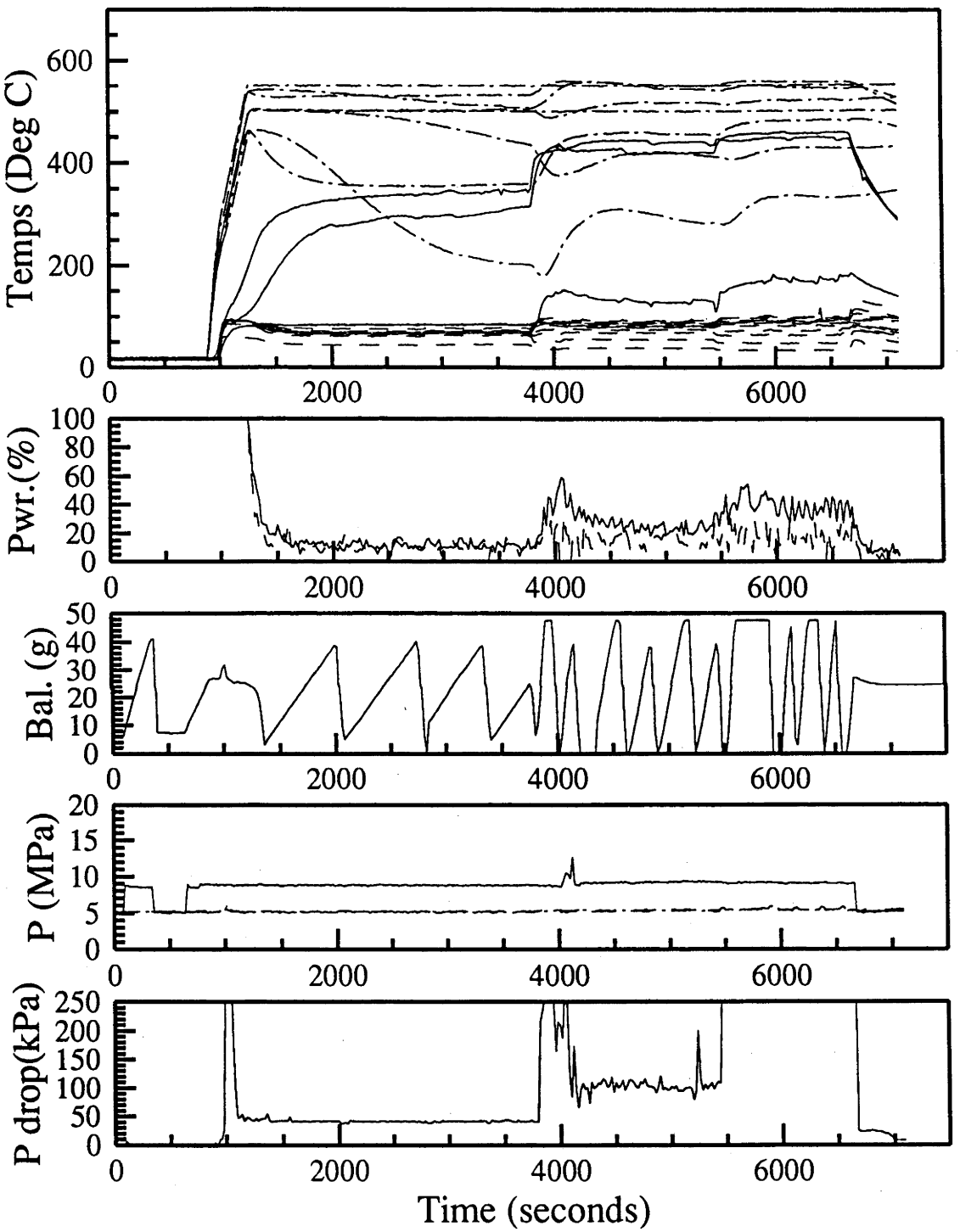

Figure D.8: Time dependance, 8th of August 1990.

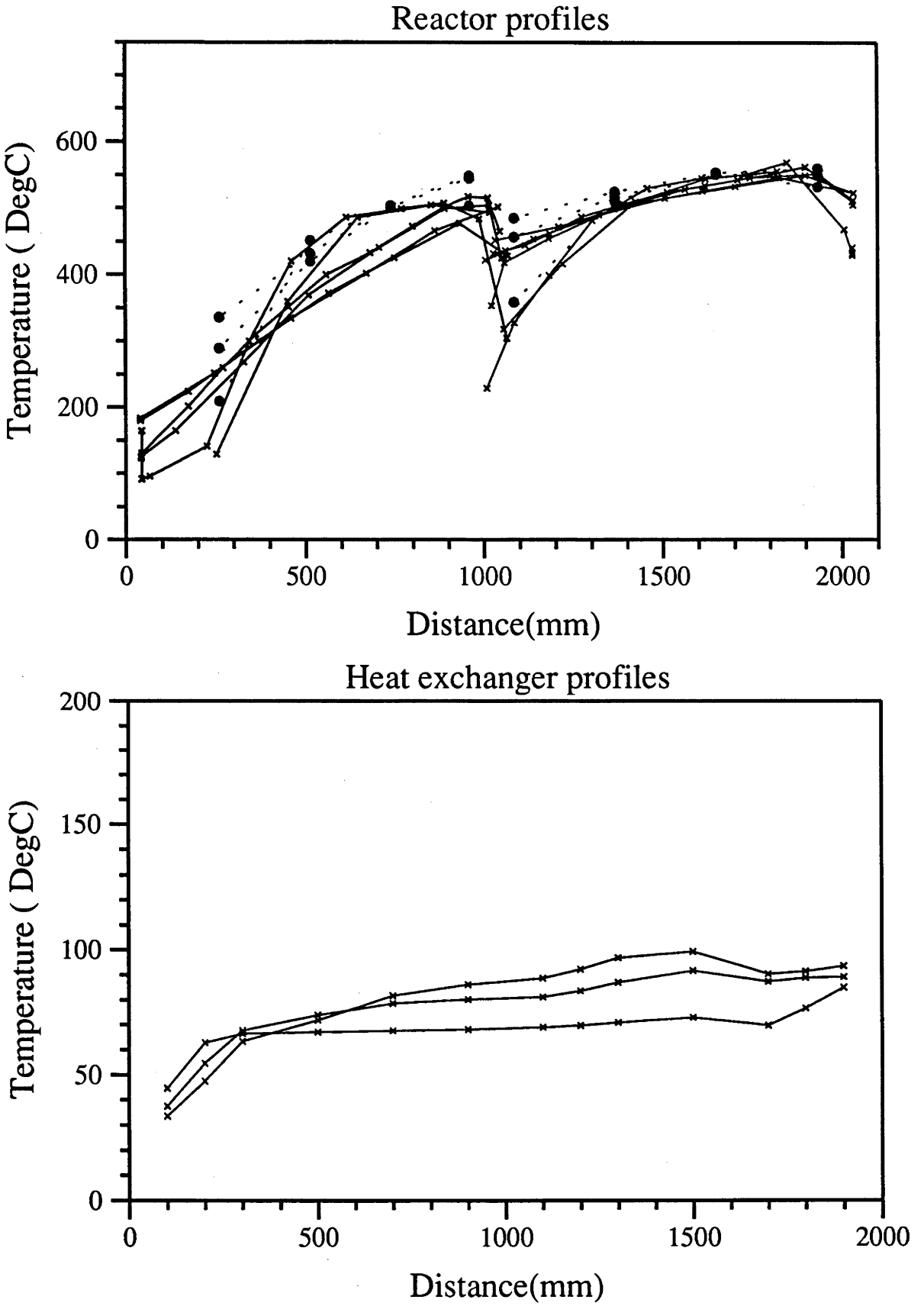

Figure D.9: Steady state temperature profiles, 8th of August 1990.

15th of October 1990

- First run following reversal of flow direction to take account of heat exchanger design (as a consequence the reactor columns 1 and 2 are encountered in reverse order by the reactants).
- Constant flow rate at $5MPa$ with 3 temperature settings investigated.
- Omitted to relocate controller thermocouples to the new "hottest" positions on flow reversal, hence set points were kept low.
- Inlet mass flow calibrated prior to power on, corrections made on the basis of variations in the pressure drop across the metering valve.

Time interval (seconds)	3000-4050	4800-5170	6000-6900	8800-9700
Pressure (MPa)	6.471±0.06	6.455±0.06	6.472±0.06	5.977±0.06
Inlet mass flow (gs^{-1})	0.1086±0.0003	0.1078±0.0003	0.1084±0.0003	0
Reaction extent	0.423±0.02	0.371±0.02	0.324±0.02	
Pressure drop (kPa)	32±10	26±9	20±6	0
	First chamber (column 2)			
Temperature setpoint ($°C$)	500	475	450	450
Heater power (W)	384±38	404±40	389±30	28.7±7
Inlet temp ($°C$)	95.0±2	95.1±2	95.4±2	
Outlet temp ($°C$)	575±20	562±20	550±20	
	Second chamber (column 1)			
Temperature setpoint ($°C$)	500	475	450	450
Heater power (W)	227.7±8	206.1±18	149.2±7	64.6±6
Inlet temp ($°C$)	425±10	415±10	400±10	
Outlet temp ($°C$)	475±20	450±20	425±20	
	Heat exchanger			
Inlet cold end temp ($°C$)	20.3±1	20.3±1	20.6±1	
Inlet hot end temp ($°C$)	99.7±3	99.5±3	99.4±3	
Outlet cold end temp ($°C$)	43.3±1	47.6±1	51.6±1	
Outlet hot end temp ($°C$)	366±15	359±15	347±15	

Table D.2: Steady state values, 15th of October 1990.

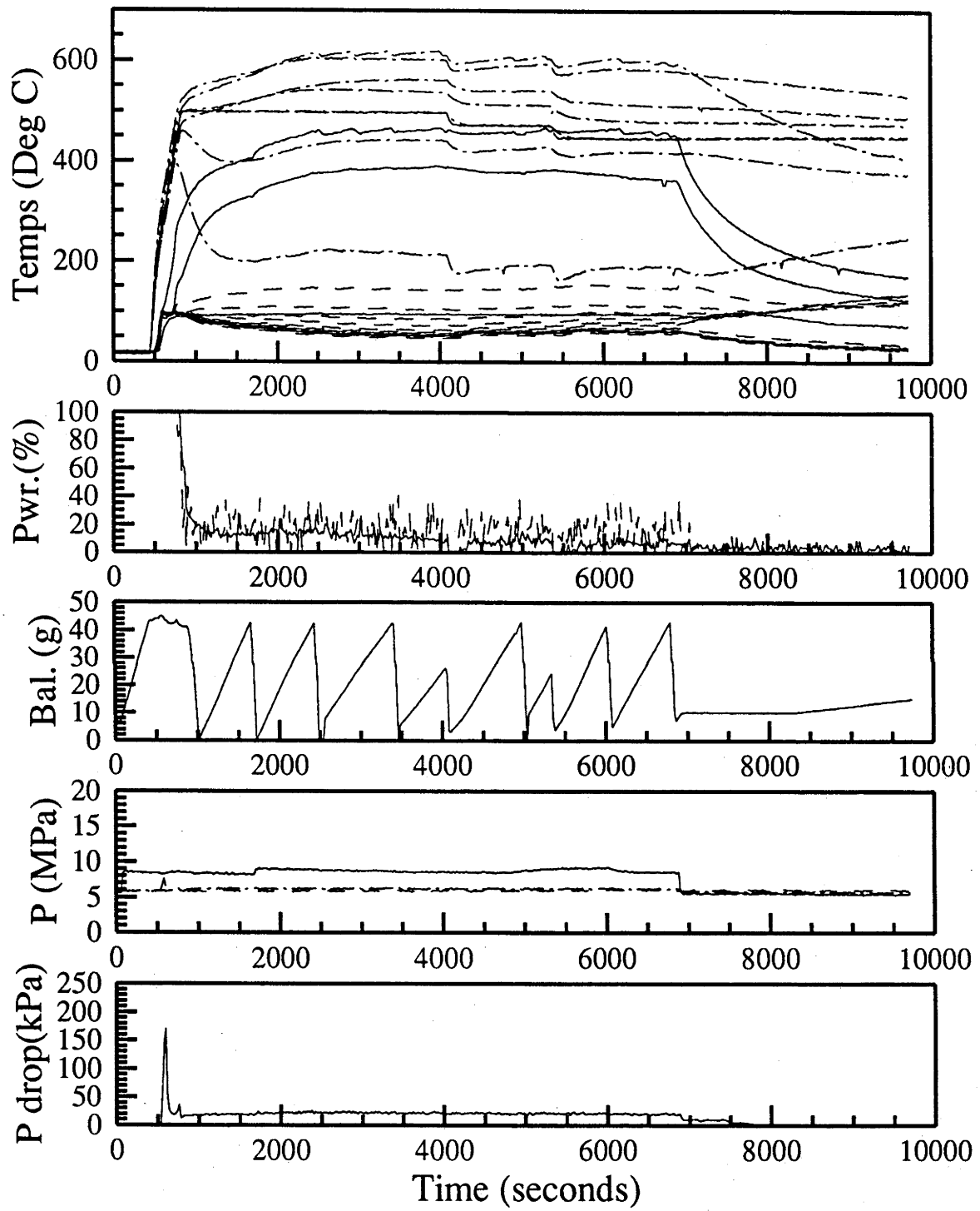

Figure D.10: Time dependance, 15th of October 1990.

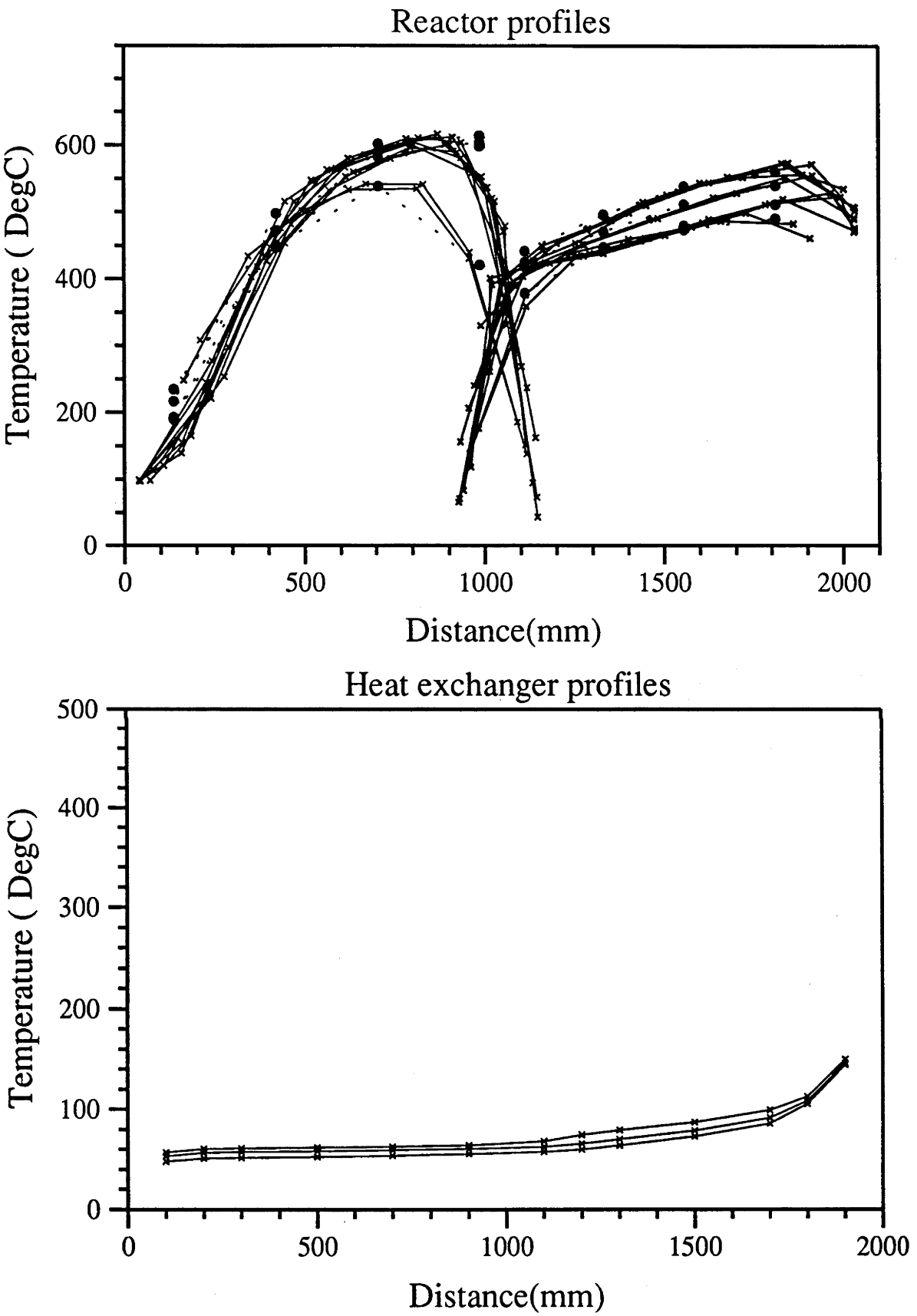

Figure D.11: Steady state temperature profiles, 15th of October 1990.

4th of November 1990

- Investigation of no flow power levels and temperature profiles to quantify heat loss processes.
- System filled with nitrogen at 420 kPa.

Time interval (seconds)	5000-6000
First chamber (column 2)	
Temperature setpoint ($°C$)	500
Heater power (W)	75.4±13
Second chamber (column 1)	
Temperature setpoint ($°C$)	500
Heater power (W)	118.1±9

Table D.3: Steady state values, 4th of November 1990.

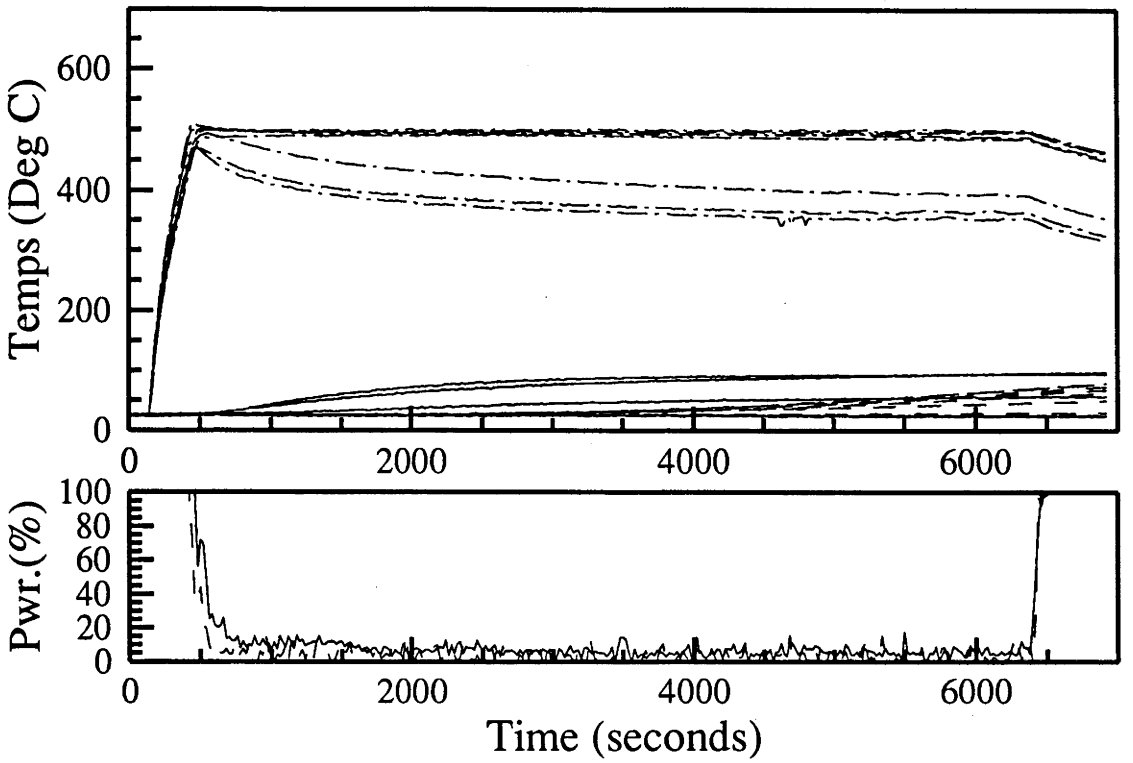

Figure D.12: Time dependance, 4th of November 1990.

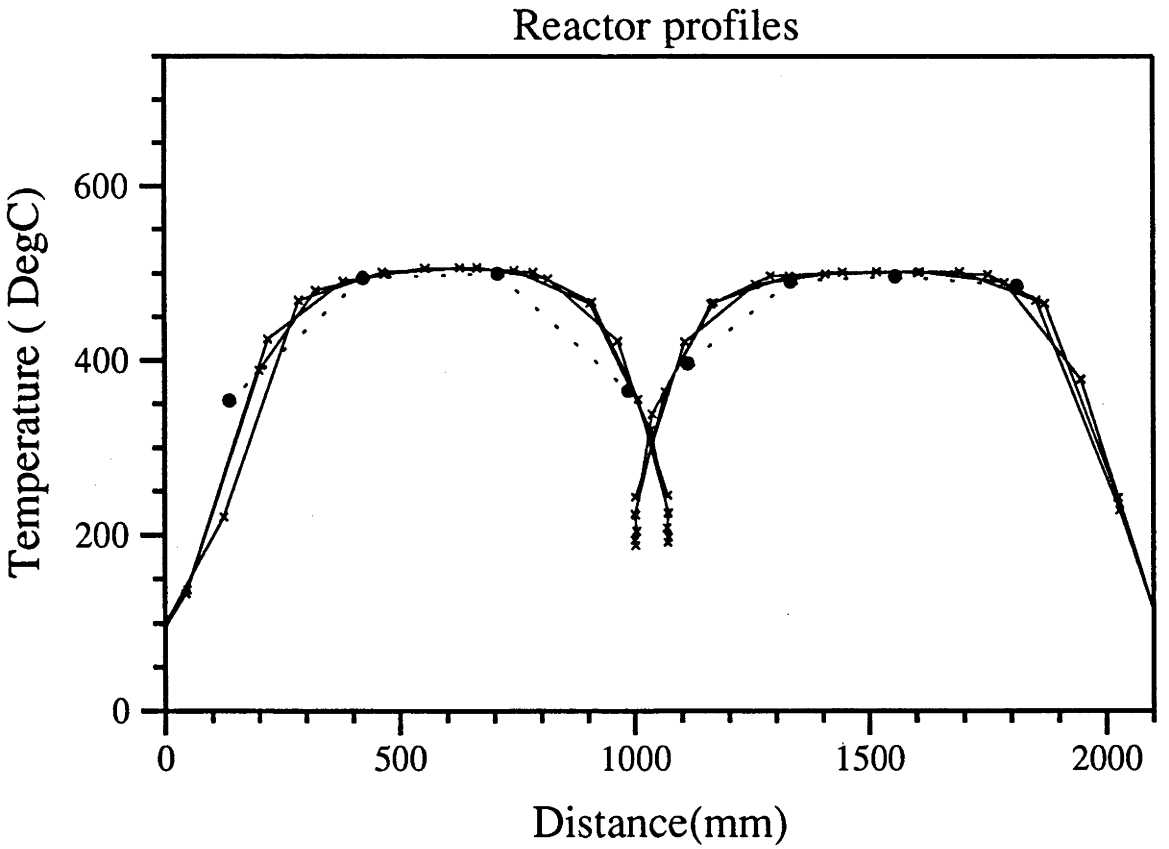

Figure D.13: Steady state temperature profiles, 4th of November 1990.

16th of November 1990

- Investigation of several setpoint temperatures at $6.6MPa$ and $0.4gs^{-1}$.
- Controller thermocouples relocated to "hottest" positions on respective reactor columns.

Table D.4: Steady state values, 16th of November 1990.

Time interval (seconds)	3400-4120	5000-5350	7200-8080	8500-8950	9300-9620	10400-10780
Pressure (MPa)	6.180±.06	6.391±.06	6.661±.06	6.583±.06	6.685±.06	6.812±.06
Inlet mass flow (gs^{-1})	.413±.005	.404±.005	.400±.005	.392±.005	.391±.005	.388±.005
Reaction extent	0.386±.02	0.324±.02	0.353±.02	0.456±.02	0.495±.02	0.527±.02
Pressure drop (kPa)	44±10	61±20	68±23	65±20	67±22	75±25
	First chamber (column 2)					
Temperature setpoint (°C)	550	575	600	625	635	650
Heater power (W)	448±50	566±90	556±60	707±110	711±110	505±100
Inlet temp (°C)	95±10	105±10	120±10	133±10	147±10	160±10
Outlet temp (°C)	515±20	530±20	545±20	562±20	585±20	600±20
	Second chamber (column 1)					
Temperature setpoint (°C)	550	575	600	625	635	650
Heater power (W)	316±20	365±20	351±30	476±80	383±40	394±50
Inlet temp (°C)	462±10	491±10	513±10	525±10	534±10	544±10
Outlet temp (°C)	475±15	512±15	537±15	550±15	561±15	574±15
	Heat exchanger					
Inlet cold end temp (°C)	23.6±1	23.4±1	22.9±1	23.3±1	24.2±1	23.6±1
Inlet hot end temp (°C)	99.6±3	102.0±3	136.9±3	145.1±3	132.7±3	206.8±3
Outlet cold end temp (°C)	64.0±1	62.1±1	57.8±1	47.8±1	44.8±1	41.2±1
Outlet hot end temp (°C)	366±15	402±15	427±15	440±15	450±15	464±15

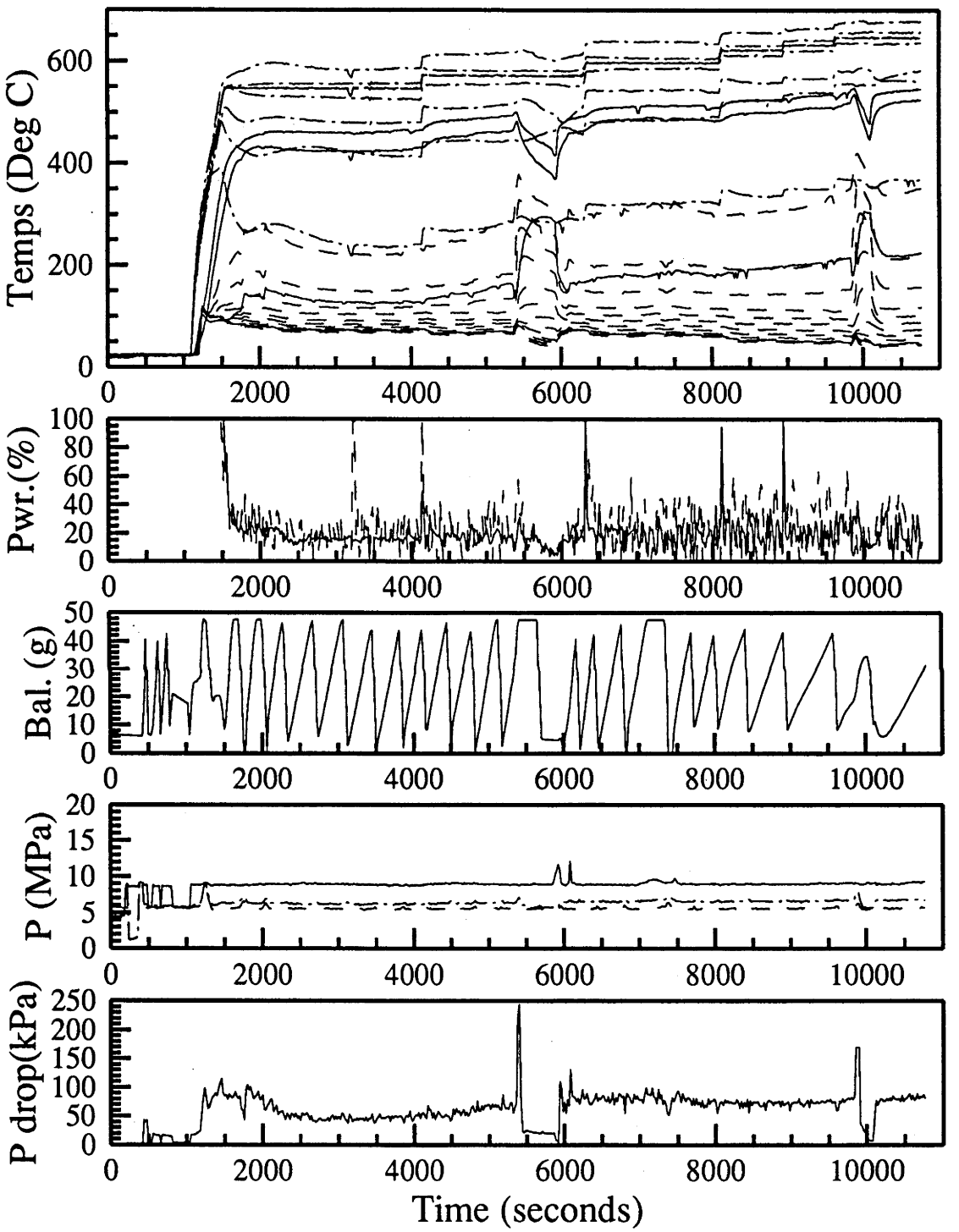

Figure D.14: Time dependance, 16th of November 1990.

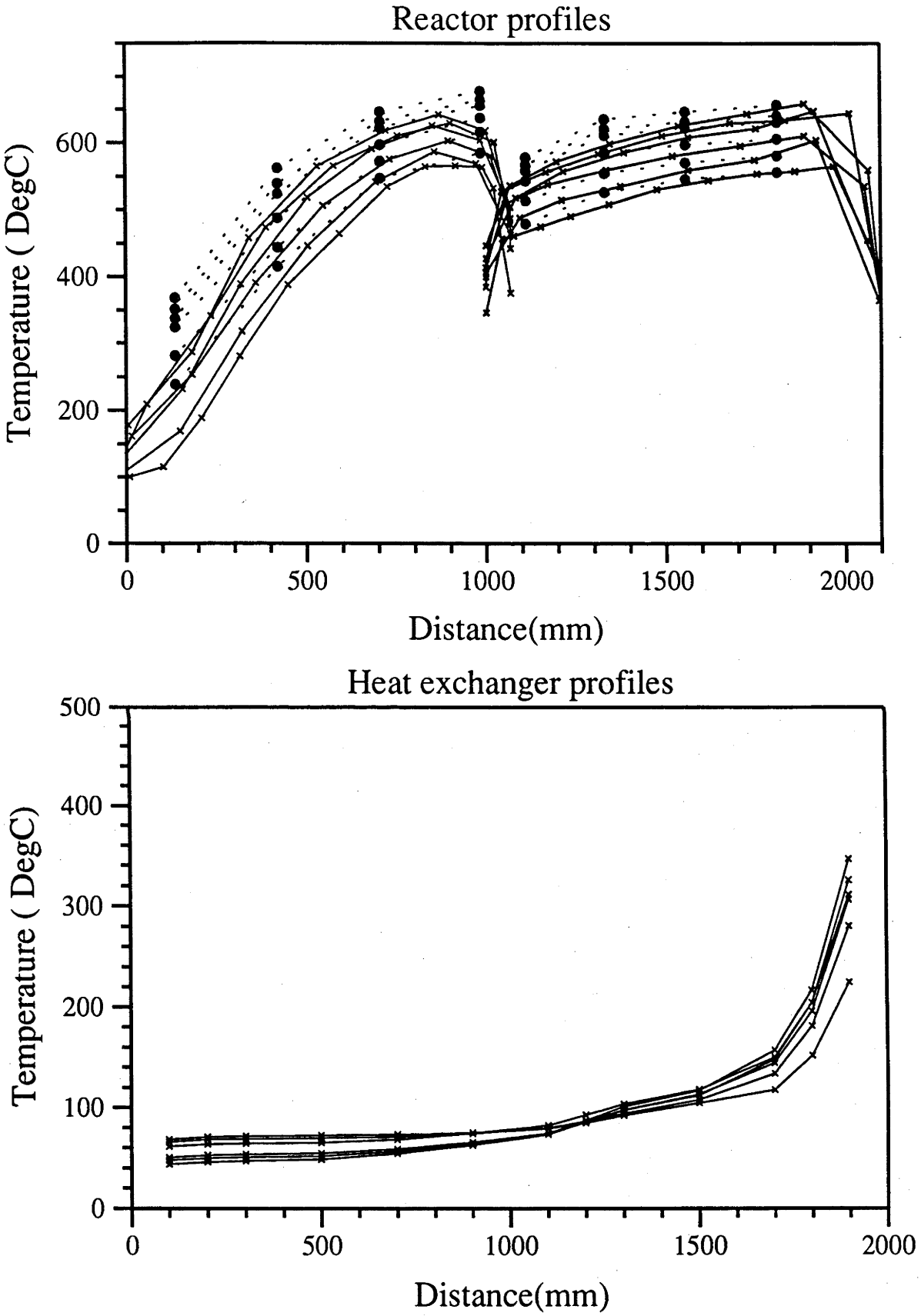

Figure D.15: Steady state temperature profiles, 16th of November 1990.

21st of November 1990

- Investigation of several setpoint temperatures at $11MPa$ and $0.47gs^{-1}0$.

Time interval (seconds)	2000-2570	3200-3640	4100-4710	5300-5800	6200-6800
Pressure (MPa)	11.90±0.1	11.99±0.1	12.06±0.1	12.07±0.1	11.97±0.1
Inlet mass flow (gs^{-1})	0.468±.006	0.472±.006	0.462±.006	0.472±.006	0.479±.006
Reaction extent	0.158±.03	0.265±.024	0.338±.02	0.416±.02	0.561±.015
Pressure drop (kPa)	31.3±10	33.8±10	32.6±10	31.1±10	19.9±10
	First chamber (column 2)				
Temperature setpoint (°C)	550	600	625	640	650
Heater power (W)	475±64	620±100	973±90	901±125	721±90
Inlet temp (°C)	208±3	220±3	227±3	226±3	210±3
Outlet temp (°C)	532±15	565±15	580±15	591±15	593±15
	Second chamber (column 1)				
Temperature setpoint (°C)	550	600	625	640	650
Heater power (W)	384±27	525±66	471±34	508±42	442±38
Inlet temp (°C)	472±15	515±15	530±15	541±15	543±15
Outlet temp (°C)	500±10	540±10	559±10	568±10	564±10
	Heat exchanger				
Inlet cold end temp (°C)	24.0±1	24.4±1	24.8±1	24.5±1	24.8±1
Inlet hot end temp (°C)	227±2	236±2	244±2	242±2	225±2
Outlet cold end temp (°C)	85.5±1	75.3±1	68.9±1	63.6±1	55.5±1
Outlet hot end temp (°C)	429±5	470±5	489±5	498±5	494±5

Table D.5: Steady state values, 21st of November 1990.

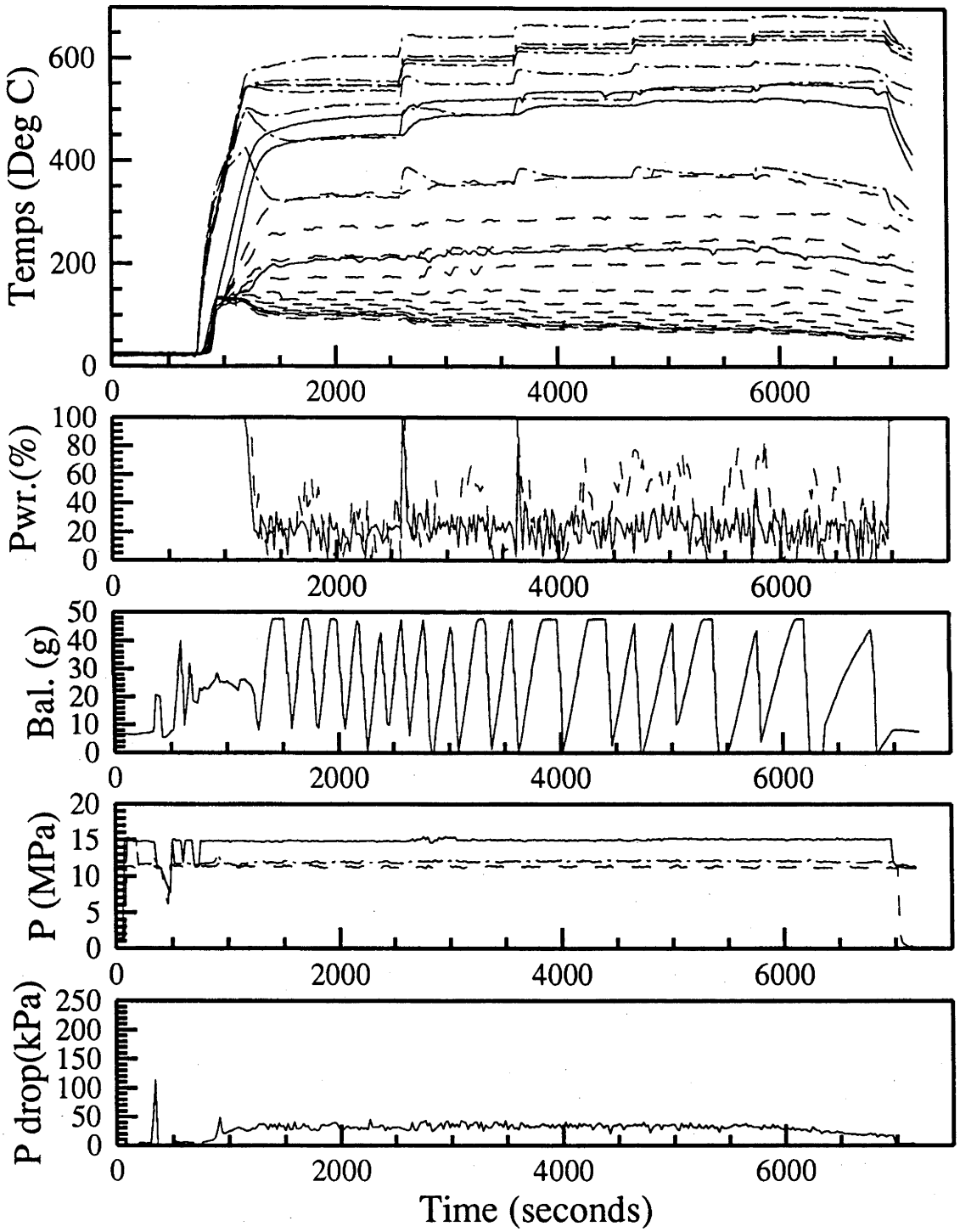

Figure D.16: Time dependance, 21st of November 1990.

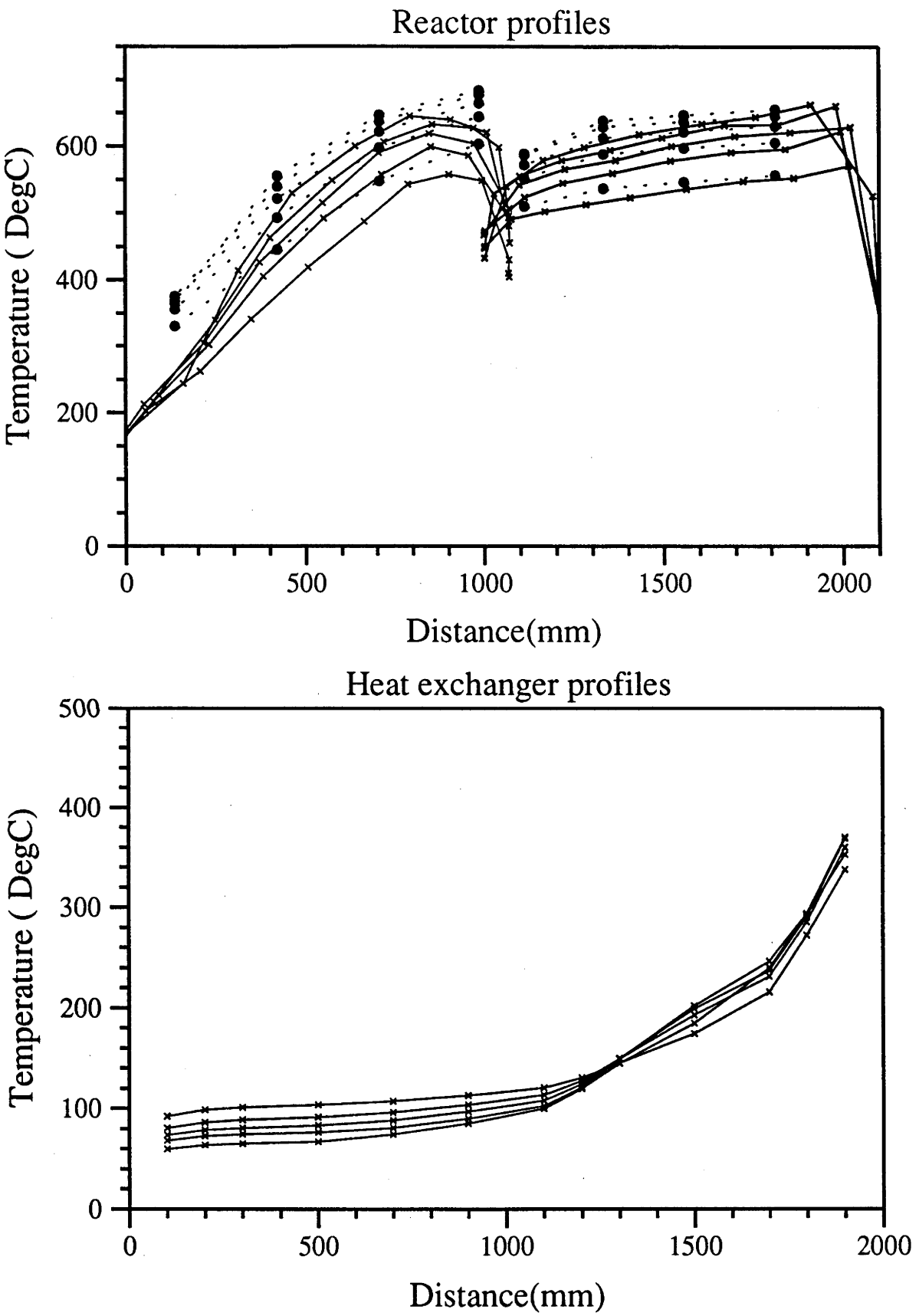

Figure D.17: Steady state temperature profiles, 21st of November 1990.

14th of January 1991

- First of a series of runs with nitrogen flow only to investigate heat transfer processes within the catalyst bed.
- Nitrogen flow rates measured with a Gilmot Rotameter.
- Single flow rate at $10MPa$ 600°C.
- Run terminated because of problems with liquid nitrogen pump.

Time interval (seconds)	4000-4200
Pressure (MPa)	9.32±0.09
Inlet mass flow (gs^{-1})	0.085±0.003
Pressure drop (kPa)	2.1±0.7
First chamber (column 2)	
Temperature setpoint (°C)	600
Heater power (W)	96±21
Inlet temp (°C)	92±20
Outlet temp (°C)	404±10
Second chamber (column 1)	
Temperature setpoint (°C)	600
Heater power (W)	203±13
Inlet temp (°C)	301±10
Outlet temp (°C)	327±20
Heat exchanger	
Inlet cold end temp (°C)	33.1±1
Inlet hot end temp (°C)	171.8±3
Outlet cold end temp (°C)	33.5±1
Outlet hot end temp (°C)	242±15

Table D.6: Steady state values, 14th of January 1991.

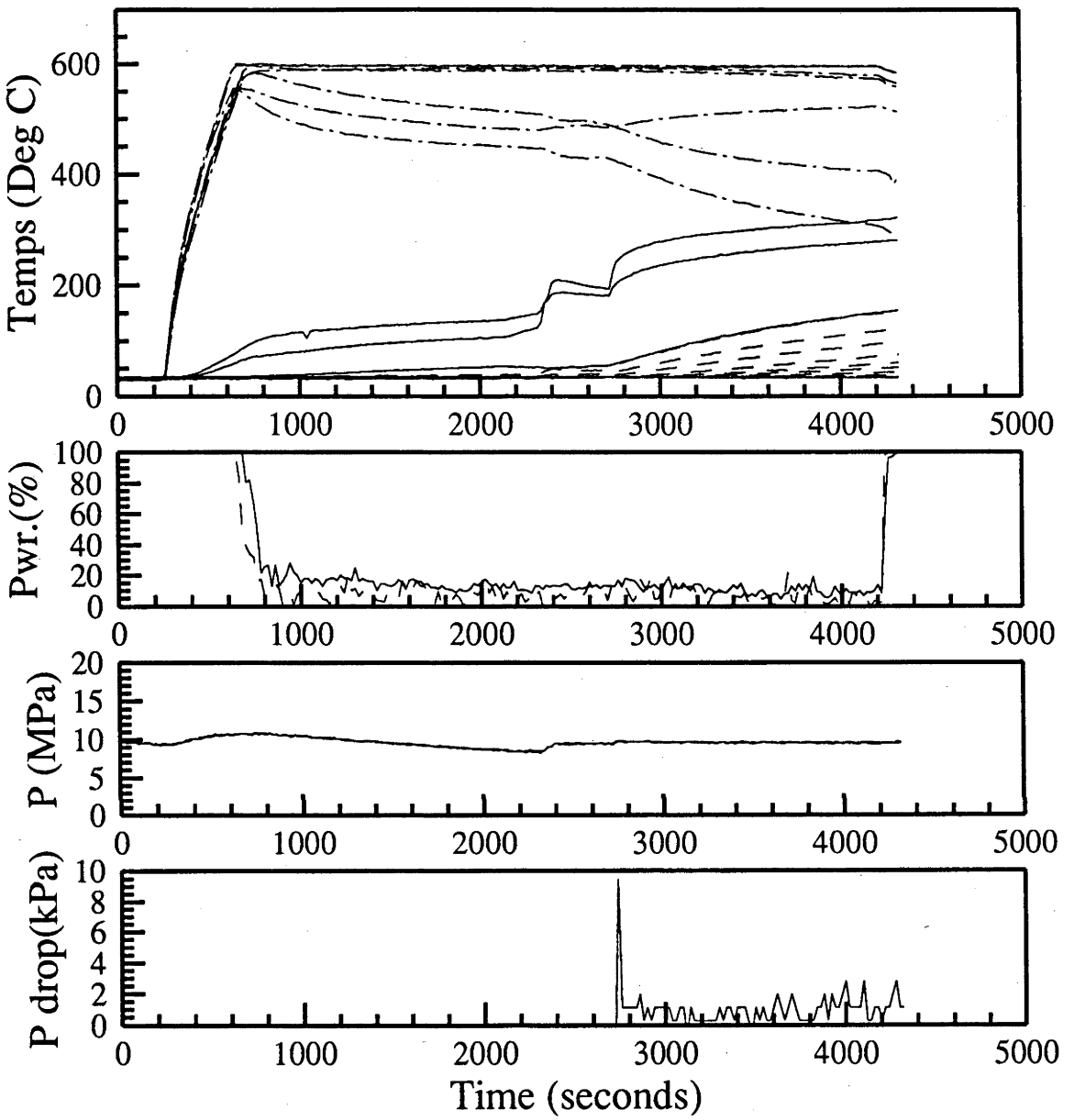

Figure D.18: Time dependance, 14th of January 1991.

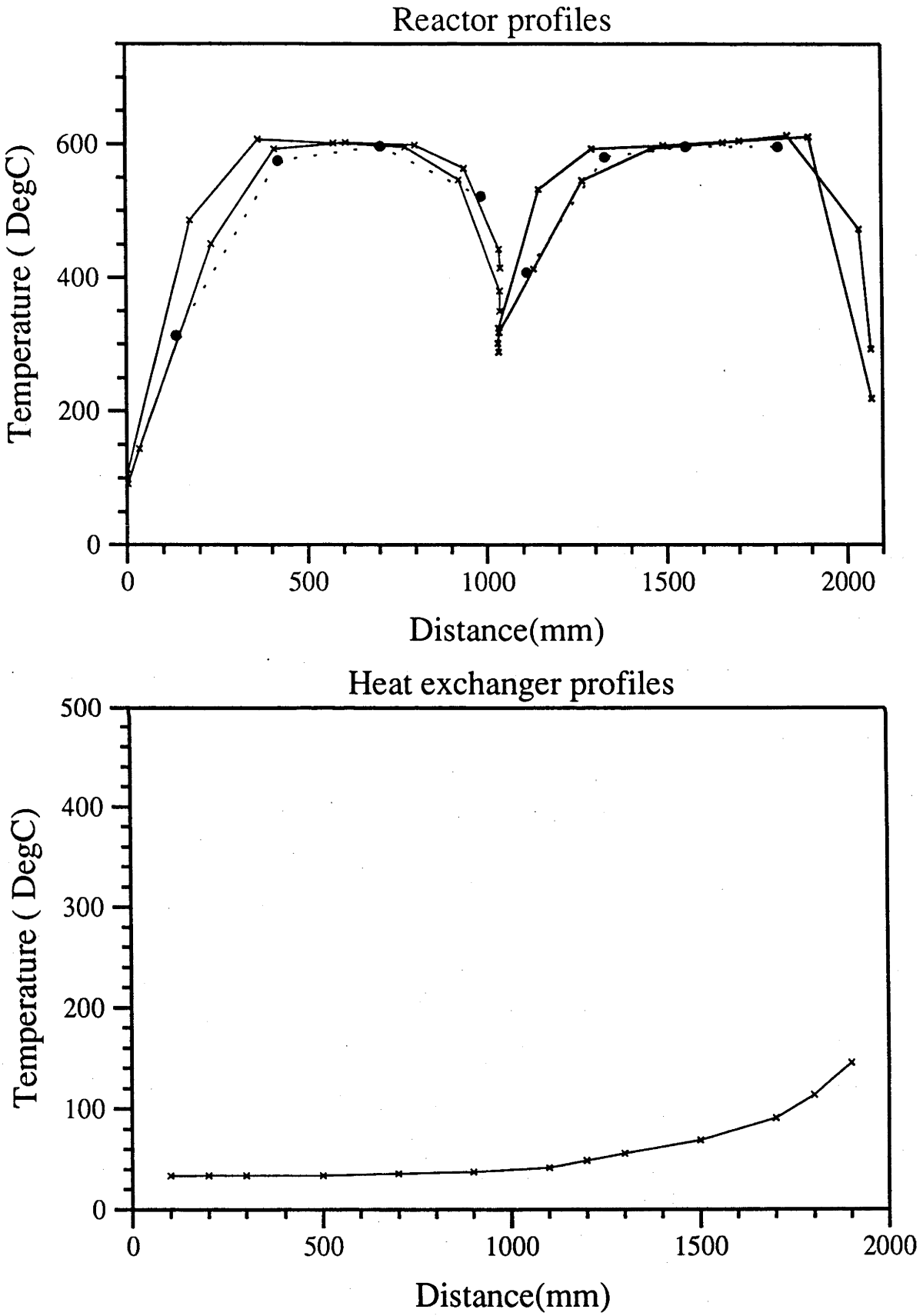

Figure D.19: Steady state temperature profiles, 14th of January 1991.

15th of January 1991

- Completion of series of flow rates at $10MPa$ 600°C setpoint.
- Data acquisition problem at 10800 seconds.

Time interval (seconds)	4000-4500	8000-8600	9800-10790	11000-11340
Pressure (MPa)	9.77±0.1	9.90±0.1	9.66±0.1	9.51±0.1
Inlet mass flow (gs^{-1})	0.085±0.003	0.255±0.01	0.676±0.02	1.179±0.03
Pressure drop (kPa)	5.7±1.2	40.6±10	156±30	282±30
	First chamber (column 2)			
Temperature setpoint (°C) 600	600	600	600	600
Heater power (W)	142±19	232±23	338±24	419±47
Inlet temp (°C)	170±20	340±10	420±10	434±10
Outlet temp (°C)	424±5	561±5	612±5	625±5
	Second chamber (column 1)			
Temperature setpoint (°C) 600	600	600	600	600
Heater power (W)	194±11	261±10	318±11	274±16
Inlet temp (°C)	305±5	463±5	542±5	563±5
Outlet temp (°C)	342±20	511±20	578±20	582±20
	Heat exchanger			
Inlet cold end temp (°C)	29.3±1	31.4±1	31.7±1	36.3±1
Inlet hot end temp (°C)	203.4±3	374.5±3	448.3±3	460.6±3
Outlet cold end temp (°C)	29.4±1	42.0±1	67.4±1	77.6±1
Outlet hot end temp (°C)	256±15	426±15	493±15	497±15

Table D.7: Steady state values, 15th of January 1991.

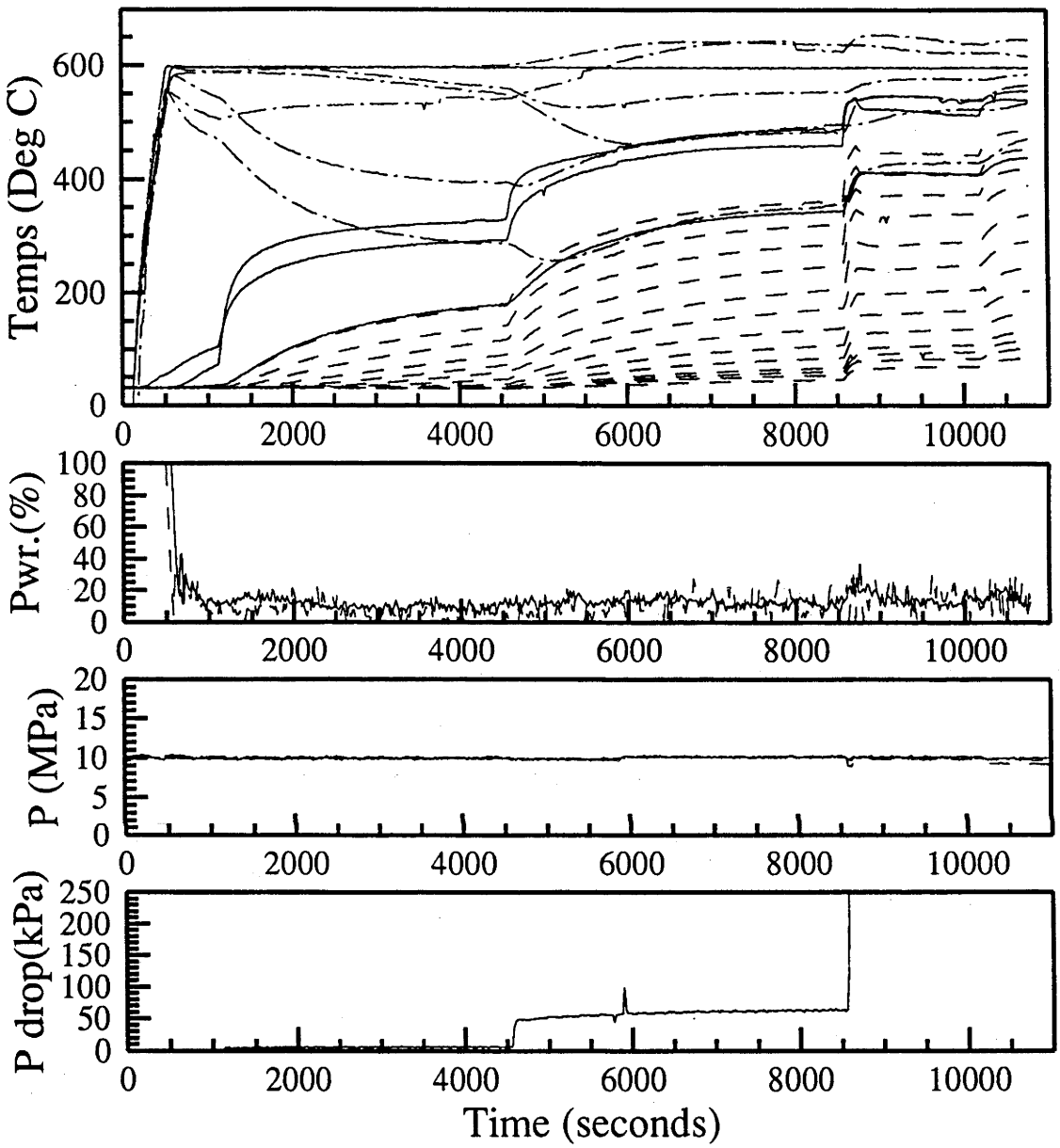

Figure D.20: Time dependance, 15th of January 1991.

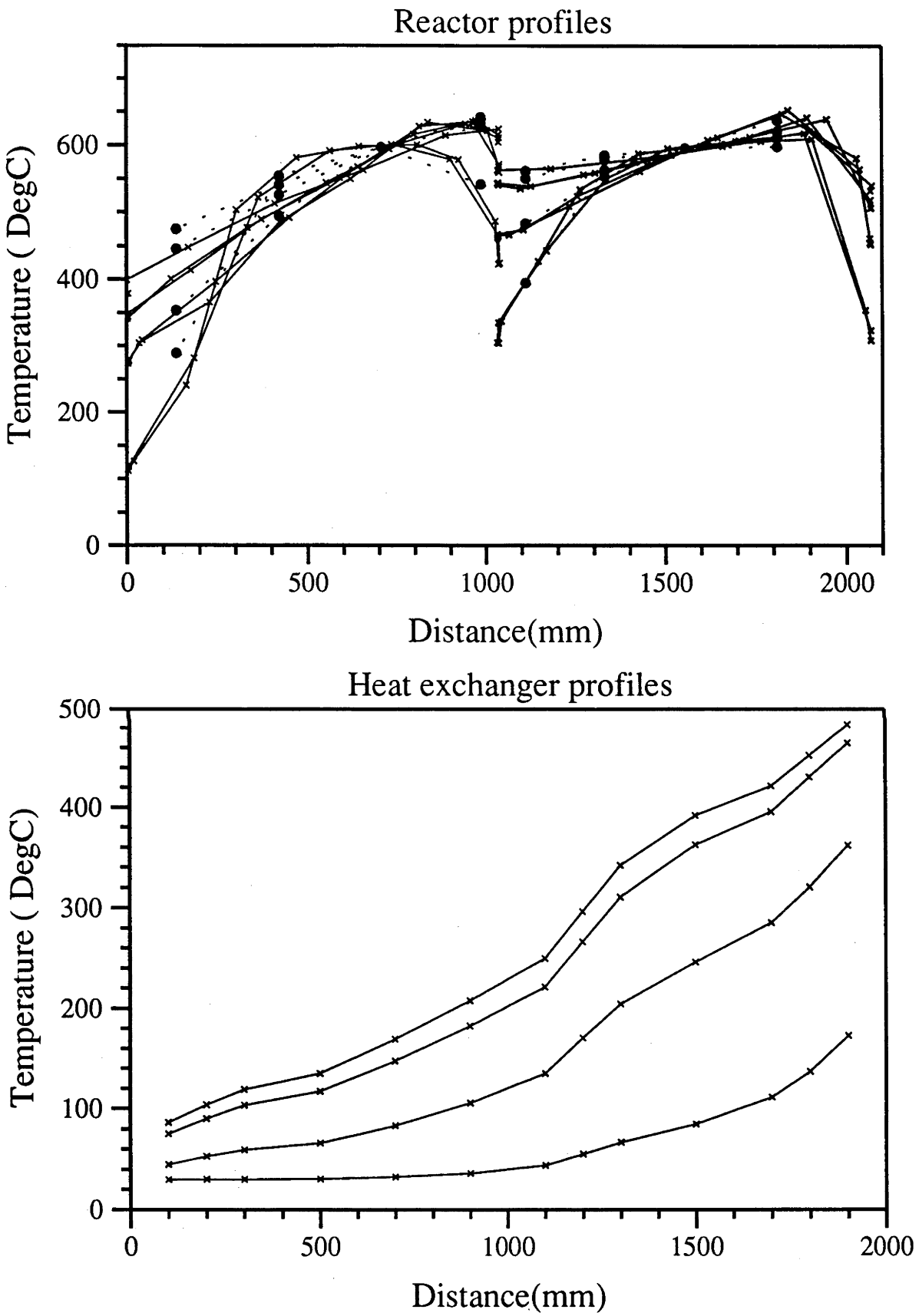

Figure D.21: Steady state temperature profiles, 15th of January 1991.

17th of January 1991

- Begining a series of setpoint temperatures with a constant nitrogen flow rate.

Time interval (seconds)	3200-3800	5400-6000	7000-7470	8400-8850	9900-10300
Pressure (MPa)	9.90±0.1	9.89±0.1	9.68±0.1	9.81±1	9.81±0.1
Inlet mass flow (gs^{-1})	0.250±0.01	0.252±0.01	0.246±0.01	0.250±0.01	0.247±0.01
Pressure drop (kPa)	51±14	55±15	55±15	69±16	83±20
	First chamber (column 2)				
Temperature setpoint ($°C$)	400	450	500	550	600
Heater power (W)	135±22	135±22	149±30	269±25	261±48
Inlet temp ($°C$)	200±10	234±10	260±10	280±10	303±10
Outlet temp ($°C$)	372±5	421±5	463±5	505±5	555±5
	Second chamber (column 1)				
Temperature setpoint ($°C$)	400	450	500	550	600
Heater power (W)	166±13	143±17	215±21	222±9	283±13
Inlet temp ($°C$)	305±5	346±5	374±5	403±5	432±5
Outlet temp ($°C$)	332±20	372±20	406±20	434±20	464±20
	Heat exchanger				
Inlet cold end temp ($°C$)	25.1±1	25.5±1	25.7±1	26.4±1	26.6±1
Inlet hot end temp ($°C$)	223.3±3	258.0±3	286.8±3	310.2±3	334.8±3
Outlet cold end temp ($°C$)	28.8±1	31.4±1	32.4±1	33.9±1	35.0±1
Outlet hot end temp ($°C$)	246±15	283±15	321±15	349±15	379±15

Table D.8: Steady state values, 17th of January 1991.

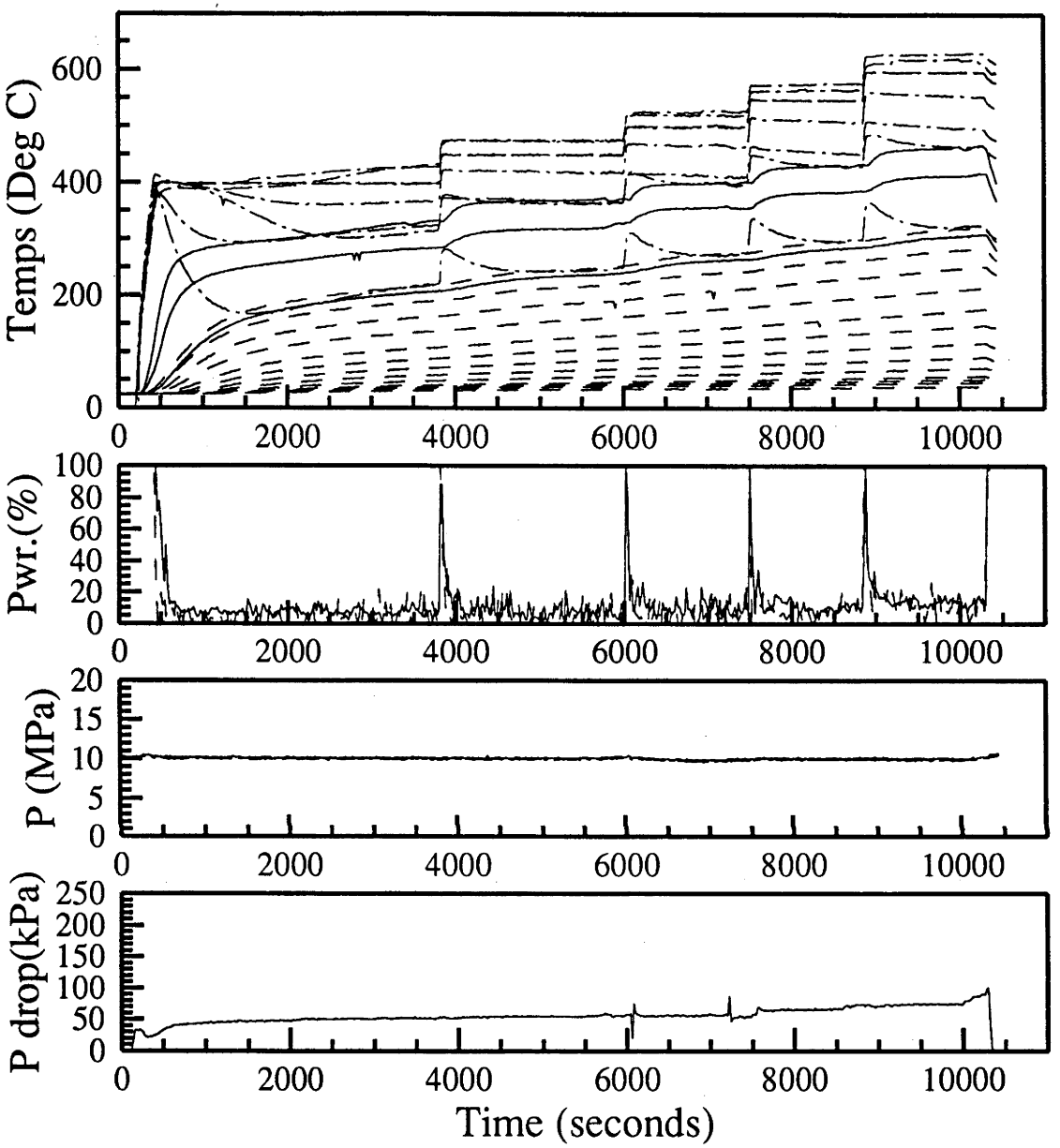

Figure D.22: Time dependance, 17th of January 1991.

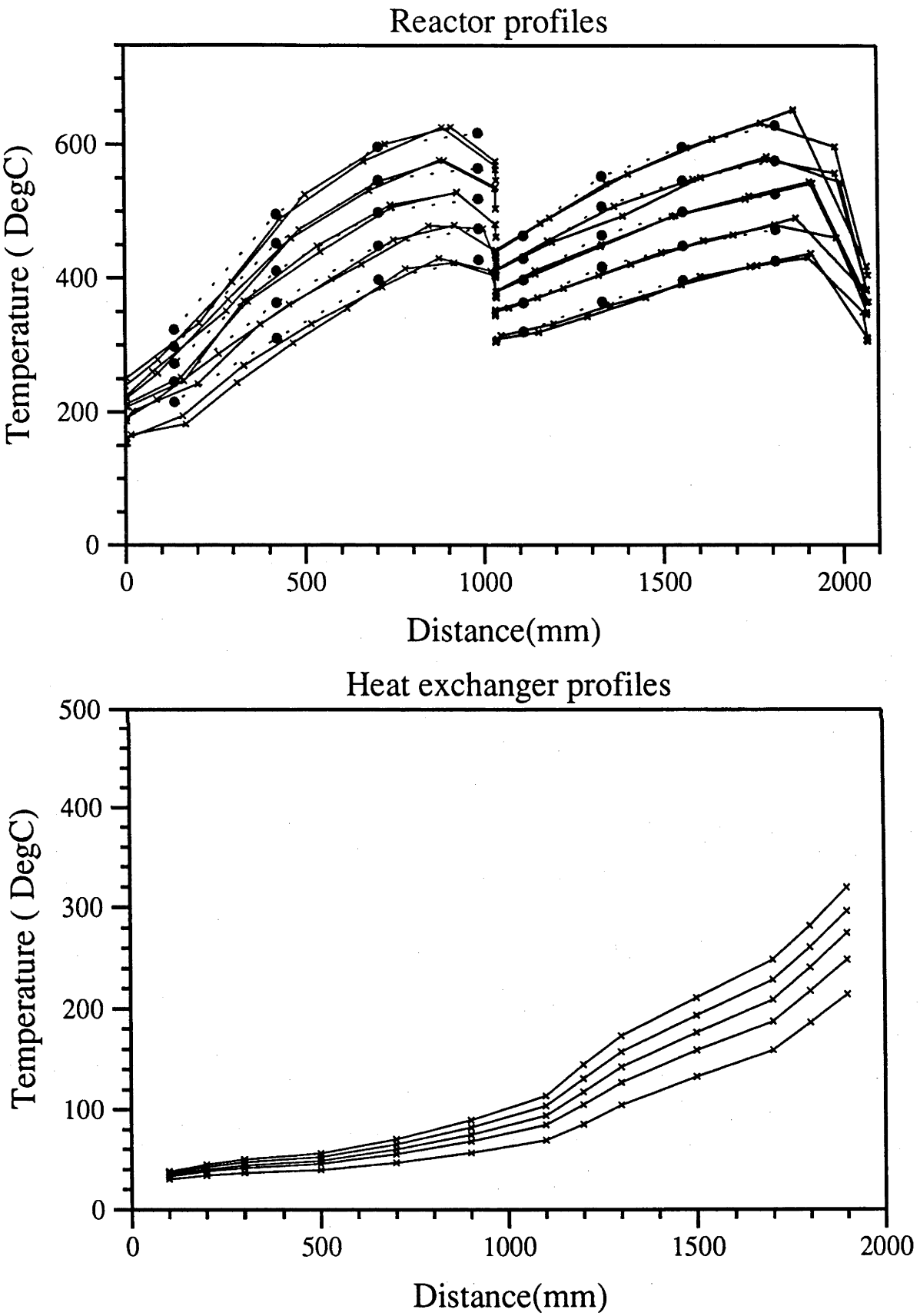

Figure D.23: Steady state temperature profiles, 17th of January 1991.

18th of January 1991

- Completion of variation of setpoint temperature for constant nitrogen flow.

Time interval (seconds)	3200-3750	5000-5590	7000-7640	9000-9800	10400-10790
Pressure (MPa)	9.95±0.1	9.99±0.1	10.01±0.1	9.97±0.1	9.96±0.1
Inlet mass flow (gs^{-1})	0.255±0.01	0.252±0.01	0.252±0.01	0.252±0.01	0.251±0.01
Pressure drop (kPa)	46±12	49±13	52±15	53±15	55±15
	First chamber (column 2)				
Temperature setpoint ($°C$)	425	475	525	575	625
Heater power (W)	165±25	231±80	148±32	263±79	281±22
Inlet temp ($°C$)	212±10	241±10	267±10	293±10	310±10
Outlet temp ($°C$)	401±5	444±5	488±5	531±5	567±5
	Second chamber (column 1)				
Temperature setpoint ($°C$)	425	475	525	575	625
Heater power (W)	181±22	230±69	216±25	348±59	255±11
Inlet temp ($°C$)	326±5	365±5	398±5	425±5	450±5
Outlet temp ($°C$)	349±20	384±20	413±20	548±20	475±20
	Heat exchanger				
Inlet cold end temp ($°C$)	23.0±1	23.7±1	25.1±1	26.5±1	27.0±1
Inlet hot end temp ($°C$)	236.6±3	267.1±3	294.3±3	323.7±3	343.5±3
Outlet cold end temp ($°C$)	27.5±1	30.1±1	32.7±1	35.1±1	36.5±1
Outlet hot end temp ($°C$)	264±15	291±15	328±15	363±15	390±15

Table D.9: Steady state values, 18th of January 1991.

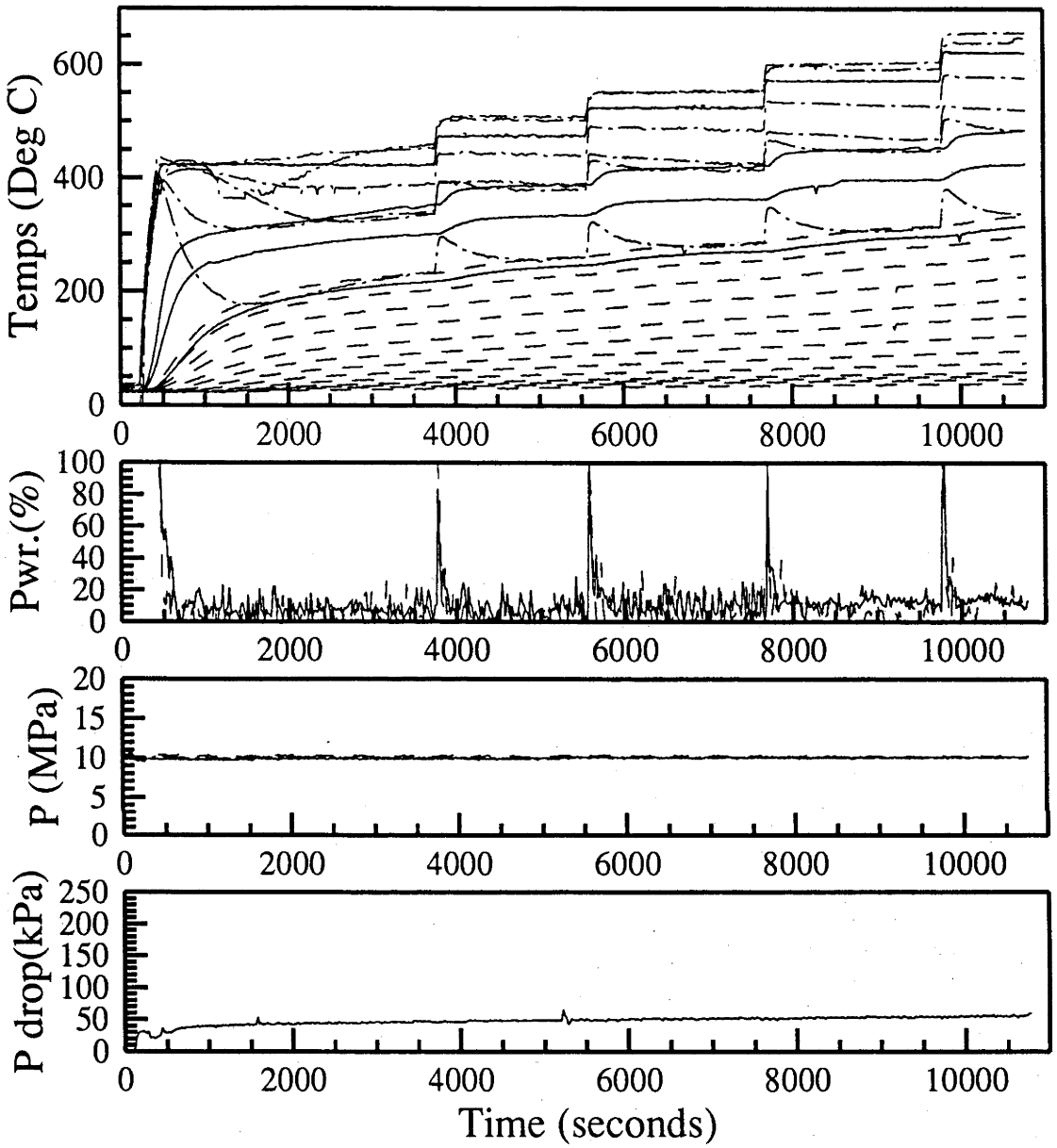

Figure D.24: Time dependance, 18th of January 1991.

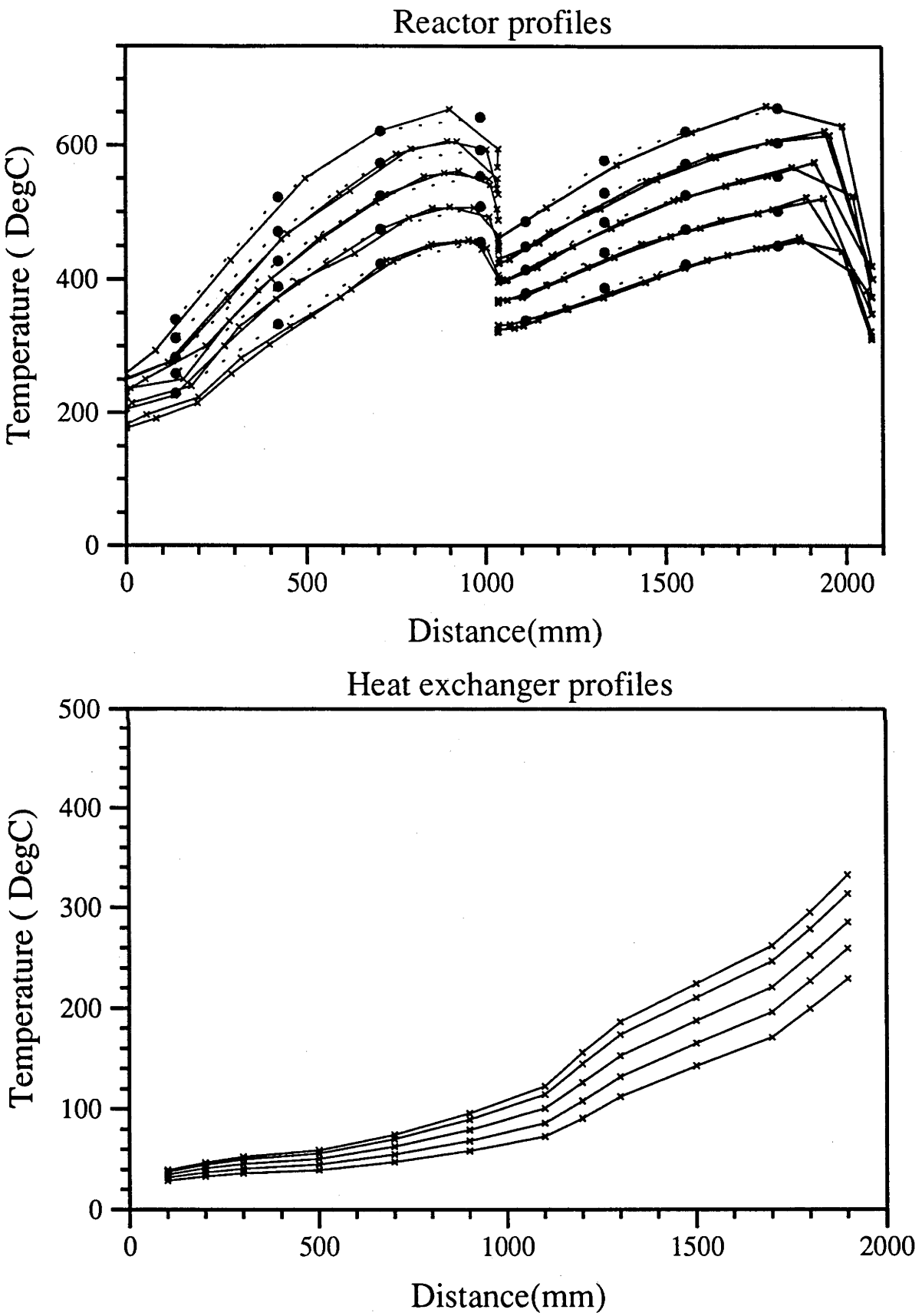

Figure D.25: Steady state temperature profiles, 18th of January 1991.

30th of January 1991

- Further investigation of no flow power levels and temperature profiles to quantify heat loss processes.
- Both heaters controlled by controller 1 to confirm apparent different heat loss from the two columns.
- Improved heater control and power measurement.
- Data acquisition faults in temperature channels at 700, 4800 and 7200 seconds.

Time interval (seconds)	8000-10700
First chamber (column 2)	
Heater power (W)	109.9±1
Second chamber (column 1)	
Temperature setpoint ($°C$)	500
Heater power (W)	100.6±1

Table D.10: Steady state values, 30th of January 1990.

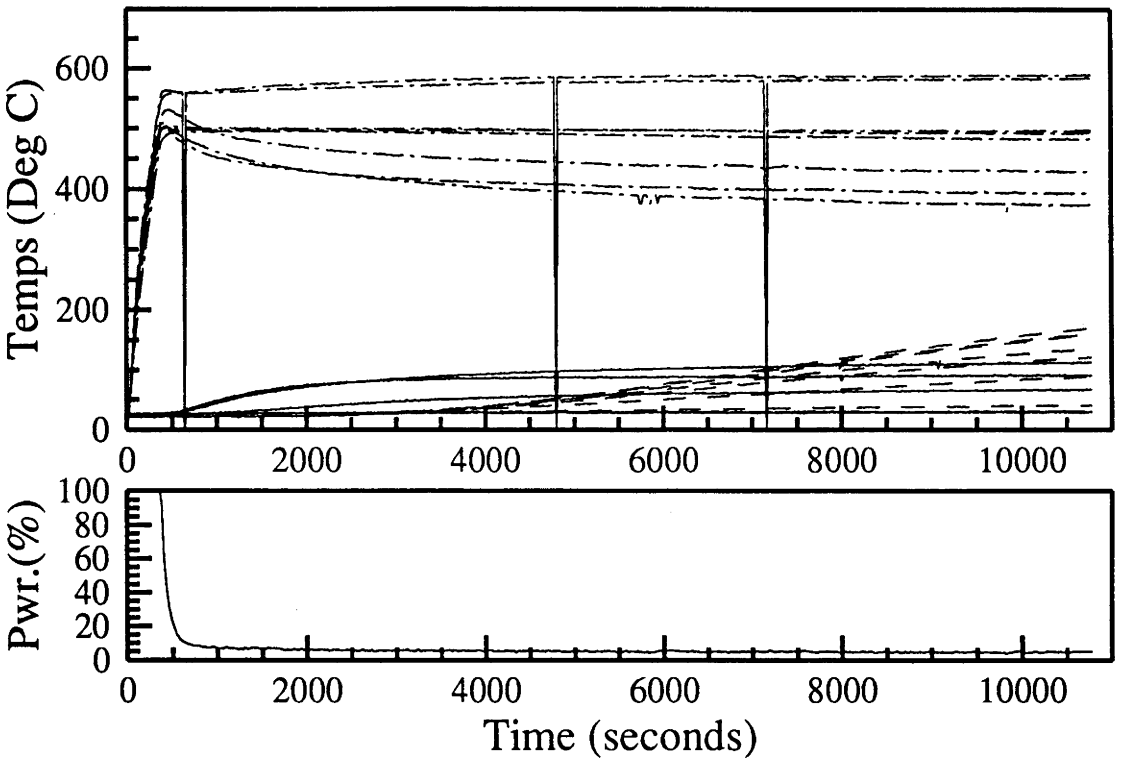

Figure D.26: Time dependance, 30th of January 1991.

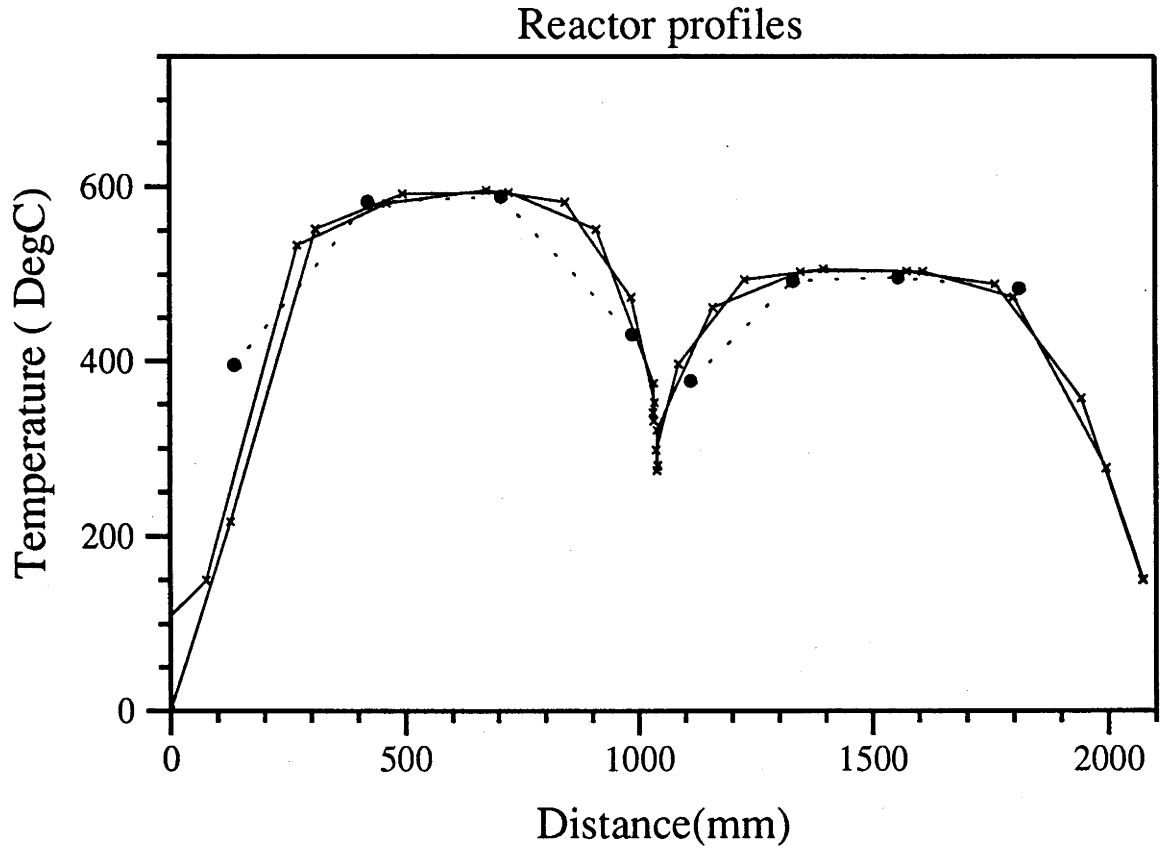

Figure D.27: Steady state temperature profiles, 30th of January 1991.

21st of February 1991

- Investigation of ammonia dissociation at several setpoints up to 675°C.
- Trial of the first prototype of the capacitance level sensor in the ammonia accumulator.
- Short test of the motor driven control valve; heater power constant and self-tuning operation of valve controller from 3500 - 5000 seconds
- Data acquisition fault at 9200 seconds.

Time interval (seconds)	2500-3800	6800-7280	7800-8200	9100-9550
Pressure (MPa)	11.98±0.1	11.97±0.12	12.16±0.1	12.03±0.1
Inlet mass flow (gs^{-1})	0.2956±0.006	0.3113±0.006	0.3064±0.006	0.3006±0.006
Reaction extent	0.330±0.025	0.474±0.02	0.566±0.028	0.7024±0.015
Pressure drop (kPa)	60.5±15	56.5±15	51.5±13	28.8±9
	First chamber (column 2)			
Temperature setpoint (°C)	600	625	650	675
Heater power (W)	582.3±4	589±4	652±9	662.9±4
Inlet temp (°C)	200±5	213±5	226±5	240±5
Outlet temp (°C)	580±15	600±15	620±15	640±15
	Second chamber (column 1)			
Temperature setpoint (°C)	600	625	650	675
Heater power (W)	361.1±2	373.1±2	426±4	441.2±2
Inlet temp (°C)	525±10	540±10	555±10	570±10
Outlet temp (°C)	535±20	556±20	579±20	600±20
	Heat exchanger			
Inlet cold end temp (°C)	27.6±1	28.1±1	28.5±1	28.4±1
Inlet hot end temp (°C)	228.6±3	243.3±3	260.1±3	269.6±3
Outlet cold end temp (°C)	72.5±1	62.6±1	53.7±1	63.6±1
Outlet hot end temp (°C)	455±10	473±10	493±10	505±10

Table D.11: Steady state values, 21st of February 1991.

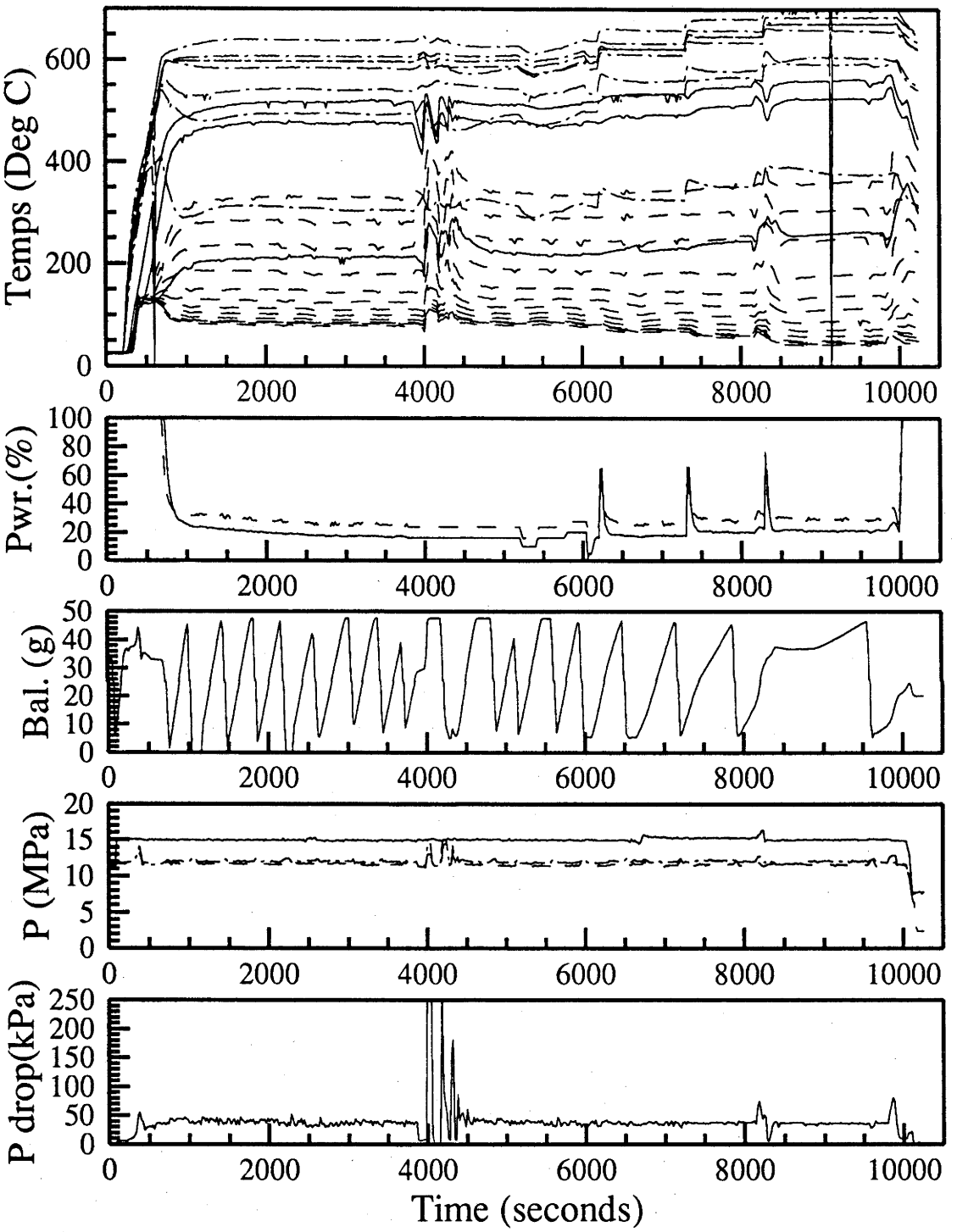

Figure D.28: Time dependance, 21st of February 1991.

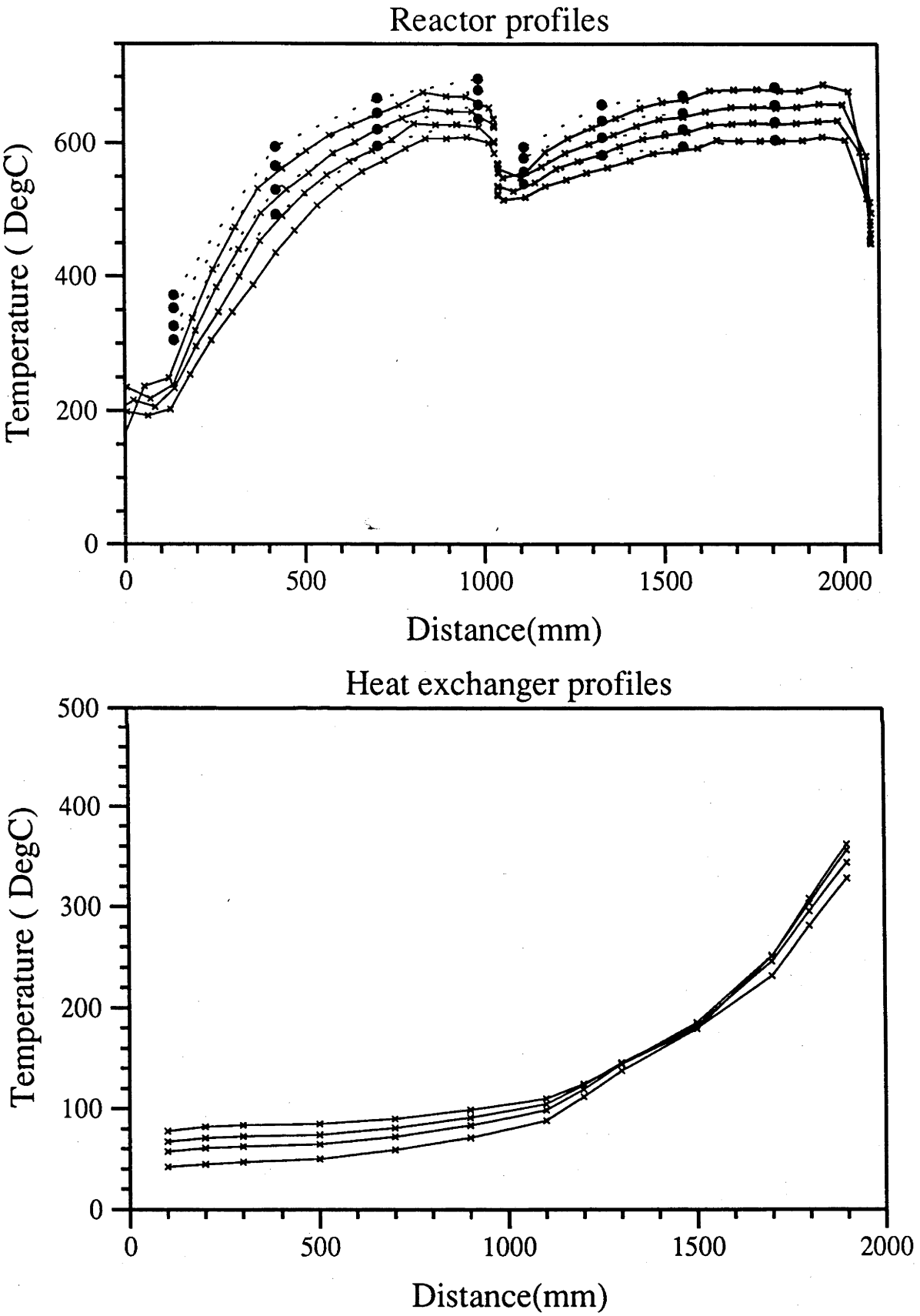

Figure D.29: Steady state temperature profiles, 21st of February 1991.

26th of February 1991

- Second trial of motor driven valve attempt to self tune controller failed due to incorrect valve position operating range.
- Data acquisition faults at 3200 and 4600 seconds.

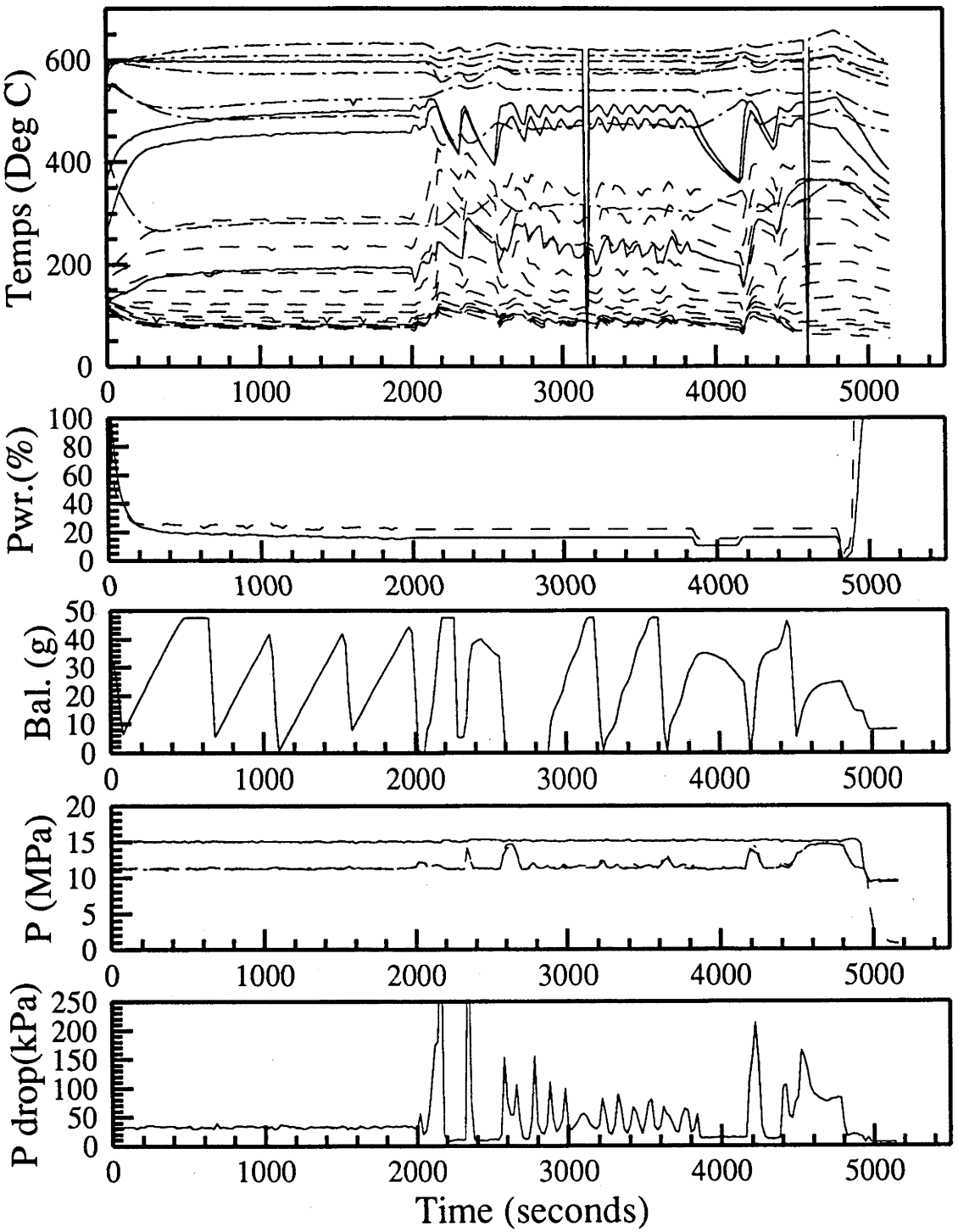

Figure D.30: Time dependance, 26th of February 1991.

6th of March 1991

- Further investigation of no flow power levels and temperature profiles.
- Both heaters controlled by controller 1 to confirm apparent different heat loss from the two columns.
- Slower internal temperature scan with improved scan speed control.

Time interval (seconds)	7500-9600
First chamber (column 2)	
Heater power (W)	127.6±1
Second chamber (column 1)	
Temperature setpoint ($°C$)	570
Heater power (W)	117.7±1

Table D.12: Steady state values, 6th of March 1991.

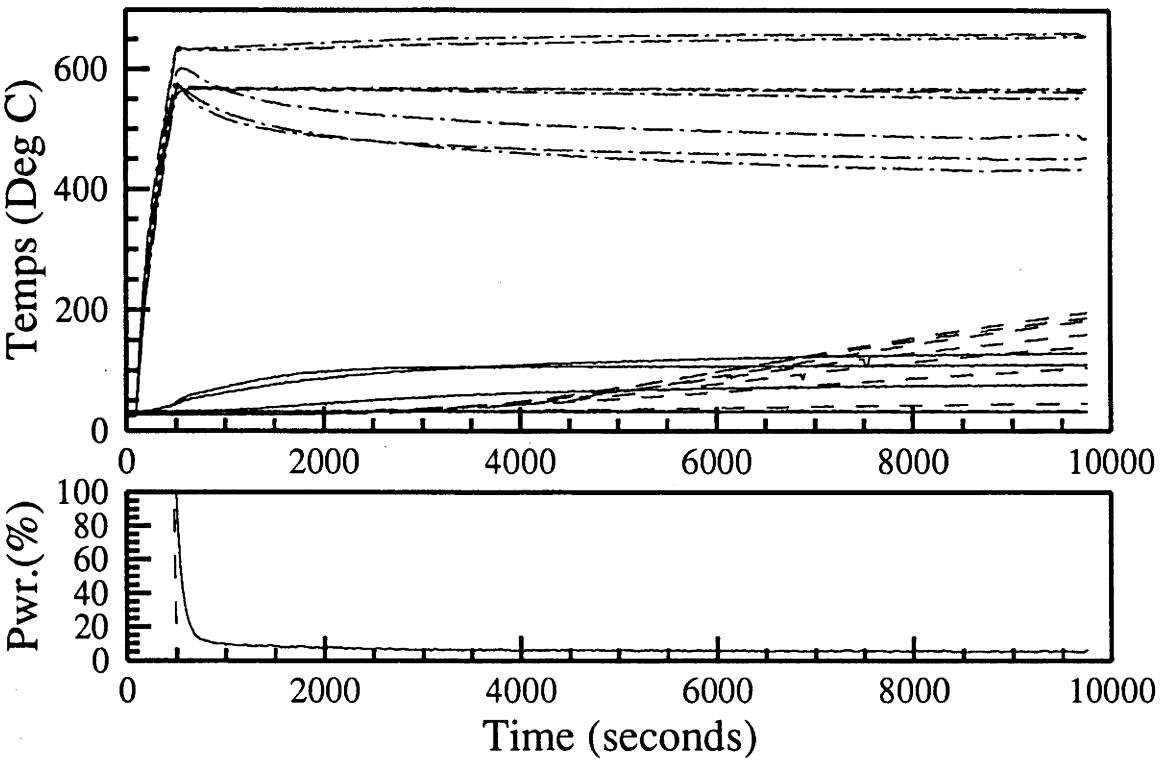

Figure D.31: Time dependance, 6th of March 1991.

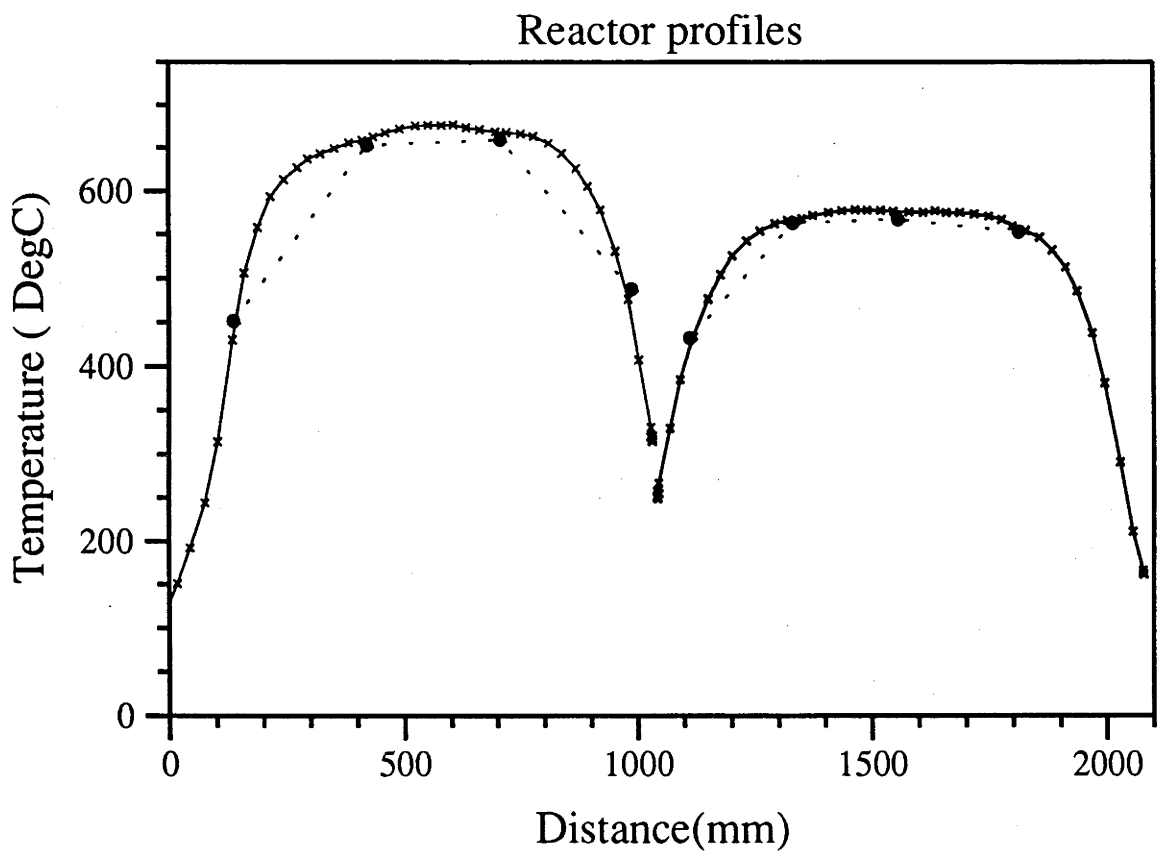

Figure D.32: Steady state temperature profiles, 6th of March 1991.

8th of March 1991

- Further unsuccessful test of motor driven valve.
- Data acquisition fault at 4800 seconds.

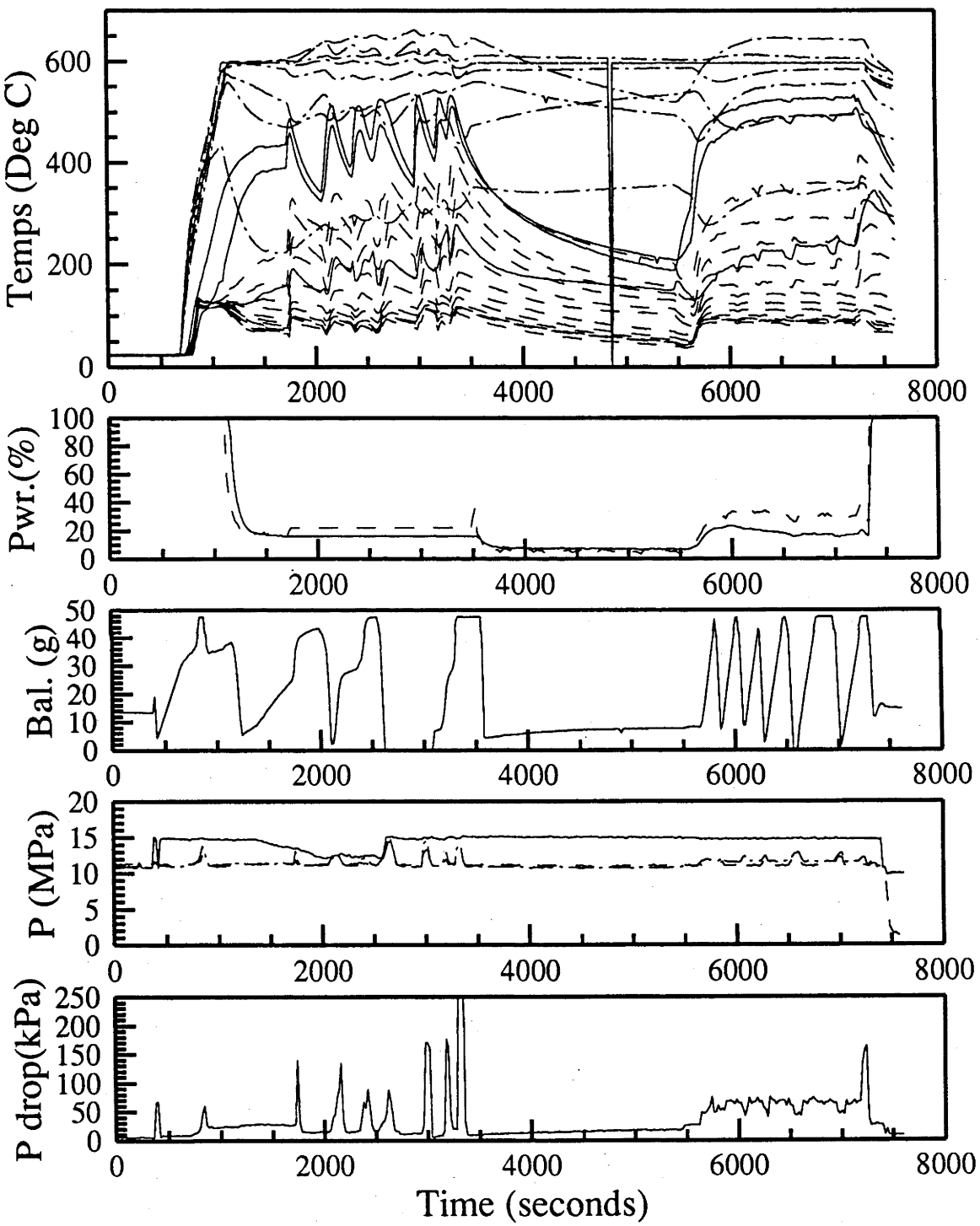

Figure D.33: Time dependance, 8th of March 1991.

11th of March 1991

- First solar flux simulation run.
- Heater powers determined by variable dc voltage input to controller one.
- Successful operation of valve controller with wide proportional band only.
- Accumulator run dry and refilled at 5100 seconds.
- Temporary blockage of exit valve at 6600 seconds.

Time interval (seconds)	0-7750	7750-8500	8500-12740
Accumulator pressure (MPa)	15.04±0.3	15.9±0.3	16.1±0.3
Exit pressure (MPa)	11.4±0.1	10.8±0.1	10.6±0.2
Maximum heater power (W)		847	
Temperature setpoint ($°C$)	525	600	625
Proportional band ($°C$)	75	75	75

Table D.13: System parameters, 11th of March 1991.

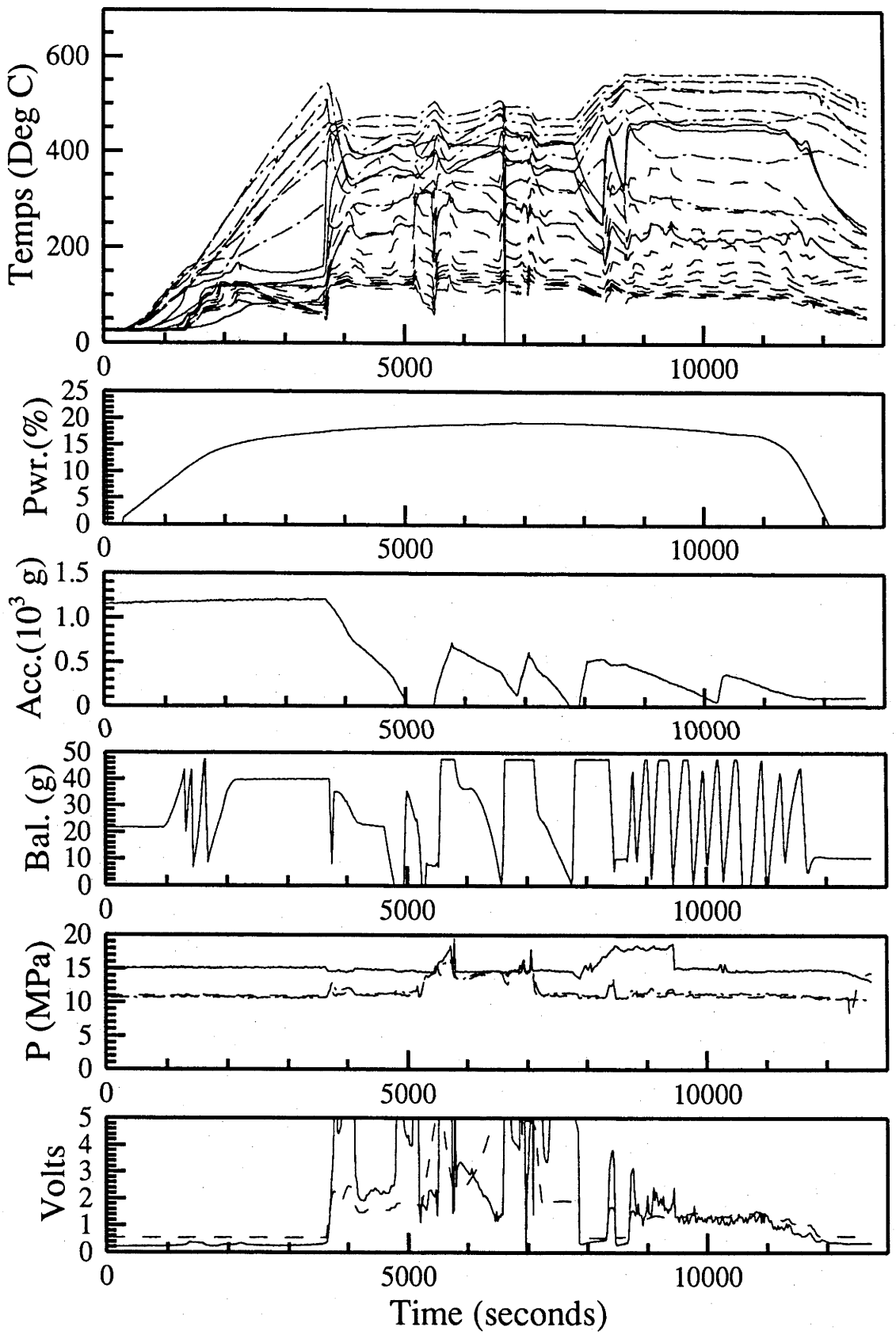

Figure D.34: Time dependance, 11th of March 1991.

21st of March 1991

- Solar flux simulation run at higher temperature.
- Temperature measurement for valve controller shifted to first reaction chamber (column 2).
- Higher value of $\frac{dT}{dx}$ contributed to slight instability with first combination of parameters.
- ammonia level sensor inoperable.

Time interval (seconds)	0-5750	5750-6300	6300-9300
Accumulator pressure (MPa)	12.3±0.1	11.4±0.1	12.4±0.1
Exit pressure (MPa)	10.3±0.1	9.6±0.1	10.3±0.1
Maximum heater power (W)	953		
Temperature setpoint ($°C$)	625	625	710
Proportional band ($°C$)	75	75	150

Table D.14: System parameters, 21st of March 1991.

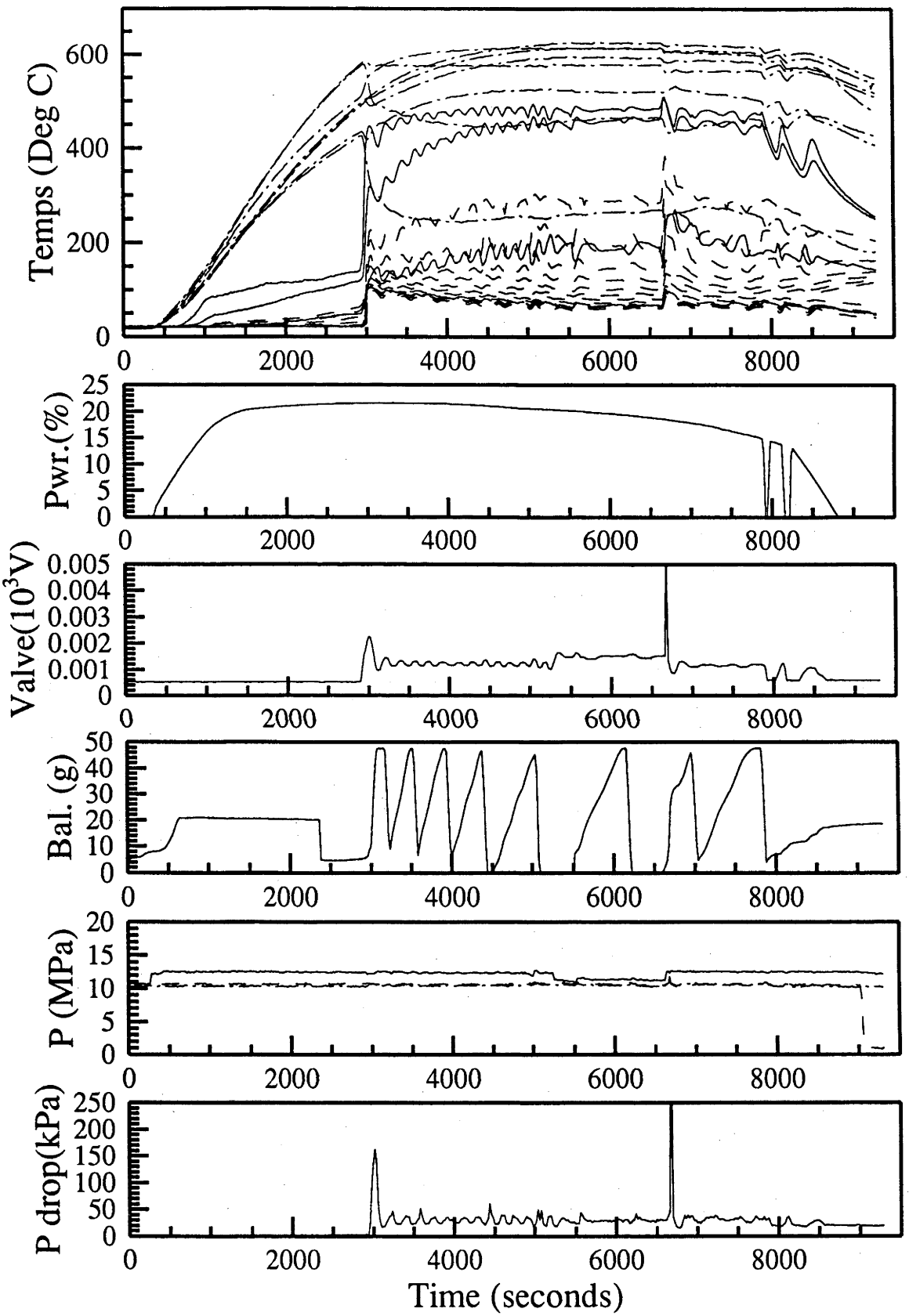

Figure D.35: Time dependance, 21st of March 1991.

27th of March 1991

- Primarily a comparison of fast and slow internal temperature scans.
- Two setpoints tested at $10MPa$, $0.35gs^{-1}$.
- Ammonia run dry and refilled at 5800 seconds.

Time interval (seconds)	3000-4500	6700-7690
Pressure (MPa)	12.81±0.1	12.96±0.1
Inlet mass flow (gs^{-1})	0.343±0.01	0.365±0.01
Reaction extent	0.308±0.044	0.414±0.034
Pressure drop (kPa)	54.3±10	56.7±10
	First chamber (column 2)	
Temperature setpoint (°C)	625	650
Heater power (W)	754.3±7	811.5±9
Inlet temp (°C)	223±5	243±5
Outlet temp (°C)	603±5	628±5
	Second chamber (column 1)	
Temperature setpoint (°C)	625	650
Heater power (W)	436.8±4	468.1±5
Inlet temp (°C)	560±5	585±5
Outlet temp (°C)	575±15	594±15
	Heat exchanger	
Inlet cold end temp (°C)	23.8±1	23.3±1
Inlet hot end temp (°C)	258.9±4	283.8±2
Outlet cold end temp (°C)	71.6±1	64.8±1
Outlet hot end temp (°C)	492±5	511±5

Table D.15: Steady state values, 27th of March 1991.

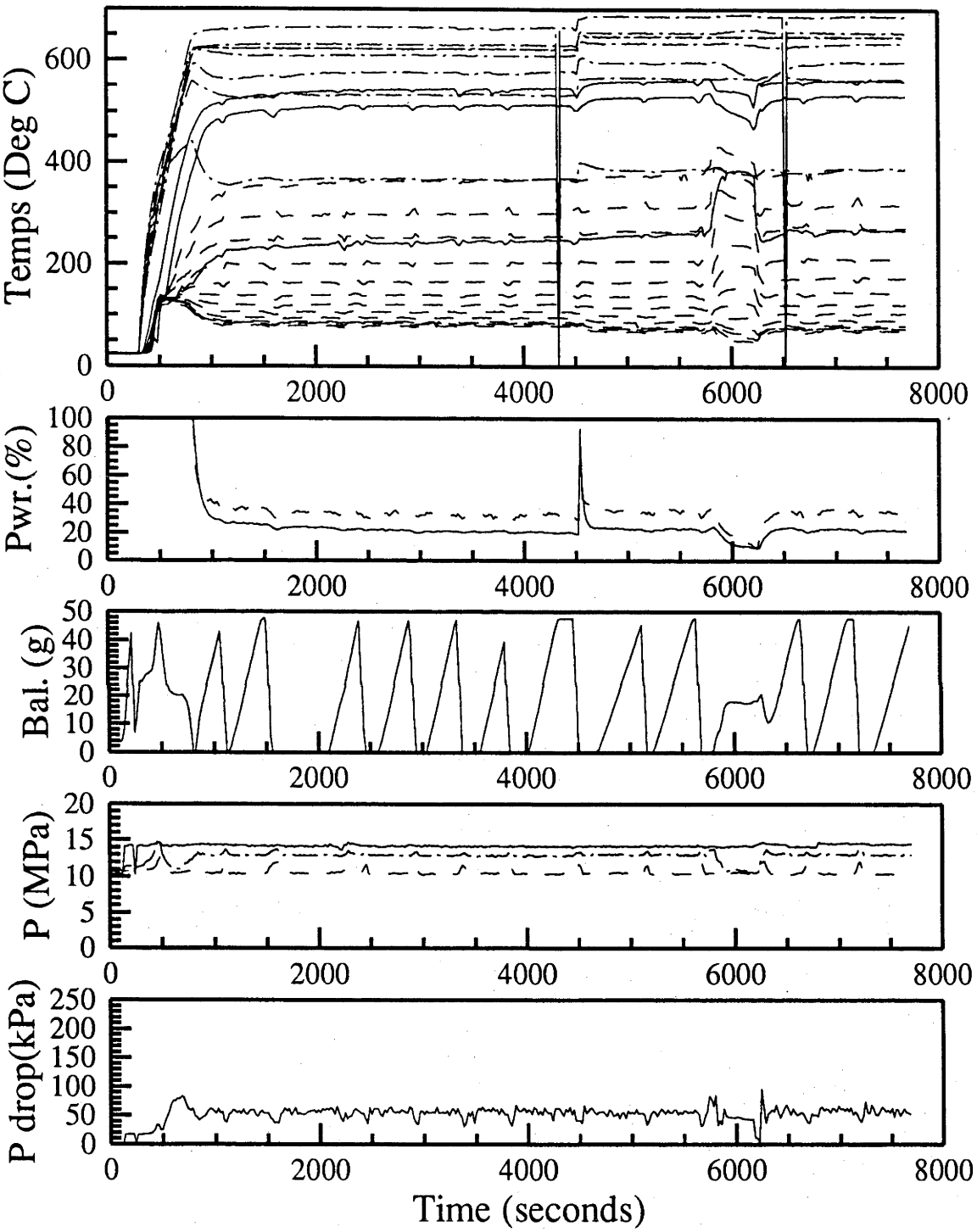

Figure D.36: Time dependance, 27th of March 1991.

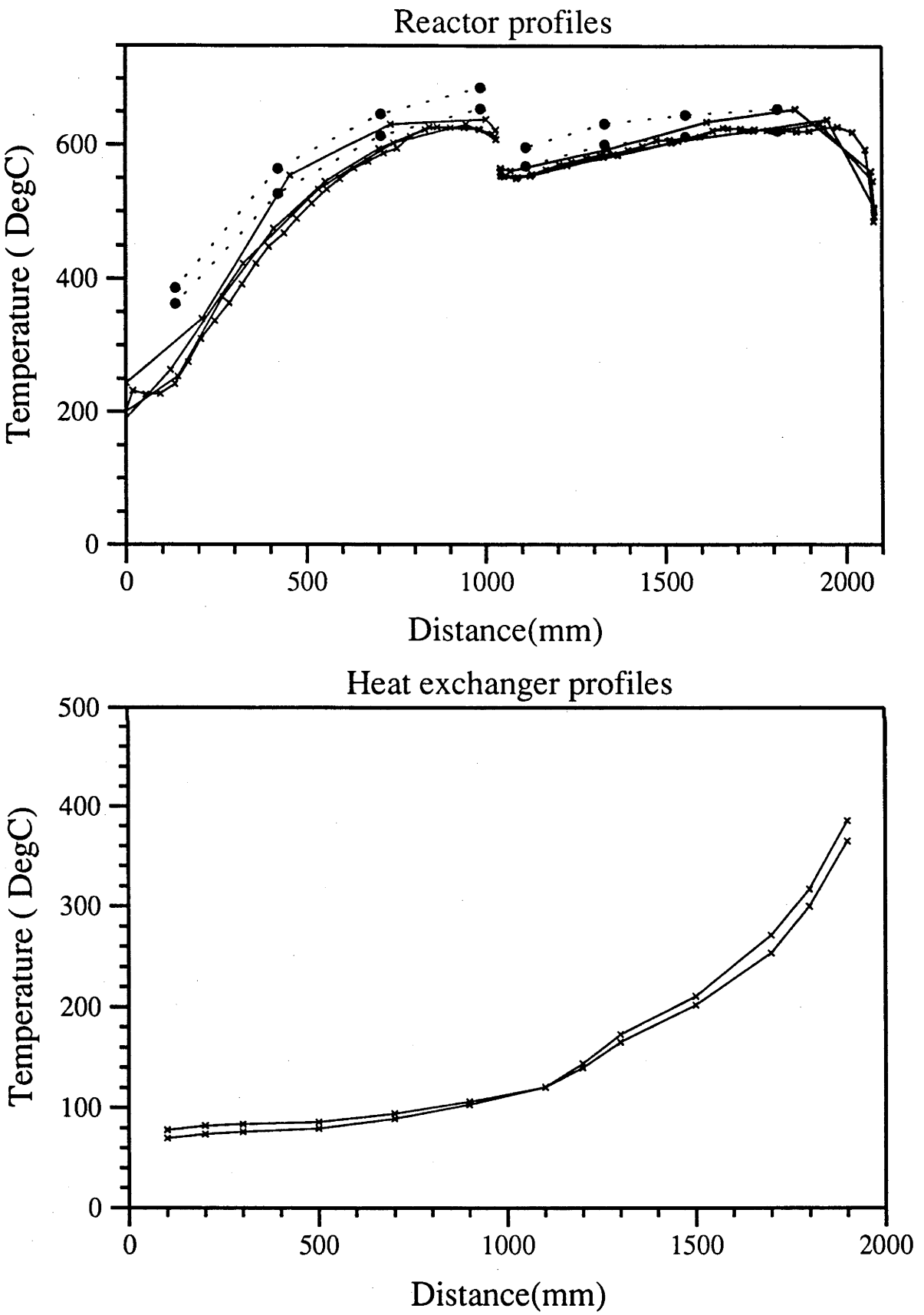

Figure D.37: Steady state temperature profiles, 27th of March 1991.

3rd of April 1991

- Further investigation of no flow power levels and temperature profiles.
- Lower temperatures to investigate temperature dependance of heat loss process.

Time interval (seconds)	7000-8500
First chamber (column 2)	
Temperature setpoint ($°C$)	450
Heater power (W)	41.19±0.3
Second chamber (column 1)	
Temperature selpoint ($°C$)	450
Heater power (W)	86.65±0.5

Table D.16: Steady state values, 3rd of April 1991.

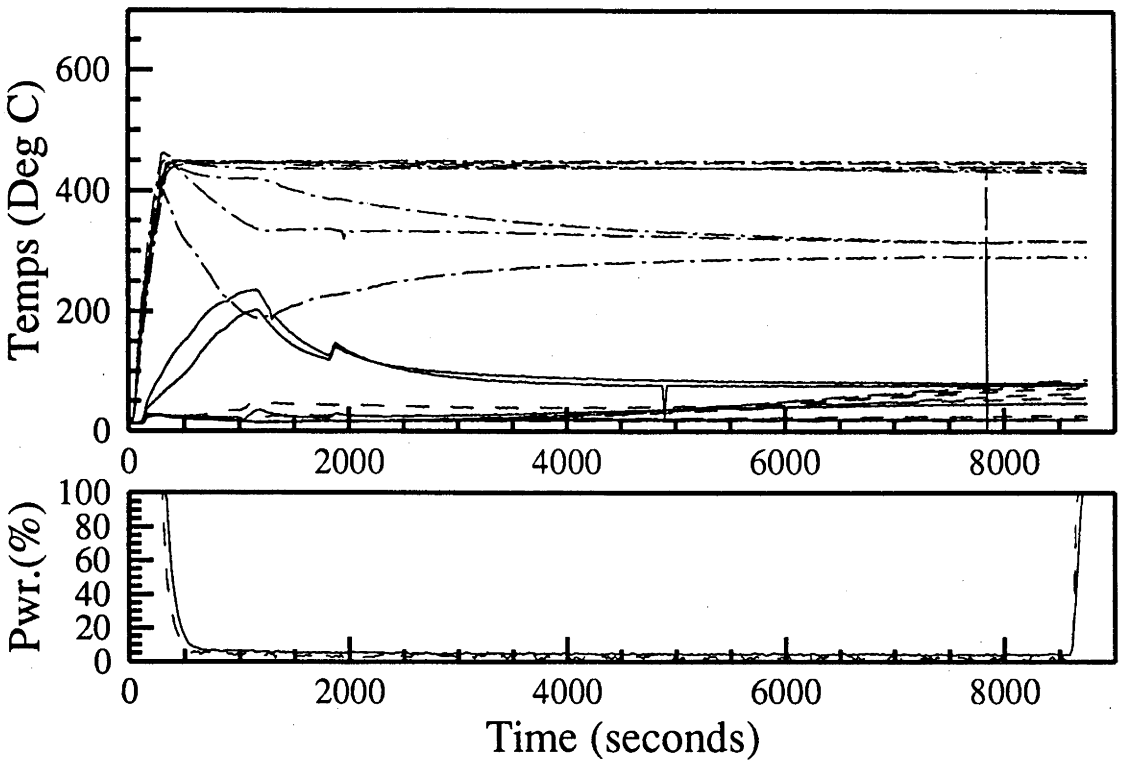

Figure D.38: Time dependance, 3rd of April 1991.

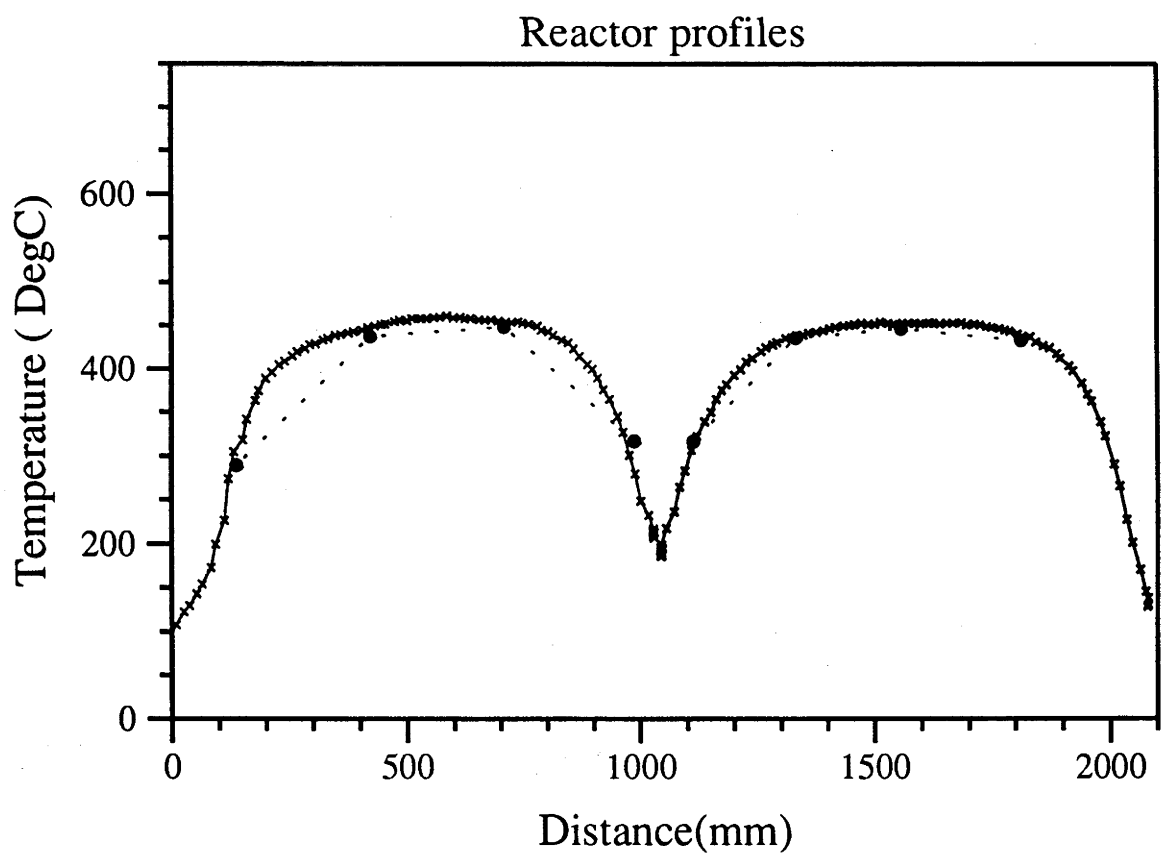

Figure D.39: Steady state temperature profiles, 3rd of April 1991.

5th of April 1991

- Successful complete solar flux cycle simulation.
- Simulation of intermitant cloud at 4750 - 5500 seconds.
- Second prototype ammonia level sensor working well.
- Data acquisition fault at 5000 seconds.

Accumulator pressure (MPa)	11.1±0.1
Exit pressure (MPa)	10.1±0.1
Maximum heater power (W)	1045
Temperature setpoint ($°C$)	710
Proportional band ($°C$)	150

Table D.17: System parameters, 5th of April 1991.

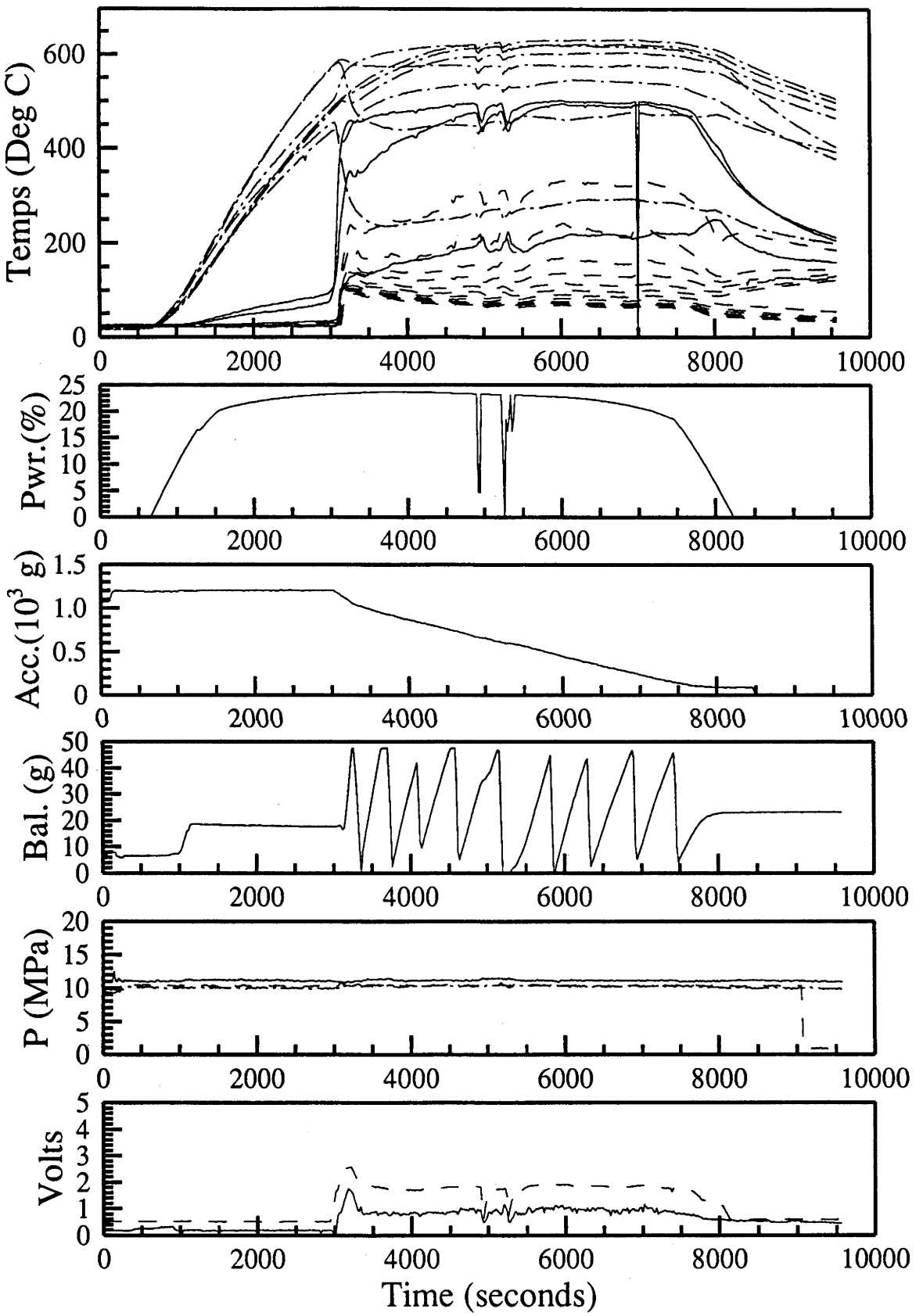

Figure D.40: Time dependance, 5th of April 1991.

8th of April 1991

- Starting an investigation of the effect of pressure for setpoint temperatures of 650°C and mass flow $0.2gs^{-1}$.
- Problems with time values due to attempt to incorporate variable sample rate.
- Loss of data acquisition from 7005 to 7305 seconds.
- Data acquisition faults at 3800 and 7800 seconds.

Time interval (seconds)	4000-4550	7555-7945
Pressure (MPa)	10.65±0.01	7.0185±0.01
Inlet mass flow (gs^{-1})	0.2391±0.0035	0.2055±0.007
Reaction extent	0.510±0.015	0.634±0.02
Pressure drop (kPa)	21.75±8	26.2±8
	First chamber (column 2)	
Temperature setpoint (°C)	650	650
Heater power (W)	696.5±7	606.7±6
Inlet temp (°C)	181.0±2	190.0±2
Outlet temp (°C)	618.0±4	610.0±5
	Second chamber (column 1)	
Temperature setpoint (°C)	650	650
Heater power (W)	437.6±3	384.1±2.3
Inlet temp (°C)	552.5±2	542.0±2
Outlet temp (°C)	600.0±5	595.0±5
	Heat exchanger	
Inlet cold end temp (°C)	19.54±1	19.21±1
Inlet hot end temp (°C)	246.7±1	225.7±3
Outlet cold end temp (°C)	48.0±1	31.74±1
Outlet hot end temp (°C)	506±4	501±4

Table D.18: Steady state values, 8th of April 1991.

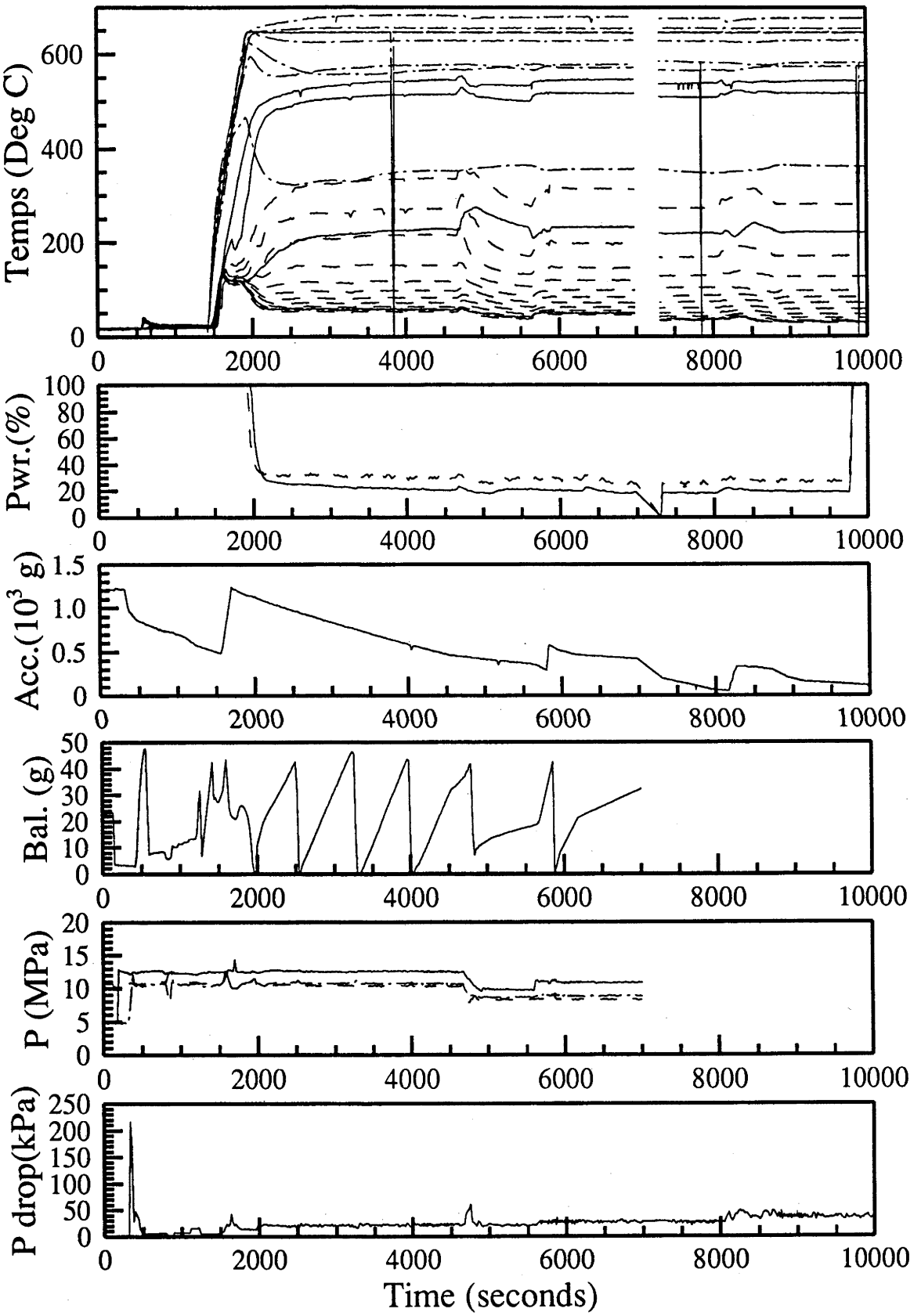

Figure D.41: Time dependance, 8th of April 1991.

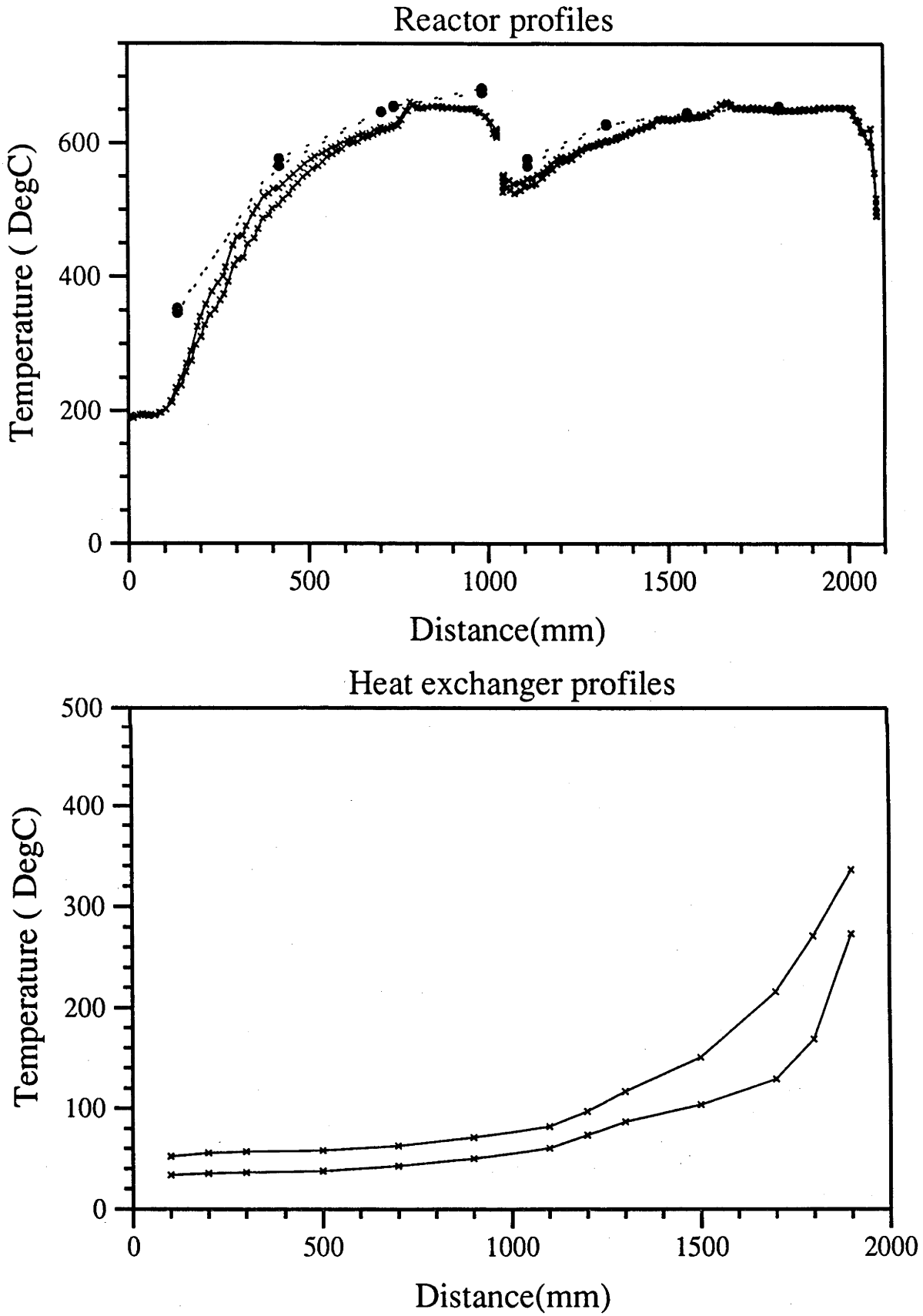

Figure D.42: Steady state temperature profiles, 8th of April 1991.

10th of April 1991

- Completion of the investigation of pressure dependance.
- Data acquisition faults at 1600, 3300 and 6700 seconds.

Time interval (seconds)	2650-3350	4000-4600	5350-6000	6500-7100	7600-8200
Pressure (MPa)	14.32±0.1	16.02±0.07	12.32±0.05	9.013±0.03	7.132±0.02
Inlet mass flow (gs^{-1})	0.2903±.007	0.348±.01	0.2516±.005	0.2347±.005	0.2903±.007
Reaction extent	0.392±.02	0.490±.02	0.509±.015	0.520±.016	0.574±.02
Pressure drop (kPa)	18±6	15±5	16±5	21±7	24±7
	First chamber (column 2)				
Temperature setpoint ($°C$)	650	650	650	650	650
Heater power (W)	752.6±6	703.4±6	625.6±5	623.4±5	623.6±4
Inlet temp ($°C$)	232.0±4	246.0±4	215.0±4	225.0±4	220.0±4
Outlet temp ($°C$)	620.0±5	620.0±5	616.0±5	610.0±5	607.0±5
	Second chamber (column 1)				
Temperature setpoint ($°C$)	650	650	650	650	650
Heater power (W)	444.5±3	399.8±2	383.9±5	390.6±2	392.8±2
Inlet temp ($°C$)	562.0±5	573.0±5	556.0±5	548.0±5	545.0±5
Outlet temp ($°C$)	590.0±15	590.0±15	590.0±15	590.0 ±15	570.0±15
	Heat exchanger				
Inlet cold end temp ($°C$)	23.4±1.3	22.6±1	21.9±1	22.7±1	21.8±1
Inlet hot end temp ($°C$)	272±8	283.7±2	267.6±2	246±8	233.1±2
Outlet cold end temp ($°C$)	63.1±2	64.6±1	53.7±1	45.1±1	37.6±1
Outlet hot end temp ($°C$)	503±5	495±5	495±5	501±5	502±5

Table D.19: Steady state values, 10th of April 1991.

Time interval (seconds)	8600-9200	9500-10070	10400-11000	11400-12000
Pressure (MPa)	5.265±0.03	5.873±0.026	6.523±0.015	7.840±0.015
Inlet mass flow (gs^{-1})	0.2481±.0054	0.2173±.0053	0.2108±.005	0.2097±.005
Reaction extent	0.6590±0.02	0.6201±0.018	0.6014±0.017	0.5635±0.016
Pressure drop (kPa)	28±8	26±8	24±6	21±6
	First chamber (column 2)			
Temperature setpoint ($°C$)	650	650	650	650
Heater power (W)	603.4±6	584.1±5	592.9±5	579.6±5
Inlet temp ($°C$)	225.0±4	203.0±4	200.0±4	200.0±4
Outlet temp ($°C$)	610.0±5	600.0±5	607.0±5	608.0 ±5
	Second chamber (column 1)			
Temperature setpoint ($°C$)	650	650	650	650
Heater power (W)	388.3±2	384.6±2	379.6±2	371.8±2
Inlet temp ($°C$)	537.0±5	531.0±5	532.0±5	533.0±5
Outlet temp ($°C$)	578.0±15	596.0±15	570.0±15	570.0 ±15
	Heat exchanger			
Inlet cold end temp ($°C$	22.1±1	21.8±1	21.8±1	22.0±1
Inlet hot end temp ($°C$)	162.6±4	171.5±2	178.3±1.5	204.5±1.5
Outlet cold end temp ($°C$)	26.8±1	29.3±1	32.4±1	38.4±1
Outlet hot end temp ($°C$)	513.1±1.3	511.3±1	509.7±1	507.5±1

Table D.20: Steady state values, 10th of April 1991 continued.

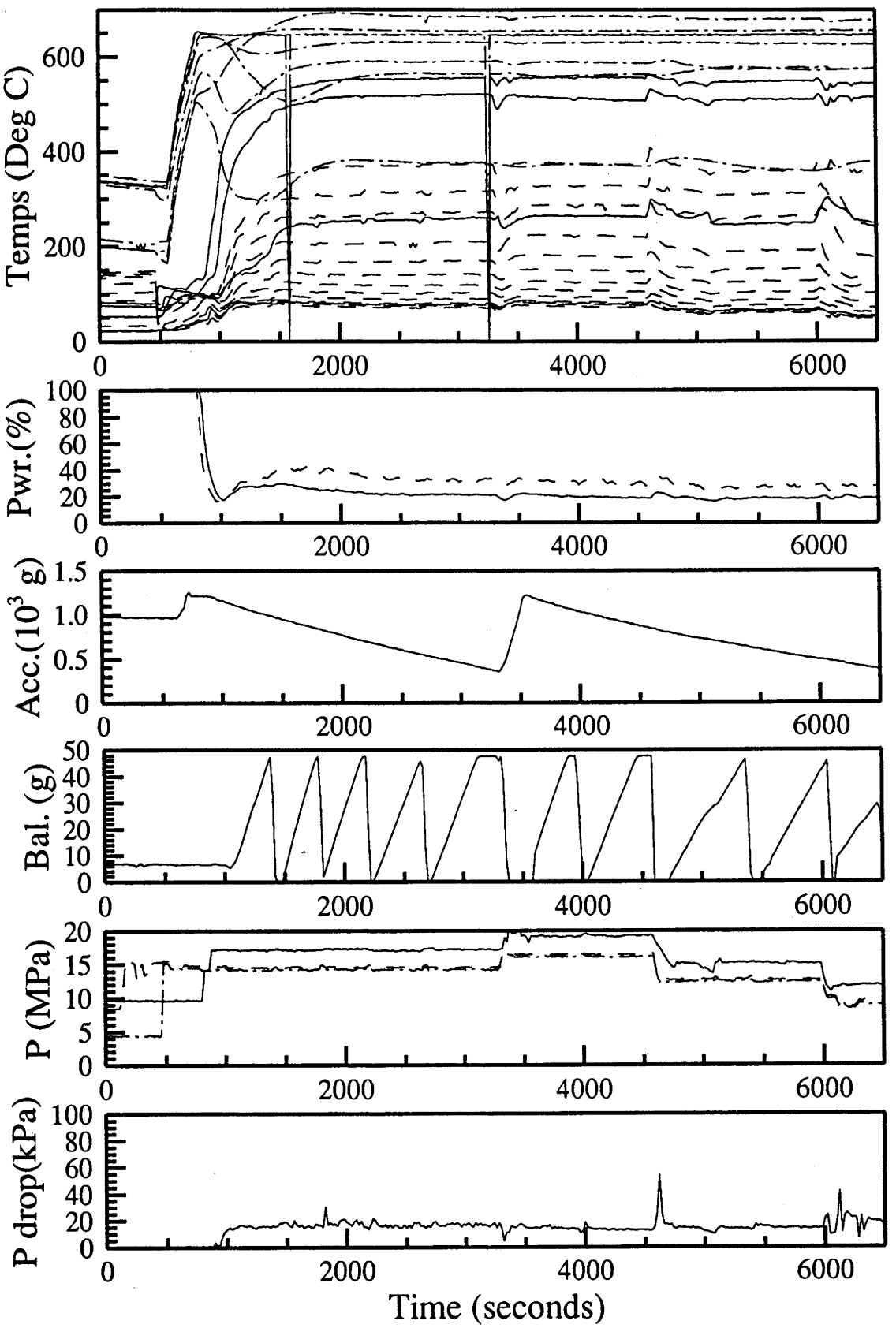

Figure D.43: Time dependance, 10th of April 1991.

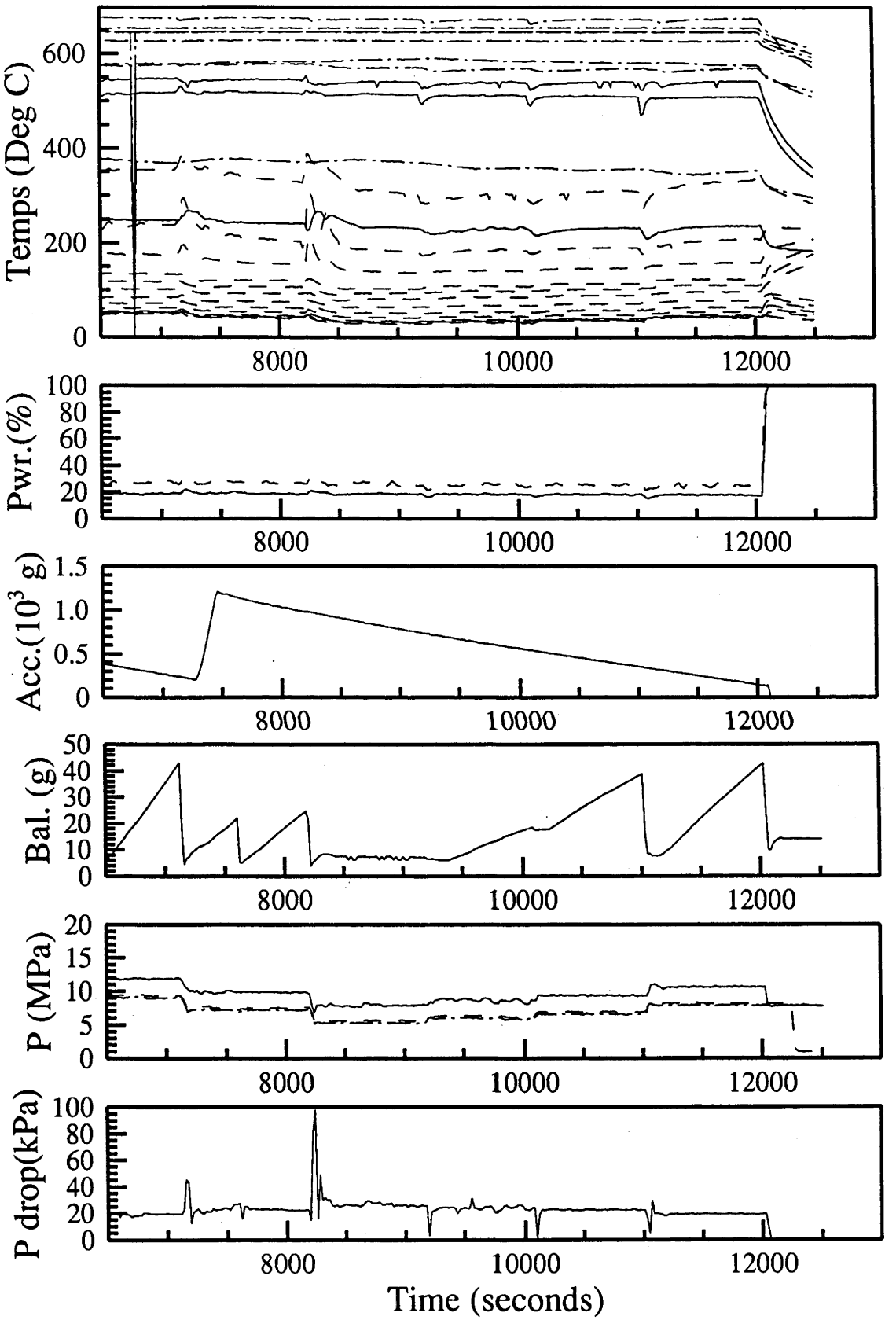

Figure D.44: Time dependance, 10th of April 1991 continued.

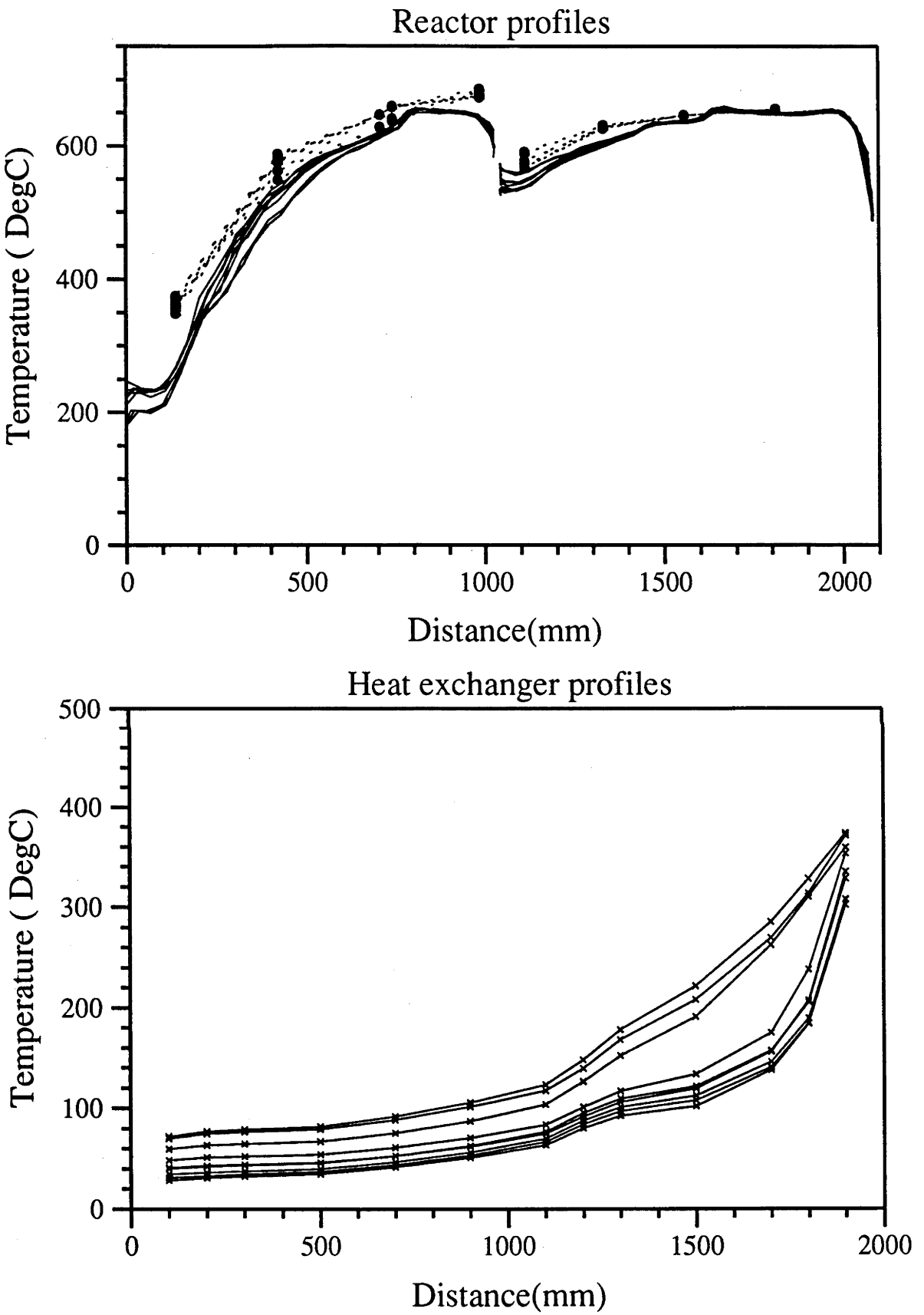

Figure D.45: Steady state temperature profiles, 10th of April 1991.

16th of April 1991

- Investigation of several flow rates at a nominal pressure of $10 MPa$, and temperature controller set points $650°C$.
- Data acquisition faults at 3840 and 10820 seconds.

Time interval (seconds)	4600-5350	8000-8700	10000-10750
Pressure (MPa)	9.836±0.014	9.859±0.014	9.942±0.018
Inlet mass flow (gs^{-1})	0.0878±0.0015	0.1377±0.002	0.3380±0.0015
Reaction extent	0.777±0.012	0.714±0.011	0.422±0.015
Pressure drop (kPa)	28±8	29.5±8	75.6±20
	First chamber (column 2)		
Temperature setpoint ($°C$)	650	650	650
Heater power (W)	417.1±3.2	451.7±3.6	805.1±3.3
Inlet temp ($°C$)	130.0±4	152.0±4	230.0±4
Outlet temp ($°C$)	572.0±5	586.0±5	623.0±5
	Second chamber (column 1)		
Temperature setpoint ($°C$)	650	650	650
Heater power (W)	311.1±1.2	307.9±1	463.1±1.3
Inlet temp ($°C$)	458.0±5	485.0±5	563.0±5
Outlet temp ($°C$)	550.0±15	550.0±15	610.0±15
	Heat exchanger		
Inlet cold end temp ($°C$)	19.8±1	19.1±1	18.5±1
Inlet hot end temp ($°C$)	172.8±2	171.4±3	271.7±2
Outlet cold end temp ($°C$)	22.7±1	29.5±1	55.7±1
Outlet hot end temp ($°C$)	408±5	441±5	514±5

Table D.21: Steady state values, 16th of April 1991.

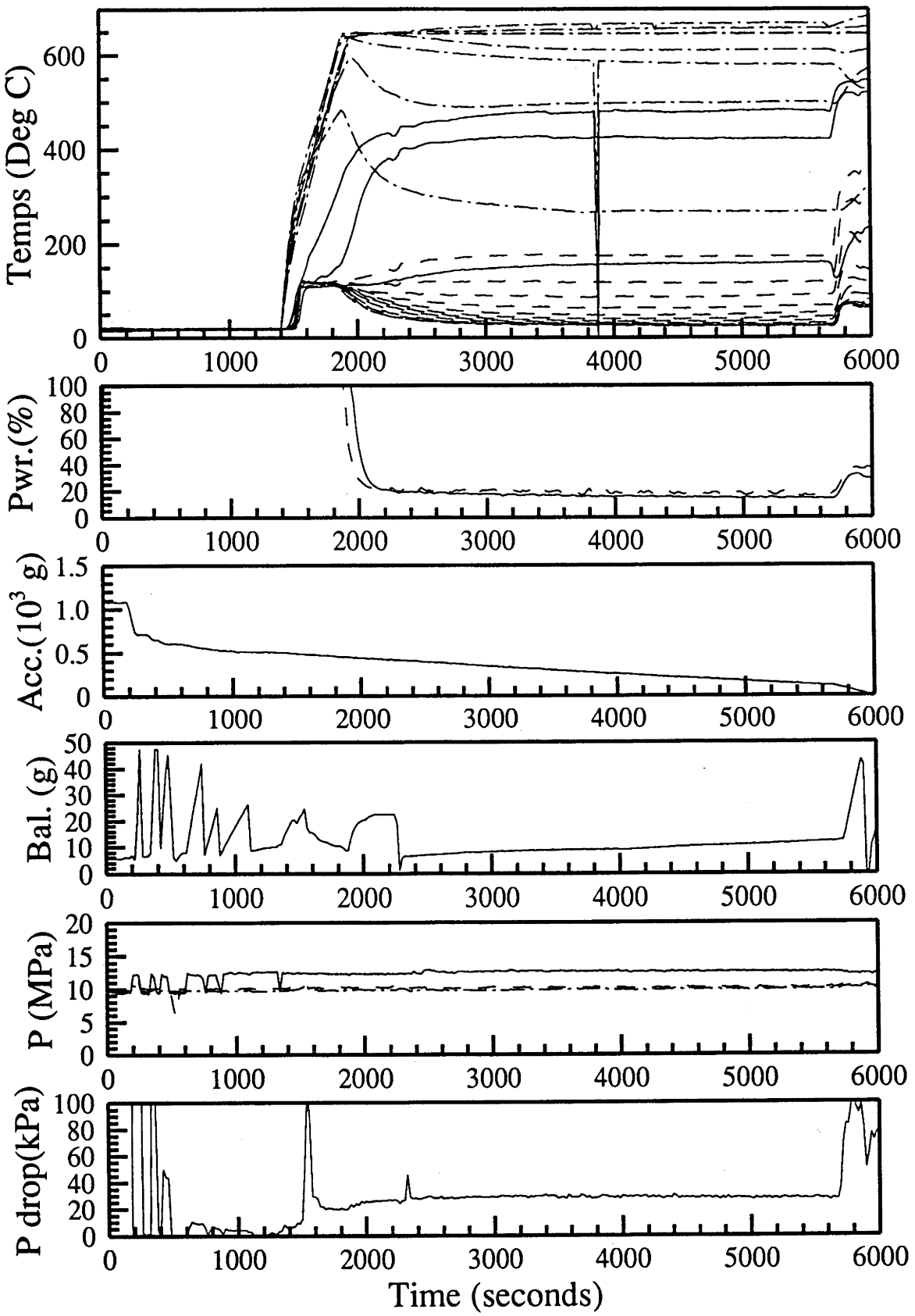

Figure D.46: Time dependance, 16th of April 1991.

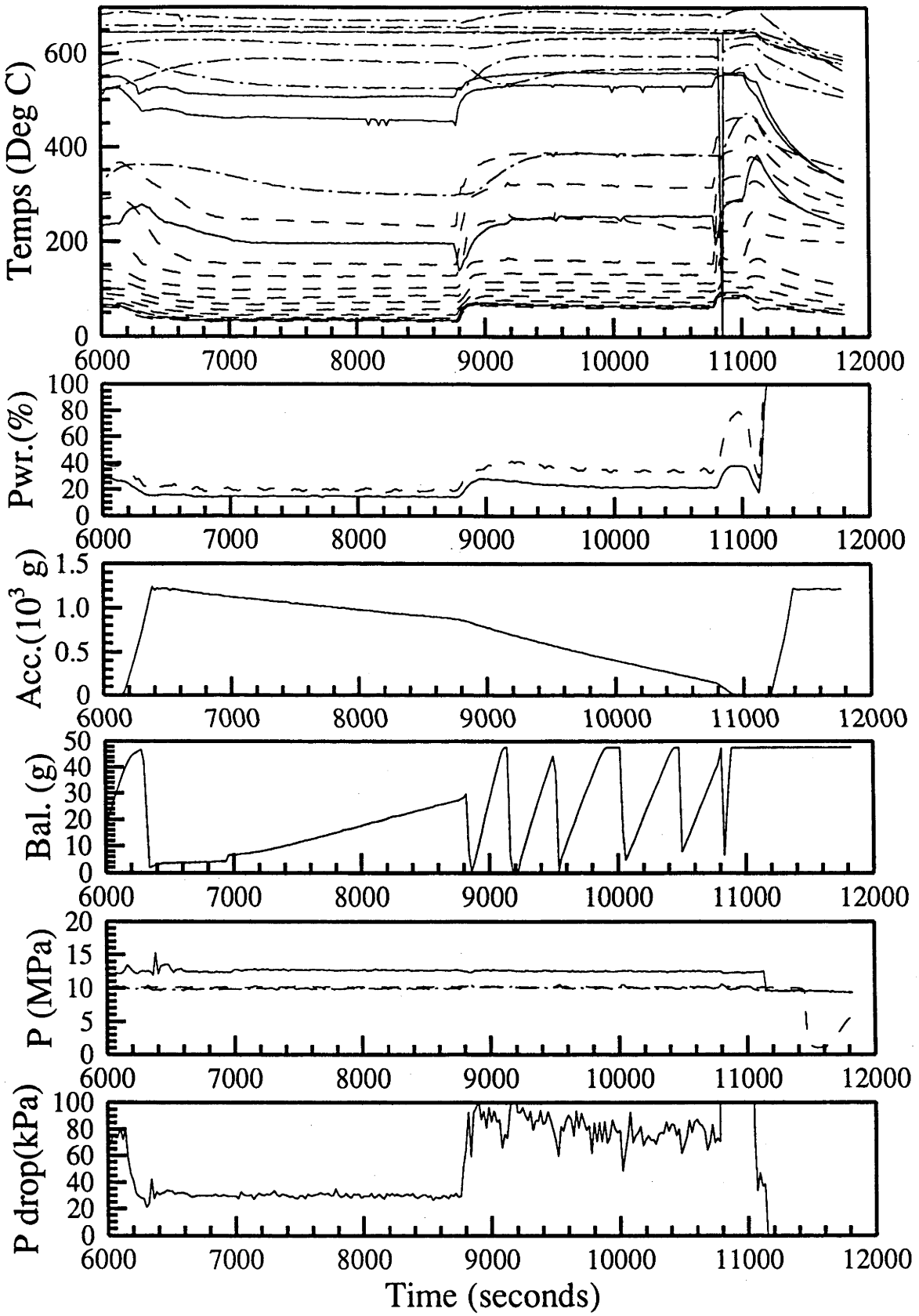

Figure D.47: Time dependance, 16th of April 1991 continued.

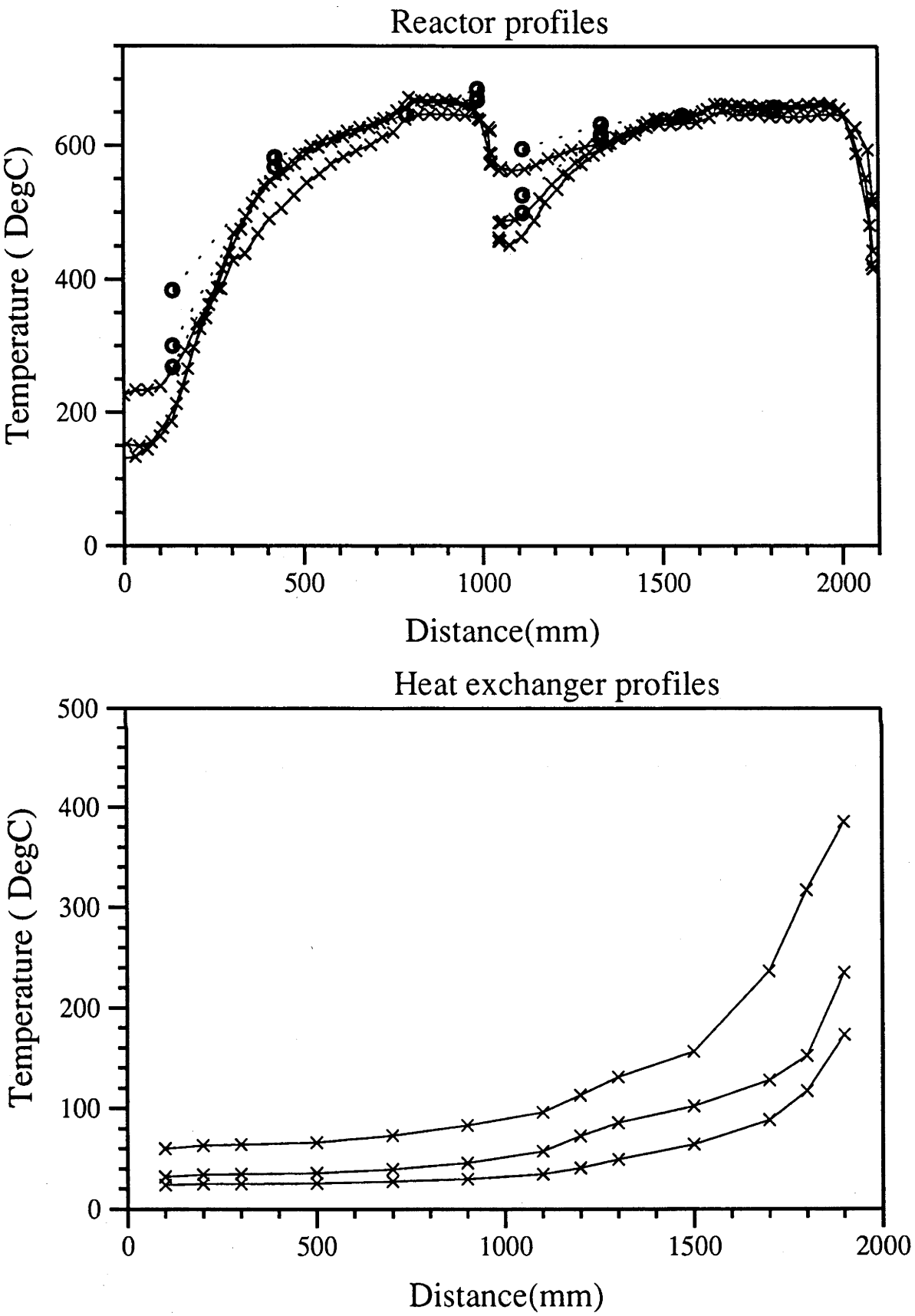

Figure D.48: Steady state temperature profiles, 16th of April 1991.

18th of April 1991

- Completion of flow rate variation investigation.
- Two intervals at higher temperature at end to test upper limit of reactor capacity.
- Data acquisition fault at 7800 seconds.

Time interval (seconds)	3800-4300	5600-6250	6850-7450	8100-8650
Pressure (MPa)	9.87±0.02	10.01±0.02	10.50±0.03	10.83±0.03
Inlet mass flow (gs^{-1})	0.2414±0.006	0.7913±0.003	1.174±0.005	1.465±0.02
Reaction extent	0.529±0.02	0.270±0.02	0.236±0.024	0.240±0.024
Pressure drop (kPa)	22±7	227±20	1018±30	1698±30
	First chamber (column 2)			
Temperature setpoint ($°C$)	650	650	650	650
Heater power (W)	692±6	1276±5	1538±10	1660±5
Inlet temp ($°C$)	192.0±4	284.0±4	295.0±4	313.0±4
Outlet temp ($°C$)	560.0±15	617.0±5	609.0±5	604.0±5
	Second chamber (column 1)			
Temperature setpoint ($°C$)	650	650	650	650
Heater power (W)	457.6±2	689±2	784.4±2	820±3
Inlet temp ($°C$)	540.0±15	586.0±2	584.0±5	582.0±5
Outlet temp ($°C$)	560.0±15	600.0±15	588.0±15	586.0±15
	Heat exchanger			
Inlet cold end temp ($°C$)	20.8±1	19.2±1	17.7±1	16.5±1
Inlet hot end temp ($°C$)	228.5±2	302.0±2	312.3±2	324.5±2
Outlet cold end temp ($°C$)	45.9±1	71.3±1	79.2±1	81.7±1
Outlet hot end temp ($°C$)	487±5	535±5	539±5	541±5

Table D.22: Steady state values, 18th of April 1991.

Time interval (seconds)	9450-9940	10250-10750	11200-11660	12000-12450
Pressure (MPa)	10.37±0.03	10.75±0.02	10.85±0.03	10.82±0.04
Inlet mass flow (gs^{-1})	0.958±0.01	1.192±0.006	1.250±0.008	1.146±0.02
Reaction extent	0.321±0.025	0.220±0.03	0.283±0.022	0.267±0.04
Pressure drop (kPa)	839±30	1139±20	1771±30	1871±40
	First chamber (column 2)			
Temperature setpoint ($°C$)	650	650	675	700
Heater power (W)	1222±6	1589±6	1686±4	1860±9
Inlet temp ($°C$)	286.0±4	310.0±4	320.0±4	325.0±4
Outlet temp ($°C$)	617.0±5	608.0±5	625.0±5	640.0 ±5
	Second chamber (column 1)			
Temperature setpoint ($°C$)	650	650	675	675
Heater power (W)	649.2±3	772.5±1	886.3±1.5	818.7±2
Inlet temp ($°C$)	584.0±5	583.0±5	600.0±5	610.0±5
Outlet temp ($°C$)	588.0±15	587.0±15	604.0±15	614.0 ±15
	Heat exchanger			
Inlet cold end temp ($°C$)	18.3±1	17.3±1	16.6±1	16.4±1
Inlet hot end temp ($°C$)	302.6±2	321.6±2	333.7±2	335.6±2
Outlet cold end temp ($°C$)	72.8±1	80.0±1	74.1±1	71.2±1
Outlet hot end temp ($°C$)	533±5	537±5	554±5	558±5

Table D.23: Steady state values, 18th of April 1991 continued.

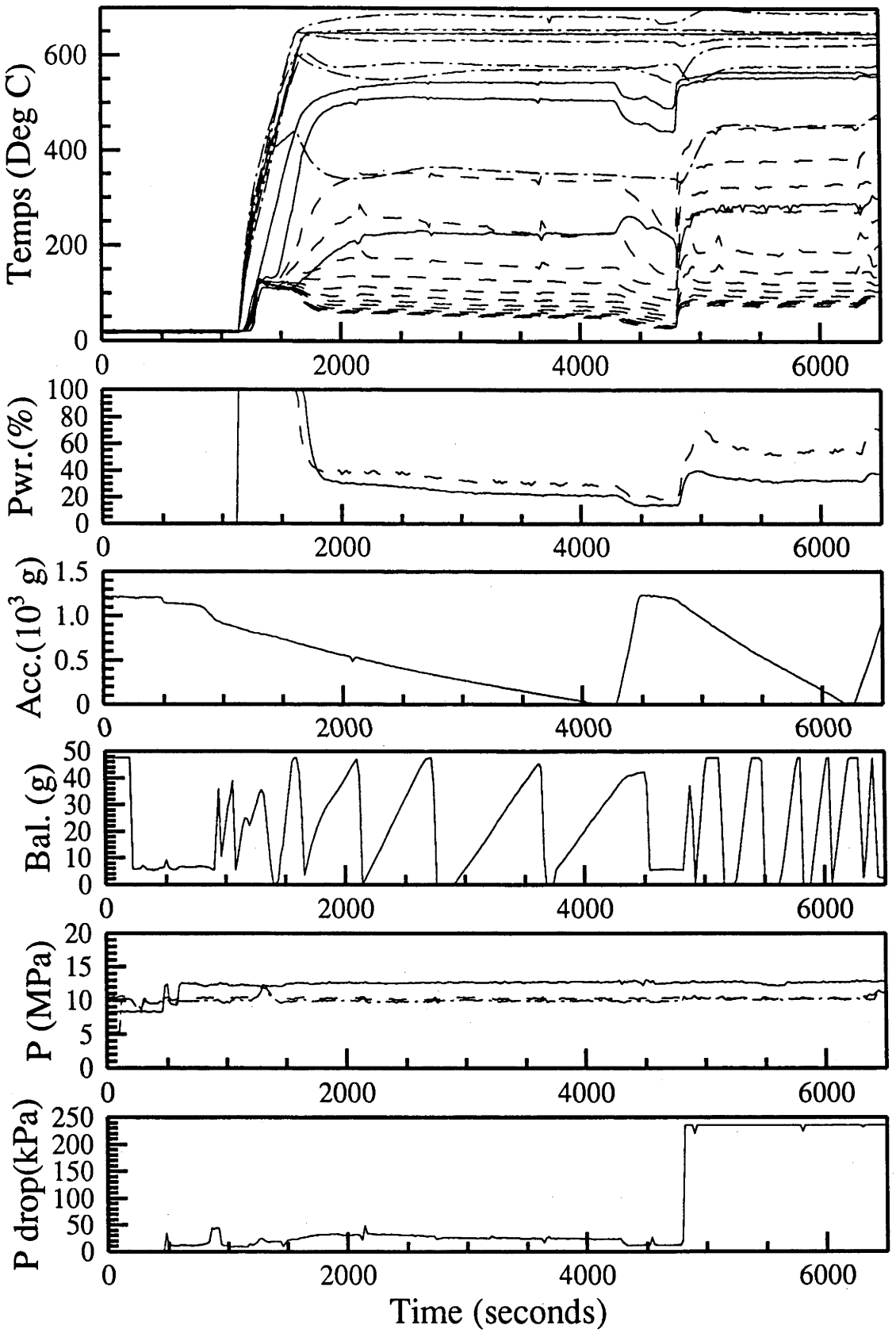

Figure D.49: Time dependance, 18th of April 1991.

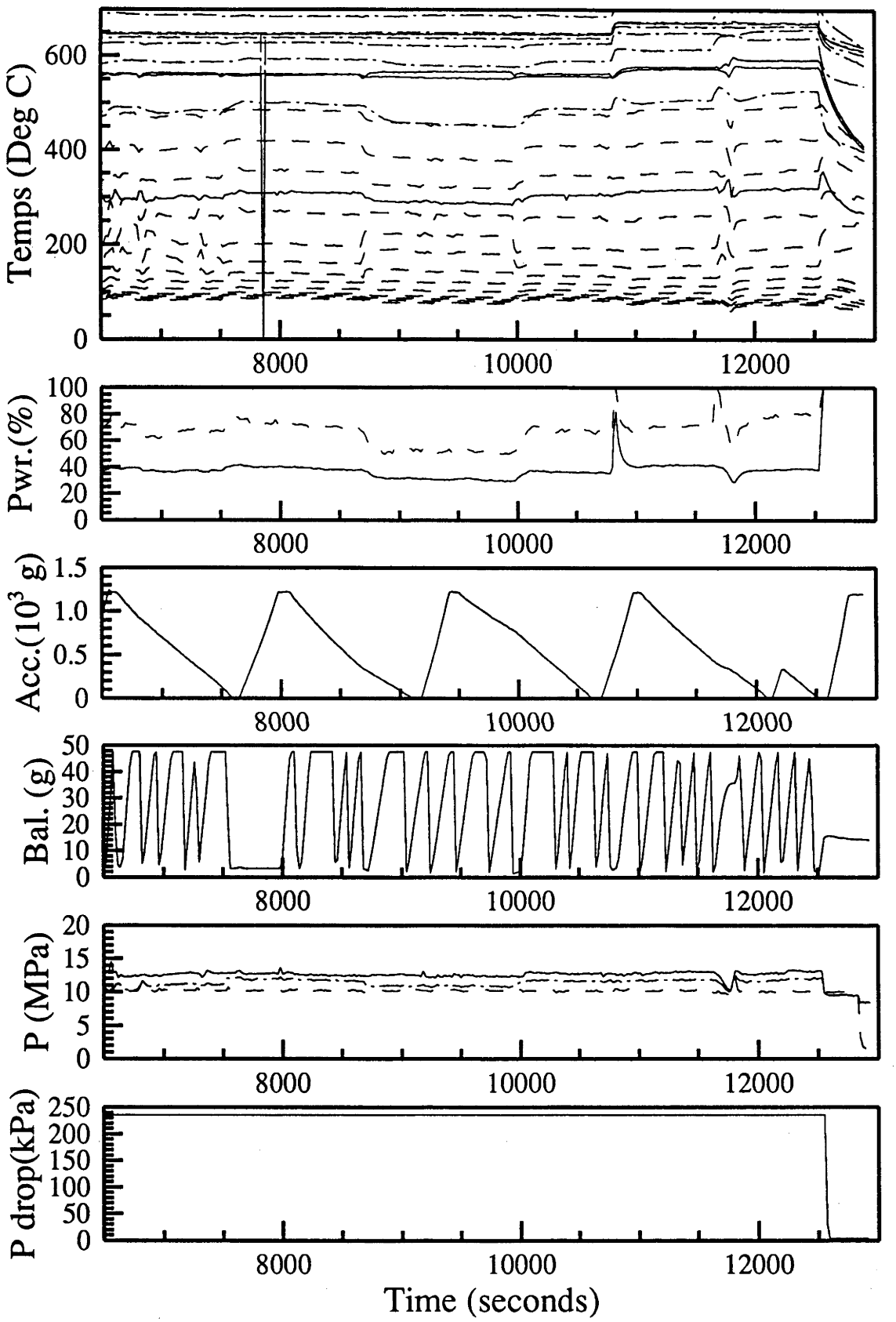

Figure D.50: Time dependance, 18th of April 1991 continued.

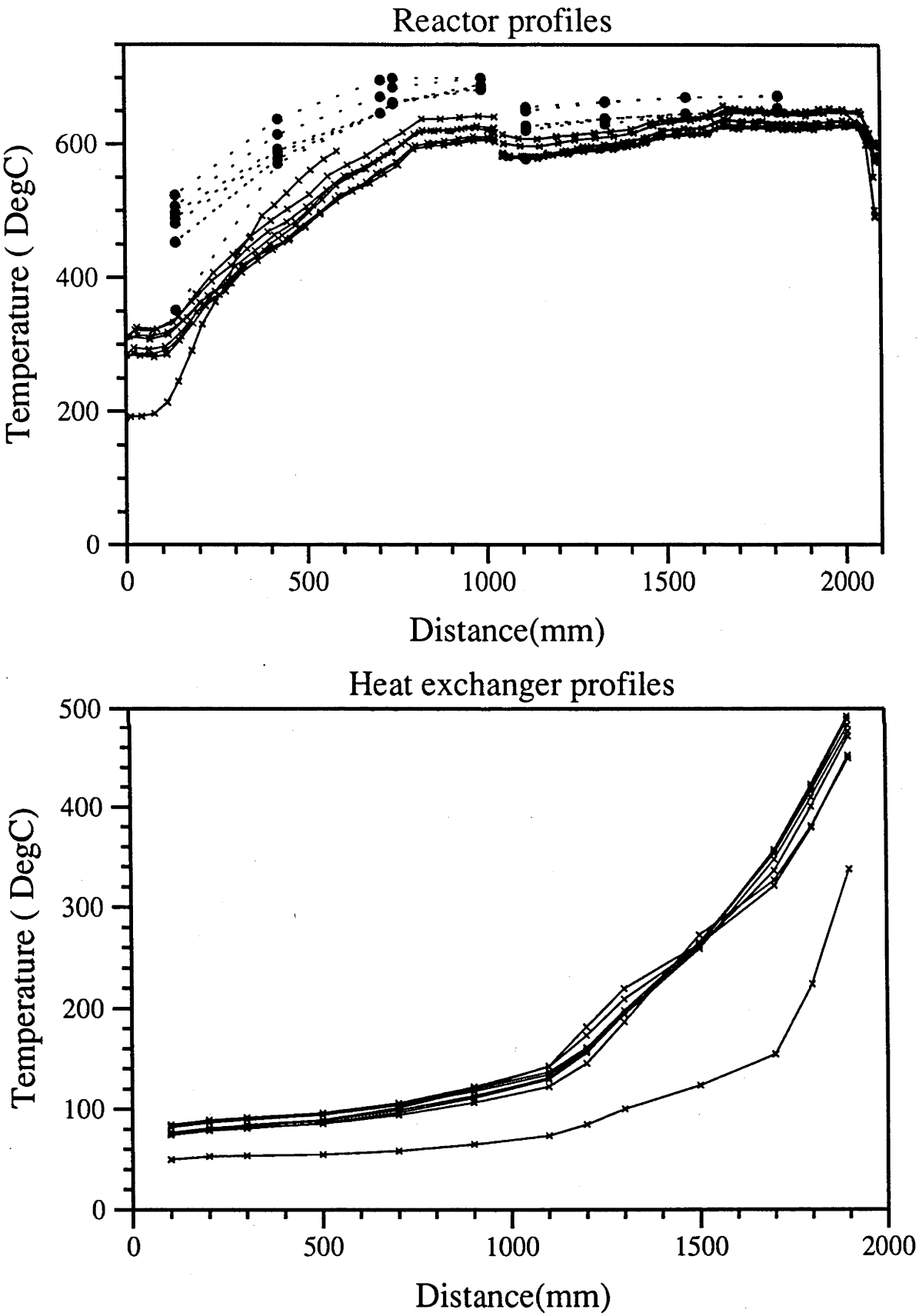

Figure D.51: Steady state temperature profiles, 18th of April 1991.

28th of May 1991 A

- Single run with nitrogen for examination of internal temperature profile using a slow probe scan.

Time interval (seconds)	2200-3450
Pressure (MPa)	10.32±0.1
Inlet mass flow (gs^{-1})	0.629±0.02
Pressure drop (kPa)	185±10
First chamber (column 2)	
Temperature setpoint (°C)	650
Heater power (W)	371.3±4
Inlet temp (°C)	392±3
Outlet temp (°C)	654±5
Second chamber (column 1)	
Temperature setpoint (°C)	650
Heater power (W)	291.3±2
Inlet temp (°C)	570±5
Outlet temp (°C)	605±5
Heat exchanger	
Inlet cold end temp (°C)	13.9±1
Inlet hot end temp (°C)	431.7±2
Outlet cold end temp (°C)	41.6±1
Outlet hot end temp (°C)	490±10

Table D.24: Steady state values, 28th of May 1991 A.

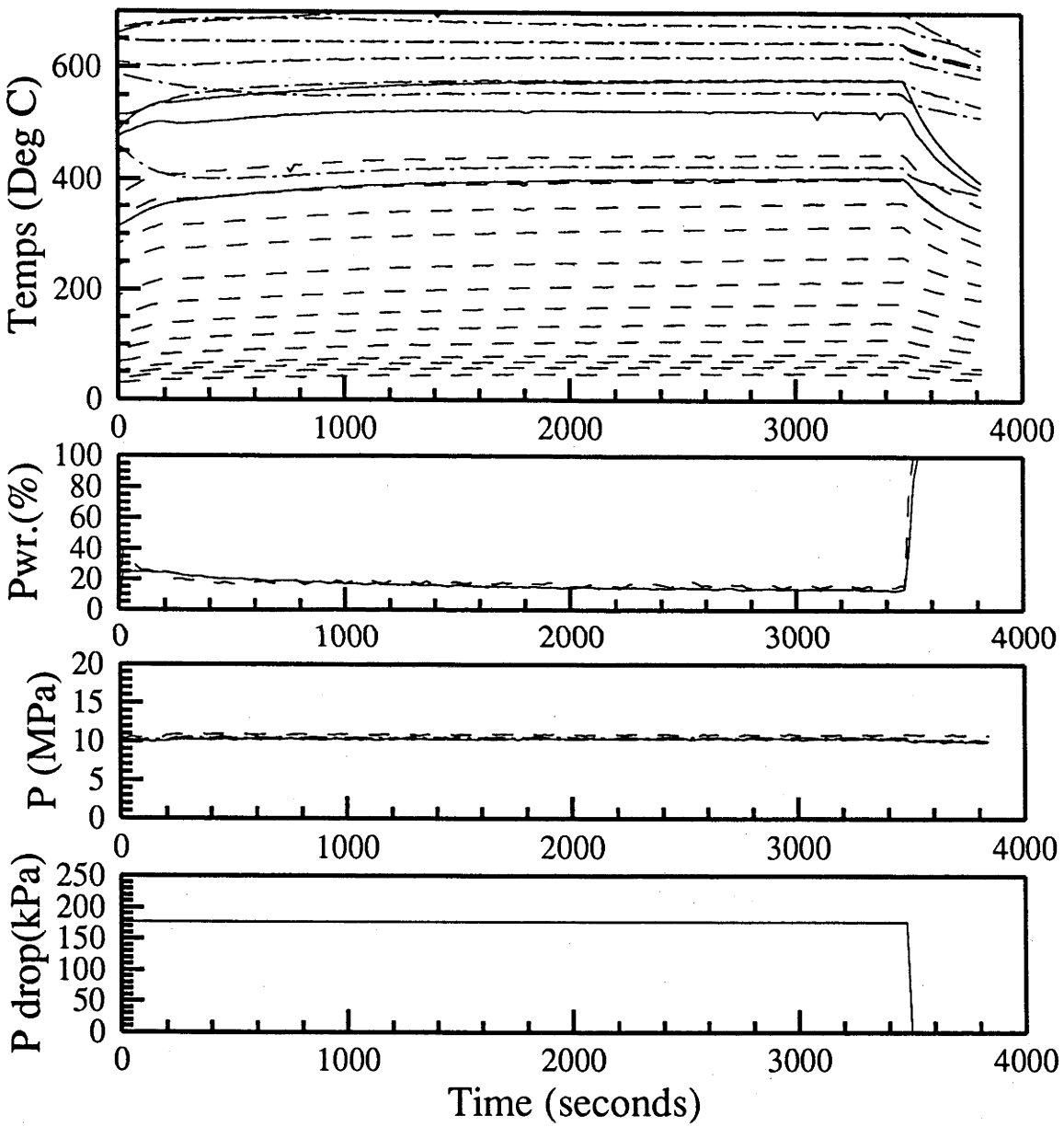

Figure D.52: Time dependance, 28th of May 1991, first run.

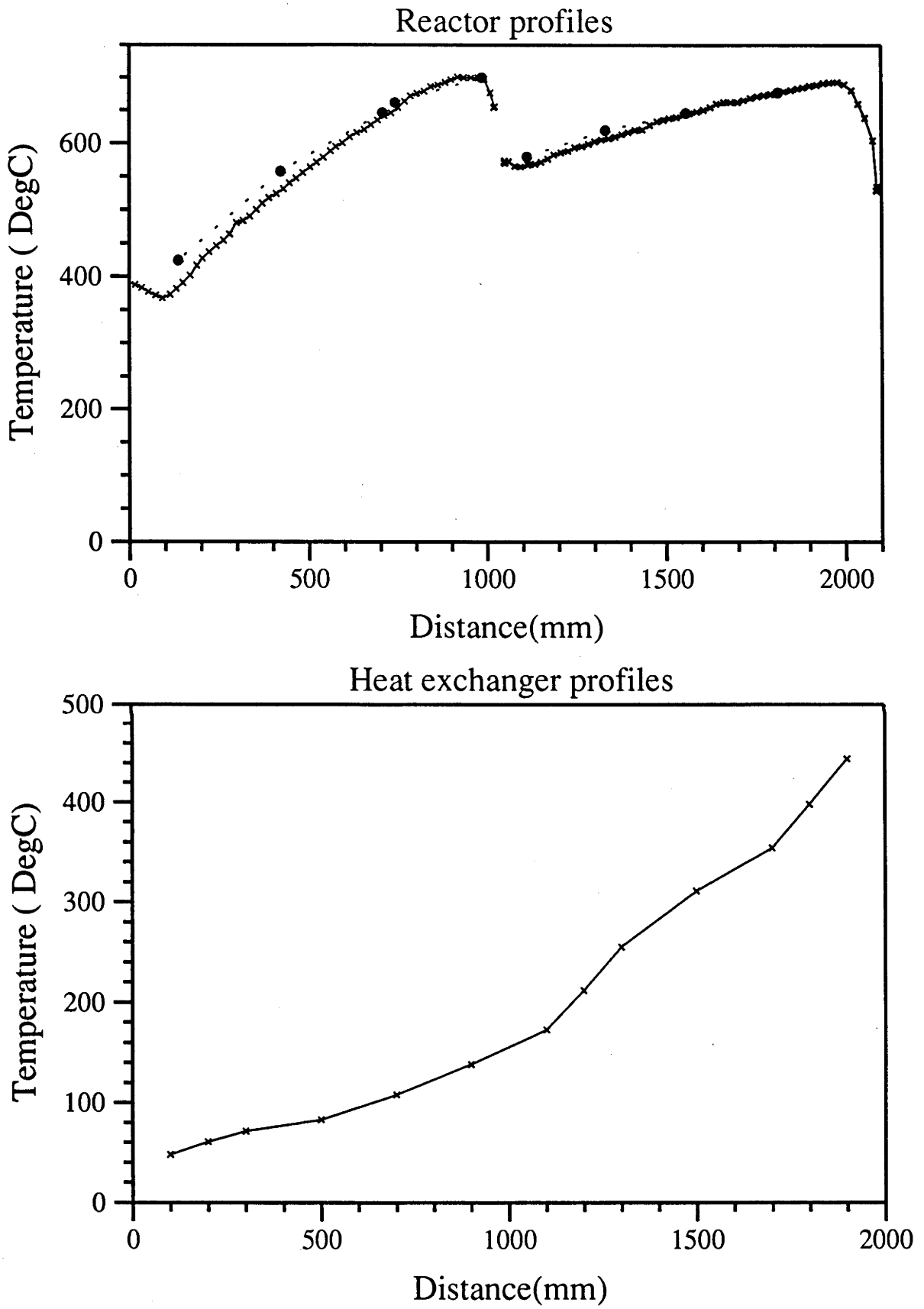

Figure D.53: Steady state temperature profiles, 28th of May 1991, first run.

28th of May 1991 B

- Testing the limit of reactor performance at higher temperatures.
- 4 setpoints investigated for $0.4gs^{-1}$ $10MPa$.
- temperature measurements saturated at $700°C$

Time interval (seconds)	3200-4400	5500-5900	6780-7720	7620-8050
Pressure (MPa)	10.67±0.1	10.69±0.1	10.64±0.1	10.65±0.1
Inlet mass flow (gs^{-1})	0.507±0.01	0.434±0.009	0.396±0.006	0.331±0.005
Reaction extent	0.407±0.02	0.473±0.03	0.619±0.01	0.693±0.02
Pressure drop (kPa)	195±10	228±10	221±10	242±10
	First chamber (column 2)			
Temperature setpoint ($°C$)	650	675	700	720
Heater power (W)	911.7±9	924.9±9	984.3±10	1094.6±10
Inlet temp ($°C$)	250±2	265±2	274±5	298±5
Outlet temp ($°C$)	625±4	638±4	660±4	675±4
	Second chamber (column 1)			
Temperature setpoint ($°C$)	650	675	700	720
Heater power (W)	517.4±5	549.3±5	612.5±6	674.7±7
Inlet temp ($°C$)	572±4	583±4	603±4	617±4
Outlet temp ($°C$)	610±5	620±10	650±15	680±10
	Heat exchanger			
Inlet cold end temp ($°C$)	14.2±1	14.2±1	13.6±1	13.5±1
Inlet hot end temp ($°C$)	276.3±2	294.5±2	310.5±2	330.7±2
Outlet cold end temp ($°C$)	61.6±1	50.5±1	40.8±1	33.4±1
Outlet hot end temp ($°C$)	519±10	533±10	543±10	569 ±10

Table D.25: Steady state values, 28th of May 1991 B.

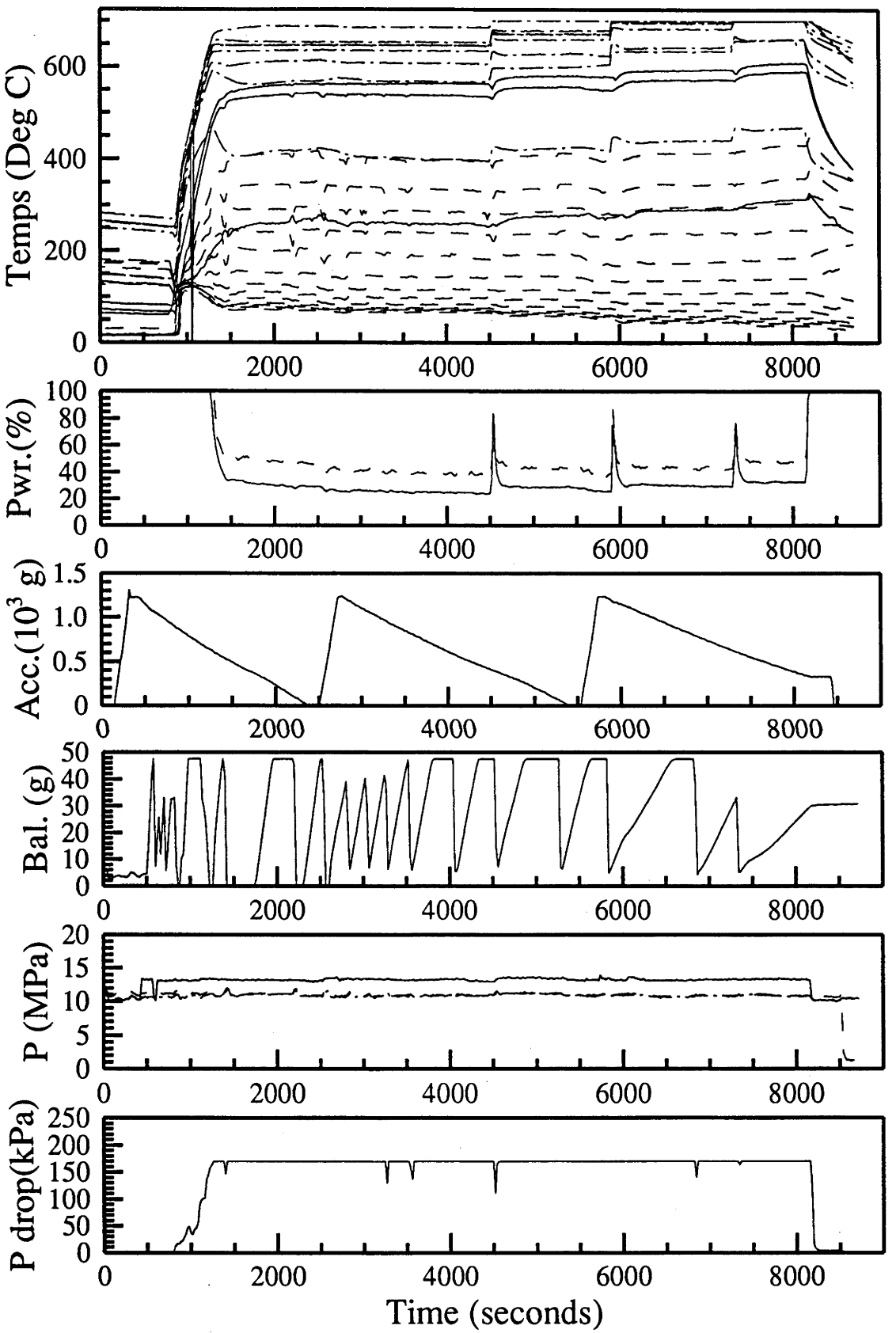

Figure D.54: Time dependance, 28th of May 1991, second run.

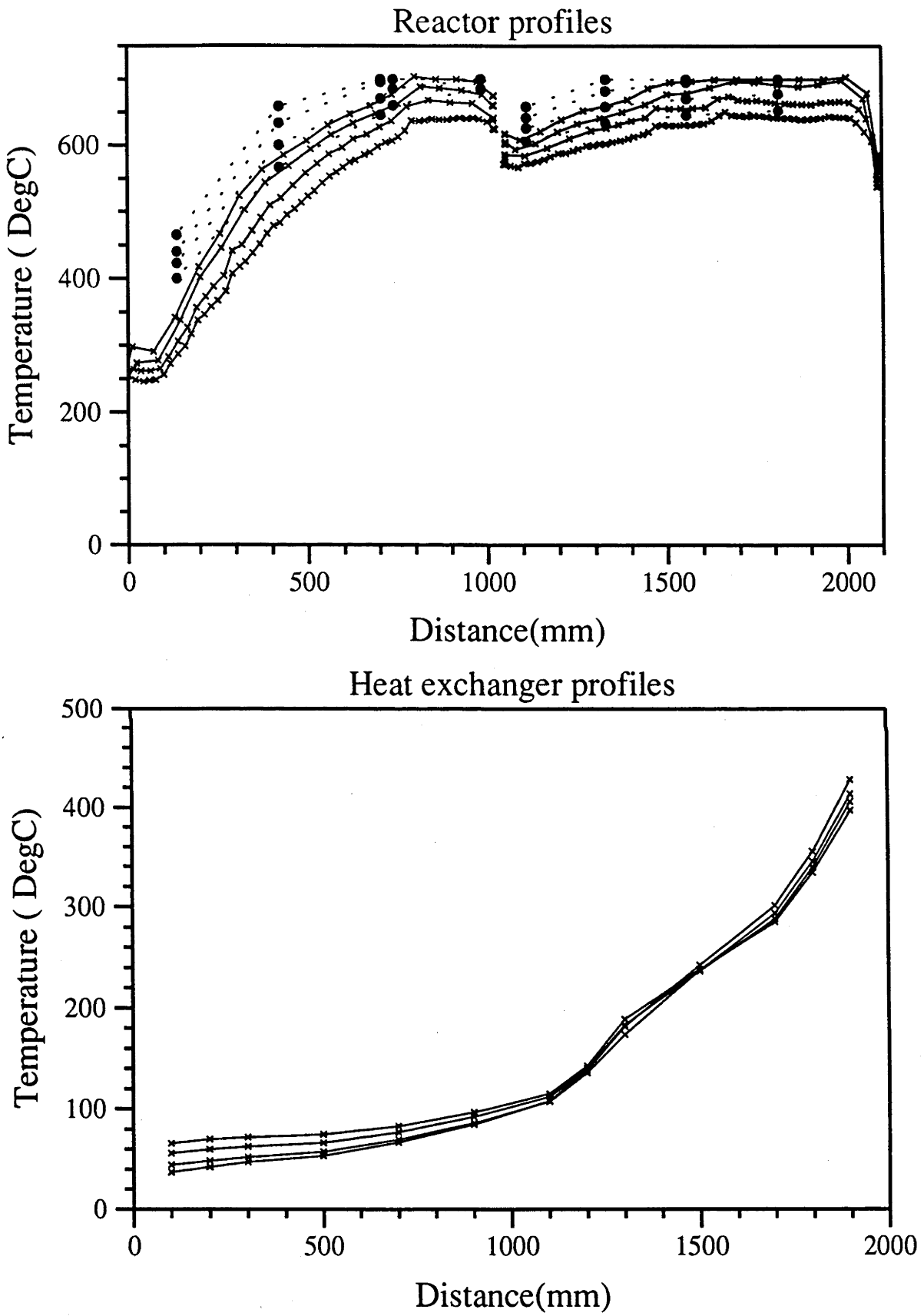

Figure D.55: Steady state temperature profiles, 28th of May 1991, second run.